NNT : 2018SACLX100

THÈSE DE DOCTORAT

de

L'Université Paris-Saclay

École doctorale de mathématiques Hadamard (EDMH, ED 574)

Établissement d'inscription : Ecole polytechnique

Laboratoire d'accueil : Centre de mathématiques appliquées de Polytechnique, UMR 7641 CNRS

Spécialité de doctorat : Mathématiques appliquées

Perle GEOFFROY-DONDERS

Homogenization method for topology optimization of structures built with lattice materials

Date de soutenance : 17 décembre 2018

Après avis des rapporteurs :
Martin BENDSOE (DTU, Danemark)
Éric BONNETIER (Université Joseph Fourier, Grenoble)

Jury de soutenance :

Grégoire ALLAIRE	(CMAP) Directeur de thèse
François ALOUGES	(CMAP) Examinateur
Samuel AMSTUTZ	(Université d'Avignon) Examinateur
Martin BENDSOE	(DTU) Rapporteur
Éric BONNETIER	(Université Joseph Fourier) Rapporteur
François JOUVE	(Université Paris Diderot) Examinateur
Olivier PANTZ	(Laboratoire J. A. Dieudonné) Codirecteur de thèse
Pierre SEPPECHER	(Université de Toulon) Examinateur

Contents

Introduction

The art of structure is where to put holes, wrote the architect and researcher Robert Le Ricolais. This could be a one-sentence summary of the context and the motivations of this thesis. It raises few questions. What does the art of structure consists here in? Why do we talk about holes, while the goal is to design structures. At first sight it seems contradictory. And consequently, what is the interest of the holes in a structure? To conclude, how can we in fact decide where to put holes or not?

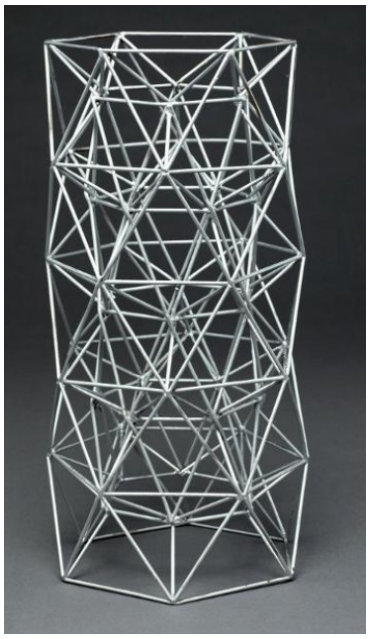

Figure 1: *Automorphic Compression Member*, Robert Le Ricolais, 1962 (©Centre Pompidou)

What we mean by *art of structure* in this thesis, is the optimal design of structures, known also as shape and topology optimization. Let us give here an example. In the industry, when a mechanical structure is designed, it has to satisfy specifications in order to fulfil its physical purpose and to not fail during its use. However, those specifications can be satisfied by several different structures. Some will be lighter than the others, or more easy to produce. Hence, we have some freedom to design the final structure and we can choose among the admissible shapes, the better one according to a supplementary criteria. This criteria is chosen depending on the context of the problem. A very common one is the volume of the shape. Indeed by reducing it, raw materials can be saved, and the shapes would be consequently cheaper. In aerospace industry, the final weight of the structures is a crucial question, with economic but also ecological impacts. The lighter the aircraft, the lower the fuel consumption.

Shape and topology optimization is a large and well studied domain of applied mathematics. Several methods have been developed in order to optimize structures. The two most well known are the SIMP (Solid Isotropic Material with Penalization) method [Bendsoe 2003] and the level-set method [Osher 2006]. The approach of the SIMP method consists in optimizing the local

density of a fictitious material, then penalizing it in order to yield a black and white structure. Holes appear in the final structure where the density is equal to zero. In the level-set method, the optimization process runs directly on the boundaries of the structure, and so on its holes. Hence in those two distinct methods, the design of the holes is a key point. They are called topology optimization method. Indeed, in 2D, the topology is linked to the number of the holes in the considered shape. In 3D, this is quite more complex. The topology also depends on the nature of the holes: it could be cavities or loops (like a torus). This answers to our second question (why speaking about holes) but not on the third: what interest do we have to perforate structures in order to optimize them?

Figure 2: Porous structure of a bone: frontal longitudinal midsection of upper femur, from [Gray 1918]

One answer could be found in observing nature, where porous material and structures are common. We focus on a particular example: the bones. The bones of all vertebrates are porous. They feature an external solid and full layer (the cortical bone) and are filled with a porous matrix (the trabecular bone), see Figure 2. Some birds bones are even mostly empty, with only internal trusses to reinforce the whole structure. Their design gives to bones strength and solidity, but also lightness. Hence, holes do not mean necessarily fragility, but quite the contrary in several cases: a clever balance between strength and lightness. Numerous human constructions take advantage of this observation, from the Roman Colosseum and its arcades to the Eiffel tower. Less raw material is required, but the solidity and the longevity are not compromised, as attested by the two thousands years old Colosseum. In fact, porous material are mathematically shown to be optimal for numerous applications of shape optimization. In the following, we will focus on a particular class of porous materials: the *lattice materials*. In the literature, lattice material designates sometimes periodic microstructures featuring only bars. But here, we keep a larger definition : a periodic mix of void and material, without any restriction on the periodic pattern.

The last question remains: how to design holes in the structure. As seen above, several optimization methods exist to optimize the topology, and consequently the holes in a structure.

The SIMP method and the level-set method are based on finite elements and so require to mesh the working domain (the domain where the structure is designed). If we want to consider lattice material, and so microscopic holes in the structures, the mesh should be fine enough to capture their shapes. Such approaches are prohibitive to compute numerically in practice. A solution is given by the homogenization method [Murat 1985]. It consists in averaging the physical behaviour of the lattice material at a mesoscopic scale. By this mean, we define a new equivalent full media, that has a similar behaviour as the lattice material. We call it the effective material. This effective material being homogeneous, it does not exhibit small scale structures. Then a relatively coarse mesh can be used to run the numerical optimization algorithm.

The geometry of the chosen lattice is characterized by some parameters and its orientation. For example, we can consider the periodic 2D square cells perforated by a central rectangular hole, parametrized by its length and height, see Figure 3. The effective behaviour of the lattice material depends on those parameters. By optimizing their distribution in the working domain, we modulate locally the lattice material. This approach was first numerically implemented and popularized by Bendsoe and Kikuchi [Bendsøe 1988] in the 80's. But two limitations put it aside progressively in favour of the SIMP method.

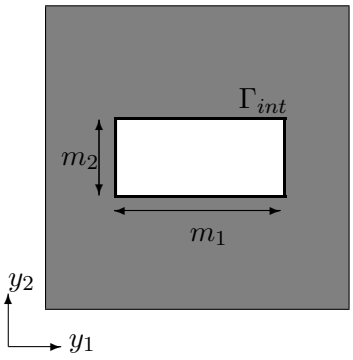

Figure 3: Example of parametrized periodic lattice material: a periodic square cell is perforated by a rectangular holes, whose length and height parametrize the geometry of the microstructure

First, lattice structures are not manufacturable using the traditional fabrication processes, like foundry, because of their microscopic structure and their complex topology. Thanks to the recent advances in additive manufacturing processes, this problem is partly solved. Lattice structures are indeed now manufacturable. But numerous investigations are currently led in order to improve the process and to modelize it, notably from a thermic point of view in order to characterize the residual stresses or the eventual defects in the structure. Nevertheless, this led to a resurrection of the homogenization method.

The second limitation is related to the deshomogenization of the optimized structure. The homogenization method yields an optimized but also homogenized structure: this is not a genuine shape, like in the SIMP method or in the level-set method, straightly manufacturable. Hence we have to construct from the effective design a genuine shape. This deshomogenization process replace the traditional penalization step. When the orientation of the lattice cells is uniform, this is not a big challenge. The periodic size of the deshomogenized cells is chosen, then on each cell we use the average parameters to design the local microstructure. Still the

connectivity between adjacent cells has to be carefully ensured. But when the orientation cells is also optimized, this orientation has to be taken into account during the deshomogenization process. Pantz and Trabelsi [Pantz 2008] proposed to introduce a diffeomorphism: a regular grid of lattice material is distorted with this diffeomorphism in order to locally orientate the cells, see Figure 4.

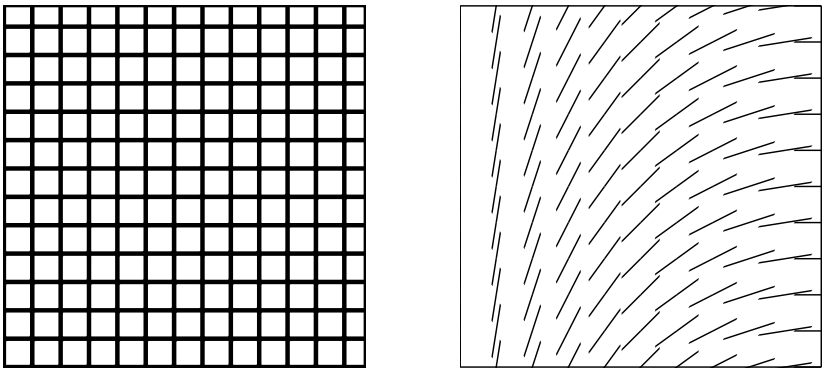

(a) Regular grid

(b) Direction field

(c) Distorted grid

Figure 4: A regular grid (a) is associated to a direction field (b), giving the local orientation of each cell: it yields a distorted grid (c)

Contents of the thesis

This thesis is composed of two parts. The first provides an introduction to shape optimization (Chapter 1), and to homogenization method (Chapter 2).

The second part is dedicated to the contributions of this thesis. We focus on the mechanical domain of linear elasticity.

In Chapter 3, we present a shape optimization method based on homogenization method to optimize structures made of modulated isotropic lattice material in 2D and in 3D. First we introduce isotropic microstructures in 2D an in 3D parametrized by their density, see Figure 5(a) and we compute their effective mechanical properties. Second, we present the optimization algorithm based on a gradient descent method. The minimization of several objective functions is investigated: the compliance in single-load and multiple-loads test cases, see Figure 5(b) or the L^2-norm of the stress tensor for example. Third, we present a method to deshomogenize the optimized homogenized structures, ensuring the connectivity and the smoothness of the final shapes, see Figure 5(c). We emphasize that optimized structures have been proved to be manufacturable by additive manufacturing process, see Figure 6, our deshomogenization method yielding the generation of geometric files compatible with additive machines drivers.

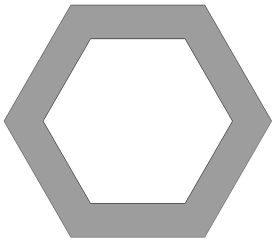

(a) An isotropic periodic microstructure, parametrized by its density

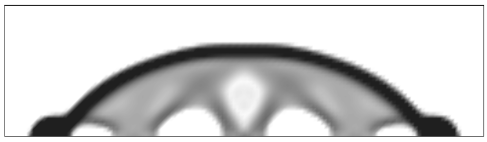

(b) Optimized density of a bridge for multiple-loads compliance minimization problem

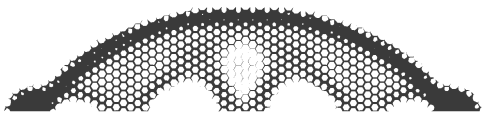

(c) Deshomogenized structure

Figure 5: Results (bottom) of topology optimization of 2D structures built with isotropic lattice materials (top)

In Chapter 4, we present a shape optimization method based on homogenization method to optimize structures made of modulated orthotropic lattice material in 2D, see Figure 3 for an example of orthotropic microstructure. The method is developed for compliance minimization problems in single-load test cases. The main difference with the previous chapter consists in adding the orientation of the cells to our method. Indeed, isotropic lattice materials do not require to be oriented, what greatly simplifies the deshomogenization step. But anisotropic, and in particular here orthotropic, microstructures are more optimal, what explains our interest into them. Thanks to Pedersen formulas [Pedersen 1989], the optimal orientation of an orthotropic

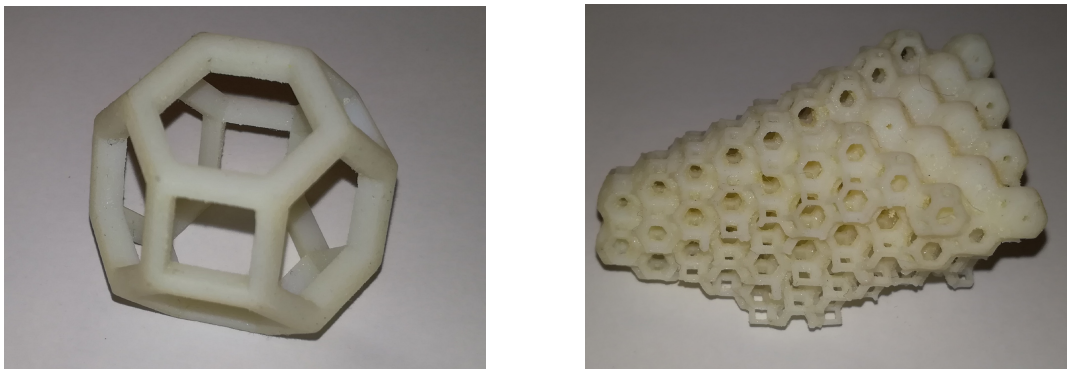

(a) (b)

Figure 6: Printed structures (b) made of modulated isotropic lattice material (a)

material is known to be given by the local principal directions of the stress. Hence at each iteration of the optimization algorithm, the minimization process according to the orientation is a global minimization method. The optimal orientation of an orthotropic microstructure and its optimized density are displayed in Figures 7(a) and 7(b) for a cantilever case (the structure is clamped on the left side and a vertical load is applied on the middle of the right side). To take into account the optimal orientation of the cells during the deshomogenization step, a conformal transformation is introduced. It requires beforehand a regularization of the orientation in order to satisfy a conformality constraint. A deshomogenized structure for the cantilever case is displayed on Figure 7(c). This work has been published in [Allaire 2018]. In a supplementary section, this method is shown to be efficient also for stress minimization problems.

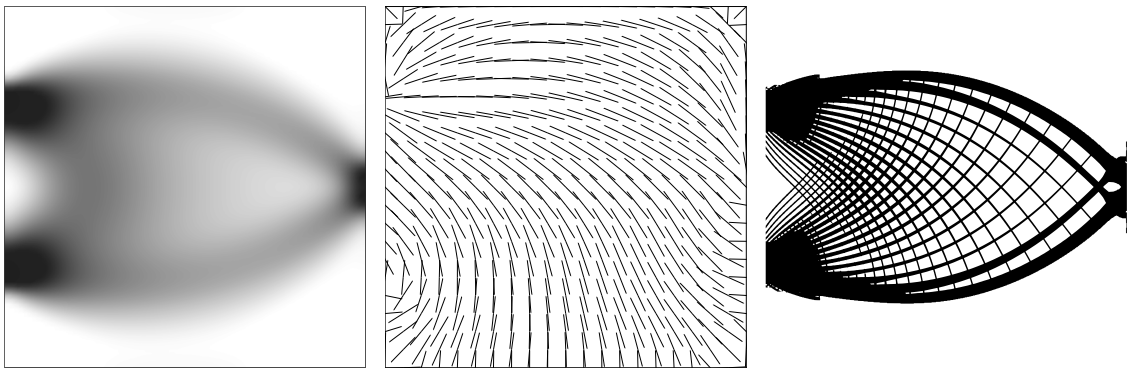

(a) Optimized density (b) Optimized orientation of the cells (c) Deshomogenized structure

Figure 7: Result of topology optimization of 2D structures built with orthotropic lattice materials for the cantilever case

Chapter 5 is dedicated to the deshomogenization step in the general case in 2D, namely when the working domain is perforated and when the optimized orientation features singularities, see Figure 8. We present a regularization method based on Ginzburg-Landau and Modica-Mortola

energies for the orientation of the cells in order to improve the deshomogenized structures.

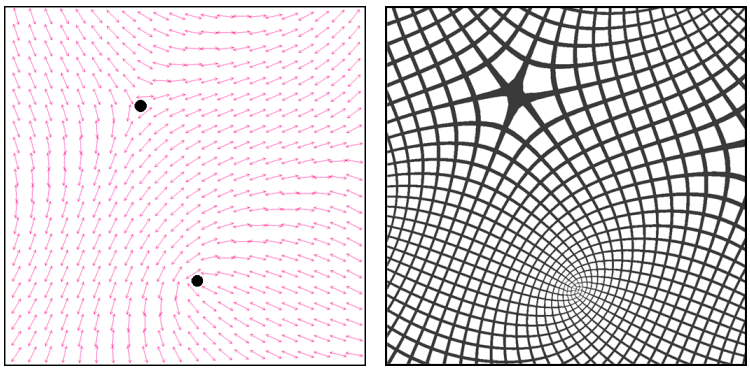

(a) Orientation vector field featuring two singularities (black points)

(b) Projection of a regular square grid

Figure 8: Projection (right) of a regular square grid according to an orientation field featuring singularities (left)

Chapter 6 is the fruit of a collaboration with Jonas Martinez (INRIA Nancy). We perform shape optimization of structures made of stochastic materials, using the homogenization approach, see Figure 9(c). These materials, developed by Jonas Martinez and based on Voronoi cells are either isotropic or orthotropic, see Figures 9(a) and 9(b). This work has been submitted for publication.

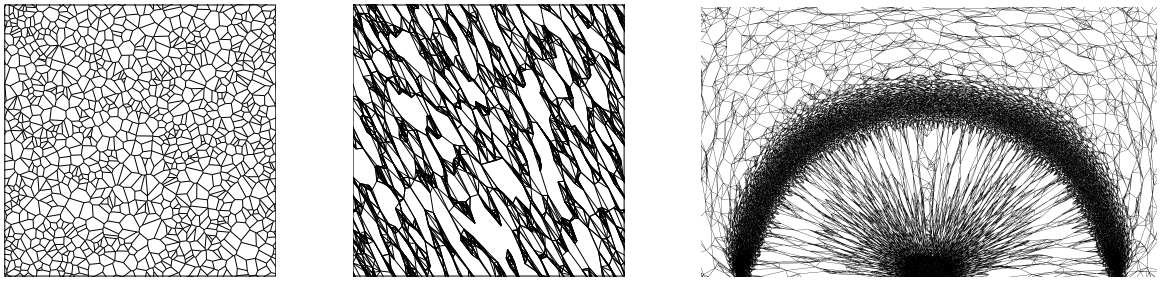

(a) Isotropic stochastic microstructure

(b) Orthotropic stochastic microstructure

(c) Deshomogenized structure of the optimized design of a bridge for a compliance minimization problem

Figure 9: 3D results (right) of topology optimization of structures built with orthotropic lattice material (right)

In Chapter 7, we propose an extension to 3D case of Chapter 4: a shape optimization method for structures made of modulated orthotropic lattice material is presented, see Figure 10(a) for an orthotropic microstructure. Nevertheless, modeling the orientation of periodic cells in 3D is more complex than in 2D. The approach proposed here relies on the introduction of a rotation matrix. A regularization method of the orientation in 3D is also developed, based on the regularization of the rotation matrix. Contrary to 2D cases, conformal mappings in 3D are very restrictive. Hence we propose an adapted deshomogenization process: a diffeomorphism is

still introduced, but which is no longer necessarily conformal. A deshomogenized structure of an optimized design for a cantilever case is displayed on Figure 10(b): orientation of the cells is respected and the final genuine shape is smooth.

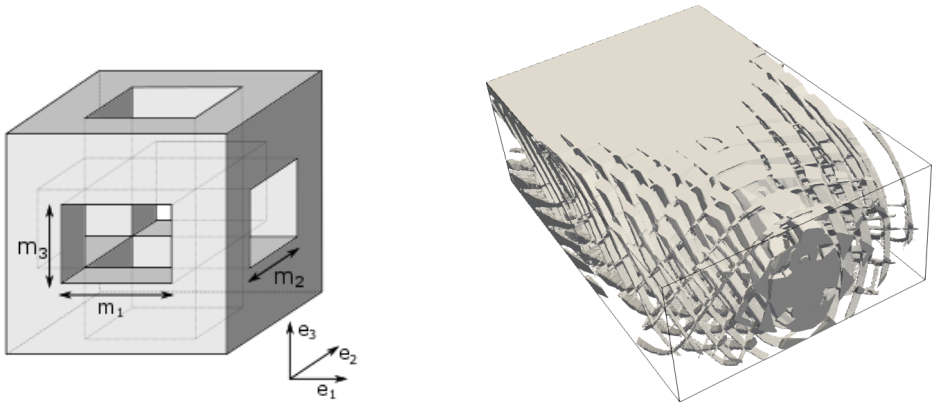

(a) 3D orthotropic periodic microstructure and its parametrization

(b) Deshomogenized structure of the optimized design of a cantilever for a compliance minimization problem

Figure 10: Projection (right) of a optimized design of a 3D cantilever for a compliance minimization problem (left)

Finally, a limitation of the approach by homogenization is the absence of a well-defined external border for the optimized homogenized structure. Thus, neither geometric constraint nor design-dependent loads can easily be taken into account. In Chapter 8, we propose a solution, by coupling the homogenization method and the level-set method. The method is tested for a coating constraint, see Figure 11. Thanks to the level-set method the external border of the structure is clearly identified. Hence it enables to force the density on an external layer of given width to be equal to one: the final shape is said to be coated. The method is also successfully tested for a design-dependent load, namely a uniform hydraulic pressure load.

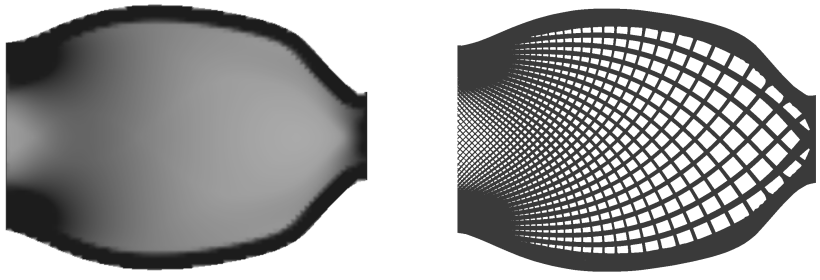

(a) Optimized density

(b) Deshomogenized structure

Figure 11: Results of topology optimization of a cantilever under a coating constraint by coupling homogenization and level-set methods

Scientific communications

The work presented in this thesis led to the following communications.

Journal articles

- **Topology optimization of modulated and oriented periodic microstructures by the homogenization method**, P. Geoffroy-Donders, G. Allaire and O. Pantz, Computers and Mathematics with Applications, March 2018
- **3-d topology optimization of modulated and oriented periodic microstructures by the homogenization method**, P. Geoffroy-Donders, G. Allaire and O. Pantz, submitted
- **Topology optimization of parametrized stochastic microstructures**, P. Geoffroy-Donders and J. Martinez, submitted

Communications

- **Optimisation de structures composées de cellules périodiques modulées orthotropes par la méthode d'homogénéisation**, CSMA 2017, Giens, France, May 2017
- **Optimization of oriented and parametric cellular structures by the homogenization method**, WCSMO 2017, Braunschweig, Germany, June 2017
- **Topology optimization of elastic cellular structures by the homogenization method, using isotropic cells**, SimAm 2017, München, Germany, October 2017
- **Optimisation de structures 3D composées de matériau lattice par la méthode d'homogénéisation**, CANUM 2018, Cap d'Agde, France, May 2018
- **Optimization of modulated and oriented periodic microstructures in presence of singularities in the orientation field**, ECCM-ECFD 2018, Glasgow, Scotland, July 2018
- **Optimization of infill structures with coupled homogenization and level-set methods**, ECCM-ECFD 2018, Lisbon, Portugal, September 2018

Seminars

- **Homogenization method for lattice structure topology optimization**, Mandel symposium, LMS, Ecole polytechnique, Palaiseau, France, June 2016
- **Topological optimization of graded and oriented cellular structures, by the homogenization method**, Friedrich-Alexander Universität, Erlangen, Germany, December 2017

Posters

- **Homogenization method for lattice structure topology optimization**, CANUM 2016, Obernai, France, May 2016
- **Homogenization method for lattice structure topology optimization**, PICOF 2016, Autrans, France, June 2016
- **Optimization of cellular structures by the homogenization method in 2D**, Journée des doctorants de Safran Tech, Châteaufort, France, June 2017
- **Optimization of cellular structures by the homogenization method in 3D**, Journée des doctorants de Safran Tech, Châteaufort, France, June 2018

Part I

Preliminaries

Chapter 1

Shape optimization

Contents

1.1 Shape optimization problem

1.1.1 Introduction

Three ingredients have to be given in order to define a shape optimization problem:

1. the physical behaviour of the shape to optimize, here we focus on the case of linear elasticity.
2. the set $\mathcal{U}_{ad}$ of admissible shapes, which includes the constraints due to the mechanical behaviour of the structure and the ones due to chosen description of the shape, other may be taken into account, like volume constraint for example.
3. the objective, also known as the cost function, often denoted J in the following. It is usually a physical characteristic, like the compliance of the structure, or a geometrical characteristic, like the volume of the structure.

   The general optimization problem reads as:

$$\min_{\Omega \in \mathcal{U}_{ad}} J(u(\Omega)) \,,$$

where Ω denotes the structure and will depend of the chosen description of the structures, and $u(\Omega)$ is a physical value, solution of the equation modeling the physical behaviour of the structure.

1.1.2 Three categories of problem

The shape optimization problem can be classified in three main categories:

- parametric shape optimization: the admissible structures are parametrized with few parameters, like the width of a bar or the radius of a circular hole. The subset of admissible structures $\mathcal{U}_a d$ is necessarily small, but the optimization process may be reasonably easy to compute and implement numerically. This process may be used for industrial purposes, when the main shape of the structure is already fixed, like the shape optimization of an airplane [El Majd 2008, Joshi 2009].
- geometric shape optimization: the admissible structures are described by their borders, which can move, but without changing the topology of the shape. Hence, for example, all the admissible structures have the same number of holes. This approach may be similar to the parametric one when the borders are described by spline functions or Nurbs [Schramm 1993], [Wall 2008]
- topology optimization: the admissible structures are not parametrized and their topology is not fixed. This approach is the more general in the sense where the set of admissible shapes is the largest. In the following, we will focus on this kind of shape optimization.

1.1.3 Existence of optimal shapes

This counter example is taken from [Allaire 2007]. The problems consists in optimizing the distribution of two isotropic phases in the domain $D = (0,1)^2$. Their respective elasticity coefficients are denoted α and β, with $0 < \alpha < \beta$.

Let χ be the characteristic function of the subset of D fulfilled with the phase β. The global elasticity coefficient of the membrane is given by:

$$a_\chi = \chi\beta + (1-\chi)\alpha\,.$$

A unit horizontal load is applied on the domain: on the left and on the right boundary, in the outward normal direction, see Figure 1.1(a). This boundary is denoted Γ_N.

The displacement u_χ of the membrane is the unique solution in $H^1(D)/\mathbb{R}$ of:

$$\begin{cases} -\operatorname{div}(a_\chi \nabla u_\chi) = 0 & \text{in } D \\ a_\chi \nabla u_\chi \cdot n = 1 & \text{on } \Gamma_N \\ a_\chi \nabla u_\chi \cdot n = 0 & \text{on } \partial D \setminus \Gamma_N \end{cases} \tag{1.1}$$

The objective function is the compliance of the structure:

$$J(\chi) = \int_{\Gamma_N} u_\chi ds\,.$$

We take into account a volume constraint on the phase β, and no other geometric constraint on the final structure. The set of admissible shapes is given by:

$$\mathcal{U}_{ad} = \left\{ \chi \in L^\infty(D, \{0;1\}) \,|\, \frac{1}{|D|}\int_D \chi(x)dx = \theta \right\}\,,$$

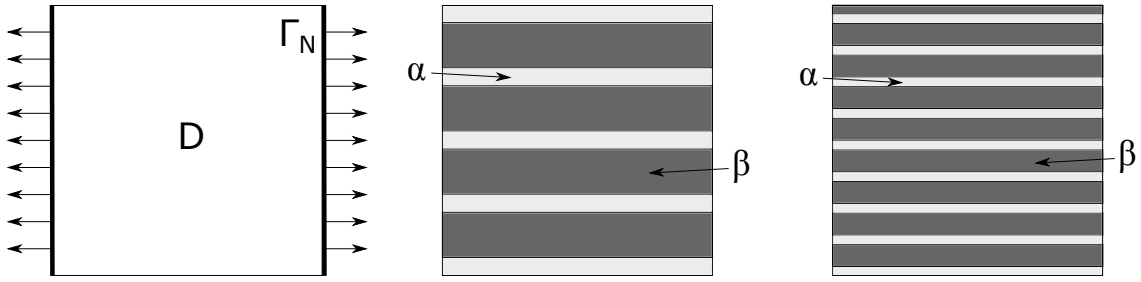

(a) Boundary conditions

(b) Admissible distribution of phases α and β

(c) Improvement of the shape (b), using thinner layers of material

Figure 1.1: Counter example of existence: load case of a membrane (left), admissible shapes (center and right)

where $\theta \in [0;1]$ is the fixed proportion of phase β.

The minimization problem reads as:

$$\begin{cases} \inf & J(\chi)\,. \\ \chi \in \mathcal{U}_{ad} & \\ u_\chi \text{ solution of (1.1)} & \end{cases}$$

In the absence of the volume constraint, the stiffer membrane is clearly the one filled exclusively with the stronger material β. Hence the problem consists in finding the best way to distribute the weaker material in D.

We explain here the mechanical principal on which the proof relies, we refer to [Allaire 2007] for the complete proof. Since the forces are horizontal, the principal directions of the stress will tend to be horizontal too. In order to not perturbate this stress field, the weaker material should be distributed along thin horizontal inclusions. In fact, making these inclusions thinner and thinner, we can always improve a given admissible shape, see Figures 1.1(b) and 1.1(c). Such a sequence of shapes will not converge to a classical shape. The minimum of the cost function is reached by a mix of phases α and β in respective proportions $(1-\theta)$ and θ, namely a composite material.

1.1.4 Obtaining existence

Given the previous counter example, the existence of an optimal shape can be obtained using two strategies.

The first approach consists in reducing the set of admissible shapes to forbid sequences which converge to composite material. For example, we can add a perimeter constraint, see [Ambrosio 1993, Henrot 2006], or a topological constraint to limit the number of holes in the shapes, see [Chambolle 2003] or [Šverák 1993], or even regularity constraints on the admissible shapes, see [Henrot 2006].

The second approach is quite the contrary: it consists in relaxing the problem, by enlarging the subset of admissible shapes to homogenized ones, meaning shapes made of composite

material. The characteristic function $\chi \in L^\infty(D, \{0;1\}$ is then replaced by a density function $\theta \in L^\infty(D, [0;1])$. Moreover, the microstructure of the shape, originally parametrized by χ is no longer given by the density function θ. Hence the physical behaviour of the composite materials has to be specified, using homogenized elasticity tensors. This is the object of the homogenization method, presented in detail in Chapter 2.

In this thesis, we use the second approach: we optimize structures made of composite materials.

1.2 Classical shape optimization methods

We present here the most well-known shape optimization methods. The two first, namely the level-set method and the SIMP method, are used to optimize macroscopic shapes: no composite material is allowed. Hence the only way to use these approaches to design shape featuring a microstructure consists in explicitly describing the microscopic details, which is numerically prohibitive.

The third and the fourth presented methods, namely the homogenization method and the multi-scale approach, are based on a homogenized description of the microstructures, and are consequently the appropriate strategies to optimize structures made of composite material. In the homogenization method, only a family of composite materials is admissible. The optimized structures feature the chosen kind of periodic cells, locally modulated. In the multi-scale approach, there is no constraint on the microstructure: this one is also optimized.

1.2.1 Level-set method

The level-set method was introduced by Osher and Sethian [Osher 1988], see also textbooks [Osher 2006] and [Sethian 1999]. It is used in a wide range of domains, from image analysis to front propagation. Since the first papers [Sethian 2000, Osher 2001, Allaire 2002b, Wang 2003], it became a very common approach in shape optimization. Its main advantage relies on the fact that the optimized structures are black and white structures. No penalization is required, contrary to other methods, like the SIMP method, presented in the next section.

The structures are described through a level-set function ψ, defined on the working domain D. The border of the shape is given by the zeros of this function, its interior by the negative values of ψ, and its exterior by the positive ones, see Figure 1.2. The optimization is done with a gradient-based algorithm. The partial derivative of the cost function with respect to the shape gives the descent direction, in the form of a velocity field. The shape is then updated by advection of the initial shape with the computed velocity field.

We do not give details here about this method. We refer to [Henrot 2006], [Allaire 2007] for theoretical results about the differentiation of criteria with respect to a shape. The numerical implementation of this method is described in [Allaire 2002b] or in [Allaire 2006] for the particular finite elements software Freefem++.

One of the limitation of this method relies on the fact that changes of topology may be difficult to achieve. Thanks to the notion of topological derivative (see [Céa 2000, Amstutz 2006, Novotny 2012, Sokolowski 2001]), the sensitivity of the objective function to the creation of small

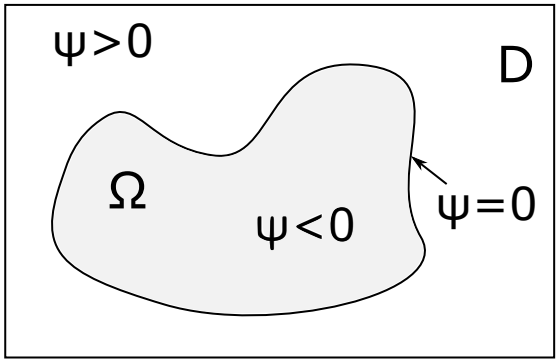

Figure 1.2: Description of a shape with a level-set function ψ

holes is quantified. Coupled with the level-set method, holes can be wisely created during the optimization process, meaning that changes in the topology are reachable.

Thanks to the level-set method, an initial shape can be hugely improved in terms of the objective function. Nevertheless, only a local minimum can be reached. Indeed, as seen previously, the existence of a global minimum is not ensured without strong geometric constraints on the admissible structures (for example a minimum perimeter of the shape or a maximal number of holes). Otherwise, in some cases, a sequence of structures featuring even more microscopic holes and converging to no genuine shape, could possibly be constructed in order to improve the cost function.

Numerically, this will not happen. Indeed, the domain is discretized using a mesh and the level-set function is discretized by a finite element function. The size of the holes could not be smaller than the size of the edges of the mesh: infinite number of microscopic holes can not be computed. Hence, numerically, the optimized structure is only a local minimum.

1.2.2 SIMP method

The Solid Isotropic Material with Penalization (SIMP) method was first introduced by Bendsoe in [Bendsøe 1989], we refer to [Bendsoe 2003, Zhou 1991] for more details. This method can be seen as a simplification of the homogenization method, which is briefly presented in the next section, and into details in the Chapter 2. However, due to the great success of this method in the shape optimization community, we present it separately.

We present here the SIMP method in the case of the linear elasticity, for a review of this method, one can read [Rozvany 2009]. An isotropic material is characterized by its Hooke's law tensor A. We introduce a fictitious material made of void and the previous isotropic material. This fictitious material is parametrized by its density θ. No assumption is made about the eventual microstructure of the material, which in fact may not correspond to any mixture of void and of the phase A, see [Bendsøe 1999] for an interpretation of the grey material as a microstructured material. The elasticity Hooke's law tensor for the fictitious material is represented as a power law of the density: $\theta^p A$, with $p > 0$. We emphasize that for density equal to one, the fictitious material is the phase A. For a density equal to zero, the fictitious

material corresponds to void. Hence, when the density takes only the two values one and zero on the working domain, it describes a genuine shape. The interior of the shape is characterized by $\theta = 1$ and its exterior by $\theta = 0$.

The optimization process consists in optimizing the distribution of the density field θ in the working domain. This is an easy task of parametric optimization. The intermediate densities are then penalized in order to yield a black and white solution, which describes a genuine shape. In practice, the value of the exponent p is progressively increased during the optimization process until it reaches $p = 3$. In the main cases, with this value the grey densities are autopenalized. It may occur that some grey densities still persist. To solve this problem, filters on the density field have been proposed [Bourdin 2001, Fuchs 2005, Sigmund 2007], but also alternative elasticity law for the fictitious material [Bruns 2005]. To address the problems of checkerboard effect or of mesh dependency, slight modifications of this method have been proposed [Sigmund 1998].

Like for the level-set method, numerically, the optimized structure is only a local minimum for the objective function. Moreover the final optimized structure can not feature too thin details, and even less a microstructure, due to discretization on a mesh. These both methods yield optimized macroscopic structures, meaning that they feature only one scale of material.

Hence, those methods are not appropriate to optimize structures built with modulated microstructure. This would imply to use a very thin mesh and would be too time-consuming.

1.2.3 Homogenization method

The mathematical framework of the homogenization method is given in Chapter 2. Here, we only briefly present the principles of this method.

The homogenization method was one of the earliest method of topology optimization. It has been introduced in the early eighties by mathematicians [Kohn 1986, Lurie 1982, Murat 1985] (see the textbook [Allaire 2002a] for more references), and popularized by the seminal paper [Bendsøe 1988] which was the first one to numerically treat a realistic problem in the elasticity setting (the previous numerical works were restricted to an anti-plane elasticity setting, namely a scalar equation). Despite its great success, the homogenization method progressively faded away because it was surpassed by a much simpler method and as efficient in most cases, the so-called SIMP method, previously presented.

However, the appearance of mature additive manufacturing technologies which are able to build finely graded microstructures (sometimes called lattice materials) may drastically change the picture and we could well see a resurrection of the homogenization method for such applications. Indeed, homogenization is the right technique to deal with microstructured materials where anisotropy plays a key role, a feature which is absent from SIMP. Homogenization theory allows to replace the microscopic details of the structure (typically a complex networks of bars, trusses and plates) by a simpler effective elasticity tensor describing the mesoscopic properties of the structure. Therefore, the analysis of the structure is greatly accelerated since there is no need to mesh or represent on a fixed mesh all the microscopic details of its shape.

There is however one final hurdle, once an optimal composite structure has been obtained. Indeed the homogenized optimized structure is not a genuine shape, and so is not straightforwardly manufacturable.

In this thesis, we propose a method, inspired by [Pantz 2008], to project the optimal mi-

crostructure at a chosen finite length scale to get a global and detailed picture of the optimal microstructure.

1.2.4 Multi-scale methods

The homogenization method relies on the optimization of the microstructure. Nevertheless, the set of admissible microstructures is generally reduced to a family of parametrized microstructures: a square cell perforated by a square in [Bendsøe 1988], a perforated hexagon in [Zhang 2015], a square perforated by an ellipse in [Geihe 2013], or a truss [Daynes 2017] in for example.

How to choose an appropriate family of composite material is not obvious. Hence, several methods based on a multiscale optimization have been proposed to bypass this question. The material distributions in microscale and macroscale are optimized simultaneously.

The microstructure is sometimes optimized but taken uniform in the working domain, see [Xie 2012] or [Liu 2008]. But methods have also been developed in order to modulate locally the microstructures, see [Kim 2000], [Rodrigues 2002], [Luo 2007] or [Yan 2014]. The major part of those optimization algorithms use evolutionary methods ([Xie 2012], [Zuo 2013]...), or gradient-based methods ([Rodrigues 2002]).

Chapter 2

Homogenization

Contents

2.1 H-convergence in linear elasticity

We present briefly the homogenization theory in the case of linear elasticity. For more details, we refer to [Tartar 1978], Chapter 2 of [Kawohl 2007] and to the textbook [Allaire 2002a].

2.1.1 Strong and weak convergences

Let Ω be an open set in $\mathbb{R}^N$. Let $L^p(\Omega)$ be the Lebesgue space, meaning the space of all measurable functions u in Ω, such that:

$$||u||_{L^p(\Omega)} = \begin{cases} (\int_\Omega |u(x)|^p dx)^{\frac{1}{p}} & \text{for } 1 \leq p < +\infty \\ \sup_{x\in\Omega} |u(x)| & \text{for } p = +\infty \end{cases}$$

is finite. $L^p(\Omega)$ is a Banach space, where two types of convergence are defined, namely the strong and the weak convergences, whose definitions are given below.

Definition 2.1.1. A sequence u_ε is said to **converge strongly** in $L^p(\Omega)$ to a limit u if:

$$\lim_{\varepsilon\to 0} ||u_\varepsilon - u||_{L^p(\Omega)} = 0\,.$$

The strong convergence is denoted by:

$$u_\varepsilon \to u \quad \text{in } L^p(\Omega) \text{ strongly}\,.$$

Definition 2.1.2. For $1 \leq p < +\infty$, the dual space of $L^p(\Omega)$ is $L^q(\Omega)$, with $\frac{1}{p} + \frac{1}{q} = 1$. A sequence u_ε is said to **converge weakly** in $L^p(\Omega)$ to a limit u if:

$$\forall \phi \in L^q(\Omega) \quad \lim_{\varepsilon \to 0} \int_\Omega u_\varepsilon(x)\phi(x)dx = \int_\Omega u(x)\phi(x)dx\,.$$

The weak convergence is denoted by:

$$u_\varepsilon \rightharpoonup u \quad \text{in } L^p(\Omega) \text{ weakly}\,.$$

For $p = +\infty$, despite $L^1(\Omega)$ is not the dual space of $L^\infty(\Omega)$, a sequence u_ε would be said to **weak * converge** in $L^\infty(\Omega)$ to a limit u if:

$$\forall \phi \in L^1(\Omega) \quad \lim_{\varepsilon \to 0} \int_\Omega u_\varepsilon(x)\phi(x)dx = \int_\Omega u(x)\phi(x)dx\,.$$

We recall also the definition of the convergence in the sense of distributions for further purposes.

Definition 2.1.3. A sequence $u_\varepsilon \in L^1_{\text{loc}}(\Omega)$ is said to converge in the sense of distributions to u if:

$$\forall \phi \in \mathcal{D}(\Omega) \quad \lim_{\varepsilon \to 0} \int_\Omega \phi(x)u_\varepsilon(x)dx = \int_\Omega \phi(x)u(x)dx\,,$$

where $\mathcal{D}$ is the set of smooth functions with compact support in Ω.

2.1.2 H-convergence

The following theorems and results are given in the particular case of the linear elasticity. Obviously, the homogenization theory is not restricted to this problem and is far more general. For general and theoretical results, one could report to [Tartar 1985, Allaire 2002a]. For an historic presentation of the homogenization theory, one could read the chapter 2 of [Kawohl 2007].

The behaviour of an elastic phase is modelized through a positive definite fourth order tensor, namely its Hooke's law A. Let $\mathcal{M}^4_N$ be the set of fourth order tensor acting on symmetric matrices : $A \in \mathcal{M}^4_N$.

We now introduce the sets $\mathcal{M}_{\alpha,\beta}$ of admissible Hooke's laws, because they are compact for the topology of the H-convergence, see Theorem 2.1.1.

Definition 2.1.4. Let $\alpha > 0$ and $\beta > 0$ be two positive constants. The set of admissible Hooke's law $\mathcal{M}_{\alpha,\beta}$ is defined by:

$$\mathcal{M}_{\alpha,\beta} = \{A \in \mathcal{M}^4_N \text{ such that } \forall \xi \in \mathcal{M}^s_N \quad A\xi : \xi \geq \alpha|\xi|^2 \text{ and } A^{-1}\xi : \xi \geq \beta|\xi|^2\}\,.$$

We recall that the definition of H-convergence which follows is given for the particular case of linear elasticity.

Definition 2.1.5. A sequence of Hooke's law $A^\varepsilon(x)$ is said to converge in the sense of homogenization, or simply to H**-converge**, to an homogenized Hooke's law $A^*(x) \in L^\infty(\Omega, \mathcal{M}_{\alpha,\beta})$ if for any right hand side $f \in H^{-1}(\Omega)^N$, the sequence u_ε of solutions of:

$$\left\{ \begin{array}{ll} -\operatorname{div}(A^\varepsilon(x)e(u_\varepsilon)(x)) = f(x) & \text{in } \Omega \\ u_\varepsilon = 0 & \text{on } \partial\Omega \end{array} \right. \tag{2.1}$$

satisfies

$$\begin{array}{l} u_\varepsilon \rightharpoonup u \quad \text{weakly in } H_0^1(\Omega)^N \\ A^\varepsilon e(u_\varepsilon) \rightharpoonup A^* e(u) \quad \text{weakly in } L^2(\Omega; \mathcal{M}_N^s) \end{array} , \tag{2.2}$$

where u is the unique solution of the homogenized equation:

$$\left\{ \begin{array}{ll} -\operatorname{div}(A^*(x)e(u)(x)) = f(x) & \text{in } \Omega \\ u = 0 & \text{on } \delta\Omega \end{array} \right. . \tag{2.3}$$

The following theorem, due to Tartar and Murat is a fundamental one of the homogenization theory, it is a compactness result: any bounded sequence of $\mathcal{M}_{\alpha,\beta}$ admits a H-converging subsequence:

Theorem 2.1.1. *For any sequence $A^\varepsilon(x)$ of Hooke's laws in $L^\infty(\Omega, \mathcal{M}_{\alpha,\beta})$, there exists a subsequence, still denoted by A^ε and an homogenized Hooke's law $A^*(x) \in L^\infty(\Omega, \mathcal{M}_{\alpha,\beta})$ such that A^ε H-converges to A^*.*

A proof of this theorem is given in [Tartar 1978], an English translation is available in [Murat 1997]. This general theorem does not give any formula for the H-limit. In fact, we have explicit formula only for few particular cases, like periodic media.

2.1.3 Periodic homogenization

Let the periodic cell be the unit cube $Y = (0,1)^N$.

Let the Lebesgue space $L^p_\#(Y)$ be the set of Y-periodic functions in $L^p_{\text{loc}}(\mathbb{R}^N)$, the norm for this space is the norm $||f||_{L^p(Y)}$.

Let the Sobolev space $H^1_\#(Y)$ be the set of Y-periodic functions of $H^1_{\text{loc}}(\mathbb{R}^N)$, the norm for this space is the norm $||f||_{H^1(Y)}$.

Let $A \in L^\infty(Y, \mathcal{M}_{\alpha,\beta})$ be a Y-periodic admissible Hooke's law. Let A^ε be the sequence of admissible Hooke's laws defined by:

$$A^\varepsilon(x) = A(\frac{x}{\varepsilon}) . \tag{2.4}$$

The theorem 2.1.1 ensures that the sequence A^ε has a H-converging subsequence. In fact, according to the following theorem, the whole sequence H-converges, and there is an explicit formula for its H-limit.

Theorem 2.1.2. *The sequence A^ε, defined by (2.4), H-converges to a constant homogenized fourth order tensor $A^* \in \mathcal{M}_{\alpha,\beta}$ defined by its coefficients:*

$$A^*_{ijkl} = \int_Y A(y)(e_{ij} + e(w_{ij})) : (e_{kl} + e(w_{kl}))dy , \tag{2.5}$$

where $e_{ij} = \frac{1}{2}(e_i \otimes e_j + e_j \otimes e_i)$ is the canonical basis of the symmetric tensors of order 2, and the functions $w_{ij} \in H^1_\sharp(Y, \mathbb{R}^N)$ (with $1 \le i, j \le N$) are the unique solutions, up to an additive constant, of the cell problems:

$$\left\{ \begin{array}{ll} \operatorname{div}(A(e_{ij} + e(w_{ij})) = 0 & \text{in } Y \\ y \to w_{ij} & Y\text{-periodic} \end{array} \right. \tag{2.6}$$

The particular interest of Theorem 2.1.2 relies on the fact that any H-limit can be reached by a converging sequence of periodic Hooke's laws:

Theorem 2.1.3. *Let A^ε be a sequence of Hooke's law in $L^\infty(\Omega, \mathcal{M}_{\alpha,\beta})$, which H-converges to a limit A^*. Let $A^*_{x,\varepsilon,h}$ be the periodic homogenized matrix defined, for any $x \in \Omega$ and any sufficiently small positive $h > 0$, by:*

$$(A^*_{x,\varepsilon,h})_{ijkl} = \int_Y A^\varepsilon(x+hy)(e_{ij} + e(w^{ij}_{x,\varepsilon,h}) : (e_{kl} + e(w^{kl}_{x,\varepsilon,h})dy\,,$$

where $(w^{ij}_{x,\varepsilon,h})_{1\leq i,j\leq N}$ is the family of solutions in $H^1_\#(Y)/\mathbb{R}$ of the cell problems:

$$\begin{cases} \operatorname{div}(A^\varepsilon(e_{ij} + e(w^{ij}_{x,\varepsilon,h})) = 0 & \text{in } Y \\ y \to w^{ij}_{x,\varepsilon,h} & Y\text{-periodic} \end{cases}. \tag{2.7}$$

There exists a subsequence h going to zero such that, for almost every $x \in \Omega$:

$$\lim_{h\to 0}\lim_{\varepsilon\to 0} A^*_{x,\varepsilon,h} = A^*(x)$$

The theorem 2.1.3 is a density result, since any general H-limit can be approached by periodic H-limits.

In particular, periodic homogenization is perfectly appropriate to study modulated cellular structures. Indeed, let us consider a periodic cell whose design is parametrized by finite parameters $p \in \mathbb{R}^{n_p}$. Thanks to the theroem 2.1.2, the homogenized Hooke's law $A^*(p)$ of the cell can be computed for any parameters p. Let be the domain Ω be tiled by periodic cells of size ε. Let $p^\varepsilon(x) : \Omega \to \mathbb{R}^{n_p}$ be the function of parameters of the periodic cells: it is a piecewise constant function. We assume that p^ε converges weakly to p^*.

Let $A^\varepsilon(x) \in L^\infty(\Omega, \mathcal{M}_{\alpha,\beta})$ be the Hooke's law of this modulated cellular structure. Then the theorem 2.1.3 ensures that the sequence A^ε H-converges to the Hooke's law $A^*(p^*(x))$, when the size ε of the periodic cells is going to zero.

We now have all the results in order to compute effective Hooke's laws with homogenization method for modulated cellular structures. However, there are few other questions to be answered before using homogenization theory to any linear elastic problem. Indeed the definition 2.1.5 is given for particular boundary conditions. We will see it can be extended to others. Moreover, we give in the following more results in order to be able to compute some quantities, like energy and eigenfrequencies.

2.1.4 Irrelevance of the boundary conditions

Proposition 2.1.4. *Let $A^\varepsilon(x)$ be a sequence of Hooke's laws in $L^\infty(\Omega, \mathcal{M}_{\alpha,\beta})$ that H-converges to $A^*(x)$. Any sequence z_ε such that:*

$$\begin{cases} -\operatorname{div}(A^\varepsilon e(z_\varepsilon)) = f_\varepsilon \to f & \text{strongly in } H^{-1}_{loc}(\Omega)^N \\ z_\varepsilon \rightharpoonup z & \text{weakly in } H^1_{loc}(\Omega)^N \end{cases}$$

satisfies:

$$A^\varepsilon e(z_\varepsilon) \rightharpoonup A^* e(z) \quad \textit{weakly in } L^2_{loc}(\Omega, \mathcal{M}^s_N)$$

Before exposing the proof of this proposition, we give the following fundamental result, which is a generalization of the *div-curl* lemma, also called *compensated compactness* lemma [Tartar 1979]. One can refer to Theorem 3.1 of [Francfort 1986] for more details.

We recall that, the product of two sequences which respectively converges weakly to u and v does not converge weakly to the product $u\,v$. The div-curl lemma and its generalization, state that if the derivatives verify some convergence, the product converge in the sense of distributions.

Lemma 2.1.5. *Let u_ε and v_ε be two sequences in $L^2(\Omega, \mathcal{M}^s_N)$ such that*

$$\begin{cases} u_\varepsilon \rightharpoonup u & \textit{weakly in } L^2(\Omega, \mathcal{M}^s_N) \\ \operatorname{div}(u_\varepsilon) \to \operatorname{div}(u) & \textit{strongly in } H^{-1}(\Omega) \end{cases},$$

and

$$\begin{cases} v_\varepsilon \rightharpoonup v & \textit{weakly in } L^2(\Omega, \mathcal{M}^s_N) \\ \forall i,j,k,l \in \{1,..,N\}, & \dfrac{\partial v_{\varepsilon,jl}}{\partial x_i \partial x_K} + \dfrac{\partial v_{\varepsilon,ik}}{\partial x_j \partial x_l} - \dfrac{\partial v_{\varepsilon,jk}}{\partial x_i \partial x_l} - \dfrac{\partial v_{\varepsilon,il}}{\partial x_j \partial x_k} \to \\ & \dfrac{\partial v_{jl}}{\partial x_i \partial x_K} + \dfrac{\partial v_{ik}}{\partial x_j \partial x_l} - \dfrac{\partial v_{jk}}{\partial x_i \partial x_l} - \dfrac{\partial v_{il}}{\partial x_j \partial x_k} \quad \textit{strongly in } H^{-2}(\Omega, \mathcal{M}^N) \end{cases} \tag{2.8}$$

Then

$$u_\varepsilon : v_\varepsilon \to u : v \quad \textit{in the sense of distributions.}$$

The term *compensated* comes from the fact that specific derivatives of each sequence converge in order to compensate each other.

The second condition of (2.8) is automatically satisfied for sequences of symmetric matrices v_ε which are strain tensor, meaning can be written $v_\varepsilon = (\nabla a_\varepsilon + \nabla a_\varepsilon^T)/2$. Indeed this linear combination of partial derivatives is equal to zero for such matrices.

Proof. We give here a proof of the proposition 2.1.4.

Let ω be a compactly embedded subset of Ω. Since z_ε converges weakly to w in $H^1_{\text{loc}}(\Omega)^N$, $e(z_\varepsilon)$ converges weakly to $e(z)$ in $L^2_{\text{loc}}(\Omega)^N$. Moreover $\nabla \wedge e(z_\varepsilon)(\Omega)^N) = 0 = \nabla \wedge e(z)$.

Since z_ε is bounded in $H^1(\omega)^N$, the product $A^\varepsilon e(z_\varepsilon)$ is bounded in $L^2(\omega)^N$, and so converges weakly to $\sigma \in L^2(\omega)^N$, up to a subsequence still denoted by ε. The strong convergence of the divergence of the product is an assumption of the proposition.

The goal is to prove $\sigma = A^* e(z)$ in ω.

Let $\phi \in \mathcal{D}(\Omega)$ such that $\phi \equiv 1$ on ω. Let $\lambda \in \mathcal{M}^s_N$ be a symmetric matrix. Let the function $w(x) = \phi(x)\lambda\, x$, then we have $e(w)(x) = \lambda$ in ω.

Let the test function w_ε be the solution in $H_0^1(\Omega)^N$ of:

$$\begin{cases} -\operatorname{div}(A^\varepsilon e(w_\varepsilon) = -\operatorname{div}(A^* e(w)) & \text{in } \Omega \\ w_\varepsilon = 0 & \text{on } \partial\Omega \end{cases}.$$

Thanks to the H-convergence of A^ε, we get:

$$w_\varepsilon \rightharpoonup w \quad \text{weakly in } H_0^1(\Omega)^N,$$

and so

$$e(w_\varepsilon) \rightharpoonup e(w) \quad \text{weakly in } L^2(\Omega)^N.$$

Moreover, $e(w_\varepsilon)$ satisfies the second condition of (2.8), since it is a strain tensor.

From the H-convergence of A^ε, we also get that $A^\varepsilon e(w_\varepsilon)$ converges weakly to $A^* e(w)$ in $L^2(\Omega)^N$. Moreover, we have $\operatorname{div}(A^\varepsilon e(w_\varepsilon)) = \operatorname{div}(A^* e(w))$ and so the strong convergence in $H^{-1}(\Omega)$.

Since $A^\varepsilon \in \mathcal{M}_{\alpha,\beta}$, A is coercive, we then have:

$$A^\varepsilon(e(z_\varepsilon) - e(w_\varepsilon)) : (e(z_\varepsilon) - e(w_\varepsilon)) \geq \alpha |e(z_\varepsilon) - e(w_\varepsilon)|^2 \geq 0 \quad \text{almost everywhere in } \omega.$$

By application of the div-curl lemma, we get:

$$(\sigma - A^*\lambda) : (e(z) - \lambda) \geq 0 \quad \text{a. e. in } \omega.$$

Let $x_0 \in \omega$ be a point where the above inequality holds. By taking $\lambda = e(z)(x_0) + t\mu$, with $t > 0$ and $\mu \in \mathcal{M}_N^s$ and dividing by t and letting t going to zero:

$$-(\sigma(x_0) - A^* e(z)(x_0)) : \mu \geq 0\,.$$

Since this inequality holds for any $\mu \in \mathcal{M}_N^s$, necessarily:

$$\sigma(x) = A^* e(z)(x) \quad \text{a. e. in } \omega.$$

Hence all converging subsequences of $A^\varepsilon(e(z_\varepsilon)$ converges to the same limit for any subset $\omega \subset \Omega$, the entire sequence converges weakly to $A^* e(z)(x)$ in $L^2_{\text{loc}}(\Omega, \mathcal{M}_N^s)$.

□

2.1.5 Convergence of the energy

In shape optimization in linear elasticity, a classic objective consists in minimizing the compliance of the final structure, meaning maximizing its rigidity. Taking a sequence of structures, whose Hooke's laws H converge to A^*, the following proposition ensures that the energy, and so the compliance, of the structures converges to the energy of the homogenized structure.

Proposition 2.1.6. *Let $A^\varepsilon(x)$ be a sequence of Hooke's laws in $L^\infty(\Omega, \mathcal{M}_{\alpha,\beta})$ that H-converges to $A^*(x)$. For any right hand side $f \in H^{-1}(\Omega)^N$, the sequence u_ε of solutions of:*

$$\begin{cases} -\operatorname{div}(A^\varepsilon(x) e(u_\varepsilon)(x)) = f(x) & \text{in } \Omega \\ u_\varepsilon = 0 & \text{on } \partial\Omega \end{cases} \tag{2.9}$$

satisfies:

$$A^\varepsilon e(u_\varepsilon) : e(u_\varepsilon) \rightharpoonup A^* e(u) : e(u) \quad \textit{in the sense of distributions}$$

and

$$\int_\Omega A^\varepsilon e(u_\varepsilon) : e(u_\varepsilon) dx \to \int_\Omega A^* e(u) : e(u)$$

where u is the weak limit of u_ε in $H_0^1(\Omega)^N$ and so the solution of the homogenized equation (2.3).

Proof. We give here the proof of the proposition 2.1.6 to illustrate a simple application of the div-curl lemma. Since $A^\varepsilon(x)$ H-converges to $A^*(x)$, we get:

$$A^\varepsilon e(u_\varepsilon) \rightharpoonup A^* e(u) \quad \text{in } L^2(\Omega, \mathcal{M}_N^s)$$

Since

$$\forall x \in \Omega \quad \operatorname{div}(A^\varepsilon(x) e(u_\varepsilon)(x)) = f(x) = \operatorname{div}(A^*(x) e(u)(x)) \,,$$

we have:

$$\operatorname{div}(A^\varepsilon e(u_\varepsilon) \to \operatorname{div}(A^* e(u)) \quad \text{strongly} \,.$$

Besides, from

$$u_\varepsilon \rightharpoonup u \quad \text{in } H_0^1(\Omega)^N \,,$$

we get

$$e(u_\varepsilon) \rightharpoonup e(u) \quad \text{in } L^2(\Omega)^N \,.$$

Moreover, $e(w_\varepsilon)$ satisfies the second condition of (2.8), since it is a strain tensor.

By application of the generalized div-curl lemma 2.1.5, we get the convergence of $A^\varepsilon e(u_\varepsilon) : e(u_\varepsilon)$ in the sense of distributions in Ω to $A^* e(u) : e(u)$.

For the second result of the proposition, we recall that u_ε converges weakly to u in $H_0^1(\Omega)$ and consequently:

$$\int_\Omega f \cdot u_\varepsilon dx \to \int_\Omega f \cdot u dx \,.$$

An integration by parts of the elasticity problems gives respectively:

$$\begin{array}{l} \displaystyle\int_\Omega A^\varepsilon e(u_\varepsilon) : e(u_\varepsilon) dx = \int_\Omega f \cdot u_\varepsilon dx \\ \displaystyle\int_\Omega A^* e(u) : e(u) dx = \int_\Omega f \cdot u dx \end{array} \,,$$

which leads eventually to the desired result.

□

Remark 1. *The second result of the proposition 2.1.6 can be extended to other boundary conditions only if they are fixed, in order to proceed to the integration by parts of the elasticity problems. This is the case for any elasticity problems studied in the present work.*

2.1.6 Corrector results

In linear elasticity, we made the assumption that the stress and the strain are always linked together through the Hooke's law, no matter their values. However in real elasticity, several phenomena (plasticity or buckling for example) may occur when the stress exceeds some threshold. So, in shape optimization, it would be relevant to estimate the limit, if it exists, of:

$$J_\varepsilon = \int_\Omega k(x)|\sigma_\varepsilon|^2 dx\,, \tag{2.10}$$

where k is a non-negative function. It is a weighting factor, thanks which the evaluation of the stress can be localized.

We recall that σ_ε converges weakly to σ and that the product of two weakly converging sequences does not generally converge weakly to the product of the weak limits. Hence to pass to the limit in (2.10), strong convergence is required for the sequence σ_ε.

From a mechanical point of view, this means that in a composite, the microstructure induces local stress. But the homogenized, meaning the average, stress does not report this local stress. Amplification, or corrector, factors are required to estimate local stress from the average one.

Definition 2.1.6. Let $(X^{ij})_{1\leq i,j\leq N}$ be the family functions of $H^1(\Omega)^N$ defined by their coefficients:

$$X^{ij}_k = x_j\delta_{ik} \tag{2.11}$$

In particular, we have:

$$e(X^{ij}) = e_{ij} \tag{2.12}$$

We now introduce the corrector tensors:

Definition 2.1.7. Let A^ε be a sequence of Hooke's laws in $L^\infty(\Omega, \mathcal{M}_{\alpha,\beta})$ that H-converges to A^*. Let $(w^{ij}_\varepsilon)_{1\leq i,j\leq N}$ be a family of functions in $H^1(\Omega)$ such that:

$$\begin{array}{rcl} w^{ij}_\varepsilon & \rightharpoonup & X^{ij} \text{ weakly in } H^1(\Omega)^N \\ g^{ij}_\varepsilon = \operatorname{div}(A^\varepsilon e(w^{ij}_\varepsilon)) & \to & g_{ij} = \operatorname{div}(A^* e_{ij}) \text{ strongly in } H^{-1}(\Omega)^N \end{array} \tag{2.13}$$

The fourth order tensor W^ε defined by its coefficients:

$$W^\varepsilon_{ijkl} = (e(w^{ij}_\varepsilon))_{kl}$$

is called a corrector tensor.

The existence of the functions w^{ij}_ε is at the heart of the proof of theorem 2.1.1 by Tartar and Murat. They are called correctors or oscillating test functions. They are introduced in the proof to define the homogenized tensor A^*. It is so quite natural that they are involved in the correction of A^* in order to compute the strong limit of the stress, as we will see in the following. We emphasize they are not uniquely defined, but only up to a strongly convergent additive term, which leads to the following lemma:

Lemma 2.1.7. *Let A^ε be a sequence of Hooke's laws in $L^\infty(\Omega, \mathcal{M}_{\alpha,\beta})$ that H-converges to A^*. If there exist two corrector tensor W^ε and $\tilde{W}^\varepsilon$, then their difference converges strongly to zero in $L^2_{loc}(\Omega, \mathcal{M}^4_N)$.*

In the periodic case, the oscillating test functions can be given explicitly by the solutions w_{ij} of the cell problem (2.7):

$$w_\varepsilon^{ij}(x) = X^{ij} + \varepsilon w_{ij}(\frac{x}{\varepsilon})\,, \tag{2.14}$$

which leads to:

$$e(w_\varepsilon^{ij})(x) = e_{ij} + (e_y(w_{ij}))(\frac{x}{\varepsilon})\,.$$

Indeed, by rescaling the cell problem (2.7), we eventually get:

$$\mathrm{div}(e(w_\varepsilon^{ij})) = 0 = \mathrm{div}(A^* e_{ij}) \text{ in } \Omega\,,$$

since A^* is homogeneous in Ω in the periodic case, and the so-defined w_ε^{ij} satisfies (2.13)

Hence, the corrector tensor is given by:

$$W_{ijkl}^\varepsilon = I_{ijkl}^4 + (e_y(w_{ij}))_{kl}(\frac{x}{\varepsilon})\,,$$

where I^4 is the fourth order identity tensor, and e_y is the operator e with respect to the periodic variable y.

Lemma 2.1.8. *Let A^ε be a sequence of Hooke's laws in $L^\infty(\Omega, \mathcal{M}_{\alpha,\beta})$ that H-converges to A^*. Then we have:*

$$\begin{aligned} W^\varepsilon &\rightharpoonup I^4 \text{ weakly in } L^2(\Omega, \mathcal{M}_N^4) \\ A^\varepsilon W^\varepsilon &\rightharpoonup A^* \text{ weakly in } L^2(\Omega, \mathcal{M}_N^4) \\ (W^\varepsilon)^T A^\varepsilon W^\varepsilon &\rightharpoonup A^* \text{ in } \mathcal{D}'(\Omega, \mathcal{M}_N^4) \end{aligned} \tag{2.15}$$

Theorem 2.1.9. *Let A^ε be a sequence of Hooke's laws in $L^\infty(\Omega, \mathcal{M}_{\alpha,\beta})$ that H-converges to A^*. Let u_ε be the solution of (2.1), which converges weakly (up to a subsequence still denoted u_ε) to u, the solution of the homogenized equation (2.3).*

Then:

$$e(u_\varepsilon) = W^\varepsilon e(u) + r_\varepsilon\,,$$

where r_ε converges strongly to zero in $L^1_{loc}(\Omega, \mathcal{M}_N^s)$.

With the settings of theorem 2.1.9, we have:

$$\sigma_\varepsilon = A^\varepsilon e(u_\varepsilon) = A^\varepsilon W^\varepsilon e(u) + A^\varepsilon r_\varepsilon = P^\varepsilon \sigma + A^\varepsilon r_\varepsilon$$

where P^ε is the fourth order tensor defined by:

$$P^\varepsilon = A^\varepsilon W^\varepsilon A^{*-1}\ ,.$$

The sequence P^ε converges weakly to I^4, thanks to lemma 2.1.8.

The objective function (2.10) can then be rewritten:

$$\begin{aligned} J_\varepsilon &= \int_\Omega k(x)|\sigma_\varepsilon|^2 dx \\ &= \int_\Omega k(x)|P^\varepsilon \sigma|^2 dx + 2\int_\Omega k(x)(A^\varepsilon r_\varepsilon : P^\varepsilon \sigma dx) + \int_\Omega k(x)|A^\varepsilon r_\varepsilon|^2 dx) \end{aligned} \tag{2.16}$$

We focus in the following in the case of periodic homogenization.

Proposition 2.1.10. *In periodic homogenization, assuming that the solution u of the elasticity problem is $W^{1,\infty}(\Omega,\mathbb{R}^N)$, the objective function (2.10) converges, when ϵ is going to zero, to:*

$$J = \int_\Omega k(x) P^* \sigma : \sigma dx$$

where σ is the associated constraint tensor to the displacement u and

$$P^* = \frac{1}{|Y|}\int_Y A(y)W(y)A^{*-1}A(y)W(y)A^{*-1}dy\,.$$

Before to display the proof of this proposition, we recall the following lemma, see Lemma 1.3.19 in [Allaire 2002a]:

Lemma 2.1.11. *Let $f(y) \in L^2_\#(Y)$ be a periodic function. The sequence f_ε, defined by*

$$f_\varepsilon(x) = f(\frac{x}{\varepsilon})$$

converges weakly in $L^2_{loc}(\mathbb{R}^N)$ to the average: $\frac{1}{|Y|}\int_Y f(y)dy$.

Proof. **Proof of Proposition 2.1.10**

Thanks to Meyers theorem (see Theorem 1.3.41 in [Allaire 2002a]), the displacement u_ε, solution of (2.1), is known to belong to $W_0^{1,p}(\Omega)$, with $p > 2$ the Meyers exponent (p independent of ε). Hence, its symmetrized gradient $e(u_\varepsilon)$ is L^p-bounded.

Likewise, the solutions w_{ij} of the cell problem (2.7) belong to $W^{1,p}(Y)$, and W_ε is L^p-bounded.

We recall that we assume here $e(u)$ to be L^∞-bounded.

Hence, $r_\varepsilon = W_\varepsilon e(u) - e(u_\varepsilon)$ is L^p-bounded. Thanks to Lemma 1.2.5 in [Allaire 2002a], since r_ε converges strongly to zero in $L^1_{\text{loc}}(\Omega, \mathcal{M}^s_N)$, it also converges strongly to zero in $L^2(\Omega, \mathcal{M}^s_N)$.

Recalling that A_ε is L^∞-bounded, the third term of (2.16) converges to zero.

The second term of (2.16) converges also to zero, since σ is assuming to be L^∞-bounded.

We conclude using Lemma 2.1.11. □

The term *amplification* tensor stands for the fact that the L^2 norm of the homogenized stress σ is amplified by this tensor in order to reach the convergence.

In the particular case of laminated composite material, an explicit formula of the correctors is due to Briane [Briane 1994] in conductivity. This result has been extended to linear elasticity [Allaire 2004a] and implemented for shape optimization.

Remark 2. *Other assumptions in Proposition 2.1.10 could be chosen, like regularity on the solutions w_{ij} of the cell problem (2.7), leading to W_ε to be L^∞-bounded. However, microstructures featuring sharp corners are used in this thesis: such assumption can not be considered here.*

2.1.7 Eigenfrequencies

Homogenization theory stands also for dynamic problems and eigenvalue problems. Let Ω be a bounded subset of $\mathbb{R}^N$. Let $A \in L^\infty(\Omega, \mathcal{M}_{\alpha,\beta})$ be an admissible Hooke's law. We recall that the spectral problem in linear elasticity reads as:

$$\begin{cases} -\operatorname{div}(A^*(x)e(u)(x)) = \lambda\rho(x)u(x) & \text{in } \Omega \\ u = 0 & \text{on } \partial\Omega \end{cases}, \tag{2.17}$$

where the unknown $\lambda > 0$ is an eigenvalue, and $u \in H_0^1(\Omega)^N$ is an associated nonzero eigenvector. There is a countable infinite number of solutions λ: the eigenvalues are a positive unbounded sequence. They are labeled by increasing order.

Homogenization theory gives a convergence result for the eigenfrequencies λ, as stated in the following theorem:

Theorem 2.1.12. *Let A^ε be a sequence of Hooke's laws in $L^\infty(\Omega, \mathcal{M}_{\alpha,\beta})$ that H-converges to A^*. Let ρ_ε be a sequence of positive functions, such that:*

$$0 < \rho_- \leq \rho_\varepsilon(x) \leq \rho_+ < \infty\,,$$

*which converges weakly * in $L^\infty(\Omega, \mathcal{M}_{\alpha,\beta})$ to a limit $\rho(x)$.*

Let $(\lambda_\varepsilon^m)_{m\geq 1}$ be the eigenvalues, labeled by increasing order, and $(u_\varepsilon^m)_{m\geq 1}$ be associated normalized eigenvectors ($||u_\varepsilon^m||_{L^2(\Omega)^N} = 1$) of the spectral problem:

$$\begin{cases} -\operatorname{div}(A^\varepsilon(x)e(u_\varepsilon^m)(x)) = \lambda_\varepsilon^m\rho_\varepsilon(x)u_\varepsilon^m(x) & \text{in } \Omega \\ u_\varepsilon^m = 0 & \text{on } \partial\Omega \end{cases}. \tag{2.18}$$

Then for any fixed $m \geq 1$,

$$\lim_{\varepsilon\to 0} \lambda_\varepsilon^m = \lambda^m\,,$$

and, up to a subsequence, u_ε^m converges weakly in $H_0^1(\Omega)^N$ to u^m, a normalized eigenvector associated to λ^m, which are solutions of the homogenized eigenvalue problem:

$$\begin{cases} -\operatorname{div}(A^*(x)e(u^m)(x)) = \lambda^m\rho(x)u^m(x) & \text{in } \Omega \\ u^m = 0 & \text{on } \partial\Omega \end{cases}. \tag{2.19}$$

Moreover $(\lambda^m)_{m\geq 1}$ is the complete family of eigenvalues of (2.19), labeled in increasing order.

We emphasize that several eigenvectors may be associated to the same eigenvalue, and so the convergence of the sequence u_ε^m can only be ensured up to a subsequence.

2.2 Composite material

We focus here on composite materials, made of two isotropic phases A and B in $\mathcal{M}_{\alpha,\beta}$. Their shear moduli and Lamé coefficients are respectively μ_A, μ_B and λ_A, λ_B. We assume that:

$$0 < \mu_B \leq \mu_A\,, \quad 0 < \lambda_B \leq \lambda_A\,.$$

Let $\chi_\varepsilon \in L^\infty(\Omega, \{0,1\})$ be a family of scalar characteristic functions, which converges weakly * to $\theta \in L^\infty(\Omega, [0;1])$. Let $A^\varepsilon \in L^\infty(\Omega, \mathcal{M}_{\alpha,\beta}$ be a sequence of Hooke's laws defined by:

$$A^\varepsilon(x) = \chi_\varepsilon(x)A + (1-\chi_\varepsilon(x))B\,.$$

The sequence A^ε, up to a subsequence still denoted A^ε, H-converges, thanks to Theorem 2.1.1. The H-limit A^* is the homogenized tensor of the composite material made of phase A in proportions θ and phase B in proportions $(1-\theta)$, with a microstructure defined by the sequence $(\chi_\varepsilon)_{\varepsilon>0}$.

Definition 2.2.1. Let $\theta \in L^\infty(\Omega, [0;1])$ be density function. The set $\mathcal{G}_\theta$ is defined as the set of all H-limits A^* associated to the density θ.

Generally, there is no formula for the H-limit A^* of A^ε. Hence, the set $\mathcal{G}_\theta$ can not be explicitly characterized. This is a huge limitation to perform shape optimization with the whole set of composite materials. A solution consists in reducing the set of admissible composites to families of composites, for which the effective elastic properties can be computed. To start, we focus on a particular class of composites : the sequential laminates. Then we recall the Hashin-Shtrikman bounds on the elastic properties of isotropic composites from $\mathcal{G}_\theta$, which will serve as reference. To conclude we briefly present the design of microstructures, an important research field in shape optimization.

Remark 3. *The H-limit A^* is not the Hooke's law defined by: $(\theta A + (1-\theta)B)$. Indeed, this would imply that the local microstructure of the composite does not affect its homogenized elastic behaviour. Only the proportions of each phase (θ for A and $(1-\theta$ for B) would control the homogenized Hooke's law. Moreover the homogenized Hooke's law would be isotropic. All of this is obviously false. To illustrate this, we can consider the composite made of equal layers of phases A and B in the direction $(0,1)$, see Figure 2.1. It would collapse for a vertical load but stay very strong for a horizontal load: it is clearly not isotropic.*

2.2.1 Sequential laminates

We focus here on a particular class of two-phase composites: the sequential laminates.

Single laminated composites. The definition of a single laminated composite relies on the following result of H-convergence (see Lemma 1.4.10 in [Allaire 2002a]):

Lemma 2.2.1. *Let $\chi_\varepsilon(x_1) \in L^\infty(\mathbb{R}; \{0,1\})$ be a sequence of scalar characteristic functions that converges weakly $*$ to a limit $\theta(x_1)$ in $L^\infty(\mathbb{R}; [0,1])$. Let A^ε be a sequence of matrices in $L^\infty(\Omega, \mathcal{M}_{\alpha,\beta})$ defined as:*

$$A^\varepsilon(x_1) = \chi_\varepsilon(x_1)A + (1-\chi_\varepsilon(x_1))B\,.$$

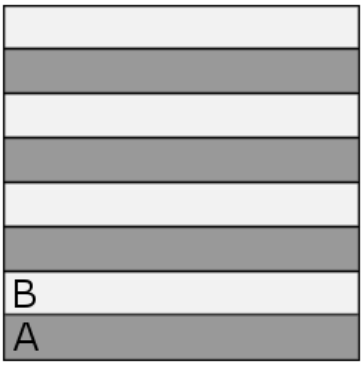

Figure 2.1

The sequence A^ε H-converges to A^*, which depends only on x_1 and is defined by:

$$\theta(A^* - B)^{-1} = (A - B)^{-1} + (1 - \theta) f_B(e_1)\,,$$

where $f_B(e_1)$ is a positive nondefinite fourth order tensor defined, for any symmetric matrix ξ by:

$$f_B(e_1)\xi : \xi = \frac{1}{\mu_B}(|\xi e_1|^2 - (\xi e_1 \cdot e_1)^2) + \frac{1}{2\mu_B + \lambda_B}(\xi e_1 \cdot e_1) e_1 \otimes e_1\,. \tag{2.20}$$

The composite A^* is said to be a single lamination in the direction e_1 of the two phases A and B in proportions θ and $(1 - \theta)$.

The single laminated composites define a whole family of composite materials, parametrized by the proportion of lamination θ and the direction of lamination.

Moreover, a single laminated composite can also be laminated, defining an enlarged family of composite materials.

Sequential laminated composites.

Lemma 2.2.2. *Let $(e_i)_{1\le i\le p}$ be a set of unit vectors. Let θ be a volumic fraction in $[0;1]$. For any collection of non-negative real numbers $(m_i)_{1\le i\le p}$ satisfying:*

$$\sum_{i=1}^{p} m_i = 1 \quad \textit{and} \quad \forall i \in \{1,..,p\}\, m_i \ge 0\,,$$

there exists a rank-p sequential laminate $A*_p$, with matrix A and core B, in proportions θ and $(1 - \theta)$, respectively, with lamination directions $(e_i)_{1\le i\le p}$ such that:

$$(1 - \theta)(A_p^* - A)^{-1} = (B - A)^{-1} + \theta \sum_{i=1}^{p} m_i f_A(e_i)\,,$$

where f_A is given by (2.20). The numbers $(m_i)_{1\le i\le p}$ are called the lamination parameters.

On Figure 2.2, we display the sequential construction of a sequence of composite materials converging to a rank-2 laminate.

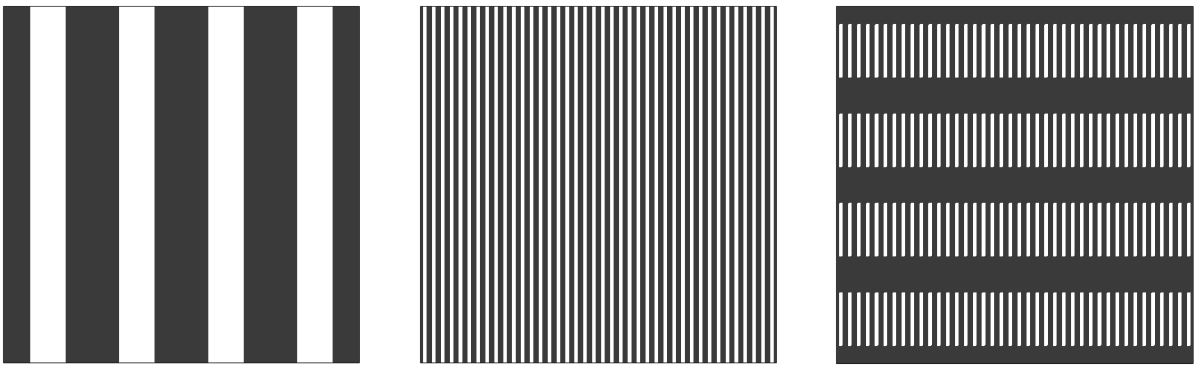

(a) First lamination, in direction e_1

(b) Change of scale

(c) Second lamination, in direction e_2

Figure 2.2: Process of to construct a sequential laminated composite

The first lamination between the two phases A and B is done in the direction e_1, see Figure 2.2(a). This new material, namely a single laminated composite, is seen as an homogenized material. This is a key point in the proof of the explicit formula of the elastic properties of the sequential laminates. Hence, the characteristic size ε of the single laminated composite is drastically reduced, what we call a change of scale, see Figure 2.2(b). Finally, this new effective material is laminated in direction e_2 with the previous matrix A, see Figure 2.2(c). We emphasize that without a change of scale between two laminations, the constructed composite will not converge to a sequential laminates. The process for laminated composites of higher ranks is exactly the same: the new material is seen as an effective material, thanks to a change of scale, then laminated in the appropriate direction.

2.2.2 Hashin Shtrikman bounds

The following theorem is due to Hashin and Shtrikman [Hashin 1963], Francfort and Murat proved that Hashin Shtrikman bounds are reached by sequential laminates [Francfort 1986].

Theorem 2.2.3. *Let A^* be an isotropic homogenized tensor in $\mathcal{G}_\theta$:*

$$A^* = 2\mu^* I_4 + (\kappa^* - \frac{2\mu^*}{N}) I_2 \otimes I_2 \,,$$

where κ^* is its bulk modulus and μ^* its shear modulus.

Then κ^* and μ^* satisfy:

$$\frac{\theta}{\kappa^* - \kappa_B} \leq \frac{1}{\kappa_A - \kappa_B} + \frac{1-\theta}{2\mu_B + \lambda_B}, \tag{2.21}$$

$$\frac{1-\theta}{\kappa_A - \kappa^*} \leq \frac{1}{\kappa_A - \kappa_B} - \frac{\theta}{2\mu_A + \lambda_A}, \tag{2.22}$$

and

$$\frac{\theta}{\mu^* - \mu_B} \leq \frac{1}{\mu_A - \mu_B} + \frac{2(1-\theta)(N-1)(\kappa_B + 2\mu_B)}{(N^2+N-2)\mu_B(2\mu_B + \lambda_B)}, \tag{2.23}$$

$$\frac{1-\theta}{\mu_A - \mu^*} \leq \frac{1}{\mu_A - \mu_B} - \frac{2\theta(N-1)(\kappa_A + 2\mu_A)}{(N^2+N-2)\mu_A(2\mu_A + \lambda_A)}, \tag{2.24}$$

Furthermore, the lower bounds (2.21) and (2.23) and the upper bounds (2.22) and (2.24) are respectively simultaneously attained by an isotropic rank-p sequential laminate with $p \leq (N+3)(N+2)(N+1)N/24$. *Optimality is achieved with* $p = 3$ *when* $N = 2$ *(in 2D), and with* $p = 6$ *when* $N = 3$ *(in 3D).*

In the following, the upper Hashin Shtrikman bounds will be our references for composite material. The composite materials in the presented work are made of an isotropic phase and void. Hence, we give the upper bounds κ_{HS} and μ_{HS} in this particular case:

$$\kappa_{HS} = \kappa_A - \frac{\kappa_A(1-\theta)(2\mu_A + \lambda_A)}{2\mu_A + \lambda_A - \kappa_A\theta} = \kappa_A\theta\frac{2\mu_A + \lambda_A - \kappa_A}{2\mu_A + \lambda_A - \kappa_A\theta} \tag{2.25}$$

and

$$\begin{aligned}\mu_{HS} &= \mu_A\theta\frac{(N^2+N-2)(2\mu_A+\lambda_A) - 2(N-1)(\kappa_A+2\mu_A)}{(N^2+N-2)(2\mu_A+\lambda_A) - 2\theta(N-1)(\kappa_A+2\mu_A)} \\ &= \begin{cases} \mu_A\theta\dfrac{\kappa_A}{\kappa_A + (1-\theta)(\kappa_A+2\mu_A)} & \text{when } N=2 \\ \mu_A\theta\dfrac{20\mu_A - 9\kappa_A)}{5(4\mu_A+3\kappa_A) - 6\theta(N-1)(\kappa_A+2\mu_A} & \text{when } N=3 \end{cases}\end{aligned} \tag{2.26}$$

The SIMP method. In the Solid Isotropic Material with Penalization (SIMP) method, the Hooke's law is represented as a power law of the density, the maximal exponent is 3. The bulk and the shear moduli with respect to the density are respectively represented on Figures 2.3(a) and 2.3(b), for three values of the exponent: 1 (linear law), 2 (quadratic law) and 3 (cubic law). The upper Hashin Shtrikman for a composite of isotropic material and void is also displayed on those figures, as references. The linear and quadratic materials are above the upper Hashin Shtrikman bounds for any density: they are fictitious material in the sens where no composite material reach those elastic properties for the same density. The cubic material satisfies the Hashin Shtrikman bounds for density lower than 70%: up to this point, the cubic material may match composite material. However, we do not have any information of which kind of microstructure it could be. Moreover, for greater densities, the cubic material turns also fictitious. Hence the SIMP method is not appropriate for shape optimization with microstructures. The penalization part is mandatory in order to reach real material (by opposition with fictitious materials), namely void and full material.

2.2.3 Design of a periodic microstructure

As seen previously, the set $\mathcal{G}_\theta$ is very large and can not be explicitly characterized. There exists an infinite choice of microstructures: to choose an adapted class of composites for a given minimization problem is not an easy task, see the textbook [Milton 2002] for more details about

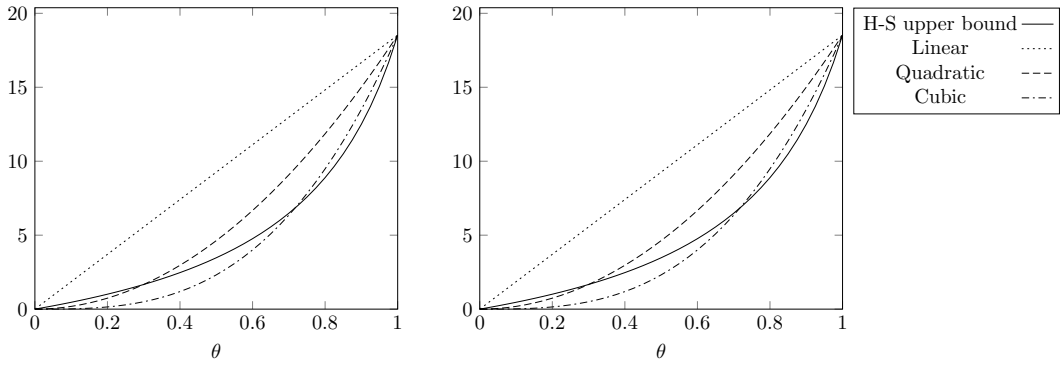

(a) $\kappa^*(\theta)$ (b) $\mu^*(\theta)$

Figure 2.3: Hashin Shtrikman (H-S) upper bound of bulk (left) and shear (right) moduli in 2D, with linear, quadratic and cubic laws

composite materials in numerous physical domains. Microstructures have been theoretically elaborated in order to reach some specific properties, like the sequential laminates, the coated confocal ellipsoid [Tartar 1985] or the Vigdergauz cells [Vigdergauz 1999]. Other microstructures have also been optimized using shape optimization methods: see [Sigmund 1994a] and [Michailidis 2014], or [Hyun 2002] for isotropic microstructures, [Guest 2006] for optimized cells for permeability to fluids, [Lin 2004] for optimization of biomaterials...

In this thesis, the chosen periodic microstructures should satisfy some criteria. First, it should be manufacturable, using additive manufacturing process. This imply that the microstructure can feature only one scale of material: rank-2 or more laminated composite are then excluded. For 3D microstructures, other constraints have to be taken into account, depending on the process of fabrication. For example, for metal additive manufacturing, the microstructure has to be drilled from end to end, otherwise metallic powder could be trapped in the final structure. Second, we consider only lattice material, meaning a mixing of an isotropic elastic phase and void. Third, the geometry of the microstructure has to be easily parametrizable, to perform the optimization process only over few parameters. To finish, the microstructure should explore, within the realm of the possible, a large range of elastic properties. In particular, it has to reach complete void and full material. This excludes for example a square perforated with an ellipse.

Part II

Contributions

Chapter 3

Topology optimization of 2D and 3D structures built with isotropic lattice materials

Contents

3.1 Introduction

We present a shape optimization method based on homogenization method to optimize structures made of modulated isotropic lattice material in 2D and in 3D. Two characteristics of the isotropic microstructures make them of high interest for shape optimization. First, there is no need to orientate them locally in the domain, what simplifies the optimization process but also the deshomogenization one. Second their geometry is parametrized by only one parameter, their density for example. Hence the distribution of only one parameter has to be optimized. One could notice that the optimization process is then very close to the SIMP method. Nevertheless, we recall that no fictitious material is used here. The homogenized elasticity tensor of the isotropic lattice material has to be computed, and taken into account during the optimization process. It is not approximated by a power law of the density.

In Section 1, we introduce isotropic microstructures in 2D an in 3D parametrized by their density. We compute their homogenized elasticity tensor, and the corresponding stress amplification tensor.

In Section 2, we present the optimization algorithm based on a gradient descent method. The optimization of several objective functions is investigated: the minimization of the compliance in single-load and multiple-loads test cases, the optimization of the displacement, the minimization of the L^2-norm of the stress tensor and the maximization of the first eigenfrequency. The isotropy of the cells is not optimal in some minimization problems, for example the minimization of the compliance for single-load case. Indeed the microstructure has to support constraints in two orthogonal directions simultaneously, when itself has no privileged strength direction. But isotropic microstructures appear to be highly adapted for other particular optimization problems, for example the minimization of the compliance for multiple-loads case.

In Section 3, two methods to deshomogenize the optimized homogenized structures are presented. The first one relies on a local approach: each cell of the deshomogenized structure is separately computed according to the local average density. In the second method, a global one, a level-set function, depending on the optimized density of the cells is introduced to describe the final structure. This strategy ensures the connectivity and the smoothness of the final shapes.

3.2 Isotropic microstructures

3.2.1 Cell designs

We present in this section, three isotropic microstructures in 2D and one in 3D. Only one parameter is retained here to modulate the cells : their density. Other equivalent parameters could be chosen, as the width of the bars. More parameters could have been retained in order to design a morphing between different types of isotropic cells.

classical honeycomb. The classical honeycomb is a regular hexagon perforated by a hexagonal hole, see Figure 3.1(a). This kind of cell is parametrized by its density, whose range is $[0; 1]$: the cell varies from void to full material.

Let θ be the density of the cell: $\theta \in [0; 1]$. Let m be the relative width of the bars, with respect to the size of the cell: $m \in [0; \frac{\sqrt{3}}{2}]$. Those two quantities are linked to each other:

$$m = \frac{\sqrt{3}}{2}(1 - \sqrt{1 - \theta}) \tag{3.1}$$

Reinforced honeycomb. The reinforced honeycomb cell is a regular hexagon with its three diagonals, see Figure 3.1(b). The periodic pattern can be seen as a truss of three groups of parallel bars. All the bars have the same width. They are equally spaced and oriented : the angle between two bars of different groups is equal to $\frac{\pi}{3}$. As the classical honeycomb, this kind of cell is parametrized by its density and varies from void to full material.

Let θ be the density of the cell: $\theta \in [0; 1]$. Let m be the relative width of the bars, with respect to size of the cell: $m \in [0; \frac{1}{2\sqrt{3}}]$. Those two quantities are linked to each other:

$$m = \frac{1}{2\sqrt{3}}(1 - \sqrt{1 - \theta}) \tag{3.2}$$

Smooth honeycomb. The smooth honeycomb is similar to the classic one, except that the interior corners are rounded, see Figure 3.1(c). Moreover, when the density increases to go to 1, the central hole converges to a circle, whose diameter is going to 0. Contrary to the previous kinds of cell and because of the smoothened corners, this kind of cell can not reach formally complete void. This cell is not parametrized using its density for practical reason, but by another parameter, $h \in [0;1]$. Indeed, in order to design this kind of cell, a parametric curve Γ_h is introduced and represents the border of the hole. This curve depends on h. We introduce some notations before giving its polar equation.

Let the vector $v(t) = (\cos(t), \sin(t))^T$ and let the vectors n_i, with $i \in \{0,1,2\}$ be respectively the normal vectors of the three diagonals of the honeycomb :

$$n_0 = \begin{pmatrix} 0 \\ 1 \end{pmatrix}, \quad n_1 = \begin{pmatrix} \frac{\sqrt{3}}{2} \\ \frac{1}{2} \end{pmatrix}, \quad n_2 = \begin{pmatrix} \frac{\sqrt{3}}{2} \\ -\frac{1}{2} \end{pmatrix}. \tag{3.3}$$

Eventually, the polar equation of Γ_h is:

$$r(t) = h\frac{\sqrt{3}}{2}\left(\sum_{i=0}^{2} |v(t)\cdot n_i|^p\right)^{-\frac{1}{p}} \quad \text{with } t \in [0; 2\pi] \tag{3.4}$$

where p is a positive coefficient which depends potentially of h. Here we took $p = 4 + 20h^2$.

We emphasize the fact that h is homogeneous to a distance, like m in the previous designs of hexagonal cells. The three kinds of honeycomb cells are hence parametrized quite the same way.

The polar equation of Γ_h relies on some following remarks and can easily be extended to other polygons. A regular unit hexagon $\mathcal{H}$ is the set of points whose maximal distances from the three diagonals is equal to $\frac{\sqrt{3}}{2}$, see Figure 3.1(b). Let $M(r,t)$ be a point, labeled with its polar coordinates: M is a point of the regular unit hexagon if and only if:

$$M(r,t) \in \mathcal{H} \quad \Leftrightarrow \quad r \max_i |v(t)\cdot n_i| = \frac{\sqrt{3}}{2}.$$

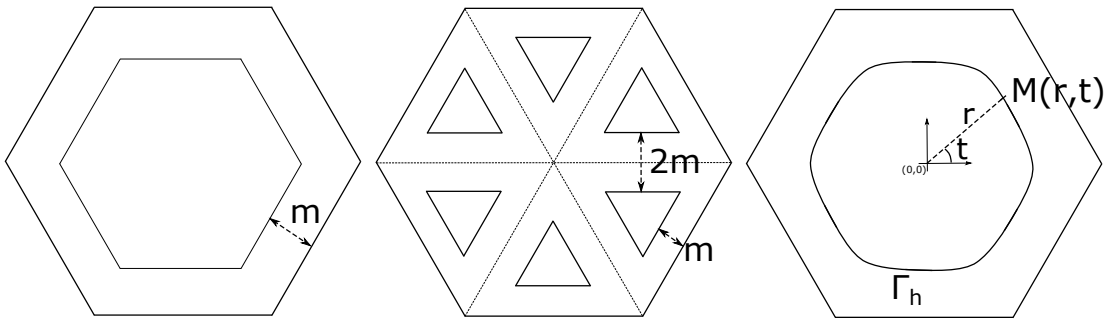

(a) classical honeycomb (b) Reinforced Honeycomb (c) Smooth Honeycomb

Figure 3.1: Periodic isotropic cells in 2D

We then get the polar equation of $\mathcal{H}$:

$$r(t) = \frac{\sqrt{3}}{2}(\max_i |v(t) \cdot n_i|)^{-1} .$$

Let us recall that:

$$(\sum_{i=0}^{2} |v(t) \cdot n_i|^p)^{-\frac{1}{p}} \to_{p \to +\infty} \max_i |v(t) \cdot n_i| .$$

The polar equation of Γ_h comes from combining the polar equation of $\mathcal{H}$ and the above limit. The scalar parameter h is added in order to adjust the diameter of the inner hole.

The interest of this design relies on its smooth rounded corners. Indeed, sharp corners are known in mechanics to concentrate high stress. Smooth corners will generate lower local concentration of stress, see [Neuber 1961], for the impact of smooth rounded corners on the performances in fatigue, see also [Abad 2013].

Remark 4. *Those cells are qualitatively similar to the celebrated Vigdergauz hexagonal cells [Vigdergauz 1999], which are known to be extremal composites in the sense that they minimize the energy. However, for practical issues, we do not implement the Vigdergauz composites: the hole boundary is described through a complex parametrization. Moreover, we do not claim that our smooth honeycomb cells reach particular elastic properties. Our only goal consisted in reducing the stress concentration, localized around the sharp corners of the classical honeycomb.*

Tetrakaidecahedron. In 3D, isotropic cells are less easy to design. The most known one is the regular tetrakaidecahedron, also called Kelvin foam, (in [Li 2006]n, it is numerically shown to yield an isotropic homogenized Hooke's law). Other isotropic cells, with particular properties, have been designed, like sequential laminates in [Francfort 1986]. But for our purpose, an easily parametrizable cell is required. That is why, we focus on the tetrakaidecahedron cell.

A unit tetrakaidecahedron features fourteen faces: six unit squares and eight regular unit hexagons, see Figure 3.2. Several approaches are possible in order to design a parametrized isotropic cell from this one, whose density range is $[0; 1]$. A naive approach consists in adding a central tetrakaidecahedron inclusion, whose characteristic size is going from 0 to 1. However, we keep in mind that the final structure has to be manufacturable using additive manufacturing processes, including metallic ones. No inclusion is permitted because metal powder would be trapped inside during the process and could not be removed at the end. Then, the cell should be drilled from end to end. Hence, through holes are drilled from each face to its opposite face, see Figure 3.3. As previously, we introduce a single parameter $m \in [0; 1]$ to characterize the cell: it is the ratio of the homothety between the hole in a face and the external border of this face, the same for all faces. When $m = 0$, there is no hole and the cell is full. When $m = 1$, the hole occupies all the faces and the cell is completely void.

3.2.2 Homogenized Hooke's laws of the microstructures

Let Y be the periodic cell pattern: either the regular hexagon in 2D or the regular tetrakaidecahedron in 3D, and not a square or a cube. The periodicity of the cells is defined by the same displacement on two opposite and parallel faces. Hence, in 2D for hexagonal cells, there are

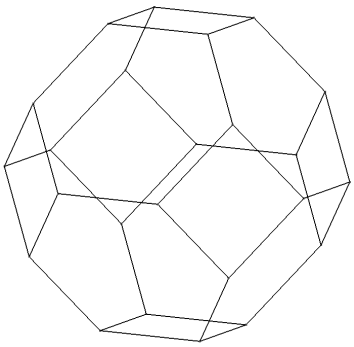

Figure 3.2: Tetrakaidecahedron

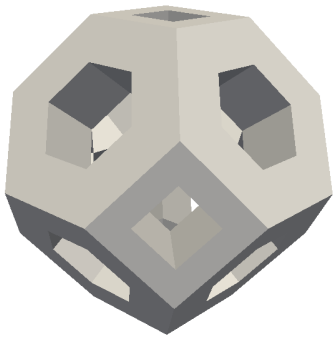

Figure 3.3: Periodic isotropic cells in 3D

classical honeycomb – Reinforced honeycomb – Smooth honeycomb – Kelvin foam

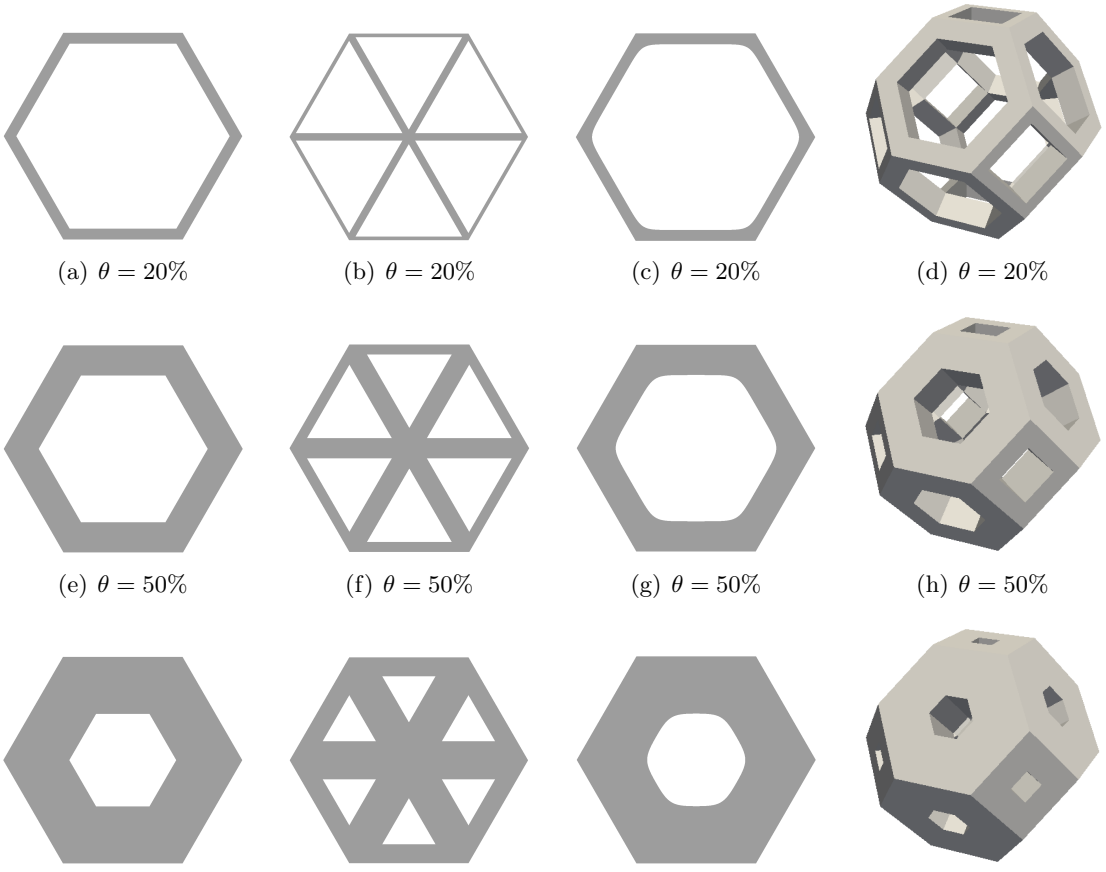

(a) $\theta = 20\%$ (b) $\theta = 20\%$ (c) $\theta = 20\%$ (d) $\theta = 20\%$

(e) $\theta = 50\%$ (f) $\theta = 50\%$ (g) $\theta = 50\%$ (h) $\theta = 50\%$

(i) $\theta = 80\%$ (j) $\theta = 80\%$ (k) $\theta = 80\%$ (l) $\theta = 80\%$

Figure 3.4: Periodic isotropic cells according to their density θ

three directions of periodicity, and in 3D for the tetrakaidecahedron cell, there are seven directions of periodicity. Let Y_0 be the solid domain in Y, Γ_{int} be the boundary of the holes, and n its normal vector. Let $|Y|$ be the volume of Y.

Let A be the constant elasticity tensor of the isotropic solid phase. Let μ be its shear modulus, κ its bulk modulus and $\lambda = \kappa - \frac{2\mu}{N}$ its Lamé coefficient. Hence A is defined by:

$$A = 2\mu I_{2N} + \lambda I_N \otimes I_N \,.$$

Let a given macroscopic domain be periodically tiled with cells εY_0, where $\varepsilon > 0$ is the periodicity size. When $\varepsilon \to 0$, the periodic medium can be considered homogeneous, with an effective elasticity tensor A^*.

As seen in (Part 1 chapter 2), the coefficients of the homogenized tensor A^* are given by:

$$A^*_{ijkl} = \frac{1}{|Y|}\int_{Y_0} A(e_{ij} + e(w_{ij}) : (e_{kl} + e(w_{kl})dy \quad \forall i,j,k,l \in \{1,..N\}\,, \tag{3.5}$$

where w_{ij} are the so-called correctors, solutions of the following cell problems:

$$\begin{cases} \text{div}(A(e_{ij} + e(w_{ij})) = 0 & \text{in } Y_0 \\ A(e_{ij} + e(w_{ij})n = 0 & \text{on } \Gamma_{\text{int}} \\ y \mapsto w_{ij}(y) & Y_0\text{-periodic} \end{cases}, \tag{3.6}$$

with $e_{ij} = \frac{1}{2}(e_i \otimes e_j + e_j \otimes e_i)$, a basis of the symmetric tensors of order 2. We emphasize that in (3.5), the coefficients are divided by the area of the periodic cell Y. Generally, the periodic cell is taken unitary, in order to bypass this point. But with complicate cells like the tetrakaidecahedron, one could prefer to design a cell whose characteristic length is equal to 1. If so, one should not forget to rescale the computed coefficients.

We recall that the homogenized elasticity tensor A^* is isotropic. Hence, its Hooke's law A^* is given by:

$$A^* = 2\mu^* I_{2N} + \lambda^* I_N \otimes I_N \,,$$

where μ^* is the homogenized shear modulus and λ^* the homogenized Lamé coefficient. The homogenized bulk modulus is defined by: $\kappa^* = \lambda^* + \frac{2\mu^*}{N}$. Then, these homogenized coefficients are also given by:

$$\begin{cases} \mu^* &= A^*_{ijij} \\ \lambda^* &= A^*_{iijj} \\ \kappa^* &= A^*_{iijj} + \frac{2}{N}A^*_{ijij} \end{cases} \qquad \forall i,j \in \{1,..,N\} \text{ such that } i \neq j\,. \tag{3.7}$$

Hashin-Shtrikman bounds. As seen in (Part 1, Chapter 2), the bulk and the shear moduli of any isotropic two-phase composite material are bounded by the Hashin Shtrikman bounds [Hashin 1963]. Here, the first isotropic phase is the phase A in proportions θ, and the second is void, in proportions $1-\theta$. The upper bounds μ_{HS} and κ_{HS} for the homogenized shear and bulk moduli are respectively:

$$\forall \theta \in [0;1] \quad \begin{cases} \mu^*(\theta) &= \mu\theta \dfrac{(N^2+N-2)(2\mu+\lambda)-2(N-1)(\kappa+2\mu)}{(N^2+N-2)(2\mu+\lambda)-\theta(N-1)(\kappa+2\mu)} \\ \kappa^*(\theta) &= \kappa\theta \dfrac{\mu}{2\mu+\lambda-\kappa\theta} \end{cases} . \tag{3.8}$$

Numerical results. We recall that each cell is parametrized by its density θ. The set of effective elasticity tensors $\{A^*(\theta)|\theta \in L^\infty(D,[0,1])\}$ has to be characterized. The homogenized Lamé coefficients are computed for a discrete sample of parameters values. From those data, a surrogate model for the constitutive law is then constructed by linear interpolation.

Since considered cells $Y_0(\theta)$ are specifically chosen in order to design an isotropic homogenized media, only two coefficients of A^*, for example A^*_{1122} and A^*_{1212}, could be computed in order to fully characterize the effective tensor A^*. However, all the coefficients have been computed, in order to confirm numerically the isotropy.

The range of the density θ is regularly discretized with 50 elements, in 2D and with 20 elements in 3D. The cell's problems (3.6) are solved using the finite element solver FreeFem++ [Hecht 2012] for each value of the discretized density. Eventually, the homogenized tensor $A^*(\theta)$ is computed with (3.5).

The Young modulus of the solid phase A is $E = 15$ GPa and its Poisson's ratio is $\nu = 0.35$. The void (when $\theta = 0$) is replaced by an ersatz material, in order to avoid undefined tensor when the elasticity problem is solved. Its elasticity tensor is equal to 0.01% of the tensor of the solid phase A.

The isotropy implies some equalities between the coefficients of A^*:

$$\forall i,j,k,l,p \in \{1,..,N\} \quad \begin{cases} A^*_{iijk} = 0 \\ A^*_{iiii} = A^*_{jjjj} \\ A^*_{iijj} = A^*_{kkll} \\ A^*_{iiii} = A^*_{jkjk} + A^*_{llpp} \end{cases} . \tag{3.9}$$

The associated relative errors to those equalities have been computed for each design of cell and all the samples of density. For the classical honeycomb and for the reinforced one, the errors are lower than 10^{-3}, and for the smooth honeycomb, the errors are lower than 10^{-4}. These values are low enough to be imputed to numerical errors. The isotropy of the honeycomb cells is confirmed.

The homogenized bulk modulus κ^* and the homogenized shear modulus μ^* are respectively displayed on Figures 3.5(a) and 3.5(b). As a reference, the upper Hashin-Shtrikman bound (3.8) is also displayed. In each case, the moduli are smooth increasing functions of the density: the more material, the stronger the cell. This behaviour according to the density ensures that the optimization algorithms will converge. In the case of the bulk modulus, the classic and the smooth honeycomb cells are very closed to the upper Hashin-Shtrikman bound. The bulk modulus of the reinforced honeycomb is a bit lower. The upper bound of the shear modulus is clearly respected by all the kinds of hexagonal cells. The shear moduli of the classic and the smooth honeycombs are both very closed and a bit lower than the reinforced honeycomb. Indeed, the reinforced honeycomb features diagonals which greatly help to support the shear.

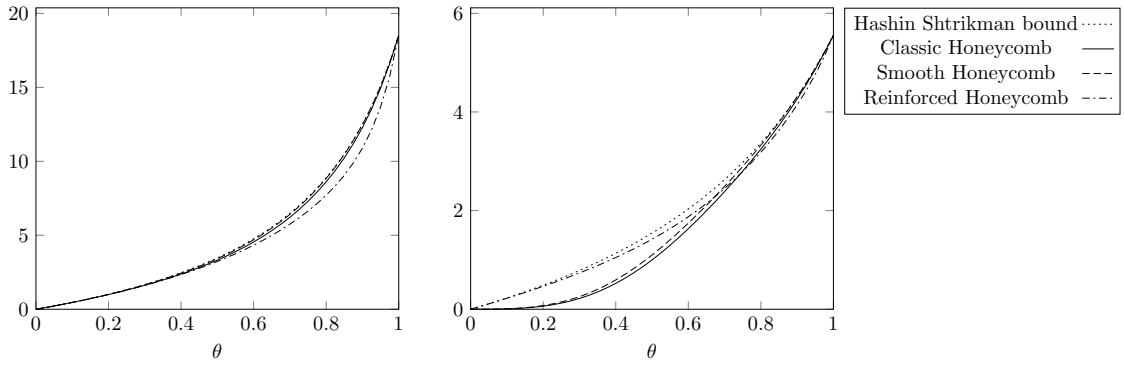

(a) $\kappa^*(\theta)$ (b) $\mu^*(\theta)$

Figure 3.5: Homogenized bulk (left) and shear (right) moduli in 2D for the several kinds of hexagonal cells

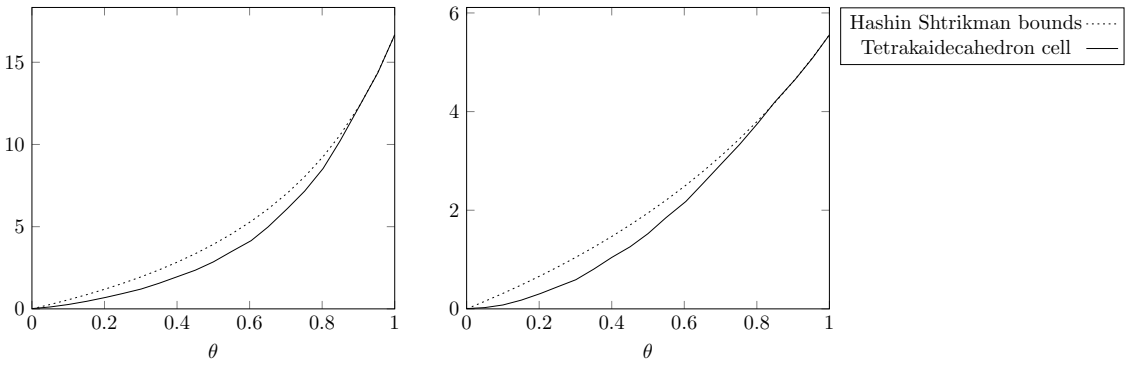

(a) $\kappa^*(\theta)$ (b) $\mu^*(\theta)$

Figure 3.6: Homogenized bulk (left) and shear (right) moduli in 3D for the tetrakaidecahedron cells

For the tetrakaidecahedron (in 3D), the homogenized bulk modulus κ^* and the homogenized shear modulus μ^* are respectively displayed on Figures 3.6(a) and 3.6(b). The upper bound of Hashin Shtrikman, given by (3.8) are also displayed on those Figures. The computed homogenized elastic moduli satisfy the upper bound.

3.2.3 Correctors matrices

The microscopic heterogeneities may cause stress concentration. The real stress distribution is different from the macroscopic homogenized stress.

This is due to the fact that the stress for a microstructure of size ε, denoted by σ_ε does not converge strongly to $(A^*e(u^*))$ when ε is going to zero.

As seen in Chapter 2, a stress amplification factor may be introduced in order to compute a L^2-norm criteria on the stress. This is not a pointwise maximum, as it could requested for

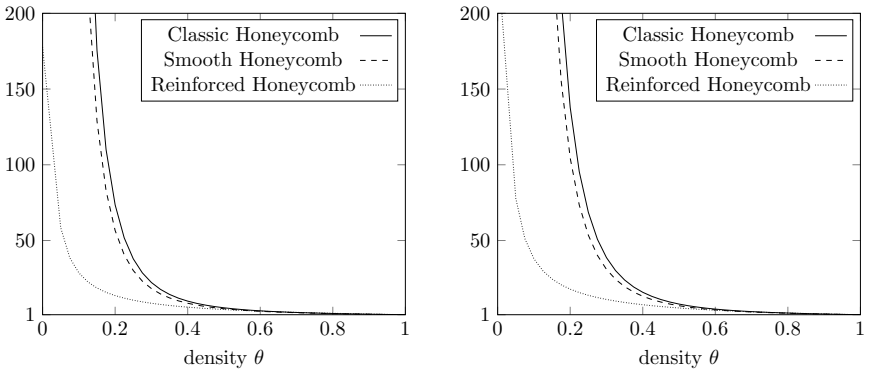

(a) P^*_{1111}, for compression load (b) P^*_{1212}, for shear load

Figure 3.7: L^2- norm of the corrected stress depending on the density of the microstructures

example to know if the material is plastic not.

We recall from Section 2.1.6 of Chapter 2, that the coefficients of the corrector tensor W are given by:

$$W_{ijkl} = I^4_{ijkl} + e(w_{ij})_{kl}\,,$$

where w_{ij} is the solution of the cell problem (3.6).

Let $P^*(\theta)$ be the amplification tensor defined by:

$$P^*(\theta) = \frac{1}{|Y|}\int_{Y_0} AW(y)A^*(\theta)^{-1}AW(y)A^*(\theta)^{-1}\,dy\,, \tag{3.10}$$

see Section 2.1.6 of Chapter 2 for more details.

Numerical results The amplification tensor $P^*(\theta)$ has been computed in 2D for the three isotropic microstructures, on the same scheme than their homogenized elasticity tensor A^*.

Let $\sigma_1 = 1.e_{11}$ be a unit stress in direction x_1, and $\sigma_2 = \frac{1}{\sqrt{2}}(e_{12}+e_{21})$ be a unit shear stress. Their L^2-norms are equal to one on a unit square. Let a unit square be fulfilled with the above isotropic microstructures. We assume that the homogenized stress tensor is equal respectively to σ_1 and σ_2. The L^2- norm of the corrected stresses can be computed using the amplification tensor P^*: their values are respectively given by P^*_{1111} and by P^*_{1212}. It has been computed for several densities of the microstructures.

The results are displayed on Figures 3.7(a) and 3.7(b). For small densities, the corrected stress norm blows up: the local stress in the thin bars can not be approximated by the homogenized stress. For high densities, the corrected stress norm converges to one, which is the homogenized stress norm. The amplification factor is the lower for the reinforced honeycomb. One can check that the correction factor is smaller for the smooth honeycomb than for the classical honeycomb. Indeed the smooth rounded corners concentrate lower stresses than sharp corners.

3.3 Optimization with isotropic cells

Let $J^*(\theta)$ the relaxed cost function for composite material, made of one kind of the previous isotropic cells, and so, parametrized by its density θ. In all the cases, the volume is constrained to be equal to V. Hence the minimization problem reads as:

$$\min_{\int_D \theta = V} J^*(\theta)\,. \tag{3.11}$$

3.3.1 Minimization of the compliance: single load case

The objective is to find the most rigid structure, made of isotropic composite material, when the structure is submitted to a given load. The cost function is here the compliance of the structure:

$$J^*(\theta) = \int_{\Gamma_N} g \cdot u^* ds = \min_{\tau \in H_0} \int_D A^{*-1}\tau : \tau dx\,,$$

where

$$H_0 = \left\{ \tau \in L^2(D, \mathcal{M}_N^s) \text{ such that } \begin{array}{l} \operatorname{div}(\tau) = 0 \text{ in } D \\ \tau n = g \text{ on } \Gamma_N \\ \tau n = 0 \text{ on } \Gamma \end{array} \right\}.$$

The optimization problem can be recast as a minimization problem over the stress field σ and the density field θ of the microstructure:

$$\begin{array}{c} \inf \\ \sigma \in H_0 \\ \theta \in L^\infty(D,[0,1]) \\ \int_D \theta = V \end{array} \quad \int_D A^{*-1}(\theta)\sigma : \sigma dx\,.$$

This problem is solved by an alternate minimization algorithm [Allaire 2002a], minimizing successively with respect to the stress field σ and to the density θ of the microstructure. It is an algorithm of type *Optimality criteria*. The corresponding Lagrangian is introduced:

$$\mathcal{L}(\theta, \sigma, \ell) = \int_D A^{*-1}(\theta)\sigma : \sigma dx + \ell(\int_D \theta dx - V)\,, \tag{3.12}$$

where ℓ is the Lagrange multiplier associated to the volume constraint.

Stress field. Minimizing with respect to the stress field σ for a given density θ, and so for a given design of the structure, consists in solving the elasticity problem with a material of elasticity tensor equal to $A^*(\theta)$ in D.

Let V_D be the set defined by:

$$V_D = \{v \in H^1(D, \mathbb{R}^2) \text{ such that } v = 0 \text{ on } \Gamma_D\} \tag{3.13}$$

The elasticity problem can be recast as a variational formulation:

$$\forall v \in V_D \quad \int_D A^*(\theta)e(u) : e(v)dx = \int_{\Gamma_N} g \cdot v ds\,.$$

Numerically, we use P_1 finite elements to compute the displacement u.

Density field. For a given stress field σ, the minimization with respect to the density θ is performed using the projected gradient algorithm. Since the problem is self-adjoint, the descend direction is given by the derivative of $\mathcal{L}$ with respect to θ:

$$\left\langle \frac{\partial \mathcal{L}}{\partial \theta}(\theta, \sigma, \ell), h \right\rangle = -\int_D (\frac{\partial A^*}{\partial \theta}(\theta) A^{*-1}(\theta)\sigma : A^{*-1}(\theta)\sigma - \ell) h dx \,.$$

The descent direction $h = d\theta$ has to be selected such that:

$$\left\langle \frac{\partial \mathcal{L}}{\partial \theta}(\theta, \sigma, \ell), d\theta \right\rangle < 0 \,,$$

which is achieved by choosing

$$d\theta = \frac{\partial A^*}{\partial \theta}(\theta) A^{*-1}(\theta)\sigma : A^{*-1}(\theta)\sigma - \ell \quad \text{in } D \,.$$

At iteration n the density is updated by:

$$\theta^{n+1} = P_{|0,1|}(\theta^n + p d\theta) \,, \tag{3.14}$$

where $p > 0$ is the step size and $P_{|0,1|}$ is the projection operator on the interval $[0; 1]$.

The value of the Lagrange multiplier ℓ is computed at each iteration by a dichotomy process designed to respect the volume constraint. Indeed the volume constraint has to be respected at each iteration. We emphasize that the exact value of ℓ to respect the volume constraint can not be analytically given, because of the projection operator on the density.

Numerically, the partial derivative for the Lagrangian, denoted by $\frac{\partial \mathcal{L}}{\partial \theta}$ is regularized using a H^1 equivalent norm, by solving the following variational formulation:

$$\forall h \in H^1(D, \mathbb{R}) \quad \int_D (\frac{\partial \mathcal{L}}{\partial \theta} h + \eta^2 \nabla \frac{\partial \mathcal{L}}{\partial \theta} \cdot \nabla h) dx = -\int_D (\frac{\partial A^*}{\partial \theta}(\theta) e(u) : e(u) - \ell) h dx \,,$$

where $\eta > 0$ is a small coefficient, which typically depends on the size of the elements of the mesh. The purpose of this small coefficient is to numerically regularize the partial derivative on a length scale of order η and to limit the checkerboard effect. In practice, we use an adaptive step size p. At each iteration, if the newly computed homogenized structure is accepted (i.e. if its compliance is lower than the one of the previous structure), the step size p is increased of 20%. On the contrary, if it is rejected, the step size is divided by 2.

Algorithm. Here is the complete optimization algorithm:

1. Initialization of the density θ in order to respect the volume constraint:

$$\forall x \in D \quad \theta^0(x) = \frac{V}{\int_D 1 dx}$$

2. Iteration until convergence, for $n \geq 0$:

   (a) Computation of σ^n through a problem of linear elasticity with $A^*(\theta^n)$ as elasticity tensor.

   (b) Updating the density θ^{n+1} using (3.14).

Numerical results The above algorithm has been implemented in FreeFem++, [Hecht 2012]. All the unknowns are discretized using P_1 finite elements.

The test case here is a cantilever. The domain size is 20×20. The structure is clamped on a central segment of length 10 on its left boundary. A unit vertical load is applied on a central segment of length 1 on its right boundary. The boundary conditions are displayed on Figure 3.8. The volume constraint is fixed to 23% of the working domain. The three isotropic microstructures have been tested, and also the material corresponding to the upper bound of Hashin-Shtrikman, as a reference for the other tests.

The convergence history is displayed on Figure 3.9. The algorithm converges quickly and smoothly for each microstructure. We emphasize that the lower curve corresponds to the upper bound of Hashin-Shtrikman. It reaches the lowest compliance. The optimized compliance for the three other microstructures are almost equal to each other.

The optimized densities for each microstructure is displayed on Figure 3.10. The structure with the upper bound of Hashin-Shtrikman still features grey material. But the structures with the three isotropic microstructures are autopenalized: they are black and white structures. The structures with respectively the classic and the smooth honeycomb microstructures are quite similar. This can be explained by the fact that their homogenized elasticity tensor are very closed, as seen in the previous Section. The structure with the reinforced honeycomb is very different from them : it recalls the structure with the upper bound of Hashin-Shtrikman. Indeed, its homogenized elasticity tensor is quite closed to the upper bound of Hashin-Shtrikman. The optimized path could possibly be similar in the both cases, even if the reinforced honeycomb finally autopenalized.

We emphasize that those structures are local minima, which explains the difference kind of autopenalized structures. This is no limitation of the method.

The fact that optimized structures for real isotropic microstructures are autopenalized suggests that those microstructures are not optimal for the compliance minimization problem in single load cases. Indeed, the local microstructure has to be designed in order to support the stress in privileged directions, namely the principal directions of the stress. However, because of their isotropy, they are no stronger in a particular direction, but equally in the whole directions. In Chapter 4, we investigate orthotropic microstructures for this problem and prove their efficiency. Indeed, orthotropic microstructures can be oriented in order to align their principal directions to the ones of the stress.

For isotropic microstructures, other shape optimization problems are investigated in the following of this Chapter, in particular multiple loads test cases. Indeed, for such cases, the local microstructure should be able to support stresses in several directions. Their isotropy could then a great advantage.

3.3.2 Minimization of the compliance: multiple loads case

The objective is to find the most rigid structure on average, when the structure is submitted to n_l several loads separately. For each load i, let g_i be the surface load, applied on $\Gamma_{N_i} \subset \partial D$.

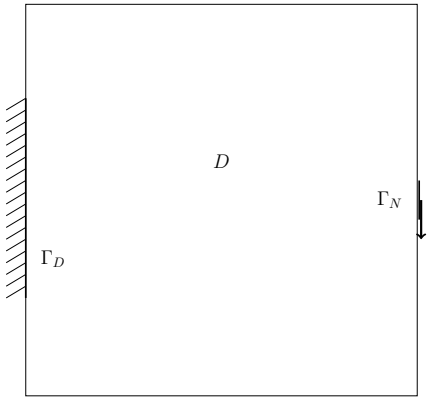

Figure 3.8: Boundary conditions for the cantilever problem

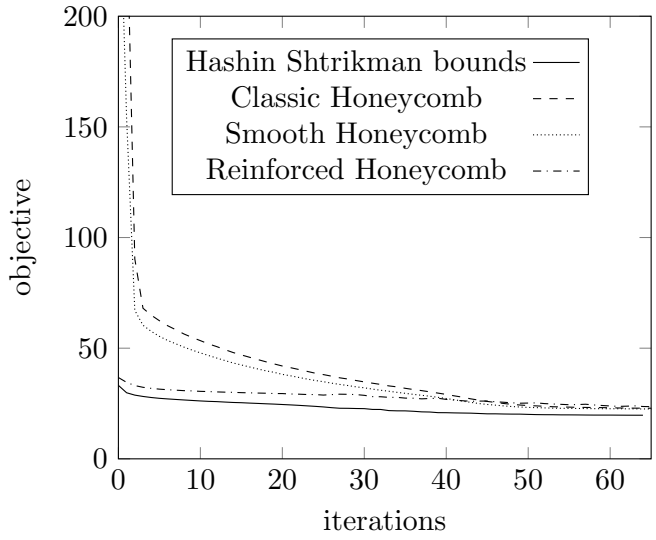

Figure 3.9: Convergence history of the objective function for the cantilever, in the single-load compliance minimization problem

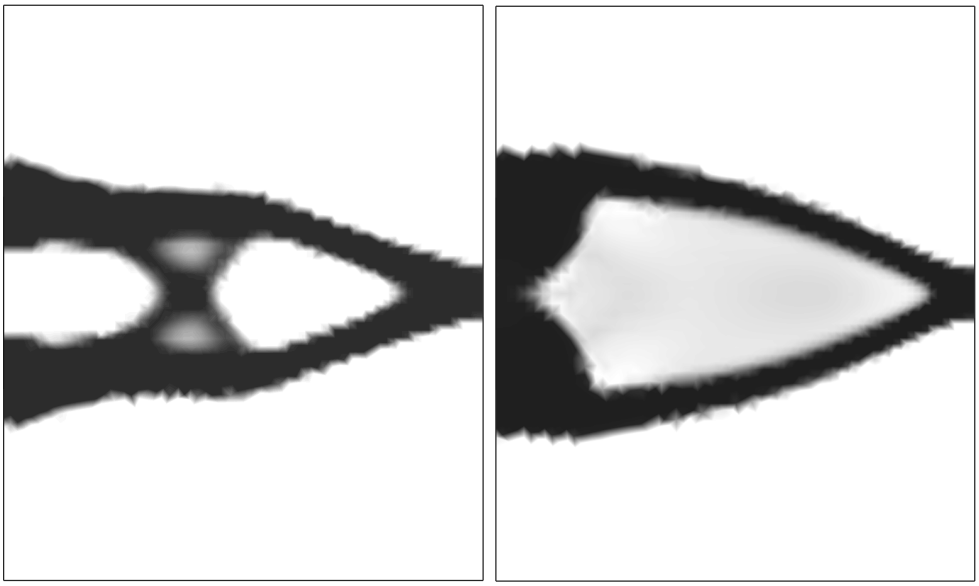

(a) classical honeycomb, $J^* = 22.86$ (b) Reinforced honeycomb, $J^* = 22.21$

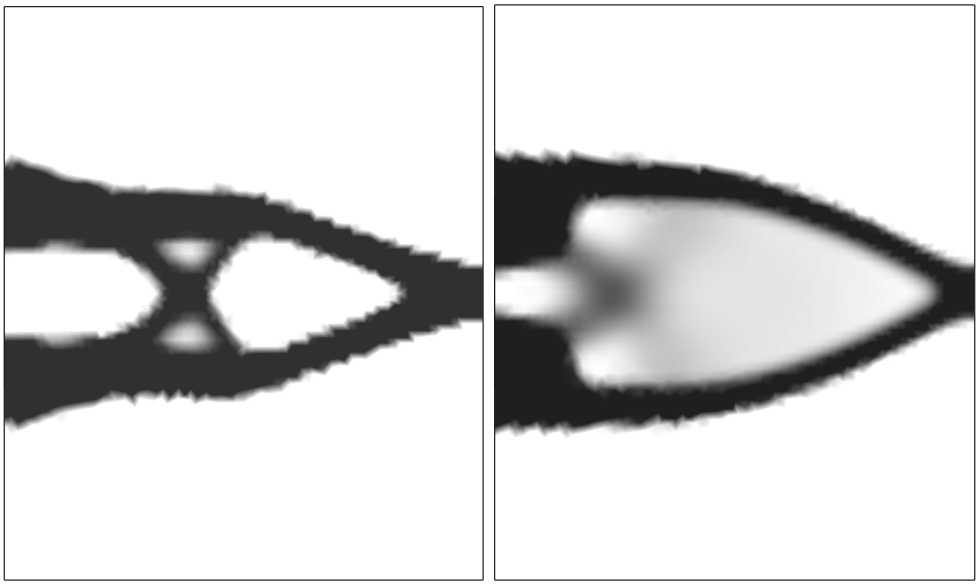

(c) Smooth honeycomb, $J^* = 22.47$ (d) Hashin Shtrikman upper bound, $J^* = 19.71$

Figure 3.10: Optimized densities for several isotropic microstructures in the cantilever test case, for the single-load compliance minimization problem

The cost function is then the sum of the compliances of the structure for each load case:

$$J^*(\theta) = \sum_{i=1}^{n_l} \int_{\Gamma_{N_i}} g_i \cdot u_i^* ds = \sum_{i=1}^{n_l} \min_{\tau \in H_{0,i}} \int_D A^{*-1}\tau : \tau dx \,,$$

where

$$H_{0,i} = \left\{ \tau \in L^2(D, \mathcal{M}_N^s) \text{ such that } \begin{array}{l} \mathrm{div}(\tau) = 0 \text{ in } D \\ \tau n = g_i \text{ on } \Gamma_{N_i} \\ \tau n = 0 \text{ on } \Gamma \end{array} \right\} .$$

As previously this optimization problem can be rescast as a minimization over the stress fields σ_i, for each load case i, and over the density field θ of the microstructure:

$$\inf_{\substack{\theta \in L^\infty(D,[0,1]) \\ \int_D \theta = V}} \sum_{i=1}^{n_l} \inf_{\sigma \in H_{0,i}} \int_D A^{*-1}(\theta)\sigma : \sigma dx \,.$$

We introduce the corresponding Lagrangian:

$$\mathcal{L}(\theta, \sigma_1, .., \sigma_{n_l}, \ell) = \sum_{i=1}^{n_l} \int_D A^{*-1}(\theta)\sigma_i : \sigma_i dx + \ell(\int_D \theta dx - V) \,, \tag{3.15}$$

with ℓ the Lagrange multiplier associated to the volume constraint.

As in the single-load case, the minimization with respect to the stress fields σ_i consists in solving the ealsticity problem for each load case i separately.

To minimize with respect to the density θ, we used a projected gradient algorithm. The problem is still self-adjoint and so he descent step is given by the partial derivative of $\mathcal{L}$ with respect to θ, namely:

$$\left\langle \frac{\partial \mathcal{L}}{\partial \theta}(\theta, \sigma_1, .., \sigma_{n_l}, \ell), h \right\rangle = \int_D \ell \, h \, dx - \sum_{i=1}^{n_l} \int_D (\frac{\partial A^*}{\partial \theta}(\theta) A^{*-1}(\theta)\sigma_i : A^{*-1}(\theta)\sigma_i) h dx \,.$$

The optimization algorithm is then identical to the previous one for single-load case, except that n_l elasticity problems have to be solved and that the descent step $d\theta$ for the density is given by:

$$d\theta = \sum_{i=1}^{n_l} \frac{\partial A^*}{\partial \theta}(\theta) A^{*-1}(\theta)\sigma : A^{*-1}(\theta)\sigma - \ell \quad \text{in } D \,.$$

Numerical results The above algorithm has been implemented in FreeFem++ for a bridge case. The domain size is 22×13. The structure is clamped on symmetric segments of length 1 on the bottom border. Unit vertical loads are applied separately on segments of length 1 on the bottom border. The boundary conditions are displayed on Figure 3.11. The volume constraint is fixed to 10% of the working domain. As previously, the three isotropic microstructures have been tested, and also the material corresponding to the upper bound of Hashin-Shtrikman, as a reference for the other tests.

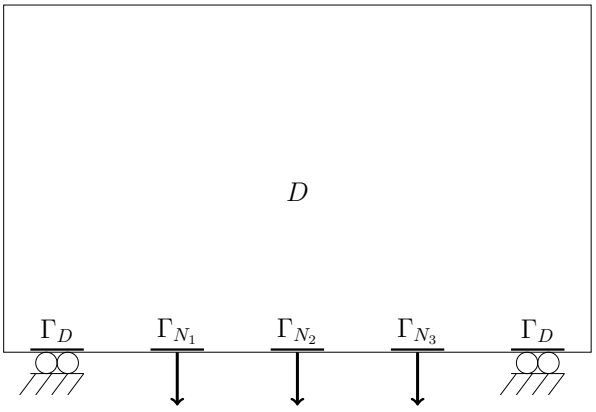

Figure 3.11: Boundary conditions for the bridge with multiple loads

The convergence history is displayed on Figure 3.12. The algorithm converges quickly and smoothly for each microstructure. We emphasize that the lower curve corresponds to the bound of Hashin-Shtrikman. It reaches the lowest compliance. The optimized compliance for the three other microstructures are almost equal to each other.

The opitmized densities for each microstructure is displayed on Figure 3.13. The structures with respectively the classic and the smooth honeycomb microstructures are again quite similar. The structure with the reinforced honeycomb is very different from them : it recalls the structure with the upper bound of Hashin-Shtrikman. Each optimized structure features grey densities. They are not autopenalized. Hence the isotropic microstructures seem to be efficient microstructure for compliance minimization in multiple loads cases. That can be explained by the fact that the local microstructure should be able to support stresses in several directions, namely the principal directions of the stress for each load. Their isotropy is then a great advantage.

We emphasize that the lower compliance is reached by the upper bound of Hashin-Shtrikman. This seems legit, since the upper bound are for the more rigid isotropic material for a gievn density. The reinforced honeycomb microstructure reachs the second lower optimized compliance. This microstructure is more rigid thant the classical honeycomb. It should a priori be preferred fot compliance minimization problems.

We also implemented this algorithm for 3D cases. Two different load cases have been tested, they are displayed on Figure 3.14.

Various iso-surfaces of the optimal density field θ for each test case are plotted respectively on Figures 3.15 and 3.16. The optimized structure is clearly not a black and white design. High densities are reached only around where Dirichlet and Neumann boundary conditions are applied. The major part of the domain is filled with intermediate or grey densities.

3.3.3 Displacement optimization

The objective function is given by:

$$J^*(\theta) = \int_{\Gamma_T} (u^* - u_T)^2 dx \,.$$

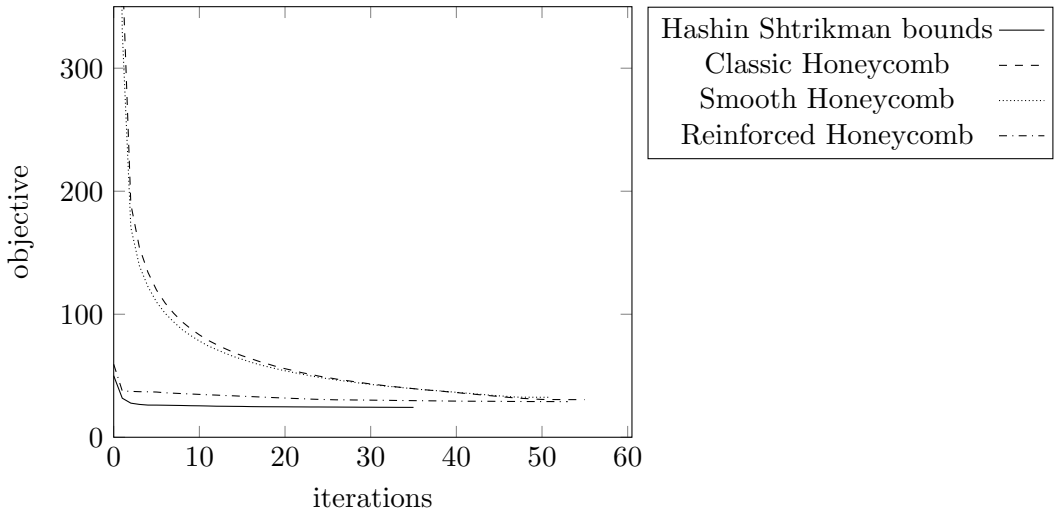

Figure 3.12: Convergence history of the objective function for the multiple loads test case, in compliance minimization problem

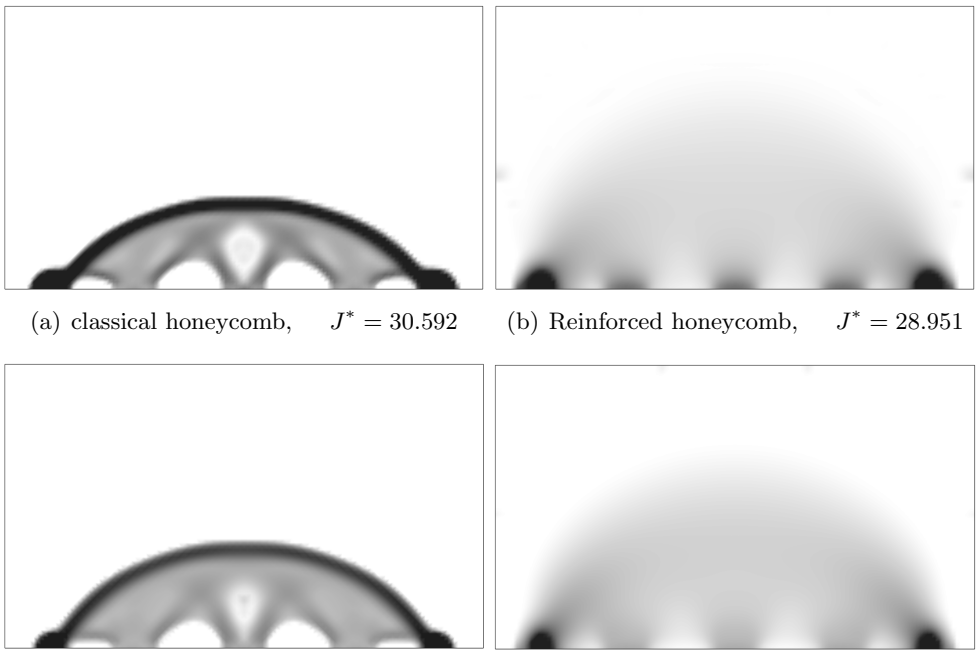

(a) classical honeycomb, $J^* = 30.592$ (b) Reinforced honeycomb, $J^* = 28.951$

(c) Smooth honeycomb, $J^* = 32.508$ (d) Hashin Shtrikman upper bound, $J^* = 24.285$

Figure 3.13: Optimized density for the multiple loads test case, in the compliance minimization problem

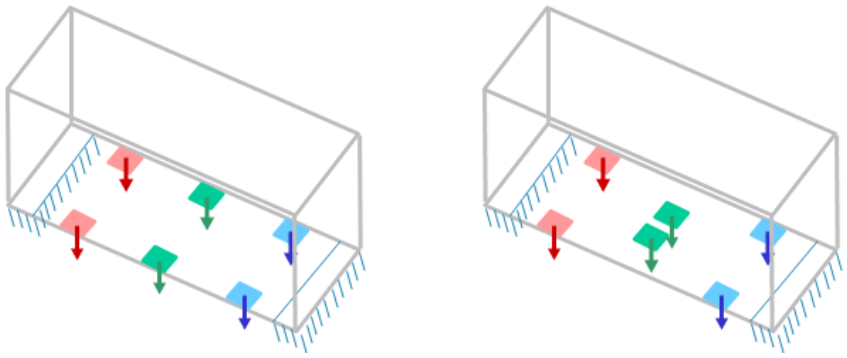

(a) First test case (b) Second test case

Figure 3.14: Load cases for the 3D multiple loads test case, each color of the loads is applied separately

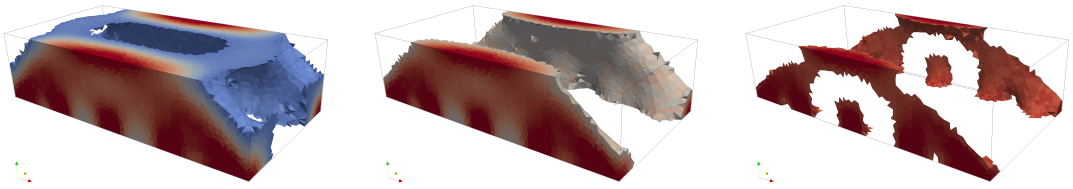

(a) $\theta \leq 15\%$ (b) $\theta \leq 50\%$ (c) $\theta \leq 85\%$

Figure 3.15: Threshold of the domain according to the optimized density θ for the first test case, in the multiple loads compliance minimization problem

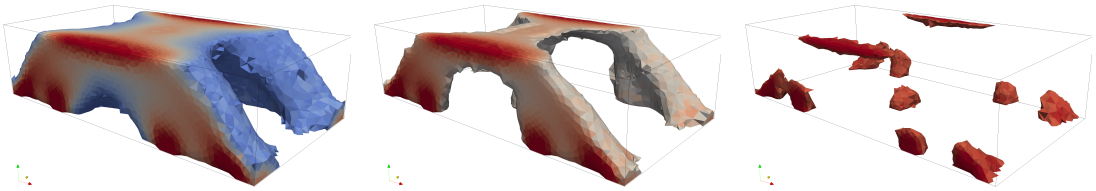

(a) $\theta \leq 15\%$ (b) $\theta \leq 50\%$ (c) $\theta \leq 85\%$

Figure 3.16: Threshold of the domain according to the optimized density θ for the second test case, in the multiple loads compliance minimization problem

where u_T is a target displacement.

This problem, contrary to the compliance minimization problem, is not self-adjoint. In order to define the associated adjoint problem, we use the Céa method. First, we introduce the following Lagrangian:

$$\mathcal{L}(v,q,\theta,\ell) = \int_D A^*(\theta)e(v) : e(q)dx - \int_{\Gamma_N} g\cdot q\,dx + \int_{\Gamma_T}(v-u_T)^2dx + \ell(\int_D \theta dx - V)\,, \quad (3.16)$$

where $q \in H^1_{\Gamma_D}(D)^N$ plays the role of the Lagrange multiplier for the elasticity equation, seen as a constraint and $\ell \in \mathbb{R}$ the Lagrange multiplier for the volume constraint. Second, we compute the partial derivatives of $\mathcal{L}$. We note (u,p) a stationary point of $\mathcal{L}$.

The partial derivative of $\mathcal{L}$ with respect to q in the direction $\psi \in H^1_{\Gamma_D}(D)^N$ is given by:

$$< \frac{\partial \mathcal{L}}{\partial q}, \psi >= \int_D A^* e(v) : e(\psi) - \int_{\Gamma_N} g\cdot\psi\,dx\,. \quad (3.17)$$

At the stationary point (u,p), this derivative is equal to zero and leads to the variational formulation of the elasticity problem.

The partial derivative of $\mathcal{L}$ with respect to v in the direction $\psi \in H^1_{\Gamma_D}(D)^N$ is given by:

$$< \frac{\partial \mathcal{L}}{\partial v}, \psi >= \int_D A^* e(\psi) : e(q) + \int_{\Gamma_T} 2\psi(v-u_T)dx\,. \quad (3.18)$$

At the stationary point (u,p), this derivative is equal to zero and leads to the adjoint problem:

$$\forall \psi \in H^1_{\Gamma_D}(D)^N \quad \int_D A^* e(p) : e(\psi) = -\int_{\Gamma_T} 2\psi(u-u_T)dx\,. \quad (3.19)$$

The partial derivative of the Lagrangian $\mathcal{L}$ with respect to the density θ of the microstructure, at the stationary point (u,p) is given by:

$$< \frac{\partial \mathcal{L}}{\partial \theta}(u,p,\theta,\ell), h >= \int_D (\frac{\partial A^*}{\partial \theta}(\theta)e(u) : e(p) + \ell)h\,dx \quad (3.20)$$

The descent direction $h = d\theta$ has to be selected such that:

$$\left\langle \frac{\partial \mathcal{L}}{\partial \theta}(u,p,\theta,\ell), d\theta \right\rangle < 0\,,$$

which is achieved by choosing

$$d\theta = -\frac{\partial A^*}{\partial \theta}e(u) : e(p) - \ell \quad \text{in } D\,.$$

At iteration n the density is updated by:

$$\theta^{n+1} = P_{|0,1|}(\theta^n + pd\theta)\,,$$

where $p > 0$ is the step size and $P_{|0,1|}$ is the projection operator on the interval $[0;1]$.

The value of the Lagrange multiplier ℓ is computed at each iteration by a dichotomy process designed to respect the volume constraint.

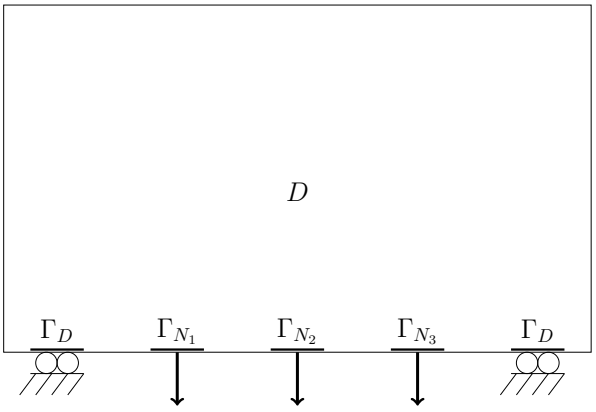

Figure 3.17: Boundary conditions for the gripping mechanism

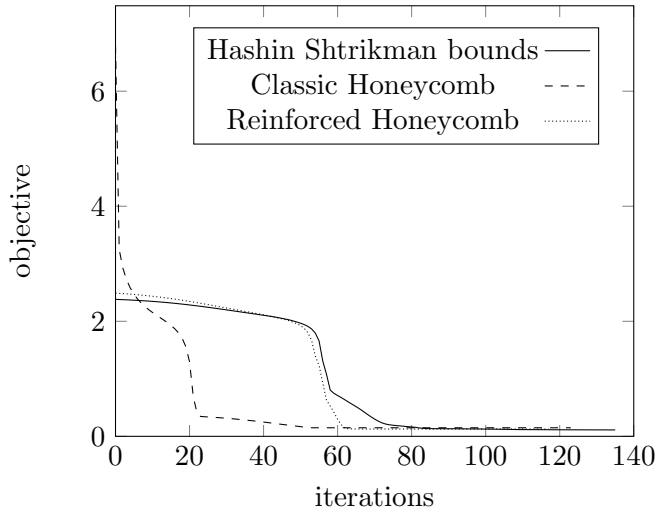

Figure 3.18: Convergence history of the objective function for the displacement optimization

Numerical results The above algorithm has been implemented in FreeFem++ for a gripping mechanism. The boundary conditions are displayed on Figure 3.17. Numerically we took part of the symmetry of the structure. The black areas are not optimizable: the density is fixed to one there. A unit vertical load is applied on the right corners. The vertical target displacement is equal to two on the jaw on the left. The horizontal displacement is not constrained. The volume constraint is fixed to 20%.

The convergence history is displayed on Figure 3.18. The optimized densities for the classical honeycomb and the upper Hashin-Shtrikman bound are displayed on Figure 3.19, with the displacement of the optimized structures.

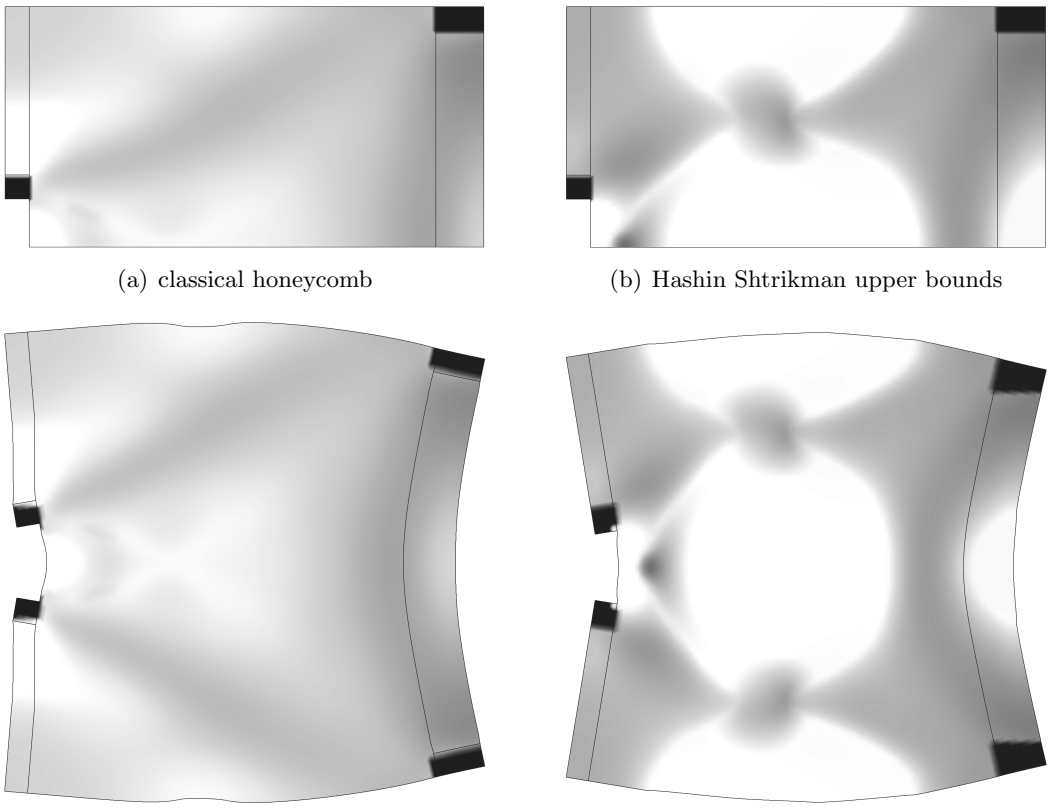

(a) classical honeycomb (b) Hashin Shtrikman upper bounds

(c) classical honeycomb (d) Hashin Shtrikman upper bounds

Figure 3.19: Optimized structures for the displacement optimization (top) and their displacement (bottom)

3.3.4 Stress minimization

The objective function is given by:

$$J^*(\theta) = \int_D P^*(\theta)\sigma : \sigma \, dx = \int_D P^*(\theta)A^*(\theta)e(u) : A^*(\theta)e(u) \, dx \,,$$

where P^* is the corrector tensor defined by (3.10), σ the stress tensor, solution of the elasticity problem and u the displacement.

In order to define the associated adjoint problem, we use the Céa method. Let $\mathcal{L}$ be the Lagrangian defined by:

$$\mathcal{L}(v,q,\theta,\ell) = \int_D A^*(\theta)e(v) : e(q) \, dx - \int_{\Gamma_N} g \cdot q \, ds + \int_D P^*(\theta)A^*(\theta)e(v) : A^*(\theta)e(v) \, dx + \ell\Big(\int_D \theta \, dx - V\Big) \,,$$

where $q \in H^1_{\Gamma_D}(D)^N$ plays the role of the Lagrange multiplier for the elasticity equation, and $\ell \in \mathbb{R}$ the Lagrange multiplier for the volume constraint.

The partial derivative of $\mathcal{L}$ with respect to q in the direction $\psi \in H^1_{\Gamma_D}(D)^N$ is given by:

$$< \frac{\partial \mathcal{L}}{\partial q}, \psi >= \int_D A^*(\theta)e(v) : e(\psi) \, dx - \int_{\Gamma_N} q \cdot \psi \, dx \,.$$

At the stationary point, this derivative is equal to zero and leads to the variational formulation of the elasticity problem.

The partial derivative of $\mathcal{L}$ with respect to v in the direction $\psi \in H^1_{\Gamma_D}(D)^N$ is given by:

$$< \frac{\partial \mathcal{L}}{\partial v}, \psi >= \int_D A^*(\theta)e(q) : e(\psi) \, dx + 2 \int_D P^*(\theta)A^*(\theta)e(v) : A^*(\theta)e(\psi) \,.$$

At the stationary point, this derivative is equal to zero and leads to the variational formulation of the adjoint problem. Let $p \in H^1_{\Gamma_D}(D)^N$ be the adjoint.

The partial derivative of $\mathcal{L}$ with respect to θ, at the point (u,p), in the direction h is given by:

$$\begin{aligned} < \frac{\partial \mathcal{L}}{\partial \theta}(u,p,\theta,\ell), h >= & \int_D \Big(\frac{\partial A^*}{\partial \theta}(\theta)e(u) : e(p)\Big)h \, dx \\ & + \int_D \Big(\frac{\partial P^*}{\partial \theta}(\theta)A^*(\theta)e(u) : A^*(\theta)e(p)\Big)h \, dx \\ & + 2\int_D \Big(P^*(\theta)\frac{\partial A^*}{\partial \theta}(\theta)e(u) : A^*(\theta)e(u)\Big)h \, dx \\ & + \int_D \ell h \, dx \,. \end{aligned}$$

Hence, the descent direction $d\theta$ is given by:

$$\begin{aligned} d\theta = &- \frac{\partial A^*}{\partial \theta}(\theta) e(u) : e(p) \\ &- \frac{\partial P^*}{\partial \theta}(\theta) A^*(\theta) e(u) : A^*(\theta) e(p) \\ &- 2P^*(\theta) \frac{\partial A^*}{\partial \theta}(\theta) e(u) : A^*(\theta) e(u) \\ &- \ell \,. \end{aligned}$$

At iteration n the density is updated by:

$$\theta^{n+1} = P_{|0,1|}(\theta^n + p d\theta) \,,$$

where $p > 0$ is the step size and $P_{|0,1|}$ is the projection operator on the interval $[0; 1]$.

The value of the Lagrange multiplier ℓ is computed at each iteration by a dichotomy process designed to respect the volume constraint.

Numerical results The above algorithm has been implemented in FreeFem++ for a cantilever case. The domain size is 20×20. The structure is clamped on a central segment of length 10 on its left boundary. A unit vertical load is applied on a central segment of length 1 on its right boundary. The boundary conditions are displayed on Figure 3.20. The three isotropic microstructures have been tested. The bound of Hashin-Shtrikman can not be used here as reference. Indeed, the corrector tensor P^* is computed for a given microstructure. But no microstructure featuring one scale of material can reach the bounds of Hashin-Shtrikman.

The history of convergence is displayed on Figure 3.21. The algorithm converges quickly and smoothly for the three microstructures. The optimized densities are displayed on Figure 3.22. The optimized structures with classic and smooth honeycomb microstructures are autopenalized: they are black and white structure. The optimized structure with reinforced honeycomb microstructure features grey densities. However, its final stress is higher than the one of autopenalized structures. Either the optimization process is trapped in a local minimum, or the optimization is so slow for this microstructure that is not yet finished. In both cases, the optimized structure is not optimal. We emphasize that, despite what parameters we used, we never reach better structure for this microstructure. To conclude, the considered isotropic microstructures are not adapted to this problem. Other kind of microstructures, not necessarily isotropic, should be investigated.

3.3.5 Maximization of the first eigenfrequency

In order to reduce noise or avoid possible resonance with external low frequencies, the first eigenfrequency of the structure has to maximized.

We recall from Part 1 Chapter 2 that the homogenized spectral problem in linear elasticity reads to:

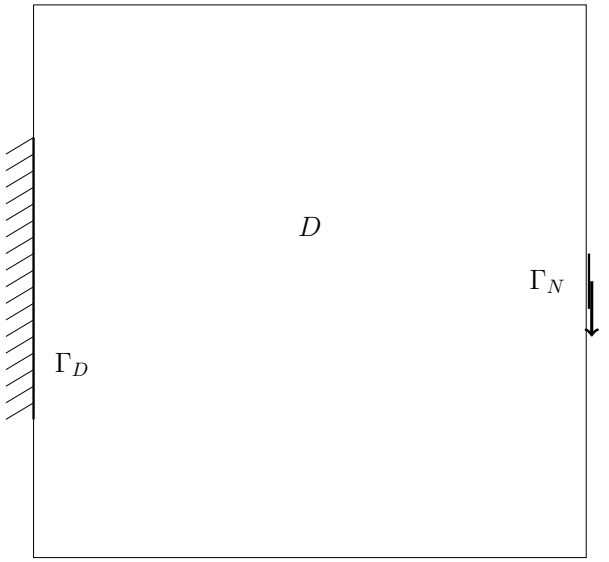

Figure 3.20: Boundary conditions for the stress minimization problem

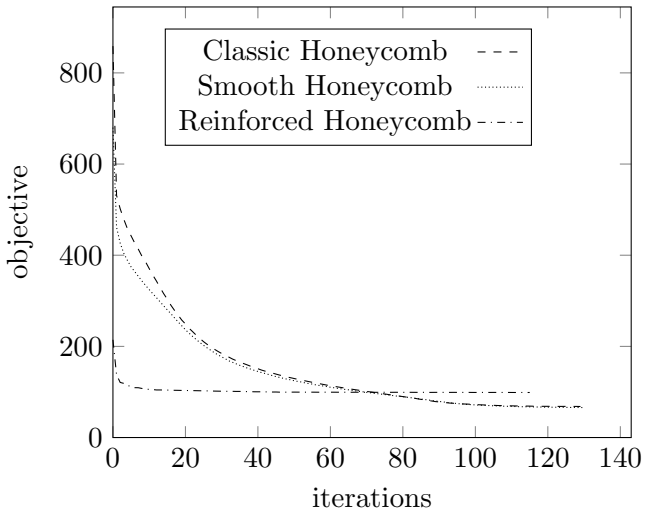

Figure 3.21: Convergence history of the objective function for the stress minimization problem

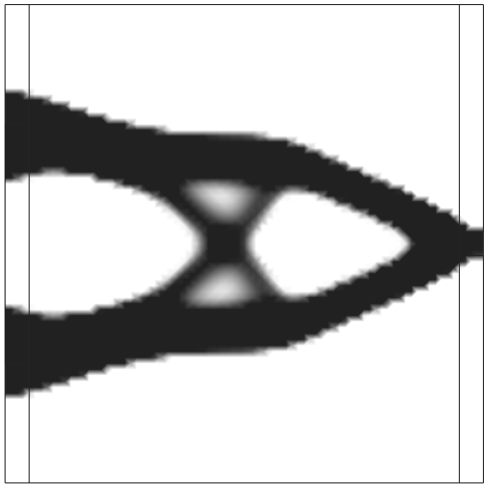

(a) classical honeycomb

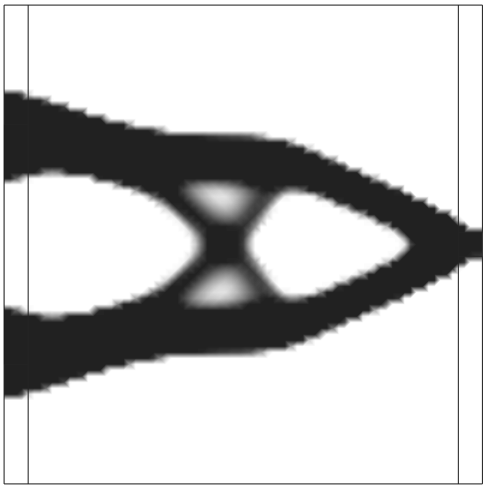

(b) Smooth honeycomb

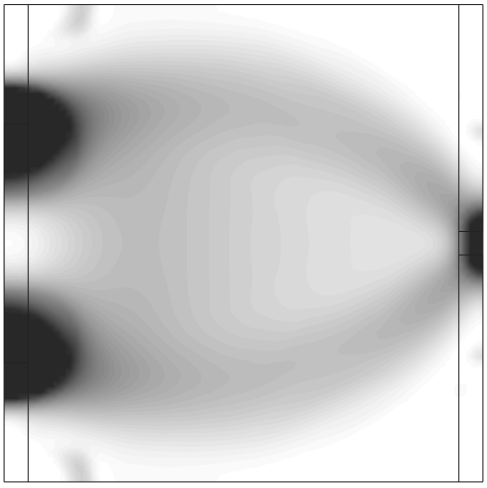

(c) Reinforced honeycomb

Figure 3.22: Optimized structures for the stress minimization

$$\begin{cases} -\operatorname{div}(A^*(x)e(u)(x)) = \omega^2\rho\theta(x)u(x) & \text{in } \Omega \\ A^*(x)e(u)ns = 0 & \text{on } \Gamma_N \\ u = 0 & \text{on } \Gamma_D \end{cases}, \tag{3.21}$$

where ρ is the material density of the phase A, in which the composite is made.

This problem admits a countably infinite family of positive eigenvalues $(\omega_i^2)_{i\in N^*}$. The first eigenvalue ω_1^2 is defined by:

$$\omega_1^2 = \min_{u\in H^1_{\Gamma_D}(D)^N} \frac{\int_D A^*(\theta)e(u) : e(u)ds}{\int_D \rho\theta|u|^2dx}.$$

Since the cost function is here $J^*(\theta) = \omega_1^2$, the optimization problems is given by:

$$\sup_{\substack{\theta\in L^\infty(D,[0,1]) \\ \int_D\theta = V}} \min_{u\in H^1_{\Gamma_D}(D)^N} \frac{\int_D A^*(\theta)e(u) : e(u)ds}{\int_D \rho\theta|u|^2dx}$$

We assume the first eigenvalue ω_1 to be simple at the current state. The cost function is Gateaux differentiable, see Lemma 5.2.16 in [Allaire 2002a]. The descent direction $d\theta$ is then given by:

$$d\theta = -\frac{1}{\int_D \rho_A\theta|u|^2}(\frac{\partial A^*}{\partial\theta}(\theta)e(u) : e(u) + \omega_1^2\rho_A|u|^2) - \ell\,,$$

where u is solution of (3.21) for the first eigenvalue ω_1, ρ_A is the massic density of the isotropic material A, which forms, with void, the microstructure.

Optimization algorithm

1. Initialization of the density
2. Iteration until convergence, for $n \geq 0$
   (a) Computation of the first eigenvalue ω_1^n and the first eigenvector u^n with the density θ^n
   (b) Updating of the density by $\theta^{n+1} = P_{|0,1|}(\theta^n + pd\theta)$, with $p > 0$ the step size. The value of the Lagrange multiplier ℓ is computed by dichotomy.

Implementation The above algorithm has been implemented in FreeFem++. All the unknowns are discretized using P_1 finite elements. The eigenvalue problem is solved with algorithm already implemented in FreeFem++. As usual, the descent direction is interpolated, using a H^1 equivalent norm, by solving a following variational formulation :

$$\forall h \in H^1(D,\mathbb{R}) \quad \int_D d\theta\, h + \eta^2\nabla d\theta\cdot\nabla h\, dx = -\int_D (\frac{1}{\int_D \rho_A\theta|u|^2}(\frac{\partial A^*}{\partial\theta}(\theta)e(u) : e(u) + \omega_1^2\rho_A|u|^2) + \ell)h\, dx\,,$$

with $\eta > 0$ a small coefficient, which typically depends on the size of the elements of the mesh.

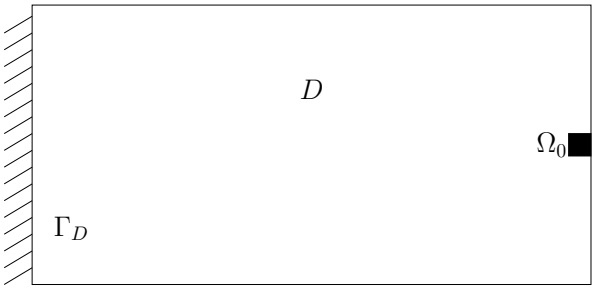

Figure 3.23: Boundary conditions for the maximization of the first eigenfrequency problem

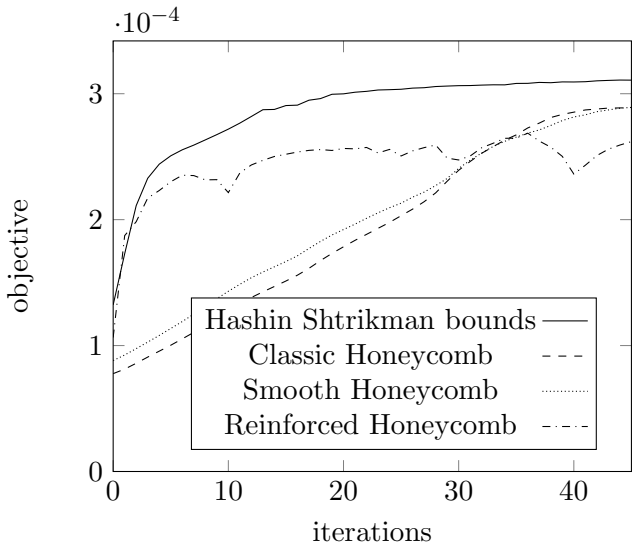

Figure 3.24: Convergence history of the objective function for the maximization of the first eigenfrequency problem

Numerical results We applied this algorithm to a cantilever case, for several microstructures. The domain size is 20×10. A square of size 1×1, denoted Ω_0 is non optimizable: the density of the material is fixed to one in this area, see Figure 3.23.

The history of the objective function is displayed on Figure 3.24. The optimized density, for each microstructure, is displayed on Figure 3.25. The algorithm converges quickly and smoothly for the upper bound of Hashin-Shtrikman. It is slower with classical and smooth honeycomb microstructures, and laborious with reinforced microstructure. The optimized density for any microstructure is autopenalized (black and white structure). There is no interest to keep grey material for the eigenfrequency maximization problem, with isotropic microstructure. Other types of microstructures should be investigated for this problem.

We emphasize that the four optimized structures seem to be identical on Figure 3.25. However, there are slight differences, and the optimized first eigenfrequencies are not equal to each other. For example, some grey material is still present in the optimized structure with the reinforced honeycomb. This could explain why this structure has the lowest eigenfrequency.

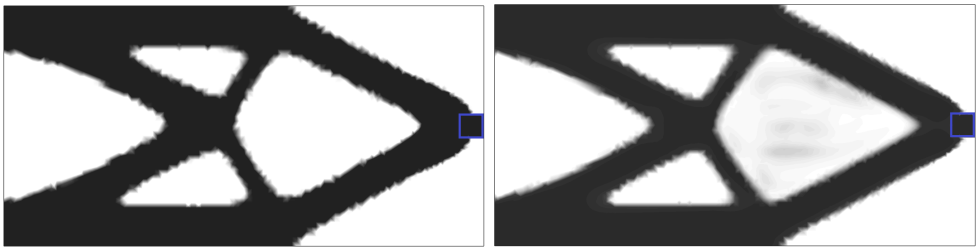

(a) classical honeycomb (b) Reinforced honeycomb

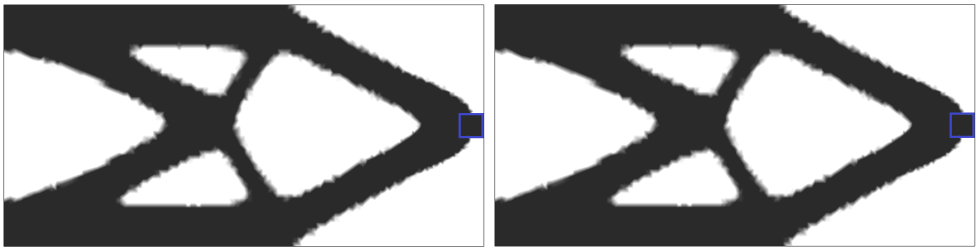

(c) Smooth honeycomb (d) Hashin Shtrikman upper bound

Figure 3.25: Optimized structures for the maximization of the first eigenfrequency problem

3.3.6 Discussion

Several optimization problems have been investigated for the use of isotropic microstructure. The microstructure tend to autopenalize in numerous cases. Since, the upper bound of Hashin-Shtrikman have also this tendency, we can only conclude that modulated isotropic microstructures are not adapted to those problems. Concerning the compliance minimization problem for single load cases for example, orthotropic rank-2 laminates are known to be optimal [Allaire 2002a]. Hence, it sounds coherent that isotropic microstructures are not relevant. In [Zhang 2015], structures are optimized with classical honeycomb microstructures. But, in order to keep grey densities, the gradient of the density is bounded in the domain: black and white structures are no longer admissible. This strategy certainly leads to grey structures, but they have no chance to be more optimal than structures optimized with the SIMP method or the level-set method.

The compliance minimization problem for multiple load cases stands out from the crowd: the microstructures do not auto-penalized. Isotropic microstructures appear to be meaningful in those cases.

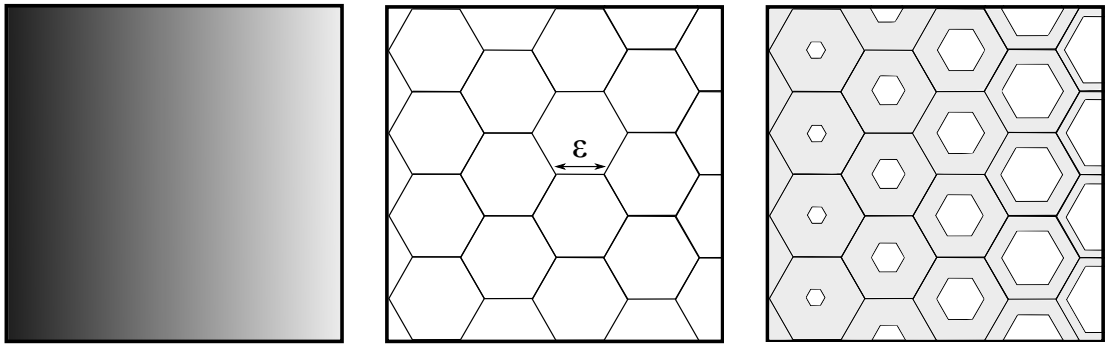

(a) Density field (b) Tesselation of the domain for a given periodic size ε (c) Design of each cell separately

Figure 3.26: Local deshomogenization approach: example in 2D with honeycomb cells for an arbitrary density field

3.4 Deshomogenization process

The homogenized structures are not straightly manufacturable. Indeed, only the local density of the cells is given but this does not describe a classical shape. The idea is to construct a sequence of classical shapes that actually converges toward the homogenized structure. In order to converge to the homogenized structure, the size of the periodic cells of the elements of the above sequence has to converge to zero. The size of the cells will be denoted ε, and the elements of the sequence will be denoted Ω_ε.

Two main approaches are possible in order to construct such a sequence. The first method is a local approach and leads to regular cells, in the sense where each cell is exactly the one described above. But this method is very time consuming since each cell has to be constructed separately. In the second method, the said global one, the final structure is described through a level-set function and is really fast to be computed. However, the cells may be not regular ones in the sense where the width of the bars of a given cell may be not constant in the whole cell.

3.4.1 Local approach : projection on each cell

This method appears as the most intuitive. It has been used for example in [Zhang 2015], in the same context: how to project optimized homogenized structures on explicit cellular structures. First, the size of the periodic cell ε is fixed. Second, the whole domain D is paved using the periodic pattern: hexagons in 2D or tetrakaidecahedra in 3D, see Figure 3.26(b). The density in each cell remains to be computed. Several approaches are possible in order to construct a sequence of shapes converging to the homogenized design. The density of each cell may be defined as the density of the homogenized structure on the center of the cell, or as the average density on the whole cell. When the density for a given cell is computed, the corresponding microstructure is projected in the corresponding tile, see Figure 3.26(c). At the end, the structures feature only regular cells.

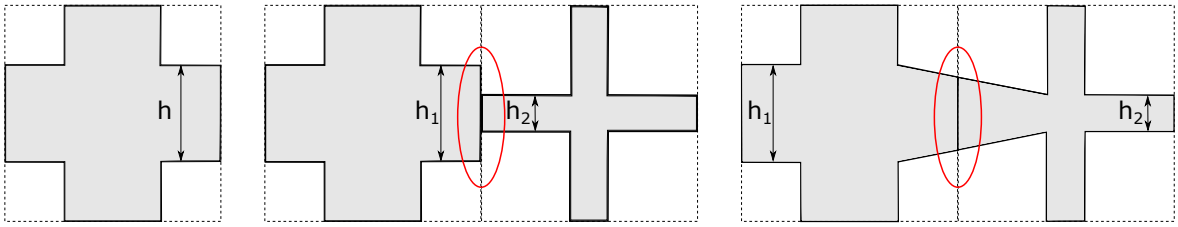

(a) Another periodic cell: the cross

(b) Non smooth interface with the local deshomogenization method

(c) Smooth interface with the interpolating approach

Figure 3.27: Two local strategies to deshomogenize optimization results made of cross cells in 2D

However, the final structures are not ensured to be smooth. This matter does not exist here in 2D thanks to the design of the cells: the common side between two hexagons is always filled. But for other types of cells, one may face this problem. An example is displayed on Figure 3.27. The periodic cell is a regular cross, parametrized by h the width of the bars, see Figure 3.27(a). If two adjacent cells are parametrized by different h, the final structure will no be smooth at the interface, in red on Figure 3.27(b). A solution consists in interpolating the geometric parameters of both cells at the interface, see Figure 3.27(c).

With the chosen isotropic cells, this problem appears in 3D. Indeed, two neighbours cells have a common holed face. As soon as their densities are not exactly the same, see Figure 3.28(a), the holes do not match on both sides of the common face. On Figure 3.28(b), a slice of the both previous cells is displayed. The border of the common hole is displayed in yellow. One can check that this border is not smooth. The interpolating method has been implemented in 3D for two neighbours cells of different density. The result is displayed on Figure 3.28(c). The border of the common hole is displayed in yellow: one can check that it is smooth.

We implemented this deshomogenization method in Python, for the 3D optimized structures. Deshomogenized structures for the multiple loads compliance minimization are displayed on Figures 3.29(a) and 3.29(b). The output of the Python script is 3D geometric file ('.obj'): it can be printed straightforwardly. We successfully printed tests structures made of modulated periodic tetrakaidecahedron cells, see Figure 3.30

When the size of the periodic cell is going to 0, the number of periodic cells increases drastically. The local deshomogenization approach may required efficient geometric algorithms in order to be efficient. An other solution is given by the second approach, where the cells are not computed one by one, but all simultaneously, no matter of their numbers.

3.4.2 Global approach : using the level-set method

In this method, the cellular structure Ω_ε is implicitly given by a level-set function $\psi_\varepsilon : D \to \mathbb{R}$:

$$\begin{cases} \psi_\varepsilon(x) = 0 & \text{if } x \in \partial\Omega \\ \psi_\varepsilon(x) < 0 & \text{if } x \in \Omega \\ \psi_\varepsilon(x) > 0 & \text{if } x \in D \setminus \Omega \end{cases} . \tag{3.22}$$

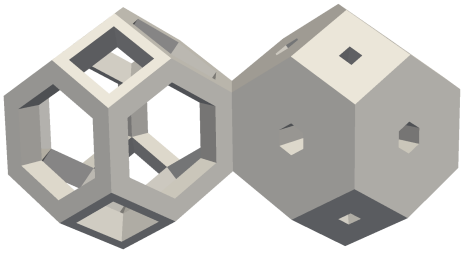

(a) Two neighbour tetrakaidecahedron cells

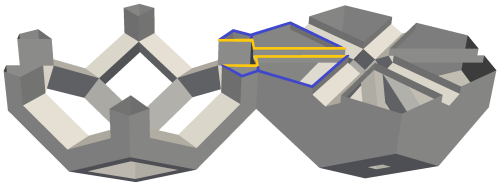

(b) Design of a sharp interface (yellow)

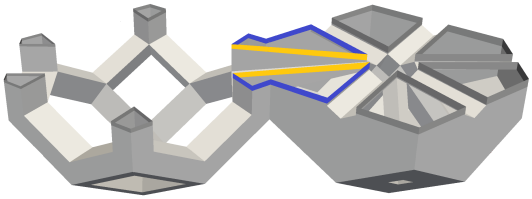

(c) Design of a smooth interface (yellow) between neighbour cells

Figure 3.28: Two local strategies to deshomogenize optimization results in 3D

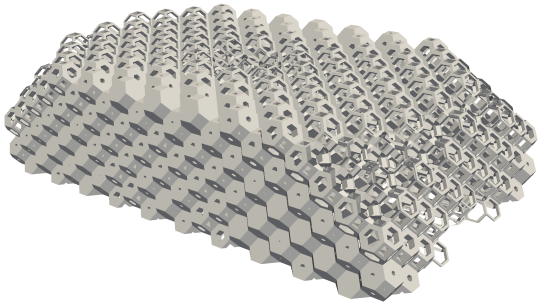

(a) First load case

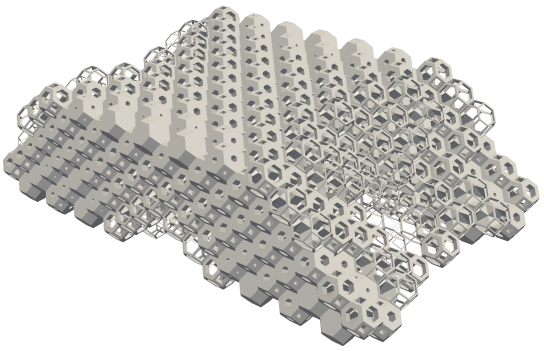

(b) Second load case

Figure 3.29: Deshomogenization of optimal homogenized structures in 3D in a multiple loads test case

(a) Tetrakaidecahedron cell (b) Four cells of different densities (c) Test structure made of modulated tetrakaidecahedron cells

Figure 3.30: Printed structures made of tetrakaidecahedron microstructures (the geometric files are produced by our Python script to deshomogenize structures)

3.4.2.a Level-set function for the reinforced honeycomb

The reinforced honeycomb is the union of three sets of parallel bars, rotated of 0, $\frac{\pi}{3}$ and $\frac{2\pi}{3}$ from the horizontal, see Figure 3.31. The three sets of parallel bars $\Omega_{\varepsilon,i}$ are respectively given by the level-set $\psi_{\varepsilon,i}$:

$$\psi_{\varepsilon,i}(x) = -\cos(\frac{2\pi}{\varepsilon}\frac{\sqrt{3}}{2}(x_1,x_2)^T \cdot n_i) + \cos(2\pi\frac{\sqrt{3}}{2}m(x))\,, \tag{3.23}$$

where $m(x)$ is the relative width of bar corresponding to the density θ, it is defined by (3.2). The complete network of bars Ω_ε is the union of the three sets of parallel bars. It is described by the level-set ψ_ε:

$$\psi_\varepsilon(x) = \min_{i\in\{0,1,2\}} \psi_{\varepsilon,i}(x)$$

For hexagons of side ε, parallel bars are distant from their neighbours of $\frac{\sqrt{3}}{2}\varepsilon$. The distance of a point from one of the diagonals of the hexagon is given by the scalar product with the unit normal vectors n_i. Hence, thanks to the even and periodic function cosine, the first term of (3.23) defines the set of parallel bars of normal n_i and with a periodicity equal to $\frac{\sqrt{3}}{2}\varepsilon$. The second term adjusts the local width of the bar, with respect to m, by thresholding the cosine function at the adapted value.

We compute the final structure Ω_ε for several values of ε, in $D = [-1;1]^2$, in the case of a radial

$$\theta = 1. - 0.5(x_1^2 + x_2^2)\,. \tag{3.24}$$

The results are displayed on Figure 3.32. The smaller ε, the thinner the final structure. As predicted, the cells are not exactly reinforced honeycomb, since the local width of the bar is given by the local density: the width of the bars is smooth in the whole domain, it does not feature any discontinuity as in the first projection approach.

3.4.2.b Level-set function for the classical honeycomb

Let ε bet the size of the side of the hexagonal cell. The classical honeycomb network does not feature infinite bars, but only segments. As previously those segments can be divided in three

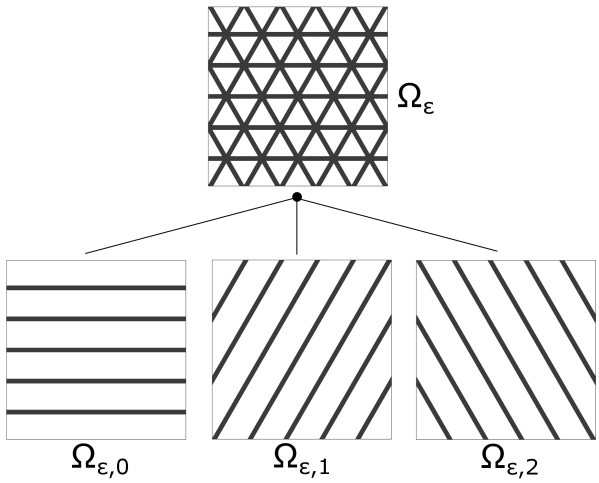

Figure 3.31: Process to describe a reinforced honeycomb cell with a level-set function

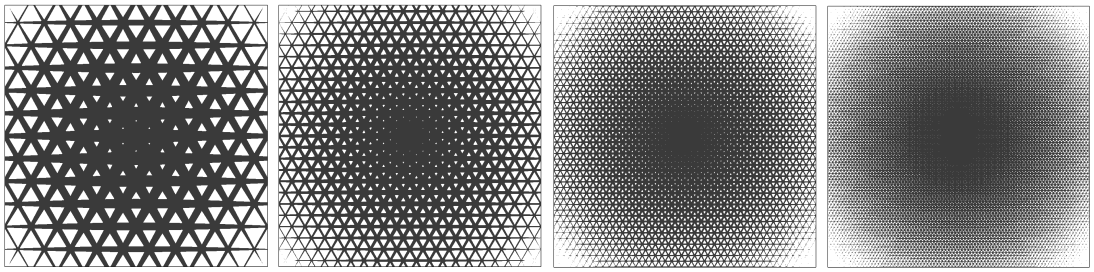

(a) $\varepsilon = 1$ (b) $\varepsilon = 0.5$ (c) $\varepsilon = 0.25$ (d) $\varepsilon = 0.125$

Figure 3.32: Projection of a radial density θ over a reinforced honeycomb composite, for several sizes of cell ε

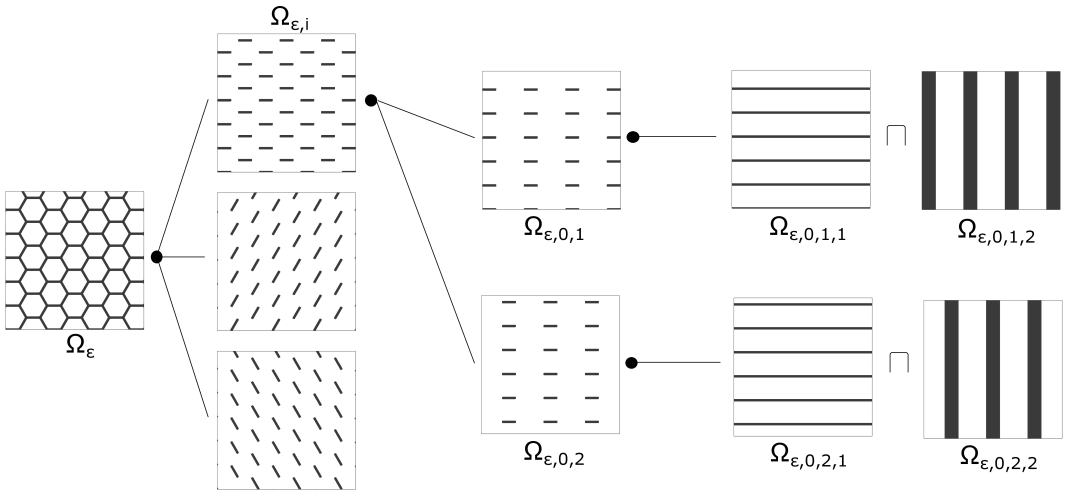

Figure 3.33: Process to describe a classical honeycomb cell with a level-set function

sets, $\Omega_{\varepsilon,i}$, according to their normal, n_i. Considering one set of segments, it can be divided in two subsets see Figure 3.33, of periodic segments: $\Omega_{\varepsilon,i,1}$ and $\Omega_{\varepsilon,i,2}$. Finally each of those subsets can be described as the intersection between two sets of bars, orthogonal to each other : $\Omega_{\varepsilon,i,j,1}$ and $\Omega_{\varepsilon,i,j,2}$. The first subset, $\Omega_{\varepsilon,i,j,1}$, has a periodicity of $\sqrt{3}\varepsilon$ and the width of the bars depends on m:

$$\Omega_{\varepsilon,i,j,1}(m) = \{x \in D \text{ such that } \cos(\frac{2\pi\sqrt{3}}{\varepsilon}(x_1,x_2)^T \cdot n_i + j\pi) \geq \cos(2\pi\frac{\sqrt{3}}{2}m(x))\}\,,$$

where the term $j\pi$ is here to shift the second subset of segments with respect to the first one. The second subset, $\Omega_{\varepsilon,i,j,2}$, has a periodicity of 3ε and the width of the bars is fixed to ε:

$$\Omega_{\varepsilon,i,j,2} = \{x \in D \text{ such that } \cos(\frac{2\pi}{3\varepsilon}(x_1,x_2)^T \cdot n_i + j\pi + (2\delta_{i,2}-1)\frac{\pi}{3}) \geq \cos(\frac{\pi}{3})\}\,,$$

where $\delta_{i,j}$ is the Kronecker delta. The purpose of the term featuring the Kronecker delta is to adjust all the segments together. Here the origin $(0,0)$ of the domain D corresponds to the upper left corner of the hexagon. Obviously, the displayed level-set description is not unique and can be translating in order to place the origin $(0,0)$ of the domain D wherever one would like in the periodic cell. We chose this one because of its relative simplicity.

As previously, we compute the final structure Ω_ε for several values of ε, in $D = [-1;1]^2$, in the case of a radial density, given by (3.24). The results are displayed on Figure 3.34. The same remarks, as with reinforced honeycomb, are still valid here.

3.4.2.c Numerical results

Optimized structures for compliance minimization in the multiple loads bridge, see Section 3.3.2, have been deshomogenized with the above method. We emphasize that all the optimization was done on quite a coarse mesh (about 10^4 vertices). But the construction of genuine shapes is done on a very thin mesh (about 10^6 vertices), in order to catch the smaller details of the shapes.

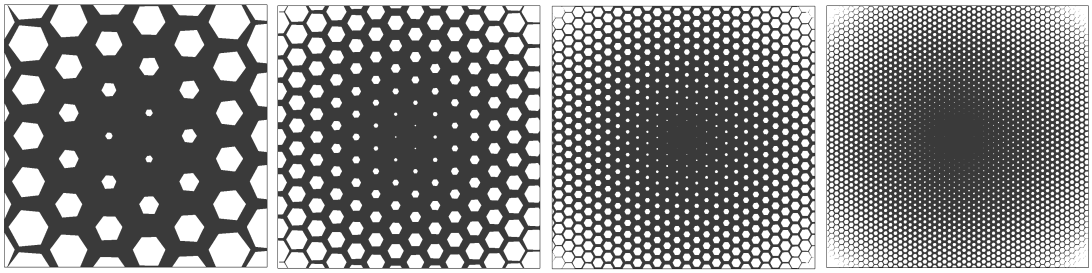

(a) $\varepsilon = 1$ (b) $\varepsilon = 0.5$ (c) $\varepsilon = 0.25$ (d) $\varepsilon = 0.125$

Figure 3.34: Projection of a radial density θ over a classical honeycomb composite, for several sizes of cell ε

However, only the level-set functions are computed at this step: the use of a thin mesh is not time-consuming.

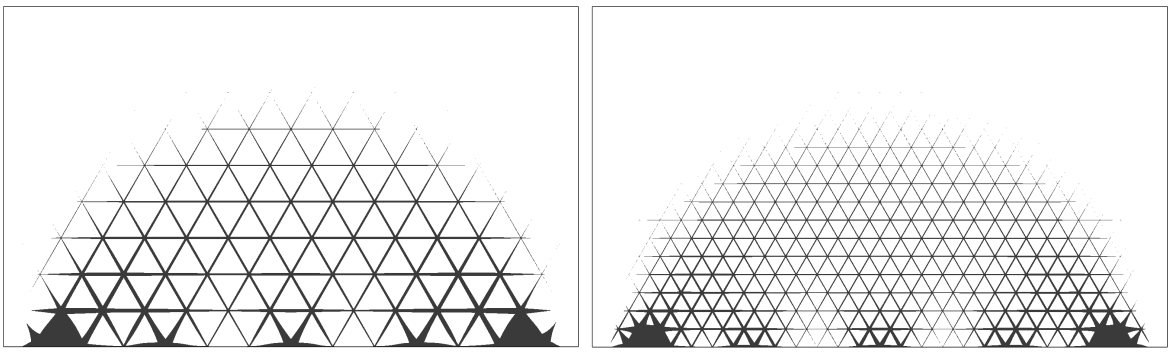

(a) $\varepsilon = 1.6$ (b) $\varepsilon = 0.8$

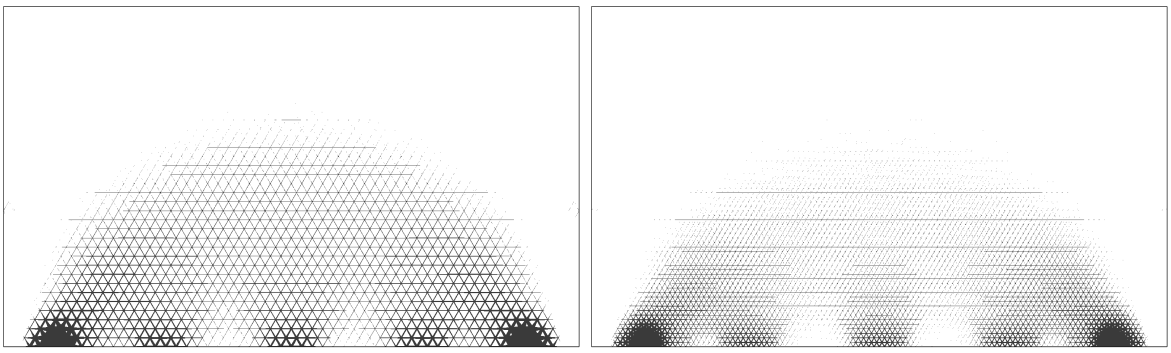

(c) $\varepsilon = 0.4$ (d) $\varepsilon = 0.2$

Figure 3.35: Projection of a radial density θ over a classical honeycomb composite, for several sizes of cell ε

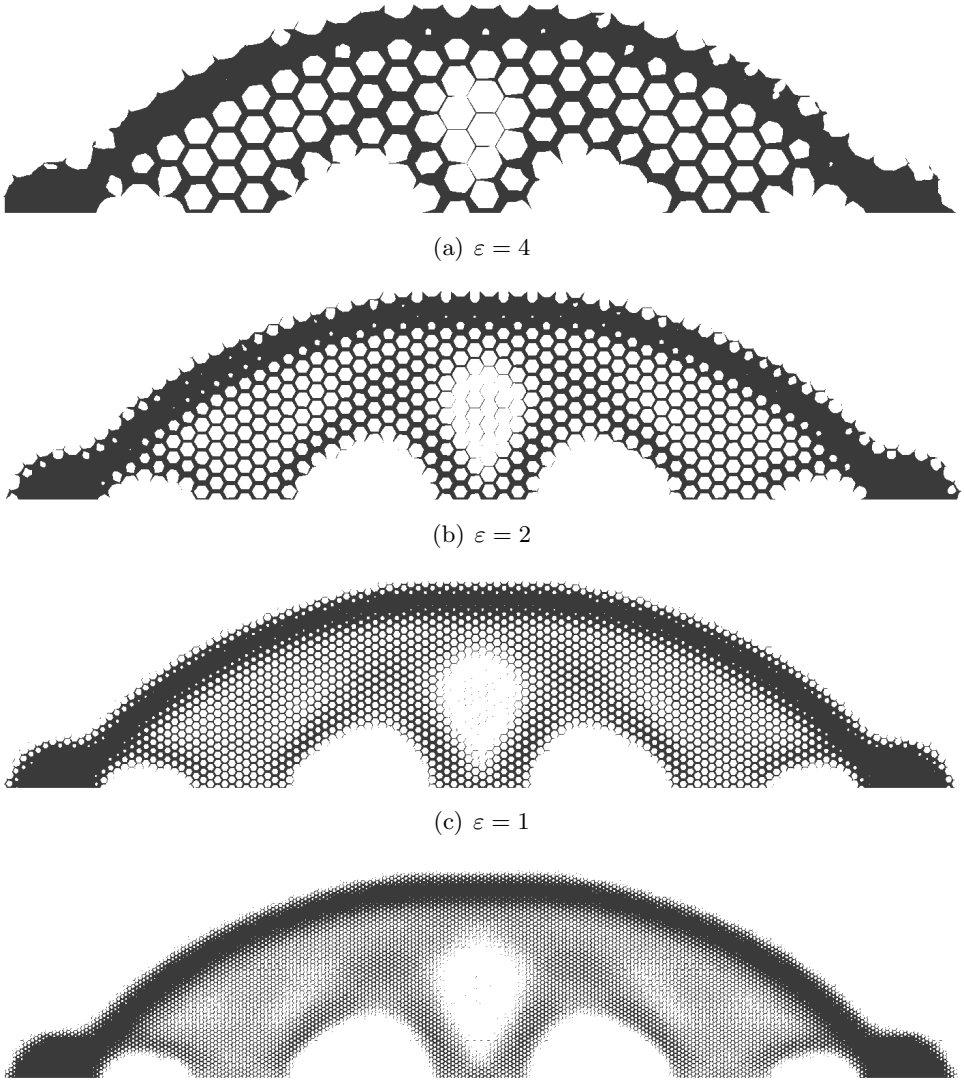

(a) $\varepsilon = 4$

(b) $\varepsilon = 2$

(c) $\varepsilon = 1$

(d) $\varepsilon = 0.5$

Figure 3.36: Projection of a radial density θ over a classical honeycomb composite, for several sizes of cell ε

Chapter 4

Topology optimization of 2D structures built with orthotropic lattice materials

Contents

This chapter, at the exception of Section 7, is the following published article:
Topology optimization of modulated and oriented periodic microstructures by the homogenization method, P. Geoffroy-Donders, G. Allaire and O. Pantz, Computers and Mathematics with Applications, March 2018

Abstract. This paper is concerned with the topology optimization of structures made of periodically perforated material, where the microscopic periodic cell can be macroscopically modulated and oriented. The main idea is to optimize the homogenized formulation of this problem, which is an easy task of parametric optimization, then to project the optimal microstructure at a desired length-scale, which is a delicate issue, albeit computationally cheap. The main novelty of our work is, in a plane setting, the conformal treatment of the optimal orientation of the microstructure. In other words, although the periodicity cell has varying parameters and orientation throughout the computational domain, the angles between its members or bars are conserved. The main application of our work is the optimization of so-called lattice materials which are becoming increasingly popular in the context of additive manufacturing. Several numerical examples are presented for compliance minimization in 2-d.

4.1 Introduction

Topology optimization of structures is nowadays a well developed field with many different approaches and a wealth of applications. One of the earliest method of topology optimization was the so-called homogenization method, introduced in the early eighties by mathematicians [Kohn 1986], [Lurie 1982], [Murat 1985] (see the textbook [Allaire 2002a] for more references), and popularized by the seminal paper [Bendsøe 1988] which was the first one to numerically treat a realistic problem in the elasticity setting (the previous numerical works were restricted to an anti-plane elasticity setting, namely a scalar equation). Despite its great success, the homogenization method progressively faded away because it was surpassed by a less rigorous method, but much simpler and as efficient in most cases, the so-called SIMP method introduced in [Bendsøe 1989], [Zhou 1991] (see the textbook [Bendsoe 2003] for a more complete account). The SIMP method is said to be less rigorous because it uses fictitious isotropic materials while the homogenization relies on true composite materials, possibly anisotropic. However, as soon as penalization of intermediate densities is put in action, there is no need of using true composite materials, which have complicated effective properties and require much more modeling and computational efforts than the simple material interpolation involved in SIMP. This is the key for the immense popularity of SIMP which is the most commonly used method in commercial topology optimization software.

However, the appearance of mature additive manufacturing technologies which are able to build finely graded microstructures (sometime called lattice materials) may drastically change the picture and we could well see a resurrection of the homogenization method for such applications. Indeed, homogenization is the right technique to deal with microstructured materials where anisotropy plays a key role, a feature which is absent from SIMP. Homogenization theory allows to replace the microscopic details of the structure (typically a complex networks of bars, trusses and plates) by a simpler effective elasticity tensor describing the mesoscopic

properties of the structure. Therefore, the analysis of the structure is greatly accelerated since there is no need to mesh or represent on a fixed mesh all the microscopic details of its shape. There is however one final hurdle, once an optimal composite structure has been obtained, which is the projection of the optimal microstructure at a chosen finite length scale to get a global and detailed picture of the optimal microstructure. This is the most delicate part of this homogenization approach and the one where the present paper is most contributing.

We follow the lead of the pioneering paper [Pantz 2008] which was the first to propose such a post-treatment of the homogenization method in topology optimization. The main idea is to project the optimal microstructure on a fine mesh of the overall structure in a smoothly varying way. This implies that locally the microstructure is deformed and oriented to adapt to its macroscopic variations. We depart from the work [Pantz 2008] and improve it in several aspects.

First, in [Pantz 2008], rank-two laminates were used during the optimization process. The advantage is that such rank-two laminates have explicit effective properties and are known to be optimal for 2-d compliance minimization. The drawback is that they are difficult to manufacture since they are featuring two well separated length scales. To circumvent this problem, during the post-processing or projection step, those rank-two laminates were arbitrary replaced by periodic composites, whose behavior are close – but still different – from the rank-2 laminates used during the optimization stage. As a consequence, the sequence of projected shapes were not exactly converging toward the computed optimal composite shape. In the present article, we lift this inconsistency. At all stages of our method, we use the same microstructure, namely periodic square cells with rectangular holes like in [Bendsøe 1988]. Other parametrized periodicity cell would be acceptable in our approach (for other examples, see 3 for triangular or hexagonal cells, or see 6 for stochastic microstructures).

Second, in [Pantz 2008], rectangular and squared cells were assumed to behave similarly. This simplified greatly the projection step. Here, we do not make such an approximation. We construct a sequence of genuine shapes based on a square lattice. As a consequence, we have to enforce a conformality property to the underlying lattice of the periodic composite, namely that, after deformation and orientation, right angles in the microstructures should stay right angles (see Figure 4.1). Note that a side effect of the conformality condition is that it imposes to the rotation field of the cells to be harmonic and thus regular. In [Pantz 2008], a different regularization was applied.

Third, we have greatly simplified the projection step. A major obstacle is related to the fact that the orientation of the cells are only defined up to a rotation of angle π. In [Pantz 2008], a quite unnatural trick was used to get over this problem. It led to a verbose formulation during the regularization step of the orientation of the cells. We propose here a different solution that consists in replacing the computational domain by an abstract manifold. It is worthy to note that our method is ready to use in the presence of singularities of the lattice, that is when no coherent orientation of the cells does exist (see [Pantz 2010]). Eventually, in a last post-processing operation, we clean the projected structure by removing disconnected bars or bars that have a free hanging end point.

At this point, let us mention the recent work [Groen 2017] which is proposing yet another homogenization method in the spirit of [Pantz 2008].

The content of this paper is the following. Section 4.2 is devoted to a presentation of

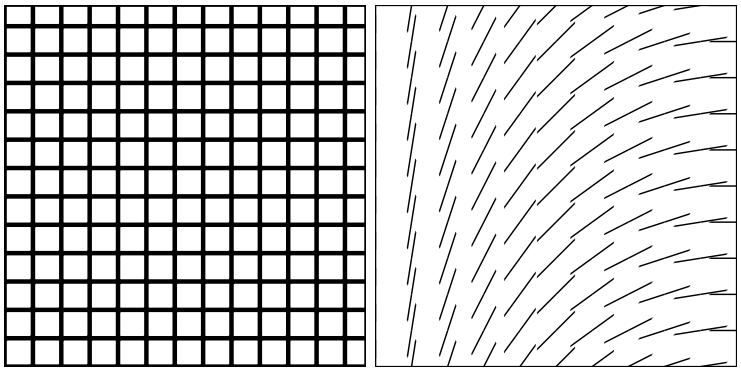

(a) Regular grid (b) Direction field

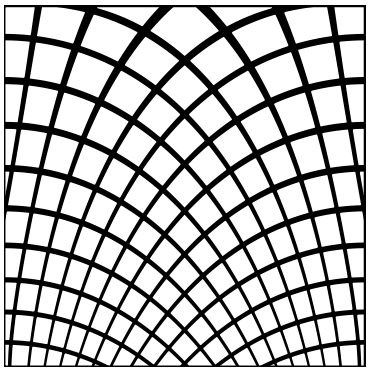

(c) Distorted grid

Figure 4.1: A regular grid (a) is associated to a direction field (b), giving the local orientation of each cell: it yields a distorted grid (c)

our setting. We focus on 2-d compliance minimization for a single load state equation (the generalization to other objective functions, multiple load problems, or 3-d requires additional ideas, see 7). We briefly recall the necessary ingredients of the homogenization approach and we explain our three-steps strategy. First, choose a parametrized periodicity cell and pre-compute its effective properties for the entire range of its parameters. Second, perform a topology optimization of the composite structure, which turns out to be a simple parametric optimization problem since our periodicity cell is parametrized. Third, apply a post-processing step which amounts to project, at a specified length scale, a modulated and oriented periodicity cell.

Section 4.3 deals with the pre-processing step of computing the effective properties of our parametrized periodicity cell which, here, is a square cell with a rectangular holes (thus having two parameters for the hole, on top of the orientation angle). We recall the homogenization formulas, based on the notion of cell problems [Allaire 2002a] and we compute the derivatives, with respect to the parameters, of the effective or homogenized tensor.

Section 4.4 deals with topology optimization for a 2-d compliance problem with a set of admissible designs which are the homogenized tensors of Section 4.3. Therefore, it is a parametric optimization problem and solving it is quite standard. Here we rely on a projected gradient algorithm for the hole parameters and optimality criteria for its orientation.

Section 4.5 is the main novelty of the present work, devoted to the post-processing of the homogenized result of Section 4.4, namely the projection of the optimal microstructure. Section 4.5.1 defines the way the microscopic cell is macroscopically modulated. First, the cell parameters (more precisely the width and height of the rectangular hole, see Figure 4.2) vary from point to point in the computational domain. Second, the orientation of the periodicity cell varies too. More precisely, we introduce a vector field $\varphi(x)$, the inverse of which maps the periodic square grid on a distorted grid where each cell is optimally oriented (see Figure 4.1). Section 4.5.2 introduces a conformality condition to be satisfied by the grid map φ so that right angles in the original square grid remain right angles in the deformed configuration. As proved in Lemma 4.5.1 this is equivalent for the orientation angle α to be harmonic (in two space dimensions). Section 4.5.3 explains how the orientation angle α is optimized for mechanical performance and slightly regularized. Section 4.5.4 is the heart of our approach: there, the grid map $\varphi(x)$ is deduced from the optimal angle $\alpha(x)$. Section 4.5.5 gives all the necessary computational details on how to find the grid map φ in practice. Section 4.5.6 gives the numerical results obtained with our approach. Eventually, Section 4.5.7 is devoted to a last "cleaning" step of the projected structure where disconnected bars or bars that have a free hanging end point are automatically removed.

Section 4.6 gives numerical examples of the whole process applied to other test cases including an arch, a cantilever, a MBB beam and a L-beam. We also present an example featuring singularities in the orientation field which can not be treated by our current implementation of the proposed algorithm. Nevertheless, a more careful regularization of the orientation allows us to remove the singularities and give a satisfactory optimal design. The complete description of how to remove the singularities will be the topic of the next Chapter 5.

4.2 Setting of the problem

4.2.1 Topology Optimization

Let $D \subset \mathbb{R}^N$ be a fixed smooth bounded open set (the working domain) and $\Omega \subset D$ the reference configuration of an isotropic elastic body. The structure Ω is clamped on $\Gamma_D \subset \partial\Omega$, and submitted to surface loads g on $\Gamma_N \subset \partial\Omega$. For simplicity these parts Γ_D and Γ_N of the boundary are assumed to be fixed and subsets of ∂D. We assume that the solid is made of an homogeneous isotropic linear elastic material of Hooke's law A, with Lamé coefficients λ and μ. The displacement u and the stress tensor σ are then solution of the system

$$\begin{cases} \operatorname{div}(\sigma) = 0 & \text{in } \Omega, \\ \sigma = Ae(u) & \text{in } \Omega, \\ u = 0 & \text{on } \Gamma_D, \\ \sigma \cdot n = g & \text{on } \Gamma_N, \\ \sigma \cdot n = 0 & \text{on } \Gamma = \partial\Omega \setminus (\Gamma_D \cup \Gamma_N), \end{cases}$$

where $e(u) = \frac{1}{2}(\nabla u + \nabla u^T)$ is the strain tensor (the symmetrized gradient of the displacement).

Shape and topology optimization consists to determine the domain Ω that minimizes a given objective function J,

$$\begin{aligned} &\min && J(\Omega) \\ &|\Omega| \leq V, \\ &\Gamma_D \cup \Gamma_N \subset \partial\Omega \end{aligned} \tag{4.1}$$

where $V \in \mathbb{R}^+$ is the maximum admissible volume. A typical objective function is the compliance

$$J(\Omega) = \int_{\Gamma_N} g \cdot u \, ds \, .$$

For most cost functions J, problem (4.1) does not admit a solution [Allaire 2002a]. This is due to the fact that composite shapes, made of very small microstructures, can always outperform genuine shapes made of plain material. A composite shape is described by the local density $\theta(x)$ of material and a homogenized elasticity tensor $A^*(x)$ that depends on the microstructure at the point $x \in D$. The homogenized or macroscopic displacement u^* of the structure is then solution of the system

$$\begin{cases} \operatorname{div}(\sigma) = 0 & \text{in } D, \\ \sigma = A^* e(u^*) & \text{in } D, \\ u^* = 0 & \text{on } \Gamma_D, \\ \sigma \cdot n = g & \text{on } \Gamma_N, \\ \sigma \cdot n = 0 & \text{on } \Gamma = \partial D \setminus (\Gamma_D \cup \Gamma_N). \end{cases}$$

We emphasize that the problem is now defined on the whole working domain D and no longer on a shape Ω. Then, the minimization problem should be rewritten as a minimization problem of

a relaxed cost function J^* with respect to the homogenized elasticity tensor A^* and the density θ

$$\begin{array}{c} \min \qquad J^*(\theta, A^*)\,. \\ \int_D \theta \leq V, \\ A^*(x) \in G_\theta(x) \end{array} \tag{4.2}$$

where $G_\theta(x)$ is the set of effective or homogenized Hooke's laws for microstructures of density $\theta(x)$. The main difficulties in the homogenized formulation (4.2) are, first, to compute the relaxed cost function J^* (which may be different from the original cost function J), second and most importantly, to give a complete and explicit description of the set of admissible Hooke's laws G_θ. It is only for special cases (like compliance minimization) that (4.2) can be made fully explicit [Allaire 2002a]. Furthermore, composite shapes are only mathematical ideal objects. They can not be actually build as they are made of infinitely small details. To circumvent these obstacles, following the lead of [Pantz 2008], we propose to limit the set of admissible composites to microstructures for which the Hooke's law can be numerically computed (typically, periodic composites with a square cell). Finally, we do not seek for the optimal homogenized or composite solution but for a sequence of genuine non composite shapes containing more and more details that does converge toward the optimal composite solution.

4.2.2 A three steps approach

Our goal is to construct a minimizing sequence for (4.2), where the homogenized tensors A^* are restricted to a specific class of composite materials. By minimizing sequence, we mean a sequence of classical or genuine shapes which converges to the infimum value of (4.2), and which is indexed by its length scale (or periodicity) $\varepsilon > 0$, a small parameter going to zero. To achieve this goal, our main strategy is to follow a three step approach. First, choosing a parametrized class of composite materials, we determine the subset of homogenized Hooke's laws for these allowed composite shapes, when their parameters vary. Second, we solve the relaxed or homogenized formulation (4.2) when the full set G_θ is replaced by its subset numerically found during the first step. This is typically a rather easy parametric optimization problem. Third, and most importantly, we construct a sequence of genuine shapes that does converge toward the optimal composite found during the second step. This last step is a rather computationally cheap post-processing of the previous step but it is where we put our main modeling and algorithmic efforts.

We restrict our analysis to the two dimensional case ($N = 2$) and to locally square-periodic composites. Note that it should be possible to adapt the whole method (or at least part of it) to hexagonal cells or to the three dimensional case. The first step consists in determining the properties of such materials when varying their parameters (see Section 4.3). It is a preprocessing stage which can be performed off-line and is the same, whatever the choice of objective functions, computational domain, applied loads and boundary conditions. Hooke's laws are computed by solving cells problems that describe the deformation at the scale of the microstructure. This is a very classical task in homogenization theory. Adding a rotation is obvious and does not require additional computations.

In a second step, we compute the optimal solution of the shape optimization problem (4.2)

over the previously found set of locally square-periodic composites (see Section 4.4). This is a parametric problem where the design variables are, at every point of the computational domain, the periodicity cell parameters and its orientation or angle.

Finally, the third step yields a minimizing sequence of genuine shapes, converging toward the optimal solution, and indexed by the period ε (see Section 4.5). For each given value of ε, a genuine or classical shape is obtained by projecting on a mesoscopic (or even macroscopic) scale the distorted grid of the periodicity cells. To achieve this, we deduce from the optimal orientation angle, satisfying a conformality condition, a vector field or grid map. The optimal microstructure is then projected along this grid map. A final post-processing cleaning process is also applied to remove disconnected or hanging bars.

4.3 Preprocessing : homogenized Hooke's laws of the microstructures

4.3.1 Set of admissible microstructures

From now on, we restrict ourselves to the two dimensional case (see 7 for some 3-d examples) and restrain our analysis to a simple class of composites already used in the seminal paper [Bendsøe 1988] : square cells with a rectangular central hole (see Fig.1) repeated periodically on the whole space. This class of composites is parametrized by the relative linear dimensions of the hole $m = (m_1, m_2) \in [0,1]^2$, together with the orientation α of the cell, which is the angle made by the y_1-axis of the cell with the x_1-axis of the domain D. We denote the periodic cells $Y_\alpha(m)$.

The structure of those cells as well as their Hooke's laws are not very far from those of rank-2 laminates with orthogonal lamination directions, which are optimal for single-load compliance minimization problems [Allaire 2002a]. Rank-2 laminates were used in the inspiring work [Pantz 2008]: however they are intrinsically multiscale (more precisely, they feature two well separated microscopic scales) and thus hard to manufacture. On the contrary, perforated square cells feature a single scale and are more likely to be additive manufacturable. We emphasize that the following method is not restricted to our choice of cells, and it can easily be extended to any other parametrizable cells. Particularly, some authors have optimized periodic cells for given objective function [Haslinger 1995, Barbarosie 2010a] that could be good candidates.

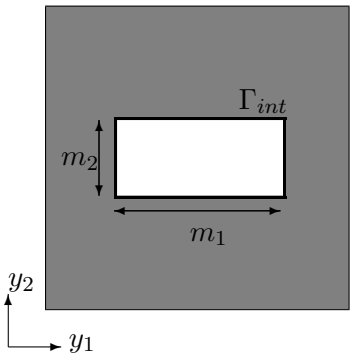

Figure 4.2: Periodicity cell $Y_0(m)$.

4.3.2 Cell problem and homogenized elasticity tensor

For the sake of brevity, only a few important results on the theory of homogenization are recalled here: the interested reader will find more details in [Allaire 2002a]. Assume that, in a given macroscopic domain, there is a periodic distribution of holes inside an isotropic elastic solid phase, with constant elasticity tensor A. The periodicity size is denoted by $\varepsilon > 0$. The rescaled periodicity cell is the unit cube $(0,1)^2$. Inside this unit periodicity cell, the solid domain is the subset $Y_0 \subset (0,1)^2$, its complement being holes with boundaries Γ_{int}. When $\varepsilon \to 0$, the

medium can be considered homogeneous, with an effective constant elasticity tensor A^*. To compute this homogenized tensor A^*, one needs so-called correctors w_{ij}, corresponding to the local displacements in the cell Y_0, defined for each pair $(i,j) \in \{1,2\}^2$ as the solutions of the following *cell problems*

$$\begin{cases} \operatorname{div}(A(e_{ij} + e(w_{ij}))) = 0 & \text{in } Y_0 \\ A(e_{ij} + e(w_{ij}))n = 0 & \text{on } \Gamma_{int} \\ y \mapsto w_{ij}(y) & (0,1)^2\text{-periodic} \end{cases} \tag{4.3}$$

where $e_{ij} = \frac{1}{2}(e_i \otimes e_j + e_j \otimes e_i)$ is a basis of the symmetric tensors of order 2, and n is the normal to the hole's boundary Γ_{int} in Y_0. The variational formulation of the cell problem (4.3) is: find $w_{ij} \in H^1_{\#}(Y_0, \mathbb{R}^2)$ such that

$$\forall \phi \in H^1_{\#}(Y_0, \mathbb{R}^2) \quad \int_{Y_0} Ae(w_{ij}) : e(\phi) + \int_{Y_0} Ae_{ij} : e(\phi) = 0\,, \tag{4.4}$$

which admits a unique solution (up to an additive translation). The tensor A^* is then given in terms of the solutions w_{ij} of the *cell problems* by

$$A^*_{ijkl} = \int_{Y_0} A(e_{ij} + e(w_{ij})) : (e_{kl} + e(w_{kl}))dy \quad \forall i,j,k,l \in \{1,2\}. \tag{4.5}$$

Restricting the analysis to periodic composites is an acceptable limitation, as the set of Hooke's laws of periodic composites is dense in the set of all possible Hooke's laws reachable with composites [Allaire 2002a]. However, restricting the set of periodic composites to square cells with rectangular holes is clearly a loss of generality since, for example, the resulting homogenized Hooke's laws are never isotropic (for intermediate densities). Exploring a larger range of periodic microstructures is an obvious line of research for future work.

4.3.3 Sensitivity of the homogenized elasticity tensor

The computation of the sensitivity of the homogenized elasticity tensor with respect to the parameters of the cell design will be based on the notion of shape derivative. We define $W^{1,\infty}_{\#}((0,1)^2;\mathbb{R}^2)$ as the set of $(0,1)^2-$ periodic Lipschitz maps from $(0,1)^2$ with value in $\mathbb{R}^2$ (the # symbol indicates that the functions are $(0,1)^2$-periodic).

Definition 4.3.1. Let $\theta \in W^{1,\infty}_{\#}((0,1)^2;\mathbb{R}^2)$. The shape derivative of a function $F(Y_0)$ is defined as the Fréchet derivative in $W^{1,\infty}$ at 0 of the application $\theta \mapsto F((\mathrm{Id}+\theta)Y_0)$

$$F((\mathrm{Id}+\theta)Y_0) = F(Y_0) + \left\langle F'(Y_0), \theta \right\rangle + o(\theta) \quad \text{with} \lim_{\theta \to 0} \frac{|o(\theta)|}{\|\theta\|_{W^{1,\infty}_{\#}}} = 0$$

where $F'(Y_0)$ is a continuous linear form on $W^{1,\infty}_{\#}((0,1)^2;\mathbb{R}^2)$.

Let $\mathcal{M}_N$ be the set of squared $N \times N$ matrices and $\mathcal{M}^s_N$ the subset of symmetric ones.

Lemma 4.3.1. *The shape derivative of A^*_{ijkl} is given by:*

$$\begin{aligned}\left\langle (A^*_{ijkl})'(Y_0), \theta \right\rangle &= \int_{Y_0} A(e_{ij} + e(w_{ij})) : (e_{kl} + e(w_{kl}))\,\mathrm{div}(\theta) dy \\ &- \int_{Y_0} A(e_{ij} + e(w_{ij})) : \langle de(w_{kl}); \theta \rangle dy \\ &- \int_{Y_0} A(e_{kl} + e(w_{kl})) : \langle de(w_{ij}); \theta \rangle dy, \end{aligned} \tag{4.6}$$

where $de(w)$ is a linear operator from $W^{1,\infty}_{\#}(Y_0; \mathbb{R}^2)$ to $L^2(Y_0; \mathcal{M}^s_2)$ defined for every $w \in H^1_{\#}(Y_0, \mathbb{R}^2)$ by

$$\langle de(w), \theta \rangle = \frac{1}{2}(\nabla w \nabla \theta + \nabla \theta^T \nabla w^T).$$

Proof. The proof is classical (see e.g. [Michailidis 2014]), thus we simply give its main idea. It relies on the Lagrangian method of Cea [Céa 1986] which amounts to introduce a Lagrangian, defined as the sum of formula (4.5) for A^*_{ijkl} and of the variational formulation (4.4). Differentiating with respect to the state variable gives the adjoint system. It turns out that the problem is self-adjoint, so no adjoint appears in (4.6). Differentiating with respect to the shape leads to the final result. □

4.3.4 Computing the homogenized elasticity tensor

The set of effective elasticity tensors $\{A^*_\alpha(m) | (m, \alpha) \in L^\infty(D, [0,1]^2 \times \mathbb{R})\}$ has to be characterized. The proposed strategy consists in computing the material properties for a discrete sample of parameters values and using the collected data to construct a surrogate model for the constitutive law (by a simple interpolation).

4.3.4.a Cell orientation

The considered cells $Y_\alpha(m)$ are not isotropic, nor are their corresponding elasticity tensors $A^*_\alpha(m)$. Therefore, their elastic behavior depends on their orientation α. Let $R(\alpha)$ a fourth-order tensor defined by :

$$\forall \xi \in \mathcal{M}^s_2 \quad R(\alpha)\xi = Q(\alpha)^T \xi Q(\alpha)$$

where $Q(\alpha) \in \mathcal{M}_2$ is the rotation matrix of angle α. Then, the dependency of $A^*_\alpha(m)$ with respect to the angle α can be made explicit as follows

$$A^*_\alpha(m) = R(\alpha)^T A^*_0(m) R(\alpha)\,. \tag{4.7}$$

Unlike the parameters $m = (m_1, m_2)$, the dependency on the orientation α is explicit and the derivative of the elasticity tensor with respect to α is also algebraically known. The numerical computation of the homogenized elasticity tensors $A^*_\alpha(m)$ can thus be restricted to the case $\alpha = 0$. Note that a rotation of the cell by an angle π does not change its Hooke's law as $R(\pi) = -\,\mathrm{Id}$. Hence the optimal orientation can only be defined modulo π.

4.3.4.b Derivatives of the homogenized elasticity tensor

In order to compute the derivative of the homogenized tensor, with respect to m_1 (respectively to m_2), we choose a specific deformation field θ in the shape derivative formula (4.6). Introducing the smooth $(0,1)^2$-periodic vector fields θ_1 and θ_2, defined by

$$\theta_1 = c_1(\sin(2\pi y_1), 0)^T \ , \quad \theta_2 = c_2(0, \sin(2\pi y_2))^T \ ,$$

where $c_1 = -\sin(\pi m_1)^{-1}, c_2 = -\sin(\pi m_2)^{-1}$ are rescaling coefficients, it is easy to check that $Y_0(m_1+\delta m_1, m_2+\delta m_2) = (\mathrm{Id} + \delta m_1\theta_1 + \delta m_2\theta_2)(Y_0(m))$, where $(\delta m_1, \delta m_2)$ is a small increment. It follows that, for $i = 1, 2$,

$$\frac{\partial A_0^*}{\partial m_i}(m) = \left\langle (A_0^*)'(Y_0), \theta_i \right\rangle \ .$$

Therefore, (4.6) leads to the sensitivities of $A_0^*(m)$ with respect to m_1 and m_2.

4.3.4.c Numerical implementation

The considered cells $Y_0(m)$ have cubic symmetry, thus the corresponding homogenized elasticity tensors $\{A_0^*(m)\}$ are orthotropic and fully characterized by only four of its entries, namely $(A_0^*(m))_{1111}, (A_0^*(m))_{1122}, (A_0^*(m))_{2222}, (A_0^*(m))_{1212}$. The three cell problems (4.3) on $Y_0(m)$ are solved using a finite element method. Once the correctors w_{11}, w_{22}, w_{12} are computed, the four independent coefficients of the elasticity tensor are obtained using equation (4.5). Similarly, the sensitivities to the parameters m_1 and m_2 are deduced from the integral formula (4.6).

We discretized the space of the parameter m describing the microstructure on a regular grid with 50 elements in each direction. We then compute numerically the effective elasticity tensors $A_0^*(m)$ for each so-defined samples of parameters $m = (m_1, m_2)$, by using the finite element solver FreeFem++ [Hecht 2012]. We emphasize the fact that rotating a periodic cell by $\pi/2$ while exchanging m_1 and m_2 leaves it invariant. Thus, the computation of the effective elasticity tensor can be restricted to the samples where $m_1 \leq m_2$.

To interpolate the effective elastic law, we take advantage of the structure of the P_1-functions in FreeFem++. Indeed, we have the value of all components of A^* and their sensitivities on each vertex of the discretization grid of m, which defines a P_1-function. Hence, there is no need to implement a specific interpolation function in FreeFem++ and during the optimization step, the call to the effective elasticity tensor is not time consuming.

We noticed from our numerical results that all the homogenized coefficients of A^* are strictly decreasing, with respect to m_1 and m_2 (as could be expected from mechanical intuition). This property must be preserved during the interpolation of the elasticity tensor. Among the several interpolation methods that were investigated, namely linear interpolation, splines, Kriging, only the linear interpolation ensures the strict monotonicity of the functions. However, using a linear interpolation, the derivatives of the interpolated tensor with respect to m_1 and m_2 are piecewise constant and discontinuous. Thus, these derivatives are not very precise and difficult to use in an optimization algorithm. Thus, we decided to interpolate the sensitivities, computed from (4.6), separately by the same P_1 algorithm. This choice makes the values of the homogenized coefficients and their sensitivities slightly inconsistent. However, in practice, the chosen interpolations are precise enough so not to impair the convergence of the gradient type algorithm used during the optimization stage.

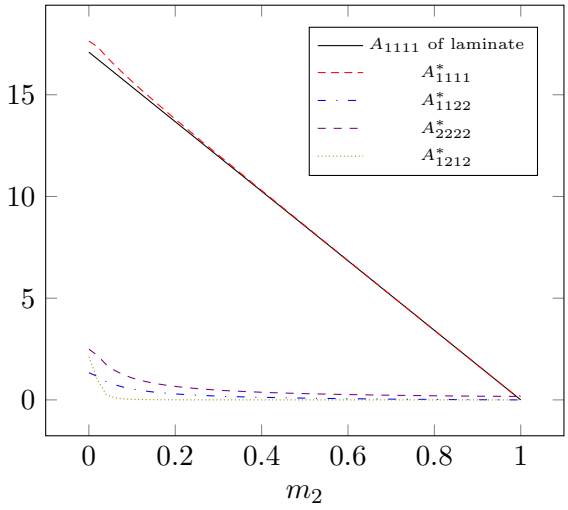

Figure 4.3: Comparison of the numerically computed components of $A_0^*((1, m_2))$ with the theoretical ones given by the rank-one laminate formula.

4.3.4.d Degeneracy issues

There exists two kinds of configurations where the $Y_0(m)$ cells are degenerate. Firstly, when one of the microstructure parameters m_i is equal to 0 but, not the other one. The square cell is full of material but features a central crack. Hence, the homogenized tensor $A_0^*(m)$ is not equal to the pure solid tensor A. Numerically, the crack is represented by a thin rectangle excluded from the mesh of the cell of width $m_i = 10^{-3}$.

Secondly, when one of the microstructure parameters m_i is equal to 1, the domain obtained by periodic repetition of the cell is no longer connected, but is rather a union of disconnected parallel bars. To avoid the degeneracy of the homogenized elasticity tensor in such a case, we impose m_i to be less than a maximal value of $(1 - 10^{-3})$. However, in the case when m_i is close to 1, the composite material is a single lamination along the y_j axis (with $j = 3 - i$) of phase A and void in respective proportions $\rho = 1 - m_j$ and $(1 - \rho) = m_j$. The homogenized elasticity tensor $A_0^*(m)$ is then algebraically known [Allaire 1997]. All of its components are equal to 0, except $(A_0^*(m))_{iiii}$ given by

$$(A_0^*(m))_{iiii} = \frac{4\mu(\lambda + \mu)}{\lambda + 2\mu}\rho$$

The Lamé coefficients of the isotropic material used numerically are : $\lambda = 12.96$ and $\mu = 5.56$, corresponding to a Young modulus $Y = 15$ and to a Poisson ratio $\nu = 0.35$. As shown in Figure 4.3, the numerical results are close to the theoretical ones of the rank-one laminate. It is therefore a justification of the above approximation which amounts to replace $m_i = 1$ by the smaller value $m_i = (1 - 10^{-3})$ when computing the homogenized tensor.

4.3.5 Numerical results and discussion

Numerical results for the entries of the homogenized tensor A^* and their derivatives as functions of the parameters m are displayed on Figure 4.4. The results are consistent, since the gradients

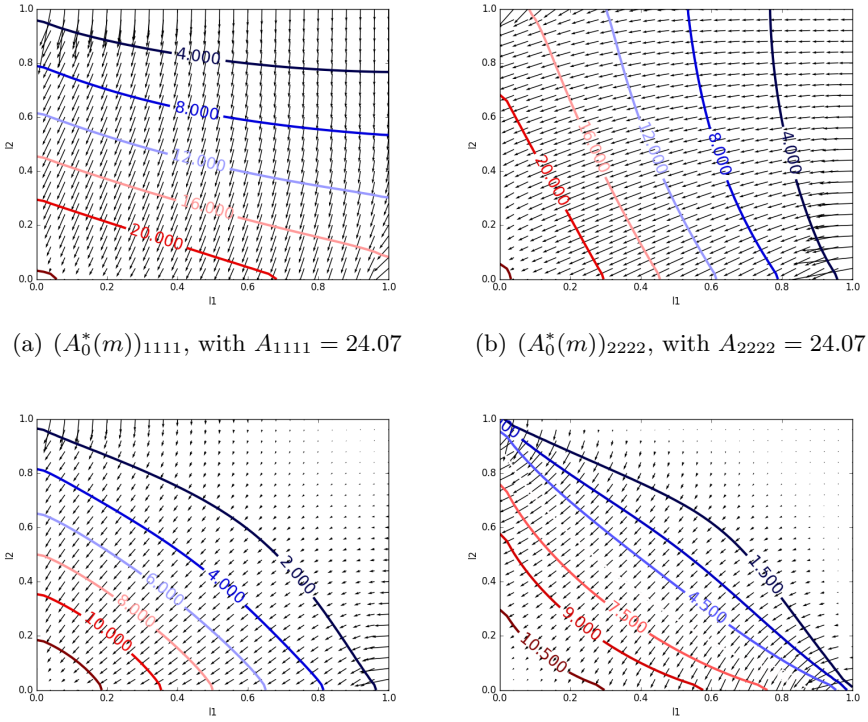

(a) $(A_0^*(m))_{1111}$, with $A_{1111} = 24.07$

(b) $(A_0^*(m))_{2222}$, with $A_{2222} = 24.07$

(c) $(A_0^*(m))_{1122}$, with $A_{1122} = 12.96$

(d) $(A_0^*(m))_{1212}$, with $A_{1212} = 11.11$

Figure 4.4: Isolines of the entries of the homogenized tensor A^* and their gradient (small arrows) according to the parameters m. The x-axis is m_1, the y-axis is m_2

are orthogonal to the isolines. When the cell is full and without crack, i.e. $m = 0$, the homogenized tensor $A_0^*(m)$ is equal to A. When the cell is close to be empty, i.e. m close to $(1, 1)$, the homogenized tensor is converging to the null tensor. Moreover, one can easily check, that the entries of $A_0^*(m)$ decrease, when m_1 is fixed and m_2 is increasing (and vice versa). In other words, the cell is globally weaker when its hole is widening in one direction or the other. However, the sensitivity of the component $(A_0^*(m))_{1111}$ to the parameter m_2 is greater than the one to the parameter m_1, see Figure 4.4(a). That is explained by the fact that, along the y_1 axis, the strength of the cell is mainly insured by the material in the areas above and below the hole, whose sizes depend on m_2. As could be expected, the homogenized elasticity tensor is quite smooth with respect to the parameter m, so it is amenable to a gradient based optimization method.

4.4 Processing: optimization among the set of periodic composite materials

4.4.1 Settings of the homogenized problem

In this paper, we focus on the compliance minimization problem, hence the cost function J defined in Section 4.2 is given by

$$J(\Omega) = \int_{\Gamma_N} g \cdot u \, ds,$$

whose relaxed version for composite material reads as

$$J^*(\theta, A^*) = \int_{\Gamma_N} g \cdot u^* \, ds,$$

which is also equal to

$$J^*(\theta, A^*) = \min_{\tau \in H_0} \int_D A^{*-1}\tau : \tau \, \mathrm{dx},$$

where

$$H_0 = \left\{ \tau \in L^2(D; \mathcal{M}_2^s) \text{ such that } \begin{array}{l} \mathrm{div}(\tau) = 0 \text{ in } D \\ \tau n = g \text{ on } \Gamma_N \\ \tau n = 0 \text{ on } \Gamma \end{array} \right\}.$$

Note that the results of the present section are not restricted to compliance minimization. For example, see 4.7.1 for a stress minimization problem.

The optimization problem defined in Section 4.2 can be recast as a minimization problem over the stress field and the admissible microstructures [Allaire 2002a]. Namely, it is equivalent to

$$\begin{array}{c} \inf \\ \sigma \in H_0 \\ m \in L^\infty(D; [0,1]^2) \\ \alpha \in L^\infty(D; \mathbb{R}) \\ \int_D \theta(m) \, \mathrm{dx} \leq V \end{array} \quad \int_D A_\alpha^{*-1}(m)\sigma : \sigma \, \mathrm{dx},$$

where

$$\theta(m) = 1 - m_1 m_2$$

is the local density of the periodic microstructure of parameters m.

In order to solve this problem, we use an alternate minimization algorithm [Allaire 2002b], minimizing successively with respect to the stress field σ, the microstructure m and the orientation α of the cell. We introduce the corresponding Lagrangian

$$\mathcal{L}(m, \alpha, \sigma, \ell) = \int_D A_\alpha^{*-1}(m)\sigma : \sigma \, \mathrm{dx} + \ell \left(\int_D \theta(m) \, \mathrm{dx} - V \right),$$

where ℓ is the Lagrange multiplier associated to the volume constraint.

Minimization w.r.t the stress field. For given design fields (m, α), the minimization with respect to the stress field σ amounts to solve the elasticity problem with a material of elasticity tensor equal to $A^*_\alpha(m)$ in D.

Minimization w.r.t the microstructure m**.** For a given stress field σ, to minimize with respect to the microstructure m, we use the projected gradient algorithm. Recall that the considered problem is self-adjoint. The descent directions are given by the derivatives of $\mathcal{L}$ with respect to m

$$\left\langle \frac{\partial \mathcal{L}}{\partial m_i}(m, \alpha, \sigma, \ell), h \right\rangle = -\int_D \left(\frac{\partial A^*_\alpha}{\partial m_i}(m) A^{*-1}_\alpha(m)\sigma : A^{*-1}_\alpha(m)\sigma + \ell m_j \right) h \, \mathrm{dx},$$

with $j = 3 - i$. We have to select a descent direction $h = dm_i$ such that

$$\left\langle \frac{\partial \mathcal{L}}{\partial m_i}(m, \alpha, \sigma, \ell), dm_i \right\rangle < 0,$$

which is achieved by choosing

$$dm_i = \frac{\partial A^*_\alpha}{\partial m_i}(m) A^{*-1}_\alpha(m)\sigma : A^{*-1}_\alpha(m)\sigma + \ell m_j \quad \text{in } D. \tag{4.8}$$

The update of the microstructure at iteration n is given by :

$$m_i^{n+1} = P_{[0,1]}(m_i^n + \mu_m dm_i) \tag{4.9}$$

where $\mu_m > 0$ is the step size and $P_{[0,1]}$ is the projection operator on the interval $[0, 1]$. The value of ℓ is updated at each iteration by a dichotomy process designed to respect the volume constraint.

Minimization w.r.t the orientation α**.** To minimize with respect to the orientation, we could use the same method as for the minimization with respect to the microstructure, but there exists a better (more efficient) algorithm than the gradient descent method to compute the optimal orientation. Pedersen [Pedersen 1989] proved that the optimal orientation of an orthotropic cell for a given displacement field is the one where the cell is aligned with the principal directions of the strain tensor. A similar result with a given stress field can easily be shown in the same way.

First, the principal (orthogonal) directions of the given stress field σ are computed. According to Pedersen formulas, we have to align the principal directions σ with the orientation of the cell. Hence, at this stage, the optimal orientation is known up to an additive multiple of $\frac{\pi}{2}$. However, by choosing to align the vector $a_1 = (\cos(\alpha), \sin(\alpha))$ with the eigenvector of σ of smallest eigenvalue (possibly negative), the angle α is defined modulo π. Note that the cases where σ is proportional to the identity are generically limited to isolated points (and thus the set of such point is of null measure). This approach is more efficient than the gradient descent method, mainly because it is a global minimization method, providing an optimal orientation at each iteration. However, this method can usually not be generalized to other objective functions.

Remark 5. *For multiple loads cases, Pedersen algorithm does not work. However, the optimal orientation at one point still only depends on the values of the local stress fields and is solution of a one dimensional minimization problem. Thus the global minimization of the cost function with respect to the orientation α remains relatively easy even without any explicit expression.*

4.4.2 Implementation

Complete optimization algorithm. The optimization algorithm is an iterative method, structured as follows :

1. Initialization of the design parameters (m, α), for example we take $m_1 = m_2$, constant satisfying the volume constraint, and $\alpha = 0$.

2. Iteration until convergence, for $n \geq 0$:

   (a) Computation of σ^n through a problem of linear elasticity with $A^*_{\alpha^n}(m^n)$ as elasticity tensor

   (b) Updating the orientation α^{n+1}, using the Pedersen formulas

   (c) Updating the design parameters m^{n+1}, using (4.8-4.9), with the parameters σ^n and α^n.

We implemented the topology optimization in the finite element software FreeFem++ [Hecht 2012] (see [Allaire 2006] for the use of FreeFem++ in optimal design). All unknowns are discretized using P_1-functions.

Stress field σ. We solve the elasticity problem, namely we compute the displacement field

$$u \in V_D := \{v \in H^1(D; \mathbb{R}^2) \text{ such that } v = 0 \text{ on } \Gamma_D\},$$

such that, for all $v \in V_D$,

$$\int_D A^*_0(m) R(\alpha)^T e(u) : R(\alpha)^T e(v) \, \mathrm{dx} = \int_{\Gamma_N} g \cdot v \, \mathrm{ds} \, .$$

We use P_1 finite elements to compute the displacement u. Afterwards, the stress tensor σ is obtained as the interpolation of the P_0-function $R(\alpha) A^*_0(m) R(\alpha)^T e(u)$ in the set of P_1 finite elements

Minimization with respect to the orientation. As recalled previously, the minimizer of $\mathcal{L}(m, \alpha, \ell, \sigma)$ with respect to α is reached when the cell is aligned with the eigenvectors of the stress tensor σ. Denote by a and b the rotation matrices of angles α and 2α, respectively,

$$a = Q(\alpha) \, , \quad b = Q(2\alpha) \, . \tag{4.10}$$

As is well known [Pedersen 1989], the Hooke's law depends on the orientation α only through the tensor $R(\alpha)$ which, in turns, only depends on the rotation matrix b. If we choose the first column a_1 to be aligned with the eigenvector of σ of smallest eigenvalue, we get that

$$b_1 = \frac{1}{\sqrt{(\sigma_{11} - \sigma_{22})^2 + 4\sigma_{12}^2}} (\sigma_{11} - \sigma_{22}, 2\sigma_{12})^T \, .$$

Remark 6. *In practice, Voigt notations are used, in order to replace tensors product by matrix product. Hence, a second-order tensor ξ is represented by the following vector :*

$$\{\xi\} = \left(\xi_{11}, \xi_{22}, \frac{\xi_{12} + \xi_{21}}{\sqrt{2}} \right)^T \, .$$

And the fourth-order tensor $R(\alpha)$ can be represented by a matrix, which is expressed only using the vector $b_1 = (b_{11}, b_{21})$

$$\{R(\alpha)\} = \begin{pmatrix} \frac{1+b_{11}}{2} & \frac{1-b_{11}}{2} & -\frac{b_{21}}{\sqrt{2}} \\ \frac{1-b_{11}}{2} & \frac{1+b_{11}}{2} & \frac{b_{21}}{\sqrt{2}} \\ \frac{b_{21}}{\sqrt{2}} & -\frac{b_{21}}{\sqrt{2}} & b_{11} \end{pmatrix}. \tag{4.11}$$

Minimization with respect to the cell parameters m**.** At each iteration, the descent directions for both parameters m_1 and m_2 are computed using (4.8). Numerically, the fields m_1 and m_2 are P_1-functions. Thus, the partial derivatives for the Lagrangian, denoted by $\frac{\partial \mathcal{L}}{\partial m_i}$ are interpolated, using a H^1 equivalent norm, by solving the following variational formulation : $\forall h \in H^1(D, \mathbb{R})$

$$\int_D \left(\frac{\partial \mathcal{L}}{\partial m_i} h + \eta^2 \nabla \frac{\partial \mathcal{L}}{\partial m_i} \cdot \nabla h \right) \mathrm{dx} = - \int_D \left(\frac{\partial A_0^*}{\partial m_i}(m) R(\alpha)^T e(u) : R(\alpha)^T e(u) + \ell m_j \right) h \, \mathrm{dx}$$

with $\eta > 0$ a small coefficient, which typically depends on the size of the elements of the mesh. The purpose of this small coefficient is to numerically regularize the partial derivatives on a length scale of order η and to limit the checkerboard effect [Sigmund 1998]. The update of the fields is then given by

$$m_i^{n+1} = \max\left(0, \min\left(1, m_i^n - \mu_m \frac{\partial \mathcal{L}}{\partial m_i}\right)\right).$$

In practice, we use an adaptive step size μ_m. At each iteration, if the newly computed homogenized structure is accepted (i.e. if its compliance is lower than the one of the previous structure), the step size μ_m is increased of 20%. On the contrary, if the newly computed structure is rejected, the step size is divided by 2.

The Lagrange multiplier ℓ is computed so that the volume constraint

$$\int_D \theta(m) = V$$

is satisfied almost exactly. To this end, we use a dichotomy process (note that the variational formulation that defines $\partial \mathcal{L}/\partial m_i$ has not to be solved at each iteration of the dichotomy, as the dependency on ℓ is linear).

4.4.3 Numerical results and discussion

We have numerically implemented the optimization algorithm for the bridge problem, see Figure 4.5 for the boundary conditions. The domain size is 22×13 and it is discretized by a structured triangular mesh. Taking 4 nodes per unit length on the boundary yields a mesh with 18304 triangles and 9293 vertices. The volume constraint is fixed to 30% of the working domain. The algorithm converged quickly and smoothly, see Figure 4.6. The results are displayed on Figure 4.7. The optimized design parameters m_1 and m_2 in Figures 4.7(c) and 4.7(d) are most of the time not equal (when they are different from the extreme values 0 and 1), and the optimized orientation (Figure 4.7(b)) is almost radial. This is a clear manifestation that the obtained optimal composite is anisotropic.

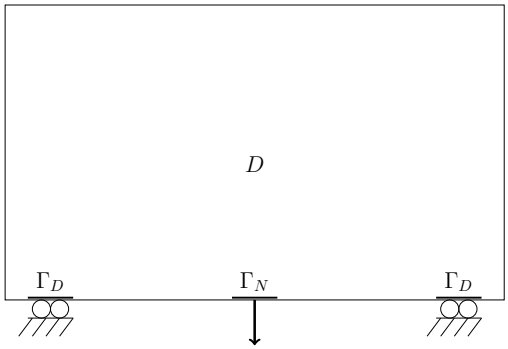

Figure 4.5: Boundary conditions for the bridge problem

The minimal compliance for a single-load case is known to be reached by rank-2 laminates [Allaire 2002a]. We have also computed the optimal design for such laminates. The results are displayed in Figure 4.8 (note that the m_1 and m_2 parameters have a different signification for rank-2 laminates). The two optimized designs, respectively with square cells and laminates, are closed to each other. Indeed, both feature a radial structure, with high density on the main arch and in the loading areas. Moreover, the final compliance 2.141 for the locally periodic square cells case is closed to the optimal one 2.100 for rank-2 laminates: the difference is less than 2%. This can be seen as a justification of our choice of such cells. For the sake of comparison, the same test case has been performed with the Solid Isotropic Material with Penalization (SIMP) method: the elastic law is represented as a power law of the density (the maximal exponent is 3). The optimal compliance obtained by this method is equal to 2.38, which is 11% greater than the final compliance reached by the homogenization method. The discretized mesh was the same than the one for the homogenization method. In order to obtain a mesh independent design (and to avoid checkerboards), a sensitivity filter was applied. The radius of the filter was equal to three mesh-element sizes. The optimal design is displayed on Figure 4.9(b). The optimal design without penalization (i.e. with exponent 1) was also computed and, of course, displays large grey areas, see Figure 4.9(a). Its compliance is equal to 1.99, a much lower value than that for the homogenization method, as it is expected [Allaire 2002a], since the SIMP method (with exponent 1) is equivalent to use fictitious isotropic material which do not fit into the Hashin-Shtrikman bounds. Hence, the optimized compliance is much lower than the previous ones, including the compliance reached by the rank-2 laminates which is the global optimum.

We also ran several tests with additional constraints on the design parameters, denoted by B, C, D and E. The previous one is denoted by A. The test cases and the results are summarized in Table 4.1, sorted according to the final compliance. The lower compliance is reached when we optimize with respect to the three variables, m_1, m_2 and α. In this case, the set of admissible shapes is the largest and contains all other used subsets.

When the orientation of the cells is fixed to zero (cases B and D, see Figures 4.10 and 4.11), the anisotropy of the cells is no longer an asset. The optimized design is then self-penalized. Only small areas of intermediate density are visible. Most of the domain is either made of void or plain material. Indeed the best strategy to bear stress, when the cell is not aligned with the principal directions of σ, is to be strong in all directions, and so to be isotropic.

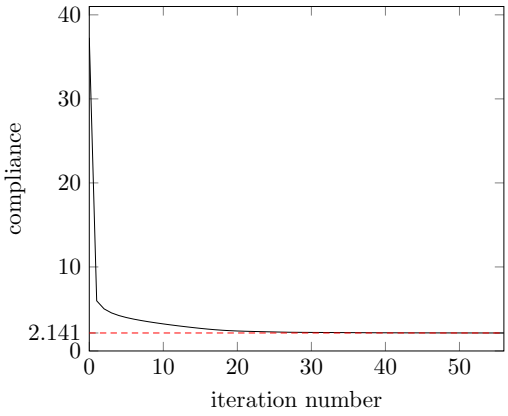

Figure 4.6: Convergence history of the objective function (compliance) for the bridge

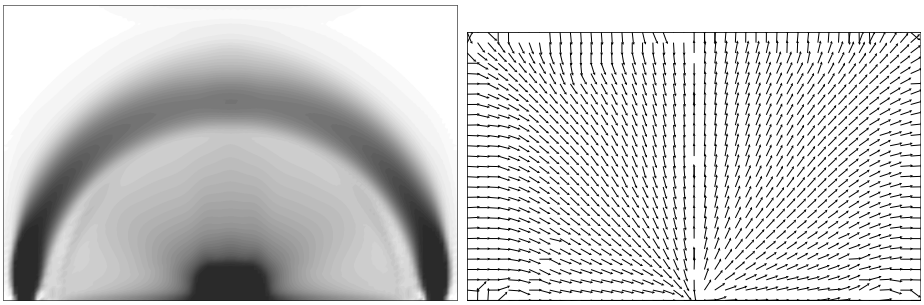

(a) Density (b) Orientation of the cells

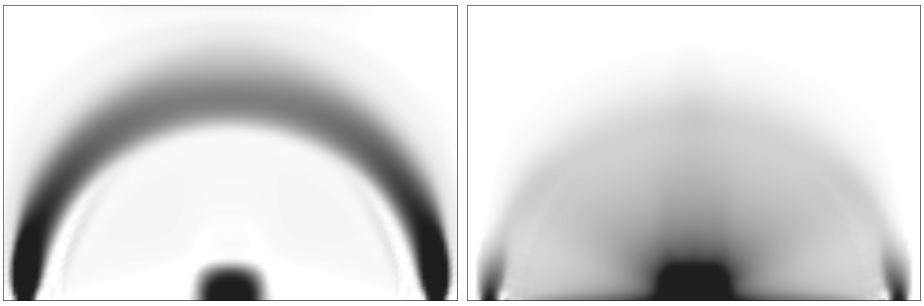

(c) m_1 (d) m_2

Figure 4.7: Optimized design of the bridge, case A : no constraint on the design variables.

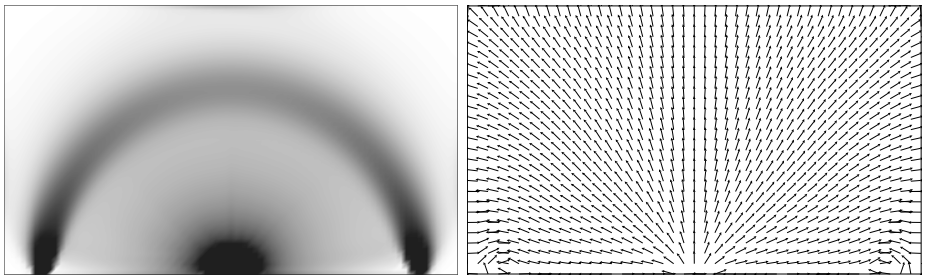

(a) Density (b) Orientation of the cells

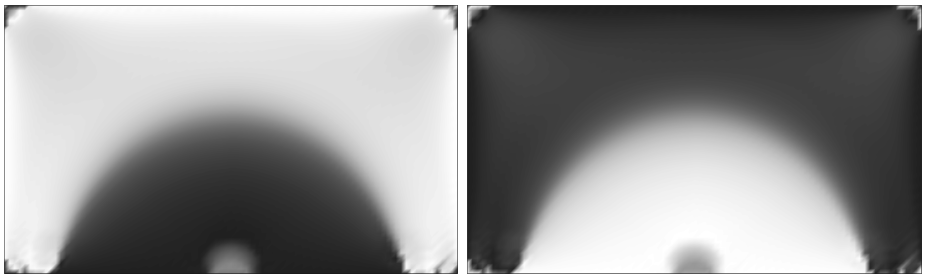

(c) m_1 (d) m_2

Figure 4.8: Optimized design of the bridge with rank-2 laminates

(a) Density (b) Density

Figure 4.9: Optimized design of the bridge with penalized (a) and non penalized (b) SIMP method

Case	Constraint on m	Constraint on α	Optimal compliance
A	none	none	2.141
B	none	$\alpha = 0$	2.524
C	$m_1 = m_2$	none	2.549
D	$m_1 = m_2$	$\alpha = 0$	2.600
E	$m_1 = m_2 = \sqrt{0.7}$	none	5.121
reference	$m_1 = m_2 = \sqrt{0.7}$	$\alpha = 0$	37.410

Table 4.1: Test Cases

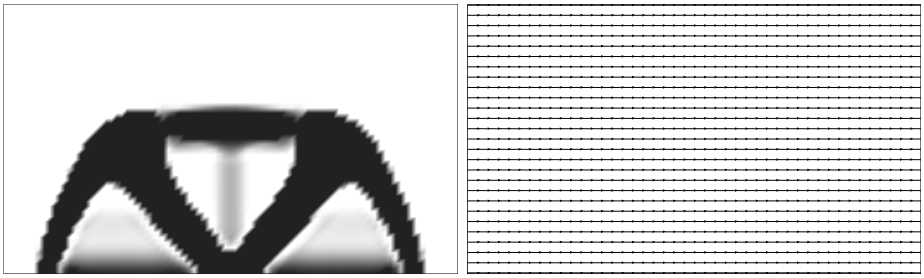

(a) Density (b) Orientation of the cells

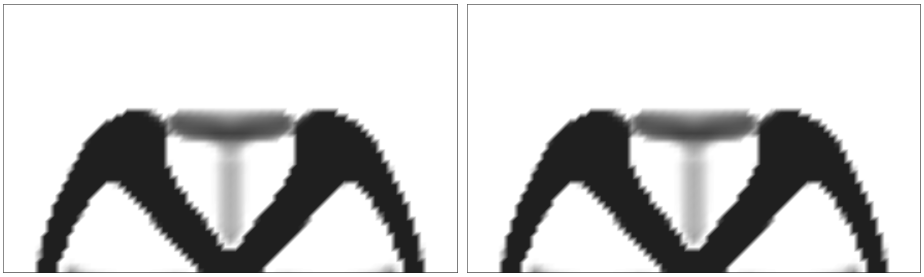

(c) m_1 (d) m_2

Figure 4.10: Optimized design of the bridge, case B : $\alpha = 0$.

When the dimensions of the holes are fixed (case E), the optimal orientation of Pedersen is still valid. The optimized orientation is closed to the one of case A. However, the optimized compliance is much greater. Nevertheless, the compliance is decreased by 87% compared to the reference value.

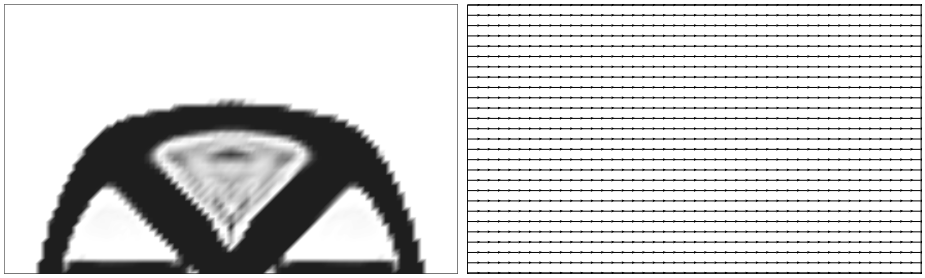

(a) Density (b) Orientation of the cells

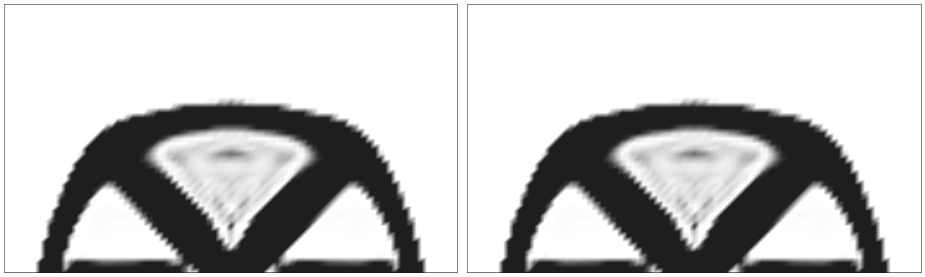

(c) m_1 (d) m_2

Figure 4.11: Optimized design of the bridge, case D : $m_1 = m_2$ and $\alpha = 0$.

4.5 Post-Processing : projection of the optimized microstructure

The last step is to construct a sequence of classical or genuine shapes that actually converges toward the computed optimal composite. This sequence is indexed by a small positive parameter $\varepsilon > 0$ which is the size of the period of the periodic composite. In numerical practice, one has to choose a specific value of ε and then the projection will be done for this chosen periodicity. Of course, the smaller ε, the more detailed will be the resulting genuine shape.

In section 4.5.1 we define a set of sequences of shapes that converge toward square periodic composites. Each sequence of shapes is defined by the micro-structure m of the composite and a mapping function φ. As shown in section 4.5.2 each reachable square periodic composite has to be build on a conformal lattice. Equivalently, the Laplacian of the orientation of the cells has to be a harmonic function. This condition is enforced to the optimal composite by pursuing the optimization while imposing this extra constraint (section 4.5.3). It remains to compute the mapping function φ to completely define a sequence of genuine shapes converging toward the optimum obtained. To be able to cope with the fact that the orientation if defined up to a rotation of angle π, we introduce an abstract manifold on which the mapping function is defined (section 4.5.4). Its computation then reduced itself to solve two linear problems (section 4.5.5).

4.5.1 Sequences of shapes

Projection of the optimized design, case without optimal orientation. First, we consider the case where the orientation of the cell is constant in the whole domain D. Our unit

cells (rectangular hole in a square) can be analytically defined by

$$Y_0(m) = \Big\{ y \in [0,1]^2 \text{ such that } \cos(2\pi y_1) \geq \cos(\pi(1-m_1)) \\ \text{or } \cos(2\pi y_2) \geq \cos(\pi(1-m_2)) \Big\}.$$

Hence, to build a cellular structure $\Omega_\varepsilon(m)$, we have to pave the domain D with cells $\varepsilon Y_0(m)$. However, the hole size m is varying inside D so the periodicity cell is macroscopically modulated, as is classical in homogenization. Thus the genuine shape $\Omega_\varepsilon(m)$ is defined by

$$\Omega_\varepsilon(m) = \Big\{ x \in D \text{ such that } \cos\left(2\pi\frac{x_1}{\varepsilon}\right) \geq \cos(\pi(1-m_1(x))) \\ \text{or } \cos\left(2\pi\frac{x_2}{\varepsilon}\right) \geq \cos(\pi(1-m_2(x))) \Big\},$$

where $m_1(x), m_2(x)$ are functions defined on D with values in $[0,1]$. The values of m_1 and m_2 are not necessarily constant in each cell of the structure. Hence, the cellular structure $\Omega_\varepsilon(m)$ do not exactly feature square cells with rectangular holes. But, since the size ε is going to 0, if the functions m_1 and m_2 are continuous, the sequence of cellular structures is converging to the composite of local Hooke's law equal to $A_0^*(m)$.
An other approach is to compute on each cell, the mean value of the dimensions parameter m_1 and m_2 on the cell [Zhang 2015]. With this method, each shape of the minimization sequence is composed of square cells as defined previously. However, its implementation can be time-consuming : for each shape of the sequence, we have to determine each cell of the lattice and its dimension parameters before constructing the final design. Hence, in the following, we will use the previous formulation.

The cellular structures can be defined using level-sets. We introduce two level-set functions $f_{\varepsilon,i}^m \in \mathcal{C}(D;\mathbb{R})$, one for each direction

$$f_{\varepsilon,i}^m(x) = -\cos\left(\frac{2\pi x_i}{\varepsilon}\right) + \cos(\pi(1-m_i(x))).$$

and the level set function

$$F_\varepsilon^m = \min(f_{\varepsilon,1}^m, f_{\varepsilon,2}^m).$$

The final structure $\Omega_\varepsilon(m)$ is then defined by

$$\Omega_\varepsilon(m) = \{x \in D \text{ such that } F_\varepsilon^m(x) \leq 0\}.$$

The construction of a minimizing sequence is immediate : we just have to update the size ε in the previous level set function.

Projection of the optimized design, case with optimized orientation. The crucial point is to take into account the optimized orientation of the cell. Indeed, neither gap nor overlap is allowed between two cells. Hence, cells have to be slightly deformed to ensure the connectivity of the final structure. A map $\varphi = (\varphi_1, \varphi_2)$ from D into $\mathbb{R}^2$ is introduced for this purpose :

the inverse of this map distorts a regular grid of squares in order to orientate each square at the optimized orientation α. Then, the previous projection method can be applied on this new grid. The final shape, now denoted $\Omega_\varepsilon(\varphi, m)$, is still defined by a level set function, the same as previously except that the coordinates are now given by the map function φ:

$$f_{\varepsilon,i}^{\varphi,m}(x) = -\cos\left(\frac{2\pi\varphi_i(x)}{\varepsilon}\right) + \cos(\pi(1 - m_i(x))). \tag{4.12}$$

$$F_\varepsilon^{\varphi,m} = \min(f_{\varepsilon,1}^{\varphi,m}, f_{\varepsilon,2}^{\varphi,m}). \tag{4.13}$$

$$\Omega_\varepsilon(\varphi, m) = \{x \in D \text{ such that } F_\varepsilon^{\varphi,m}(x) \leq 0\}. \tag{4.14}$$

Remark 7. *The map φ is introduced in order to take into account the optimal orientation of the cell. Hence, φ depends only on the angle field α. In particular, φ does not depend on the size ε of the cells. Once φ has been computed, it could be used for any value of this scale parameter.*

4.5.2 Conformality condition

As seen above, we introduce here a map φ in order to construct a minimizing sequence of genuine shapes that converges to the optimal composite. We emphasize that the cells featured in those genuine shapes have to converge to square cells, in order that their effective elasticity tensor converges to A^*. To perform this, we require that φ locally preserves all angles: it is a conformal map. In other words, a small square cell is deformed by φ into another almost square cell since the angles between the cell sides, and their diagonals too, are unchanged. This conformality requirement is not specific to square cells. It should be imposed to other types of periodicity cells, like hexagonal cells, in order that the minimizing sequence of genuine shapes converges to the optimal composite A^*.

To respect the local orientation, the gradient of φ has to be aligned with the axis of the cell given by $a = Q(\alpha)$. Moreover, the proportions of the cell have to be preserved in order to converge to a true square and not simply to a rectangle: $|\nabla\varphi_1| = |\nabla\varphi_2| = e^r$, where $r \in H^1(D)$ is a (scalar) dilation field. The exponential form has been chosen in order to simplify the following equation, and to impose easily the condition of positiveness. Hence,

$$\nabla\varphi = e^r Q(\alpha). \tag{4.15}$$

It is a classical result that, provided the rotation field is regular, the existence of a compatible conformal mapping φ is equivalent to the harmonicity of the orientation α. We recall the proof of this result which holds true only in two space dimensions.

Lemma 4.5.1. *Let α be a regular orientation field and D be a simply connected domain. There exists a mapping function φ and a dilatation field r satisfying (4.15) if and only if*

$$\Delta\alpha = 0 \text{ in } D. \tag{4.16}$$

Proof. Recall that in 2-d the rotational or curl of a vector field $u = (u_1, u_2)$ is defined as $\operatorname{curl} u = \nabla \wedge u = \frac{\partial u_2}{\partial x_1} - \frac{\partial u_1}{\partial x_2}$, where $\wedge$ is the 2-d cross product of vectors. Of course, the rotational of a gradient vanishes. Conversely, as D is assumed to be simply connected, a vector-valued map is a gradient if and only if its rotational vanishes. Therefore, there exists a map φ which verifies (4.15) if and only if the rotational of the right hand side vanishes, namely $\operatorname{curl} e^r Q(\alpha)$. Recall from (4.10) that $a = Q(\alpha)$ with columns a_1, a_2. Therefore

$$\operatorname{curl}\left(e^r Q(\alpha)\right) = 0 \Leftrightarrow \forall i \in \{1,2\}, \quad \nabla r \wedge a_i = -\nabla \wedge a_i.$$

Since (a_1, a_2) is an orthonormal basis, ∇r can be rewritten as

$$\nabla r = (-\nabla \wedge a_2)a_1 + (\nabla \wedge a_1)a_2. \tag{4.17}$$

We compute

$$\nabla \wedge a_1 = \frac{\partial \alpha}{\partial x_1}\cos(\alpha) + \frac{\partial \alpha}{\partial x_2}\sin(\alpha) \text{ and } \nabla \wedge a_2 = -\frac{\partial \alpha}{\partial x_1}\sin(\alpha) + \frac{\partial \alpha}{\partial x_2}\cos(\alpha). \tag{4.18}$$

Coupling equations (4.17) and (4.18) leads to

$$\nabla r = \left(-\frac{\partial \alpha}{\partial x_2}, \frac{\partial \alpha}{\partial x_1}\right)^T. \tag{4.19}$$

Finally, the dilation factor r does exist if and only if, the left hand side of (4.19) is curl free, which leads to the harmonic condition (4.16) on the orientation field α.

□

4.5.3 Optimization over feasible locally square periodic composites

The orientation α given by the optimization does not necessarily respect the conformality condition. In order to enforce this condition, we pursue the optimization algorithm while imposing the harmonicity of α. The only step that differs from the optimization algorithm of section 4.4 concerns the minimization with respect to α. We can no longer simply align the periodicity cells with the principal directions of the stress as it leads to solutions that does not satisfy the conformality condition. Moreover, we slightly change the cost function by adding a small regularization term on the orientation. Thus, the optimization with respect to the orientation reduces to the minimization of

$$\int_D \left(A^*_\alpha(m)^{-1}\sigma : \sigma + \eta^2 |\nabla \alpha|^2\right) \mathrm{dx},$$

under the constraint

$$\int_D \nabla \alpha \cdot \nabla q \ \mathrm{dx} = 0 \text{ for all } q \in H^1_0(D).$$

Remark 8. *The regularization term in the above minimization problem is the usual L^2-norm of the angle gradient. Other choices are possible, including more "local" criteria. For example, one could replace this gradient norm by a least square difference between the angle and its filtered version, obtained by a local convolution. We did not try this idea since the gradient norm works nicely. Note that the conformality constraint is already non-local and thus the additional computational cost of minimizing the gradient norm is somehow negligible.*

We recall that the dependence of the Hooke's law with respect to the orientation is explicitly known by (4.7). Moreover, the tensor $R(\alpha)$ depends only on b_1, see (4.11), where

$$(b_1, b_2) = b = a^2 = Q(\alpha)^2 = Q(\beta),$$

with $\beta = 2\alpha$ or equivalently

$$b_1 = (\cos(\beta), \sin(\beta)). \tag{4.20}$$

Let $S(b_1) = R(\alpha)$. As shown by formula (4.11), $S(b_1)$ is an affine function of b_1. Since (4.7) can be rewritten as

$$A^*_\alpha(m) = S(b_1)^T A^*_0(m) S(b_1),$$

we are left with the minimization problem of

$$\int_D \left(A^*_0(m)^{-1} S(b_1)\sigma : S(b_1)\sigma + \eta^2 |\nabla\beta|^2 \right) \mathrm{dx}$$

under the constraints (4.20) (relating b_1 and β) and

$$\int_D \nabla\beta \cdot \nabla q \ \mathrm{dx} = 0, \ \text{for all } q \in H^1_0(D).$$

This minimization problem can not be solved exactly because of the non linear constraint (4.20). At each iteration n, we approximate this constraint by its linearization around the current state. We compute δb_1^n and $\delta\beta^n$ that minimizes

$$\int_D A^*_0(m)^{-1} S(b_1^n + \delta b_1)\sigma : S(b_1^n + \delta b_1)\sigma \ \mathrm{dx} + \eta^2 \int_D |\nabla(\beta^n + \delta\beta)|^2 \ \mathrm{dx}$$

under the constraint

$$\int_D \nabla(\beta^n + \delta\beta) \cdot \nabla q \ \mathrm{dx} = 0, \ \text{for all } q \in H^1_0(D)$$

and the linearized constraint

$$\delta b_1 = (-\sin(\beta^n), \cos(\beta^n))\delta\beta.$$

Note that, we have

$$\nabla\beta^n = b_1^n \wedge \nabla b_1^n,$$

and thanks to the linearized constraint,

$$\nabla\delta\beta = b_1^n \wedge \nabla\delta b_1.$$

Thus, we can rewrite the linearized minimization problem solely as the variational problem consisting in finding $\delta b_1^n \in H^1(D;\mathbb{R}^2)$ and $p^{n+1} \in H^1_0(D)$ such that for all test functions $\delta c \in H^1(D;\mathbb{R}^2)$ and $q \in H^1_0(D)$,

$$2\int_D A^*_0(m)^{-1} S(b_1^n + \delta b_1^n)\sigma : S'(\delta c)\sigma \ \mathrm{dx} + 2\eta^2 \int_D (b_1^n \wedge \nabla(b_1^n + \delta b_1^n)) \cdot (b_1^n \wedge \nabla\delta c) \ \mathrm{dx} + \int_D (b_1^n \wedge \nabla\delta c) \cdot \nabla p^{n+1} \ \mathrm{dx} = 0 \tag{4.21}$$

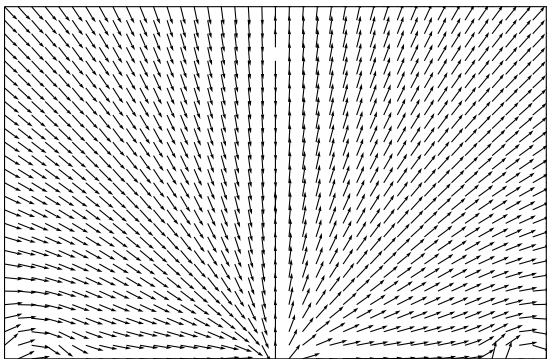

Figure 4.12: Regularized Orientation for the bridge case

and

$$\int_D (b_1^n \wedge \nabla(b_1^n + \delta b_1^n)) \cdot \nabla q \, \mathrm{dx} = 0. \tag{4.22}$$

In (4.21), p^{n+1} is the Lagrange multiplier, corresponding to the constraint (4.22) and $S'(\delta c)$ is the directional derivative of $S(b_1)$ in the direction δc. Recall that S is affine so S' is easy to determine.

The vector field b_1 is then updated after renormalization of $b_1^n + \delta b_1^n$

$$b_1^{n+1} = \frac{b_1^n + \delta b_1^n}{|b_1^n + \delta b_1^n|}. \tag{4.23}$$

Regularization algorithm. The above algorithm is structured as follows :

1. Initialization of the design parameters (m, b) with the results of the optimization without the conformality constraint.

2. Iteration until convergence, for $n \geq 0$:

   (a) Computation of the strain tensor $e(u^n)$ through the problem of linear elasticity.

   (b) Computation of the increment δb_1^n by solving the variational problem (4.21,4.22).

   (c) Updating of the orientation with (4.23).

   (d) Updating of the design parameters m^n, using (4.8,4.9), with the parameters b^n, where the Lagrange multiplier ℓ for the volume constraint in (4.8) is again computed by dichotomy.

Numerical Results. We implemented this algorithm for the optimized bridge (case A). Regularized orientation is displayed in Figure 4.12 and a comparison between the optimized orientation and the regularized orientation is displayed in Figure 4.13. There is no significant difference concerning the dimension parameters m. Hence they are not produced here.

The regularized orientation is not far from the optimized one. The regularization occurred mainly in areas where density is closed to 0 or to 1, i.e. where the homogenized material is almost isotropic and the orientation has no significant impact on the Hooke's law. Moreover, the singularity at the point $(0, 0)$ is put outside of the working domain D by the regularization algorithm. This is crucial to compute the mapping φ, but does not really degrade the final

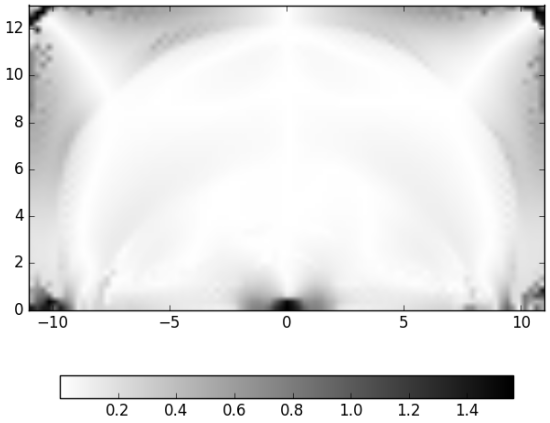

Figure 4.13: Angle difference in radian between the optimized orientation and the regularized orientation for the bridge case

design since in the vicinity of the singularities the density is equal to 1. The compliance of the regularized structure is equal to 2.169, to be compared with the value 2.141 for case A: the degradation of the solution is lower than 2%.

4.5.4 Reconstruction of a sequence of shapes

Once the optimal locally square periodic composite that satisfies the conformality condition has been computed, it remains to determine the corresponding grid map φ from D into $\mathbb{R}^2$, that satisfies (4.15). As shown in the proof of Lemma 4.5.1, the dilation field r of the cells is given by

$$\nabla r = (\nabla \wedge a_1)a_2 - (\nabla \wedge a_2)a_1.$$

Thus, it can be computed simply by minimizing

$$\int_D |\nabla r - (\nabla \wedge a_1)a_2 + (\nabla \wedge a_2)a_1|^2 \, \mathrm{dx} \tag{4.24}$$

over the maps $r \in H^1(D)$. If the orientation α is coherent on the working domain D, the computation of φ reduced to the minimization of

$$\int_D |\nabla \varphi - e^r a|^2 \, dx$$

over the fields $\varphi \in H^1(D;\mathbb{R}^2)$. Unfortunately, as a consequence of the property of central symmetry of the periodicity cells, $a = Q(\alpha)$ is only defined up to a sign. There are two ways to bypass this issue. The first and obvious one (see [Groen 2017]) would be to determine a coherent orientation of a over D (what could be done proceeding from one triangle to its neighbors and so on). The second option is based on the introduction of a covering space $\mathcal{D}$ over D and to define φ on $\mathcal{D}$ rather than on D itself (we will give more details soon). A minor advantage of this second approach relies on the fact that it saves us the computation of a coherent rotation field a. More important, even if we discard this possibility in the current article, such a coherent

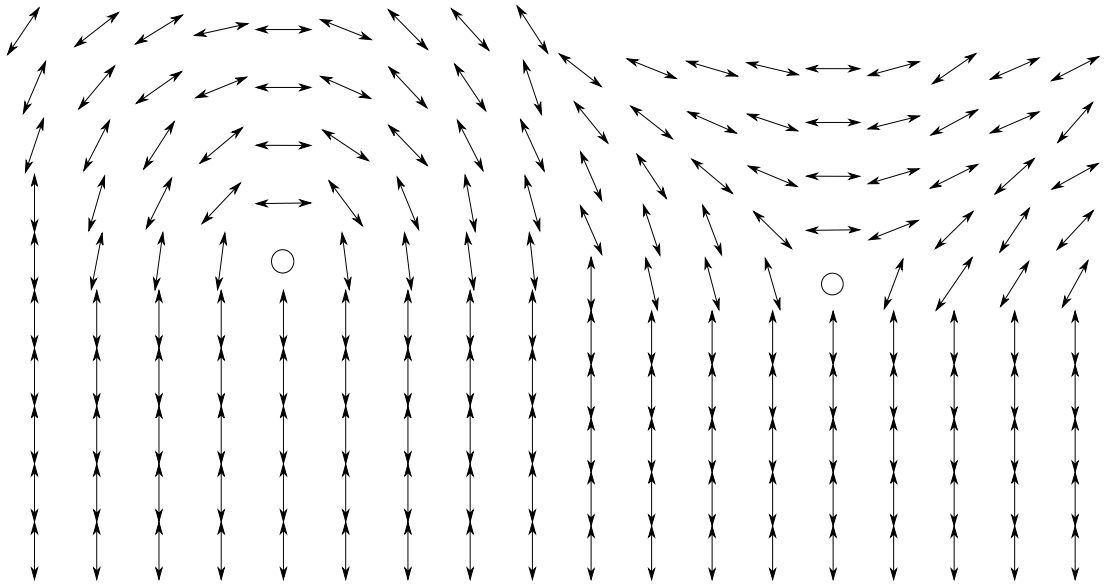

(a) Positive singularity (b) Negative singularity

Figure 4.14: The two canonical type of singularities of the field a_1. The field a_1 is not coherently orientable in those cases, as the vector a_1 rotates of an angle of $\pm\pi$ along circles which are enclosing the singularities.

orientation does not necessarily exists in the presence of singularities like the ones displayed in Figure 4.14). Hence, the first option can not be extended to encompass the general case contrarily to the second one that we retain here (a rapid description of the way the singularities could be treated in this context can be found in [Pantz 2010], for a detailed description see Section 1 of Chapter 5). In this section, we introduce the manifold $\mathcal{D}$ and recast the problem that defines the grid map. The reader mainly interested in the practical implementation could skip this part for section 4.5.5.

An abstract manifold. We introduce the cover space of D

$$\mathcal{D} = \{(x, T) \in D \times \mathrm{SO}(2) \text{ such that } T^2 = b(x)\},$$

where $\mathrm{SO}(2)$ is the set of rotations in $\mathbb{R}^2$. It is a submanifold of the space $D \times \mathrm{SO}(2)$. The rotation field a is assume to be locally orientable, meaning that D can be covered by open sets U for each of which there exists a map $T_U \in \mathcal{C}(U, \mathrm{SO}(2))$ such that for all $x \in U$, $T_U(x)^2 = b(x)$. The map T_U defines two charts g_U^+ and g_u^- of the manifold $\mathcal{D}$ given by

$$\begin{array}{rcl} g_U^+ : U & \to & \mathcal{D} \\ x & \mapsto & (x, T_U(x)) \end{array} \quad \text{and} \quad \begin{array}{rcl} g_U^- : U & \to & \mathcal{D} \\ x & \mapsto & (x, -T_U(x)). \end{array} \tag{4.25}$$

In the present article, we assume the rotation field a of the optimal design to be without singularities (and thus orientable). Thus, $\mathcal{D}$ is simply the union of two copies of D consisting of the two possible orientations of a. Nevertheless, we will not use this feature in the following.

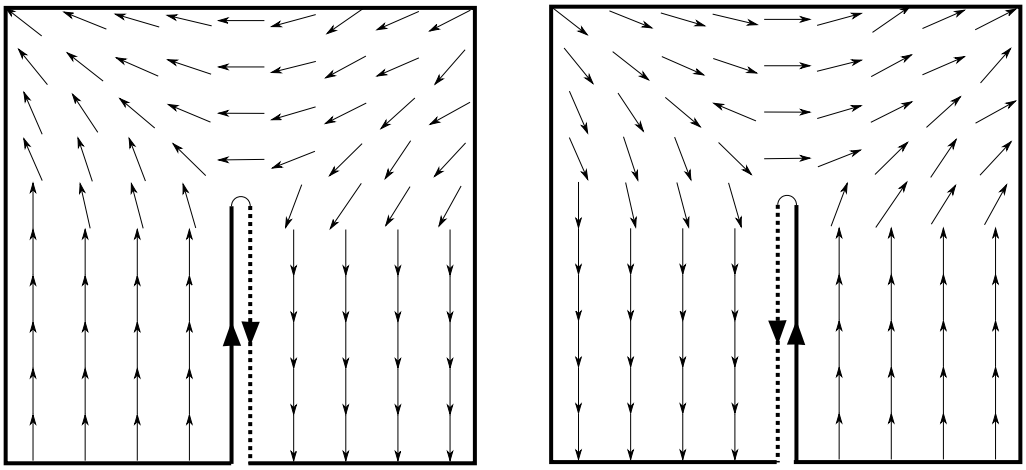

Figure 4.15: Representation of the manifold $\mathcal{D}$ in the presence of a singularity.

Its makes our method relatively easy to extend so to encompass the case with singularities, what will be done in a future work. Before digging into deeper details in the next section, let us illustrate how $\mathcal{D}$ can be represented if the field a contains singularities.

The Figure 4.15 gives such a representation of the manifold $\mathcal{D}$ in the presence of a negative singularity. The manifold $\mathcal{D}$ is obtained starting with two copies of the initial domain D (a square in the present case). Each of them is cut along the same path connecting the singularity to the boundary of D. Then, they are glued together along this very path. On Figure 4.15 the thick (respectively the dotted) lines are glued together. Contrarily to the case without singularity, $\mathcal{D}$ is connected but not simply connected and can not be embedded in $\mathbb{R}^2$. Another representation of $\mathcal{D}$ is given by the Figure 4.16 as a submanifold of $D \times \mathrm{SO}(2) \simeq D \times \mathbb{R}/2\pi\mathbb{Z}$. In this case, the manifold $\mathcal{D}$ looks as a screw in the cylinder $D \times (0, 2\pi)$ whose axis is parallel to the z-direction and located at the very position of the singularity in D. The top and bottom parts of the screw are identified.

Finally, we endow $\mathcal{D}$ with a differential structure through the projection p_D onto D. In particular, it induces a gradient operator on $\mathcal{D}$ and a second linear form $p_D^*(\,\mathrm{dx})$, the pull-back of second linear form dx defined on D. For sake of simplicity, we will denote $p_D^*(\,\mathrm{dx})$ simply dx in the following.

Construction of φ**.** We change our working space from D to $\mathcal{D}$, meaning that we are now seeking for a grid map φ from $\mathcal{D}$ into $\mathbb{R}^2$ such that

$$\nabla\varphi = e^r T \tag{4.26}$$

for all $(x, T) \in \mathcal{D}$ and for some function $r(x)$. The operator ∇ in (4.26) is not the standard gradient on the manifold $\mathcal{D}$ but is rather defined by

$$\nabla\varphi(x, T) = \nabla\varphi_U(x),$$

where U is an open subset of D,

$$\varphi_U(x) = \varphi \circ g_U(x),$$

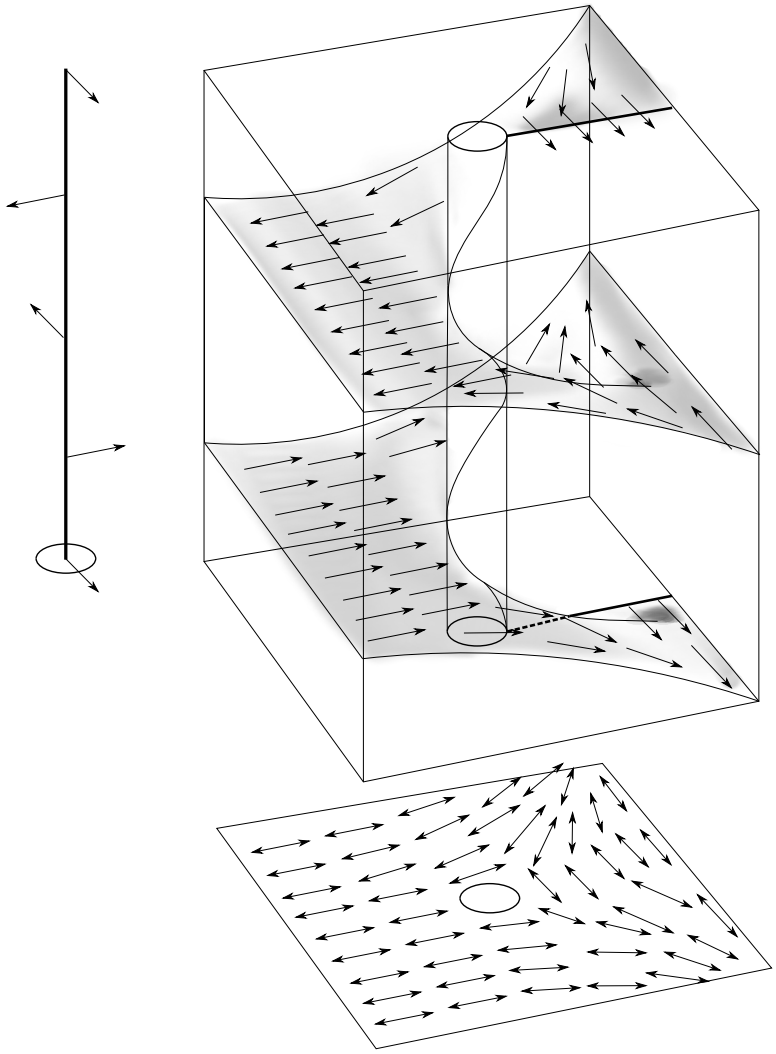

Figure 4.16: Submanifold $\mathcal{D}$ in $D \times \mathbb{R}/2\pi\mathbb{Z}$.

and g_U is a chart of the neighborhood of (x,T) like in (4.25). Moreover, without loss of generality, we can assume that

$$\varphi(x,-T) = -\varphi(x,T). \tag{4.27}$$

Indeed, if φ satisfies (4.26), then the map $(x,T) \mapsto (\varphi(x,T) - \varphi(x,-T))/2$ still satisfies (4.26) together with the antisymmetric property (4.27). Thus, if the conformality condition (4.16) is satisfied, the map φ can be defined as the solution of

$$\min_{\varphi\in\mathcal{V}} \int_{\mathcal{D}} |\nabla\varphi - e^r T|^2 \,\mathrm{dx}, \tag{4.28}$$

over the maps φ in

$$\mathcal{V} := \left\{\varphi \in H^1(\mathcal{D};\mathbb{R}^2) \text{ such that } \varphi(x,-T) = -\varphi(x,T) \text{ for all } (x,T)\in\mathcal{D}\right\}.$$

Previously in this section we assumed that D can be covered by open sets U where the rotation field a is coherently orientable. From now on, let us be more specific in assuming that those open sets U are the cells K of a mesh covering D. In other words, there exists a finite family $\mathcal{T}$ of disjoint open subsets K such that

$$\overline{D} = \cup_{K\in\mathcal{T}} \overline{K},$$

and such that the rotation field a is coherently orientable on all K. We denote $T_K : K \to \mathrm{SO}(2)$ such an orientation on K. We have

$$\begin{aligned}\int_{\mathcal{D}} |\nabla\varphi - e^r T|^2 \,\mathrm{dx} &= \sum_{K\in\mathcal{T}} \int_{p_D^{-1}(K)} |\nabla\varphi - e^r T|^2 \,\mathrm{dx} = \\ &\qquad \sum_{K\in\mathcal{T}} \int_{g_K^+(K)\cup g_K^-(K)} |\nabla\varphi - e^r T|^2 \,\mathrm{dx} \\ &= \sum_{K\in\mathcal{T}} \int_K \left|\nabla(\varphi\circ g_K^+) - e^r T_K(x)\right|^2 \mathrm{dx} + \int_K \left|\nabla(\varphi\circ g_K^-) + e^r T_K(x)\right|^2 \mathrm{dx}\end{aligned}$$

with $g_K^\pm = \mathrm{Id}\times(\pm T_K)$. In particular, for all $\varphi\in\mathcal{V}$, due to the antisymmetry condition, we get

$$\int_{\mathcal{D}} |\nabla\varphi - e^r T|^2 \,\mathrm{dx} = 2\sum_{K\in\mathcal{T}} \int_K \left|\nabla(\varphi\circ g_K^+) - e^r T_K(x)\right|^2 \mathrm{dx}. \tag{4.29}$$

4.5.5 Practical computation of the grid map φ

Solving (4.28) using a classical finite element software seems at first sight far form straightforward, mainly because the solution φ is defined over the manifold $\mathcal{D}$ and not a two dimensional open subset of $\mathbb{R}^2$.

We use P_1 finite elements to discretize φ. To build the bilinear form of the variational formulation, we introduce an interpolation operator from $\mathcal{V}_h$, the Lagrange finite elements of degree one on $\mathcal{D}$ that satisfies the antisymmetry condition (4.27), onto the space W_h of P_1 discontinuous Galerkin elements on D.

The finite element space $\mathcal{V}_h$**.** Let $\mathcal{T}_h$ be a regular mesh of D. We assume that on each triangle K of the mesh, the rotation field a is locally orientable, meaning that, on each K, there exists a regular map T_K with values in SO(2) such that

$$T_K(x)^2 = b(x) \text{ for all } x \in K. \tag{4.30}$$

Such a coherent orientation field T_K is easy to define and more details are given at the end of this section. We also choose an orientation T_i at each vertex x_i of the mesh such that

$$T_i^2 = b(x_i). \tag{4.31}$$

The manifold $\mathcal{D}$ can be endowed with a mesh, whose elements are $g_K^+(K) = (\mathrm{Id} \times T_K)(K)$ and $g_K^-(K) = (\mathrm{Id} \times (-T_K))(K)$ and whose vertices are (x_i, T_i) and $(x_i, -T_i)$, where x_i spans the vertices of $\mathcal{T}_h$ and K its triangles. A P_1 finite element on $\mathcal{D}$ is defined by its values on the nodes (x_i, T_i) and $(x_i, -T_i)$. Moreover, for any element $\varphi \in \mathcal{V}_h$ we have from (4.27)

$$\varphi(x_i, -T_i) = -\varphi(x_i, T_i).$$

Thus $\varphi \in \mathcal{V}_h$ is uniquely determined by the values $\varphi(x_i, T_i)$. It follows that $\mathcal{V}_h$ is of the same dimension than V_h, the space of P_1 Lagrange finite elements over D. An element $\varphi \in \mathcal{V}_h$ is completely defined by a vector $\{\varphi\}$ of coordinates

$$\varphi_i = \varphi(x_i, T_i).$$

The finite element space W_h**.** We denote by W_h the space of P_1 discontinuous finite elements on D with values in $\mathbb{R}^2$. Any element $\psi \in W_h$ is uniquely defined by its values at each vertices of each triangle $K \in \mathcal{T}_h$, that is by a vector

$$\psi_{3k+l} = \psi|_{K_k}(x_i),$$

with k the index of the k-th triangle K_k of $\mathcal{T}_h$ and x_i is the l-th vertex of the triangle K_k (where $l \in \{0, 1, 2\}$).

The interpolation I^h ***from*** $\mathcal{V}_h$ ***onto*** W_h**.** We are now in a position to introduce an interpolation operator I^h from $\mathcal{V}_h$ (the P_1 antisymmetric finite elements on $\mathcal{D}$ with values in $\mathbb{R}^2$) onto W_h (the P_1 Galerkin discontinuous finite elements over D with values in $\mathbb{R}^2$). Let φ be an element of $\mathcal{V}_h$. For all triangle $K \in \mathcal{T}_h$, we define

$$(I^h\varphi)|_K = \varphi \circ g_K^+. \tag{4.32}$$

We recall that $g_K^+ = \mathrm{Id} \times T_K$ as in (4.25). In other words, the restriction of $I^h\varphi$ to K is equal to the restriction of φ on the corresponding triangle endowed with the chosen orientation T_K. From a practical point of view, the interpolation matrix from $\mathcal{V}_h$ to W_h is sparse and defined for all index k of a triangle, for all $l \in \{0, 1, 2\}$ and for all index i of a vertex by

$$I^h_{3k+l,i} = \begin{cases} +1 & \text{if } T_i = \quad T_{K_k}(x_i) \text{ and } x_i \text{ is the } l\text{-th vertex of } K_k \\ -1 & \text{if } T_i = -T_{K_k}(x_i) \text{ and } x_i \text{ is the } l\text{-th vertex of } K_k \\ 0 & \text{if } x_i \text{ is not the } l\text{-th vertex of } K_k \end{cases} \tag{4.33}$$

Computation of φ. The map φ from $\mathcal{V}_h$ into $\mathbb{R}^2$ is the minimizer of

$$G(\varphi) := \int_{\mathcal{D}} |\nabla\varphi - e^r T|^2 \, \mathrm{dx}\,.$$

We recall that from (4.29) that

$$G(\varphi) = 2 \sum_{K\in\mathcal{T}_h} \int_K \left|\nabla(\varphi \circ g_K^+) - e^r T_K(x)\right|^2 \, \mathrm{dx}\,.$$

Thanks to (4.32), this functional can be rewritten as

$$G(\varphi) = 2 \sum_{K\in\mathcal{T}_h} \int_K |\nabla I^h(\varphi) - e^r T_K|^2 \, \mathrm{dx}\,.$$

Thus, the minimizer is the solution of the variational formulation consisting in finding $\varphi \in \mathcal{V}_h$ such that for all for all $\psi \in \mathcal{V}_h$,

$$\sum_{K\in\mathcal{T}_h} \int_K \nabla I^h(\varphi) : \nabla I^h(\psi) \, \mathrm{dx} = \sum_{K\in\mathcal{T}_h} \int_K e^r T_K : \nabla I^h(\psi) \, \mathrm{dx}\,.$$

Introducing the bilinear form

$$\mathcal{A}(\Phi, \Psi) = \sum_{K\in\mathcal{T}_h} \int_K \nabla\Phi : \nabla\Psi \ \mathrm{dx} \tag{4.34}$$

on W_h and the linear form (also on W_h)

$$L(\Psi) = \sum_{K\in\mathcal{T}_h} \int_K e^r T_K : \nabla\Psi \, \mathrm{dx}, \tag{4.35}$$

The map $\varphi \in \mathcal{V}_h$ is such that for all $\psi \in \mathcal{V}_h$,

$$\mathcal{A}(I^h(\varphi), I^h(\psi)) = L(I^h(\psi)). \tag{4.36}$$

It only requires to assemble the matrices associated with the bilinear and linear forms $\mathcal{A}$ and L on the space of Galerkin discontinuous functions to obtain the system satisfied by φ.

Remark 9. *If (as we consider here), the rotation field of the periodicity cells is coherently orientable, the manifold $\mathcal{D}$ is made of two disconnected copies of D and φ is defined up to a constant. This constant can be fixed by adding a small penalization of the L^2-norm of φ in the definition of the bilinear form $\mathcal{A}(\cdot,\cdot)$,*

$$\mathcal{A}(\Phi, \Psi) = \sum_{K\in\mathcal{T}_h} \int_K \left(\nabla\Phi : \nabla\Psi + \eta^2 \Phi \cdot \Psi\right) \mathrm{dx},$$

with $0 < \eta \ll 1$.

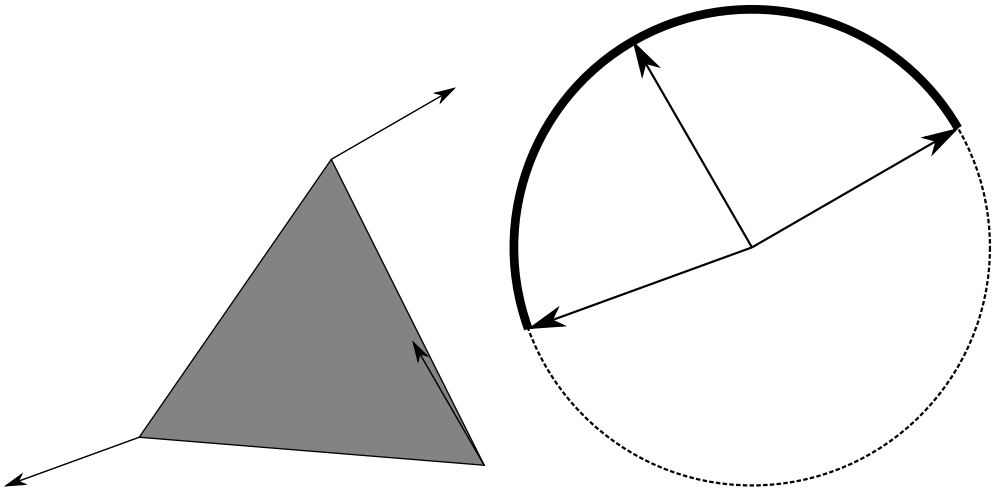

(a) Field b on a triangle ... (b) ... and its image in S^1.

Figure 4.17: Field $b_1 = (\cos(\beta), \sin(\beta))$ that defines the rotation of the periodicity cells.

Coherent local orientation. It remains to determine a local coherent orientation on each triangle of the mesh in order to be able to define the interpolation operator I^h form $\mathcal{V}_h$ onto W_h.

Let us consider a practical example. We recall that the output of the homogenization step is a rotation field b. During this phase of the optimization, we use P_1 Lagrange finite elements to discretized this field. Hence, we can consider each triangle of the mesh separately.

Figure 4.17(a) displays the vector field b_1 on the nodes of a triangle, while Figure 4.17(b) shows the image of this field on S^1 (the bold part of the circle). We have now to choose coherent values of the vector a_1 on each node of this triangle (we recall that $a^2 = b$). Two choices are possible at each node of the triangle as illustrated by Figure 4.18. This leads to eight options for the orientation of the triangle. If the triangle does not contain any singularity, two of them define a coherent orientation (see Figure 4.19). The possible orientations of a_1 are simply obtained by the condition that the scalar product between all couples of values taken by the vector a_1 at nodes should be positive. Hence, it suffices to choose an arbitrary orientation for one vertex and to orient the others accordingly. Doing so, we obtain a rotation field T_K on each triangle K. Note that the chosen orientation is not continuous from on triangle to the other. Moreover, such a coherent orientation does not exists if the triangle contains a singularity, a case that is disregarded in this article.

Sequence of shapes. In conclusion, after the regularization algorithm described in section 4.5.3, the sequence of shapes is constructed in three steps

1. Choosing a coherent orientation T_K on each triangle and an orientation T_i on each vertex of the mesh $\mathcal{T}_h$ of the working domain D (4.30-4.31).

2. Build the interpolation matrix I^h defined by (4.33).

3. Build the matrix A^h and the vector L^h in the space of P_1 discontinuous finite elements

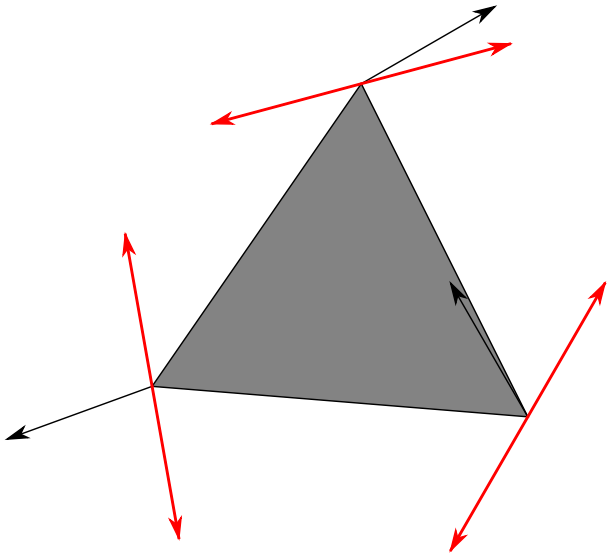

Figure 4.18: Field $a_1 = (\cos(\alpha), \sin(\alpha))$ is defined up to a sign at the nodes.

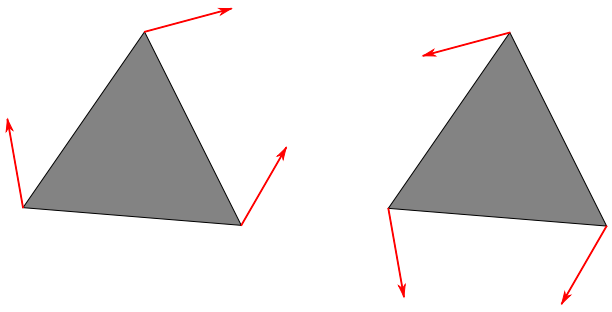

Figure 4.19: The two possible orientations of a_1 on a triangle.

associated to the bilinear and linear forms $\mathcal{A}$ and L (4.34-4.35).

4. Compute the component $\{\varphi\} = (\varphi_i)$ of the coordinates of grid map φ in the base of $\mathcal{V}_h$ defined by the chosen orientation T_i.

$$(I^h)^T A^h I^h \{\varphi\} = L^h I^h$$

5. The sequence of shapes is implicitly defined by (4.12-4.14)

$$\Omega_\varepsilon(\varphi, m) = \Omega_\varepsilon(I_h(\varphi), m) = \{x \in D \text{ such that } F_\varepsilon^{I_h(\varphi),m} \leq 0\}.$$

Remark 10. *Both $\Omega_\varepsilon(\varphi, m)$ and $\Omega_\varepsilon(I_h(\varphi), m)$ do define the same sequence of shapes due to the antisymmetry property of the grid map φ.*

Remark 11. *In all our examples the computational domain D is a simply connected domain in the plane (i.e., without holes). The connectivity property of D does not play any role in the pre-processing and processing steps (see Sections 4.3 and 4.4) but it has some impact in the present post-processing step. In particular, Lemma 4.5.1 (about the conformality condition on the angle α) is stated only for simply connected domains. This is linked somehow to the singularity issue: for example, a radial vector field has a singularity at the origin in a ball but no singularity in a corona. Therefore, the conformality condition, as well as the presence and the removal of singularities, are different for domains with or without holes. The generalization of our algorithm in such a case is work under progress. Note that it is not difficult to take into account non-optimizable zones where the material density is fixed, either to 1 or to 0 (more precisely, to the minimal value imposed by the upper bound $1 - 10^{-3}$ imposed on the microstructure parameters m_i). In such a case, the conformality condition is enforced everywhere in the domain D, including the non-optimizable zones.*

4.5.6 Numerical results

We implemented the above algorithm in Freefem++ [Hecht 2012]. Here, we consider the bridge test case. The computed map φ is displayed in Figure 4.20. However, φ is defined up to its sign on D. Hence for better readability of the figures, we displayed the absolute value of φ. On Figure 4.20(a) (resp. 4.20(b)), the vector a_2 (resp. a_1) is also displayed. Hence, we can easily check that the isolines of $|\varphi_i|$ are orthogonal to the vector a_i. The computed map φ respects the regularized optimal orientation of the microstructure. On Figure 4.21 one can check that the regular square grid, projected by φ, is conformal, namely all lines cross at right angles.

The sequence of genuine or classical shapes can now be constructed using the simple formulas (4.12), (4.14). We displayed in Figure 4.22 several shapes $\Omega_\varepsilon(\varphi, m)$ for various values of ε. Those shapes are very smooth. They feature rectangular holes, oriented according to α. The smaller ε, the closer from the homogenized optimal design the shape $\Omega_\varepsilon(\varphi, m)$ is.

For the sake of comparison, the elasticity problem for each of these classical shapes has been solved on a fine mesh (316 250 elements), using the same ersatz material for void than in the optimization process (0.1% of the elastic tensor of the isotropic material). The resulting compliances for various values of the cell characteristic size ε are displayed on Figure 4.23 (each dot corresponds to one value of ε). Their relative volume, defined as the ratio between the

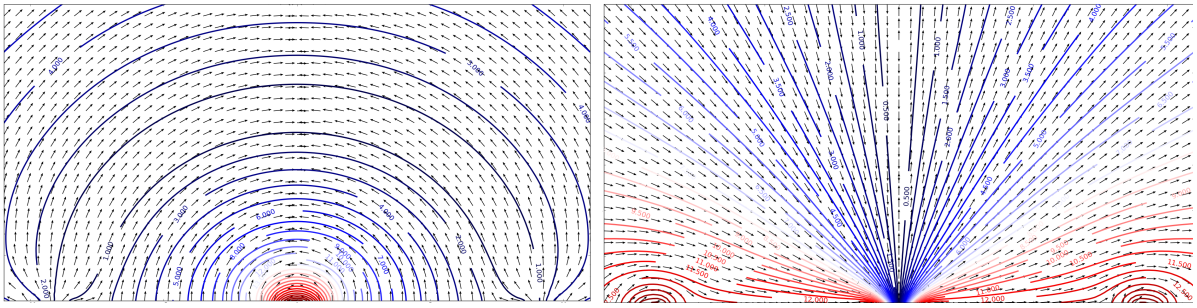

(a) $|\varphi_1|$ and a_2 (b) $|\varphi_2|$ and a_1

Figure 4.20: Map φ (isolines) and the vectors a_i (arrows) for the bridge case

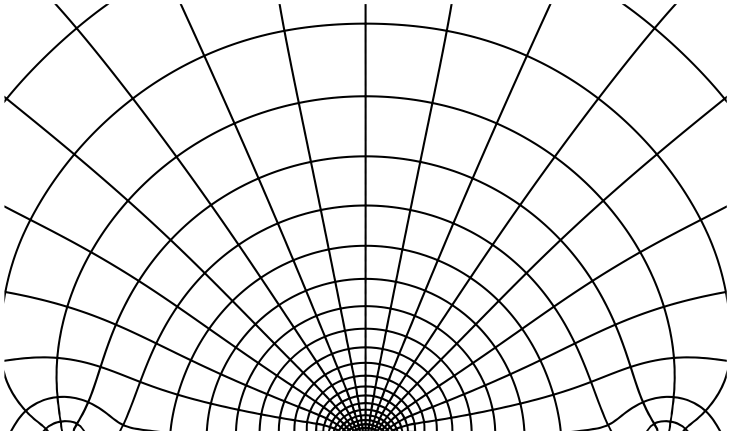

Figure 4.21: Projection of a regular grid through the map φ for the bridge case

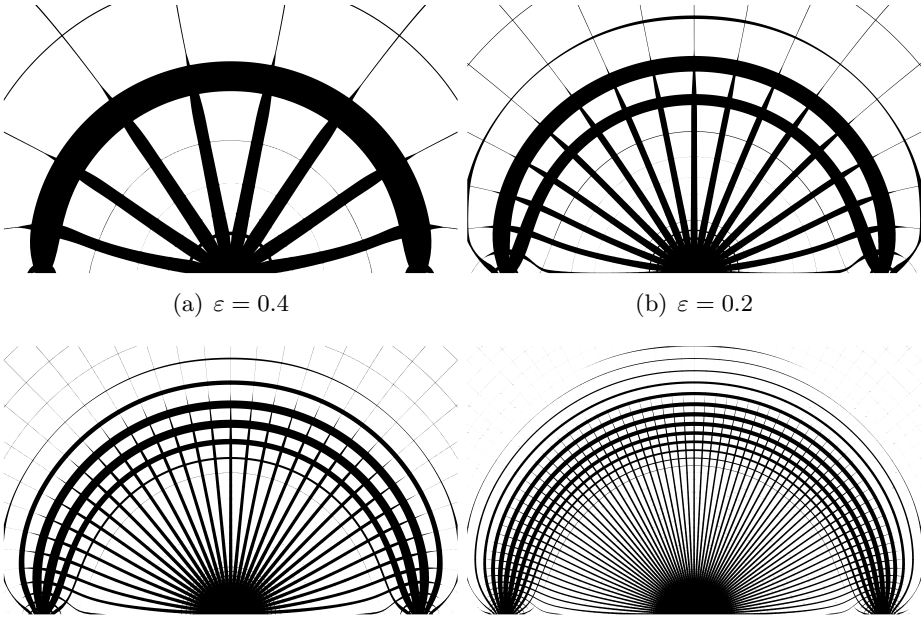

(a) $\varepsilon = 0.4$ (b) $\varepsilon = 0.2$

(c) $\varepsilon = 0.1$ (d) $\varepsilon = 0.05$

Figure 4.22: $\Omega_\varepsilon(\varphi, m)$ for several ε in the case of the bridge

actual volume of the shape and the target one, is also plotted. The compliance of the genuine shapes is close to the optimal value of the homogenized design but slightly above. As soon as ε is small enough, these compliances are lower than that for an optimized shape using no lattice material (here, the reference is the shape obtained by the SIMP method, see Figure 4.9). The variations of the compliance are mostly caused by the variations of the volume. Indeed, a smaller volume induces a larger compliance. As a matter of fact, the projection post-processing phase does not ensure a preservation of the total volume. However, such volume errors are smaller for smaller ε. Nevertheless, for too small values of ε, the mesh may not be fine enough to capture accurately the details of the shapes, which can alter the evaluation of the compliance. Note that the compliance values for the SIMP design and the homogenized design are computed on a coarser mesh. But we check that their compliances on the fine mesh are almost the same (the relative differences are of the order of 1%).

4.5.7 Post-processing of the final structures

The above shapes are not straightforwardly manufacturable. Indeed, they can feature very thin bars, some of them not even connected to the principal structure, as well as very tiny holes. We propose here a simple post-treatment in order to get manufacturable shapes. More clever ideas could certainly be implemented but we leave this to future work.

Let $h_{min} > 0$ be the minimal manufacturable length scale or feature size, meaning the smallest possible width of bars and diameter of holes which can be effectively built. We do not allow for details or features smaller than h_{min} in the post-processed shape. Recall that ε is our choice of a global size of cells. Then, locally after deformation, the cell size is $h_c(x) = \varepsilon e^{-r(x)}$,

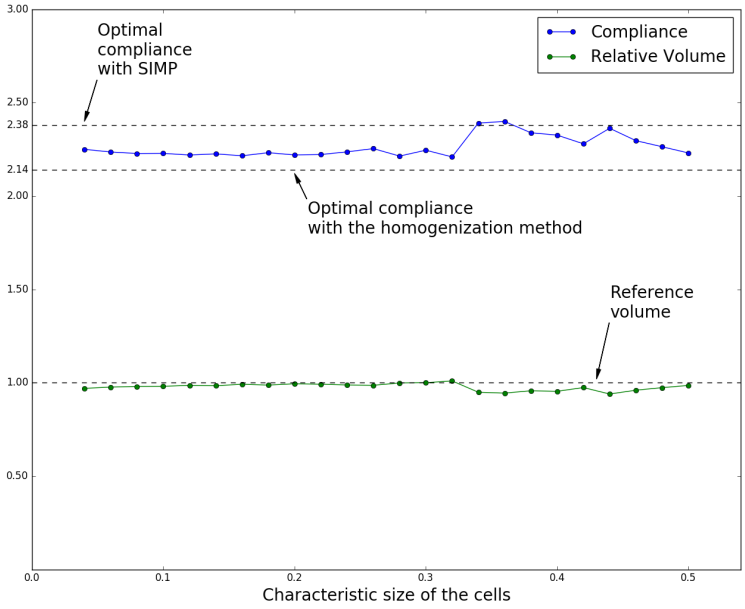

Figure 4.23: Compliance and relative volume of the genuine shapes according to the cell characteristic size ε

which is varying from point to point. Hence, the local widths of bars and holes are respectively given by $(1 - m_i(x))h_c(x)$ and $m_i(x)h_c(x)$.

In the following, we distinguish two regimes, depending of the local size of the cell $h_c(x)$. First, if the local cell size is too small, a hole and a bar of minimal width cannot coexist: we have to choose between a completely full or void cell. Hence, if $h_c < 2h_{min}$, a thresholding is applied separately to each field m_i: it is assigned the value 0 if $m_i < 0.5$ and 1 otherwise.

Second, when $h_c \geq 2h_{min}$, our post-processing criteria about the widths of the bar and the hole is satisfied if:

$$\forall i \in \{1, 2\} \quad \frac{h_{min}}{h_c} \leq m_i \leq 1 - \frac{h_{min}}{h_c}\,. \tag{4.37}$$

Failing (4.37), we simply threshold the values of m_1 and m_2, according to the functions displayed on Figure 4.24 in order to reach void or full material.
The thresholded m is then denoted $\tilde{m}$.

Let $O_\varepsilon(\varphi, \tilde{m})$ be the shape obtained from $\Omega_\varepsilon(\varphi, \tilde{m})$ by filling its closed holes, see Figure 4.25(e). Numerically, the complement of $O_\varepsilon(\varphi, \tilde{m})$ is computed step by step, by evaluating the sign of $F_\varepsilon^{\varphi,\tilde{m}}$. If it is positive, the current vertex belongs to the complement $O_\varepsilon^c(\varphi, \tilde{m})$ and then its neighbors, which are not already visited, are added to a list of vertices, which should be tested. Otherwise, the current vertex does not belong to $O_\varepsilon^c(\varphi, \tilde{m})$: no particular action is required and so we keep going with the next vertex of our list.

Then, the subset $O_\varepsilon(\varphi, \tilde{m})$ is regularized in order to remove the disconnected bars or the bars that have one free end point. Numerically, we explore all the vertices of the complement as follows. For any given vertex, we check all other vertices not further away than a distance h_{min}: if this vertex belongs to the complement too, all vertices between them are added to the complement. In this way, we suppress all disconnected bars and all bars that have one free end

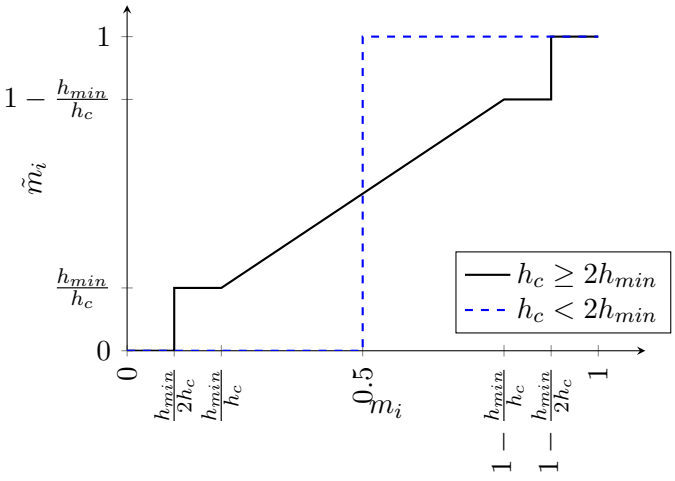

Figure 4.24: Thresholds for the post-treatment, or $\tilde{m}_i$ as a function of m_i, in order to fulfill a minimal feature size h_{min}

point, which are not too wide, of $O_\varepsilon(\varphi, \tilde{m})$. This new subset is denoted $\tilde{O}_\varepsilon(\varphi, \tilde{m})$, see Figure 4.25(f).

Finally, the post-processed structure is given by the intersection $\tilde{\Omega}_\varepsilon(\varphi, \tilde{m}) = \Omega_\varepsilon(\varphi, \tilde{m}) \cap \tilde{O}_\varepsilon(\varphi, \tilde{m})$, see Figure 4.25(g). Several post-processed structures $\tilde{\Omega}_\varepsilon(\varphi, \tilde{m})$ for the bridge case are displayed on Figure 4.26.

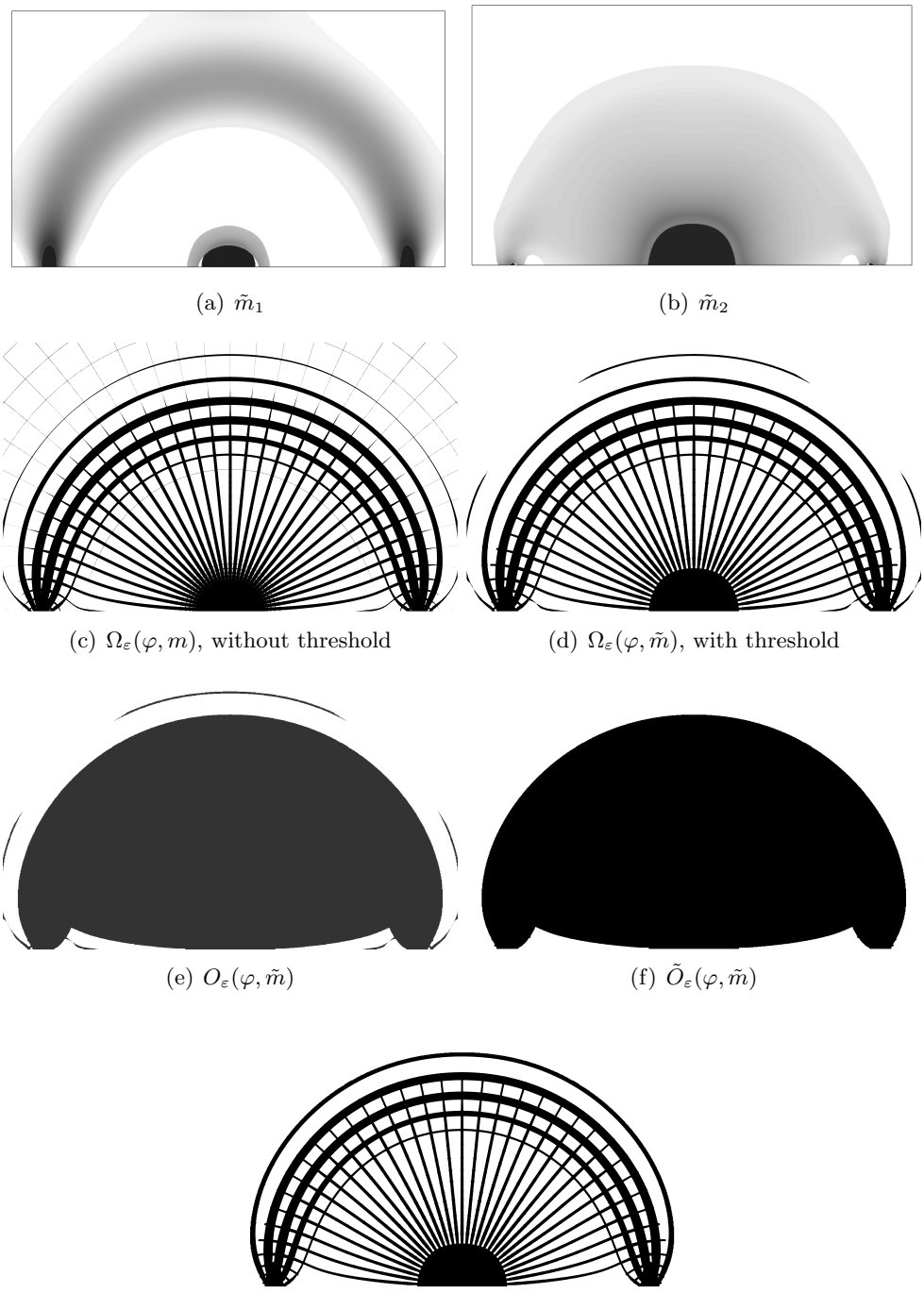

(a) $\tilde{m}_1$

(b) $\tilde{m}_2$

(c) $\Omega_\varepsilon(\varphi, m)$, without threshold

(d) $\Omega_\varepsilon(\varphi, \tilde{m})$, with threshold

(e) $O_\varepsilon(\varphi, \tilde{m})$

(f) $\tilde{O}_\varepsilon(\varphi, \tilde{m})$

(g) Post-processed structure $\tilde{\Omega}_\varepsilon(\varphi, \tilde{m})$

Figure 4.25: Results of the post-treatment for the bridge case, with a minimal feature size $h_{min} = 0.05\varepsilon$ (here : $\varepsilon = 0.1$)

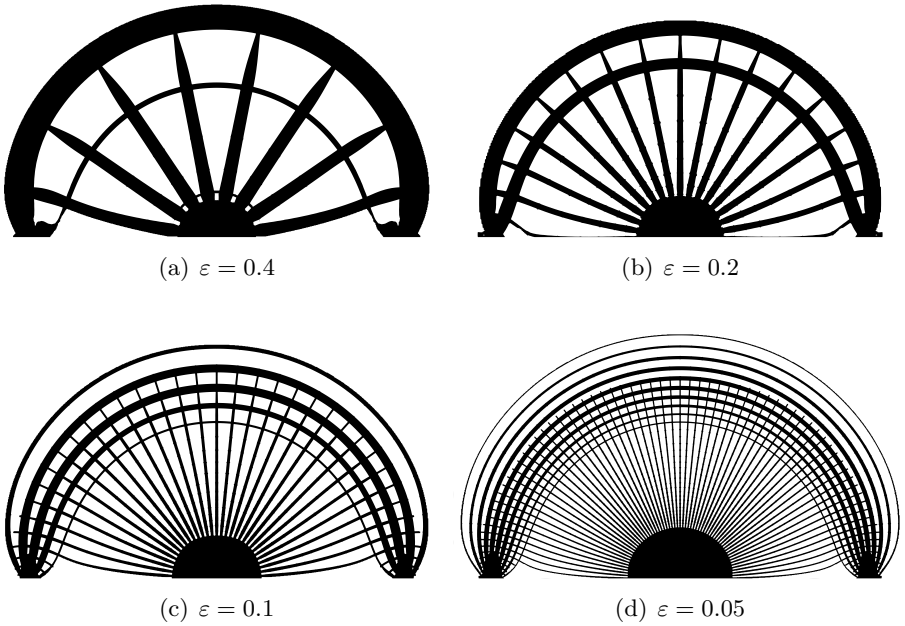

(a) $\varepsilon = 0.4$ (b) $\varepsilon = 0.2$

(c) $\varepsilon = 0.1$ (d) $\varepsilon = 0.05$

Figure 4.26: Post-processed structures $\tilde{\Omega}_\varepsilon(\varphi, \tilde{m})$ for several ε in the case of the bridge

4.6 Other numerical examples

We applied the whole method to the several cases: optimization of an arch (Figure 4.27), a cantilever (Figure 4.27), a MBB beam (Figure 4.28) and a L-beam (Figure 4.29). As in the case of the bridge, used previously to illustrate our approach, the volume constraint is fixed to 30% of the working domain and the number of iterations during the optimization – before regularization – is set to 200. The number of vertices is in all cases, lower than 9000 and the numbers of triangles to 18000.

For the arch (Figure 4.27) the domain size is 22×13 and a unit vertical load is applied at the middle of the bottom border on an interval of length 2. The Dirichlet boundary condition is applied on two symmetric intervals of length 1 starting at a distance 1 from the sides. The resulting compliance for the homogenized design is 1.558.

For the cantilever (Figure 4.27), the domain size is 20×20. The Dirichlet boundary condition is applied on a central interval of length 10 on the left side. A unit vertical load is applied in the center of its right side on a segment of length 1. The resulting compliance for the homogenized design is 2.729.

For the MBB beam (Figure 4.28), the domain size is 30×10. We took advantage of the symmetry, by running the algorithm just on the half of a complete beam. Then the structure is allowed to slide on its left side. A unit vertical load is applied in the upper left corner on a segment of length 1. The resulting compliance for the homogenized design is 13.626

For the L-beam (Figure 4.29), the domain size is 10×10. The structure is clamped on its upper side, and is submitted to a unit vertical load in the center of its right side on a segment of 20% of the total length. The resulting compliance for the homogenized design is 6.581.

For each case, we have represented: (a) the applied loads and the boundary conditions; (b-c) the optimal orientation of the periodicity cells before and after regularization; (d) the underlying lattice on which the optimal composite is built; (e-g) the optimal density and microstructure parameters; (h-j) the sequence of shapes before post-processing, and after (k-n).

The orientation fields of all those cases do not feature any singularity after regularization, which is a necessary condition for our method to apply. In the case of the L-beam, the orientation field in Figure 4.29(b) presents two singularities. Both have been ejected during the regularization step as seen on Figure 4.29(c). Note that the orientation field before and after regularization are significantly different (it turns with an angle of order $\pi/2$ on some areas). We would like to draw the attention of the reader to the fact that it is not universal: in some cases, no matter how strong the regularization is chosen, singularities do persist. We perform a last test case, the so-called electrical mast (see Figure 4.30), to illustrate this fact: two negative singularities, located inside the domain, cannot neither be removed nor pushed toward the boundary during the regularization step (see Figure 4.30(b)). The application of our method failed in this case, as it is not designed to deal with the presence of singularities. This is illustrated by Figure 4.30(c), where the computed grid is clearly not correctly aligned with the optimal orientation of the cells in the vicinity of the singularities. To overcome this problem, at least two different strategies can be considered. One consists in modifying the regularization in a way that force more effectively the singularities to be eliminated. For instance, this can be done by adding a penalization of the singularities to the cost function. We have implemented such a method and are indeed able to remove the singularities from the optimal shape as shown in Figures 4.30(d) and 4.30(e). Another option, already mentioned previously, is to adapt the projection step so that it is able to take singularities into account. These approaches are not presented here, but will be the topic of the next Chapter 5.

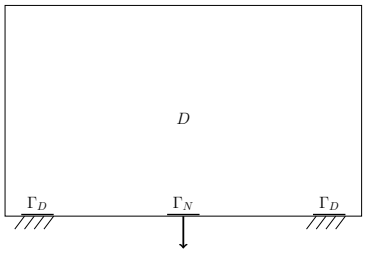

(a) Load case

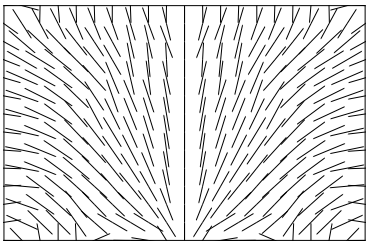

(b) Optimized orientation

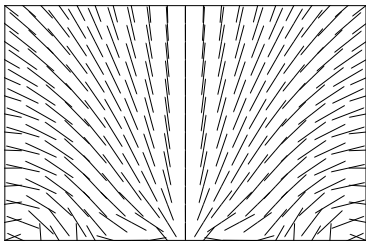

(c) Regularized orientation

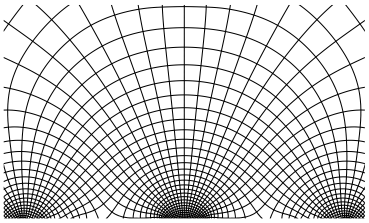

(d) Projection of a regular grid through φ

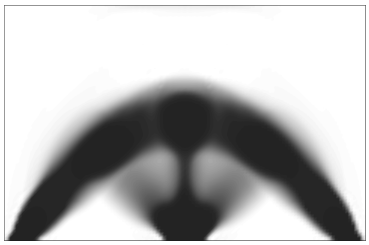

(e) Density

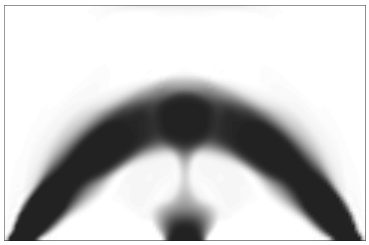

(f) m_1

(g) m_2

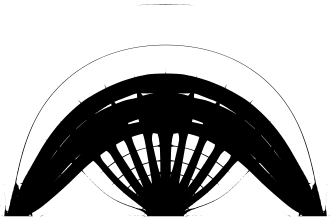

(h) $\Omega_\varepsilon(\varphi, m)$, $\varepsilon = 0.2$

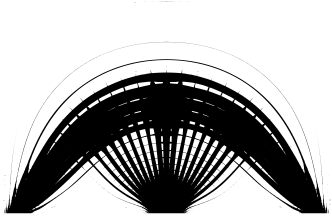

(i) $\Omega_\varepsilon(\varphi, m)$, $\varepsilon = 0.1$

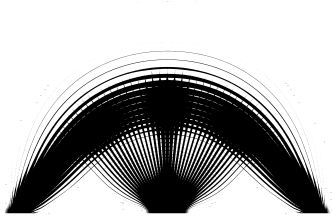

(j) $\Omega_\varepsilon(\varphi, m)$, $\varepsilon = 0.05$

(k) $\tilde{\Omega}_\varepsilon(\varphi, \tilde{m})$, $\varepsilon = 0.2$

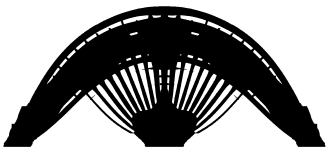

(l) $\tilde{\Omega}_\varepsilon(\varphi, \tilde{m})$, $\varepsilon = 0.1$

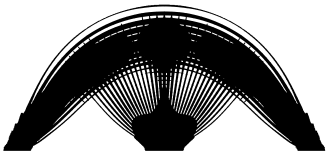

(m) $\tilde{\Omega}_\varepsilon(\varphi, \tilde{m})$, $\varepsilon = 0.05$

Figure 4.27: Complete process for an arch case

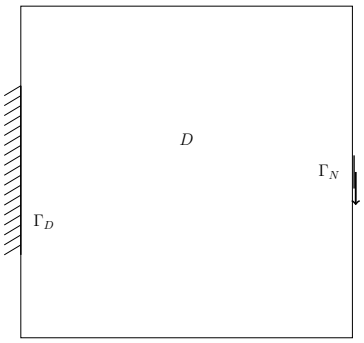

(a) Load case

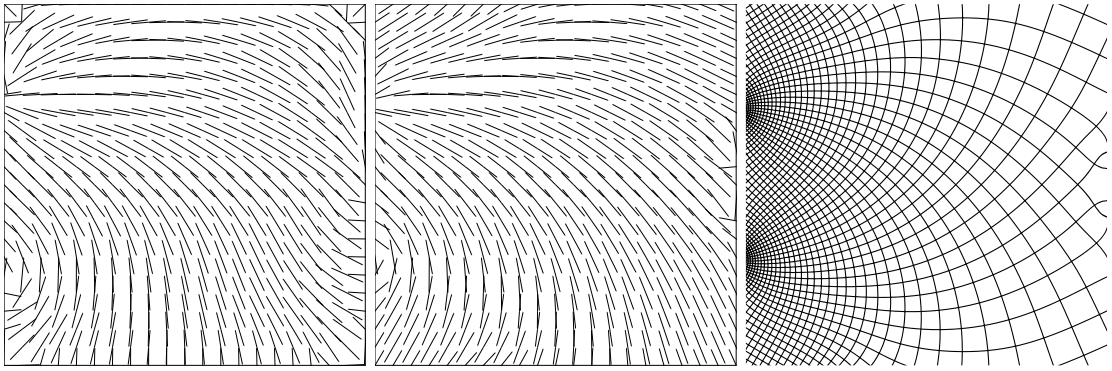

(b) Optimized orientation (c) Regularized orientation (d) Projection of a regular grid through φ

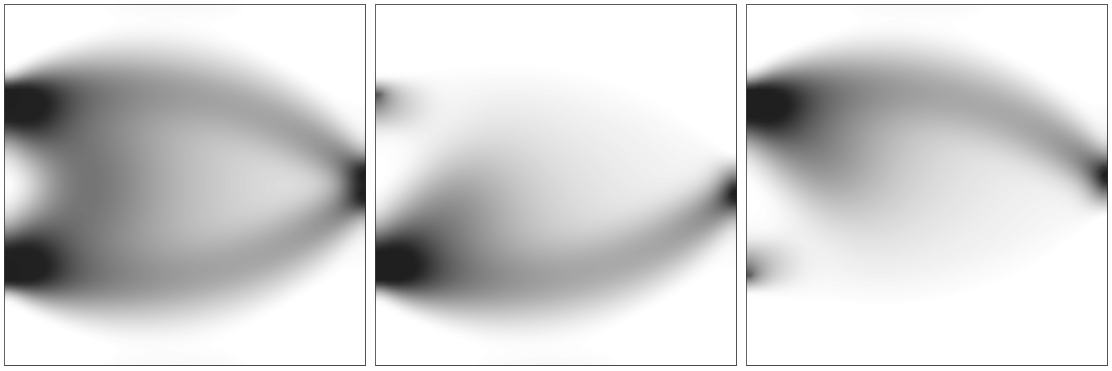

(e) Density (f) m_1 (g) m_2

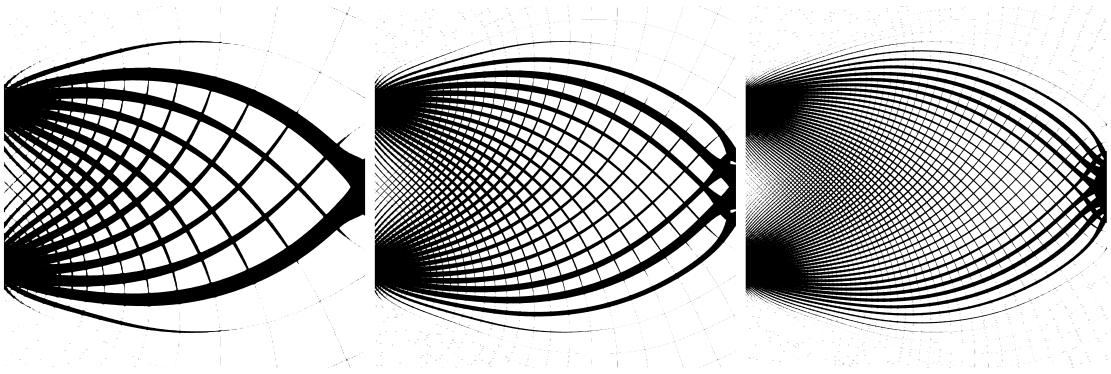

(h) $\Omega_\varepsilon(\varphi, m)$, $\varepsilon = 0.2$ (i) $\Omega_\varepsilon(\varphi, m)$, $\varepsilon = 0.1$ (j) $\Omega_\varepsilon(\varphi, m)$, $\varepsilon = 0.05$

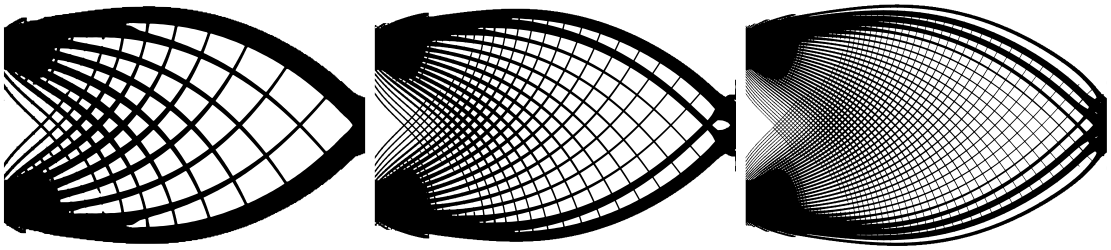

(k) $\tilde{\Omega}_\varepsilon(\varphi, \tilde{m})$, $\varepsilon = 0.2$ (l) $\tilde{\Omega}_\varepsilon(\varphi, \tilde{m})$, $\varepsilon = 0.1$ (m) $\tilde{\Omega}_\varepsilon(\varphi, \tilde{m})$, $\varepsilon = 0.05$

Figure 4.27: Complete process for a cantilever case

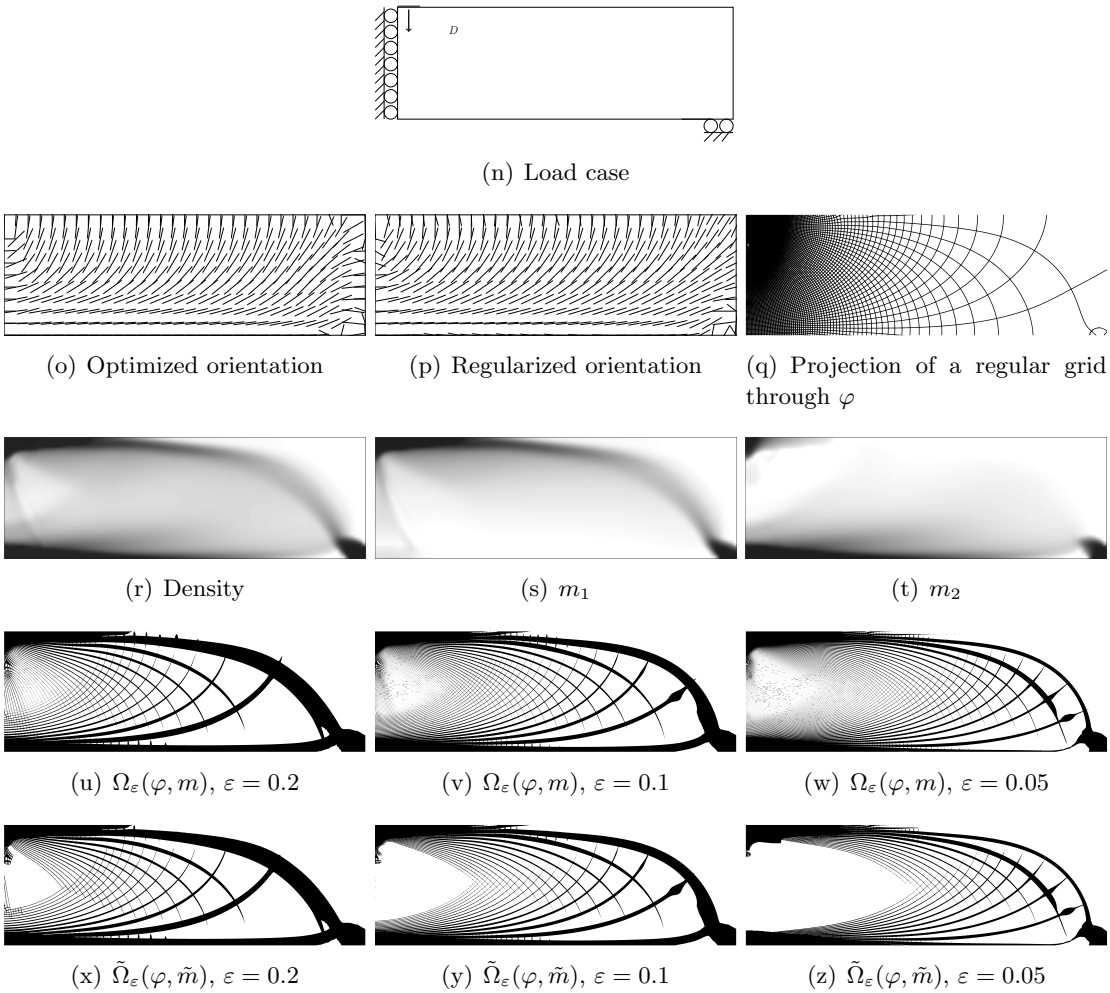

(n) Load case

(o) Optimized orientation (p) Regularized orientation (q) Projection of a regular grid through φ

(r) Density (s) m_1 (t) m_2

(u) $\Omega_\varepsilon(\varphi, m)$, $\varepsilon = 0.2$ (v) $\Omega_\varepsilon(\varphi, m)$, $\varepsilon = 0.1$ (w) $\Omega_\varepsilon(\varphi, m)$, $\varepsilon = 0.05$

(x) $\tilde{\Omega}_\varepsilon(\varphi, \tilde{m})$, $\varepsilon = 0.2$ (y) $\tilde{\Omega}_\varepsilon(\varphi, \tilde{m})$, $\varepsilon = 0.1$ (z) $\tilde{\Omega}_\varepsilon(\varphi, \tilde{m})$, $\varepsilon = 0.05$

Figure 4.28: Complete process for a MBB beam

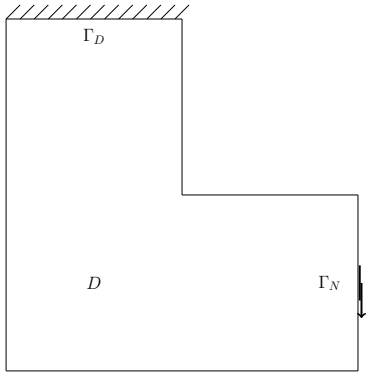

(a) Load case

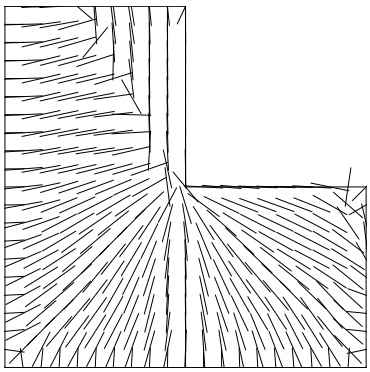

(b) Optimized orientation

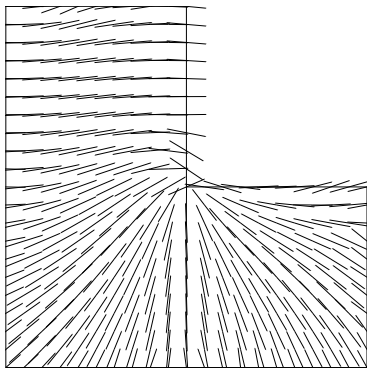

(c) Regularized orientation

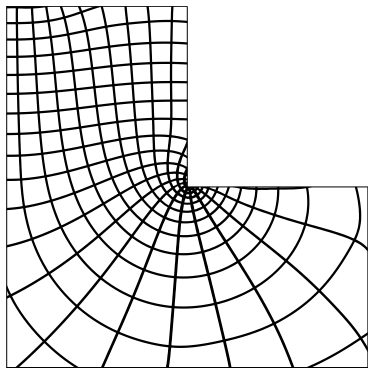

(d) Projection of a regular grid through φ

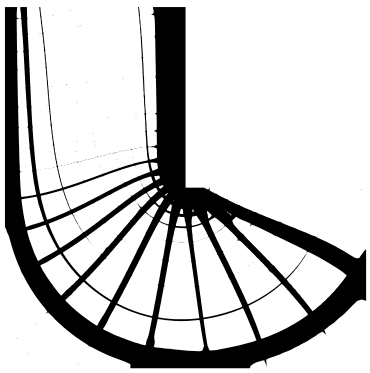

(e) $\Omega_\varepsilon(\varphi, m)$, $\varepsilon = 0.2$

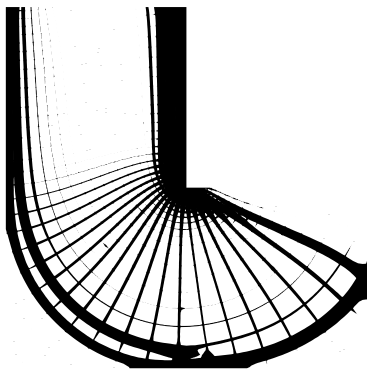

(f) $\Omega_\varepsilon(\varphi, m)$, $\varepsilon = 0.1$

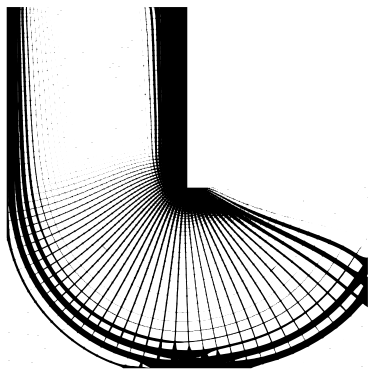

(g) $\Omega_\varepsilon(\varphi, m)$, $\varepsilon = 0.05$

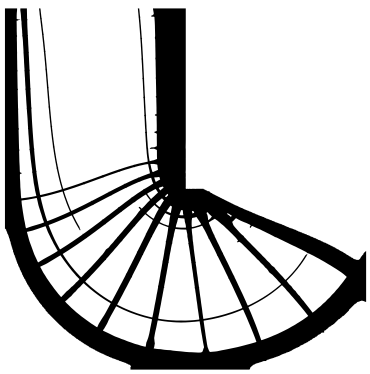

(h) $\tilde{\Omega}_\varepsilon(\varphi, \tilde{m})$, $\varepsilon = 0.2$

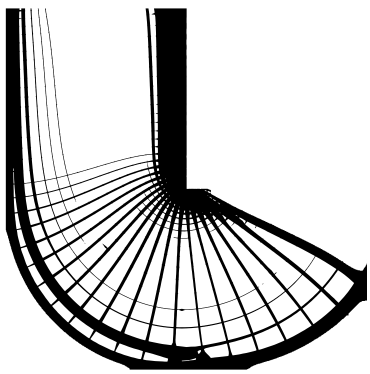

(i) $\tilde{\Omega}_\varepsilon(\varphi, \tilde{m})$, $\varepsilon = 0.1$

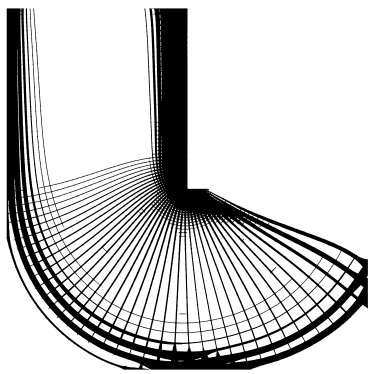

(j) $\tilde{\Omega}_\varepsilon(\varphi, \tilde{m})$, $\varepsilon = 0.05$

Figure 4.29: Complete process for a L-beam

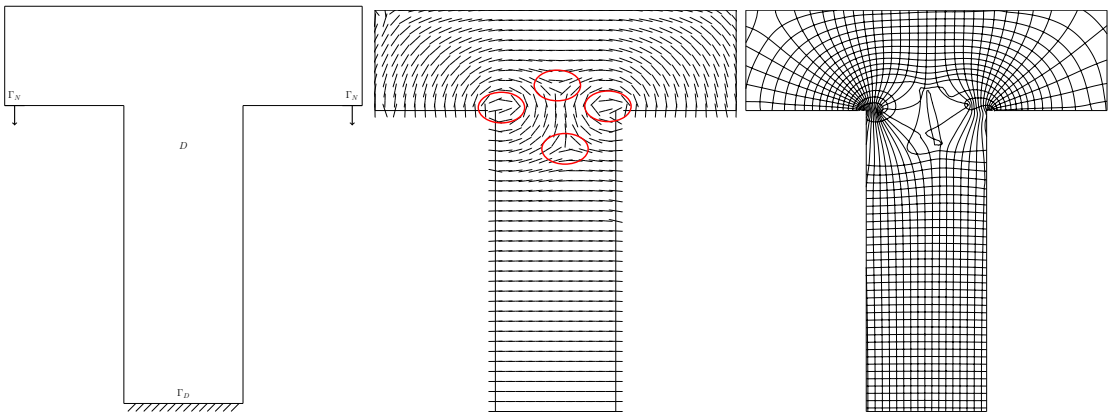

(a) Load case (b) Regularized orientation (c) Distorted grid

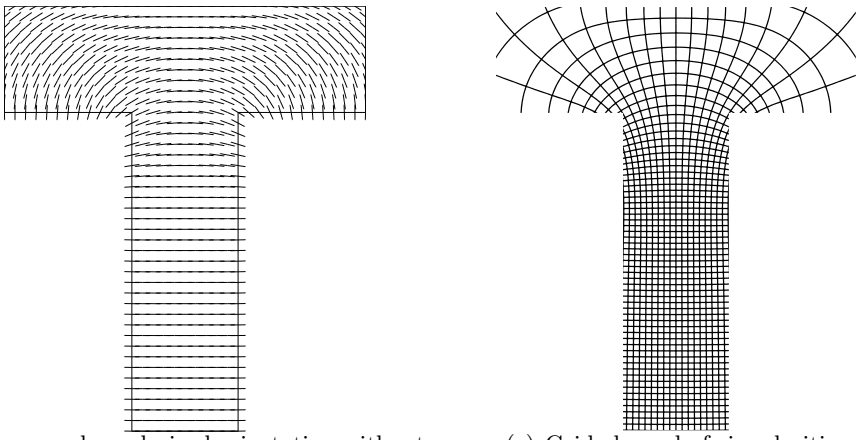

(d) Improved regularized orientation without anymore singularities (e) Grid cleaned of singularities

Figure 4.30: The electrical mast test case: singularities persist in the optimized orientation field, even after regularization

4.7 Stress minimization problem

We focus on the stress minimization problem in this section.

4.7.1 Preprocessing: amplification tensor P^*

We recall that the microscopic heterogeneities may cause stress concentration. The real stress distribution is different from the macroscopic homogenized stress.

This is due to the fact that the stress for a microstructure of size ε, denoted by σ_ε does not converge strongly to $(A^*e(u^*))$ when ε is going to zero.

As seen in Chapter 2, a stress amplification factor may be introduced in order to compute a L^2-norm criteria on the stress. This is not a pointwise maximum.

Hence the objective function in this case is:

$$J(m,\alpha) = \int_D P^*(m)R(\alpha)^T\sigma : R(\alpha)^T\sigma dx\,,$$

where σ is the homogenized stress tensor, solution of the elasticity problem and $P^*(m)$ is the amplification tensor, corresponding to the microstructure, see Section 2.1.6 of Chapter 2. $P^*(m)$ is defined by:

$$P^*(m) = \int_{Y_0} A(y)W(y)A^*(m)^{-1}A(y)W(y)A^*(m)^{-1}\,dy\,, \tag{4.38}$$

where W is the corrector tensor, see Section 2.1.6 of Chapter 2. Its coefficients are given by:

$$W_{ijkl} = I^4_{ijkl} + e(w_{ij})_{kl}\,,$$

where w_{ij} is the solution of the cell problem (4.3).

4.7.1.a Numerical implementation

The set of amplification tensor $\{P^*m | m \in L^\infty(D,[0,1]^2)\}$ has to be characterized. The proposed strategy is the same that the one used to characterize the effective homogenized tensor A^*. It consists in computing the amplification tensor for a discrete sample of parameters values and using the collected data to construct a surrogate model by a simple interpolation.

We discretized the space of the parameter m describing the microstructure on a regular grid with 20 elements in each direction. Then the amplification tensor is numerically computed for each samples of parameters m, by using the finite element solver FreeFem++.

For each sample, the three cell problems (4.3) on $Y_0(m)$ are solved. The amplification tensor $P^*(m)$ is then computed with (4.38).

Like for the effective homogenized tensor, we take advantage of the P_1-functions in FreeFem++ to interpolate the amplification tensor law.

The coefficients of P^* are displayed for $m_2 = 0.5$ on Figure 4.31. These coefficients can be interpreted as the amplification value of the L_2 norm of the effective stress, for particular load cases: compression load in directions e_1 (resp. e_2) for P_{1111} (resp. P_{2222}) and shear load for P_{1212}.

For small values of m_1 all the coefficients are closed to one: there is no amplification of the effective stress. Indeed, when $m_1 = 0$, the density of the cell is equal to one, the cell is full,

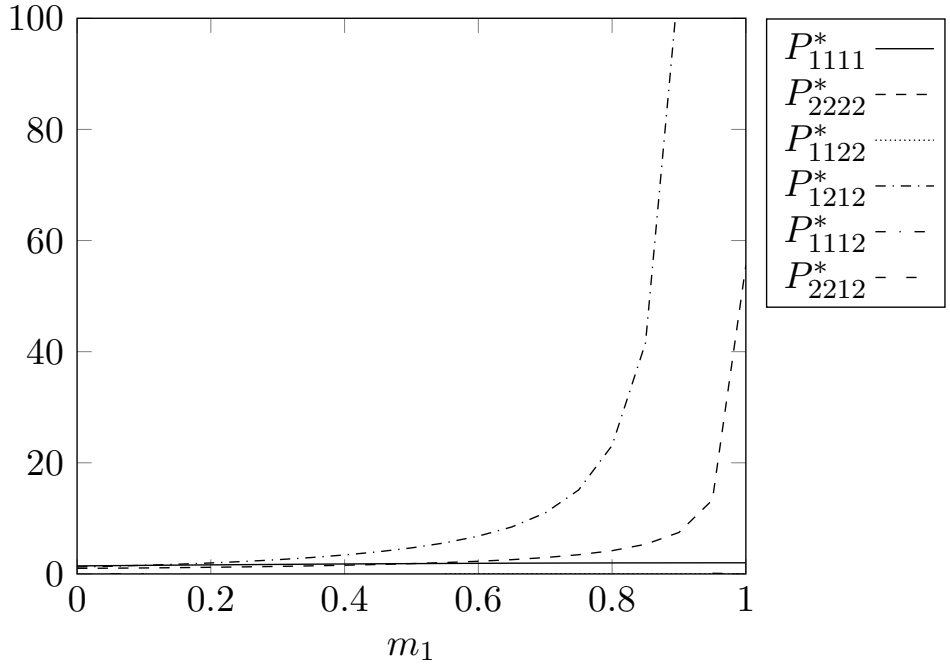

Figure 4.31: $P^*(m1, 0.5)$

so the microstructure does not concentrate any stress. The coefficients P_{2222} and P_{1212} explode when m_1 is going to one: the microstructure concentrates a lot of local stress. The coefficient P_{1111} increases from 1 to around 2 when m_1 is going from zero to one. Indeed, the width of the hole in the direction e_1 has little impact on the behaviour of the cell for a compression load in direction e_1.

4.7.2 Processing: optimization among the set of periodic composite materials

The cost function is $J(m, \alpha) = \int_D P^*(m) R(\alpha)^T \sigma : R(\alpha)^T \sigma dx$, with σ is the effective stress tensor, solution of the elasticity problem. The optimization problem reads as:

$$\begin{gathered} \inf \qquad J(m, \alpha)\,, \\ \sigma \in H_0 \\ m \in L^\infty(D; [0,1]^2) \\ \alpha \in L^\infty(D; \mathbb{R}) \\ \int_D \theta(m)\ \mathrm{dx} \leq V \end{gathered}$$

where $\theta(m) = 1 - m_1 m_2$ is the density of the periodic microstructure of parameters m and V the target volume.

In order to solve this problem, we use an algorithm closed to the one for the compliance minimization. We give here only the elements that have to be adjusted, due to the fact that this problem is not self-adjoint. For the complete algorithm, one can refer to Section 4.4.

Minimization with respect to the design parameters m**.** We use the Céa method [Céa 1986] to compute the adjoint state and then the derivatives of the objective function. The corresponding Lagrangian L to the minimization problem is:

$$L(m,\alpha,v,q,\ell) = \int_D A_0^*(m)R(\alpha)^T e(v) : R(\alpha)^T e(q))dx - \int_{\Gamma_N} g\cdot q\, ds + \int_D P^*(m)A_0^*(m)R(\alpha)^T e(v) : A_0^*(m)R(\alpha)^T e(v)dx + \ell\left(\int_D \theta(m)dx - V\right), \quad (4.39)$$

where ℓ is the Lagrange multiplier associated to the volume constraint, and $v, q \in H^1_{\Gamma_D}(D)^N$.

The partial derivative of L with respect to q in the direction $\psi \in H^1_{\Gamma_D}(D)^N$ is given by:

$$\left\langle \frac{\partial L}{\partial q}, \psi \right\rangle = \int_D A_0^*(m)R(\alpha)^T e(v) : R(\alpha)^T e(\psi)dx - \int_{\Gamma_N} g\cdot\psi\, ds\,.$$

At the stationary point, this derivative is equal to zero and leads to the variational formulation of the elasticity problem.

The partial derivative of L with respect to v in the direction $\psi \in H^1_{\Gamma_D}(D)^N$ is given by:

$$\left\langle \frac{\partial L}{\partial v}, \psi \right\rangle = \int_D A_0^*(m)R(\alpha)^T e(q) : R(\alpha)^T e(\psi)\, dx + 2\int_D P^*(m)A_0^*(m)R(\alpha)^T e(v) : A_0^*(m)R(\alpha)^T e(\psi)\, dx\,. \quad (4.40)$$

At the stationary point, this derivative is equal to zero and leads to the variational formulation of the adjoint problem. Its solution, the adjoint state, is denoted p.

The partial derivative of the cost function with respect to m is equal to the partial derivative of the Lagrangian L at the state (u,p):

$$\frac{\partial J}{\partial m_i}(m,\alpha) = \int_D \frac{\partial A_0^*}{\partial m_i}R(\alpha)^T e(u) : R(\alpha)^T e(p))\, dx + \int_D \frac{\partial P_0^*}{\partial m_i}R(\alpha)^T\sigma : R(\alpha)^T\sigma)\, dx + 2\int_D P^*(m)\frac{\partial A_0^*}{\partial m_i}R(\alpha)^T e(u) : A_0^*(m)R(\alpha)^T e(u)\, dx \quad (4.41)$$

In the optimization algorithm, the adjoint problem has to be solved before computing the descent direction for the design parameters m. The descent direction is then given by:

$$dm_i = -\frac{\partial J}{\partial m_i}(m,\alpha) + \ell m_j \quad \text{in } D\,.$$

Minimization with respect to the orientation α**.** The optimal orientation of the microstructure in order to minimize the corrected stress, for a given effective stress is not explictly known. It the corrector tensor P^* was known to be orthotropic, this optimal orientation would be given by the Pedersen formulas. It would be align with the principal directions of the stress tensor.

We do not have theoretically such a result. However, numerically, we notice that the coefficients P^*_{1112} and P^*_{2212} are almost equal to zero, see Figure 4.31. Moreover, it seems reasonable to align the principal directions of the cell with the principal directions of the stress, in order to minimize this last one. Hence, we used a heuristic here: the optimization with respect to the orientation is done exactly like in the compliance minimization problem.

4.7.2.a Numerical results

We have numerically implemented the optimization algorithm for the cantilever case, the boundary conditions are displayed on Figure 4.28(a). The volume constraint is fixed to 30% of the working domain. The algorithm converged quickly and smoothly , see Figure 4.32 (solid line). The results are displayed on Figure 4.33. The obtained composite is anisotropic: the optimized design parameters m_1 and m_2, see Figures 4.33(b) and 4.33(c) are not equal, and the orientation is not uniform, see Figure 4.33(d). The facts that the microstructure does not autopenalized and that the algorithm converges smoothly justify the heuristic used to optimize with respect to the orientation. This orthotropic microstructure is a good candidate for this problem, since it does not autopenalize. To compare, we also ran a test with fixed orientation: α is taken equal to zero on the whole domain, and is not updated during the optimization process. The optimized density of the final structure is displayed on Figure 4.34. It is autopenalized: the final structure is black and white. The history of convergence is also displayed on Figure 4.32 (dashed line). The cost function decreases but its final value is much greater than the optimized cost function when the orientation is not fixed. Hence the heuristic used to optimize on the orientation is efficient: thanks to it, the cost function reaches lower values.

4.7.3 Post-processing: projection of the optimized microstructures

4.7.3.a Regularization of the orientation

The optimized orientation, see Figure 4.33(d) does not respect the conformality condition (4.16). Like previously, we pursue the optimization algorithm while imposing the harmonicity of the angle α.

We take the same notations as previously, in particular $\beta = 2\alpha$ and $b_1 = (\cos(\beta), \sin(\beta))$. In order to regularize the orientation, we are left with the minimization problem of

$$\int_D \left(P^*(m) S(b_1)\sigma : S(b_1)\sigma + \eta^2 |\nabla \beta|^2 \right) dx$$

under the constraints

$$\int_D \nabla \beta \cdot \nabla q \, \mathrm{dx} = 0, \text{ for all } q \in H^1_0(D) \quad \text{and} \quad b_1 = (\cos(\beta), \sin(\beta)).$$

At each iteration, the first constraint is approximated by its linearization around the current state. The linearized minimization problem can finally be rewritten as the variational problem consisting in finding $\delta b_1^n \in H^1(D; \mathbb{R}^2)$ and $p^{n+1} \in H^1_0(D)$ such that for all test functions

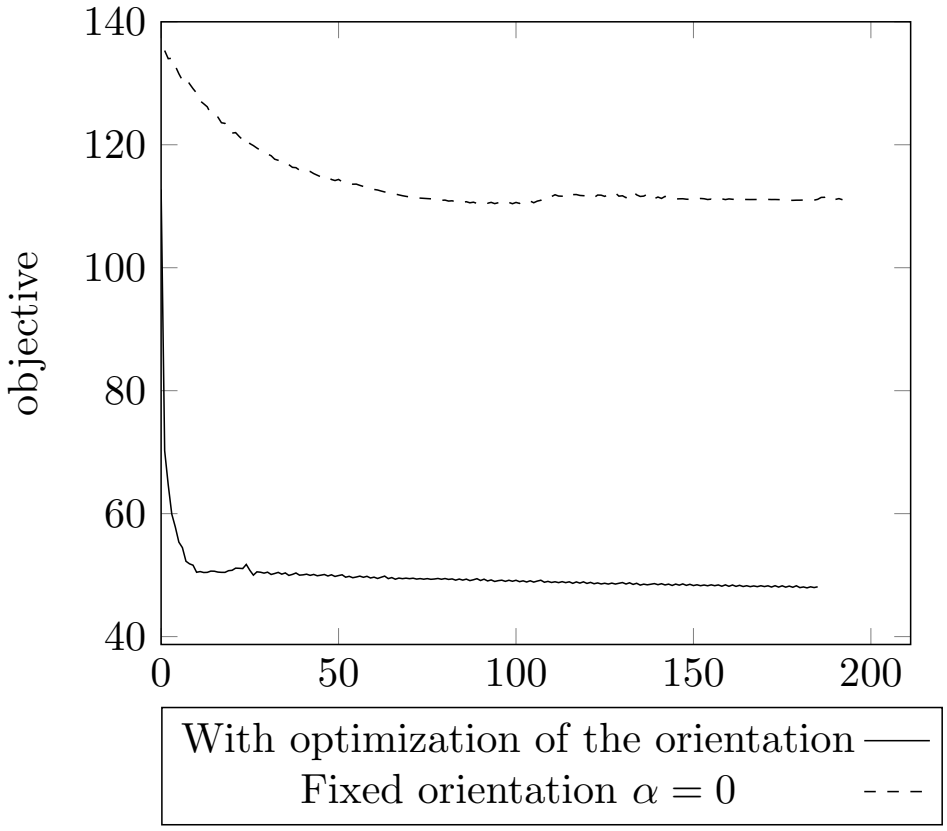

Figure 4.32: Convergence history of the objective function

.

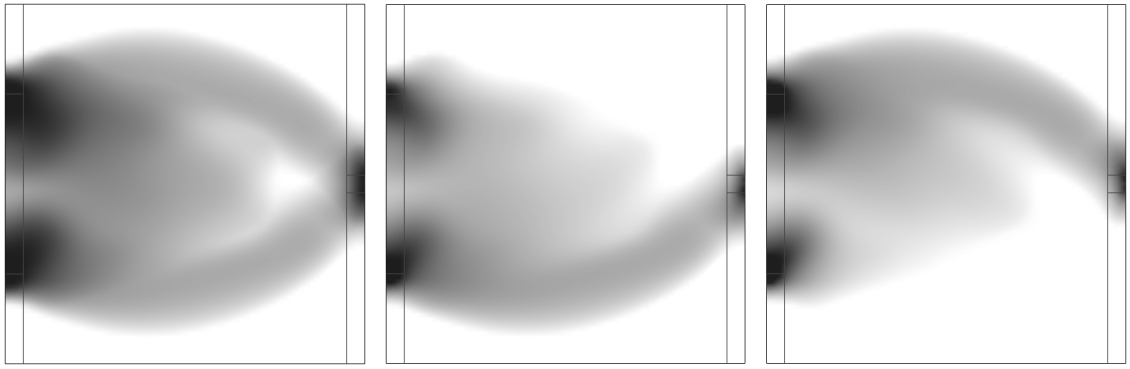

(a) Optimized Density (b) Optimized m_1 (c) Optimized m_2

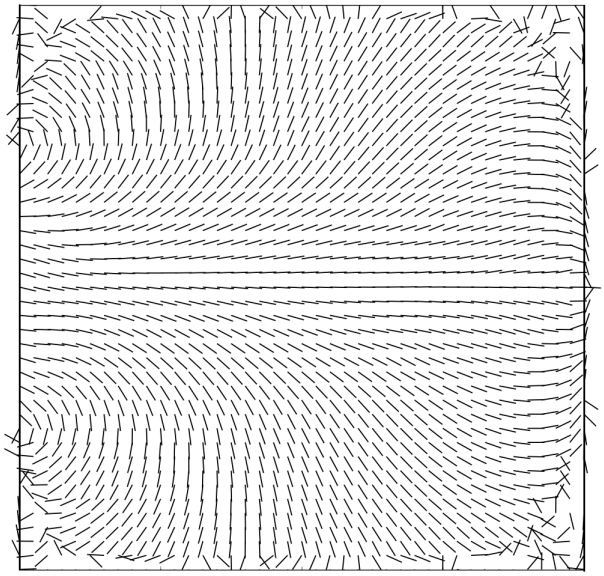

(d) Optimized Orientation

Figure 4.33: Optimized design of the cantilever for the stress minimization problem

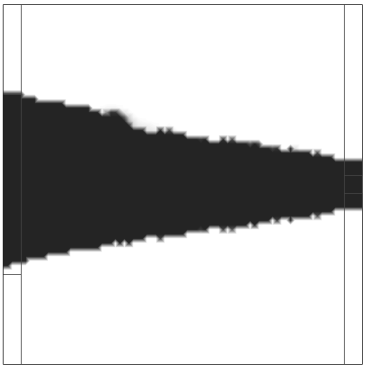

Figure 4.34: Optimized density of the cantilever, for a fixed orientation ($\alpha = 0$

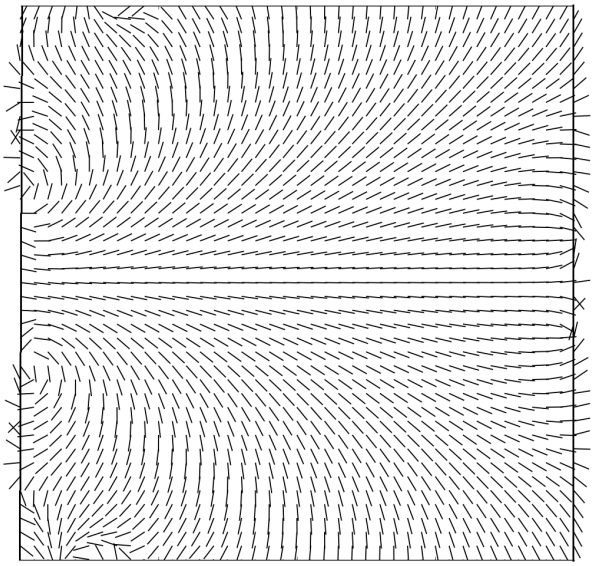

(a) Regularized Orientation

Figure 4.35: Optimized design of the cantilever for the stress minimization problem

$\delta c \in H^1(D;\mathbb{R}^2)$ and $q \in H^1_0(D)$,

$$2\int_D P^*(m)(S(b_1^n)+S'(\delta b_1^n))\sigma : S'(\delta c)\sigma\, dx + 2\eta^2 \int_D (b_1^n \wedge \nabla(b_1^n+\delta b_1^n))\cdot(b_1^n\wedge\nabla\delta c)\ \mathrm{dx} + \int_D (b_1^n\wedge\nabla\delta c)\cdot\nabla p^{n+1}\ \mathrm{dx} = 0 \quad (4.42)$$

4.7.3.b Reconstruction of a sequence of shapes

The computation of the diffeomorphism φ which distorts a regular grid in order to align the bars with a given orientation, depends only on the orientation vector field. Hence, the over presented method is valid no matter the optimization problem. We construct a sequence of genuine shapes $(\Omega_\varepsilon(\varphi,m))_{\varepsilon>0}$ converging to the optimized homogenized structure. We applied also the post-process to these structures, see Section 4.5.7. Results are displayed on Figure 4.36 for two values of ε, the period of the periodic microstructure.

Those structures are not the same as the ones optimized for the compliance minimization, see Figure 4.27. In particular, the external layers of the structure feature only parallel bars. They are not connected to each other by perpendicular bars, like the structures optimized for the compliance. That can be explained by the fact that the local stress induced in the sharp corners, at the junction of perpendicular bars, was quite important.

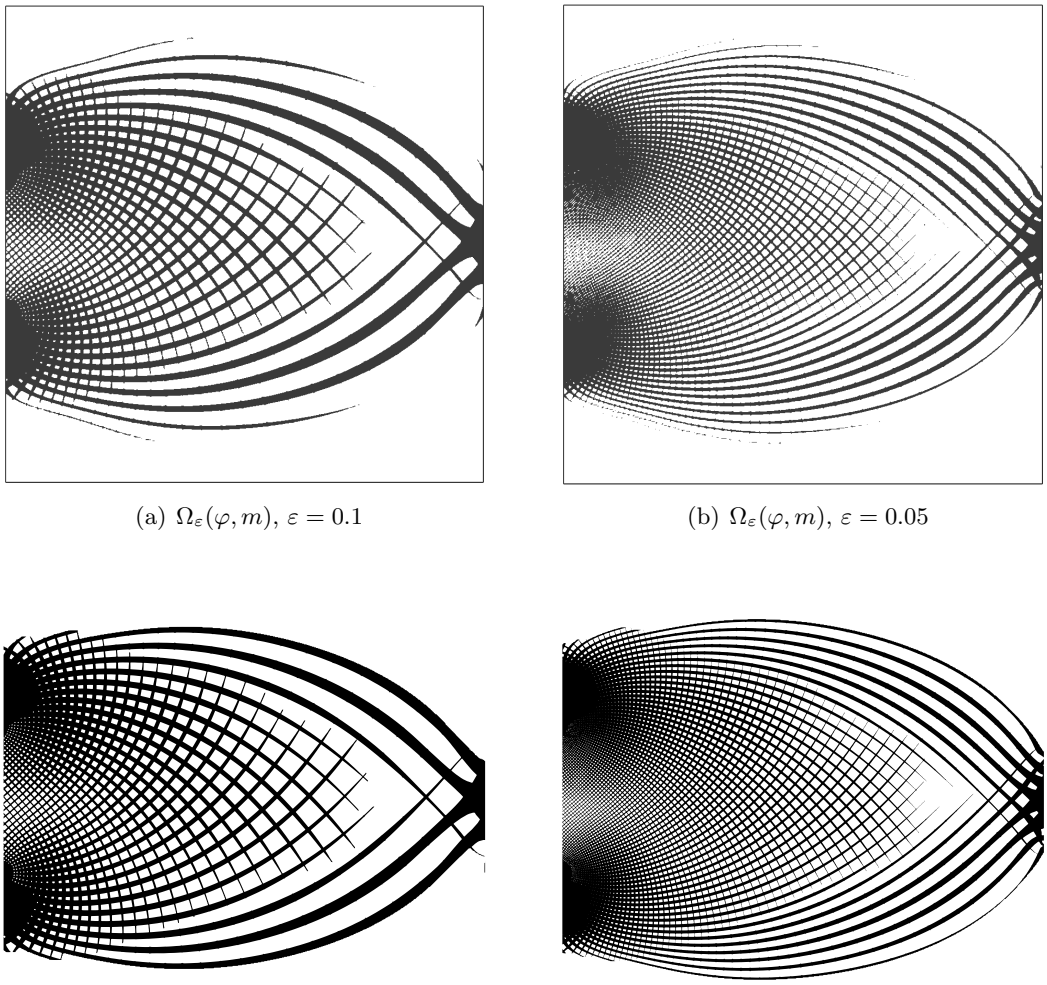

(a) $\Omega_\varepsilon(\varphi, m)$, $\varepsilon = 0.1$

(b) $\Omega_\varepsilon(\varphi, m)$, $\varepsilon = 0.05$

(c) $\tilde{\Omega}_\varepsilon(\varphi, \tilde{m})$, $\varepsilon = 0.1$

(d) $\tilde{\Omega}_\varepsilon(\varphi, \tilde{m})$, $\varepsilon = 0.05$

Figure 4.36: Deshomogenized structures $\Omega_\varepsilon(\varphi, m)$ and Post-processed structures $\tilde{\Omega}_\varepsilon(\varphi, \tilde{m})$ for several ε

Chapter 5

Projection of 2D optimized structures in the general case

Contents

5.1 Introduction

In the previous chapter, we presented how to compute a diffeomorphism, which distorts a regular grid in order to align each bar with a given direction. However, this initial method is not valid in the general case, especially when the domain D features holes and when the orientation field features singularities. Indeed, on a non simply connected domain, an irrotational vector field is not necessarily the gradient of a function.

Section 5.2 is dedicated to the theoretical computation of such a diffeormorphism. First, we introduce general results of differential geometry. Thanks to these settings, we determine the necessary conditions to integrate a vector field on a not simply connected domain. The idea consists in ripping the domain D in order to connect the holes to the exterior of D. This new

subset $\tilde{D}$ is now simply connected. Thanks to Poincaré lemma, see 5.2.2, an irrotational vector field on $\tilde{D}$ is the gradient of a function f. *Correction functions* are then introduced, to ensure the continuity of the function f along the cut lines. Then, this method is extended to cases where the orientation vector is known up to a π rotation. Indeed, optimized orientation vector field is generally not unequivocally defined. As in Chapter 4, the extended method relies on the introduction of a specific manifold. Results about integrability of antisymmetric vector fields defined on this manifold are given.

In Section 5.3, we focus on the numerical computation of the diffeomorphism in the general case. First, singularities of a vector field are defined, then we give a method to spot them in the domain. Singularities and holes of the domain can be treated the same way, thanks to correction functions. Second, we explain how to numerically compute those functions. Third the computation of the diffeomorphism is performed: it is equivalent to a minimization problem. To conclude, the numerical algorithm is successfully tested for vector fields featuring singularities and for perforated domains.

Section 5.4 deals with the regularization of vector fields featuring singularities. Thanks to an energy of Ginzburg-Landau, singularities of a vector field can be kept, while the conformality condition is satisfied. By considering also an energy of Modica Mortola, singularities can be removed of the orientation vector field. Those regularization methods are successfully tested on the optimized orientation of an electric mast.

5.2 Integrability of a vector field

5.2.1 Elements of differential geometry

We give here some classical results of differential geometry, one could read the textbooks [Weintraub 1997] or [Do Carmo 2012] for more details.

5.2.1.a Generalities

Fundamental correspondence. There is a fundamental correspondence between the differential forms and the functions, see section I.3 of [Weintraub 1997]. Hence, some results about the differential forms are directly transposable to the vector fields: they are straightly given for vector fields in the following. We refer to the previous textbooks for more details.

Closed and exact forms. A vector field v is said to be closed, if and only if $\nabla \wedge v = 0$. The vector field v is also called a curl-free or irrotational vector field.

A vector field v is said to be exact, if and only if there is a function f such that $\nabla f = v$. The vector field v is also called a conservative vector field.

There is a link between exact and closed vector fields, as stated in the following proposition, but no equivalence.

Proposition 5.2.1. *Every $\mathcal{C}^1$ conservative vector field is an irrotational vector field.*

Proof. Let v be a $\mathcal{C}^1$ conservative vector field. Hence, there is a function f such that: $\nabla f = v$. Recall the following identity of vector calculus to conclude: any $\mathcal{C}^2$ scalar field f satisfies

$\nabla \wedge (\nabla f) = \frac{\partial}{\partial x_1}\frac{\partial f}{\partial x_2} - \frac{\partial}{\partial x_2}\frac{\partial f}{\partial x_1} = 0.$ □

The Poincaré lemma (see Theorem 2, section 4.3 in [Do Carmo 2012]) gives a partial converse to this proposition, if the considered domain is simply connected.

Lemma 5.2.2. *Poincaré Lemma*
Let D be a simply connected open subset of $\mathbb{R}^2$, meaning that every closed curve in D can be continuously deformed to a point through deformations that stay in D, in particular, D features no hole.
Then every irrotational vector field on D is conservative.

5.2.1.b Non simply connected domain

The following theorem states that the linear integral around $(0,0)$ of an irrotational vector field defined on $\mathbb{R}^2 \setminus \{(0,0)\}$ does not depend of the chosen curve:

Theorem 5.2.3. *Let v be an irrotational vector field on $D = \mathbb{R}^2 \setminus \{(0,0)\}$. Let S^1 be the unit circle in $\mathbb{R}^2$, oriented counterclockwise, centered in $(0,0)$. Hence, for any simple closed curve γ_0 on D containing $(0,0)$ and oriented counterclockwise:*

$$\int_{S^1} v \cdot dr = \int_{\gamma_0} v \cdot dr\,.$$

Proof. We start to prove the above result for a particular kind of closed curves: the circles S^d of radius d, centered in $(0,0)$ and oriented counterclockwise.

The domain D is divided into two simple connected regions: $D^+ = D \cap (\mathbb{R} \times \mathbb{R}^+)$ and $D^- = D \cap (\mathbb{R} \times \mathbb{R}^-)$. The vector field v is still irrotational on D^+ (resp. on D^-).

We assume here that $d < 1$ without loss of generalities: the proof is exactly the same with $d > 1$ except that the orientation of some curves has to be reversed.

Let T^+ and T^- be two oriented straight line segments, from $(1,0)$ to $(d,0)$ and respectively from $(-d,0)$ to $(-1,0)$, see Figure 5.1.

Let $S^{d,+} = S^d \cap D^+$ and $S^{d,-} = S^d \cap D^-$.

The curve γ^+ defined by: $\gamma^+ = S^{1,+} \cup T^+ \cup -S^{d,+} \cup T^-$ is closed in D^+, see Figure 5.1(b). Let Ω be the region bounded by γ^+. Thanks to Green's theorem, we get: $\int_{\gamma^+} v \cdot dr = \int_\Omega \nabla \wedge v \, dx = 0$.

The curve γ^- defined by: $\gamma^- = S^{1,-} \cup -T^+ \cup -S^{d,-} \cup -T^-$ is closed in D^-, see Figure 5.1(c). Thanks to Green's theorem, we get also: $\int_{\gamma^-} v \cdot dr = 0$.

Since $\gamma^+ + \gamma^- = S^1 - S^d$, we have:

$$\int_{S^1} v \cdot dr - \int_{S^d} v \cdot dr = 0\,.$$

The proof of the general case is almost identical. Let γ_0 be a simple closed curve on D containing $(0,0)$ and oriented counterclockwise. Let $d > 0$ such that S^d contains γ_0, see Figure 5.2(a). Indeed, since γ_0 is closed, it is bounded.

As previously, the closed curves S^d and γ_0 are divided into two parts, see Figure 5.2(b), and two oriented straight line segments are introduced.

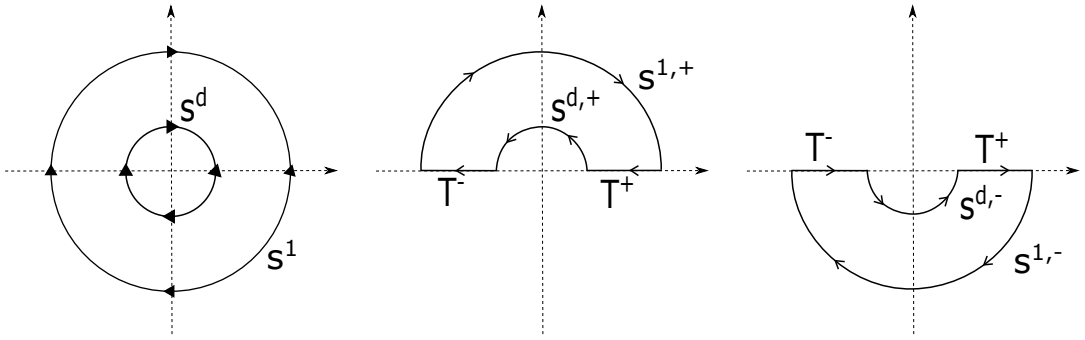

(a) S^1 and S^d (b) γ^+ (c) γ^-

Figure 5.1

We emphasize that γ_0 may intersect the horizontal axis in several points. Let $T = \{t \in \mathbb{R} | (t, 0) \in \gamma_0\}$ the set of the abscissas of the intersection points between γ_0 and the horizontal axis. We recall that T is bounded: $T \subset [-d, d]$.

Let $t^+ = \max(T)$ and $t^- = \min(T)$. The curve γ_0 is cut in $(t^+, 0)$ and $(t^-, 0)$. The straight segments T^+ and T^- are respectively defined from these points to S^d.

The closed curves γ^+ and γ^- are respectively defined as previously by: $\gamma^+ = S^{d,+} + T^+ - \gamma_0^+ + T^-$ and $\gamma^- = S^{d,-} - T^+ - \gamma_0^- - T^-$

The domains D^+ and D^- are no longer relevant. Nevertheless the domains bounded by the closed curves γ^+ and γ^- are simply connected sets of $\mathbb{R}^2$. We can conclude by similar arguments, thanks to Green's theorem.

□

The above theorem can easily be generalized to any perforated domain:

Corollary 5.2.4. *Let $D \subset \mathbb{R}^2$ be a connected domain featuring holes: D is not simply connected.*

Let v be an irrotational vector field on D.

Let γ_i be a simple closed curve, oriented counterclockwise and containing the i-th hole of D and no other one.

Then, $\int_{\gamma_i} v \cdot dr$ is independent of the curve γ_i which satisfies the above conditions. The value of the linear integral of v around the i-th hole will be denoted $c_i(v)$ in the following:

$$c_i(v) = \int_{\gamma_i} v \cdot dr \,. \tag{5.1}$$

The sketch of the proof is quite the same the one of the previous theorem, hence it is not displayed here.

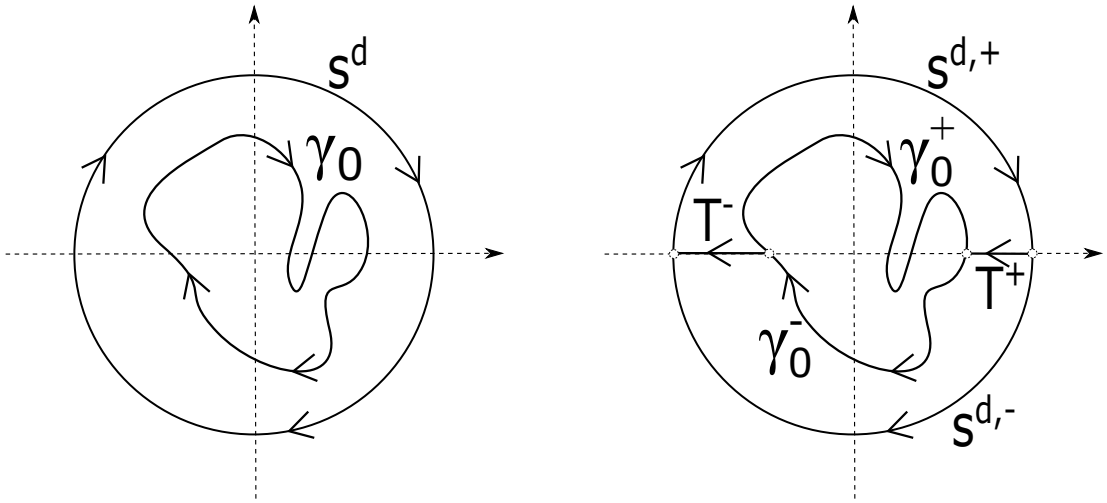

(a) (b)

Figure 5.2

5.2.2 Integrability of irrotational vector fields on non simply connected domains

5.2.2.a How to correct an irrotational vector field on a non simply connected domain

Let $D \subset \mathbb{R}^2$ be a connected domain featuring a finite number n_H of holes. Its holes will be denoted $(H_i)_{1\leq i\leq n_H}$, will be assumed to be smooth and not reduced to one point.

Let v be an irrotational vector field defined on D. Because D is not simply connected, the Poincaré Lemma 5.2.2 can not be used here. In order to use it, we have to construct from D a new domain $\tilde{D}$, simply connected. The idea is to cut the domain D in order to connect the holes H_i to the exterior of the domain.

For each hole H_i, let Γ_i be an arbitrary C^1 curve joining the external border of D and the border of the i-th hole H_i of D. Since D is assumed to feature a finite number of holes, we can construct a family of pairwise disjoint curves $(\Gamma_i)_{1\leq i\leq n_H}$, see Figure 5.3.

The domain $\tilde{D} = D \setminus \{\Gamma_i\}_{1\leq i\leq n_H}$ is simply connected. Hence, we get en integrability result for irrotational vector fields on the domain $\tilde{D}$:

Proposition 5.2.5. *Let v be an irrotational vector field on D. There exists a function $f \in C^1(\tilde{D}, \mathbb{R})$ such that:*

$$v = \nabla f \quad \text{on } \tilde{D}\,.$$

The jump of f through Γ_i is constant and equal to $c_i(v)$, for all $i \in \{1, .., n_H\}$.

Before giving the proof of this proposition, we recall the following classic proposition:

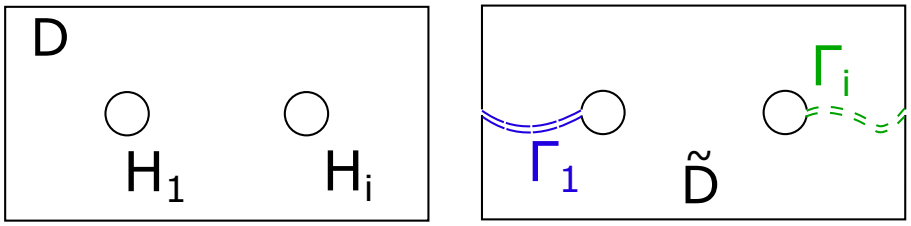

Figure 5.3: Cutting D (left) along curves Γ_i connecting the holes to the exterior of D led to a simply connected domain $\tilde{D}$ (right)

Proposition 5.2.6. *Let $a, b \in \tilde{D}$ (possibly $a = b$), let γ be a curve in $\tilde{D}$ joining a to b. Let f be a $C^1(\tilde{D}, \mathbb{R})$ be a function on $\tilde{D}$. Then we have:*

$$\int_\gamma \nabla f \cdot dr = f(b) - f(a)\,.$$

Proof. **Proof of Proposition 5.2.5**
On $\tilde{D}$, the vector field v (still denoted v for the sake of simplicity) is always irrotational. Thanks to Poincaré Lemma 5.2.2, there exists a function $f \in C^1(\tilde{D}, \mathbb{R})$ such that:

$$v = \nabla f\,.$$

We focus now on the behaviour of the function f around the curves Γ_i.

Let $a \in \Gamma_i$. As f is defined on $\tilde{D}$, f is not defined on a. Let $(a_n^+)_{n\geq 0}$ (resp $(a_n^-)_{n\geq 0}$ be a sequence of points in $\tilde{D}$, which are all on the same side of Γ_i. We assume that those sequences converge to a, meaning $||a_n^\pm - a|| \underset{n\to+\infty}{\longrightarrow} 0$. Let $(\gamma_n)_{n\geq 0}$ be a sequence of curves in $\tilde{D}$ joining a_n^- to a_n^+, see Figure 5.4. Thanks to the proposition 5.2.6, we get:

$$\int_{\gamma_n} v \cdot dr = f(a_n^+) - f(a_n^-)\,. \tag{5.2}$$

Since f is continuous, the sequences $(f(a_n^\pm)_{n\geq 0}$ are converging, we denote their respective limits $f(a^+)$ and $f(a^-)$. By passing to the limit in (5.2) we get:

$$c_i(v) = f(a^+) - f(a^-)\,.$$

This result does not depend on the choice of the point a of Γ_i. Hence the jump of f through the curve Γ_i is constant and equal to $c_i(v)$. □

Thanks to Proposition 5.2.5, an irrotational vector field is integrable on $\tilde{D}$. However we would like an integrability result on the whole domain D. Because of its jump through the curves Γ_i, the function f can not be continuously extended to the whole domain D. Hence, we propose to introduce the so-called *correction functions*. The purpose of these functions is to take into account the jump of the function f through the curves Γ_i.

We first define the set of continuous $\mathbb{R}/\mathbb{Z}$-valued functions:

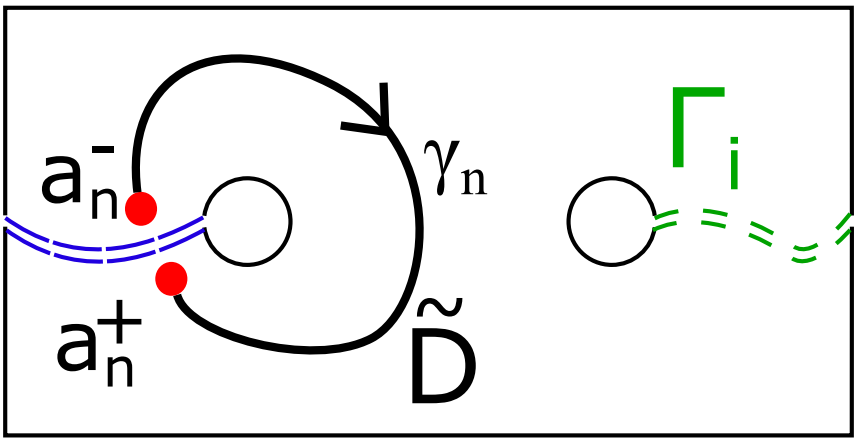

Figure 5.4: Curves γ_n crossing the cut lines Γ_j

Definition 5.2.1. We introduce the set $C^1(D, \mathbb{R}/\mathbb{Z})$ of $\mathbb{R}/\mathbb{Z}$-valued functions, which are continuous in $\mathbb{R}/\mathbb{Z}$ and twice derivable, their first derivatives are in the classical set $C^1(D, \mathbb{R}^2)$ and their second derivatives in $C(D, \mathcal{M}(\mathbb{R})^2)$. We recall that $\mathbb{R}/\mathbb{Z}$ is the quotient space $\mathbb{R}$ by $\mathbb{Z}$, also known as the unit torus.

Since $\mathbb{R}/\mathbb{Z}$ is a differentiable manifold locally similar to $\mathbb{R}$, the local notion of gradient is well defined for these functions. However, in order to prevent confusion between the gradients of $\mathbb{R}$-valued functions and of $\mathbb{R}/\mathbb{Z}$-valued functions, the gradient of the last ones will be denoted $\tilde{\nabla}$ in the following.

We can now define the correction functions:

Definition 5.2.2. Let $(\gamma_j)_{1\leq j\leq n_H}$ be a family of simple closed curves, clockwise oriented and containing respectively only the hole H_j.

A function $\psi_i \in C^1(D, \mathbb{R}/\mathbb{Z})$ is said to be a correction function for the hole H_i if and only if:

$$\forall \gamma_j \subset D \quad \int_{\gamma_j} \tilde{\nabla}\psi_i \cdot dr = \delta_{ij} \,,$$

where δ_{ij} is the Kronecker delta.

We emphasize that the choice of the curves of the family $(\gamma_j)_{1\leq j\leq n_H}$ has no impact on the definition of the correction functions, thanks to Corollary 5.2.4.

We will give further proofs of existence of correction functions, by construction. We assume for the moment their existence.

Theorem 5.2.7. *Let $D \subset \mathbb{R}^2$ be a connected domain featuring n_H holes. Let $0 < \eta < \eta_m$ be a small scalar. Let $(\psi_i)_{1\leq i\leq n_H}$ be a family of correction functions.*

Let v be an irrotational vector field on D. Let $c_i(v)$, defined by (5.1), be the value of the linear integral of v around the i-th hole.

Then there exists $\varphi \in C^1(D, \mathbb{R})$, such that :

$$v = \nabla\varphi + \sum_{i=1}^{n_H} c_i(v)\tilde{\nabla}\psi_i \,.$$

Proof. Let $\tilde{D}$ be the simply connected domain defined as previously.

Let w be a vector field defined on D as the vector field, corrected with the correction functions. It is given by:

$$w = v - \sum_{i=1}^{n_H} c_i(v)\tilde{\nabla}\psi_i \,.$$

The corrected vector field is obviously irrotational on D, since v is irrotational.

Hence, thanks to Poincaré Lemma 5.2.2, there exists a function $\varphi \in C^1(\tilde{D}, \mathbb{R})$ such that:

$$w = \nabla\varphi \quad \text{on } \tilde{D} \,.$$

Thanks to Proposition 5.2.5, the jump of φ through the curve Γ_i is equal to:

$$c_i(w) = \int_{\gamma_i} v \cdot dr - \sum_{i=1}^{n_H} c_i(v) \int_{\gamma_i} \tilde{\nabla}\psi_i \cdot dr = c_i(v) - \sum_{i=1}^{n_H} c_i(v)\delta_{ij} = 0 \,.$$

Hence the function φ defined on $\tilde{D}$, can continuously be extended to the whole domain D. To conclude, we have:

$$v = \nabla\varphi + \sum_{i=1}^{n_H} c_i(v)\tilde{\nabla}\psi_i \,.$$

□

5.2.2.b Existence of correction functions

We recall the settings. Let $D \subset \mathbb{R}^2$ be a connected domain featuring a finite number n_H of holes. Its holes are denoted $(H_i)_{1\leq i\leq n_H}$, are assumed to be smooth and not reduced to one point.

We assume that the border of each hole H_i can be joined to the exterior of the domain D by a straight line Γ_i, of normal n_i, see Figure 5.5. We assume also that the straight lines $(\Gamma_i)_{1\leq i\leq n_H}$ are pairwise disjoint.

Let $\eta_m > 0$ be the scalar defined by:

$$\eta_m = \frac{1}{2} \min_{1\leq i<j\leq n_H} d(\Gamma_i, \Gamma_j) \,,$$

where d is the usual euclidian distance.

Let $0 < \eta < \eta_m$, and let $l \in C^1(\mathbb{R}, \mathbb{R}/\mathbb{Z})$ be the function defined by:

$$l(t) = \begin{cases} 0 & \text{if } |t| > \eta \\ \frac{1}{4}(\cos(\frac{\pi}{\eta}t) + 1) & \text{if } 0 \leq t \leq \eta \\ -\frac{1}{4}(\cos(\frac{\pi}{\eta}t) + 1) & \text{if } -\eta \leq t < 0 \end{cases} \tag{5.3}$$

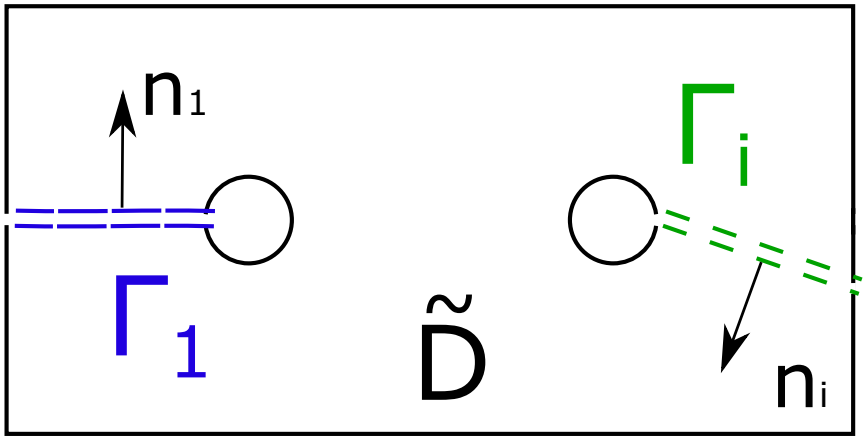

Figure 5.5: Cutting D with straight lines Γ_i

We emphasize that the function l is $\mathbb{R}/\mathbb{Z}$-valued and so is continuous in zero.

For each hole H_i, the domain D is cut along a line of normal $n_i^{\perp}$ crossing the hole H_i, see Figure 5.6. It subdivides the domain D in two parts: the open subset Ω_i containing Γ_i and $D \setminus \Omega_i$.

Proposition 5.2.8. *Let $M_i \in \Gamma_i$. Let $\psi_i \in C^1(D, \mathbb{R}/\mathbb{Z})$ be the function defined by:*

$$\psi_i(x) = \begin{cases} l((x - M_i) \cdot n_i) & \text{if } x \in \Omega_i \\ 0 & \text{if } x \notin \Omega_i \end{cases}$$

ψ_i is a correction function for the hole H_i.

Proof. We recall that the function ψ_i is $\mathbb{R}/\mathbb{Z}$ valued. Its gradient $\tilde{\nabla}\psi_i$ is irrotational on D.

From Corollary 5.2.4, the value of linear integral of $\tilde{\nabla}\psi_i$ around the hole H_j does not depend on the choice of the simple closed curve, oriented counterclockwise and containing the hole H_j.

Around the holes H_j, $j \neq i$

We recall that $\eta < \eta_m$. Hence, for each hole H_j with $j \neq i$, there exists a simple closed curve γ_j, oriented counterclockwise and containing only the hole H_j such that $d(\Gamma_i, \gamma_j) > \eta$, see Figure 5.7. This leads to $\tilde{\nabla}\psi(x)$ is equal to zero for all $x \in \gamma_j$ and so:

$$\int_{\gamma_j} \tilde{\nabla}\psi_i \cdot dr = 0\,.$$

Around the hole H_i

Let $x \in \Gamma_i$, such that $\gamma = \{x + t\,\eta\,n_i \mid t \in [-1; 1]\}$ is included in D. Let γ_2 be a curve joining

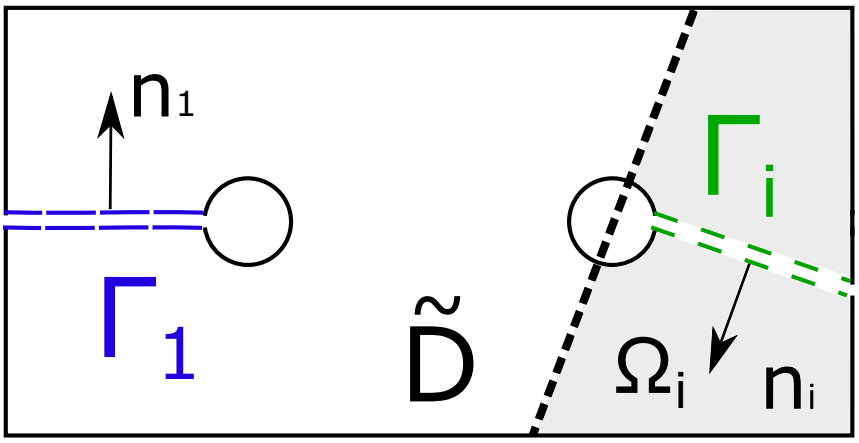

Figure 5.6: Definition of Ω_i

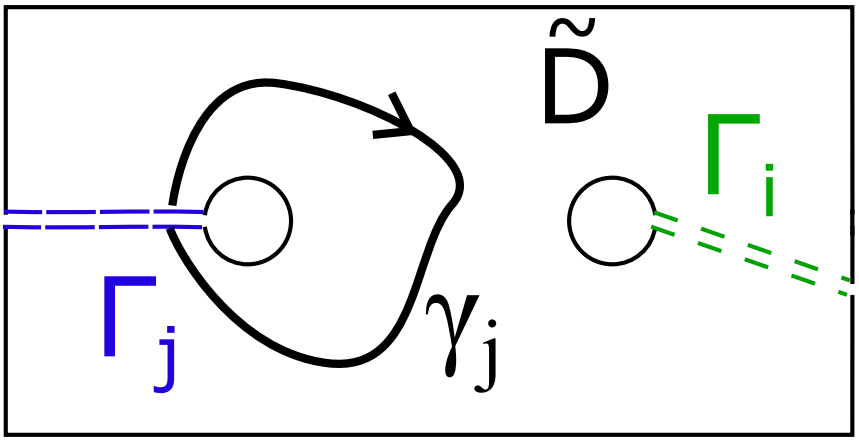

Figure 5.7: Integration of $\nabla\psi_i$ around holes H_j, $j \neq i$

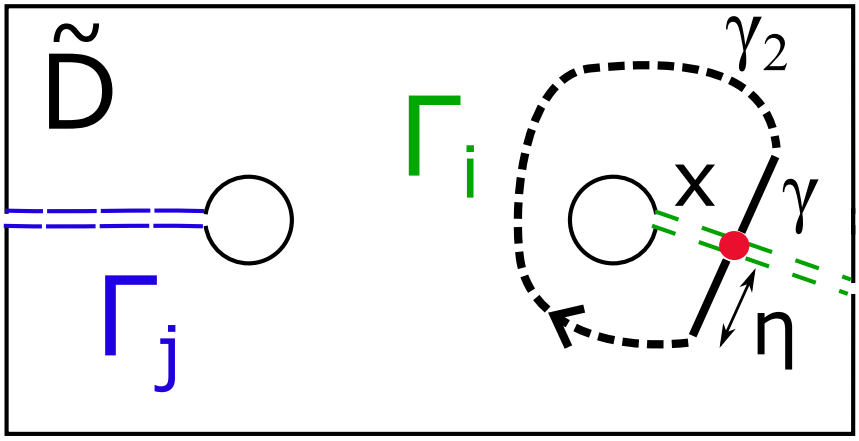

Figure 5.8: Integration of $\nabla\psi_i$ around the hole H_i

the points $x + \eta n_i$ and $x - \eta n_i$, without crossing Γ_i, see Figure 5.8. Let $\gamma_i = \gamma + \gamma_2$. Then

$$\begin{aligned} \int_{\gamma_i} \tilde{\nabla}\psi_i \cdot dr &= \int_{\gamma} \tilde{\nabla}\psi_i \cdot dr + \int_{\gamma_2} \tilde{\nabla}\psi_i \cdot dr \\ &= \int_{\gamma} \tilde{\nabla}\psi_i \cdot dr \\ &= \pm(\psi(x - \eta n_i) - \psi(x_i)) + (\psi(x_i) - \psi(x + \eta n_i)) \\ &= \pm(0 + 0.5) + (0.5 - 0) = \pm 1 \end{aligned} \tag{5.4}$$

Strictly speaking, the sign of $\int_{\gamma_i} \tilde{\nabla}\psi_i \cdot dr$ depends on the orientation of the normal n_i. It can be replaced by $-n_i$ without loss of generality in order to get $+1$ and not -1.

□

We make here the assumption that the curves Γ_i could be straight lines. It is not always the case, see Figure 5.9.

The previous process to construct a correction function ψ_i, when Γ_i is a straight line can be transposed to the case where Γ_i is only a C^1 curve:

Proposition 5.2.9. *The function ψ_i defined by:*

$$\forall x \in \Gamma_i, \forall t \in \mathbb{R} \quad \psi_i(x + t\, n_i(x)) = \begin{cases} l(t) & \text{if } x + t\, n_i(x) \in \Omega_i \\ 0 & \text{else} \end{cases},$$

where $n_i(x)$ is the normal of Γ_i in point x, is a correction function for the hole H_i.

However, two points have to be carefully satisfied. First, the curve has to be continuously extended outside of the domain D, on its both extremities. On Figure 5.9, the point z does not belong to D, but because the curve Γ_i is extended, the ray from this point exists. This ray is essential to define the correction function, because it is the only one to reach points where the

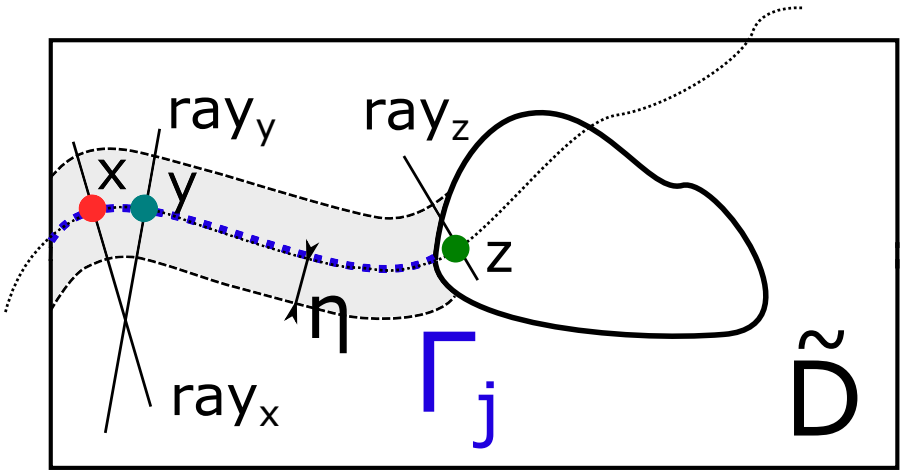

Figure 5.9: Definition of correction functions, when Γ_i is not a straight line

correction function is not equal to zero.
Second, the function ψ is defined along the rays coming from Γ_i. Hence the width η of the tube around Γ_i has to be chosen small enough in order that the rays do not intersect each other on a distance of η. This depends on the local curvature of the curve Γ_i. On Figure 5.9, the rays from the points x and y do intersect each other, but on a distance greater than η. If it is not the case, the correction function is not well defined at the intersection point, because it comes from multiple rays.

5.2.3 Exact functions on a differentiable manifold

Let $D \subset \mathbb{R}^2$ be an open subset featuring n_H holes $(H_i)_{1 \leq i \leq n_H}$.

Let v_1 and v_2 be two orthogonal vector fields on D defined up to their sign. Like in Section 5.3 of Chapter 4, we introduce a submanifold $\mathcal{D}$ of the space $D \times SO(2)$ in order to compute the grid map φ required to distort a regular grid according to the vector fields v_1 and v_2. We recall that $SO(2)$ is the set of rotations in $\mathbb{R}^2$.

We change our working space from D to $\mathcal{D}$. Hence, the vector fields to integrate are no longer defined on a subset of $\mathbb{R}^2$, but on a differentiable submanifold $\mathcal{D}$ of $D \times SO(2)$. However, all the previous results are still valid for such a space, and the proofs are identical. In particular, the Poincaré lemma 5.2.2.

We recall the settings and the notations of Chapter 4. Let $D \subset \mathbb{R}^2$, and $\alpha \in H^1(D, \mathbb{R}/\pi\mathbb{Z})$ an orientation field defined on D. We emphasize that this orientation field is defined up to π. Let $a_1 = (\cos(\alpha), \sin(\alpha))$ and $a_2 = (-\sin(\alpha), \cos(\alpha))$ be two vector fields defined on D. Those vectors are defined up to their sign. They may feature discontinuities in their direction: they will be said to be non coherently oriented. We will denote $a = (a_1, a_2)$ in the following.
We introduce $\beta = 2\alpha$: it is defined modulo 2π. Hence the vector fields $b_1 = (\cos(\beta), \sin(\beta))$ and $b_2 = (-\sin(\beta), \cos(\beta))$ are coherently defined. We will denote $b = (b_1, b_2)$ in the following.

We introduce the following submanifold of $D \times SO(2)$:

$$\mathcal{D} = \{(x, T) \in D \times SO(2) \text{ such that } T^2 = b(x)\}.$$

The domain D featuring holes, the manifold $\mathcal{D}$ is also perforated. For each hole H_i of D, two scenarios may occur: either the field a can be coherently oriented around the hole, possibly, by changing its sign, see Figure 5.10(a), or it can not, see Figure 5.10(c). In the first case, the manifold $\mathcal{D}$ around the hole H_i is locally the union of two copies of a neighbourhood of H_i, consisting of the two possible orientations of a, see Figure 5.10(b). The manifold features two distinct holes, that will be denoted H_i^+ and H_i^-.

In the second case, the manifold $\mathcal{D}$ around the hole H_i is locally connected, contrary to the previous case. A representation of $\mathcal{D}$ is displayed on Figure 5.10(d). Each copy of the neighbourhood of the hole H_i is cut along the same path. Then, they are glued together along this very path. On Figure 5.10(d), the solid (respectively the dashed) lines are glued together.

5.2.3.a Integrability conditions of an irrotational vector field on the manifold $\mathcal{D}$.

The method to integrate an irrotational vector field v on the manifold $\mathcal{D}$ follows the same steps that in $\mathbb{R}^2$. First the manifold $\mathcal{D}$ is cut in order to have simply connected domains, on which the vector field v is integrable, thanks to Poincaré lemma. Second, the jumps of the primitives of v, through the cut lines, are explicitly given by linear integrals of v along particular closed curves. Third, a family of corrections functions are introduced. To conclude a corrected vector field w defined as a linear combination of v and of the gradients of the correction functions is introduced. The primitives of this irrotational vector field w over the simply connected domains are shown to be continuously glued together.

Cutting the manifold $\mathcal{D}$. The domain D is perforated by n_H holes. Like in the previous section, we define a family of pairwise disjoint, smooth curves $(\Gamma_i)_{1\leq i\leq n_H}$, joining the holes H_i to the external border of the domain D. The domain D can be cut along these curves, yielding the domain $\tilde{D} = D \setminus \{\Gamma_i\}_{1\leq i\leq n_H}$.

For each $i \in \{1, .., n_H\}$, the subset $\{(x, T) \in \mathcal{D} \text{ such that } x \in \Gamma_i\}$ of $\mathcal{D}$ consists in two disjoint curves. They will be arbitrarily denoted Γ_i^+ and Γ_i^-. The manifold $\mathcal{D}$ is cut along these $2n_H$ curves, yielding two disjoint copies of $\tilde{D}$, see Figure 5.11. They are arbitrarily denoted $\tilde{D}^+$ and $\tilde{D}^-$.

A family of simple closed curves on $\mathcal{D}$. We introduce here a family of simple closed curves on $\mathcal{D}$. The hole H_1 is assumed to be a hole around which the field a can not be coherently oriented, possibly by renumbering the holes. We emphasize that the case where the field a can be coherently oriented around every hole, can be treated like in the previous Section in $\mathbb{R}^2$. The introduction of the manifold $\mathcal{D}$ is not be required in such a case.

Let the curve Γ_1^+ be the reference curve. Let γ_1^- be a simple closed curve going through the curves Γ_1^+ and Γ_1^-, see Figure 5.12(a).

For the holes H_i, $i \neq 1$, around which a can not be coherently oriented, let $\gamma_i^\pm$ be a simple closed curve going through the curves Γ_1^+ and $\Gamma_i^\pm$, see Figures 5.12(b) and 5.12(c). We emphasize that going through those curves, make switch the current copy of $\tilde{D}$ on which we are. Hence, by

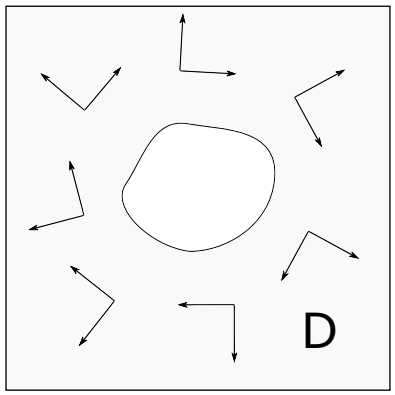

(a) Domain D

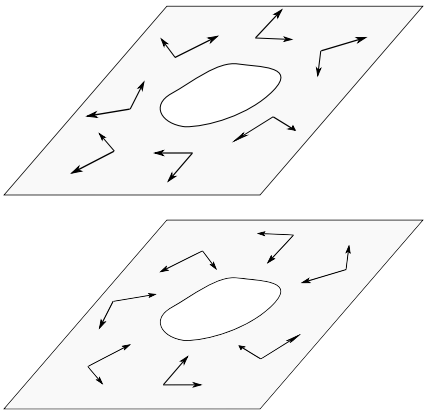

(b) Manifold $\mathcal{D}$

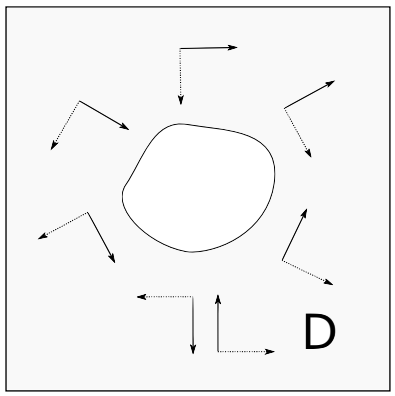

(c) Domain D

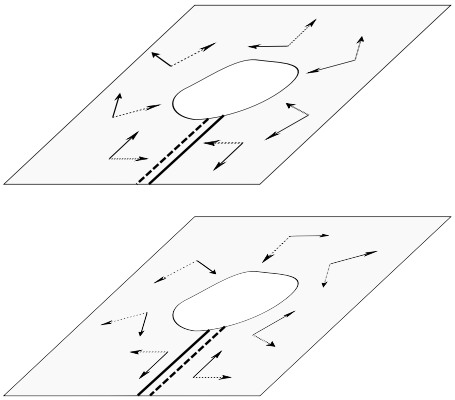

(d) Manifold $\mathcal{D}$

Figure 5.10: A perforated domain D (left) leads to two manifolds $\mathcal{D}$ (right), depending on whether the vector field is coherently orientable around the hole (top), or not (bottom). On (d), the solid (respectively dashed) lines are glued together.

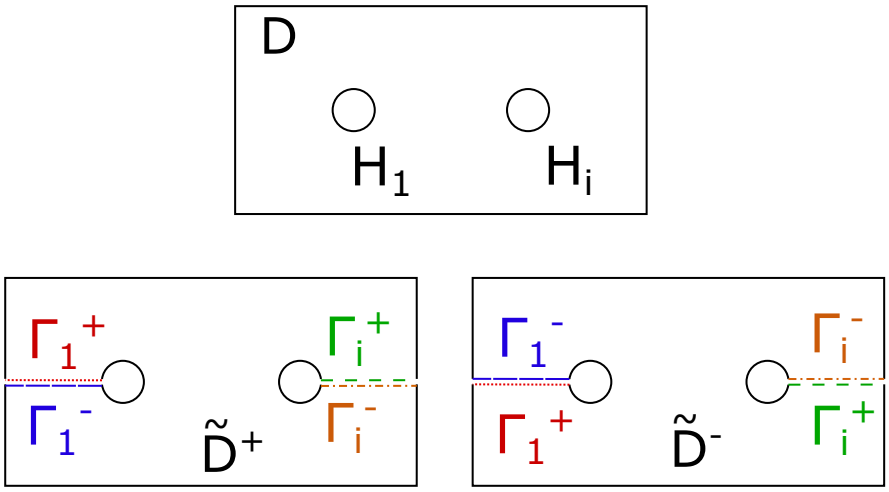

Figure 5.11: From a perforated domain D (top), a manifold $\mathcal{D}$ is introduced. This manifold $\mathcal{D}$ is cut along the curves $\Gamma_i^{\pm}$, this leads to two disconnected copies of the simply connected domain $\tilde{D}$. To find back the manifold, those copies have to be glued together along the cut lines $\Gamma_i^{\pm}$ (the segments of the same color are connected in the manifold $\mathcal{D}$).

crossing two of them, we switch twice and so go back to the copy on which we start the closed curve.

For the holes H_i, around which a can be coherently oriented, when the curves $\Gamma_i^{\pm}$ are crossed, the current copy of $\tilde{D}$ stays unchanged. Hence, let $\gamma_i^{\pm}$ be a simple closed curve going through the curves $\Gamma_i^{\pm}$, see Figures 5.12(d) and 5.12(e).

Integration of an irrotational vector field on the subset $\tilde{D}^+$ and $\tilde{D}^-$.

Proposition 5.2.10. *Assuming all the previous settings.*

Let v be an irrotational vector field defined on the manifold $\mathcal{D}$.

There exists two functions f^+ and f^-, respectively defined on $\tilde{D}^+$ and on $\tilde{D}^-$, such that:

$$\begin{aligned} \nabla f^+ &= v \quad \text{on } \tilde{D}^+ \\ \nabla f^- &= v \quad \text{on } \tilde{D}^- \end{aligned}$$

and such that:

- *the difference between f^+ and f^- through Γ_1^+ is equal to zero,*
- *for holes H_i around which the field a can not be coherently oriented, the difference between f^+ and f^- through $\Gamma_i^{\pm}$, different of Γ_1^+, is equal to $c_i^{\pm}(v) = \int_{\gamma_i^{\pm}} v \cdot dr$,*
- *for holes H_i around which the field a can be coherently oriented, the jump of f^+ (resp f^-) through Γ_i^+ (resp. Γ_i^-) is equal to $c_i^+(v) = \int_{\gamma_i^+} v \cdot dr$, (resp. $c_i^-(v) = \int_{\gamma_i^-} v \cdot dr$).*

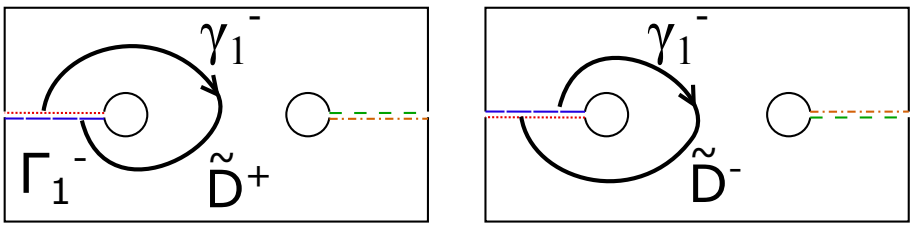

(a) γ_1^-

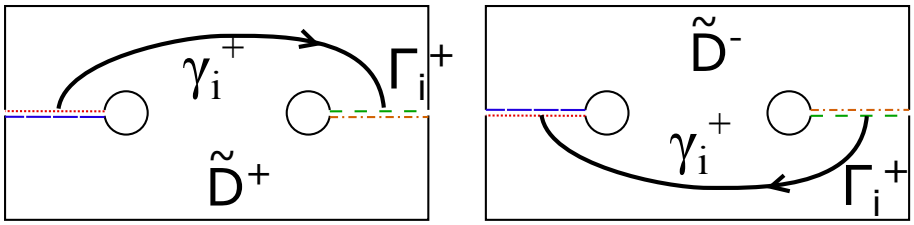

(b) γ_i^+, when the field a is non coherently orientable around H_i

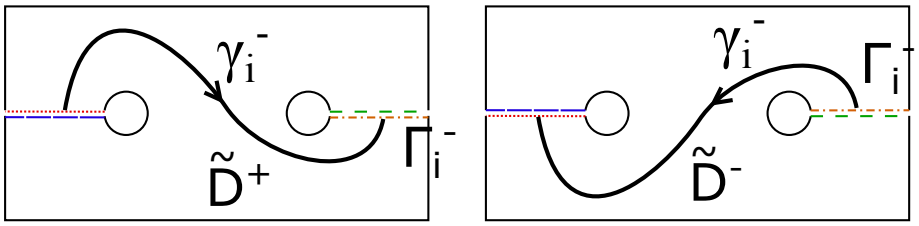

(c) γ_i^-, when the field a is non coherently orientable around H_i

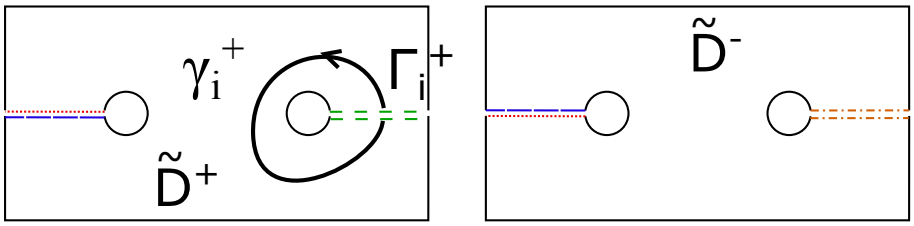

(d) γ_i^+, when the field a is coherently orientable around H_i

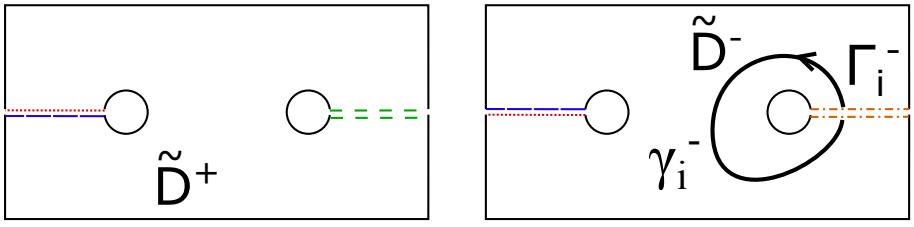

(e) γ_i^+, when the field a is coherently orientable around H_i

Figure 5.12: Definition of the curves $\gamma_i^{\pm}$, crossing the corresponding curve $\Gamma_i^{\pm}$

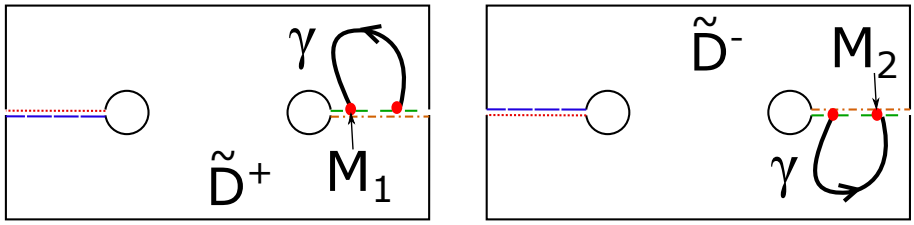

Figure 5.13: Difference between f^+ and f^- through Γ_i^+

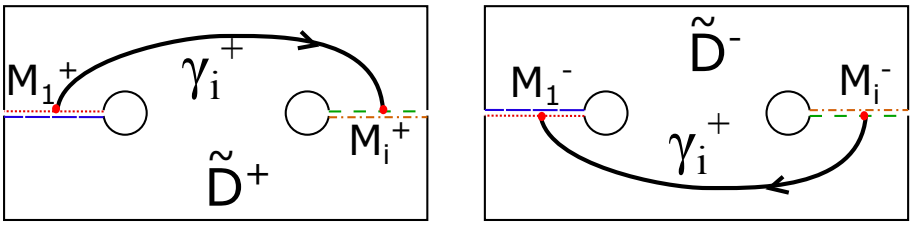

Figure 5.14: Difference between f^+ and f^- through Γ_i^+

Proof. The vector field v is irrotational on the simply connected domain $\tilde{D}^+$ (resp. on $\tilde{D}^-$). Thanks to Poincaré lemma 5.2.2, there exists a function f^+ (resp. f^-) such that $\nabla f^+ = v$ on $\tilde{D}^+$ (resp $\nabla f^- = v$ on $\tilde{D}^-$).

Let $M \in \Gamma_1^+$, and $f^+(M)$ (resp. $f^-(M)$ the limit of f^+ (resp. of f^-) on M. We can assume that $f^+(M) = f^-(M)$. If not, we can add the constant $f^+(M) - f^-(M)$ to the function f^-, without altering its gradient.

For holes H_i around which a can not be coherently oriented:
The difference between f^+ and f^- through Γ_i^+ (resp. Γ_i^-) is uniform, as we can see below. It will be denote Δf_i^+ (resp. Δf_i^-). Let $M_1, M_2 \in \Gamma_i^+$, (resp. Γ_i^-) let γ in $\mathcal{D}$ be a closed curve joining M_1 and M_2 by crossing twice Γ_i^+, (resp. Γ_i^-) see Figure 5.13. Then, since v is irrotational on $\mathcal{D}$, we have thanks to the Green's theorem:

$$\int_\gamma v \cdot dr = 0 = (f^-(M_1) - f^+(M_1)) + (f^+(M_2) - f^-(M_2)) .$$

The linear integral of v along the closed curve γ_i^+ (resp. γ_i^-)can be explictly given using the values of the primitives f^+ and f^-, see Figure 5.14:

$$c_i^+(v) = \int_{\gamma_i^+} = (f^+(M_i) - f^+(M_1)) + f^-(M_1) - f^-(M_i) = \Delta f_i^+ - \Delta f_1^+ = \Delta f_i^+ .$$

Likewise, $c_i^-(v) = \Delta f_i^-$

For holes H_i around which a can be coherently oriented:
The jump of f^+ (reps. f^-) through Γ_i^+ (resp. Γ_i^-) is uniform, and will be denoted Δf_i^+ (resp. Δf_i^-). Let $M_1, M_2 \in \Gamma_i^+$ (resp. Γ_i^-), let γ in $\mathcal{D}$ be a closed curve joining M_1 and M_2 by crossing

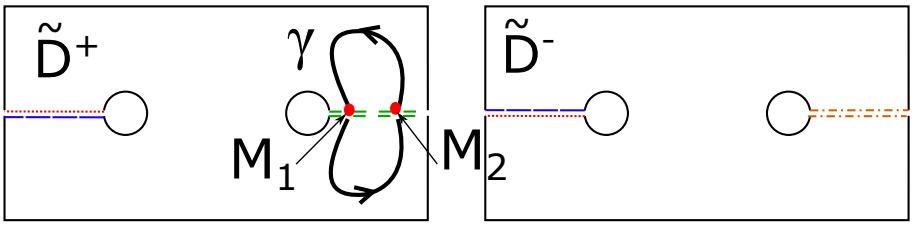

Figure 5.15: Jump of f^+ through Γ_i^+

twice Γ_i^+, (resp Γ_i^+) see Figure 5.15. Then, since v is irrotational on $\mathcal{D}$, we have thanks to the Green's theorem:

$$\int_\gamma v \cdot dr = 0 = (f^+(M_1^+) - f^+(M_1)^-) - (f^+(M_2^+) - f^-(M_2^-))\,,$$

where $f^+(M_i^+)$ is the limit of f^+ in M_i on one side of the cut line Γ_i^+, and $f^+(M_i^-)$ the limit on the other side.

The linear integral of v along the closed curve γ_i^+ (resp. γ_i^-) is equal to the jump Δf_i^+ (resp. Δf_i^-).

□

Correction of an irrotational vector field. We introduce the so-called correction functions.

Definition 5.2.3. Let $i \in \{2, .., n_H\}$. A function $\psi_i^+ \in C^1(\mathcal{D}, \mathbb{R}/\mathbb{Z})$ is said to be a correction function if and only if:

$$\int_{\gamma_i^+} \tilde{\nabla}\psi_i^+ \cdot dr = 1\,,$$

$$\forall j \in \{2, .., n_H\}, j \neq i, \quad \int_{\gamma_j^+} \tilde{\nabla}\psi_i^+ \cdot dr = 0\,,$$

$$\forall j \in \{1, .., n_H\}, \quad \int_{\gamma_j^-} \tilde{\nabla}\psi_i^+ \cdot dr = 0\,.$$

Let $i \in \{1, .., n_H\}$. A function $\psi_i^- \in C^1(\mathcal{D}, \mathbb{R}/\mathbb{Z})$ is said to be a correction function if and only if:

$$\int_{\gamma_i^-} \tilde{\nabla}\psi_i^- \cdot dr = 1\,,$$

$$\forall j \in \{1, .., n_H\}, j \neq i, \quad \int_{\gamma_j^-} \tilde{\nabla}\psi_i^6 \cdot dr = 0\,,$$

$$\forall j \in \{2, .., n_H\}, \quad \int_{\gamma_j^+} \tilde{\nabla}\psi_i^- \cdot dr = 0\,.$$

We assume their existence for the moment.

Theorem 5.2.11. *Assuming the previous settings.*

Let v be an irrotational vector field on $\mathcal{D}$. Let $c_i^{\pm}(v)$ be the coefficients defined by $c_i^{\pm}(v) = \int_{\gamma_i^{\pm}} v \cdot dr$.

Let $(\psi_i^+)_{2\leq i\leq n_H}$ and $(\psi_i^-)_{1\leq i\leq n_H}$ be families of correction functions, defined by Definition 5.2.3.

There exists $\varphi \in C^1(\mathcal{D}, \mathbb{R})$ such that

$$v = \nabla\varphi + \sum_{i=2}^{n_H} c_i^+(v)\tilde{\nabla}\psi_i^+ + \sum_{i=1}^{n_H} c_i^-(v)\tilde{\nabla}\psi_i^- .$$

Proof. Let the corrected vector field w be defined by:

$$w = v - \sum_{i=2}^{n_H} c_i^+(v)\tilde{\nabla}\psi_i^+ - \sum_{i=1}^{n_H} c_i^-(v)\tilde{\nabla}\psi_i^- .$$

This vector field is irrotational on $\mathcal{D}$. Moreover the value $c_i^{\pm}(w)$ of its linear integral along the curves $\gamma_i^{\pm}$ is equal to zero:

$$\begin{array}{rcl} c_i^{\pm}(w) & = & \int_{\gamma_i^{\pm}} w \cdot dr \\ & = & \int_{\gamma_i^{\pm}} v \cdot dr - \sum_{i=2}^{n_H} c_i^+(v) \int_{\gamma_i^{\pm}} \tilde{\nabla}\psi_i^+ \cdot dr - \sum_{i=1}^{n_H} c_i^-(v) \int_{\gamma_i^{\pm}} \tilde{\nabla}\psi_i^- \cdot dr \ \cdot \\ & = & c_i^{\pm}(v) - c_i^{\pm}(v) = 0 \end{array}$$

Thanks to Proposition 5.2.10, there exists two functions f^+ and f^-, respectively defined on $\tilde{D}^+$ and on $\tilde{D}^-$, such that $\nabla f^+ = v$ on $\tilde{D}^+$ and $\nabla f^- = v$ on $\tilde{D}^-$.

The manifold $\mathcal{D}$ is obtained from $\tilde{D}^+$ and $\tilde{D}^-$, by gluing them together along the cut lines $\Gamma_i^{\pm}$.

Thanks to Proposition 5.2.10, the differences between the functions f^+ and f^-, and also their respective jumps (when the field a can be coherently oriented around the considered hole H_i), through the cut lines $\Gamma_i^{\pm}$ are respectively equal to $c_i^{\pm}(w) = 0$ The functions f^+ and f^- can then be continuously extended to the whole manifold $\mathcal{D}$, defining a new function φ on $\mathcal{D}$. The continuity of its gradient on the whole manifold $\mathcal{D}$ is ensured by the fact that $\nabla\varphi = v$ on the subdomains $\tilde{D}^+$ and $\tilde{D}^-$.

□

Correction functions on a manifold.

Proposition 5.2.12. *Let $\eta > 0$, and $i \in \{1, .., n_H\}$.*

Let $\psi_i \in D$ be the correction function defined at Proposition 5.2.9.

Let Ω_i^+, (resp. Ω_i^-) be the open subset of $\mathcal{D}$ defined as the tubular space around Γ_i^+ (resp. Γ_i^-). The functions defined by:

$$\psi_i^+(x,T) = \begin{cases} \psi_i(x) & \text{if } (x,T) \in \Omega_i^+ \\ 0 & \text{else} \end{cases}$$

and

$$\psi_i^-(x,T) = \begin{cases} \psi_i(x) & \text{if } (x,T) \in \Omega_i^- \\ 0 & \text{else} \end{cases}$$

are correction functions.

Proof. The proof consists in computing the linear integral of the gradient of the over-defined functions along the curves $\gamma_i^{\pm}$. It is similar to the proof of Proposition 5.2.5, and so it is not reproduced here. □

5.2.3.b Integration of an antisymmetric irrotational vector field.

Theorem 5.2.13. *Let v be an antisymmetric irrotational vector field on $\mathcal{D}$, meaning:*

$$\forall (x,T) \in \mathcal{D} \quad v(x,T) = -v(x,-T)\,.$$

Let $c_i(v)$ be the coefficient defined by $c_i(v) = \int_{\gamma_i^+} v \cdot dr$, for $2 \le i \le n_H$.

There exist $(\psi_i)_{2\le i\le n_H} \in C^1(\mathcal{D}, \mathbb{R}/\mathbb{Z})$, antisymmetric functions, and $\varphi \in C^1(\mathcal{D},\mathbb{R})$, an antisymmetric function too, such that :

$$v = \nabla\varphi + \sum_{i=2}^{n_H} c_i(v)\tilde{\nabla}\psi_i \quad \text{on } \mathcal{D}\,.$$

Proof. Thanks to Theorem 5.2.11, there exists $\varphi \in C^1(\mathcal{D},\mathbb{R})$ such that:

$$v = \nabla\varphi + \sum_{i=2}^{n_H} c_i^+(v)\tilde{\nabla}\psi_i^+ + \sum_{i=1}^{n_H} c_i^-(v)\tilde{\nabla}\psi_i^-\,,$$

where $c_i^{\pm}(v) = \int_{\gamma_i^{\pm}} v \cdot dr$.

Values of $c_i^{\pm}(v)$**.** The curve γ_1^- can be split in two curves γ^+ and γ^- on respectively D^+ and D^-. Then we get:

$$\begin{aligned} c_1^-(v) &= \int_{\gamma_1^-} v \cdot dr \\ &= \int_{\gamma^+} v \cdot dr + \int_{\gamma^-} v \cdot dr \\ &= \int_{\gamma^+} v \cdot dr - \int_{\gamma^+} v \cdot dr = 0 \end{aligned}$$

For holes H_i around which the field a can not be coherently oriented:
Let γ be the closed curve defined by $\gamma = \gamma_i^+ + \gamma_i^-$, see Figure 5.16(a). This curve can be split in two curves γ^+ and γ^- on respectively D^+ and D^-.

Let γ_0 be a symmetric closed curve on $\mathcal{D}$, going twice through Γ_i, see Figure 5.16(b). It has two components: γ_0^+ and γ_0^- on respectively D^+ and D^-. Since v is antisymmetric, we get:

$$\int_{\gamma_0^+} v \cdot dr = -\int_{\gamma_0^-} v \cdot dr\,.$$

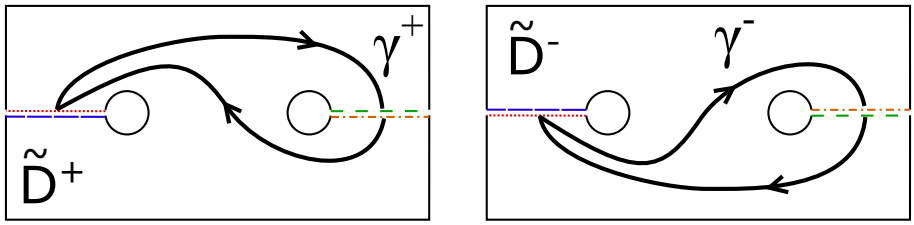

(a) Curve $\gamma_i^+ \cup \gamma_i^-$

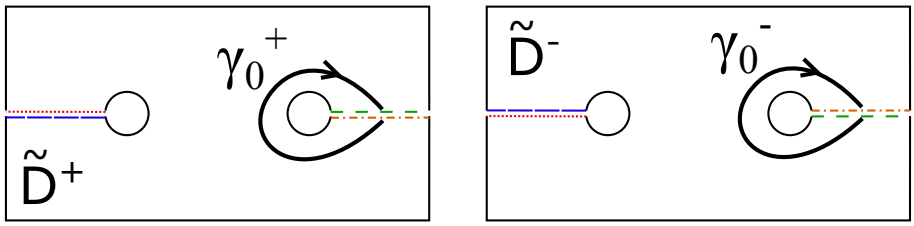

(b) Closed curve γ_0

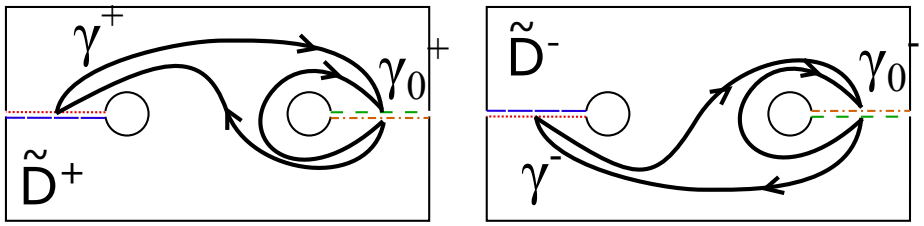

(c) Curves $\gamma^+ \cup \gamma_0^+$ and $\gamma^- \cup \gamma_0^-$

Figure 5.16: Computing $c_i(v)$ for holes around which the field a can not be coherently oriented

The curves $\gamma^+ \cup \gamma_0^+$ and $\gamma^- \cup \gamma_0^-$ are closed curves on respectively $\tilde{D}^+$ and $\tilde{D}^-$, containing no hole, see Figure 5.16(c). Thanks to Green's theorem, and since v is irrotational, we get:

$$\int_{\gamma^+} v \cdot dr + \int_{\gamma_0^+} v \cdot dr = 0$$

and

$$\int_{\gamma^-} v \cdot dr + \int_{\gamma_0^-} v \cdot dr = 0\,.$$

To conclude:

$$\int_{\gamma_0^+} v \cdot dr + \int_{\gamma_0^-} v \cdot dr \; = \int_{\gamma_i^+} v \cdot dr + \int_{\gamma_i^-} v \cdot dr \; = c_i^+(v) + c_i^-(v) = 0\,,$$

what can be rewritten : $c_i^+(v) = -c_i^-(v)$.

For holes H_i around which the field a can be coherently oriented:
We can prove likewise: $c_i^+(v) = -c_i^-(v)$.

Finally, v can be rewritten:

$$v = \nabla\varphi + \sum_{i=2}^{n_H} c_i^+(v)(\tilde{\nabla}\psi_i^+ - \tilde{\nabla}\psi_i^-)\,,$$

Antisymmetry of the correction functions Let $\psi_i^\pm$ be the correction functions defined by. For $i \geq 2$, one can notice that for all $(x,T) \in \mathcal{D}$:

$$\psi_i^+(x,T) = \psi_i^-(x,-T)\,.$$

Hence we introduce the function ψ_i defined by: $\psi_i = \psi_i^+(x,T) - \psi_i^-(x,T)$. It is an antisymmetric function.

v can be rewritten:

$$v = \nabla\varphi + \sum_{i=2}^{n_H} c_i^+(v)\tilde{\nabla}\psi_i\,,$$

Antisymmetry of the function φ. The gradient of φ is given as the sum of antisymmetric vector fields, namely v and $(\tilde{\nabla}\psi_i)_{2\leq i\leq n_H}$. Hence, it is antisymmetric too.

Let g be the function defined by $g(x,T) = \varphi(x,T) + \varphi(x,-T)$. Its gradient is given by $\nabla\varphi(x,T) + \nabla\varphi(x,-T)0$. Hence g is constant on $\mathcal{D}$, let c be this constant. Then we have:

$$\varphi(x,T) - \frac{c}{2} = -\varphi(x,T) + \frac{c}{2}\,. \tag{5.5}$$

Let ψ the function defined by: $\psi = \varphi(x,T) - \frac{c}{2}$. This function is antisymmetric thanks to (5.5), and it satisfies : $\nabla\psi = \nabla\varphi$.

Finally, we have:

$$v = \nabla\psi + \sum_{i=2}^{n_H} c_i^+(v)\tilde{\nabla}\psi_i\,,$$

where the functions ψ and ψ_i $(2 \leq i \leq n_H)$ are antisymmetric on $\mathcal{D}$.

□

5.3 Numerical implementation

We focus here on the numerical implementation of the integration method of an irrotational vector field.

5.3.1 Numerical settings of the problem

Let $D \subset \mathbb{R}^2$ be a connected open set, let $(H_i)_{1 \leq i \leq n_H}$ be the holes of D.

Let $\mathcal{T}_h$ be a regular mesh of D. Let V_h be the space of P_1 finite elements on D, and W_h the space of P_1 discontinuous Galerkin elements on D.

Let $\alpha \in V_h$ be an orientation field over D, so discretized using P_1 finite elements. It is assumed to satisfy the conformality condition, see Lemma 4.5.1 in Chapter 4.

Let $r \in V_h$ be a dilatation field, such that $\nabla r = (-\frac{\partial \alpha}{\partial x_2}, \frac{\partial \alpha}{\partial x_1})^T$, see Section 5.2 in Chapter 4 for more details.

We introduce the cover space of D:

$$\mathcal{D} = \{(x, T) \in D \times SO(2) \text{ such that } T^2 = b(x)\},$$

where

$$b(x) = \begin{pmatrix} \cos(2\alpha) & -\sin(2\alpha) \\ \sin(2\alpha) & \cos(2\alpha) \end{pmatrix}.$$

Let $\mathcal{V}_h$ be the set of Lagrange finite elements of degree one on $\mathcal{D}$ that satisfy an antisymmetry condition, namely for a function $f \in \mathcal{V}_h$: $f(x, T) = -f(x, -T)$.

Let I^h be the interpolation operator from $\mathcal{V}_h$ onto W_h. For the practical computation of this operator, one could refer to Section 5.5 of Chapter 4. Briefly, the triangles of the mesh are seen as charts of the manifold. Hence, the vector fields have to be coherently oriented in each triangle separately. However, we do not impose any adjacent triangles to be adjacent charts of $\mathcal{D}$: this is in fact not possible in presence of singularities in the vector field. The purpose of the interpolation operator is to ensure a coherent orientation of the vector fields on each triangle.

5.3.2 Singularities of a vector field

Numerically the angle α is defined by the orientation of the unit vector a_1. This vector field is discretized using P_1 finite elements: its value is known at each vertex of the mesh and interpolated on the rest of the domain. Hence, even if its norm is equal to one on the vertices, it is not necessarily the case on the rest of the domain, due to the interpolation. Where the vector a_1 is the null vector, the orientation α can not be defined. Those zeros of the vector field are called singularities. In particular, the rotational of the vector field on a singularity is not equal to zero. Hence, it is not locally integrable. In order to solve this problem, a small neighbourhood of each singularity is removed from the domain. On this new perforated subset, the vector field is irrotational: we apply the integration method presented in the previous section.

5.3.3 Spotting the singularities of a vector field

We explain here how to spot the singularities of the numerical vector fields $v_1 = e^r a_1$ and $v_2 = e^r a_2$, discretized by P_1 finite elements. We recall that a singularity of a vector field is defined as a zero of the vector field. Hence to spot the singularities of a vector field, we can simply spot its zeros.

Since a_1 and a_2 are unit vector fields, the vector fields v_1 and v_2 do not feature a zero on a vertex of the mesh. However, they may feature a zero inside a triangle of the mesh, or on the edge of the mesh. We assume in the following that the considered vector fields do not feature zeros on the edges of the mesh.

Since the vector fields v_1 and v_2 are the same up to a rotation of angle $\frac{\pi}{2}$, $p \in D$ is a zero of v_2 if and only if it is a zero of v_1. Hence it is enough to spot the zeros of only one of the vector fields, v_1 for example. However, we recall that the vector field v_1 is defined up to its sign, since the angle α is only defined modulo π. To bypass this difficulty, we introduce the well defined vector field $w = e^{2r} b_1$. This vector field w is unequivocal defined. Its root square is given by v_1. Hence $p \in D$ is a zero of v_1 if and only if it is a zero of w.

The following proposition gives criteria to spot the zeros of w:

Proposition 5.3.1. *Let K be a triangle of the mesh $\mathcal{T}_h$. Let $w \in V_h$ be a vector field, discretized by P_1 finite elements. We assume that w has no zero on the edges of the triangle.*

Let w^1, w^2 and w^3 be the value of w at the three vertices of the triangle K.

If the vector field w features a singularity in the interior of K, then there exists no half plane such that the three vectors w^1, w^2 and w^3 belong simultaneously to it. This is equivalent to the fact that at least two scalar products $w^i \cdot w^j$ are negative.

Proof. Let K be a triangle of $\mathcal{T}_h$, featuring an isolated zero of v in $x_0 \in K$. The linear interpolation of the vector field v can be written:

$$\forall x \in K \quad v(x) = A(x - x_0)\,,$$

where $A \in \mathcal{M}_{2\times 2}$ is a constant square matrix of size two.

If the matrix A is not invertible, v would be equal to zero on a whole segment in K, which necessarily meets edges of the triangle in two distinct points. This is in contradiction with the assumption that there is no zero of the vector fields on the edges of the mesh.

Consequently, the matrix A is invertible. It has two eigenvalues, possibly equal to each other λ_1 and λ_2. There exists a rotation matrix $R \in SO(2)$ such that:

$$A = R \begin{pmatrix} |\lambda_1| & 0 \\ 0 & |\lambda_2| \end{pmatrix} \begin{pmatrix} \pm 1 & 0 \\ 0 & \pm 1 \end{pmatrix},$$

where the ± 1 are in fact defined by the sign of the eigenvalues of A. Since a rotation and an homothetic transformation do not change the zeros of vector field, the study of A can be reduced to the study of the matrices of kind:

$$\begin{pmatrix} \pm 1 & 0 \\ 0 & \pm 1 \end{pmatrix}.$$

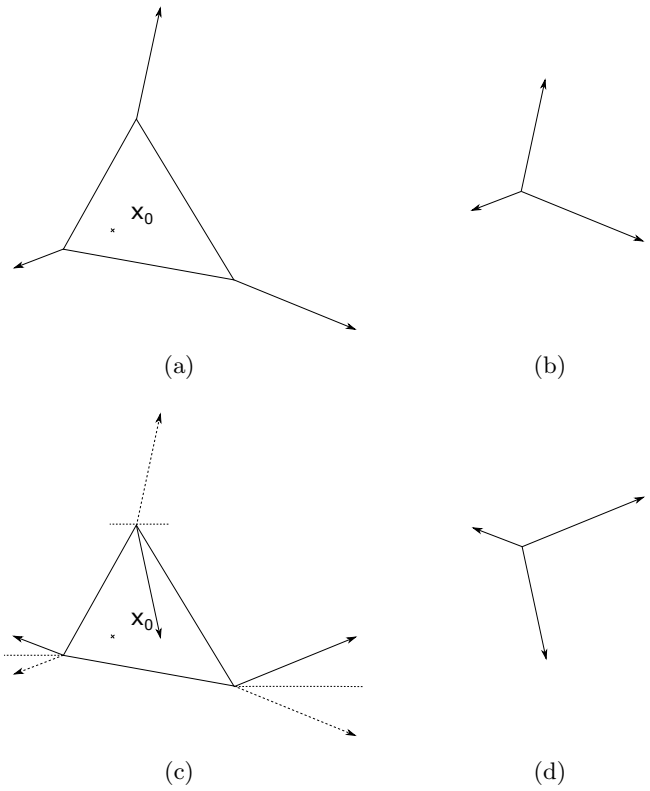

(a) (b)

(c) (d)

Figure 5.17

We develop here only two cases over the four possible. Indeed the sketch of the proofs is exactly the same. When the matrix A is equivalent to the matrix:

$$\begin{pmatrix} 1 & 0 \\ 0 & 1 \end{pmatrix},$$

the interpolation of v over the triangle K can be written: $v(x) = (x - x_0)$. The vectors v at the vertices of the triangle K is represented on Figure 5.17(a). They are displayed all together on Figure 5.17(b). One can see that those three vectors can not be drawn in the same half plane. Indeed, if it was possible, it would imply that x_0 is on an edge of the triangle K or outside K. We will say that the winding number of the vector field w on the triangle K is not equal to zero.

When the matrix A is equivalent to the matrix:

$$\begin{pmatrix} 1 & 0 \\ 0 & -1 \end{pmatrix},$$

the interpolation of v over the triangle K can be written: $v(x) = (x_1 - x_{0,1}, x_2 - x_{0,2})^T$. It is exactly the same case as previously up to an axial symmetry of axis e_2.

□

To conclude, if a triangle K of the mesh contains a singularity of the vector fields v_1 and v_2, necessarily the vectors w on the vertices of the triangle can not be drawn in the same half plane. We recall that the vector field v_1 is a root square of w. Hence if a triangle K contains a zero of v_1, the vectors v_1 on the vertices of K can not be drawn in the same quarter of plane, even after changing their sign. This leads to the following proposition, giving criteria to spot singularities of the vector fields v_1 and v_2:

Proposition 5.3.2. *Let K be a triangle of the mesh $\mathcal{T}_h$. Let $v \in V_h$ be a vector field, discretized by P_1 finite elements, defined up to its sign. We assume that v has no zero on the edges of the triangle.*

Let v^1, v^2 and v^3 be the value of v at the three vertices of the triangle K.

If the vector field v features a singularity in the interior of K, then there exists no quarter of plane such that the three vectors v^1, v^2 and v^3 belong simultaneously to it, possibly even after changing their sign. This is equivalent to:

$$\prod_{1 \leq i < j \leq 3} v^i \cdot v^j < 0 \,.$$

In practice, for each triangle of the mesh, we compute the products of the scalar product between the vectors v_1 at the vertices of the triangle. If the result is strictly negative, the triangle features a zero of v_1, which is treated in the following as a singularity.

The triangles featuring zeros could be removed from the mesh, in order to treat singularities like holes in the domain. Indeed, there is no coherent orientation of the vector field in such triangles. But numerically, there is no limitation to keep them: the computed diffeormorphism is not impacted by the presence of those triangles as we will see in the numerical results.

5.3.4 Correction functions

This section is devoted to the practical computation of the correction functions.

Let K be a triangle featuring a zero x_0 of the vector fields, see Figure 5.18(a). This zero is treated as a singularity of the vector field. Let ψ be the correction function associated to x_0. This function is defined on the manifold $\mathcal{D}$ and discretized using P_1 finite elements on the manifold. Hence, we can use P_1 discontinuous Galerkin elements on D to discretize the correction function ψ. The technical point is that we can not use the interpolation operator to compute straightly the correction functions.

To start, we have to compute a curve Γ joining the point x_0 to the external border of the domain. Numerically, Γ is discretized: it is a set of edges and vertices of the mesh, see Figure 5.18(b). We recall that a correction function is defined by (5.3). In particular, it is equal to zero on the whole domain except on a tube of size η around the curve Γ. We choose a coefficient η smaller than the minimal size of the triangle of the mesh. Hence, the correction function ψ is equal to zero on every vertex that does not belong to Γ.

The triangles which contain a vertex of Γ can be split into two subsets, according to which side of Γ they are. The triangle K which contains x_0 is the frontier between the both subsets.

From the triangle K, we are going step by step through each triangle, which contains a vertex in Γ. We have to determine if two adjacent triangles represent adjacent charts of the manifold $\mathcal{D}$.

Adjacent triangles have one common vertex belonging to Γ. If the retained coherent orientation at this vertex is the same in the both triangles, the both triangles represent in fact adjacent charts of $\mathcal{D}$. This can be easily checked by looking the value of the interpolation operator at this vertex for the both triangles. If it is the same value, we have adjacent charts, else, we have charts belonging to two distinct copies of D. On Figure 5.18(c), the retained coherent orientation of the vector fields is displayed for each triangle. On Figure 5.18(d), the values of the interpolation operator corresponding to this coherent orientation is displayed. On Figure 5.18(e), the discretization of the manifold $\mathcal{D}$ is represented. The triangles of the mesh D are colored respectively in blue and red, according to which charts of $\mathcal{D}$ they represent. We also displayed the sign of the correction function on the manifold according to which side of Γ we are looking at. We recall that the correction function is antisymmetric. To conclude, the values of the correction function on the mesh $\mathcal{T}_h$ are displayed on Figure 5.18(f): $+$ stands for $+0.5$, and $-$ for -0.5.

The correction functions for the holes of the domain D are computed exactly with the same method. The only slight difference is that the curve Γ joins a vertex of the external border of the domain to a vertex of the border of the hole.

5.3.5 Computation of the diffeomorphism

Let n_c be the sum of the number of the holes of the domain and the number of singularities in the vector fields v_1 and v_2 to integrate. Let $(\psi_i)_{1\leq i\leq n_c}$ be the n_c corresponding correction functions.

Thanks to Theorem 5.2.13, there exist n_c real coefficients $c_i \in \mathbb{R}^2$ and an antisymmetric function $\varphi \in \mathcal{C}^1(\mathcal{D}, \mathbb{R}^2)$ such that, for $j \in \{1, 2\}$:

$$e^r\, T = \nabla\varphi + \sum_{i=1}^{n_c} c_i \otimes \nabla\psi_i\,.$$

An other formulation leads to looking for $c_i \in \mathbb{R}^2$ and a map φ from $\mathcal{D}$ into $\mathbb{R}^2$ as the minimizer of:

$$\begin{aligned} G(\varphi, c_i) &= \int_{\mathcal{D}} |\nabla\varphi + \sum_{i=1}^{n_c} c_i \otimes \nabla\psi_i - e^r T|^2 dx \\ &= \int_{\mathcal{D}} |\nabla\varphi - e^r T|^2 dx + \int_{\mathcal{D}} |\sum_{i=1}^{n_c} c_i \otimes \nabla\psi_i|^2 dx + 2\int_{\mathcal{D}} (\nabla\varphi - e^r T)\cdot(\sum_{i=1}^{n_c} c_i \otimes \nabla\psi_i) dx \end{aligned}$$

In order to split the above minimization problem into two independent minimization problems, we introduce the functions $f_i \in \mathcal{C}^1(\mathcal{D}, \mathbb{R})$, solutions of the following variational problem:

$$\forall g \in \mathcal{C}^1(\mathcal{D}, \mathbb{R}),\ g \text{ antisymmetric on } \mathcal{D}, \qquad \int_{\mathcal{D}} \nabla f_i \cdot \nabla g\, dx = \int_{\mathcal{D}} \nabla\psi_i \cdot \nabla g\, dx\,.$$

In the following, we will denote: $\tilde{\psi}_i = \psi_i - f_i$. They would be referred as *orthogonalized correction functions* since the scalar product of their gradient with any conservative vector field w on $\mathcal{D}$ is equal to zero:

$$\int_{\mathcal{D}} \nabla\tilde{\psi}_i \cdot w = 0\,.$$

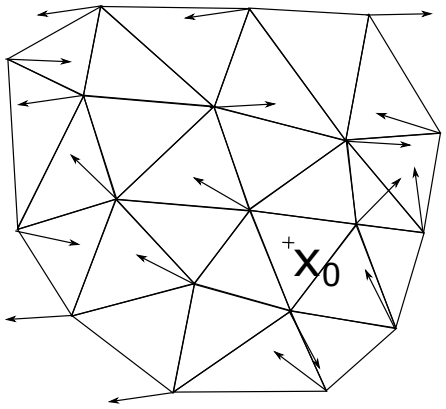

(a) A vector field featuring a singularity in x_0

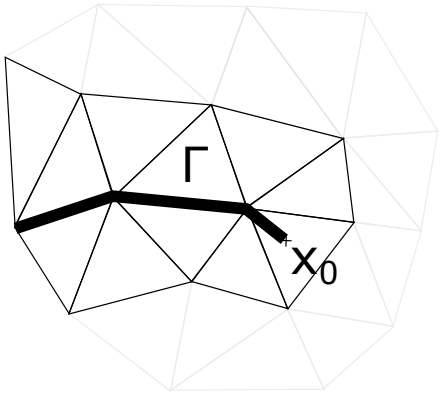

(b) Curve Γ from x_0 to the external border of the mesh and the triangles adjacent of Γ

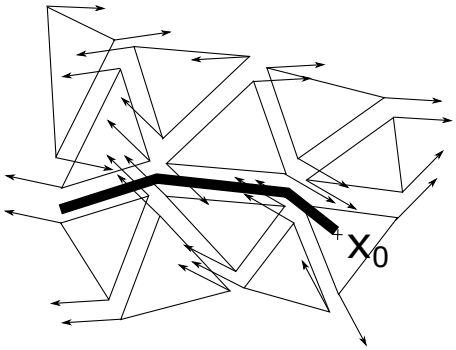

(c) Coherent orientation of the vector field on each triangle: the coherent vector field is discretized by P_1 discontinuous finite elements

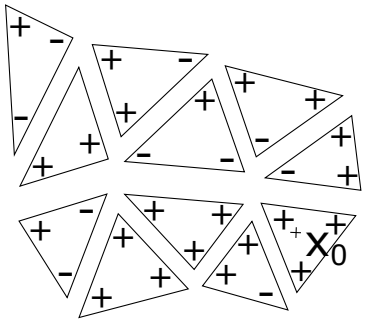

(d) Values of the interpolation operator I_h from $\mathcal{V}_h$ to W_h

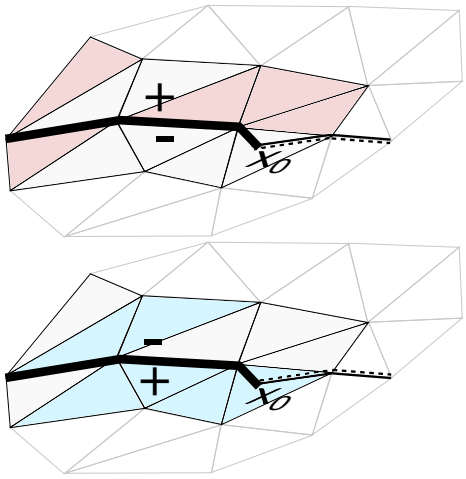

(e) Values of the correction function ψ on the manifold $\mathcal{D}$, in red and blue: the charts used for the discretization of $\mathcal{D}$ in the mesh $\mathcal{T}_h$

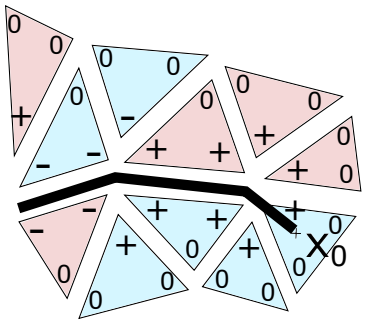

(f) Values of the correction function ψ on the mesh $\mathcal{T}_h$

Figure 5.18: Numerical construction of a correction function

We emphasize that the functions ψ_i are $\mathbb{R}/\mathbb{Z}$ valued. Hence, the product $\int_{\mathcal{D}} \nabla\tilde{\psi}_i \cdot \nabla\psi_j$, where $i, j \in \{1, ..n_H\}$, is not necessarily equal to zero.

We are looking for $c_i \in \mathbb{R}^2$ and a map φ from $\mathcal{D}$ into $\mathbb{R}^2$, minimizer of:

$$\begin{aligned}\tilde{G}(\varphi, c_i) &= \int_{\mathcal{D}} |\nabla\varphi + \sum_{i=1}^{n_c} \nabla\tilde{\psi}_i\, c_i - e^r T|^2 dx \\ &= \int_{\mathcal{D}} |\nabla\varphi - e^r T|^2 dx + \int_{\mathcal{D}} |\sum_{i=1}^{n_c} \nabla\tilde{\psi}_i\, c_i|^2 dx + 2\int_{\mathcal{D}} (-e^r T) : (\sum_{i=1}^{n_c} \nabla\tilde{\psi}_i\, c_i) dx\end{aligned}$$

The first term features only the unknown φ, and the second and the third only the unknowns c_i. Hence the minimization problem leads to two independent minimization problems.

First minimization problem The map φ from $\mathcal{D}$ into $\mathbb{R}^2$ is the minimizer of:

$$G_1(\varphi) = \int_{\mathcal{D}} |\nabla\varphi - e^r T|^2 dx\,.$$

This is the exact same minimization problem than in the case without singularities neither holes in the domain. One could refer to Section 5.5 of Chapter 4 for more details: we give here only essential elements to compute the map φ.

Numerically, φ is a map from $\mathcal{V}_h$ to $\mathbb{R}^2$. The functional G_1 can be rewritten as:

$$G_1(\varphi) = 2\sum_{K\in\mathcal{T}_h} \int_K |\nabla I^h(\varphi) - e^r T(K)|^2 dx\,,$$

where I^h is the interpolation operator from $\mathcal{V}_h$ onto W_h, and $T(K)$ the coherent vector field T on the triangle K. The minimizer of G_1 is the solution of the variational formulation consisting in finding $\varphi \in \mathcal{V}_h$ such that for all $g \in \mathcal{V}_h$:

$$\sum_{K\in\mathcal{T}_h} \int_K \nabla I^h(\varphi) : \nabla I^h(g) dx = \sum_{K\in\mathcal{T}_h} \int_K e^r T(K) : \nabla I^h(g) dx\,.$$

Second minimization problem The family of real coefficients $(c_i)_{1\le i\le n_c}$ in $\mathbb{R}^2$ is the minimizer of:

$$G_2(c_i) = \int_{\mathcal{D}} |\sum_{i=1}^{n_c} \nabla\tilde{\psi}_i\, c_i|^2 dx + 2\int_{\mathcal{D}} (-e^r T) : (\sum_{i=1}^{n_c} \nabla\tilde{\psi}_i\, c_i) dx\,.$$

This minimization problem can also be split into two independent minimization problems, according to respectively the first and the second component of T, namely, v_1 and v_2.

Let $c_{i,j}$ be the j-th component of c_i, and for $j \in \{1, 2\}$, let $G_{2,j}$ be the functional defined by:

$$G_{2,j}(c_{i,j}) = \int_{\mathcal{D}} |\sum_{i=1}^{n_c} c_{i,j}\nabla\tilde{\psi}_i|^2 dx + 2\int_{\mathcal{D}} (-e^r T) : (\sum_{i=1}^{n_c} \nabla\tilde{\psi}_i\, c_i) dx$$

Let $M \in \mathcal{M}(\mathbb{R})$ be the symmetric square matrix defined by:

$$M = (\int_{\mathcal{D}} \nabla\tilde{\psi}_i \cdot \nabla\tilde{\psi}_j dx)_{1\le i,j\le n_c}\,.$$

For $j \in \{1,2\}$, let $N_j \in \mathbb{R}^{n_c}$ be the real vector defined by:

$$N_j = (\int_{\mathcal{D}} \nabla\tilde{\psi}_i \cdot e^r v_j \, dx)_{1\leq i\leq n_c} \,,$$

and let c_j be the real vector defined by:

$$c_j = (c_{i,j})_{1\leq i\leq n_c} \,.$$

The functional $G_{2,j}$ can be rewritten as:

$$G_{2,j}(c_{i,j}) = \frac{1}{2} c_j \, M \, c_j^T - N_j \cdot c_j \,.$$

Its minimizer is classically given by the solution of: $Mc_j^T = N_j$.

Numerically, we compute the matrix M and the vector N_j using the interpolation operator I^h:

$$M_{ij} = \sum_{K\in\mathcal{T}_h} \int_K \nabla I^h(\tilde{\psi}_i) \cdot \nabla I^h(\tilde{\psi}_j) dx \,, \quad N_{j_i} = \sum_{K\in\mathcal{T}_h} \int_K \nabla I^h(\tilde{\psi}_i) \cdot e^r T(K) dx \,.$$

5.3.6 Projection of the microstructure

We have computed a diffeomorphism of D which distorts a regular grid in order to orientate locally the bars according to a given orientation. We explain here how to compute a sequence of genuine shapes from an homogenized structure made of the same periodic microstructures than in Chapter 4. We recall that this microstructure is characterized by geometric parameters $m \in [0;1]$, which are the relative dimensions of the central rectangular hole in the square cell, see Figure 4.2.

Like in Chapter 4, a sequence of genuine shapes, indexed by a small coefficient $\varepsilon > 0$, which is the size of the period of the periodic composite, is computed thanks to the diffeomorphism Φ, defined by:

$$\Phi = \varphi + \sum_{i=1}^{n_c} \tilde{\psi}_i c_i = \varphi + \sum_{i=1}^{n_c} f_i c_i + \sum_{i=1}^{n_c} \psi_i c_i \,.$$

The functions φ and f_i are continuous on $\mathbb{R}$. However the functions ψ_i are $\mathbb{R}/\mathbb{Z}$-valued. The level-set functions defining the final shapes are sine functions of the diffeomorphism. In order to avoid any discontinuity in the level-set functions, we have to ensure that the coefficients for any orthogonal test functions $\tilde{\psi}_i$ are multiples of 2π. Let $\tilde{\Phi}_{\varepsilon,j}$ be two functions defined by:

$$\tilde{\Phi}_{\varepsilon,j} = \varphi_j + \sum_{i=1}^{n_c} \varepsilon d_{i,j} \tilde{\psi}_i \,,$$

where $d_{i,j} = E\left(\dfrac{c_{i,j}}{\varepsilon}\right) \in \mathbb{Z}$, with E the floor function.

Let $f^m_{\varepsilon,i} \in \mathcal{C}(D,\mathbb{R})$ be two level-set functions defined by:

$$\begin{aligned} f^m_{\varepsilon,j}(x) &= -\cos\left(\frac{2\pi\tilde{\Phi}_{\varepsilon,j}(x)}{\varepsilon}\right) + \cos(\pi(1-m_i(x))) \\ &= -\cos\left(\frac{2\pi\varphi_{\varepsilon,j}(x)}{\varepsilon} + 2\pi\sum_{i=1}^{n_c} d_{i,j}\tilde{\psi}_i)\right) + \cos(\pi(1-m_i(x)))\,. \end{aligned}$$

Let the level-set function:

$$F^m_\varepsilon = \min(f^m_{\varepsilon,1}, f^m_{\varepsilon,2})\,.$$

The final structure $\Omega_\varepsilon(m)$ is then defined by:

$$\Omega_\varepsilon(m) = \left\{ x \in D \text{ such that } F^m_\varepsilon(x) \leq 0 \right\}.$$

Integer coefficients By taking the floor of the coefficients in $\tilde{\Phi}_{\varepsilon,j}$, we alter the exact diffeomorphism Φ. In order to prevent this, one could choose only sizes of cell ε, such that every coefficient $c_{i,j}$ is a multiple of ε. Nevertheless, this could be extremely restrictive, especially if there are a lot of singularities and holes.

In practice, we decline this: the diffeomorphism used for the projection is slightly altered, but with no significant consequence on the orientation of the microstructure, see numerical results below.

However, we can minimize the functionals $G_{2,j}$ on $\mathbb{Z}^{n_c}$. First, we compute the coefficients c_j as previously on $\mathbb{R}^{n_c}$. Second, $G_{2,j}$ is computed in $\varepsilon(d_{1,j},...,d_{n_c,j}) + \varepsilon\{0,1\}^{n_c}$. Among those vectors, the one minimizing $G_{2,j}$ is kept. Nevertheless, this method implies to compute 2^{n_c} times the functional $G_{2,j}$: it is quickly prohibitive. Optimization algorithms in integer programming could be efficient here, this approach should be investigated.

5.3.7 Numerical results

5.3.7.a Theoretical test case

In order to generate a direction field featuring singularities, we used the method developed by Sacchelli in [Boscain 2016]. Let V be the vector field defined on $\mathbb{R}^2$ by:

$$V = \left(\cos\left(\pi(x_1 + s_1 x_2)\right), \cos\left(\pi(x_2 + s_2 * x_1)\right)\right),$$

with for example here $s_1 = 0.3$ and $s_2 = -0.8$. Let $\beta \in \mathbb{R}/2\pi\mathbb{Z}$ be the angle between the vectors $(1,0)$ and V, and $\alpha \in \mathbb{R}/\pi\mathbb{Z}$ the angle defined by: $\alpha = 0.5\beta$. The direction field $a = (\cos(\alpha), \sin(\alpha))$ features singularities where $V = (0,0)$.

Let $D = [0.5;2] \times [0.25;1.75]$. The direction field a is displayed on Figure 5.19 on the subset D. Let r be the dilatation factor defined by (4.7). Let $v_1 = e^r a$, and $v_2 = e^r a^\perp$, where $a^\perp$ is a unit vector field orthogonal to a.

The projection algorithm, implemented in FreeFem++, has been tested on the above direction field a. The mesh is a regular triangular one, with 2704 vertices. The algorithm successfully

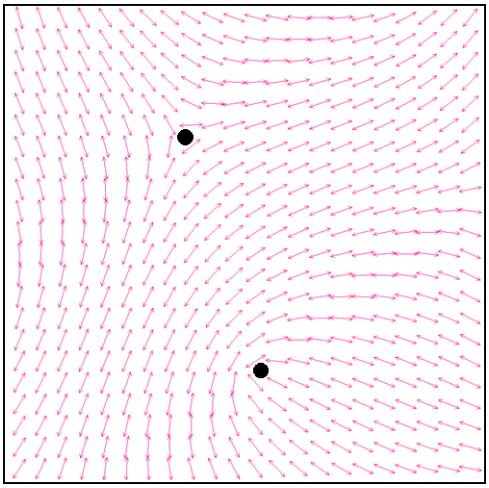

Figure 5.19: Direction field featuring two singularities (black points)

detected the two singularities of the vector field in D. We recall, that we need here only one correction function to proceed to the projection: one less than the number of singularities. The algorithm computed the orthogonalized correction function $\tilde{\psi}_1$, for the lower singularity. This function is displayed on Figure 5.20(a). It features a constant gap along the curve Γ_1, represented in red on Figure 5.20(b). The functions φ_1 and φ_2 are respectively displayed on Figures 5.20(c) and 5.20(d). They are regular and their isolines are not aligned with the vector fields v and $v^{\perp}$, which is a strong difference with the case without singularity, see Section 4.5 of Chapter 4. The projection functions $\Phi_1 = \varphi_1 + c_{11}\tilde{\psi}_1$ and $\Phi_2 = \varphi_2 + c_{12}\tilde{\psi}_1$ are displayed on Figures 5.20(e) and 5.20(f). Their isolines are respectively well aligned with the vector fields a and $a^{\perp}$. Hence the correction function corrects properly the functions φ_1 and φ_2. On Figures 5.20(g) and 5.20(h), one can check that the projection functions are not continuous through Γ_i (in red): the isolines are not well connected on both sides of Γ_i. Nevertheless, the gap is constant along Γ_i, as desired.

The projection of regular square cells, with $m = (0.8, 0.8)$, with the diffeomorphism $\tilde{\Phi}_{\varepsilon}^{-1}$ is displayed on Figure 5.21(c). At this step (and not before) we used a finer mesh, featuring 10^6 vertices, in order to catch the fine details of the structures. The size of the cell is $\varepsilon = 0.01$. The bars of the distorted grid are well aligned with the vector fields a and $a^{\perp}$. One can check that the final grid is not homotopic to a regular grid. Indeed, around the upper singularity for example, one vertex connect six square cells.

We emphasize that during the projection, we took the floor of the coefficients c_{11} and c_{12} as seen in the previous section. This ensures the projected grid to be well connected. Indeed, the result of the projection in the case where we do not take the floor of the coefficients, is displayed on Figure 5.22. Along the curve Γ_i the bars of the structure are not connected to each other. Let e be the mean of the error on the angle between the bars and the vectors a , when we take

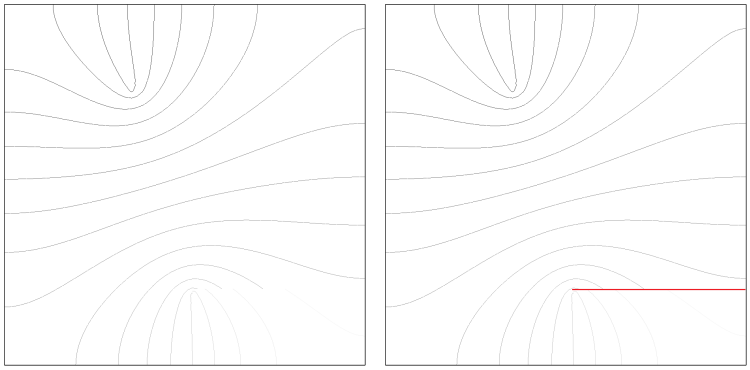

(a) $|\tilde{\psi}_1|$

(b) $|\tilde{\psi}_1|$ features a constant gap along Γ_1(in red)

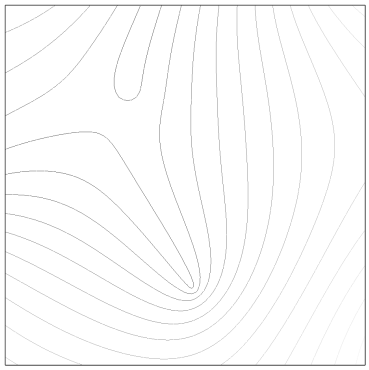

(c) $|\varphi_1|$

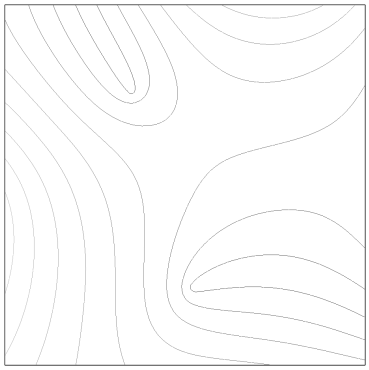

(d) $|\varphi_2|$

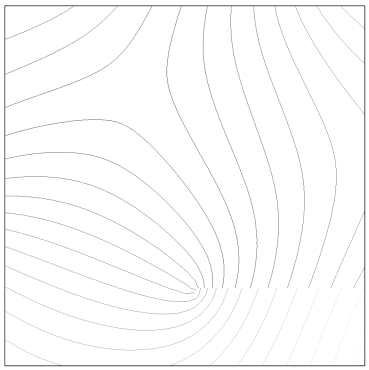

(e) $|\varphi_1 + c_{11}\tilde{\psi}_1|$

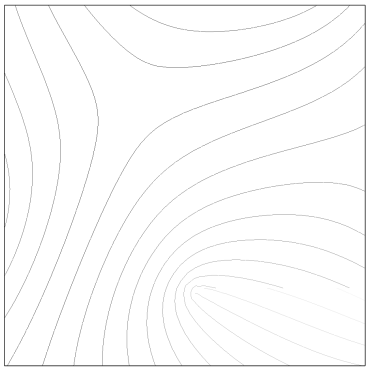

(f) $|\varphi_2 + c_{12}\tilde{\psi}_1|$

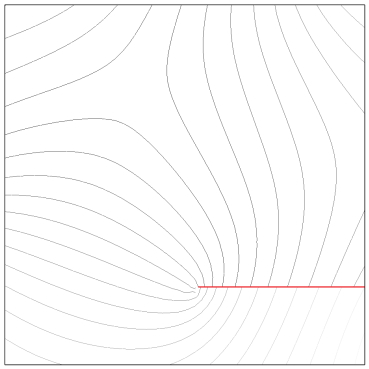

(g) $|\tilde{\Phi}_{\varepsilon,1}|$ features a constant gap along Γ_1(in red)

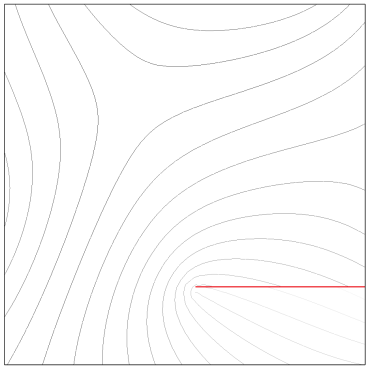

(h) $|\tilde{\Phi}_{\varepsilon,2}|$ features a constant gap along Γ_1(in red)

Figure 5.20: Isolines of the maps involved in the projection algorithm, in red the curve Γ_1 linking the singularity to the border

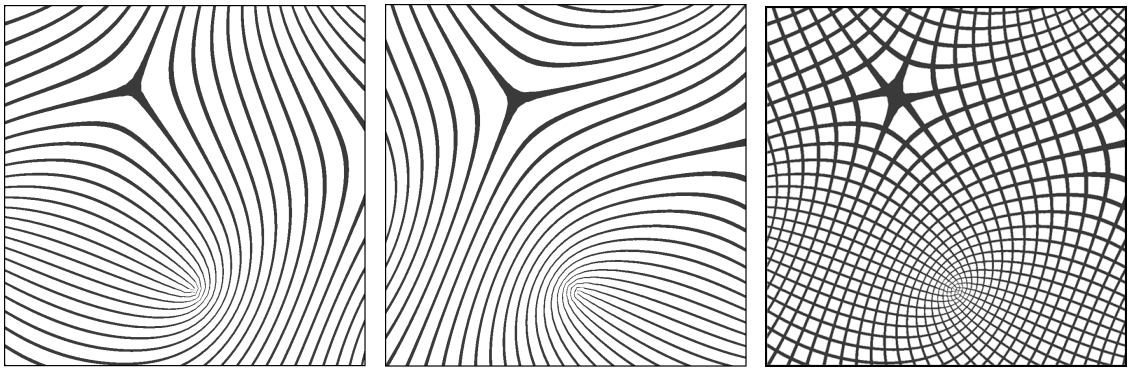

(a) (b) (c)

Figure 5.21: Projection of regular square cells according to the direction field α defined on $D = [0.5; 2] \times [0.25; 1.75]$

the floor of the coefficients. It is defined by:

$$e = \frac{\int_D a^\perp \cdot \frac{\nabla \Phi_1}{||\nabla \Phi_1||} dx}{\int_D dx}.$$

For this test case we get $e = 2.3 \cdot 10^{-3}$. This corresponds to a mean deviation of $0.13°$ of the bars in comparison to the desired orientation, which is very low. In practice, this would be perfectly tolerable.

This method can be applied to vector fields featuring many more singularities. Let the same vector field α be defined on $D = [0.8; 4.8] \times [0.1; 4.1]$ for example. On this subset, there are twenty singularities. The result of the projection of regular cells on this subset is displayed on Figure 5.23.

5.3.7.b Domain featuring a hole

The domain D of the wheel is a circle perforated in its center. Its external radius is equal to 4, its internal radius is equal to 1. The mesh is triangular, it features 2600 vertices. The structure is clamped on its internal radius. A unit load is applied on the external border. In the first case, the load is normal to the border, see Figure 5.24(a). In the second case, the load is tangential to the border, see Figure 5.25(a).

For both cases, optimized homogenized structures are computed with the method presented in Chapter 4. The microstructure is the same square periodic cell, perforated with a central rectangular hole, whose relative dimensions are given by $m \in [0; 1]^2$.

Let $\alpha \in \mathcal{C}(D, \mathbb{R}/\mathbb{Z})$ be the optimized orientation, and a the unit vector field defined by $a(\cos(\alpha], \sin(\alpha))$. Let r be the dilatation factor defined by (4.7). Let $v_1 = e^r a$, and $v_2 = e^r a^\perp$, where $a^\perp$ is a unit vector field orthogonal to a.

Normal loading The optimized density is displayed on Figure 5.24(b), and the optimized orientation on Figure 5.24(c).

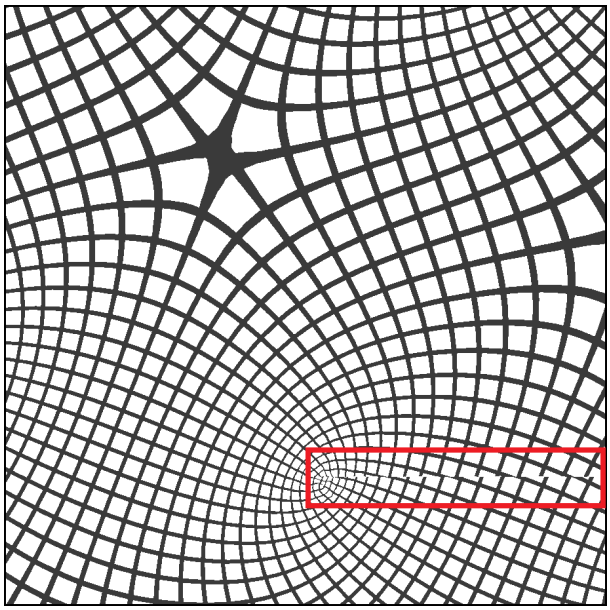

Figure 5.22: Projection of regular square cells according to the direction field α defined on $D = [0.5; 2] \times [0.25; 1.75]$ with non integer coefficients : failures in the connectivity between the bars along Γ_i (in the red rectangle)

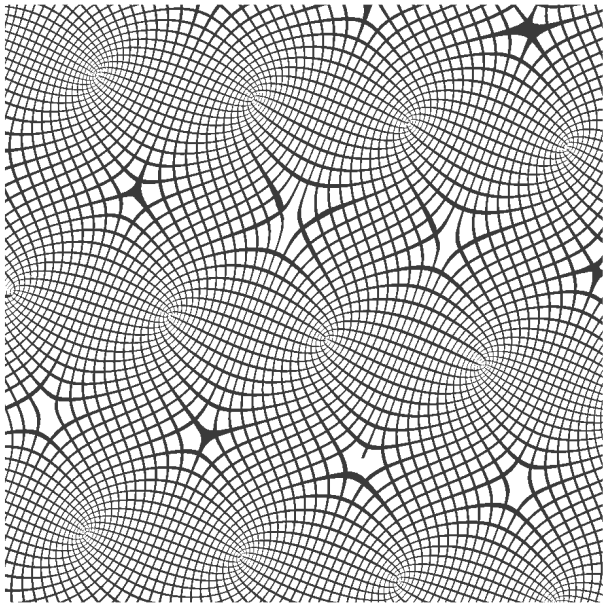

Figure 5.23: Projection of regular square cells according to the direction field α defined on $D = [0.8; 4.8] \times [0.1; 4.1]$

The function φ_1 is displayed on Figure 5.24(d). Its isolines are almost everywhere orthogonal to the vector field a. But in some areas, they are quite messy. The vector field $a^\perp$ is not conservative, a correction function is required to integrate this vector field.

The function φ_2 is displayed on Figure 5.24(e). Its isolines are perfectly aligned with a. The vector field a is indeed conservative.

The distortion of a regular grid with only the diffeormorphism φ, meaning, without any correction function, is displayed on Figure 5.24(f). One can check that the diffeormorphism is not conformal. Indeed, the cells are not dilated of the same ratio in the both direction, in spite of the dilatation factor r. The correction function is required to correct this.

The orthogonalized correction $\tilde{\psi}_1$ function is displayed on Figure 5.24(g). The corresponding curve Γ_1 is the black segment on the left half of the domain. The functions Φ_1 and Φ_2 are displayed respectively on Figures 5.24(h) and 5.24(i). We emphasize that the coefficient $c_{1,2}$ corresponding to contribution of the correction function in the direction a is equal to zero. As seen above, no correction function is required to integrate the vector field a. The isolines of the both functions are well aligned with respectively the vector fields $a^\perp$ and a.

The shape $\Omega_\varepsilon(m)$ is then computed with the diffeomorphism $\tilde{\Phi}$, with integer coefficients for the correction functions. It is displayed on Figure 5.24(l). Let $\Omega_{\varepsilon,j}(m)$ be the shape defined by:

$$\Omega_{\varepsilon,j}(m) = \{x \in D \text{ such that } f^m_{\varepsilon,j}(x) \leq 0\}\,.$$

They are respectively displayed on Figures 5.24(j) and 5.24(k). Those shapes are the distorted set of parallel bars.

Tangent loading The optimized density is displayed on Figure 5.25(b), and the optimized orientation on 5.25(c).

The functions φ_1 and φ_2 are displayed respectively on Figures 5.25(d) and 5.25(e). Their isolines are not aligned with a and $a^\perp$. Those vector fields are not conservative, a correction function is required to integrate them.

The distortion of a regular grid with only the diffeormorphism φ, meaning, without any correction function, is displayed on Figure 5.25(f). The cells are oriented according to α. The correction function is required to correct this.

The orthogonalized correction $\tilde{\psi}_1$ function is displayed on Figure 5.25(g). The corresponding curve Γ_1 is the black segment on the left half of the domain. The functions Φ_1 and Φ_2 are displayed respectively on Figures 5.25(h) and 5.25(i). The isolines of the both functions are well aligned with respectively the vector fields $a^\perp$ and a.

The shape $\Omega_\varepsilon(m)$ is then computed with the diffeomorphism $\tilde{\Phi}$, with integer coefficients for the correction functions. It is displayed on Figure 5.25(l). Let $\Omega_{\varepsilon,j}(m)$ be the shape defined by:

$$\Omega_{\varepsilon,j}(m) = \{x \in D \text{ such that } f^m_{\varepsilon,j}(x) \leq 0\}\,.$$

They are respectively displayed on Figures 5.25(j) and 5.25(k). Those shapes are the distorted set of parallel bars.

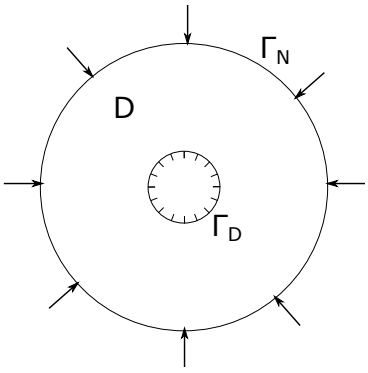

(a) Load case

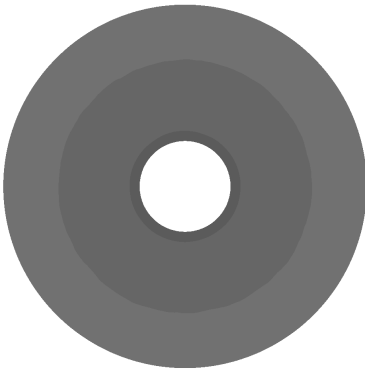

(b) Optimized density

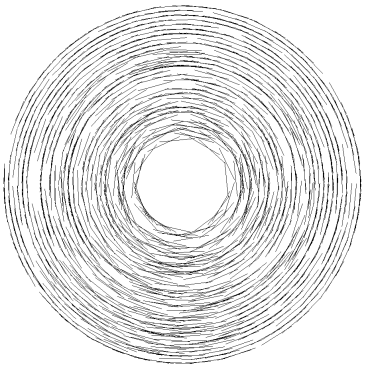

(c) Optimized orientation

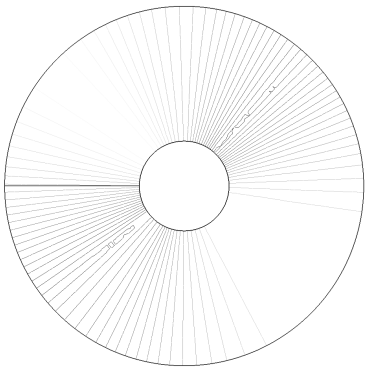

(d) $|\varphi_1|$

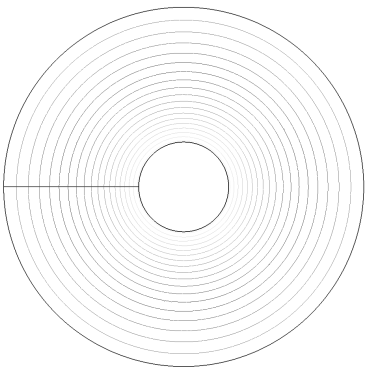

(e) $|\varphi_2|$

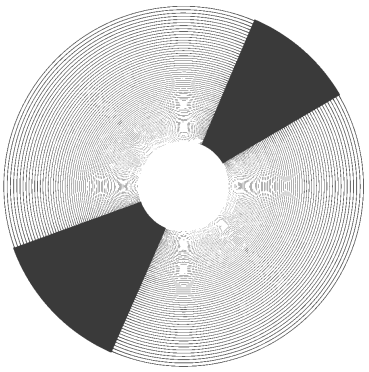

(f) Distortion of a regular grid by φ (meaning without correction function)

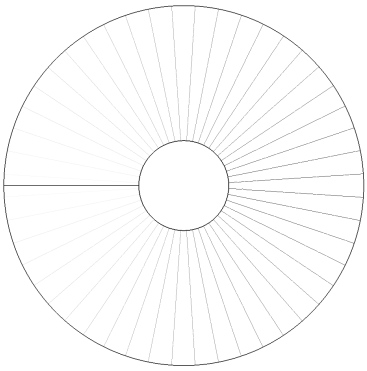

(g) Correction function: $|\tilde{\psi}_1|$

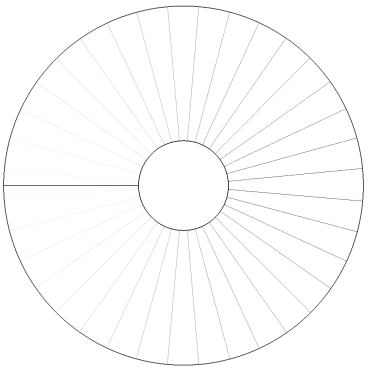

(h) $|\Phi_1| = |\varphi_1 + c_{1,1}\tilde{\psi}_1|$

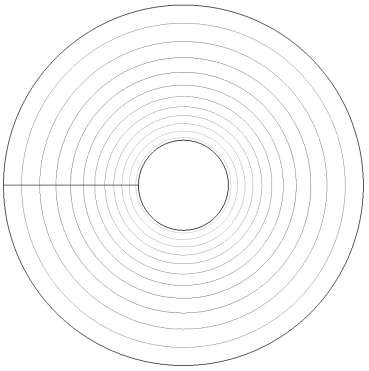

(i) $|\Phi_2| = |\varphi_2 + c_{1,2}\tilde{\psi}_1|$

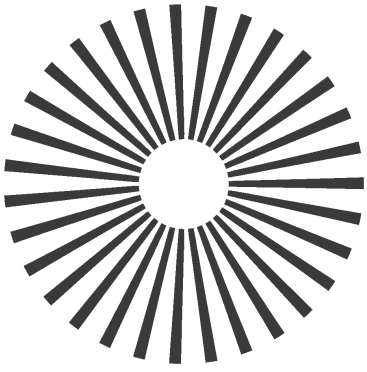

(j) $\Omega_{\varepsilon,1}(m)$

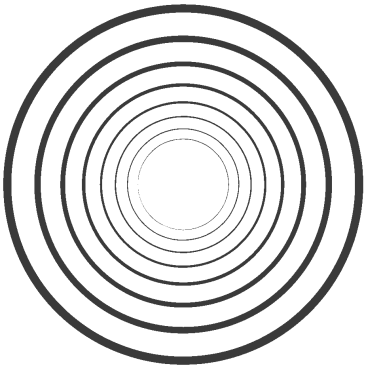

(k) $\Omega_{\varepsilon,2}(m)$

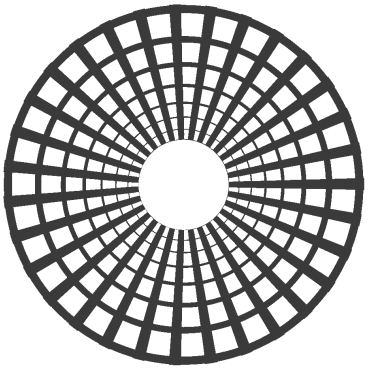

(l) $\Omega_{\varepsilon}(m)$

Figure 5.24: Projection of optimized homogenized wheel

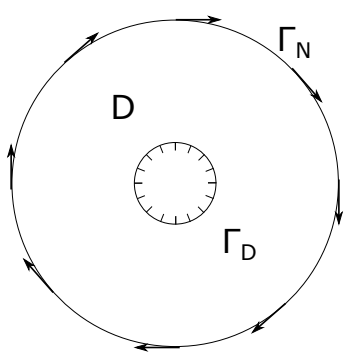

(a) Load case

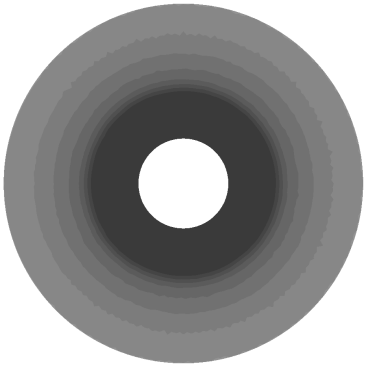

(b) Optimized density

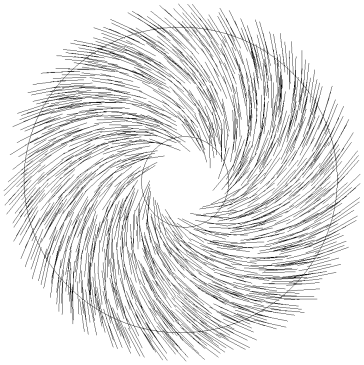

(c) Optimized orientation

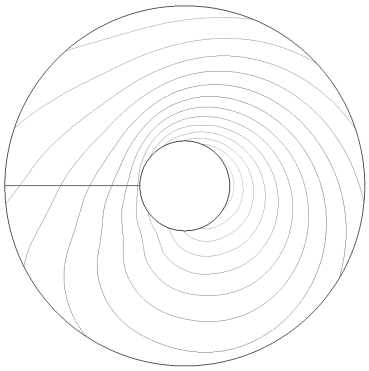

(d) $|\varphi_1|$

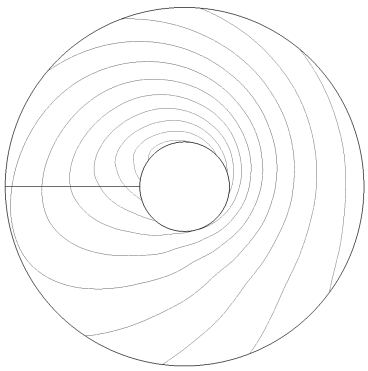

(e) $|\varphi_2|$

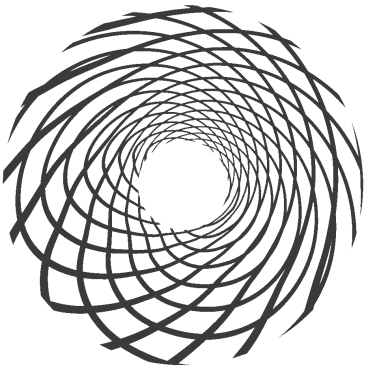

(f) Distortion of a regular grid by φ (meaning without correction function)

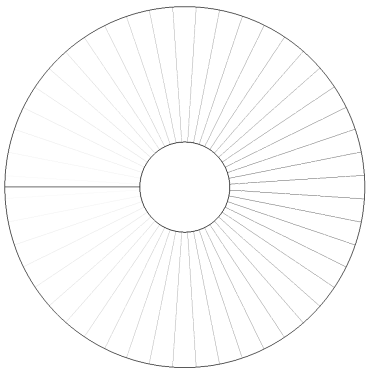

(g) Correction function: $|\tilde{\psi}_1|$

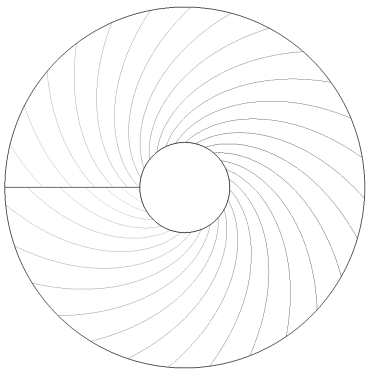

(h) $|\Phi_1| = |\varphi_1 + c_{1,1}\tilde{\psi}_1|$

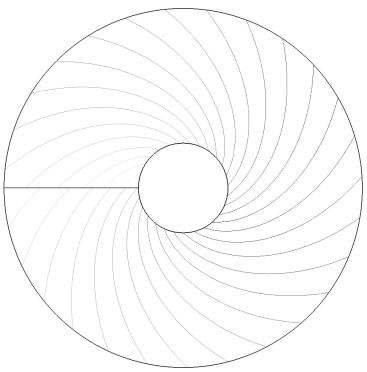

(i) $|\Phi_2| = |\varphi_2 + c_{1,2}\tilde{\psi}_1|$

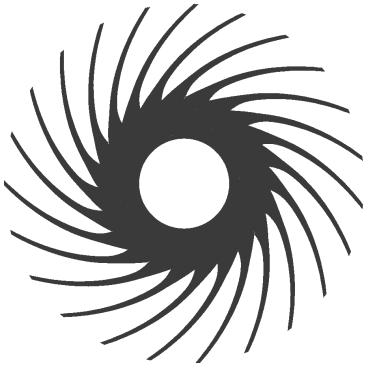

(j) $\Omega_{\varepsilon,1}(m)$

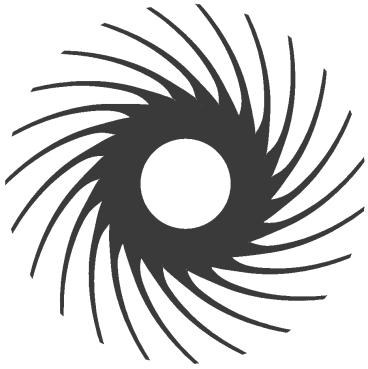

(k) $\Omega_{\varepsilon,2}(m)$

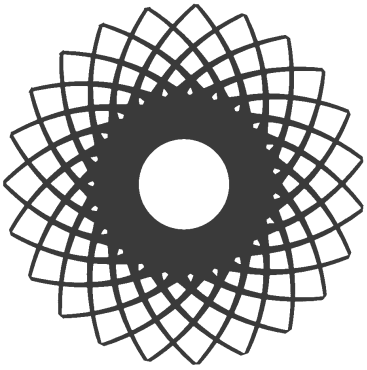

(l) $\Omega_{\varepsilon}(m)$

Figure 5.25: Projection of optimized homogenized wheel

5.4 Regularization of the orientation taking into account the singularities

5.4.1 Settings of the problem

We briefly recall the frame of Chapter 4 Section 5.3.

Let $\alpha \in L^\infty(D, \mathbb{R})$ be an orientation field which is known to minimize an objective function J. The optimal orientation field has now to satisfy the conformality condition: the set of admissible orientation is reduced. The idea is to regularize the optimal orientation field α using an iterative optimization algorithm : α will be the initial orientation.

Moreover, we add a small regularization term on the orientation to the cost function J. Indeed, in areas where the density is equal to zero or to one, the homogenized material is isotropic: any orientation is then admissible there. By adding a small penalization of the L^2-norm of α, the orientation will be regularized in those areas, without significant effect everywhere else.

The new cost function J_{reg} is given by:

$$J_{\text{reg}}(\alpha) = J(\alpha) + \eta^2 \int_D |\nabla \alpha|^2 dx \,.$$

The new minimization problem consists in minimizing J_{reg} under the constraint:

$$\int_D \nabla \alpha \cdot \nabla q \, dx = 0 \quad \text{for all } q \in H_0^1(D) \,.$$

We recall that the orientation α is defined modulo π, and hence it is not convenient to solve a minimization problem over it. We then introduced the vector field $b = (\cos(\beta), \sin(\beta))^T$, where the angle $\beta \in \mathbb{R}/2\pi\mathbb{Z}$ is given by: $\beta = 2\alpha$. The minimization problem over α was then rewritten as a minimization problem over b, see Chapter 4 Section 5.3 for more details. In the following, we will use $J_{\text{reg}}(b)$ to denote the objective function.

We recall that β is not a $\mathbb{R}$-valued function but a $\mathbb{R}/2\pi\mathbb{Z}$-valued function. Hence its classical gradient is not defined. In the following we will use in the whole domain D:

$$\nabla \beta = b \wedge \nabla b \,.$$

This method is efficient provided that the orientation field does not feature singularities. In the case of singularities, this regularization method may be able to remove them, see the L-beam test case in 4.6. But it may also fail to remove them, like in the electrical mast test case, see 4.6.

In order to remove those singularities or just to limit their number, a penalization term of the singularities may be added to the current objective function J_{reg}.

5.4.2 Regularization of the orientation with an energy of Ginzburg-Landau type

5.4.2.a Ginzburg-Landau model in superconductivity

We give here only very general elements about the Ginzburg-Landau model in superconductivity. One could read [Sandier 2008] for more details about the model.

A superconductor is a material where the electrical resistance is equal to zero under particular conditions (like low temperature). The superconductivity is also characterized by the Meissner effect : the expulsion of the magnetic field from the material, when the material is cooled and submitted to a magnetic field. There are two types of superconductor. The ones from Type I have only two states according to the applied magnetic field: normal state or superconducting state. The ones from Type II have three states: the normal and the superconducting ones, but also a mixed state. In this state, some areas of the material are superconductor but other, called vortices, are not conductor. The Ginzburg Landau model with magnetic field describes the behavior of the superconductors of Type II.

The local state of the material is described through a complex-valued function u, the order parameter: $u = 0$ corresponds to the normal state and $|u| = 1$ corresponds to the superconducting state. Hence in the mixed state, a vortex in $x \in D$ is characterized by $u(x) = 0$. The electromagnetic vector potential will be denoted $E : D \to \mathbb{R}^2$. The induced magnetic field is given by: $\nabla \wedge E$.

A parameter ϵ, known as the inverse of the Ginzburg-Landau parameter, depends only of the material. For extreme Type II superconductors, the parameter ϵ is very small. Moreover, this parameter characterizes the size of the vortices. Hence, when ϵ is going to zero, the vortices are reduced to isolated points.

If the material is in a bounded subset $\Omega \in \mathbb{R}^2$, the Ginzburg-Landau energy of (u, E) is given by:

$$\frac{1}{2}\int_\Omega |\nabla_E u|^2 + |\nabla \wedge E|^2 + \frac{1}{2\epsilon^2}(1 - |u|)^2 \, dx \,,$$

where the operator ∇_E is the covariant gradient, defined by: $\nabla_E = \nabla - iE$, see (2.5) in [Sandier 2008].

5.4.2.b Energy of Ginzburg-Landau type

We can make some analogies between the Ginzburg-Landau model and the orientation of the cells in shape optimization. Hence, the orientation, which can be seen as a complex, would correspond to the order parameter u. The singularities in the orientation would correspond to the vortices in superconductivity, if ϵ is small enough. However, there is no parallel for the electromagnetic vector potential: we introduce a new vector, also denoted E.

Other formulations of the Ginzburg-Landau energy have also been used to regularize orientation vector fields for the generation of quadrangular meshes, [Viertel 2017]. The orientation of the boundary elements is given by the normal of the frontier. It is then propagated in the volume, leading to singularities in the orientation field. We emphasize that the method to mesh coherently the domain is different from the one we presented above, but relies on the same main idea. The domain is subdivided into subsets where the orientation vector field does not feature any singularity. Those subsets are then carefully merged together, paying attention to the continuity of the mesh between two adjacent domains. Let us notice that the meshing method relies on a Ginzburg-Landau energy with $E = 0$. We also investigated this approach for regularization, but it was not concluding. Hence we kept the general formulation.

Relaxation of the minimization problem. We emphasize that the norm of the vector field u is not equal to one on the whole domain. Hence, before anything else, the previous

minimization problem, consisting in minimizing J_{reg}, has to be relaxed relaxed. Indeed the norm of the vector field b is no longer restricted to one.

When the norm of b is equal to one, we recall that the compliance is written:

$$\int_D A_0^*(m)^{-1} S(b)\sigma : S(b)\sigma \,,$$

where σ is the stress tensor, A_0^* the homogenized elasticity tensor, depending on the geometric parameters m of the microstructure, and $S(b)$ the rotation operator tensor. Let $S'(\delta b)$ be the directional derivative of $S(b)$ in the direction δb. When the Voigt notations are used, $S(b)$ and $S'(\delta b)$ are represented respectively by the matrices:

$$\{S(b)\} = \begin{pmatrix} \frac{1+b_1}{2} & \frac{1-b_1}{2} & -\frac{b_2}{\sqrt{2}} \\ \frac{1-b_1}{2} & \frac{1+b_1}{2} & \frac{b_2}{\sqrt{2}} \\ \frac{b_2}{\sqrt{2}} & -\frac{b_2}{\sqrt{2}} & b_1 \end{pmatrix} \quad \{S'(\delta b)\} = \begin{pmatrix} \frac{\delta b_1}{2} & \frac{-\delta b_1}{2} & -\frac{\delta b_2}{\sqrt{2}} \\ \frac{-\delta b_1}{2} & \frac{\delta b_1}{2} & \frac{\delta b_2}{\sqrt{2}} \\ \frac{\delta b_2}{\sqrt{2}} & -\frac{\delta b_2}{\sqrt{2}} & \delta b_1 \end{pmatrix} .$$

From now on, the norm of b can vary. Let $S_n(b)$ be the fourth-order tensor defined by: $S_n(b) = S(\frac{b}{|b|})$. Hence the compliance is written as:

$$\int_D A_0^*(m)^{-1} S_n(b)\sigma : S_n(b)\sigma \,.$$

Let $S_n'(\delta b)$ be the directional derivative of $S_n'(b)$ in the direction δb: $S_n'(\delta b) = S'((\frac{\delta b}{|b|} - \frac{b \cdot \delta b}{|b|^2})b)$.

Supplementary term in the cost function. An energy of kind of Ginzburg-Landau is added to the cost function J_{reg}:

$$I_{GL}(b, E) = \int_D (\epsilon_1 |\nabla b - b^\perp \otimes E|^2 + \epsilon_1 |\nabla \wedge E|^2 + \epsilon_1^{-1}(|b|^2 - 1)^2)\, dx \,. \tag{5.6}$$

The first term in this energy is the real correspondence to the covariant gradient in complex.

Proposition 5.4.1. *The minimum of the energy $I_{GL}(b, E)$ defined by (5.6) depends only on the number of singularities, on their type and on ϵ_1 the characteristic size of the vicinity of the singularities.*

In particular, when there is no singularity in the vector field, the minimum of this energy is equal to zero.

Proof. We refer to [Sandier 2008] for the first part of the proposition.

When there is no singularity, the angle α is defined on the whole domain. Hence the minimizer b is defined by $b = (\cos(\beta), \sin(\beta))$. It is a unit vector field: the third term of the energy is equal to zero. Moreover, we have

$$\nabla b = b^\perp \otimes \nabla \beta \,,$$

where $\nabla\beta$ is well defined on the whole domain D. Then the minimizer E is $\nabla\beta$. The first and the second terms are equal to zero. □

5.4.2.c Minimization problem and its approximation

The objective function to minimize is now:

$$J_{\text{reg, GL}}(b, E, m) = \int_D (A_0^*(m)^{-1} S(b)\sigma : S(b)\sigma + \eta^2 |\nabla b|^2) dx + \gamma I_{GL}(b, E)\,,$$

under the conformality constraint:

$$\int_D (b \wedge \nabla b) \cdot \nabla q \, dx = 0 \quad \text{for all } q \in H_0^1(D)\,. \tag{5.7}$$

The coefficient $\gamma > 0$ is the weight of the Ginzburg-Landau energy in the cost function. The corresponding Lagrangian is given by:

$$L_{\text{GL}}(b, E, m, p) = \int_D (A_0^*(m)^{-1} S(b)\sigma : S(b)\sigma + \eta^2 |\nabla b|^2) dx + \gamma I_{GL}(b, E) + \int_D (b \wedge \nabla b) \cdot \nabla p\,,$$

where $p \in H_0^1(D, \mathbb{R})$ is the Lagrange multiplier for the constraint (5.7).

We emphasize that the optimization process with respect to the geometric parameter m is unchanged, see Section 4 of Chapter 4 for more details. Indeed, none of the new terms in the objective function depends on this parameter. For the sake of clearness, the geometric parameter m will be omitted in the following equations.

A SQP (Sequential quadratic programming) type algorithm is used to solve this minimization problem with respect to b, ζ and p. At each iteration n, the Lagrangian L_{GL} is approximated, around the current state, at second order in δb, δE and δp.

The Ginzburg-Landau energy is approximated at second order in δb and δE around the state (b, E) by:

$$\begin{aligned}
I_{GL}(b + \delta b, E + \delta E) \;\simeq\; & \int_D (\epsilon_1 |\nabla b - b^\perp \otimes E|^2 + \epsilon_1 |\nabla \wedge E|^2 + \epsilon_1^{-1} (|b|^2 - 1)^2)\, dx \\
& + \int_D 2\epsilon_1 (\nabla b - b^\perp \otimes E) \cdot (\nabla \delta b - \delta b^\perp \otimes E - b^\perp \otimes \delta E)\, dx \\
& + \int_D \epsilon_1 |\nabla \delta b - \delta b^\perp \otimes E - b^\perp \otimes \delta E|^2\, dx \\
& + \epsilon_1 \int_D (2(\nabla \wedge E) \cdot (\nabla \wedge \delta E) + |\nabla \wedge \delta E|^2)\, dx \\
& + \epsilon_1^{-1} \int_D (4(|b|^2 - 1)(b \cdot \delta b) + 4(b \cdot \delta b)^2 + 2(|b|^2 - 1)|\delta b|^2)\, dx
\end{aligned}$$

The approximation at second order in δb and δp of the constraint term is given by:

$$\begin{aligned}
I_{cst}(b + \delta b, p + \delta p) \;=\; & \int_D (b + \delta b) \wedge (\nabla b + \nabla \delta b) \cdot (\nabla p + \nabla \delta p)\, dx \\
\simeq\; & \int_D (b \wedge \nabla b) \cdot \nabla p \, dx \\
& + \int_D ((b \wedge \nabla b) \cdot \nabla \delta p + (\delta b \wedge \nabla b) \cdot \nabla p + (b \wedge \nabla \delta b) \cdot \nabla p)\, dx \\
& + \int_D ((\delta b \wedge \nabla \delta b) \cdot \nabla p + (\delta b \wedge \nabla b) \cdot \nabla \delta p + (b \wedge \nabla \delta b) \cdot \nabla \delta p)\, dx
\end{aligned}$$

The regularization term over the L^2-norm of b is approximated at second order in δb by:

$$\begin{aligned} I_{reg}(b+\delta b) &= \int_D |\nabla b + \nabla \delta b|^2 \, dx \\ &\simeq \int_D |\nabla b|^2 \, dx + 2\int_D \nabla b : \nabla \delta b \, dx + \int_D |\nabla \delta b|^2 \, dx \end{aligned}$$

Finally, at iteration n, at state (β^n, E^n, p^n), we write the necessary and sufficient optimality condition of the minimization problem as the variational problem consisting in finding $(\delta b^n, \delta E^n, \delta p^n) \in ()$ such that for all test functions $(c, F, q) \in ()$:

$$\left.\begin{aligned} & \int_D A_0^{*-1}(m^n) S(b^n) S'(\delta b^n)^T A_0^*(m^n) S(b^n) e(u) : S(b^n) S'(c)^T A_0^*(m^n) S(b^n) e(u) \, dx \\ + & \int_D 2\gamma\epsilon_1 (\nabla \delta b - \delta b^\perp \otimes E - b^\perp \otimes \delta E) : (\nabla c - c^\perp \otimes E - b^\perp \otimes F) \, dx \\ + & \int_D 2\gamma\epsilon_1 (\nabla \wedge \delta E) \cdot (\nabla \wedge F) \, dx \\ + & \int_D 4\gamma\epsilon_1^{-1} (2(b \cdot \delta b)(b \cdot c) \, dx \\ + & \int_D ((\delta b^n \wedge \nabla c + c \wedge \nabla \delta b^n) \cdot \nabla p^n \, dx \\ + & \int_D (\delta b^n \wedge \nabla b^n) \cdot \nabla q + (c \wedge \nabla b^n) \cdot \nabla \delta p^n) \, dx \\ + & \int_D ((b^n \wedge \nabla \delta b^n) \cdot \nabla q + (b^n \wedge \nabla c) \cdot \nabla \delta p^n) \, dx \\ + & \int_D 2\eta^2 \nabla \delta b^n : \nabla c \, dx \end{aligned}\right\} \text{bilinear form}$$

$$\left.\begin{aligned} + & \int_D (A_0^*(m^n) S(b^n) e(u)) : S'(c) e(u) \, dx \\ + & \int_D 2\gamma\epsilon_1 (\nabla b - b^\perp \otimes E) : (\nabla c - c^\perp \otimes E - b^\perp \otimes \delta F) \, dx \\ + & \int_D 2\gamma\epsilon_1 (\nabla \wedge E) \cdot (\nabla \wedge F) \, dx \\ + & \int_D 4\gamma\epsilon_1^{-1} (|b|^2 - 1)(\delta b \cdot c) \, dx \\ + & \int_D ((b^n \wedge \nabla b^n) \cdot \nabla q + (c \wedge \nabla b^n) \cdot \nabla p^n + (b^n \wedge \nabla c) \cdot \nabla p^n) \, dx \\ + & \int_D 2\eta^2 \nabla b^n : \nabla c \, dx \end{aligned}\right\} \text{linear form}$$

$$= 0 \tag{5.8}$$

5.4.2.d Initialization of E

There is no good obvious initialization of the vector field E. Hence, to start, we take $E = (0, 0)$. Then the cost function $J_{\text{reg, GL}}$ is minimized only according to the variable E. Here again, a SQP type algorithm is used: the same approximation of the cost function, at second order

in δE is computed. It leads to solve at each iteration the variational formulation consisting in finding $\delta E \in H^1(D, \mathbb{R}^2)$ such that for all test functions $F \in H^1(D, \mathbb{R}^2)$:

$$\begin{array}{rl} & \left.\begin{array}{l} \displaystyle\int_D 2\gamma\epsilon_1 (b^\perp \otimes \delta E) : (b^\perp \otimes F)\, dx \\ \displaystyle\int_D 2\gamma\epsilon_1 (\nabla \wedge \delta E) \cdot (\nabla \wedge F)\, dx \end{array}\right\} \text{ bilinear form} \\ + & \left.\begin{array}{l} \displaystyle\int_D 2\gamma\epsilon_1 (b^\perp \otimes E) : \cdot (b^\perp \otimes \delta F)\, dx \\ \displaystyle\int_D 2\gamma\epsilon_1 (\nabla \wedge E) \cdot (\nabla \wedge F)\, dx \end{array}\right\} \text{ linear form} \\ = & \ 0 \end{array} \tag{5.9}$$

After a few iterations, (typically between ten and twelve iterations), the vector field E is initialized. Hence the minimization of the cost function over the three variables is computed. At each iteration, the variational formulation (5.8) is solved. The variables are then updated: $b^{n+1} = b^n + \delta b^n$, $E^{n+1} = E^n + \delta E^n$ and $p^{n+1} = p^n + \delta p^n$.

5.4.2.e Stabilization terms

Numerically, we add some stabilization terms to the cost function:
- $r_1 ||\delta p||^2_{L^2}$, with $r_1 = 1.e^{-2}$
- $r_2 ||\delta E||^2_{L^2}$, with $r_2 = 1.e^{-1}$.

5.4.2.f Numerical results

The above regularization method has been implemented in Freefem++.

We tested it for the electric mast test case. Indeed, the optimized orientation for this case features singularities, as seen in Section 4.6 of Chapter 4. The optimized orientation is displayed on Figure 5.26.

The orientation is regularized with the above regularization algorithm. The numerical values of the coefficients are:
- $\gamma = 1.$ for the weight of the Ginzburg Landau energy,
- $\epsilon_1 = 0.05$ for the characteristic size of the vicinity of the singularities,
- $\eta = 0.001$ for the regularization of the gradient of the angle.

The initialization of the vector field E is made in 15 iterations. The regularization of the orientation is done in 70 iterations. The convergence history of the compliance, the conformality constraint and the Ginzburg Landau energy is displayed on Figure 5.27. The conformality constraint is respected, since it goes to zero. The Ginzburg Landau energy decreases quickly. We emphasize that the energy does not go to zero, but to a constant around 9.7. Indeed, the orientation field still features singularities. Hence the minimum of the Ginzburg Landau energy is not zero, but a coefficient which depends on the number of singularities. Finally, the compliance increases slightly during the regularization process. Indeed, the cells are no longer

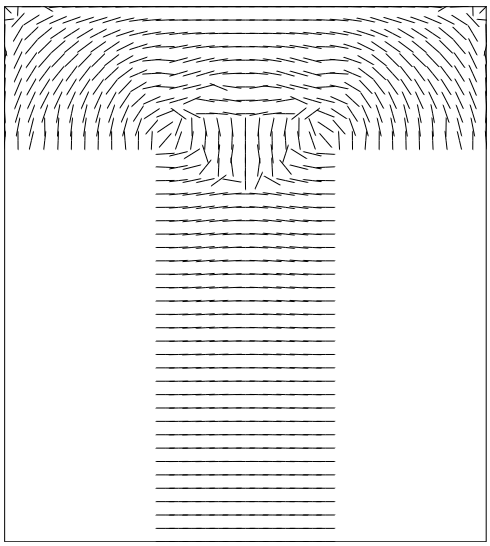

Figure 5.26: Optimal orientation for the electric mast test case

exactly aligned with the principal directions of the stress. This is an inevitable cost to pay to regularize the orientation field.

The regularized orientation is displayed on Figure 5.28(a). The regularized vector field is cleaned. It features always four singularities. But the orientation is smoother in their vicinity than previously in the optimal orientation.

The regularized vector field can be integrated with the method developed in Section 5.3. A diffeomorphism $\tilde{\Phi}$ is computed for this vector field. The projection of a regular grid through the diffeomorphism $\tilde{\Phi}$ is displayed on Figure 5.28(b). The singularities in the vector field are not a limitation to align the cells with the regularized orientation. A genuine shape $\Omega_\varepsilon(m)$ is also computed, with $\varepsilon = 0.1$. It is displayed on Figure 5.28(c).

We run again the regularization algorithm but with a higher value of ϵ_1, the characteristic size of the vicinity of the singularities. We took $\epsilon_1 = 0.25$.

The convergence history is displayed on Figure 5.29. The regularized orientation is displayed on Figure 5.30(a). Two singularities have been removed, and only two are kept. By adjusting the characteristic size of the vicinity of the singularities, it is possible to make disappear some of them. In fact, the vicinity of the lateral singularities in the electric mast case is large enough to reach the external border of the domain and consequently to put those singularities outside of the domain.

5.4.3 Regularization of the orientation using a Modica-Mortola energy

5.4.3.a Modica-Mortola energy

In order to eliminate singularities quickly, we introduce an energy of kind of Modica-Mortola:

$$I_{MM}(b,\zeta) = \int_D (\epsilon_2 |\nabla b - b^\perp \otimes \nabla\zeta|^2 + \epsilon_2^{-1} |b - (\cos(\zeta), \sin(\zeta))|^2) dx \,,$$

where $\zeta \in L^\infty(D, \mathbb{R})$.

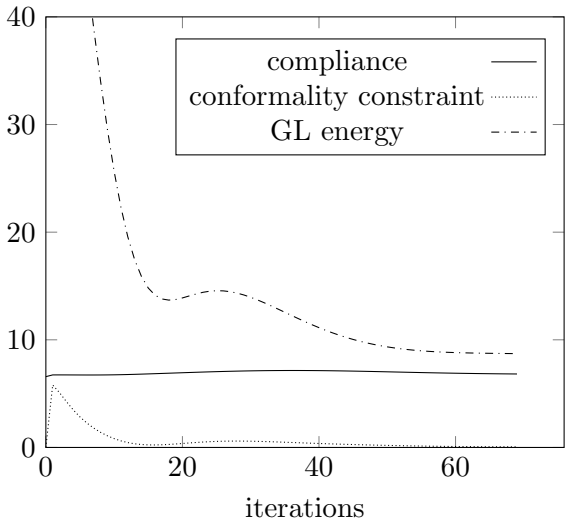

Figure 5.27: Convergence history during the regularization process, in the case where the four singularities are kept

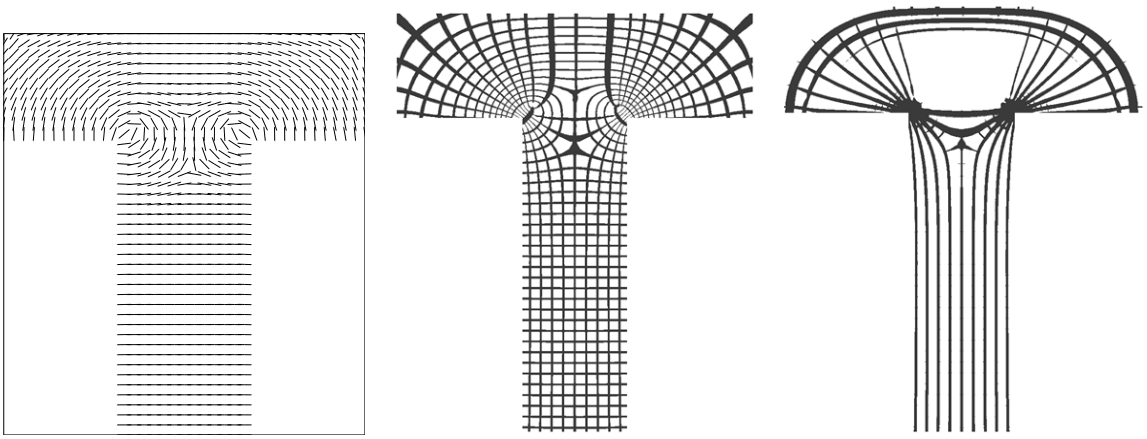

(a) Regularized orientation with Ginzburg-Landau energy

(b) Distorted grid

(c) $\Omega_\varepsilon(m)$

Figure 5.28: Electric mast test case: the four singularities are kept during the regularization process

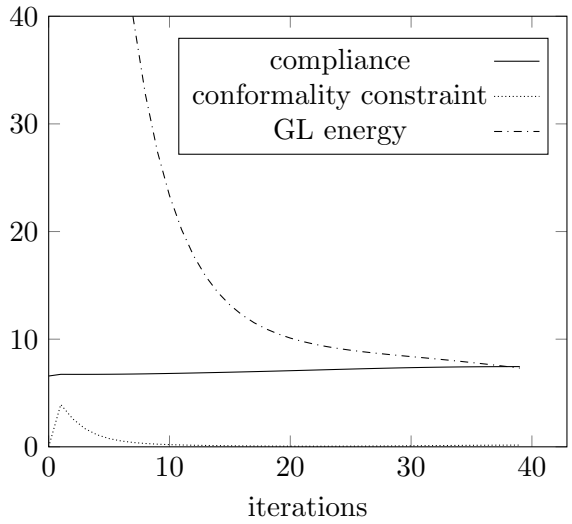

Figure 5.29: Convergence history during the regularization process, in the case where only two singularities are kept

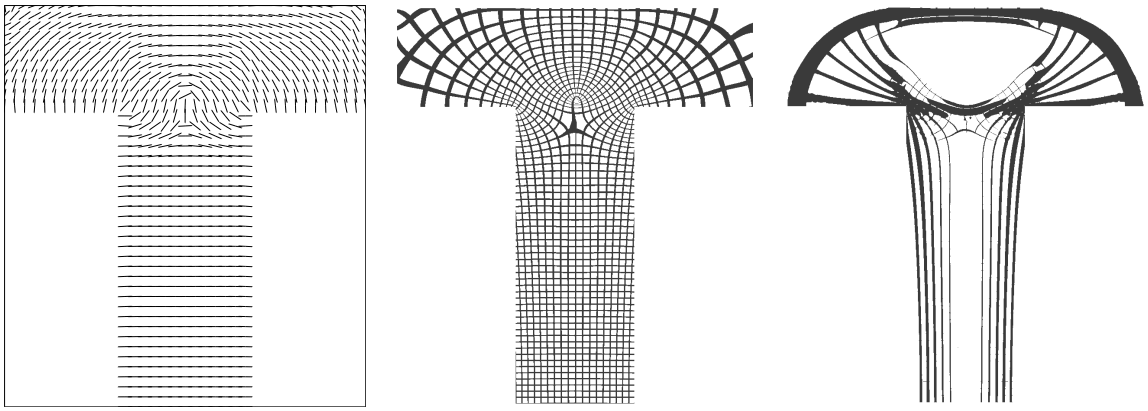

(a) Regularized orientation of the electric mast test case, with an energy of kind of Ginzburg-Landau

(b) Distorted grid

(c) $\Omega_\varepsilon(m)$

Figure 5.30: Electric mast test case: only two singularities are kept during the regularization process

If there is no singularity, the minimum of this energy is zero and it is reached when ζ is such that $(\cos(\zeta), \sin(\zeta)) = (\cos(\beta), \sin(\beta))$. The function ζ is a $\mathbb{R}$-valued "relevement" of β.

If the initial orientation features singularities, there is no $\mathbb{R}$-valued "relevement" of β. We emphasize that this energy is differentiable, thanks to the fact that the norm of b is not equal to one everywhere. Indeed, the vector b vanishes around the singularities.

5.4.3.b Minimization problem and its approximation

The objective function to minimize is now:

$$J_{\text{reg, GL-MM}}(b, E, \zeta) = J_{\text{reg, GL}}(b, E) + \gamma_2 I_{MM}(b, \zeta)\,,$$

under the constraint:

$$\int_D (b \wedge \nabla b) \cdot \nabla q \, dx = 0 \quad \text{for all } q \in H^1_0(D)\,. \tag{5.10}$$

The corresponding Lagrangian is given by:

$$L_{\text{GL,MM}}(b, E, \zeta, p) = L_{\text{GL}}(b, E, p) + \gamma I_{MM}(b, \zeta)\,,$$

where $p \in H^1_0(D, \mathbb{R})$ is the Lagrange multiplier for the constraint (5.10).

A SQP type algorithm is used to solve this minimization problem with respect to b, E, ζ and p. At each iteration n, the Lagrangian $L_{\text{GL,MM}}$ is approximated, around the current state, at second order in δb, δE, $\delta\zeta$ and δp.

5.4.3.c Approximation at second order of the Modica-Mortola energy

Both terms of the Modica-Mortola energy are respectively approximated at second order in δb and $\delta\zeta$ (denoted with $\simeq$) by:

$$\begin{aligned}
I_1(b+\delta b, \zeta+\delta\zeta) &= \int_D |\nabla(b+\delta b) - (b+\delta b)^\perp \otimes \nabla(\zeta+\delta\zeta)|^2 \, dx \\
&\simeq \int_D |\nabla b - b^\perp \otimes \nabla\zeta|^2 \, dx \\
&\quad + \int_D 2(\nabla b - b^\perp \otimes \nabla\zeta) : (\nabla\delta b - b^\perp \otimes \nabla\delta\zeta - \delta b^\perp \otimes \nabla\zeta) \, dx \\
&\quad + \int_D (|\nabla\delta b - b^\perp \otimes \nabla\delta\zeta - \delta b^\perp \otimes \nabla\zeta|^2 - 2(\nabla b - b^\perp \otimes \nabla\zeta) : (\delta b^\perp \otimes \nabla\delta\zeta)) \, dx\,,
\end{aligned}$$

and

$$
\begin{aligned}
I_2(b+\delta b,\zeta+\delta\zeta) &= \int_D |b+\delta b-(\cos(\zeta+\delta\zeta),\sin(\zeta+\delta\zeta))|^2\,dx \\
&\simeq \int_D |b-(\cos(\zeta),\sin(\zeta))|^2\,dx \\
&\quad + \int_D 2(b-(\cos(\zeta),\sin(\zeta)))\cdot(\delta b-\delta\zeta(-\sin(\zeta),\cos(\zeta)))\,dx \\
&\quad + \int_D (|\delta b-(-\sin(\zeta),\cos(\zeta))\delta\zeta|^2-(|b-(\cos(\zeta),\sin(\zeta))|^2) \\
&\qquad\qquad \cdot(\delta\zeta^2(\cos(\zeta),\sin(\zeta)))\,dx\,.
\end{aligned}
$$

The quadratic terms of both approximations are not necessarily positive. In order to avoid numerical instabilities, those terms have been neglected in the implementation, and the method is efficient in practice.

At iteration n, at state $(\beta^n, E^n, \zeta, p^n)$, we write the necessary and sufficient optimality condition of the minimization problem as a variational problem, namely the variational problem (5.8) with some supplementary terms (corresponding to the Modica-Mortola energy):
- to the linear form:

$$
\begin{aligned}
\mathfrak{A}(c,F) &= \int_D 2\gamma_2\epsilon_2(\nabla b^n - b^{n,\perp}\otimes\nabla\zeta^n):(\nabla c - b^{n,\perp}\otimes\nabla\xi - c^{\perp}\otimes\nabla\zeta^n)\,dx \\
&\quad + \int_D 2\gamma_2\epsilon_2^{-1}(b^n-(\cos(\zeta^n),\sin(\zeta^n)))\cdot(c-\xi(-\sin(\zeta^n),\cos(\zeta^n)))\,dx\,.
\end{aligned}
$$

- to the bilinear form:

$$
\begin{aligned}
\mathfrak{B}((\delta b,\delta E),(c,F)) &= \int_D 2\gamma_2\epsilon_2(\nabla\delta b^n - b^{n,\perp}\otimes\nabla\delta\zeta^n - \delta b^{n,\perp}\otimes\nabla\zeta^n):(\nabla c - b^{n,\perp}\otimes\nabla\xi - c^{\perp}\otimes\nabla\zeta^n)\,dx \\
&\quad + \int_D 2\gamma_2\epsilon_2^{-1}(\delta b^n - \delta\zeta^n(-\sin(\zeta^n),\cos(\zeta^n)))\cdot(c-\xi(-\sin(\zeta^n),\cos(\zeta^n)))\,dx
\end{aligned}
$$

5.4.3.d Stabilization terms

Numerically, a stabilization term to the cost function for the new unknown is used:
- $r_3||\delta\zeta||^2_{L^2}$, with $r_1 = 1.e^{-5}$.

5.4.3.e Numerical results

The regularization method based on the energies of Ginzburg-Landau et Modica-Mortolas, has also been implemented in Freefem++. We tested it also for the electric mast test case.

The orientation is regularized with the regularization algorithm using the both energies. The numerical values of the coefficients are:
- $\gamma = 10.$ for the weight of the Ginzburg-Landau energy,
- $\epsilon_1 = 0.2$ for the characteristic size of the vicinity of the singularities,

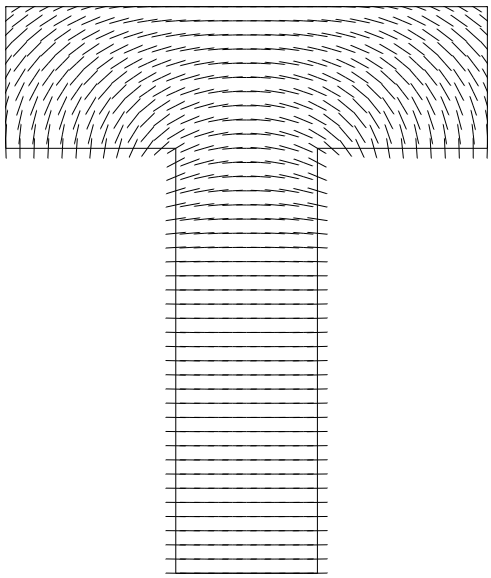

Figure 5.31: Regularized orientation with Modica-Mortola and Ginzburg-Landau energies in the electric mast test case

- $\eta = 0.001$ for the regularization of the gradient of the angle,
- $\gamma_2 = 10.$ for the weight of the Modica-Mortola energy,
- $\epsilon_2 = 0.2$.

The initialization of the vector field E is made in 70 iterations. The regularization of the orientation is done in 80 iterations. The regularized orientation is displayed on Figure 5.31. It features no longer any singularity.

Chapter 6

Topology optimization of parametrized stochastic microstructures

Contents

This chapter is a submitted article:
Topology optimization of parametrized stochastic microstructures, by P. Geoffroy-Donders and J. Martinez.

6.1 Introduction

The field of topology optimization is dedicated to the optimization of material properties within a domain [Eschenauer 2001, Rozvany 2001]. For instance, a classical scenario seeks to obtain the structure with minimal compliance under a prescribed budget of material. One of the main approaches to make topology optimization tractable is to rely on periodic microstructures [Sigmund 1994b, Sigmund 1995, Sigmund 1999]. This offers two significant advantages.

First, the periodicity allows for a compact representation, that is implicitly repeated in a regular grid covering the object. Second, the theory of periodic homogenization affords for the computation of the parameters of an equivalent homogeneous material [Allaire 2002a]. Given these, the macroscopic physical behavior of an object can be simulated while abstracting away fine scale heterogeneities.

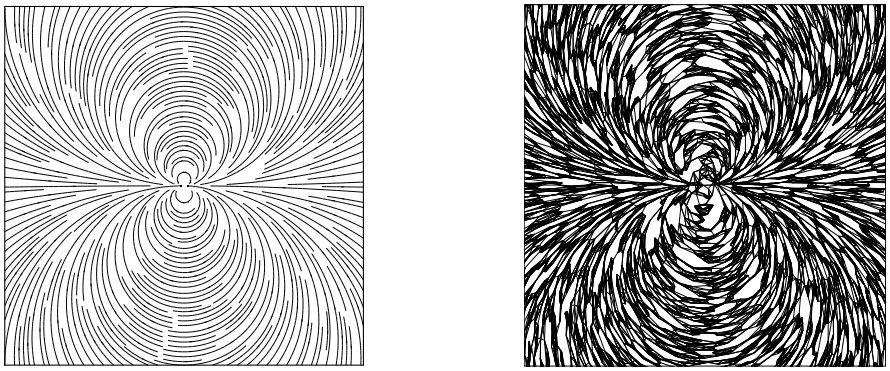

Figure 6.1: 6.1(a): A two dimensional vector field of orthotropy with a singularity in the center, which is challenging to deal with periodic microstructures. 6.1(b): Our parametric stochastic microstructures follows the orientation of orthotropy, without any particular regard about field singularities. Moreover, their geometry can be computed very efficiently, making them amenable to fill large optimization domains.

Different works have explored the topology optimization of parametrized periodic microstructures by the homogenization method [Zhang 2015, Cramer 2016a, Cramer 2016b, Wang 2017, Wang 2018b, Wang 2018a]. A promising venue of work lies in within Additive Manufacturing technologies, that allow us to physically realize the intricate designs obtained with topology optimization. In order to fabricate the results, the parametrized microstructures must be projected at some finite scale taking into account the minimum printable size. However, for periodic microstructures it remains difficult to project and continuously grade the material properties since the boundary and transition between tiles has to be carefully handled [Schumacher 2015, Cramer 2016a]. Recent efforts [Wang 2017, Du 2018] attempt to deal with this issue. The problem becomes even more acute when dealing with orthotropic microstructures, as tackled by recent works [Groen 2017, Allaire 2018]. The vector field of orthotropy orientation may exhibit singularities which are challenging to deal with (see Figure 6.1). In general, the problem of mapping a periodic domain following an arbitrary vector field is known to be hard and computationally expensive [Staten 2007], and is still an open problem in the three dimensional case.

In this work we consider two different stochastic microstructures (isotropic and orthotropic) solely parametrized by an anisotropic metric and a Poisson point process. We perform topology optimization with such microstructures by an homogenization method based akin to [Allaire 2018]. Both stochastic microstructures are amenable to efficient and scalable computation of their geometry. Unlike previous methods dealing with the projection of orthotropic microstructures [Groen 2017, Allaire 2018] the presented microstructures are able to easily follow a field of

orthotropy orientation (possibly with singularities as illustrated in Figure 6.1), without requiring any additional treatment.

The article is structured as follows. In Section 6.2 we review prior work regarding topology optimization with periodic microstructures, and the computational challenges that arise. In Section 6.3 we provide some previous definitions. In Section 6.4 we describe the two parametrized stochastic microstructures and their macroscopic linear elastic behavior. In Section 6.5 we detail the topology optimization procedure. In Section 6.6 we present some optimized results with both isotropic and orthotropic microstructures.

6.2 Related work

Optimizing for material properties. The methods optimizing for continuously spatially varying material properties (e.g. density) are of direct interest to us [Bendsøe 1988, Allaire 2002a]. Microstructures are one possible approach to map the homogenized properties to an actual material [Bendsøe 1988, Suzuki 1991, Rodrigues 2002] . It is worth noting that topology optimization via homogenization optimizes for a full elasticity tensor at every point (e.g. *free material optimization* [Bendsøe 1994, Kočvara 2007], laminate optimization [Allaire 1993]), and thus anisotropy information is available. In practice, it is difficult to physically produce materials with this type of control, and this information is often unexploited. In this work, we pursue a tighter integration between stochastic microstructures and topology optimization.

Microstructures for material design. The base tile of a periodic microstructure can be optimized through an inverse homogenization problem to target a specific material [Sigmund 1994b, Zhou 2008, Radman 2013, Andreassen 2014, Xia 2015]. Recent works [Schumacher 2015, Cramer 2016a, Wang 2017] extended this methodology to optimize families of periodic tiles with varying properties. Panetta et al. [Panetta 2015] proposed a family of isotropic tiles based on periodic truss structures. In these works, tiles with different properties can be spatially arranged to grade properties, such as obtaining varying degrees of elasticity. This requires a special treatment of the boundaries, either ensuring the tile borders are compatible across the entire tile set [Panetta 2015], or performing a global optimization step to choose tiles with best matching borders [Schumacher 2015]. Whenever using a periodic grid care must be taken where the grid intersects the object surface, as tiles are cut by the surface [Robbins 2016]. Our stochastic formulation allows us to deviate from periodic methods in order to attain better gradation properties (see Section 6.4).

Scalable computation of microstructures. Given a specific microstructure geometry the question of how to fill a target shape with this detailed geometry arises. Wang et al. [Wang 2005] conform truss lattices in a thick shell below an object's surface through an efficient procedure that directly outputs an STL model. Rosen [Rosen 2007] considers the challenges of designing parts with internal lattices and proposes a slicing algorithm which works directly from the truss skeleton. Chen [Chen 2007] extends texture mapping and signal specialized parameterization to infill volumes with density-varying truss lattices. Brennan-Craddock [Brennan-Craddock 2011] studies several approaches to apply microstructures within objects, and proposes a slicing algorithm exploiting the periodicity of the structures for efficiency. Li et al. [Li 2015] rely on such mi-

crostructures to optimize the internal cross-sections of an object. Vidimče et al. [Vidimče 2013, Vidimče 2016] explore a voxel approach to define complex procedural structures within objects, with an emphasis on multi-materials, usability, and slicing efficiency. In a similar vein, our method is scales in terms of computation, thanks to the efficient synthesis of the parametrized stochastic microstructures [Martínez 2016, Martínez 2017a].

6.3 Previous definitions

Consider a composite material, whose local microstructure is described through a set of parameters p. Thanks to the homogenization method, this composite material can be considered as homogeneous. Let $A^*(p)$ be its homogenized elasticity tensor, which depends smoothly of the parameters p. We do not develop here the homogenization theory, the reader could find more details in [Allaire 2002a]. Let $D \subset \mathbb{R}^N$, with $N = 2$ or 3, be a fixed smooth bounded open set, namely the working domain.

6.4 Parametrized stochastic microstructures

We consider parametrized microstructures induced by a Poisson point process [Moller 2003] on the domain D. The Poisson point process is specified by an intensity function $\lambda : D \to \mathbb{R}_{\geq 0}$ which is locally integrable. The intensity measure is defined as:

$$\delta(B) = \int_B \lambda(\epsilon) d\epsilon \leq \infty, B \subseteq D$$

Function $\delta(B)$ determines the expected number of points in B. Intuitively speaking, $\lambda(\epsilon)d\epsilon$ corresponds the probability for the occurrence of a point in an infinitesimally small ball with centre ϵ and volume $d\epsilon$. For an homogeneous Poisson point process λ is the mean number of points per unit volume (see Figure 6.2(b)). Let $S \subset D$ be the set of points induced by a Poisson point process with intensity function λ.

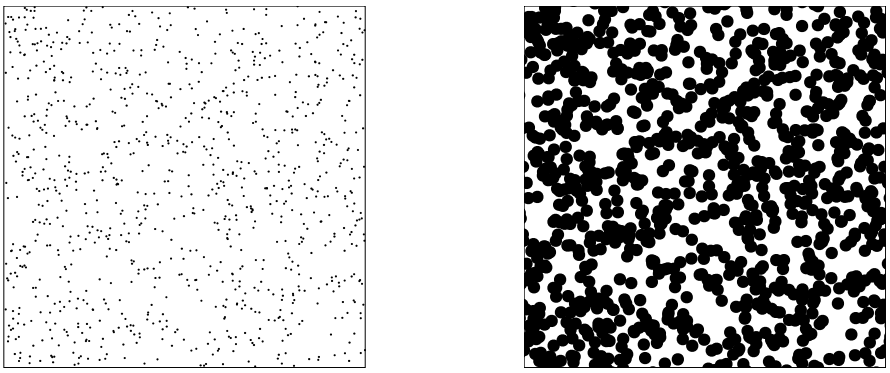

Figure 6.2: 6.2(b): Homogeneous Poisson point process ($\lambda = 1000$) in the unit square. 6.2(a): Induced microstructure with circular inclusions of radius $r = 0.017$.

6.4.1 Homogenization of stochastic microstructures

Consider a microstructure induced by an homogeneous Poisson point process D with intensity λ, and some parameters p. For instance, a microstructure made of circular inclusions centered at each point of D with radius r (see Figure 6.2(a)).

Most stochastic homogenization methods seek to establish upper and lower bounds of $A^*(p)$ [Hashin 1963]. We consider the homogenization of random periodic sample of extent $[0, \chi]^N$. It is known that this approximation converges as $\chi \to \infty$, giving back the effective coefficients of the original random operator. The variance of $A^*(p)$ between different random microstructures remains low for a large enough extent χ [Xu 2009, Savvas 2016, Martínez 2016, Martínez 2017a]. Thus, we approximate $A^*(p)$ by periodic homogenization of a random microstructures with parameters p. In particular, we compute the homogenized elasticity tensor $A^*(p)$ of the periodic sample with the publicly available FEM homogenization code of [Andreassen 2014]. We consider an isotropic base material with Young's modulus 1 and Poisson's ratio 0.3.

In the following, we present two different parametrized stochastic microstructures induced by S.

6.4.2 Voronoi microstructures

For a point $p \in D$, the set of closest points in S is:

$$C(p, S) = \{s_i \in S : \|s_i - p\| \leq \|s_j - p\|, \forall s_j \in S \setminus \{s_i\}\}$$

Where $\|\cdot\|$ corresponds to the Euclidean norm. The Voronoi edges of S are:

$$V_e(S) = \{x \in D : |C(x, S)| \geq N\}$$

Given some radius function $r : D \to \mathbb{R}_{>0}$, the Voronoi microstructure corresponds to $V_e(S) \oplus B_r$, where $\oplus$ is the Minkowski sum operator, and B_r is a closed ball centered at the origin with radius r.

In summary, the Voronoi microstructure is parametrized by $p = \{\lambda, r\}$ (see Figure 6.3).

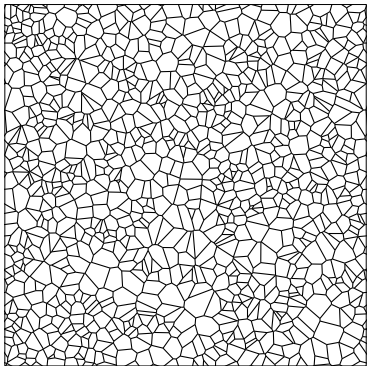

Figure 6.3: Voronoi microstructure induced by the set of points of Figure 6.2 (periodic domain), with $r = 0.003$.

For $r \to 0$ and $\lambda \to \infty$, it is known that the homogenized elasticity tensor $A^*(p)$ of stochastic Voronoi microstructures [Moller 2012] is close to an isotropic material [Gibson 1999]. An

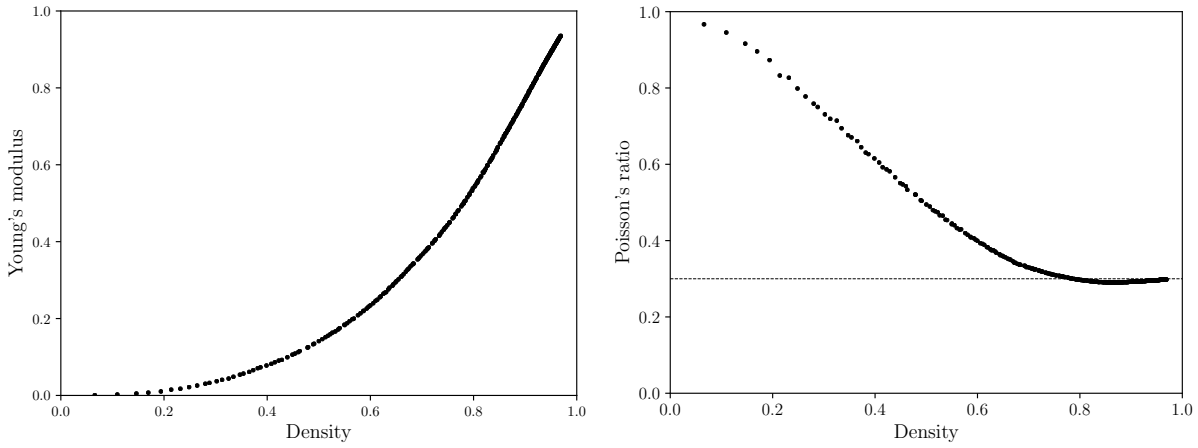

Figure 6.4: Isotropic material space of two dimensional Voronoi microstructures, showing the correlation between the overall density of the microstructure and: (6.4(a)) Young's modulus, (6.4(b)) the Poisson's ratio (base material Poisson's ratio marked with a dashed line).

isotropic elasticity tensor is defined by two independent elastic constants [Jones 1975] (e.g. Young's modulus and Poisson's ratio). Both parameters λ and r correlate in a power-law fashion with the Young's modulus [Roberts 2002, Martínez 2016]. This is illustrated by the 2D homogenization results shown in Figure 6.4.

6.4.3 k-nearest graph microstructures

Consider a graph $G_k = \{S, E\}$, where S is the set of vertices, and E is the set of edges connecting each vertex $s \in S$ to its $k > 0$ nearest (under some metric) points in $S \setminus \{s\}$.

We consider an anisotropic metric, where $\theta : D \to SO(N)$ corresponds to the metric rotation and $\xi : D \to \mathbb{R}^N_{>0}$ to the metric scaling. Let $d'(s_i, s_j)$ be the asymmetric distance between two points $s_i, s_j \in S$:

$$d'(s_i, s_j) = \sqrt{(s_i - s_j)M(s_i)(s_i - s_j)^T}$$

where

$$M(s) = \theta(s)\mathrm{diag}(\xi(s)^{-2})\theta(s)^T$$

Then, we construct the k-nearest graph with the symmetric metric:

$$d(s_i, s_j) = \frac{d'(s_i, s_j) + d'(s_j, s_i)}{2}$$

The k-nearest graph microstructure corresponds to $G_k \oplus B_r$.

In summary, the k-nearest graph microstructure is parametrized by $p = \{\lambda, r, \theta, \xi\}$ (see Figure 6.5).

For $r \to 0$ and $\lambda \to \infty$, the homogenized elasticity tensor $A^*(p)$ of stochastic k-nearest graph microstructures is close to an orthotropic material [Martínez 2017a]. An orthotropic elasticity tensor is defined by either four (in 2D) or nine (in 3D) independent elastic constants [Jones 1975] (e.g. Young's moduli, Poisson's ratios, and shear moduli varying independently along each

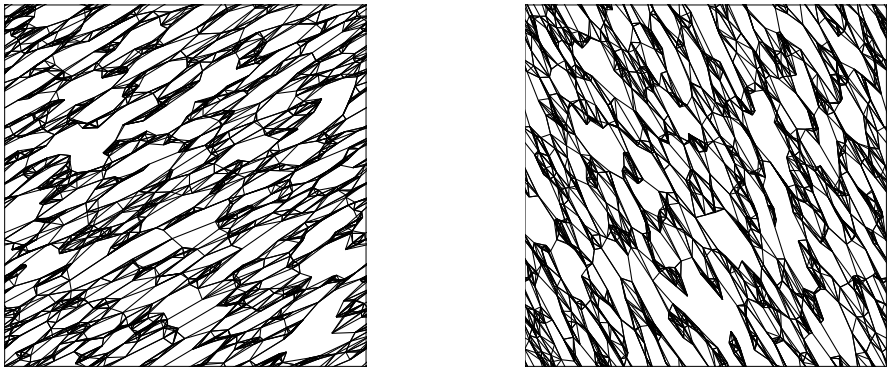

Figure 6.5: Two k-nearest graph microstructures induced by the set of points of Figure 6.2 (periodic domain), with $k = 6$, $r = 0.003$, and $\theta = R(30°)$. R corresponds to a two dimensional rotation matrix (counter-clockwise). 6.5(a): Metric scaling $\xi = \{4, 1\}$. 6.5(b): Metric scaling $\xi = \{\frac{1}{4}, 1\}$.

orthogonal axis). As shown in [Martínez 2017a], the metric rotation θ directly translates into the orientation of the orthotropic material, the metric scaling ξ correlates independently with the different orthogonal Young's moduli, and the point intensity λ correlates with the overall elastic moduli. Again, this is illustrated by the two dimensional FEM homogenization results shown in Figure 6.6.

6.4.4 Comparison with periodic microstructures

Most prior works consider parametrized periodic microstructures [Sigmund 1994b]. This offers two significant advantages. First, the periodicity allows for compact storage of the microstructure geometry. Second, periodic homogenization affords for the computation of the parameters of an equivalent homogeneous material [Allaire 2002a].

However, for periodic microstructures it remains difficult to grade the material properties since the boundary and transition between tiles has to be carefully handled [Schumacher 2015, Cramer 2016a, Wang 2017, Zhu 2017]. This problem becomes even more acute when grading anisotropic material properties (e.g. following some orthotropy material orientation). Namely, periodicity imposes strict boundary conditions that need to be carefully handled. On the contrary, stochastic microstructures do not suffer from this drawbacks, due to their less constrained formulation (see Figure 6.7).

6.4.5 Geometry computation

Microstructures are intended to fill large working domains. Most approaches explicitly store the microstructure geometry [Wang 2005, Robbins 2016, Gorguluarslan 2017]. This quickly leads to large data structures, and will eventually render impractical the geometry computation.

To avoid the aforementioned problems we consider a *procedural* computation [Lagae 2010] of stochastic microstructures, instead of explicitly storing their geometry. Consider a stochastic microstructure defined as a function $M : D \to \{0, 1\}$, 0 being void material, and 1 solid material.

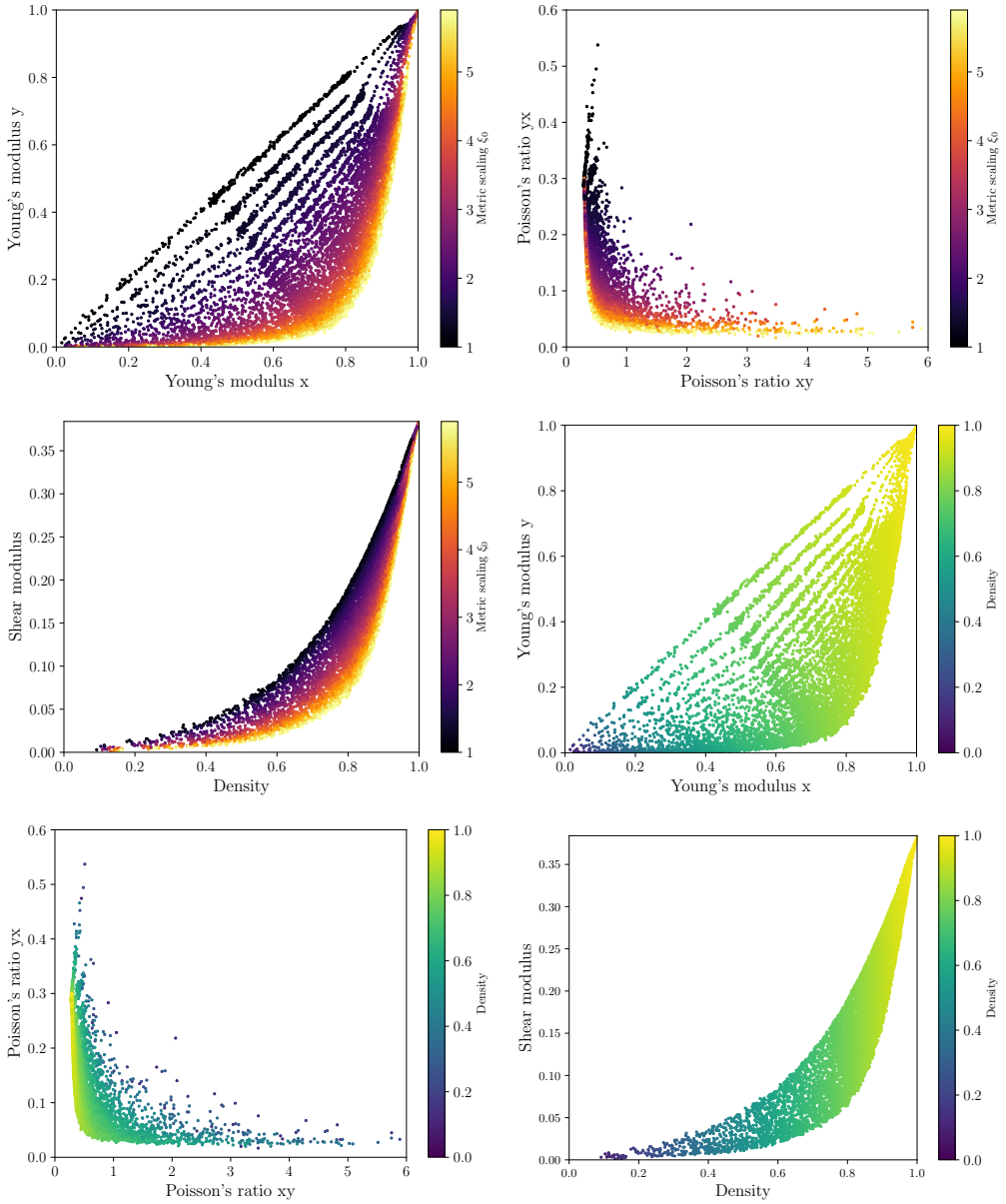

Figure 6.6: Orthotropic material space of two dimensional k-nearest graph microstructures. We sample the interval of metric scaling $\xi_0 = [1, 6]$, with fixed $\xi_1 = 1$. Correlation between 1) metric scaling (from 6.6(a) to 6.6(c)), 2) the overall density (from 6.6(d) to 6.6(f)), with the orthogonal Young's moduli (left column), the orthogonal Poisson's ratio (middle column), and the independent shear modulus (right column). When approaching higher density, the homogenized tensor converges to the base material properties.

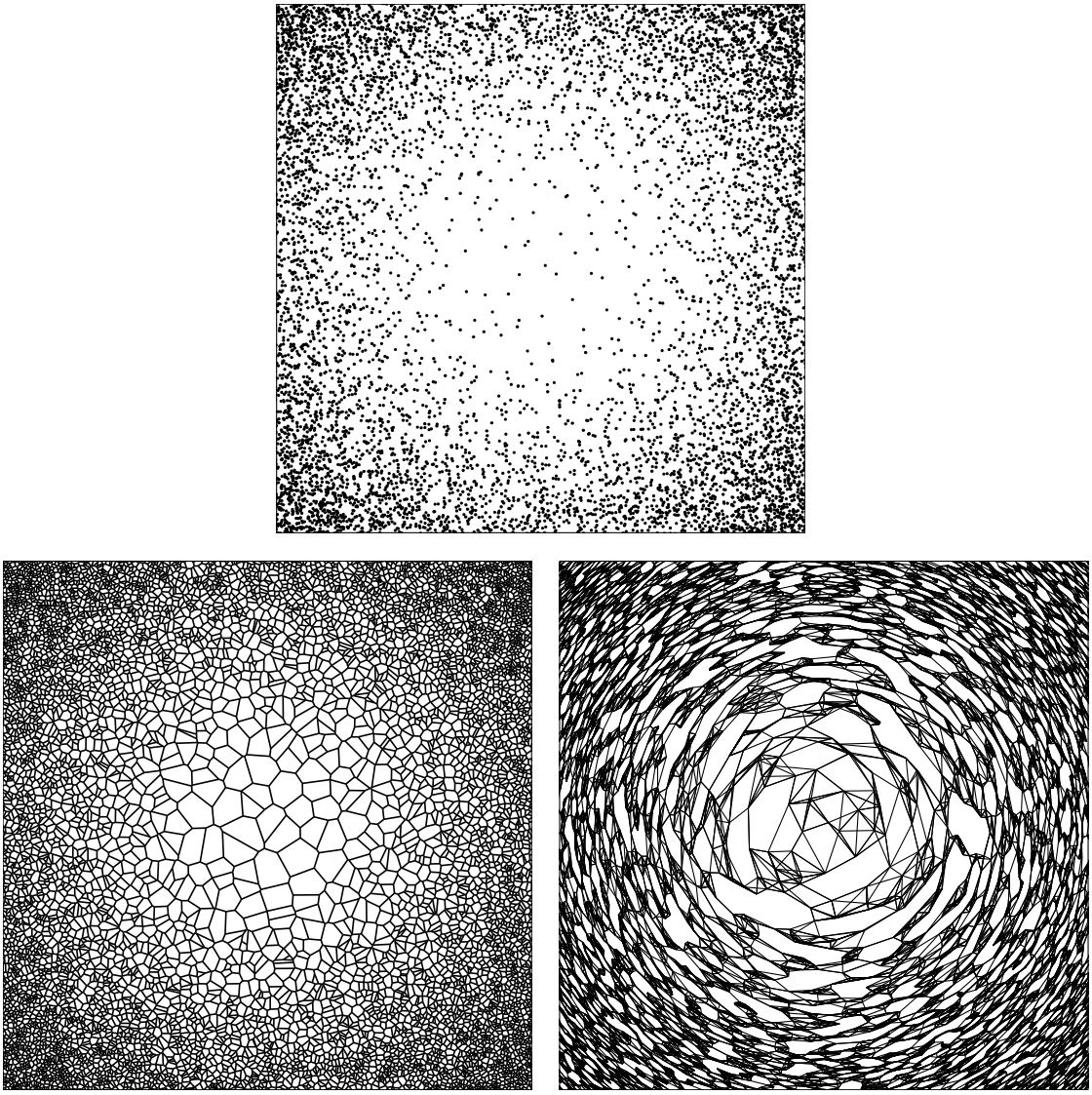

Figure 6.7: Grading material density with stochastic parametrized microstructures. 6.7(a): Inhomogeneous Poisson point process in the unit square with $\lambda(\epsilon) = 500\left(1 + 200\left\|\epsilon - [0.5, 0.5]\right\|^3\right)$. 6.7(b): Corresponding Voronoi microstructure. 6.7(c): Corresponding k-nearest microstructure with concentric variation of the metric rotation θ and a constant metric scaling $\xi = \{4, 1\}$.

M is a *procedural* function if:

- M can be evaluated for all points of D in constant time and constant memory computational complexity.
- The size of the program to compute M is constant.

The time/space complexity quantifies the amount of time/space taken by an algorithm to run as a function of the length of its output. In other words, having a constant factor implies that the algorithm complexity is independent of the output size. Thus, a procedural function trivially scales with the increase of microstructure geometry size and complexity.

A procedural computation of Voronoi microstructures [Martínez 2016] and k-nearest graph microstructures [Martínez 2017a] have already been proposed.

6.5 Optimization

6.5.1 Settings of the problem

The domain D is filled by the composite material, whose microstructure at the point $x \in D$ is given by $p(x)$. This composite structure is clamped on $\Gamma_D \subset \partial D$ and submitted to surface loads g on $\Gamma_N \subset \partial D$. The homogenized displacement u^* and the homogenized stress tensor σ^* are the solutions of the following homogenized elasticity problem:

$$\begin{cases} \operatorname{div}(\sigma^*) = 0 & \text{in } D, \\ \sigma^* = A * (p(x))e(u^*) & \text{in } D, \\ u^* = 0 & \text{on } \Gamma_D, \\ \sigma^* \cdot n = g & \text{on } \Gamma_N, \\ \sigma^* \cdot n = 0 & \text{on } \Gamma = \partial D \setminus (\Gamma_D \cup \Gamma_N), \end{cases} \tag{6.1}$$

where $e(u^*) = \frac{1}{2}(\nabla u^* + \nabla u^{*T})$ is the homogenized strain tensor, and n is the normal to ∂D.

The purpose of topology optimization is to determine the composite structure, described by the field p over the whole domain D, that minimizes a given objective function J^*, under for example a volume constraint:

$$\begin{aligned} &\min_{p} \quad J^*(p)\,, \\ &\int_D \rho(p) = V \end{aligned} \tag{6.2}$$

where ρ is the local density of the composite material and V is the target volume. In the following the objective function will be exclusively the compliance:

$$J^*(p) = \int_{\Gamma_N} g \cdot u^* ds\,. \tag{6.3}$$

We emphasize that the compliance is also equal to the minimum of an energy:

$$J^*(p) = \min_{\tau \in H_0} \int_D A^{*-1}(p(x))\tau : \tau dx\,, \tag{6.4}$$

where :

$$H_0 = \left\{ \tau \in L^2(D, \mathcal{M}_3^s) | \begin{array}{ll} \operatorname{div}(\tau) = 0 & \text{in } D \\ \tau n = g & \text{on } \Gamma_N \\ \tau n = 0 & \text{on } \Gamma \end{array} \right\}$$

Hence, the shape optimization problem 6.2 can be rewritten as:

$$J^*(p) = \inf_{\tau \in H_0} \min_{\substack{p \in \mathcal{P} \\ \int_D \rho(p) = 0}} \int_D A^{*-1}(p(x))\tau : \tau dx \,, \tag{6.5}$$

where $\mathcal{P}$ is the admissible set of the parameters p.

6.5.2 Optimization with a parametrized material

We present briefly the optimization method, one could find more details in [Allaire 2018].

General optimization process. The minimization problem 6.5 can be solved using an alternate algorithm: we minimize successively with respect to the stress tensor σ and to the material parameters p. The corresponding Lagrangian is given by:

$$\mathcal{L}(p, \sigma, \ell) = \int_D A^{*-1}(p(x))\sigma : \sigma dx + \ell(\int_D \rho(p(x))dx - V) \,,$$

where ℓ is the Lagrange multiplier associated to the volume constraint.

The minimization with respect to the stress field σ is done by solving the elasticity problem 6.1, with the current state for the material parameters p. First we compute the displacement field $u \in V_D$ solution of :

$$\forall v \in V_D \quad \int_D A^*(p(x))e(u) : e(u)dx = \int_{\Gamma_N} g \cdot v ds \,, \tag{6.6}$$

where $V_D = \{v \in H^1(D, \mathbb{R}^N | v = 0 \text{ on } \Gamma_D\}$. The stress tensor is then given by:

$$\sigma = A^*(p)e(u) \,.$$

The minimization with respect to the material parameters $p = (p_i)_{1 \leq i \leq n_p}$ is done using the projected gradient algorithm. Since we consider here only the case of the compliance, our problem is self-adjoint. Hence the descent direction dp_i is given by:

$$dp_i = \frac{\partial A^*}{\partial p_i}(p(x))A^{*-1}(p(x))\sigma : A^{*-1}(p(x))\sigma + \ell \frac{\partial \rho}{\partial p_i}(p(x)) \,. \tag{6.7}$$

The update of the material parameters at iteration n is given by:

$$p_i^{n+1} = P_{\mathcal{P}}(m_i^n + \mu dp_i) \,, \tag{6.8}$$

where $\mu > 0$ is the step size and $P_{\mathcal{P}}$ is the projection operator on the set $\mathcal{P}$ of admissible material parameters p. The Lagrange multiplier ℓ is determined by a dichotomy process in order to respect the volume constraint at each iteration. We emphasize that the several terms in the descent direction (6.7) are computed once by iteration, thanks to the linearity of (6.7) with respect to ℓ.

Consideration about the orientation of the material. In the following, we consider two kinds of material: an isotropic one and an orthotropic one. The isotropic material is only parametrized by its local density ρ. Hence the parameter p is reduced to ρ in this particular case.

Contrary to an isotropic material, an orthotropic one can be suitably oriented in the domain D, in order to support efficiently the local stress. The orientation of the material can be seen as one of the material parameters p_i. Hence the above gradient algorithm could be used on it. However, we can improve the efficiency of our algorithm using the Pedersen formulas [Pedersen 1989]: for a given stress field σ the optimal orientation of an orthotropic material in order to minimize the compliance is the one aligned with the principal directions of σ.
Let be $\tilde{p}$ be the material parameters excluding the orientation, denoted by α. Let $A_0^*(\tilde{p})$ be the homogenized elasticity tensor corresponding to the material parameters $\tilde{p}$ for a reference orientation. Let $R(\alpha)$ be a fourth order tensor defined by:

$$\forall \xi \in \mathcal{M}_N^s \quad R(\alpha)\xi = Q(\alpha)^T \xi Q(\alpha)\,,$$

where $Q(\alpha) \in SO(N)$ is the rotation matrix from the reference orientation to the orientation α. The dependency of $A^*(p)$ with respect to the orientation α is then given by:

$$A^*(p) = R(\alpha) A_0^*(\tilde{p}) R(\alpha)^T\,.$$

At each iteration, we have to minimize with respect to the orientation α. Thanks to Pedersen formulas, the optimal orientation is given by the unit eigenvectors v_1, and v_2 of the stress tensor σ. Those eigenvectors are ordered according to their respective eigenvalues : $\lambda_1 < \lambda_2$, in order to ensure the continuity of the orientation of the composite in the whole domain D. Then we have to find the angle α such that $v_1 = (\cos(\alpha), \sin(\alpha))^T$.

In fact, the rotation tensor $R(\alpha)$ depends only on the angle 2α. Let the vector $b = (\cos(2\alpha), \sin(2\alpha))^T$. b is then given by:

$$b = \frac{1}{\sqrt{(\sigma_{11} - \sigma_{22})^2 + 4\sigma_{12}^2}} (\sigma_{11} - \sigma_{22}, 2\sigma_{12})^T\,. \tag{6.9}$$

Complete optimization algorithm. The algorithm has been implemented in the finite elements software FreeFem++ [Hecht 2012]. All unknowns are discretized using P_1-functions.

Here is the complete optimization algorithm:

1. Initialization of the parameters p^0: either ρ^0 for isotropic material, or b^0 and $\tilde{p}^0$ for orthotropic material.

2. Iteration until convergence, for $n \geq 0$:

   (a) Computation of the stress field σ^n by solving the variational formulation (6.6) with p^0, using finite element method

   (b) If orthotropic material : Computation of the optimal orientation given by the vector b^{n+1}, using (6.9) with σ^n.

   (c) Computation of the gradient descent (6.7), with σ^n and p^n, then update of the parameters p^{n+1} with (6.8).

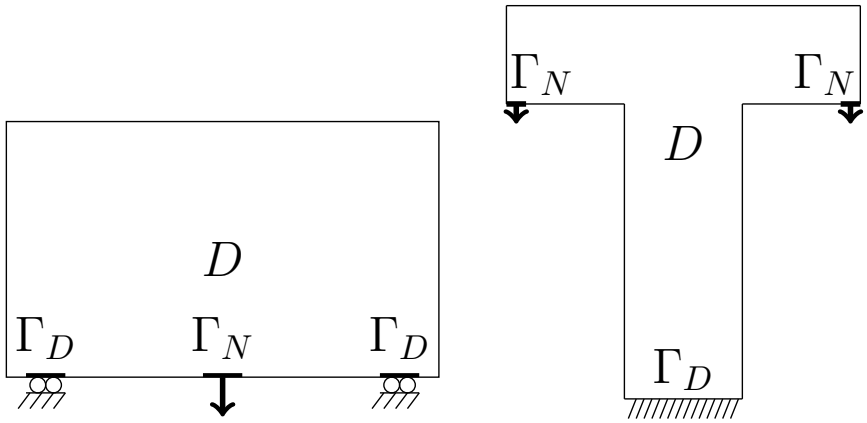

(a) Bridge (b) Electric mast

Figure 6.8: Boundary conditions for the bridge and the electric mast problems

6.6 Numerical results of the optimization

The above optimization algorithm has been implemented for a bridge problem and for an electric mast problem, with two kinds of material: Voronoi microstructures, which are isotropic, and k-nearest graph microstructures, which are orthotropic. For both cases, the volume constraint is set to $V = 30\%$.

The domain size of the bridge is 22×13, it is discretized by a triangular mesh (9000 vertices). A unit vertical load is applied at the middle of the bottom border on an interval of length 2, Γ_N, see Figure 6.8(a). A sliding boundary condition is applied on two symmetric intervals of length 1 starting at a distance 1 from the sides, Γ_D.

The electric mast is high of 20 and width of 18, its pillar is high of 15 and width of 6. It is discretized by a triangular mesh (11000 vertices). A unit vertical load is applied at the middle of the bottom border on an interval of length 1, Γ_N, see Figure 6.8(b). A Dirichlet boundary condition is applied on the bottom border, Γ_D.

6.6.1 Isotropic material

The Voronoi microstructures are parametrized by their density, ρ, linked to the radius r. We run the algorithm respectively on the bridge case and on the electrical mast case. The optimized compliance are respectively equal to 63.8 and 68.02. Results are respectively displayed on Figures 6.9 and 6.10. The microstructure auto penalized: the density is taken only two values, the upper and the lower bounds of the admissible range for the density, $[0.1; 1]$. In other words, the final structure does not feature microstructure, it is only full material and most reachable void. The final structures are very close to shapes optimized with classic shape optimization methods, like SIMP method (Solid Isotropic Material with Penalization method) [Bendsøe 1989] or level-set methods [Allaire 2004b]. Note that those methods optimize only the macroscopic distribution of the material in the whole domain D, without any consideration for microstructures.

One could conclude that Voronoi microstructures are not relevant in shape optimization. But, if they are not efficient for compliance minimization in single-load cases, other objective functions have to be investigated.

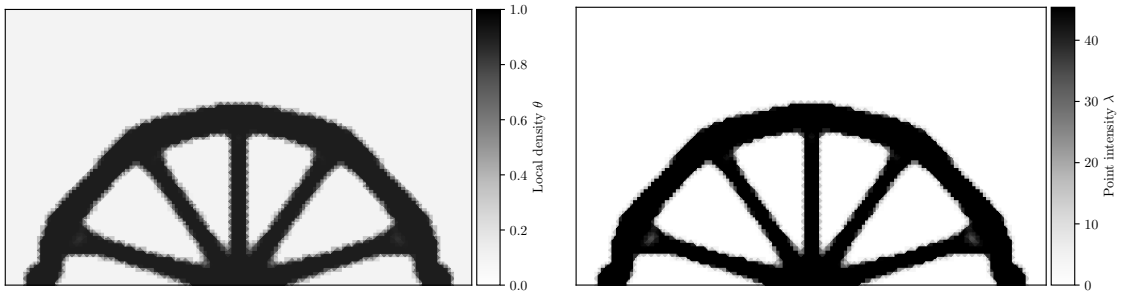

(a) Local density ρ.

(b) Point intensity λ

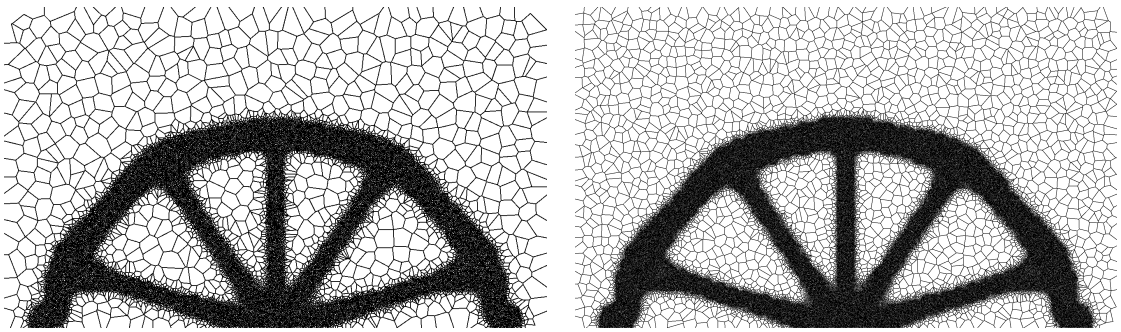

(c) $r = 0.016$, $V = 31.5\%$

(d) $r = 0.01$, $V = 30.9\%$

Figure 6.9: Isotropic case for the bridge. Volume constraint $V = 30\%$. Compliance $J^*(p) = 63.8$.

6.6.2 Orthotropic material

The k-nearest graph microstructures are parametrized by the metric orientation θ, their density $\rho \in [0.1; 1]$, and their metric scaling $\xi_0 \in [0, 6]$ (fixed $\xi_1 = 1$). We run the algorithm respectively on the bridge case and on the electric mast case. Results are respectively displayed on Figures 6.11 and 6.12. There is no autopenalization of the microstructures. Thanks to the orientation and the stretch, the material can be efficiently locally distributed to support the stress. The optimized compliances are respectively equal to 60.2 and 65.1, which is about 5% better than the optimized compliances with isotropic material.

We run another test, where the density is fixed to $\rho = 0.3$ in the whole domain. Only the orientation and the stretch are optimized. Results are displayed on Figures 6.13 and 6.14. The optimal orientation is very closed to the one, where all parameters were optimized. The optimized compliances are respectively equal to 112.4 and 140.6, which are unsurprisingly higher than the previous ones.

The density is the parameter with the better leverage for compliance minimization, but it is not efficient to optimize a microstructure only with respect to the density. All parameters have to be carefully and simultaneously optimized. Note that only compliance minimization has been

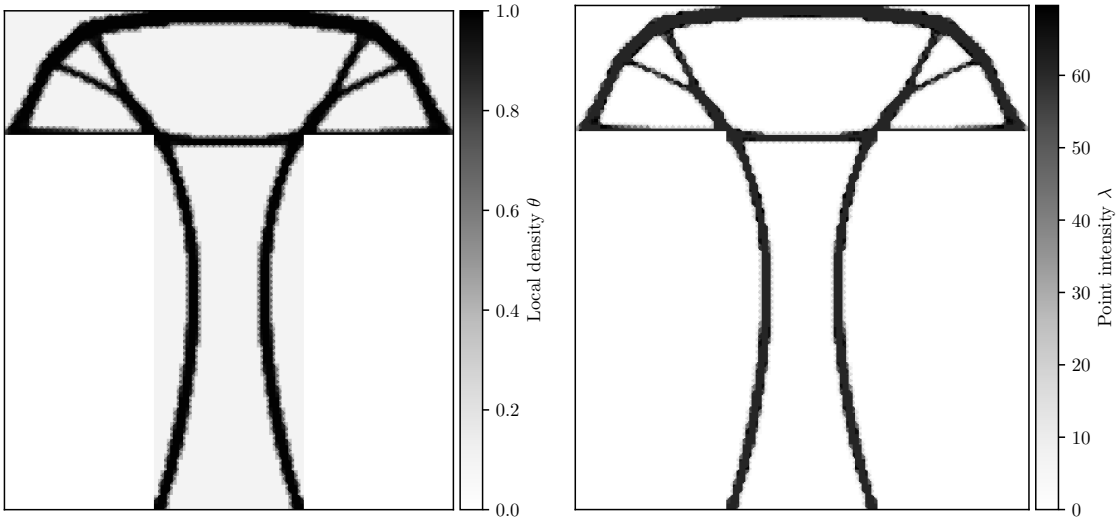

(a) Local density ρ (b) Point intensity λ

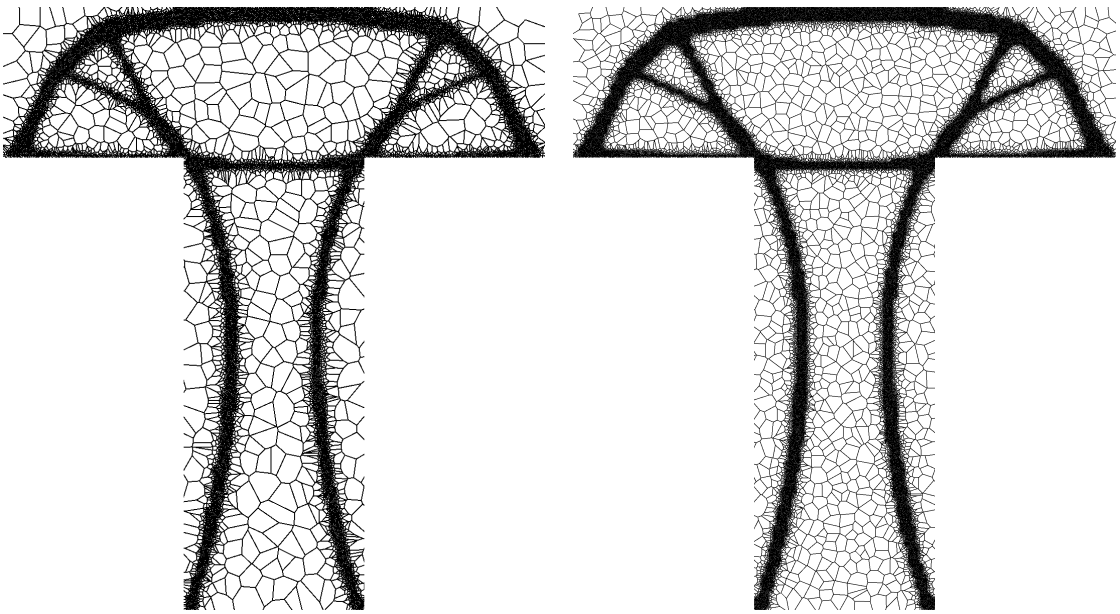

(c) $r = 0.018$, $V = 32.0\%$ (d) $r = 0.011$, $V = 31.0\%$

Figure 6.10: Isotropic case for the electric mast. Volume constraint $V = 30\%$. Compliance $J^*(p) = 68.02$.

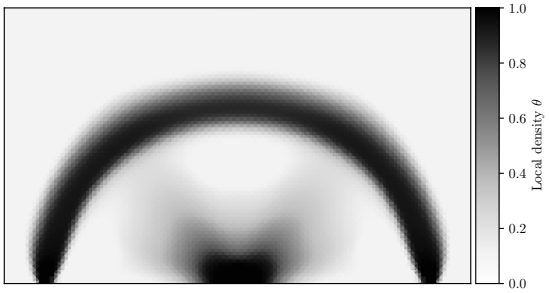

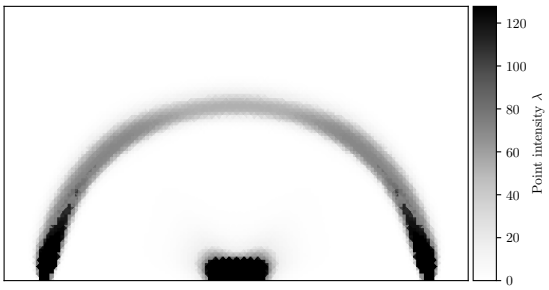

(b) Point intensity λ

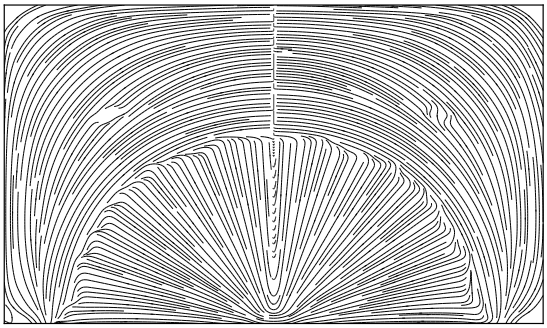

(c) Angle orthotropy

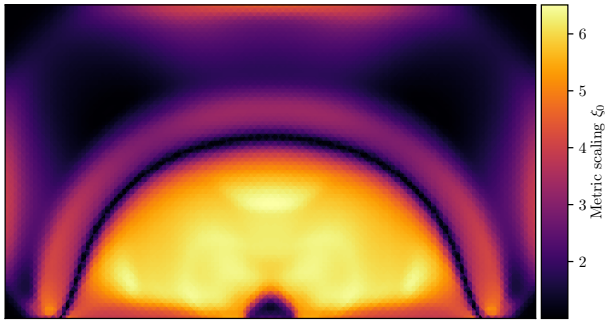

(d) Metric scaling ξ_0

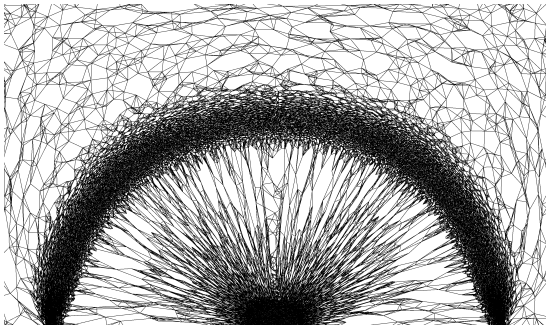

(e) $r = 0.0071$, $V = 32.31\%$

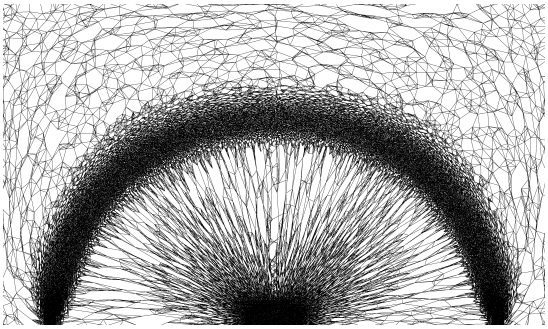

(f) $r = 0.0055$, $V = 32.02\%$

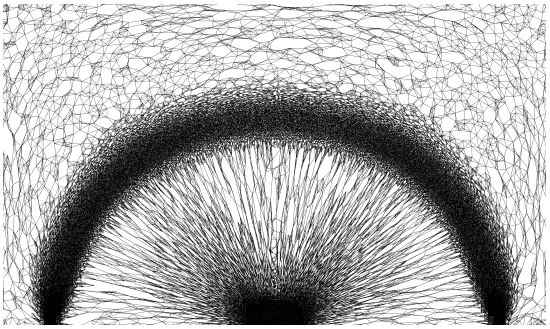

(g) $r = 0.0045$, $V = 32.01\%$

Figure 6.11: Orthotropic case. Volume constraint $V = 30\%$. Compliance $J^*(p) = 60.2$.

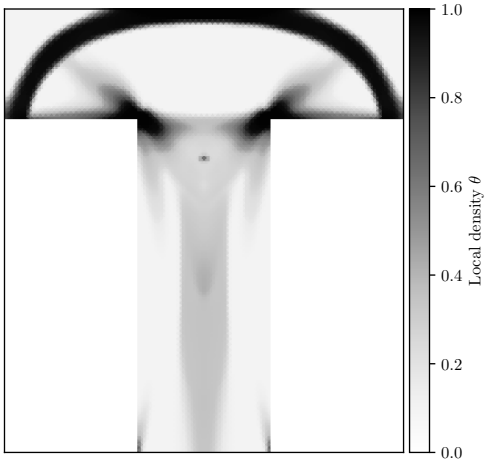

(a) Local density ρ.

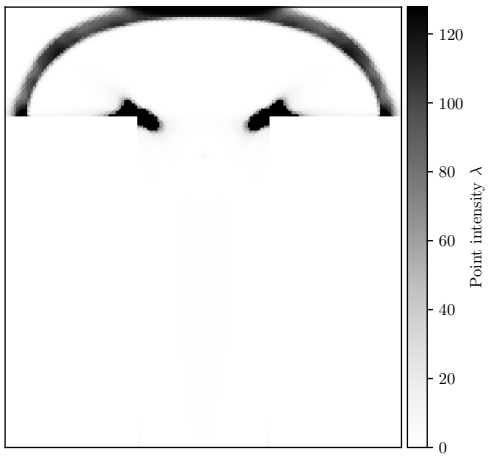

(b) Point intensity λ

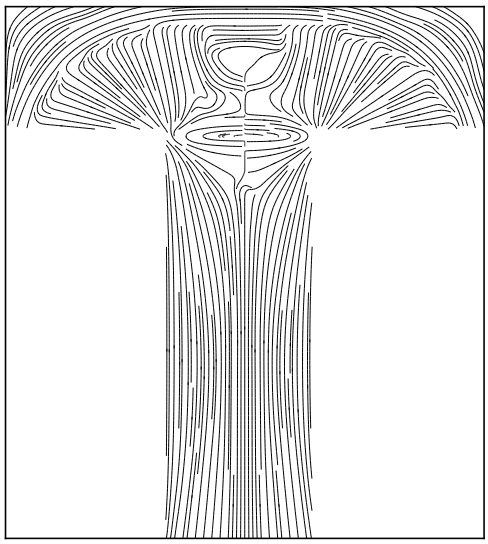

(c) Angle orthotropy

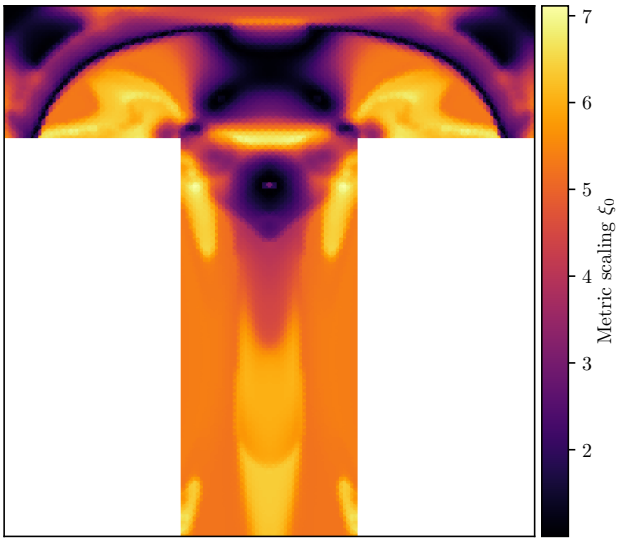

(d) Metric scaling ξ_0

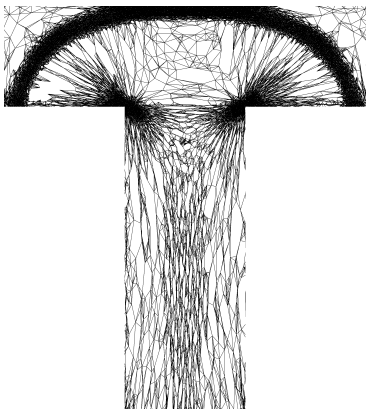

(e) $r = 0.0079$, $V = 32.93\%$

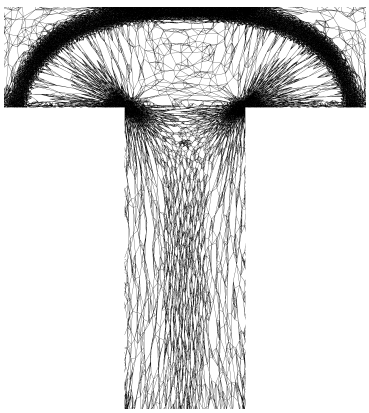

(f) $r = 0.0062$, $V = 32.85\%$

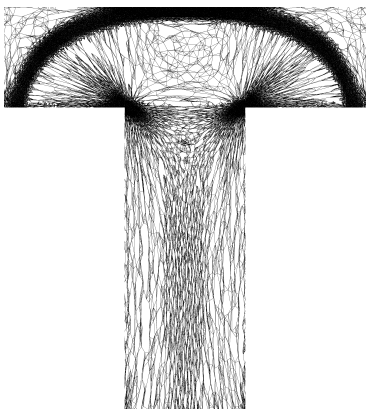

(g) $r = 0.0050$, $V = 32.69\%$

Figure 6.12: Orthotropic case. Volume constraint $V = 30\%$. Compliance $J^*(p) = 65.1$.

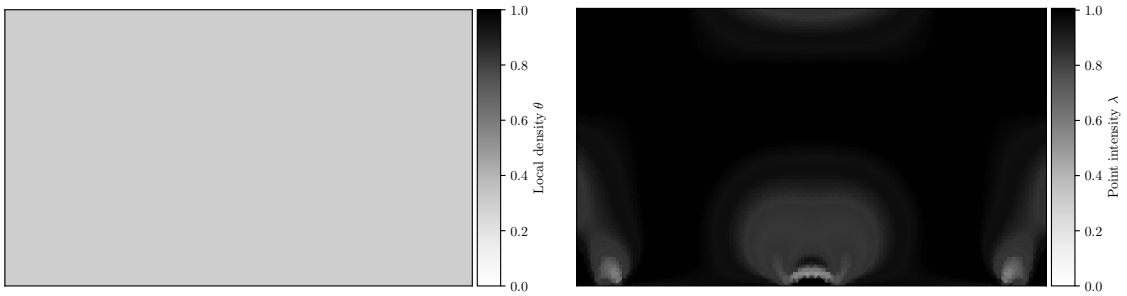

(a) Local density ρ.

(b) Point intensity λ

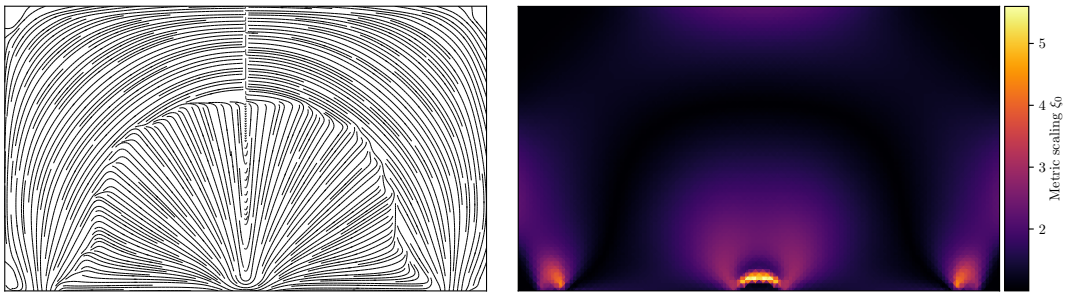

(c) Angle orthotropy

(d) Metric scaling ξ_0

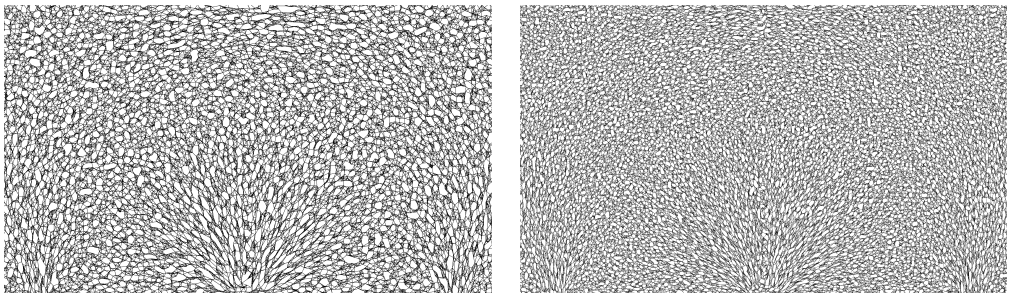

(e) $r = 0.0071$, $V = 29.4\%$

(f) $r = 0.0041$, $V = 29.5\%$

Figure 6.13: Orthotropic case with fixed density $\rho = 0.3$. Compliance $J^*(p) = 112.4$.

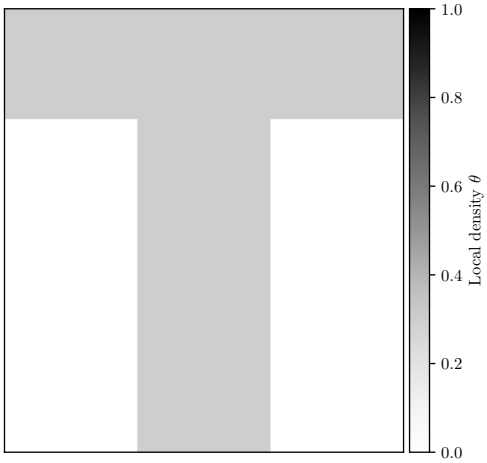

(a) Local density ρ.

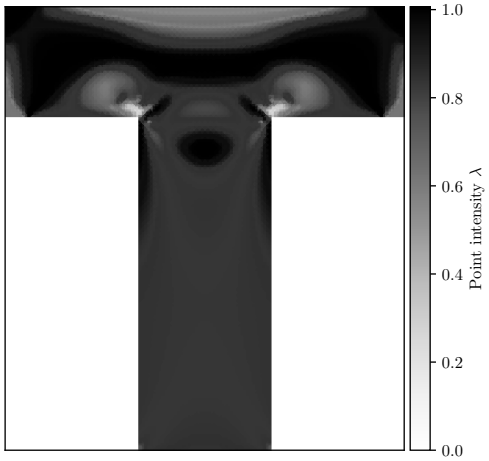

(b) Point intensity λ

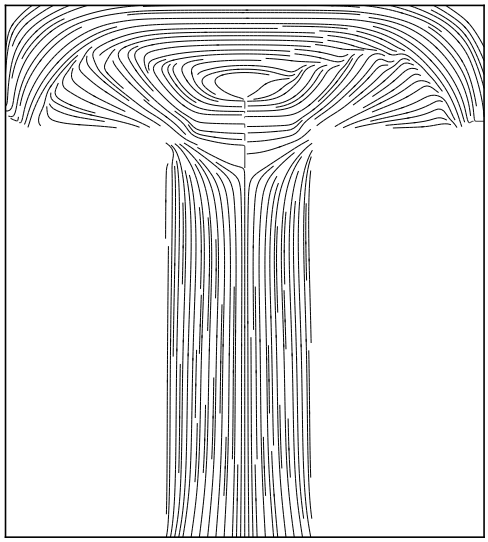

(c) Angle orthotropy

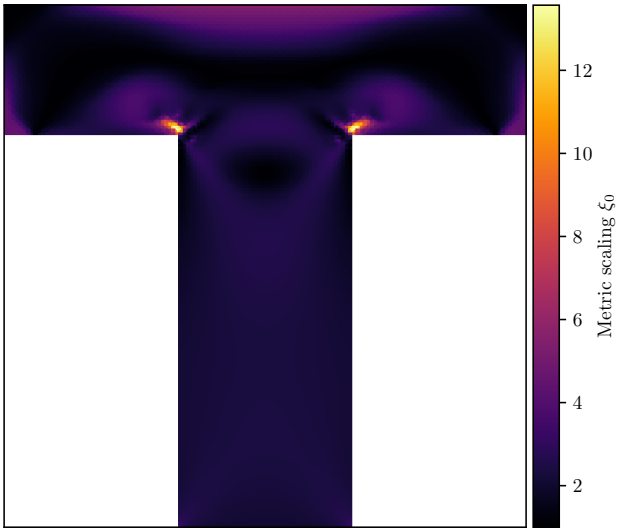

(d) Metric scaling ξ_0

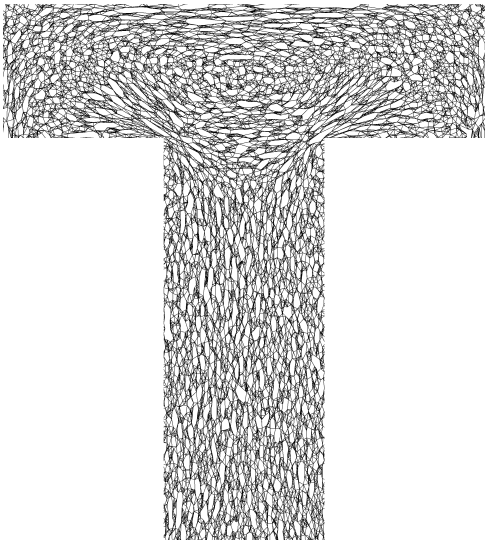

(e) $r = 0.0079$, $V = 29.9\%$

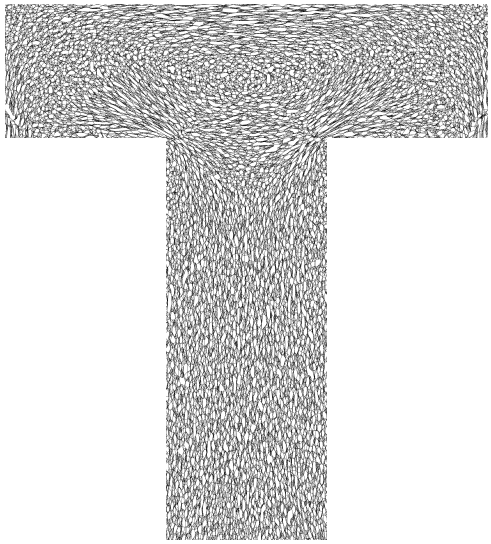

(f) $r = 0.0046$, $V = 30.1\%$

Figure 6.14: Orthotropic case with fixed density $\rho = 0.3$. Compliance $J^*(p) = 140.6$.

performed here. Other applications for those microstructures have still to be investigated in shape optimization, for example compliance minimization in multiple-loads cases for isotropic cells, or optimal filing of shapes.

6.6.3 Discussion

There exists small differences between the target volume constraint and the actual volume of the microstructure. This is largely explained by two different factors. First, the microstructure geometry being computed at a finite scale ($r > 0$). In particular, sudden changes of the local density, may lead to divergences with respect the target volume constraint as discussed in Figure 6.15. Finally, the reconstructed of the material space shown in Figures 6.4 and 6.6 is approximate, since we consider a finite periodic domain to perform the homogenization.

6.7 Conclusions and future work

We have presented an approach to perform topology optimization with parametric and stochastic microstructures, that it is notably well-suited for orthotropic materials, due to its intrinsic ability to effortlessly follow a vector field.

Although all the presented results are in 2D, the formulation of our approach naturally extends to the 3D dimensional case. We find particularly promising the case of 3D orthotropic microstructures, following an arbitrary vector field of orthotropy orientation. The problem of finding a 3D periodic parametrization is known to be particularly hard [Sokolov 2016].

As discussed in Section 6.6.3 due to the finite scale of the projected microstructures, the microstructure volume may differ from the target volume constraint. We would like to study how to compensate for this finite scale side effect, possibly by taking into account the radius of the microstructure edges r in the projection phase.

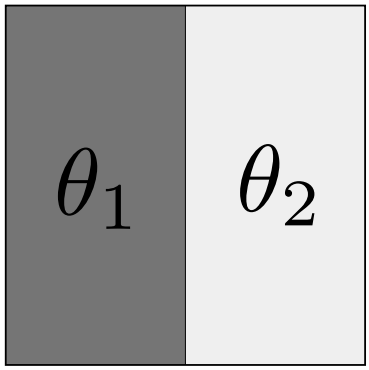

(a)

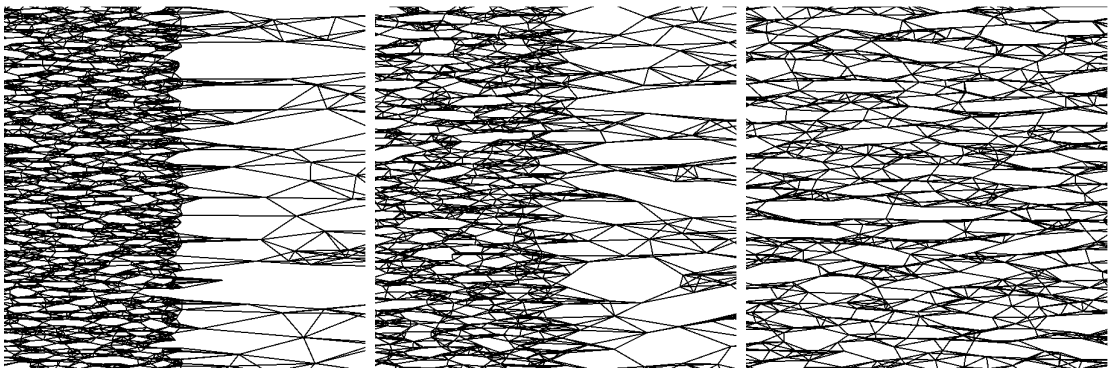

(b) $\beta = 0.1$ (c) $\beta = 0.3$ (d) $\beta = 0.5$

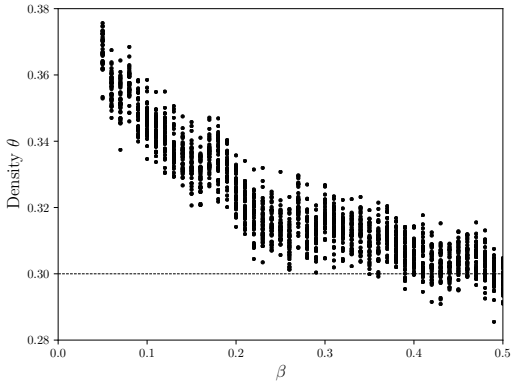

(e)

Figure 6.15: Studying the effect of abrupt changes of target density, paired with a high metric scaling $\xi_0 = 4$. Given a target overall density $\theta = 0.3$, the two different densities θ_1 and θ_2 are parametrized with $\beta \in [0, \frac{1}{2}]$ such that $\theta_1 = 2\theta\beta$ and $\theta_2 = 2\theta(1-\beta)$. Thus, $\theta = \frac{\theta_1+\theta_2}{2}$. 6.15(a): Square domain with dimension 1×1. The radius of the k-nearest microstructures is set to $r = 0.0016$. 6.15(e): Results for 40 random realizations of the same microstructure with varying $\beta \in [0.05, \frac{1}{2}]$. Due to the close interaction the microstructures in θ_1 and θ_2, for low values of β (high contrast of densities, and high metric scaling) the overall density increases significantly from the target one of $\theta = 0.3$. This likely explains why the results exhibiting a field of density with high contrast(Figures 6.11 and 6.12) show a higher overall density than the target one.

Chapter 7

Topology optimization of 3D structures built with orthotropic lattice materials

Contents

This chapter is a submitted article:
3-d topology optimization of modulated and oriented periodic microstructures by the homogenization method, by P. Geoffroy-Donders, G. Allaire and O. Pantz.

Abstract. This paper is motivated by the optimization of so-called lattice materials which are becoming increasingly popular in the context of additive manufacturing. Generalizing our previous work in 2-d we propose a method for topology optimization of structures made of periodically perforated material, where the microscopic periodic cell can be macroscopically modulated and oriented. This method is made of three steps. The first step amounts to compute

the homogenized properties of an adequately chosen parametrized microstructure (here, a cubic lattice with varying bar thicknesses). The second step optimizes the homogenized formulation of the problem, which is a classical problem of parametric optimization. The third, and most delicate, step projects the optimal oriented microstructure at a desired length scale. Compared to the 2-d case where rotations are parametrized by a single angle, to which a conformality constraint can be applied, the 3-d case is more involved and requires new ingredients. In particular, the full rotation matrix is regularized (instead of just one angle in 2-d) and the projection map which deforms the square periodic lattice is computed component by component. Several numerical examples are presented for compliance minimization in 3-d.

7.1 Introduction

The homogenization method is the ancestor of many popular and successful algorithms for topology optimization of structures. Its main idea is to introduce microstructures with a continuously variable material density as admissible designs in the optimization process. This idea was first introduced by mathematicians [Kohn 1986], [Lurie 1982], [Murat 1985] (see the textbook [Allaire 2002a] for more references), who motivated the use of such composite materials by the notion of relaxation, i.e., making the optimization well-posed. The homogenization method became popular thanks to the pioneering paper [Bendsøe 1988] which was the first one to numerically address a realistic problem in the elasticity setting. Since then, the homogenization method has been replaced by its much simplified version, the so-called SIMP method introduced in [Bendsøe 1989], [Zhou 1991] (see the textbook [Bendsoe 2003] for a more complete account), which is the most commonly used method in commercial topology optimization software, as well as in many academic contributions. Compared to the homogenization method, which relies on true composite materials, possibly anisotropic, SIMP uses only fictitious isotropic materials. Since intermediate densities (between full material and void) are penalized in the end, there is indeed no need to have a detailed knowledge and optimization of microstructures.

Nevertheless, the recent progress of additive manufacturing techniques revive the interest for the use of graded or microstructured materials since they are now manufacturable. Their range of applications is very large, from standard light-weighting mechanical structures [Wang 2013], to the design of bone scaffolds [Cramer 2016b, Khanoki 2012], passing by heat exchangers [Luo 2007].

Although homogenization theory applies to any kind of composite materials (without any restriction on the geometry of their microstructure), in this work we restrict ourselves to periodic homogenization and macroscopically modulated periodic structures. The reason for this choice is the obvious manufacturability of such periodic structures, although other choices would be possible, like (stationary) random structures (see e.g. [Martínez 2017b]). The optimization of periodic microstructure for composite materials is an old topic [Barbarosie 1997], [Barbarosie 2010a], [Barbarosie 2010b], [Haslinger 1995], [Lipton 2002], [Xia 2008]. Typically, the properties of the microstructures are homogenized (or averaged), then parametrized in order to optimize only a few scalar fields. Very often, these microstructures are anisotropic. However, their orientation is rarely taken into account and optimized, although it is well-known that their orientation is a crucial and determining parameter in topology optimization

[Allaire 2002a, Pedersen 1989]. Actually, if optimizing the microstructure orientation is not difficult, reconstructing the oriented periodic structure is a challenging issue. In particular, two neighbouring cells, if oriented differently, either overlap or leave a small gap between their sides. Therefore, the periodic structure might be not connected or would not respect an imposed volume constraint [Zhou 2008, Cramer 2016a]. Morphing approaches have been suggested [Schumacher 2015], but they are not effective as soon as the cell orientation varies in the structure. Another method, developed in 2-d [Pantz 2008, Allaire 2018, Groen 2017] alleviates this difficulty by deforming the original periodic grid with a diffeormorphism, which ensures the cohesion between cells by slightly distorting them. This diffeormorphism is defined and computed in such a way that, roughly speaking, its gradient is aligned with the optimal orientation of the periodicity cell.

The goal of the present paper is to extend this approach from the 2-d setting to the 3-d case. It is not a simple matter since many new difficulties appear, which are not merely computational issues but also modeling and theoretical issues. In particular, orientation in 2-d is easily parametrized by a single angle which, furthermore, can satisfy a conformality condition, ensuring preservation of angles upon deformation. There is no such conformality condition in 3-d and there are several different ways of modeling orientation. Here, orientation would be represented by a rotation matrix. There are two main novelties in the present work. First, we propose a new method to regularize the orientation of the cells in 3-d, which avoids the sign indeterminacy of a vector representing a direction (see Section 7.4.3). Second, we extend in 3-d our 2-d projection method [Allaire 2018] in order to reconstruct a modulated and oriented periodic structure with properties closed to the homogenized optimal design. The key difference with respect to the 2-d setting is that the projection is made direction by direction and not globally (see Section 7.5).

The content of this paper is the following. Section 7.2 introduces the optimal design problem of compliance minimization in 3-d and its relaxation using the homogenization approach.

Section 7.3 is devoted to the first or pre-processing step of our method. It amounts to choose a parametrized periodicity cell, here a cube drilled from end to end by three rectangular holes, and to compute its homogenized elasticity properties, as well as their derivatives, with respect to the cell parameters. We also discuss a representation of the cell orientation by a set of three orthogonal unit vectors (in 3-d) in Section 7.3.3.

Section 7.4 focuses on the second step of our method, namely the optimization of the homogenized formulation of the 3-d compliance problem, with respect to the periodicity cell parameters. We rely on a gradient-based algorithm where the gradient is classically computed by an adjoint approach. The optimal orientation is found analytically [Pedersen 1989], [Norris 2005] since we consider single load compliance minimization problem. However, for more general problems we could have used a more standard, albeit less efficient, gradient algorithm for the orientation (see Remark 13). The method differs from the one developed in 2-d [Allaire 2018] by the regularization of the cell orientation. Indeed, after optimization, the orientation has to be slightly regularized in order to lead to reasonable results during the post-processing step. The regularization method, presented in Section 7.4.3 is one of the main novelties of the present work. It relies on the fact that the chosen orientation representation is not unique: each three vectors can be replaced by its opposite. Hence, the regularization approach has to take into account this property. A symmetric matrix, with eigenvectors given by these three orientation vectors,

is introduced. The regularization of this matrix is then preferably chosen, rather than a direct regularization of the orientation vectors.

Section 7.5 deals with the third or post-processing step, namely the projection of the homogenized design over genuine shapes. This is the second main novelty of the present work. As in 2-d [Allaire 2018], a vector field $\varphi(x)$, which distorts a regular grid according to a given local orientation, is defined. The main difference with 2-d is that the map φ is no longer a conformal map, which would be a too restrictive requirement in 3-d. Section 7.5.2 introduces a method to compute the map φ. Numerical implementation is detailed in Section 7.5.4. The numerical results are displayed in Section 7.5.5 for a cantilever test case. We emphasize that the orientation regularization and the post processing algorithm are completely general, meaning that they are not restricted to single load compliance minimization, and that they can readily be implemented for any other optimization problem.

In Section 7.6 numerical examples of the whole process applied to a bridge and to an electrical mast are displayed.

7.2 Setting of the problem

Let $D \subset \mathbb{R}^3$ be a fixed smooth bounded open set (the working domain) and $\Omega \subset D$ the reference configuration of an isotropic elastic body. The structure Ω is clamped on $\Gamma_D \subset \partial\Omega$, and submitted to surface loads g on $\Gamma_N \subset \partial\Omega$. For simplicity these parts Γ_D and Γ_N of the boundary are assumed to be fixed subsets of ∂D. We assume that the solid is made of an homogeneous isotropic linear elastic material of Hooke's law A, with Lamé coefficients λ and μ. The displacement u and the stress tensor σ are then solutions of the system

$$\begin{cases} \operatorname{div}(\sigma) = 0 & \text{in } \Omega, \\ \sigma = Ae(u) & \text{in } \Omega, \\ u = 0 & \text{on } \Gamma_D, \\ \sigma \cdot n = g & \text{on } \Gamma_N, \\ \sigma \cdot n = 0 & \text{on } \Gamma = \partial\Omega \setminus (\Gamma_D \cup \Gamma_N), \end{cases}$$

where $e(u) = \frac{1}{2}(\nabla u + \nabla u^T)$ is the strain tensor (the symmetrized gradient of the displacement). Shape and topology optimization consists in determining the domain Ω that minimizes a given objective function J,

$$\begin{aligned} &\min && J(\Omega) \\ &|\Omega| \le V, \\ &\Gamma_D \cup \Gamma_N \subset \partial\Omega \end{aligned} \tag{7.1}$$

where $V \in \mathbb{R}^+$ is the maximum admissible volume. A typical objective function is the compliance

$$J(\Omega) = \int_{\Gamma_N} g \cdot u \, ds \, .$$

As is well known [Allaire 2002a], for most cost functions J, problem (7.1) does not admit a solution. This is due to the fact that composite shapes, made of very small microstructures,

can always outperform genuine shapes made of plain material. A composite shape is described by the local density $\theta(x)$ of material and a homogenized elasticity tensor $A^*(x)$ that depends on the microstructure at the point $x \in D$. The homogenized or macroscopic displacement u^* of the structure is then solution of the system

$$\begin{cases} \mathrm{div}(\sigma) = 0 & \text{in } D, \\ \sigma = A^* e(u^*) & \text{in } D, \\ u^* = 0 & \text{on } \Gamma_D, \\ \sigma \cdot n = g & \text{on } \Gamma_N, \\ \sigma \cdot n = 0 & \text{on } \Gamma = \partial D \setminus (\Gamma_D \cup \Gamma_N). \end{cases}$$

We emphasize that the mechanical problem is now defined on the whole working domain D and no longer on a shape $\Omega \subset D$. Then, the minimization problem should be rewritten as a minimization problem of a relaxed cost function J^* with respect to the homogenized elasticity tensor A^* and the density θ

$$\begin{array}{c} \min \qquad\qquad J^*(\theta, A^*)\,, \\ \int_D \theta(x)\,dx \le V, \\ A^*(x) \in G_\theta(x) \text{ a.e. } x \in D \end{array} \tag{7.2}$$

where $G_\theta(x)$ is the set of effective or homogenized Hooke's laws for microstructures of density $\theta(x)$. The main difficulties in the homogenized formulation (7.2) are, first, to compute the relaxed cost function J^* (which may be different from the original cost function J), second and more importantly, to give a complete and explicit description of the set of admissible Hooke's laws G_θ. It is only for special cases (like compliance minimization) that (7.2) can be made fully explicit [Allaire 2002a]. Furthermore, composite shapes are only ideal mathematical objects. Very often, optimal composites are multi-scale microstructures (like sequential laminates) which cannot be actually built as they are made of infinitely small details. To circumvent these obstacles, we restrict the set of admissible composites to periodic microstructures for which the Hooke's law can be numerically computed and, furthermore, which can be explicitly projected on a so-called lattice structure as in [Allaire 2018], [Pantz 2008]. Of course, optimizing periodic composites is an old idea that goes back at least to [Bendsøe 1988]. The new idea here is that this periodic microstructure will be projected to build a sequence of genuine non composite shapes with increasing levels of detail that converges toward the optimal periodic composite.

7.3 Preprocessing : homogenized Hooke's laws of the microstructures

7.3.1 Set of admissible microstructures

From now on, we limit our analysis to a simple class of periodic composites, which is a natural extension to 3-d of the one used in the seminal paper [Bendsøe 1988]. The periodic cell is the unit cube drilled from face to face by three cylindrical holes with rectangular cross sections (see Figure 7.1). Hence this class of composites is parametrized by its geometric parameters

$m = (m_1, m_2, m_3)$, where (m_{i-1}, m_{i+1}) denotes the size of the holes rectangular cross sections perpendicular to direction e_i. We emphasize the fact that we only have three dimensions, since each hole has a common dimension with each of the two remaining holes. The periodic cell with geometric parameters m is denoted $Y(m)$. The solid volume fraction in $Y(m)$ is $\theta(m) = 1 - m_1m_2 - m_1m_3 - m_2m_3 + 2m_1m_2m_3$. A mathematically more precise definition of the cell $Y(m)$ is given in Section 7.5.1. Moreover, the cubic cell can be freely oriented in the space. This orientation is denoted by ω (an explicit definition of ω will be given later in Section 7.3.3).

Rank 3-laminates are known to reach the optimum for single-load compliance minimization problems [Allaire 2002a]. The directions of lamination are given by the principal direction of the stress tensor and, consequently, form an orthogonal basis. There are two regimes for the optimal proportions of lamination. First, where the stress tensor is quite isotropic, the optimum laminate is a non degenerate rank-3 laminate. This microstructure features closed holes. Second, where the stress tensor is strongly anisotropic (the principal stress in one direction is much larger than in the orthogonal plane), the optimum is reached by a degenerate rank-3 laminate, namely a rank-2 laminate. Such a microstructure looks like tubular holes in the direction of the largest principal stress. In any case, those laminates feature up to three well separated microscopic scales and thus they are far from being manufacturable, even by additive manufacturing processes. Hence we have to choose a simpler microstructure, featuring a single microscopic scale, probably sub-optimal but manufacturable. Another reason for choosing the periodic cell of Figure 7.1 is that it does not contain closed holes (contrary to rank-3 laminates) and thus the metal powder can be recovered after the building process. Indeed, another possible periodic cell, which would be more similar to a rank-3 laminate, is a cubic cell with solid walls and a closed hole. However it is not manufacturable since the metal powder would be trapped in the closed hole and could not be removed Hence, our choice of periodic cell is not the union between three orthogonal planes, but their intersection, resulting in through holes. Obviously, this microstructure is not optimal, and could be improved (for example, by rounding its corners and edges to avoid local stress concentrations), possibly at the detriment of the manufacturability. Eventually, other manufacturable microstructures could be considered. For example a generalization of a rank-2 laminate (from the second regime), namely a material featuring through tubular holes, may be relevant, although not optimal, in the single-load compliance minimization problem. Other manufacturable orthotropic materials, dedicated to additive manufacturing are developed [Martínez 2017b] and could be good candidates too. We emphasize that orthotropic periodic materials whose elastic properties can be modulated through cell parameters in three orthogonal directions separately, like rank-3 laminates, are the best candidates for single-load compliance minimization problems. Indeed, in our numerical experiments, see Chapter 3, compliance minimization with isotropic cells, like Kelvin foams [Li 2006], or orthotropic cells modulated only by density, leads to black and white designs (with almost no composite zones of intermediate densities), less optimal than the structures computed by the present method. In other words, these microstructures are self-penalizing (a feature already remarked for isotropic materials in [Aubry 1999]). In any case, the present optimization method could be implemented for other orthotropic composites without any additional work.

Remark 12. *Recall that we focus here on single-load compliance minimization problems (see*

Remark 13). For other objective functions, suitable microstructures are not discussed here and should be investigated.

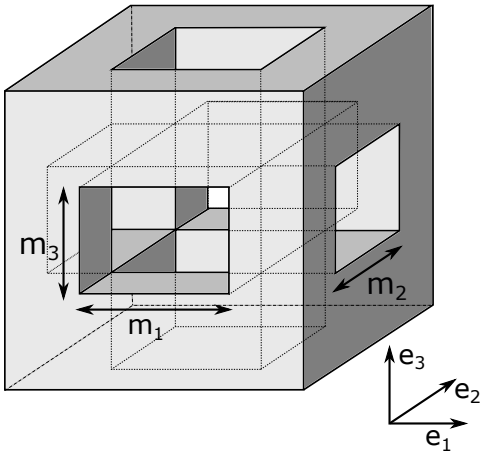

Figure 7.1: Periodicity cell $Y(m)$.

7.3.2 Cell problem and homogenized elasticity tensor

The periodic cell $Y(m)$ is the unit cube perforated by holes, the boundary of which is denoted by Γ_{int}. It defines a composite material which has a macroscopic of effective behavior characterized by an homogenized elasticity tensor A^*. In other words, the local geometry of the cell $Y(m)$ is enough to describe the elastic properties of the composite material. More detailed explanations about the homogenization method could be found on Chapter 2.

To compute this homogenized tensor A^*, one needs so-called *correctors* w_{ij}, corresponding to the local displacements in the cell $Y(m)$, defined for each pair $(i,j) \in \{1,2,3\}^2$ as the solutions of the following *cell problem*

$$\left\{ \begin{array}{cc} \mathrm{div}(A(e_{ij}+e(w_{ij}))) = 0 & \text{in } Y(m) \\ A(e_{ij}+e(w_{ij}))n = 0 & \text{on } \Gamma_{int} \\ y \mapsto w_{ij}(y) & (0,1)^3\text{-periodic} \end{array} \right. \tag{7.3}$$

where $e_{ij} = \frac{1}{2}(e_i \otimes e_j + e_j \otimes e_i)$ is a basis of the symmetric tensors of order 2 and n is the normal to the hole boundaries Γ_{int}. This problem admits a unique solution, up to an additive translation. The variational formulation of the cell problem (7.3) is: find $w_{ij} \in H^1_{\#}(Y(m),\mathbb{R}^3)$ such that

$$\forall \phi \in H^1_{\#}(Y(m),\mathbb{R}^3) \quad \int_{Y(m)} Ae(w_{ij}) : e(\phi) + \int_{Y(m)} Ae_{ij} : e(\phi) = 0\,. \tag{7.4}$$

The tensor A^* is then given in terms of the solutions w_{ij} of the *cell problems* by

$$A^*_{ijkl} = \int_{Y(m)} A(e_{ij}+e(w_{ij})) : (e_{kl}+e(w_{kl}))dy \quad \forall i,j,k,l \in \{1,2,3\}. \tag{7.5}$$

The above equation defines indeed a coercive fourth order tensor with the suitable symmetric properties of an elasticity tensor.

Since the geometry of the cell $Y(m)$ depends on the parameter m, the corresponding homogenized elastic tensor depends on the parameters m too, and it is denoted $A^*(m)$. The sensitivity of the homogenized tensor $A^*(m)$, with respect to m, is given by the same formula than in 2-d, (see Chapter 4, equation (4.6)). Since, by virtue of its definition (7.5), A^*_{ijkl} is an energy, computing the sensitivity of $A^*(m)$ is a self-adjoint problem (no adjoint are necessary) and the derivative formula is easily obtained by differentiating (7.5) with respect to the shape.

7.3.3 Cell orientation

The periodic cells $Y(m)$ may be oriented and their orientation can vary in the working domain D. Indeed, they are orthotropic: they feature three orthogonal planes of symmetry. Therefore, their elastic behavior depends also on their 3-d orientation, denoted ω. The homogenized elastic tensor will be denoted $A^*_\omega(m)$ (the orientation is in subscript in the chosen notation). Indeed, thanks to a rotation operator, the homogenized tensor $A^*_\omega(m)$ can easily be computed for any orientation ω from $A^*_{\omega_0}(m)$, where ω_0 is an arbitrary orientation. Consequently, if the orientation is fixed, the homogenized tensor can be seen as depending only on the geometric parameters. On the contrary, the geometric parameter m is an intrinsic variable of the elasticity tensor.

The modeling of the cell orientation in 3-d is a delicate problem: one could use Euler angles or quaternions for example. However our choice is dictated by the optimization method. Indeed, the optimal orientation in a compliance minimizing problem with orthotropic cells is given by the three principal directions of the stress tensor (see Section 7.4.1). Hence, we view the orientation ω as the set of three unit vectors aligned with the principal directions: $\omega = (\omega_1, \omega_2, \omega_3)$. Those vectors form an orthonormal basis, since they are eigenvectors of a symmetric matrix, here the stress tensor.

The reference orientation of the cell is the canonical basis $\omega_0 = (e_1, e_2, e_3)$, as in Figure 7.1. For simplicity, we set $A^*_{\omega_0}(m) = A^*(m)$.

Let $SO(3)$ be the special orthogonal group, and let $Q(\omega) \in SO(3)$ be the rotation matrix, whose columns are respectively the unit vectors ω_1, ω_2 and $\pm\omega_3$. We emphasize that in order to define a rotation matrix (i.e. an element of $SO(3)$), we have to ensure that its determinant is equal to 1, and not to -1: this defines the sign of $\pm\omega_3$. Eventually $Q(\omega)$ is the rotation matrix between the orientations ω_0 and ω.

Let $R(\omega)$ be the fourth-order tensor defined by :

$$\forall \xi \in \mathcal{M}_3^s \quad R(\omega)\xi = Q(\omega)^T \xi Q(\omega)\,,$$

where $\mathcal{M}_3^s$ is the set of 3×3 symmetric matrices. The dependency of $A^*_\omega(m)$ with respect to the orientation ω can be made explicit as follows:

$$A^*_\omega(m) = R(\omega)^T A^*(m) R(\omega)\,. \tag{7.6}$$

We emphasize that the knowledge of $R(\omega)$ does not define uniquely ω, since the vectors ω_i are chosen arbitrarily up to their sign. This particularity is inherited from the principal directions of the stress tensor. However, the signs of the vectors ω_i have no impact on the result of equation (7.6).

7.3.4 Numerical implementation

The set of effective elasticity tensors $\{A^*(m) \text{ such that } m \in [0,1]^3\}$ has to be characterized. The proposed strategy consists in computing the material properties for a discrete sample of parameters values and using the collected data to construct a surrogate model for the constitutive law (by a simple interpolation).

A few remarks lead to a massive reduction of the cost of this characterization. First, the considered cells are orthotropic, hence only 9 coefficients (out of 36) of the homogenized tensor $A^*_{\omega_0}(m)$ have to be computed in order to characterize it. Second, the homogenized tensor does not have to be computed on the whole admissible set $[0,1]^3$ of the geometric parameters m. Indeed, a permutation s of the parameters m_i is equivalent to a rotation of $R(s(\omega_0))$, where $s(\omega) = (\omega_{s(1)}, \omega_{s(2)}, \omega_{s(3)})$. Hence, we run the characterization of $A^*_{\omega_0}(m)$ only on the subset $\{m \in [0,1]^3 \,|\, m_1 \leq m_2 \leq m_3\}$, dividing by a factor 6 the number of samples.

The computations of $A^*(m)$ are performed with FreeFem++ [Hecht 2012]. We used a regular discretization of parameters values, with 20 elements in each direction. The homogenized tensor is numerically represented as a $P1$ function over the domain $[0,1]^3$. Hence the interpolation giving the homogenized tensor on the whole domain is automatically computed by FreeFem++. The Young modulus of the isotropic material used to design those cells is $E = 15GPa$ and its Poisson's ratio is $\nu = 0.35$.

Results for $A^*(m)$ can not be easily displayed since it would involve 3-d plots. Therefore we content ourselves in displaying only two slices of $A^*(m)$ in Figures 7.2(a) and 7.2(b). The parameter m_3 is fixed to 0.5 and the parameters m_1 and m_2 vary from zero to one. The coefficient A^*_{1111} (respectively A^*_{3333}) and its gradient are displayed on Figure 7.2(a) (respectively 7.2(b)). Those coefficients are smooth functions of m_1 and m_2. Moreover they decrease when m_1 (respectively m_2) increases, as is expected. The entry A^*_{1111} is more sensitive to a variation of m_2 when m_1 is fixed than the opposite. Indeed, the larger the $m_2 \times m_3$ rectangular hole, the weaker the cell is in the direction x_1. Moreover, when $m_2 = 0$ (resp. $m_1 = 0$), the cell features a crack of normal e_2 (resp. e_1): the homogenized properties do not reach the ones of the full material. The entry A^*_{3333} is a symmetric function of the parameters m_1 and m_2. Indeed, in the direction x_3, the more significant source of loss of rigidity comes from the $m_1 \times m_2$ rectangular hole, no matter its orientation. When $m_1 = m_2 = 0$, the cell features a crack line in the direction x_3. For a load in the same direction, the crack line has no impact: the homogenized coefficient A^*_{3333} is equal to the same coefficient of the full material: A_{3333}.

7.4 Processing: optimization among the set of periodic composite materials

7.4.1 Settings of the homogenized problem

In this paper, only compliance minimization problems, as defined in Section 7.2, are considered. Recall that its relaxed version for composite designs amounts to minimize the cost function

$$J^*(\theta, A^*) = \int_{\Gamma_N} g \cdot u^* \, ds,$$

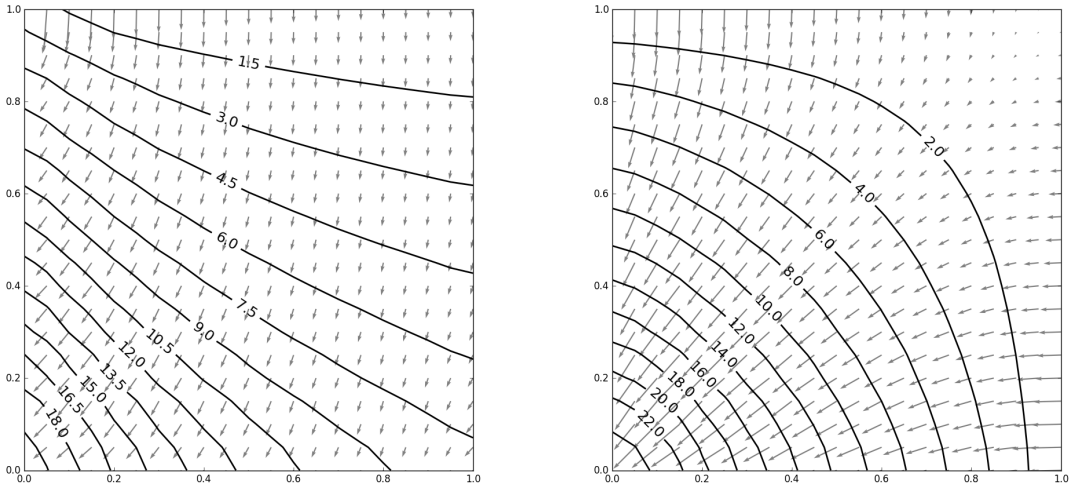

(a) $A^*_{1111}(m_1, m_2, 0.5)$ with $A_{1111} = 25.58$ (b) $A^*_{3333}(m_1, m_2, 0.5)$ with $A_{3333} = 25.58$

Figure 7.2: Isolines of the entries of the homogenized coefficients A^*_{1111} (left) and A^*_{3333} (right) and their gradients (small arrows) according to the parameters m, with $m_3 = 0.5$. The x-axis is m_1, the y-axis is m_2

which is also equal to the minimum of complementary energy

$$J^*(\theta, A^*) = \min_{\tau \in H_0} \int_D A^{*-1}\tau : \tau \, \mathrm{dx},$$

where

$$H_0 = \left\{ \tau \in L^2(D; \mathcal{M}_3^s) \text{ such that } \begin{array}{l} \operatorname{div}(\tau) = 0 \text{ in } D \\ \tau n = g \text{ on } \Gamma_N \\ \tau n = 0 \text{ on } \Gamma \end{array} \right\}.$$

Thus, this compliance minimization problem can be recast as a double minimization problem over the stress field and the admissible microstructures [Allaire 2002a]. Namely, it is equivalent to:

$$\begin{array}{c} \inf \\ \sigma \in H_0 \\ m \in L^\infty(D; [0,1]^2) \\ \omega \in L^\infty(D; W) \\ \int_D \theta(m) \, \mathrm{dx} \leq V \end{array} \quad \int_D A^{*-1}_\omega(m)\sigma : \sigma \, \mathrm{dx},$$

where

$$\theta(m) = 1 - m_1 m_2 - m_1 m_3 - m_2 m_3 + 2 m_1 m_2 m_3$$

is the local density of the periodic microstructure of parameters m and

$$W = \{(\omega_1, \omega_2, \omega_3) \in (\S^2)^3 \text{ such that } \forall i, j \in \{1,2,3\} \quad \omega_i \cdot \omega_j = \delta_{ij}\} \tag{7.7}$$

where $\S^2$ is the unit sphere in $\mathbb{R}^3$ and δ_{ij} is the Kronecker symbol.

In order to solve this problem, we use an alternate minimization algorithm [Allaire 2002a], minimizing successively with respect to the stress field σ, the cell parameters m and the orientation ω of the cell. We introduce the corresponding Lagrangian

$$\mathcal{L}(m, \omega, \sigma, \ell) = \int_D A_\omega^{*-1}(m)\sigma : \sigma \, \mathrm{dx} + \ell \left(\int_D \theta(m) \, \mathrm{dx} - V \right), \tag{7.8}$$

where ℓ is the Lagrange multiplier associated to the volume constraint.

To minimize with respect to the geometric parameters m, we use a projected gradient algorithm. Minimizing with respect to the stress field σ amounts to solve the elasticity problem with a material of elasticity tensor equal to $A_\omega^*(m)$ in D. For more details on both minimizations, which are completely similar in 3-d to the 2-case, we refer to our previous work [Allaire 2018]. However the minimization with respect to the orientation ω is different in 3-d, compared to 2-d, and is presented in full details.

Recall that there are various representations for 3-d orientation, like Euler angles or quaternions. They could be valid choices if a gradient descent method was used to compute the optimal orientation. However, this strategy may not be very efficient due to the occurrence of possible local minima. Besides, as proved by Pedersen [Pedersen 1989] in 2-d and Norris [Norris 2005] in 3-d, the optimal orientation of an orthotropic cell is given by the principal directions of the stress tensor. This result motivates our choice of modeling the orientation as the set of three unit vectors forming an orthonormal basis: $\omega = (\omega_1, \omega_2, \omega_3)$. Then the rotation matrix $Q(\omega)$ is simply the change-of-basis matrix from (e_1, e_2, e_3) to $(\omega_1, \omega_2, \pm\omega_3)$, the sign $\pm$ being chosen so that $\det Q(\omega) = 1$ (see Section 7.3.3 for more details).

At each iteration n of the optimization algorithm, the updated orientation $\omega_{n+1}(x)$ is then given by the three normalized (i.e. unit) eigenvectors of the stress tensor $\sigma_{n+1}(x)$. Moreover the vectors $(\omega_1, \omega_2, \omega_3)$ are labelled according to their associated eigenvalue (taken with their sign): from the smaller one to the larger one. Of course, unit eigenvectors are defined only up to their sign: they are not uniquely defined and only their direction is unambiguously defined. However, this sign ambiguity has no influence on the rotation operator $R(\omega)$, defined by (7.6).

Remark 13. *This approach is more efficient than the gradient descent method, mainly because it is a global minimization method, providing an optimal orientation at each iteration. However it works only for compliance minimization problem. For other objective functions, other methods should be implemented.*

The complete optimization algorithm is the same as in 2-d [Allaire 2018]. It is an iterative method, structured as follows :

1. Initialization of the design parameters (m, ω), for example we take $m_1 = m_2 = m_3$, constant satisfying the volume constraint, and $\omega = \omega_0 = (e_1, e_2, e_3)$.

2. Iteration until convergence, for $n \geq 0$:

(a) Computation of the stress σ^n through a problem of linear elasticity with $A^*_{\omega^n}(m^n)$ as elasticity tensor.

(b) Updating the orientation ω^{n+1}, using Norris formula.

(c) Updating the cell parameters m^{n+1} by one step of a projected gradient algorithm where the descent direction is given by the derivative according to m of the Lagrangian (7.8) evaluated at σ^n and ω^n.

This topology optimization algorithm was implemented in the finite element software FreeFem++ [Hecht 2012] (see [Allaire 2006] for the use of FreeFem++ in optimal design). All unknown fields are discretized using $P1$-functions.

At each iteration and for each node of the mesh, the principal directions of the stress tensor σ_{n+1} are computed thanks to the library *lapack*. They are ordered according to their respective eigenvalue. In practice, Voigt notations are used, in order to replace tensors product by matrix product. Hence, the fourth-order tensor $R(\omega)$ is represented by a 6×6 matrix. Its expression in terms of ω is given in the appendix.

7.4.2 Numerical results and discussion

The previous optimization algorithm is discussed and illustrated for a cantilever problem, for which the boundary conditions are displayed on Figure 7.3. Other examples are performed in Section 7.6. The domain size is $15 \times 10 \times 5$ and it is discretized by a tetrahedral mesh with 3604 elements and 959 vertices. This mesh is coarse, a parallel implementation would enable the use of finer meshes. Decomposition domain methods [Dolean 2015] are available in FreeFem++, hence our algorithms could be parallelized with only few additional work. This has to be investigated.

The volume constraint is fixed at 35% of the working domain. The convergence history is displayed on Figure 7.4 : the algorithm converges smoothly and quickly.

The optimized density θ and cell parameter m displayed on Figure 7.5. As usual, 3-d results are difficult to display clearly because only external borders are represented. Therefore, in Figure 7.6 various iso-surfaces of the density field are plotted. The optimized structure is clearly not a black and white design. High densities are reached only around where Dirichlet and Neumann boundary conditions are applied. The major part of the domain is filled with intermediate or grey densities. Similarly, the optimized geometric parameters (m_1, m_2, m_3) vary in their full range from 0 to 1 and they are not equal in a large region of the domain. The obtained optimal composite is clearly not isotropic. Moreover, the optimal orientation is displayed on Figures 7.7(a), 7.7(c) and 7.7(e). It is not constant in the whole domain : the obtained optimal composite takes advantage of the anisotropy of the cells.

For the sake of comparison, the same test case has been performed with different homogenized properties. Since minimal compliance for a single load-case is known to be reached by rank-3 laminates [Allaire 2002a], the optimal design for such laminates has also been computed. For the sake of brevity, the resulting design is not displayed here. The rank-3 laminate compliance is equal to 14.802 and is indeed lower than the compliance reached by our periodic optimal homogenized structure, which is 20.933. Such a large gap in performance is obviously due to

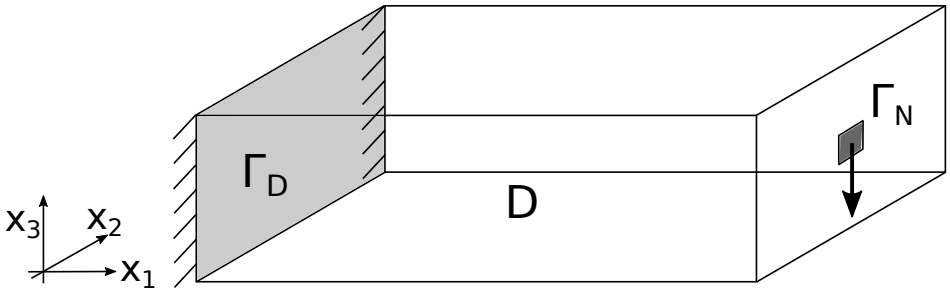

Figure 7.3: Boundary conditions for the cantilever problem

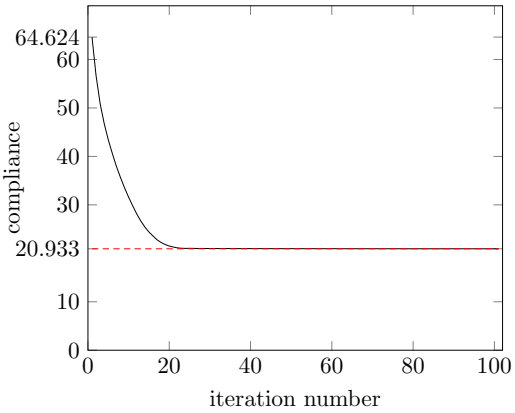

Figure 7.4: Convergence history of the objective function (compliance) for the bridge

our constraint of choosing a periodic cell with connected holes (see Figure 7.1) for manufacturability reasons, while the rank-3 laminates feature closed holes which are definitely better for structural performance. Another comparison is made with the Solid Isotropic Material with Penalization (SIMP) method, including a sensitivity filter (in order to avoid checkerboards). The homogenized tensor A^* is replaced by $\theta^p A$ where A is the pure material Hooke's law and the maximal exponent is $p = 3$ in the power law of the density. The result is displayed in Figure 7.8 since it is a black and white design, more suitable to be displayed. The optimal compliance reached by this method is 22.401, which is 7% greater than the compliance reached by the optimal periodic homogenized structure. The discretized mesh was the same for all test cases, as well as the ersatz material (0.1% of the elastic tensor of the isotropic material).

7.4.3 Regularization of the orientation

The orientation might be not very smooth in some regions, in particular in the areas of either full or zero density, in which the material is isotropic. Hence, it is possible to regularize the orientation field without changing too much the performance of the final structure. The interest in regularizing the orientation is crucial for the post-processing stage to lead to reasonable results. The orientation in those black and white areas has no influence on the performances of the homogenized structure. However, they may sensibly degrade the computation of the grid map φ, which distorts a regular grid in order to align the cells along a given local orientation,

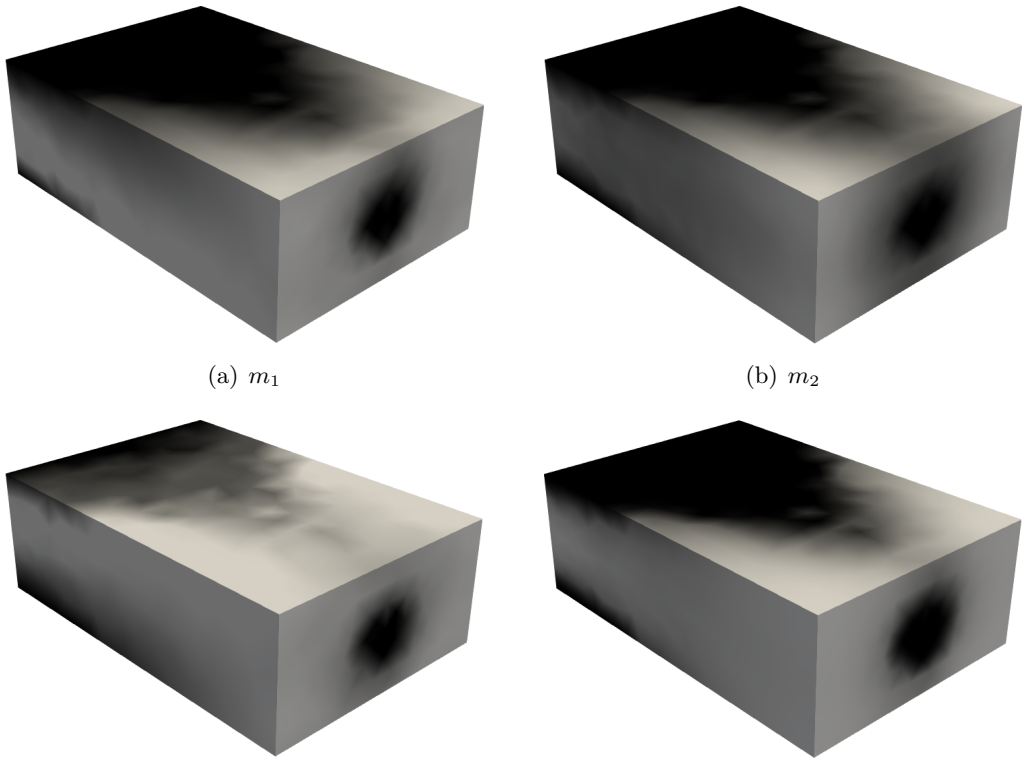

(a) m_1 (b) m_2

(c) m_3 (d) density

Figure 7.5: Optimized geometric parameters m and density of the cantilever

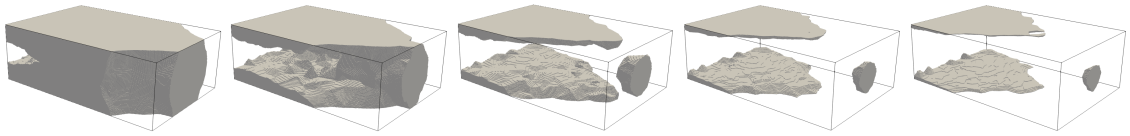

(a) $\theta \geq 10\%$ (b) $\theta \geq 25\%$ (c) $\theta \geq 50\%$ (d) $\theta \geq 75\%$ (e) $\theta \geq 90\%$

Figure 7.6: Threshold of the domain according to the optimized density θ for the cantilever case

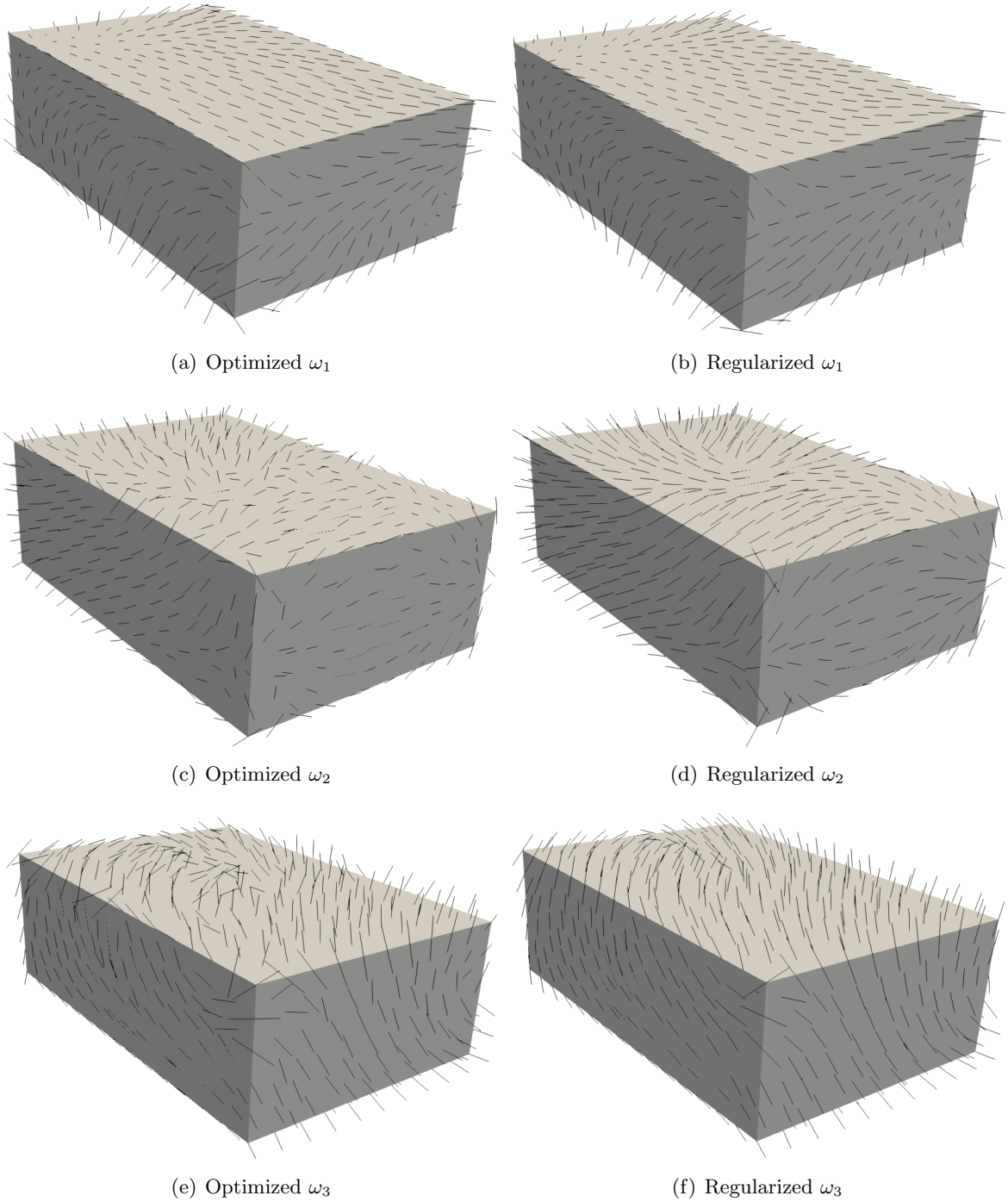

(a) Optimized ω_1

(b) Regularized ω_1

(c) Optimized ω_2

(d) Regularized ω_2

(e) Optimized ω_3

(f) Regularized ω_3

Figure 7.7: Optimized (left) and regularized (right) orientation for the cantilever case

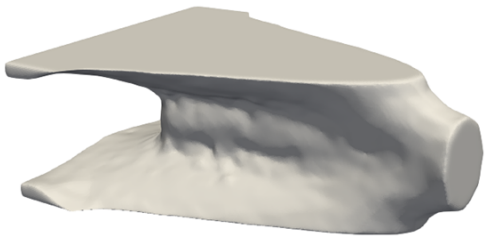

Figure 7.8: Optimized design of the cantilever with penalized SIMP method

see Section 7.5.

Classically, in order to regularize the orientation, we would like to minimize a function:

$$\sum_{i=1}^{3} ||\nabla \omega_i||^2_{L^2(D)} \,,$$

where $||\cdot||^2_{L^2(D)}$ denotes the integral over D of the (squared) Frobenius norm (the same notation shall be used for tensors of order 3 and 4 too).

However, since the orientation vectors ω_i are the principal directions of the stress tensor, they are defined locally up to their sign and can feature discontinuities. Then, there is no hope to compute directly their gradient. A possible approach would be to introduce a manifold, like in [Allaire 2018] in order to evaluate the gradients. This approach is doable but since we use an iterative algorithm in order to regularize the orientation, we should recompute interpolation operators at each iteration, which is too time-consuming.

Regularized cost function. We present here another approach, based on the fact that the ω_i are computed as the principal directions of a symmetric matrix. The main idea amounts not to regularize directly the orientation ω but rather a symmetric matrix $M(\omega)$, independent of the arbitrary chosen sign for the orientation vectors ω_i. Recall that $Q(\omega)$ is the rotation matrix from (e_1, e_2, e_3) to $(\omega_1, \omega_2, \pm\omega_3)$. Let $\mathcal{D}(\lambda)$ be the diagonal matrix, with entries $\lambda_1 = -1$, $\lambda_2 = 1$ and $\lambda_3 = 0$. We define a symmetric matrix M by

$$M(\omega) = Q(\omega)^T \mathcal{D}(\lambda) Q(\omega) \,, \tag{7.9}$$

whose eigenvalues are λ_i and associated eigenvectors are ω_i. Since we want to regularize the orientation without degrading the compliance, we introduce a new cost-function to minimize:

$$J_{\text{reg}}(m, \omega) = \int_D A^{*-1}_\omega(m)\sigma : \sigma dx + \eta^2_{\text{reg}} ||\nabla M(\omega)||^2_{L^2(D)} \,,$$

with σ the stress tensor solution of the elasticity problem and $\eta_{\text{reg}} > 0$, a small coefficient. In practice, $\eta_{\text{reg}} = 0.1$ works well.

Approximate minimization. We now describe a SQP type algorithm to minimize this cost function J_{reg} with respect to ω. The optimization process with respect to m is unchanged. At each iteration n, we approximate J_{reg} at second order in $\delta\omega$, around the current state, by

$$J_{\text{approx}}(m, \omega + \delta\omega) = J_{\text{reg}}(m, \omega) + < J'_{\text{reg}}(m, \omega), \delta\omega > + \frac{1}{2} < J''_{\text{reg}}(m, \omega)\delta\omega, \delta\omega > \,. \tag{7.10}$$

In theory, $\omega + \delta\omega$ should belong to W, defined by (7.7). Since the sign of the vectors of the orientation does not matter, we can impose without loss of generality that ω and $\omega + \delta\omega$ have the same determinant. In other words, ω and $\omega + \delta\omega$ are both either direct triads or indirect triads and we have:

$$\forall i \in \{1,2,3\} \quad \omega_i + \delta\omega_i = S\omega_i, \quad \text{where} \quad S = Q(\omega + \delta\omega)Q(\omega)^T \in SO(3)\,, \tag{7.11}$$

where $SO(3)$ is the special orthogonal group. First, we change the unknown, from $\delta\omega$ to S, in the minimization of J_{approx}. Second, we write the necessary and sufficient optimality condition of this minimization problem as the variational problem consisting in finding $S^n \in H^1(D, SO(3))$ such that for all test functions $T \in H^1(D, SO(3))$:

$$\begin{aligned} & < J'_{\text{reg}}(m, \omega^n), ((T - Id_3)\omega^n) > \\ + \quad & < J''_{\text{reg}}(m, \omega^n)((S^n - Id_3)\omega^n), ((T - Id_3)\omega^n) >= 0 \end{aligned} \tag{7.12}$$

The orientation is then updated with:

$$\omega^{n+1} = S^n \omega^n.$$

Nevertheless, problem (7.12) is still too complex. So, we approximate it by another variational problem whose unknown is no longer a field of orthogonal matrices in $SO(3)$, but a field of vectors in $\mathbb{R}^3$. This approximation is based on the following idea: since an iterative method is used for regularizing the orientation, between two iterations the orientation should not change drastically. This means that the rotation matrix S^n should be close to the identity Id_3. Hence the variational formulation (7.12) is approximated in a neighbourhood of Id_3, which is not a subset of $SO(3)$ (the numerical approximation of a neighbourhood of Id_3 in $SO(3)$ is too complicated). In what follows we explain how to construct this neighbourhood. First, the set of admissible rotation matrices S in the variational problem (7.12) is parametrized. Second, this parametrization allows us to build a neighborhood of Id_3.

Since the unknown matrix S^n in (7.12) is close to the identity, -1 is not one of its eigenvalues. The Cayley transform ensures there exists an involution between the set of skew-symmetric matrices and the set of orthogonal matrix, for which no eigenvalue is equal to -1. Hence, the set of admissible rotation matrices $SO(3)$ in the variational problem (7.12) can be restricted to:

$$\{(Id_3 - N)^{-1}(Id_3 + N) \quad | \quad N \in \mathcal{M}_3(\mathbb{R}) \,\text{such that}\, N^T = -N\}\,. \tag{7.13}$$

Using again that S^n is close to the identity Id_3, by an asymptotic expansion, we approximate (7.13) by the following neighbourhood of Id_3

$$\mathcal{V}_{Id} = \{Id_3 + 2N \quad | \quad N \in \mathcal{M}_3(\mathbb{R}) \,\text{such that}\, N^T = -N \;\text{ and }\; ||N|| << 1\}\,. \tag{7.14}$$

Skew matrices in $\mathcal{M}_3(\mathbb{R})$ can be parametrized by a vector in $\delta s \in \mathbb{R}^3$ as follows

$$F(\delta s) = \begin{pmatrix} 0 & -\delta s_3 & -\delta s_2 \\ \delta s_3 & 0 & -\delta s_1 \\ \delta s_2 & \delta s_1 & 0 \end{pmatrix}.$$

Then (7.14) can be rewritten as:

$$\mathcal{V}_{Id} = \{ Id_3 + F(\delta s) \quad | \quad \delta s \in H^1(D, \mathbb{R}^3) \quad \text{such that} \quad ||\delta s|| << 1 \} .$$

Under the hypothesis that S^n is close to Id_3, the variational problem (7.12) is approximated by a variational problem where $H^1(D, SO(3))$ is replaced by $\mathcal{V}_{Id}$. We take this opportunity to further add a penalization term on the norm of δs in order to ensure that δs is indeed small. The final approximate variational formulation is: find $\delta s^n \in H^1(D, \mathbb{R}^3)$ such that, for any test function $\delta\tau \in H^1(D, \mathbb{R}^3)$,

$$\begin{aligned} & < J'_{\text{reg}}(m, \omega^n), (F(\delta\tau)\, \omega^n) > \\ + \quad & < J''_{\text{reg}}(m, \omega^n)(F(\delta s^n)\, \omega^n), (F(\delta\tau)\, \omega^n) > \\ + \quad & \frac{1}{\eta^2_{\text{pen}}} < \delta s^n, \delta\tau >= 0 , \end{aligned} \tag{7.15}$$

where $\eta_{\text{pen}} > 0$ is a small coefficient. In practice, we take $\eta_{\text{pen}} = 1$.

Finally, to update the orientation, we compute the matrix:

$$S^n = Id_3 + F(\delta s^n) ,$$

which is not a rotation matrix, as already said. Hence ω^{n+1} is not equal to $S^n \omega^n$ but rather is given by a Gram-Schmidt orthonormalization process, applied to the set of vectors $(S^n \omega^n_1, S^n \omega^n_2, S^n \omega^n_3)$. Several approximations have been used, and their combination is not guaranteed to work well. However, in practice the algorithm converges and its implementation is rather simple.

Derivatives of J_{reg}. To make (7.15) fully explicit, we now give formulas for the derivatives of $J_{\text{reg}}(m, \omega)$ with respect to ω. From the definitions (7.9) of M and (7.11) of S, we get:

$$M(\omega + \delta\omega) = M(\omega) + \big(F^T(\delta s)\, M(\omega) + M(\omega)\, F(\delta s) \big) + F(\delta s)\, M(\omega)\, F(\delta s)^T .$$

Eventually, it leads to

$$\begin{aligned} < J'_{\text{reg}}(m, \omega), (F(\delta\tau)\delta\omega) > = & \int_D (A^{*-1}_{\omega_0}(m) R(\omega)\sigma) : (R'(F(\delta\tau)\, \omega)\sigma) dx \\ & + \eta^2_{\text{reg}} \sum_{1 \le i,j \le 3} \int_D 2 \nabla M_{i,j}(\omega) \cdot \nabla (F^T(\delta\tau)\, M + M\, F(\delta\tau))_{i,j} dx , \end{aligned}$$

and

$$\begin{aligned} < J''_{\text{reg}}(m, \omega)(F(\delta\tau)\delta\omega), (F(\delta s)\delta\omega) > = & \, 2 \int_D A^{*-1}_{\omega_0}(m) R'(F(\delta s)\omega)\sigma : R'(F(\delta\tau)\omega)\sigma dx \\ & + 2\eta^2_{\text{reg}} \sum_{1 \le i,j \le 3} \int_D 2 \nabla M_{i,j}(\omega) \cdot \nabla (F^T(\delta s)\, M\, F(\delta\tau))_{i,j} dx \\ + 2\eta^2_{\text{reg}} \sum_{1 \le i,j \le 3} \int_D & \nabla (F^T(\delta s))\, M + M\, F(\delta s))_{i,j} \cdot \nabla (F^T(\delta\tau)\, M + M\, F(\delta\tau))_{i,j} dx , \end{aligned}$$

where $R'(v)$ is the directional derivative of $R(\omega)$ in the direction v, and $A^*_{\omega_0}$ is the homogenized elasticity tensor in the reference orientation ω_0.

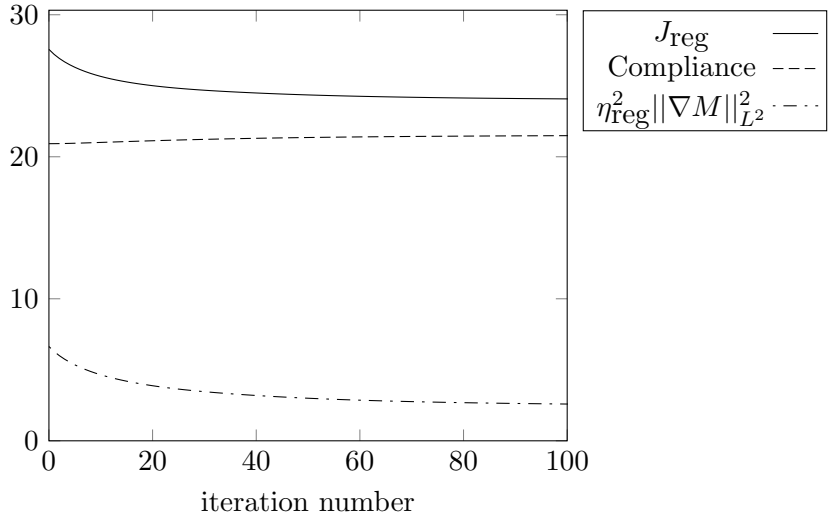

Figure 7.9: Convergence history of the regularization cost function J_{reg} for the bridge

Numerical results. The above algorithm has been implemented in FreeFem++, using again $P1$ functions for all the unknown fields. Recall that $\lambda_1 = -1$, $\lambda_2 = 1$ and $\lambda_3 = 0$. Hence the three vector fields ω_i are equally regularized. Indeed ω_1 and ω_2 have the same regularization coefficient since $|\lambda_1| = |\lambda_2|$, and the last one is fully determined by the others thanks to the orthogonality of the eigenvectors for a symmetric matrix. For the cantilever case, the regularized vector fields are displayed on Figures 7.7(b), 7.7(d) and 7.7(f). The orientation vectors are not changed much by the regularization step, except in the black and white design regions. As can be checked in Figure 7.9, during the regularization process, the compliance is only slightly increasing while the regularization term undergoes a strict decrease.

7.5 Post-Processing : projection of the optimized microstructure

The last step is to construct a sequence of classical or genuine shapes that converges toward the computed optimal composite. This sequence is indexed by a small positive parameter $\varepsilon > 0$ which is the characteristic size of the period of the periodic composite. In practice, the parameter ε is set to a value freely chosen by the user. Of course, the smaller ε, the more detailed will be the resulting genuine shape.

The main ideas are roughly the same as in 2-d, see Chapter 4 except for the following crucial points. In 2-d, we took advantage of conformal maps in 2-d in order to compute a distortion map. We can no longer make this assumption in 3-d and we present a different approach here. Moreover, the treatment of the orientation in 3-d is quite different as in 2-d, which implies to adapt our algorithms.

7.5.1 Sequences of shapes

Similarly to the 2-d case, we introduce a map $\varphi = (\varphi_1, \varphi_2, \varphi_3)$ from D into $\mathbb{R}^3$, in order to properly orient each cell locally, without connectivity failures in the final structure. This map distorts a regular grid, such that each bar in direction e_i is locally oriented along ω_i.

For all $i \in \{1, 2, 3\}$, let Y_i be defined by:

$$Y_i(m) = \left\{ y \in [0,1]^3 \text{ such that } \cos(2\pi y_i) \geq \cos(\pi(1 - m_i)) \right\}. \tag{7.16}$$

Y_i is the unit cube, cut by a central slice of normal e_i, and thickness m_i, see Figure 7.10. Our unit cells $Y_0(m)$ can then be analytically defined by:

$$Y_0(m) = \cup_{1 \leq i < j \leq 3} \left(Y_i(m) \cap Y_j(m) \right) \tag{7.17}$$

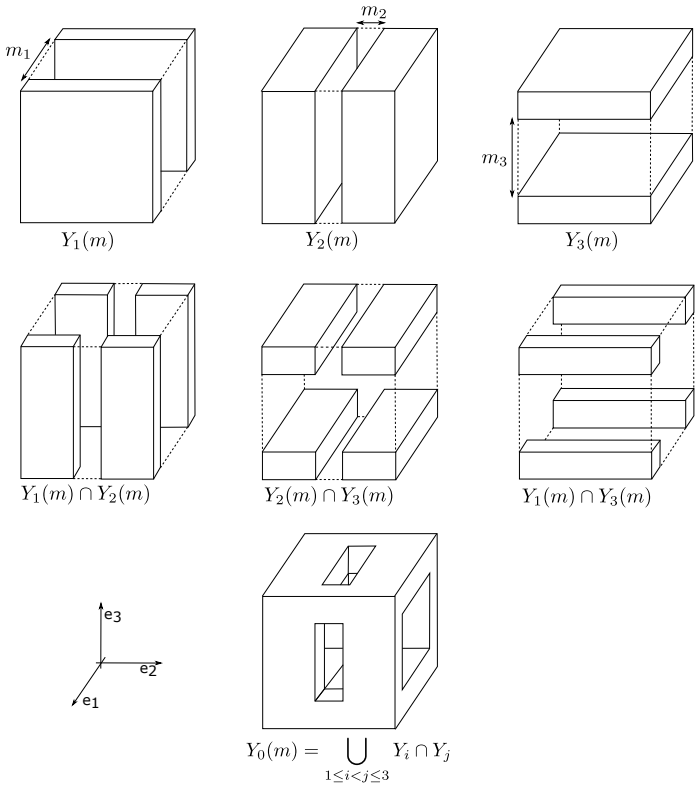

Figure 7.10: Construction of the cell $Y_0(m)$ from $Y_i(m)$.

In order to compute a sequence of genuine shapes converging to the optimized homogenized structures, we introduce ε the reference size of the cells, which is going to 0. The elements of this sequence are denoted by $\Omega_{\varphi,\epsilon}(m)$, since they depend on the map φ that gives the proper orientation. We give details about its computation further.

In periodic homogenization, we have two systems of coordinates : x, the macroscopic coordinates, and y the microscopic coordinates, indicating the position into the periodic cell. Classically, we take $y = \frac{x}{\epsilon} - E(\frac{x}{\epsilon})$ to describe a homogenized periodic structure, where $E(\cdot)$ is the

floor function.
Thanks to the map φ, that distorts the regular grid, the new macroscopic coordinates to be considered are then $\varphi(x)$. The sequence of genuine shapes is then built according to the exact same scheme as the unit cell $Y_0(m)$. Let us introduce the counterparts of $Y_i(m)$:

$$\Omega_{i,\varphi,\epsilon}(m) = \left\{ x \in D \text{ such that } \cos\left(\frac{2\pi\varphi_i(x_i)}{\epsilon}\right) \geq \cos\left(\frac{\pi(1-m_i)}{\epsilon}\right) \right\}. \tag{7.18}$$

Hence, the sequence of genuine shapes is given by:

$$\Omega_{\varphi,\epsilon}(m) = \cup_{1\leq i<j\leq 3} \left(\Omega_{i,\varphi,\epsilon}(m) \cap \Omega_{j,\varphi,\epsilon}(m)\right) \tag{7.19}$$

We emphasize that thanks to the periodicity of the cosine function, there is no need to consider the integer part of $\frac{x}{\epsilon}$ in the approximation of the microscopic coordinates.

Remark 14. *The map φ is introduced in order to take into account the optimal orientation of the cell. Hence, φ depends only on the orientation ω. In particular, φ does not depend on the size ε of the cells. Once φ has been computed, it could be used for any value of this scale parameter.*

7.5.2 Computation of the projection map φ

We are looking for a map $\varphi = (\varphi_1, \varphi_2, \varphi_3)$ from D into $\mathbb{R}^3$ such that its gradients $\nabla\varphi_i$ are aligned with ω_i. Hence, we impose for the map φ to satisfy:

$$\forall i \in \{1,2,3\} \quad \nabla\varphi_i = e^{r_i}\omega_i, \tag{7.20}$$

where r_i is a scalar field, given the local dilation of the cubic cell in the direction ω_i.

Unlike the 2-d case, we can not assume here that the three fields r_i are the same field. Indeed, if the values of r_i are locally equal to each other, infinitesimal cubes is distorted into cubes. If the fields r_i were equal everywhere to each other, then the map φ would be a conformal map. However, there is only a few conformal maps in 3-d, thanks to Liouville's theorem [Rešetnjak 1967]. Hence, it would be too restrictive to impose such a condition on the map φ.

Taking the rotational of (7.20) leads to:

$$\forall i \in \{1,2,3\} \quad (\nabla r_i \wedge \omega_i + \nabla \wedge \omega_i) = 0 \tag{7.21}$$

Those equations do not define uniquely the dilation factors r_i: they give the gradient of r_i in only two directions, the orthogonal ones to ω_i. We then penalize the third component by minimizing :

$$\forall i \in \{1,2,3\} \quad \min_{s_i} \int_D |\nabla s_i \wedge \omega_i + \nabla \wedge \omega_i|^2 + \eta_1^2 |\nabla s_i \cdot \omega_i|^2 . \tag{7.22}$$

Hence, the dilations factors are defined up to a constant, that we can fix, by small penalization of the L^2 norm of r_i.

$$\forall i \in \{1,2,3\} \quad \min_{s_i} \int_D |\nabla s_i \wedge \omega_i + \nabla \wedge \omega_i|^2 + \eta_1^2 |\nabla s_i \cdot \omega_i|^2 + \eta_2^2 |s_i|^2. \tag{7.23}$$

The minimizer $\widehat{r}_i$ is the solution of the variational formulation consisting in finding $\widehat{r}_i \in H^1(D,\mathbb{R})$ such that for all $t \in H^1(D,\mathbb{R})$:

$$\int_D (\nabla \widehat{r}_i \wedge \omega_i + \nabla \wedge \omega_i) \cdot (\nabla t \wedge \omega_i) + \eta_1^2 \, (\nabla \widehat{r}_i \cdot \omega_i)(\nabla t \cdot \omega_i) + \eta_2^2 \, \widehat{r}_i \, t = 0. \tag{7.24}$$

We emphasize that the solution $\widehat{r}_i$ of the above variational formulation does not verify the equation (7.21). Indeed, $\widehat{r}_i$ is an approximation of a theoretically perfect dilation factor r_i. In the following, we will no longer make the distinction between them, and we will indifferently write r_i.

Once the dilation factors r_i are computed for each direction, the computation of the distortion map is reduced to the following minimization problem:

$$\min_{\psi} \sum_{i=1}^{3} \int_D |\nabla \psi - e^{r_i} \omega_i|^2 \tag{7.25}$$

which can be separated in three independent minimization problems over the three components of φ. The minimizers φ_i are respectively the solutions of the variational problems consisting in finding $\varphi_i \in H^1(D,\mathbb{R})$ such that for all $\psi \in H^1(D,\mathbb{R})$:

$$\int_D (\nabla \varphi_i - e^{r_i} \omega_i) \cdot \nabla \psi = 0 \tag{7.26}$$

7.5.3 Coherent orientation

We compute separately the three components φ_i of the map φ. First, we have to compute the dilation factor r_i. We see from the variational formulation (7.24) over the dilation factor that it depends on only one of the orientation vectors, namely ω_i. Likewise, we can see from the variational formulation (7.26) over φ_i, that only the orientation vector ω_i is involved. Hence, we can consider each vector field separately.

We recall here that the representation of the optimal orientation using the vectors $\omega_\cdot$ is not unique, since it is independent of their sign.

Numerically, we only compute the principal directions of the stress tensors, without any constraint about the regularity of the fields ω_i. It might features discontinuities, coming from an uncontrolled change of sign. Because of their sign indetermination, the rotational of the vectors ω_i, like in the above variational formulation (7.24) can not be directly computed.

A first naive approach amounts to reorientate each vector field by looking over the mesh, which is not efficient in the presence of singularities in the orientation field. Therefore, we prefer a second approach, similar to the one developed in [Allaire 2018]. We introduce a manifold, defined as a two-fold covering space of the working domain. On each of those subsets the orientation vector fields are coherent and have opposed signs. Defining an atlas over those manifolds, we are now able to address this sign problem. We will give more details in the following. We do not consider the possible presence of singularities in the orientation ω in the present work.

For each i, we introduce a covering space of the working domain D:

$$\mathcal{D}_i = \{(x,T) \in D \times \S^2 \text{ such that } T \wedge \omega_i(x) = 0\}\,,$$

where $\S^2$ is the unit sphere in $\mathbb{R}^3$ (in other words, $\mathcal{D}_i$ is a submanifold of $D \times \S^2$). Let $\mathcal{U}$ be a covering of D by open sets U. Since we assume that the optimal orientation does not feature any singularity, for each open set U there exists a continuous map $T_{U,i} \in \mathcal{C}(U, \S^2)$ such that for all $x \in U$, $T_{U,i}(x) = \pm\omega_i(x)$. Two charts $g^+_{U,i}$ and $g^-_{U,i}$ of $\mathcal{D}_i$ are then defined:

$$g^+_{U,i} : \begin{array}{ccc} U & \to & \mathcal{D}_i \\ x & \mapsto & (x, T_{U,i}(x)) \end{array} \quad \text{and} \quad g^-_{U,i} : \begin{array}{ccc} U & \to & \mathcal{D}_i \\ x & \mapsto & (x, -T_{U,i}(x)) \end{array}\,. \tag{7.27}$$

If the domain D is simply connected and ω_i does not feature any singularity, the manifold $\mathcal{D}_i$ consists of two disconnected copies of the working domain D, on which the vector field ω_i is coherently oriented. Those two copies are only distinguished by the sign of T.

Integrals on the manifold $\mathcal{D}_i$. We introduce here the notion of integrals on the manifold $\mathcal{D}_i$.

Let $\mathcal{U}$ be a finite family of disjoint open subsets U covering D, and $f \in \mathcal{C}(\mathcal{D}_i, \mathbb{R})$, a continuous map. We define the integral of f over $\mathcal{D}_i$ by:

$$\int_{D_i} f(x,T)dx = \sum_{U \in \mathcal{U}} \int_U f \circ g^+_{U,i}(x)dx + \int_U f \circ g^-_{U,i}(x)dx\,, \tag{7.28}$$

where the charts $g^\pm_{U,i}$ are defined by (7.27). This definition does not depend on the family $\mathcal{U}$ of disjoint subsets.

Differential operators on the manifold $\mathcal{D}_i$. The manifold $\mathcal{D}_i$ can be endowed with a differential structure: a gradient operator and a rotational operator are induced on $\mathcal{D}_i$ as follows.

Let $x \in D$ and U be an open subset of D containing x, we define the gradient operator by:

$$\nabla f(x,T) = \nabla(f \circ g_{U,i})(x)\,,$$

where $f \in H^1(\mathcal{D}_i, \mathbb{R})$ and $g_{U,i}$ is a chart of the neighborhood of (x,T), and the rotational operator by:

$$\nabla \wedge W(x,T) = \nabla \wedge (W \circ g_{U,i})(x)\,,$$

where $W \in H^1(\mathcal{D}_i, \mathbb{R}^3)$.

Those operators do not depend of the choice of the open subset U.

Symmetric and antisymmetric maps on the manifold $\mathcal{D}_i$. We introduce the subset of symmetric maps on $\mathcal{D}_i$:

$$\mathcal{V}^s_i = \{f \in H^1(\mathcal{D}_i, \mathbb{R}) \text{ such that: } \forall (x,T) \in \mathcal{D}_i \quad f(x,-T) = f(x,T)\}$$

and of antisymmetric maps on $\mathcal{D}_i$:

$$\mathcal{V}^a_i = \{f \in H^1(\mathcal{D}_i, \mathbb{R}) \text{ such that: } \forall (x,T) \in \mathcal{D}_i \quad f(x,-T) = -f(x,T)\}\,.$$

Remark 15. *The integral of a symmetric map over the manifold $\mathcal{D}_i$ can be simply rewritten. Let $\mathcal{U}$ be a finite family of disjoint open subsets U covering D, and $f \in \mathcal{V}_i^s$. We have:*

$$\begin{aligned}\int_{D_i} f(x,T)\,dx &= \sum_{U\in\mathcal{U}} \left(\int_U f\circ g_{U,i}^+(x)\,dx + \int_U f\circ g_{U,i}^-(x)\,dx\right)\\ &= 2\sum_{U\in\mathcal{U}} \left(\int_U f\circ g_{U,i}^+(x)dx\right).\end{aligned}$$

We now have all the requirements to change our working space from D to $\mathcal{D}_i$: we are looking for a dilation map r_i from $\mathcal{D}_i$ into $\mathbb{R}$ and a grid map φ_i from $\mathcal{D}_i$ into $\mathbb{R}^3$.

Dilation map r_i**.** The dilation map r_i satisfied (7.21) on D. Therefore it also satisfies on $\mathcal{D}_i$:

$$\nabla r_i \wedge T + \nabla \wedge T = 0.$$

A solution of the above equation is also solution of the same equation where $-T$ replaces T. We emphasize that there is no unicity of the solution, since we can create a new solution from a previous one simply by adding a constant to it. Then, we assume that r_i satisfies a symmetric property on $\mathcal{D}_i$, meaning that $r_i \in \mathcal{V}_i^s$, without loss of generality. Hence, from (7.23), we compute r_i as the minimizer of:

$$\min_{s_i\in\mathcal{V}_i^s} \int_{\mathcal{D}_i} |\nabla s_i \wedge T + \nabla\wedge T|^2 + \eta^2|\nabla s_i \cdot T|^2 + \eta_N^2|s_i|^2\,dx.$$

Grid map φ_i**.** The grid map φ_i satisfies on $\mathcal{D}_i$:

$$\nabla\varphi_i = e^{r_i}T\,.$$

The opposite of a solution of the above equation is also solution of the same equation where $-T$ replaces T. As previously for the dilation maps, we emphasize there is no unicity of the solution. We assume that φ_i satisfies an antisymmetric property on $\mathcal{D}_i$, meaning that $\varphi_i \in \mathcal{V}_i^a$, without loss of generality. Hence, φ_i is the minimizer of:

$$\min_{\psi_i\in\mathcal{V}_i^a} \int_{\mathcal{D}_i} |\nabla\psi_i - e^{r_i}T|^2 dx\,.$$

7.5.4 Implementation

We present here briefly the numerical implementation using the manifolds $\mathcal{D}_i$. The reader could find more details on Chapter 4.

Let $\mathcal{T}$ be the mesh of D used during the optimization process, and $\mathcal{T}_k$, its k^{th} element (a tetrahedron). We recall that we use P_1 finite elements to discretize all fields, including the vector fields ω_i, see figure 7.12(a).

The difficulty is to represent the manifold $\mathcal{D}_i$, which is equivalent to two copies of D, using finite elements in a classical finite element solver. However, all the maps involved in this problem are either symmetric or antisymmetric on $\mathcal{D}_i$. Hence, they are completely determined by their values at (x,T), from which the other values at $(x,-T)$ are deduced by symmetry. As a consequence, a possibility would be to use only one copy of D to represent $\mathcal{D}_i$. However, this

requires to compute a coherent orientation on the whole domain D, a solution we previously declined.

Instead, we subdivide the working domain D into open subsets U whose closures covers D. In practice, the tetrahedra $\mathcal{T}_k$ of $\mathcal{T}$ are natural candidates for such purpose. Then, we work independently on each tetrahedron and compute a coherent orientation on each tetrahedron, meaning to have a continuous orientation vector field, featuring no change of sign. Hence, on each tetrahedron we can compute the rotational of the orientation vector field. The key point is that we do not require the orientation on each tetrahedron to be coherent with one another. We give more details about coherent orientation in the following.

Recall that standard P_1 conforming finite elements are used for discretization during the optimization process. However, since we work now on each tetrahedron separately, P_1 discontinuous Galerkin elements on $\mathcal{T}$ are now used for this post-processing projection. Furthermore symmetry (or antisymmetry) of the considered maps have to be taken into account, which is explained in the following.

Coherent orientation on a tetrahedron. In the whole paragraph, vector fields are discretized by their values at each vertex of the mesh. For a tetrahedron $\mathcal{T}_k$ of the mesh $\mathcal{T}$, its four vertices are denoted by $(x_j)_{1\leq j\leq 4}$. The vector field ω_i on $\mathcal{T}_k$ is defined by four vectors.

A vector field admits a coherent orientation over the tetrahedron $\mathcal{T}_k$ if there exists an affine map $\tilde{\omega}_i$ from $\mathcal{T}_k$ to $\mathbb{R}^3$ such that:

$$\forall j \in \{1,2,3,4\} \quad \text{`}\tilde{\omega}_i(x_j) = \pm\omega_i(x_j) \quad \text{and} \quad \forall x \in \mathcal{T}_k \quad \tilde{\omega}_i(x) \neq 0\,.$$

Such a coherent orientation does not necessarily exists on each tetrahedron. If not, the orientation field is said singular. In the present work, we do not treat such cases and assume that a coherent orientation does indeed exists on every element of the mesh.

In practice, for each tetrahedron, we pick a first vertex x_1, where the value $\omega_i(x_1)$ will be the reference orientation of the tetrahedron : $\tilde{\omega}_i(x_1) = \omega_i(x_1)$. For the three other vertices x_j, we choose the orientation $\tilde{\omega}_i(x_j) = \pm\omega_i(x_j)$ in order to have :

$$\tilde{\omega}_i(x_j) \cdot \tilde{\omega}_i(x_1) \geq 0\,.$$

Hence two coherent orientations could be defined on each tetrahedron, see figure (7.11), depending of the choice of the first vertex x_1 : one for each copy of D into $\mathcal{D}$.
By iterating this over the whole mesh $\mathcal{T}$ we define a P_1 discontinuous finite element on D. The different steps to construct a coherent orientation $\tilde{\omega}_i$ are represented on the Figures 7.12(a), 7.12(b) and 7.12(c). To avoid unnecessary complex figures, that would have undermined their readability, this process is illustrated in a 2-d setting, which is perfectly similar to the 3-d case.

Interpolation of symmetric maps. The value of a symmetric map $\psi \in \mathcal{V}_i^s$ at a vertex does not depend on its second variable, since $\psi(x,T) = \psi(x,-T)$. Hence, it can be represented by a standard conformal P_1 finite element function over D.

Interpolation of antisymmetric maps. We explain here how to represent an antisymmetric map of $\mathcal{D}_i$ using a standard conformal P_1 finite element function on D.

Let $\psi \in \mathcal{V}_i^a$ be an antisymmetric map. Let x_j be a vertex, and $x_{j,k}$ its copies in all tetrahedra featuring x_j. The value of ψ in each vertex $x_{j,k}$ depends on the current coherent orientation:

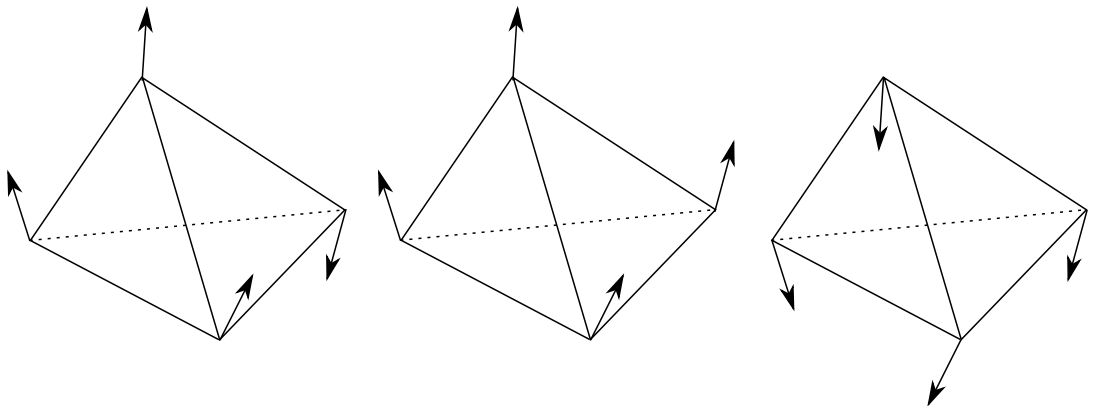

(a) ω_i (b) $\tilde{\omega}_i$ (c) $\tilde{\omega}_i$

Figure 7.11: Optimized orientation field ω_i (a) on a tetrahedron and the both possible coherent orientation fields $\tilde{\omega}_i$ from ω_i : the coherent orientation when the first vertex x_1 is the upper one (b) and the coherent orientation when the first vertex x_1 is the vertex on the right (c)

$\tilde{\omega}_i(x_{j,k}) = \pm\omega_i(x_j)$. We can order the vertices $x_{j,k}$ in two sets, X_j^+ and X_j^-, according to this sign.

All the elements of X_j^+ (resp. of X_j^-) are the same points of the manifold $\mathcal{D}$: $(x_j, \omega_i(x_j))$ (resp $(x_j, -\omega_i(x_j))$). Hence ψ is constant on X_j^+ (resp. on X_j^-). Moreover, we have $\psi(X_j^+) = -\psi(X_j^-)$.

We now have all the requirements to represent the antisymmetric maps by standard P_1 finite element functions on D. Let I be the projection operator from P_1 elements to P_1 discontinuous elements. Let g be a P_1 discontinuous finite element, see figure 7.12(d) defined by:

$$g(x_{j,k}) = \begin{cases} +1 & \text{if } \tilde{\omega}_i(x_{j,k}) = \omega_i(x_j) \\ -1 & \text{if } \tilde{\omega}_i(x_{j,k}) = -\omega_i(x_j) \end{cases}$$

Define I^a, the interpolation operator for antisymmetric maps, from P_1 finite elements on $\mathcal{D}$ to P_1 discontinuous finite element on D by $I^a = g \times I$, meaning that $I^a(\varphi)(x_{j,k}) = g(x_{j,k})\varphi(x_j)$. We emphasize that this operator is uniquely defined, but depends on the previously computed field $\tilde{\omega}_i$, the coherent orientation on each tetrahedron.

Computation of r ***and*** φ***.*** In order to compute the dilation factors and the distortion map, as seen previously, we work on each tetrahedron separately, using P_1 Galerkin discontinuous finite elements. However, as just seen, the three dilation factors r_i and the three components of the distortion map φ are represented by standard P_1 finite elements functions, composed with projection operators I and I^a.

Let $\mathcal{V}$ be the set of P_1 finite elements on $\mathcal{T}$. The dilation factor $r_i \in \mathcal{V}$ is the minimizer of:

$$\begin{aligned} \min_{s\in\mathcal{V}} \sum_{\mathcal{T}_k\mathcal{T}} \int_{\mathcal{T}_k} & |\nabla(I(s)) \wedge \tilde{\omega}_i + \nabla \wedge \tilde{\omega}_i|^2 \\ & +\eta_1^2 |\nabla(I(s) \cdot \tilde{\omega}_i|^2 \\ & +\eta_2^2 |(I(s)|^2 dx \,. \end{aligned}$$

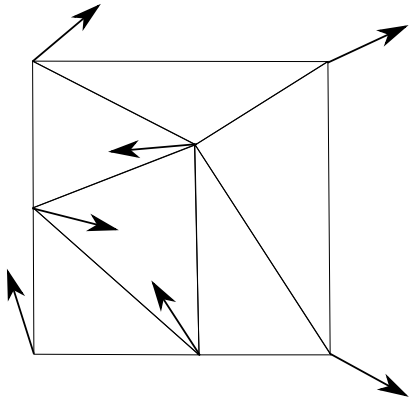

(a) Optimized orientation ω_i, defined up to its sign

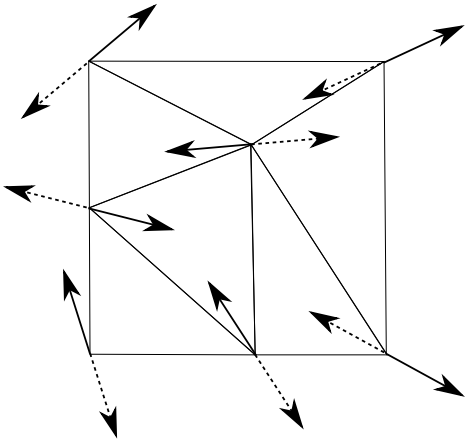

(b) Local possible orientations of the cells ω_i and $-\omega_i$, leading to the same final structure

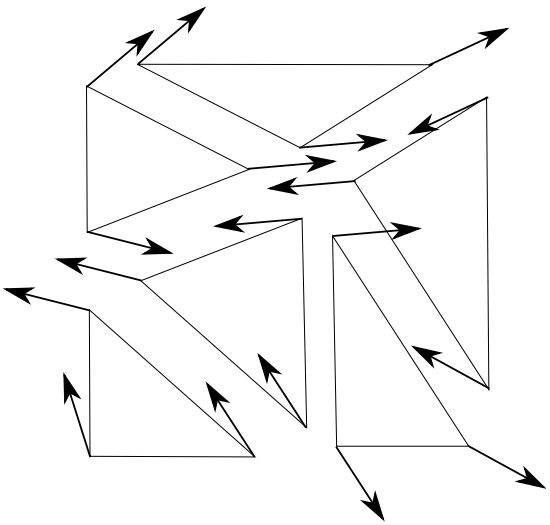

(c) Coherent orientation $\tilde{\omega}_i$ as a P_1 discontinuous finite elements

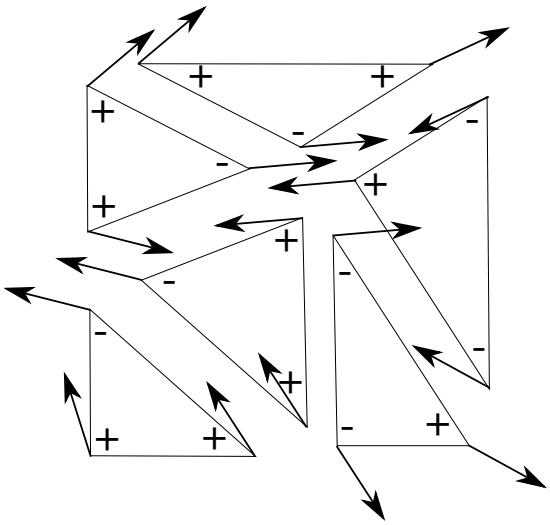

(d) $\tilde{\omega}_i$ and the interpolation map g for antisymmetric maps

Figure 7.12: Complete process to represent the manifold $\mathcal{D}$ using classical finite elements

We emphasize that the P_1 finite element functions r_i is continuous on $\mathcal{T}$.

The i^{th}-component $\varphi_i \in \mathcal{V}$ of the distortion map, is the minimizer of:

$$\min_{\psi \in \mathcal{V}} \sum_{\mathcal{T}_k \in \mathcal{T}} \int_{\mathcal{T}_k} |\nabla(I^a(\psi)) - e^{I(r_i)}\tilde{\omega}_i|^2 dx\,.$$

Although $I^a(\varphi_i)$ is a P_1 discontinuous finite element function, its absolute value $|I^a(\varphi_i)| = \varphi_i|$ is continuous on the whole mesh. Since the genuine shapes are built using the even function cos, the projection is smoothly defined by using φ_i.

Both preceding problems can be classically solved by writing the first order optimality condition, which is a standard variational formulation featuring a linear form and a bilinear form.

7.5.5 Numerical results

The above algorithm for the computation of the diffeomorphism is implemented in Freefem++ [Hecht 2012]. The projection step has been scripted in Paraview. Hence, *stl* files of the deshomogenized structures are straightforwardly generated and are ready to be printed using additive manufacturing machines. We emphasizing that the size ε of the chosen periodic cells is editable on line in order to adapt the resolution of the deshomogenized structures without any supplementary actions.

The cantilever case is chosen in order to assess our method.

The several steps of the whole process of building the distortion of a regular periodic grid are displayed on Figure 7.13. The regular grid is defined by constant geometric parameters over the whole domain D : $m_{reg} = (0.9, 0.9, 0.9)$. Note the definition of the grid is independent of the mesh.

Several shapes $\Omega_\epsilon(\varphi, m)$ for various values of the characteristic size ε of the cells are displayed in Figure 7.14. The smaller ε, the closer from the homogenized optimal design the shape $\Omega_\epsilon(\varphi, m)$.

We emphasize that small non connected components have been removed from the displayed final shapes. The final shapes are therefore connected.

On Figure 7.14, we displayed several shapes $\Omega_\epsilon(\varphi, m)$ for various values of ϵ.

7.6 Other numerical examples

We applied the whole method to a bridge case and to an electrical mast. In both cases, the volume constraint is fixed to 30% of the working domain and the number of iterations during the optimization – before regularization – is set to 200. The optimized geometric parameters and densities are not displayed for both cases. Indeed, as seen in the cantilever case, such 3-d results are difficult to displayed in 2-d, or required too many figures to be explicit. The main novelties of the present work are the regularization of the orientation and the projection step. Hence we privileged Figures for those parts.

For the bridge (Figure 7.15) the domain size is $22 \times 10 \times 12$ and a unit vertical load is applied at the middle of the bottom border on a square of length 2. The Dirichlet boundary condition

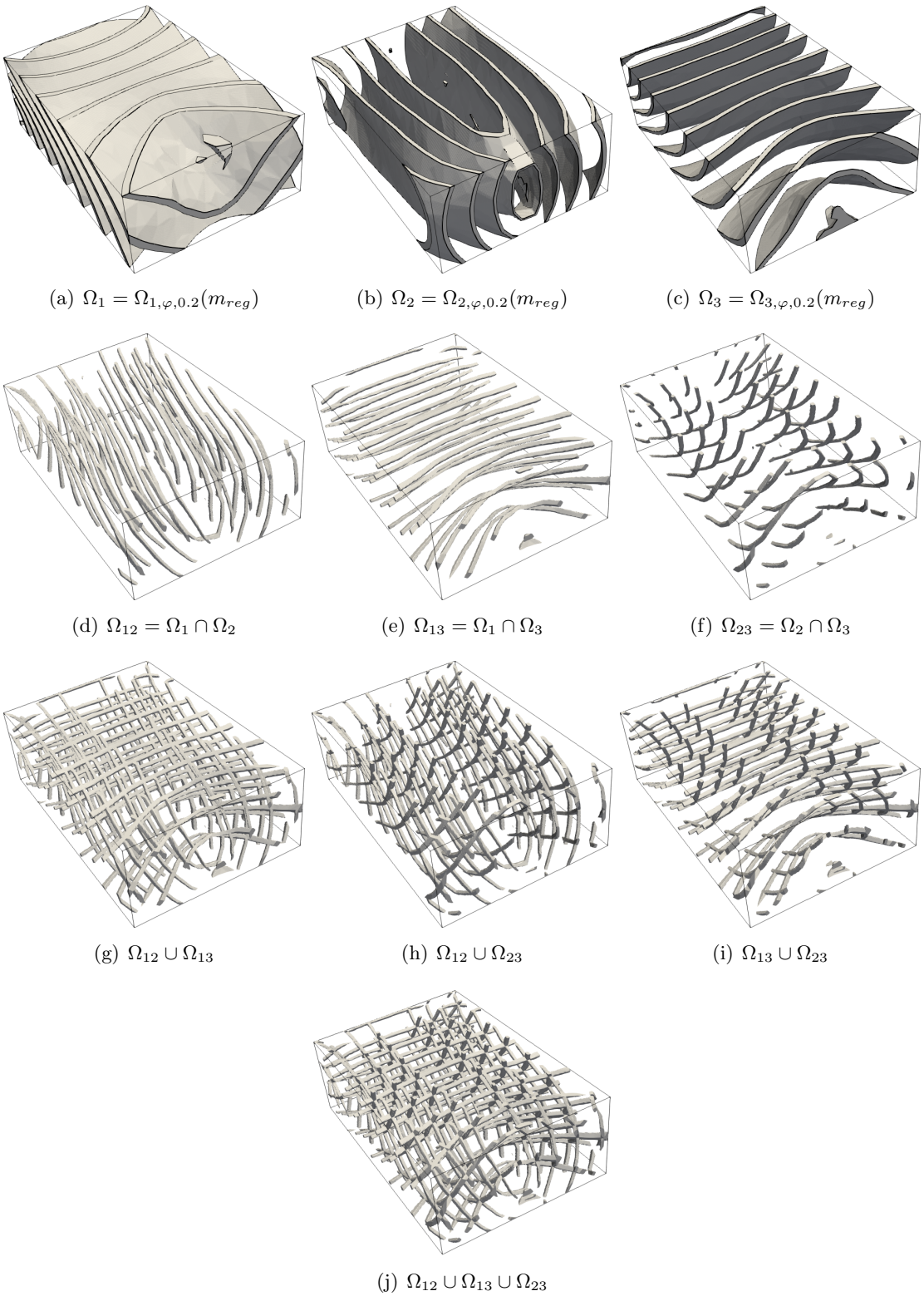

(a) $\Omega_1 = \Omega_{1,\varphi,0.2}(m_{reg})$ (b) $\Omega_2 = \Omega_{2,\varphi,0.2}(m_{reg})$ (c) $\Omega_3 = \Omega_{3,\varphi,0.2}(m_{reg})$

(d) $\Omega_{12} = \Omega_1 \cap \Omega_2$ (e) $\Omega_{13} = \Omega_1 \cap \Omega_3$ (f) $\Omega_{23} = \Omega_2 \cap \Omega_3$

(g) $\Omega_{12} \cup \Omega_{13}$ (h) $\Omega_{12} \cup \Omega_{23}$ (i) $\Omega_{13} \cup \Omega_{23}$

(j) $\Omega_{12} \cup \Omega_{13} \cup \Omega_{23}$

Figure 7.13: Distortion of a regular grid through the map φ from the cantilever case

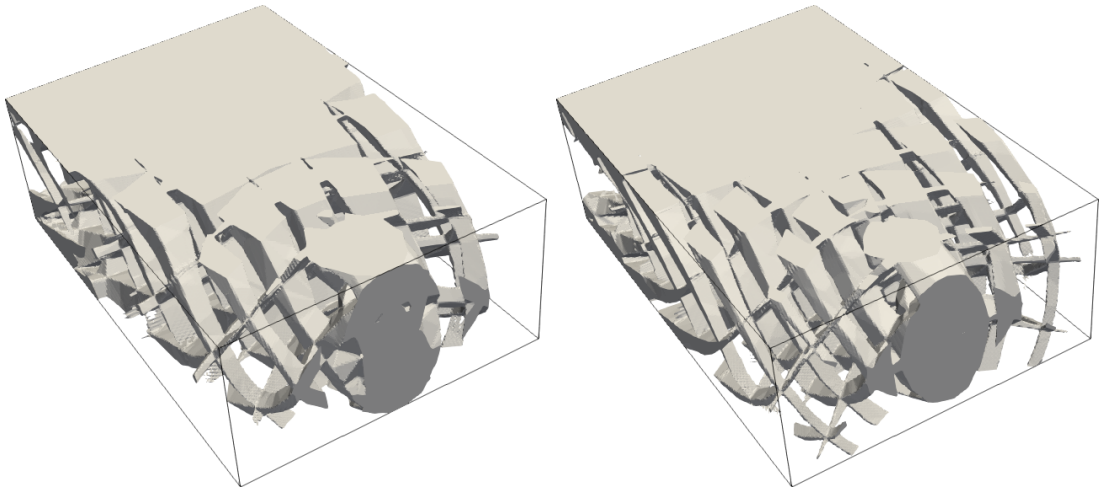

(a) $\epsilon = 0.275$

(b) $\epsilon = 0.225$

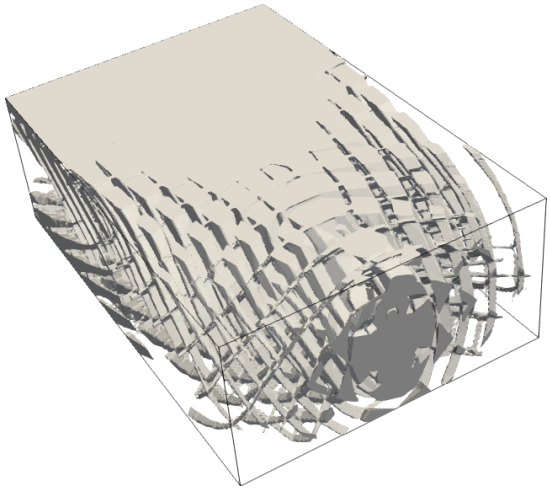

(c) $\epsilon = 0.125$

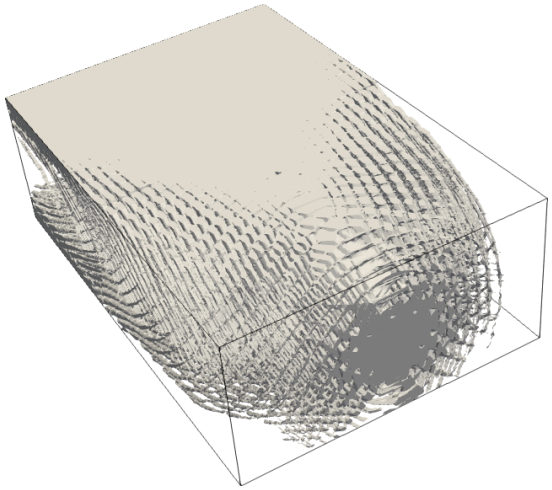

(d) $\epsilon = 0.05$

Figure 7.14: $\Omega_\epsilon(\varphi, m)$ for several ϵ in the case of the cantilever

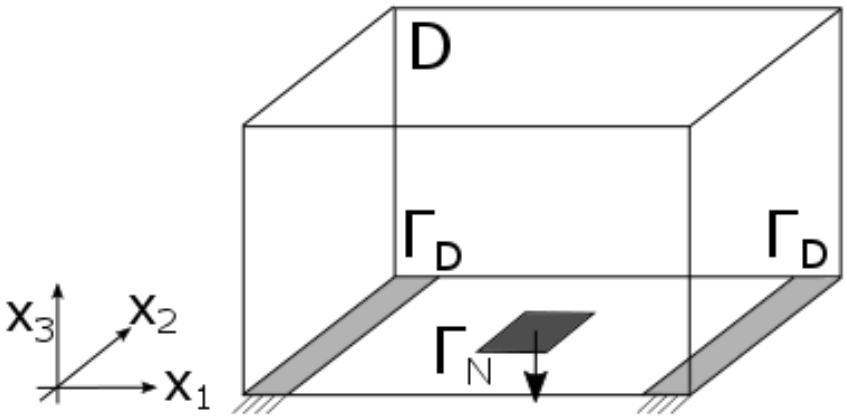

Figure 7.15: Boundary conditions for the bridge case

is applied on two symmetric rectangles, of length 1 and of width 1, on the bottom border. The resulting compliance for the homogenized design is 1.017.

The applied loads and the boundary conditions are displayed on Figure 7.15, the optimal orientation of the periodicity cells before and after regularization on Figure 7.16. The distortion of a regular grid is displayed on Figure 7.17. The sequence of final shapes is displayed on Figure 7.18.

For the electrical mast (Figure 7.19), the domain size of the pillar is $2 \times 2 \times 8$, and the domain size of the upper part is $9 \times 9 \times 3.5$. We took advantage of the symmetry, by running the algorithm just on the quarter of a complete working domain : the domain in bold on Figure 7.19. Then the structure is allowed to slide on its two intern sides. The Dirichlet boundary condition is applied on the bottom border. A unit vertical load is applied on a square of size 1 on the external corner of the bottom face of the upper part of the domain. The resulting compliance for the homogenized design on the quarter of the whole domain is 4.288.

The optimal orientation of the periodicity cells before and after regularization is displayed on Figure 7.20. The distortion of a regular grid is displayed on Figure 7.20. The sequence of final shapes is displayed on Figure 7.21, for the quarter of the domain and for the whole domain : the second ones are obtained by reflections of the first ones. The pillar is not completely full, but feature thin holes: central slices of final structures and of normal x_1 are displayed on Figure 7.22. We emphasize that nothing ensures that the phase of φ is the same for each value of ε: on a given slice, the density could seem to be not the same according to the value of ε, but it is not the case.

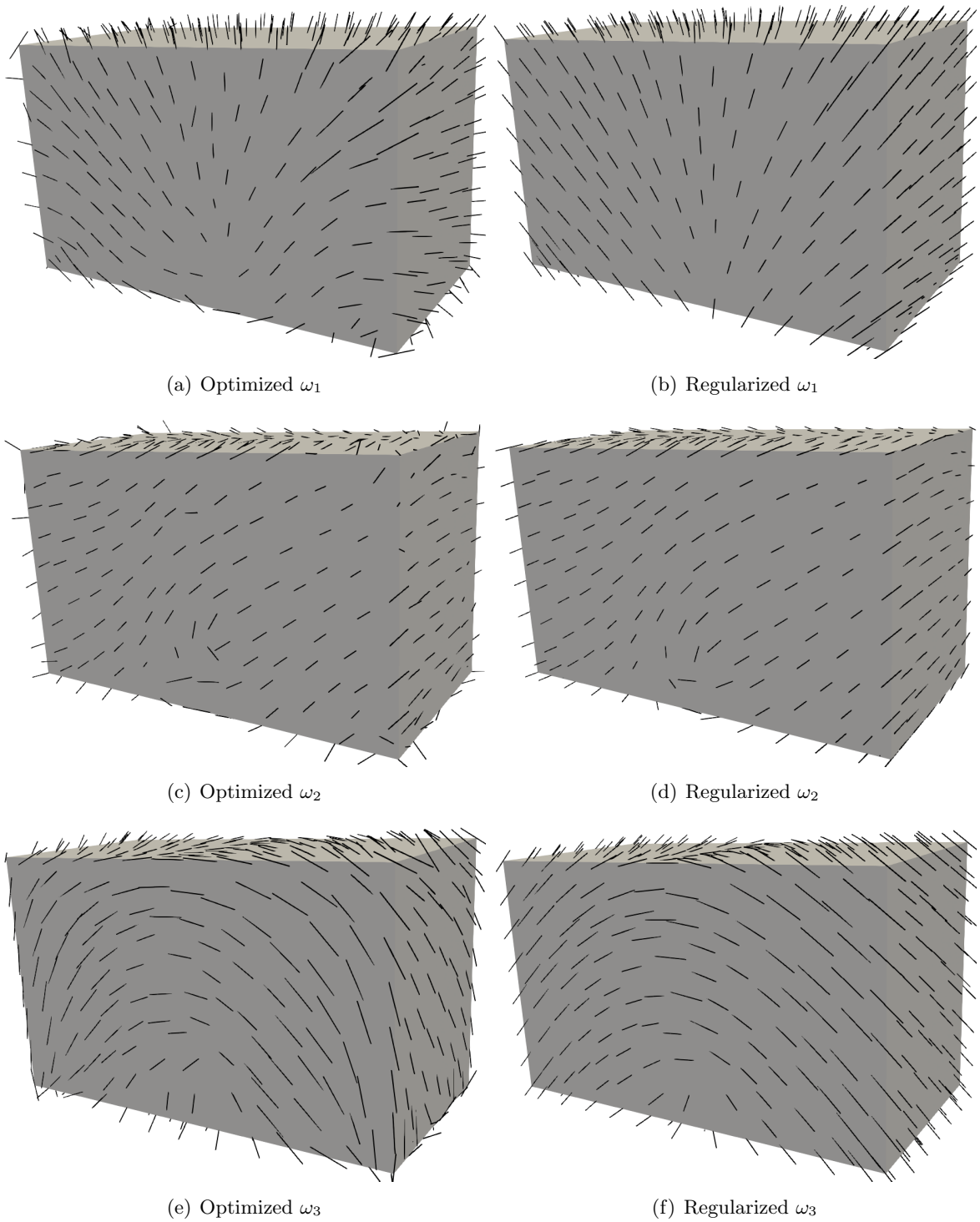

(a) Optimized ω_1

(b) Regularized ω_1

(c) Optimized ω_2

(d) Regularized ω_2

(e) Optimized ω_3

(f) Regularized ω_3

Figure 7.16: Optimized (left) and regularized (right) orientation for the bridge case

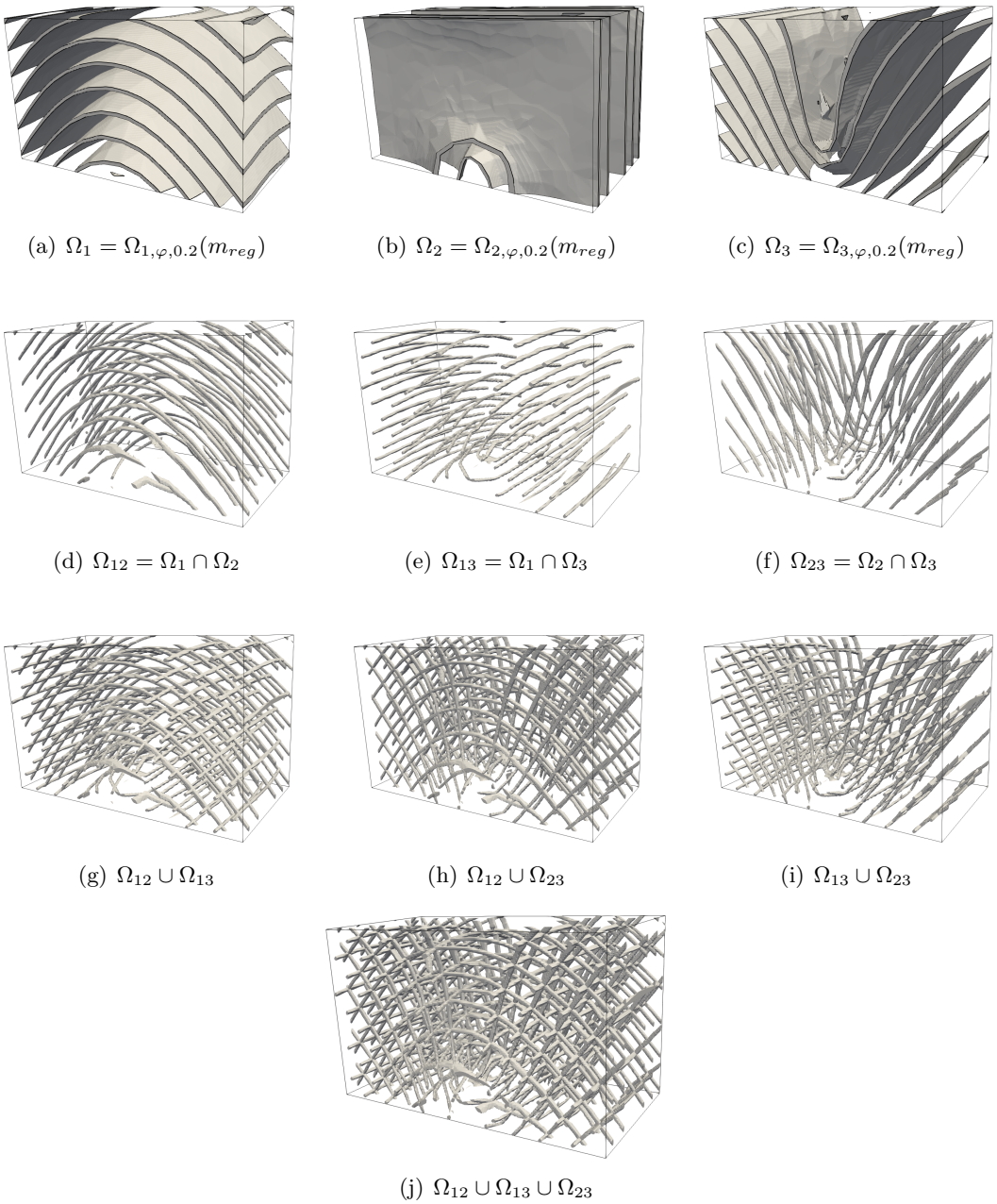

(a) $\Omega_1 = \Omega_{1,\varphi,0.2}(m_{reg})$ (b) $\Omega_2 = \Omega_{2,\varphi,0.2}(m_{reg})$ (c) $\Omega_3 = \Omega_{3,\varphi,0.2}(m_{reg})$

(d) $\Omega_{12} = \Omega_1 \cap \Omega_2$ (e) $\Omega_{13} = \Omega_1 \cap \Omega_3$ (f) $\Omega_{23} = \Omega_2 \cap \Omega_3$

(g) $\Omega_{12} \cup \Omega_{13}$ (h) $\Omega_{12} \cup \Omega_{23}$ (i) $\Omega_{13} \cup \Omega_{23}$

(j) $\Omega_{12} \cup \Omega_{13} \cup \Omega_{23}$

Figure 7.17: Distortion of a regular grid through the map φ from the bridge case

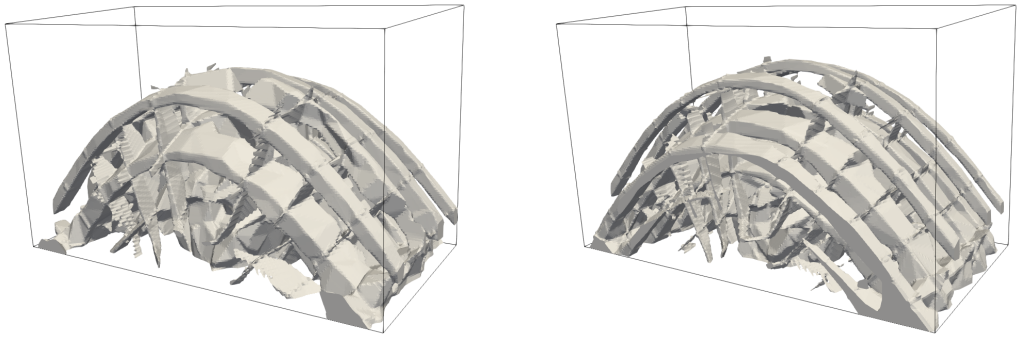

(a) $\epsilon = 0.5$ (b) $\epsilon = 0.4$

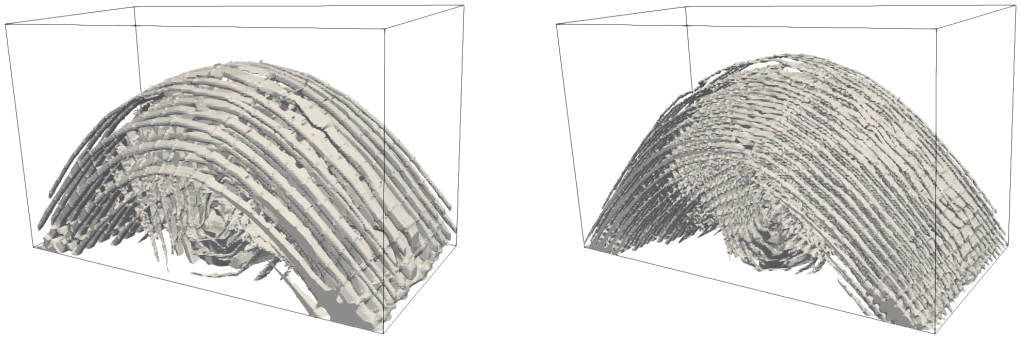

(c) $\epsilon = 0.2$ (d) $\epsilon = 0.1$

Figure 7.18: $\Omega_\epsilon(\varphi, m)$ for several ϵ in the case of the bridge

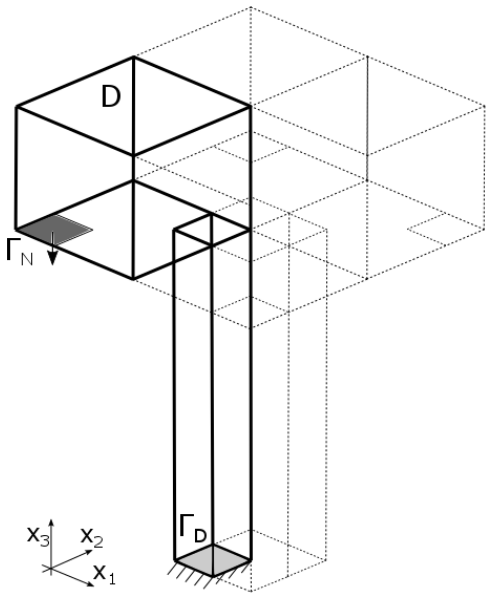

Figure 7.19: Boundary conditions for the bridge case

Appendix

In numerical practice, we use the normalized Voigt notations. Hence a symmetric tensor s of order 2, like the stress or strain tensor, is represented by a vector $\{s\}$ of size 6 with same norm:

$$\{s\} = \begin{pmatrix} s_{11} \\ s_{22} \\ s_{33} \\ \sqrt{2}s_{12} \\ \sqrt{2}s_{13} \\ \sqrt{2}s_{23} \end{pmatrix}.$$

The rotation operator $R(\omega)$, as any fourth-order tensor, is then represented by a 6×6 matrix, which is precisely defined by

$$\{R(\omega)\} = \begin{pmatrix} R_{11}(\omega) & R_{12}(\omega) \\ R_{21}(\omega) & R_{22}(\omega) \end{pmatrix}, \tag{7.29}$$

where the four sub-matrices R_{ij} of size 3×3 are respectively given by:

$$R_{11}(\omega) = \begin{pmatrix} \omega_{1,1}^2 & \omega_{2,1}^2 & \omega_{3,1}^2 \\ \omega_{1,2}^2 & \omega_{2,2}^2 & \omega_{3,2}^2 \\ \omega_{1,3}^2 & \omega_{2,3}^2 & \omega_{3,3}^2 \end{pmatrix}, \tag{7.30}$$

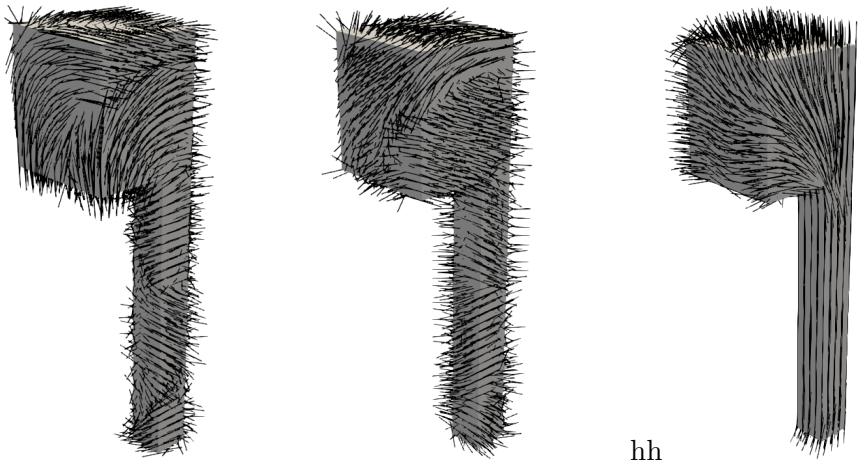

(a) Optimized ω_1 (b) Optimized ω_2 (c) Optimized ω_3

hh

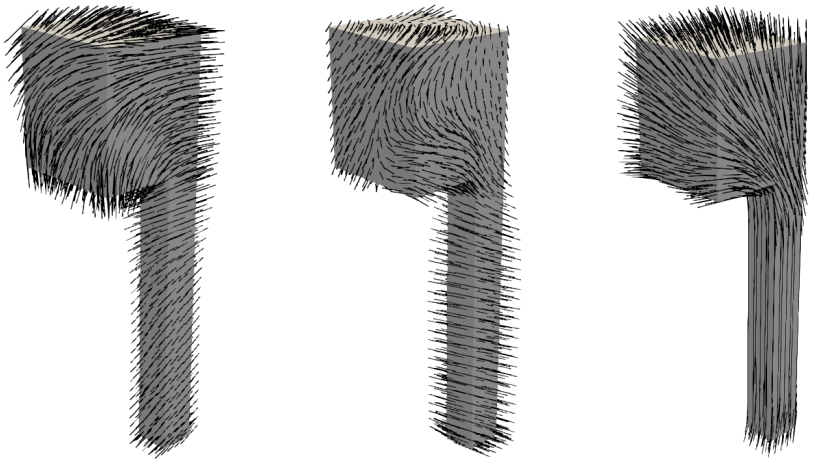

(d) Regularized ω_1 (e) Regularized ω_2 (f) Regularized ω_3

Figure 7.20: Optimized (up) and regularized (down) orientation for the electrical mast case

(a) $\Omega_1 = \Omega_{1,\varphi,\varepsilon}(m_{\mathrm{reg}})$

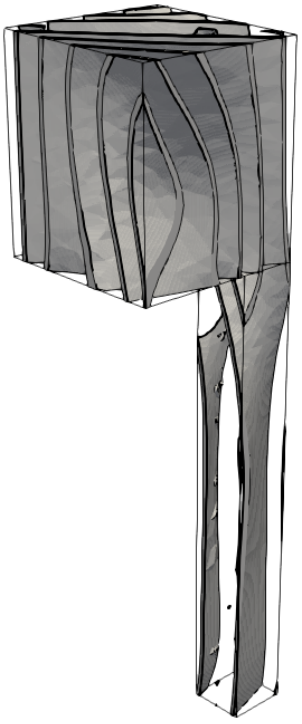

(b) $\Omega_2 = \Omega_{2,\varphi,\varepsilon}(m_{\mathrm{reg}})$

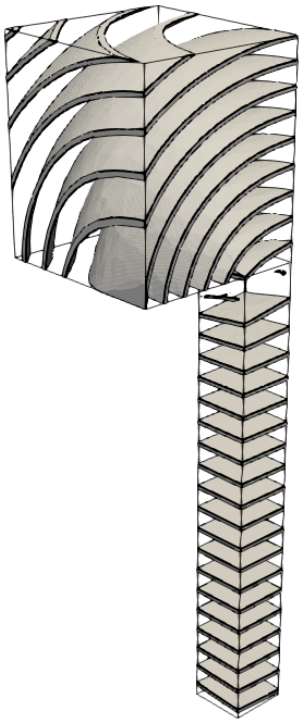

(c) $\Omega_3 = \Omega_{3,\varphi,\varepsilon}(m_{\mathrm{reg}})$

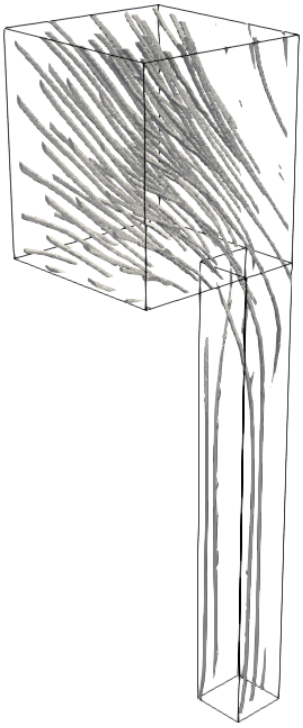

(d) $\Omega_{12} = \Omega_1 \cap \Omega_2$

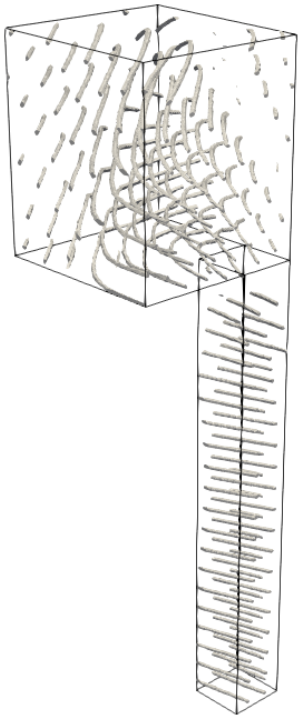

(e) $\Omega_{13} = \Omega_1 \cap \Omega_3$

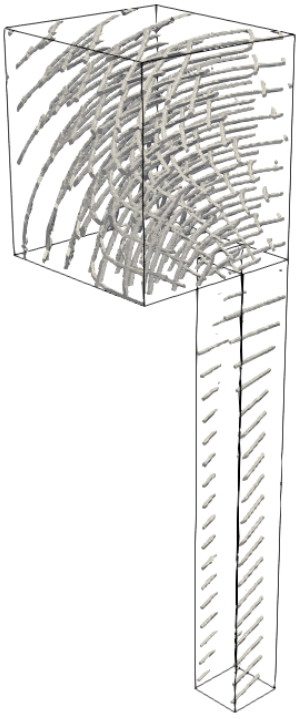

(f) $\Omega_{23} = \Omega_2 \cap \Omega_3$

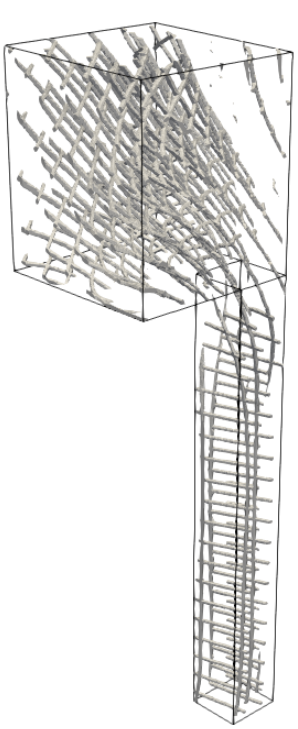

(g) $\Omega_{12} \cup \Omega_{13}$

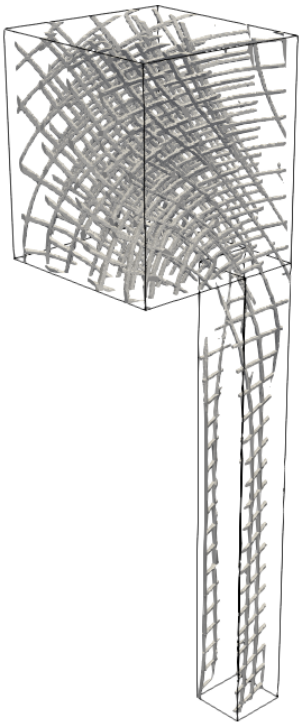

(h) $\Omega_{12} \cup \Omega_{23}$

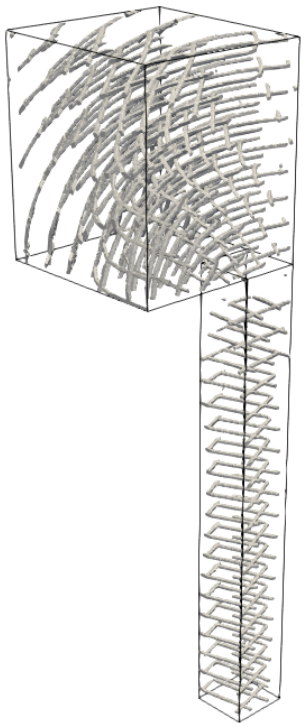

(i) $\Omega_{13} \cup \Omega_{23}$

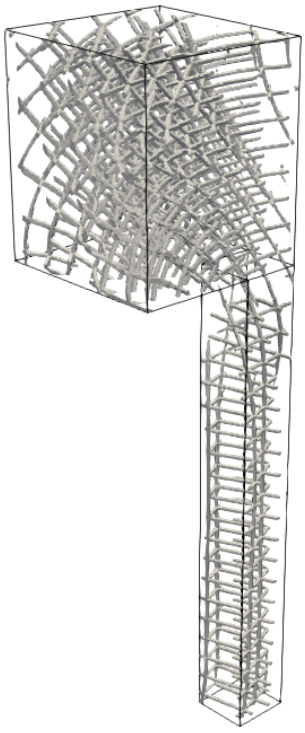

(j) $\Omega_{12} \cup \Omega_{13} \cup \Omega_{23}$

Figure 7.20: Distortion of a regular grid through the map φ from the electrical mast test case

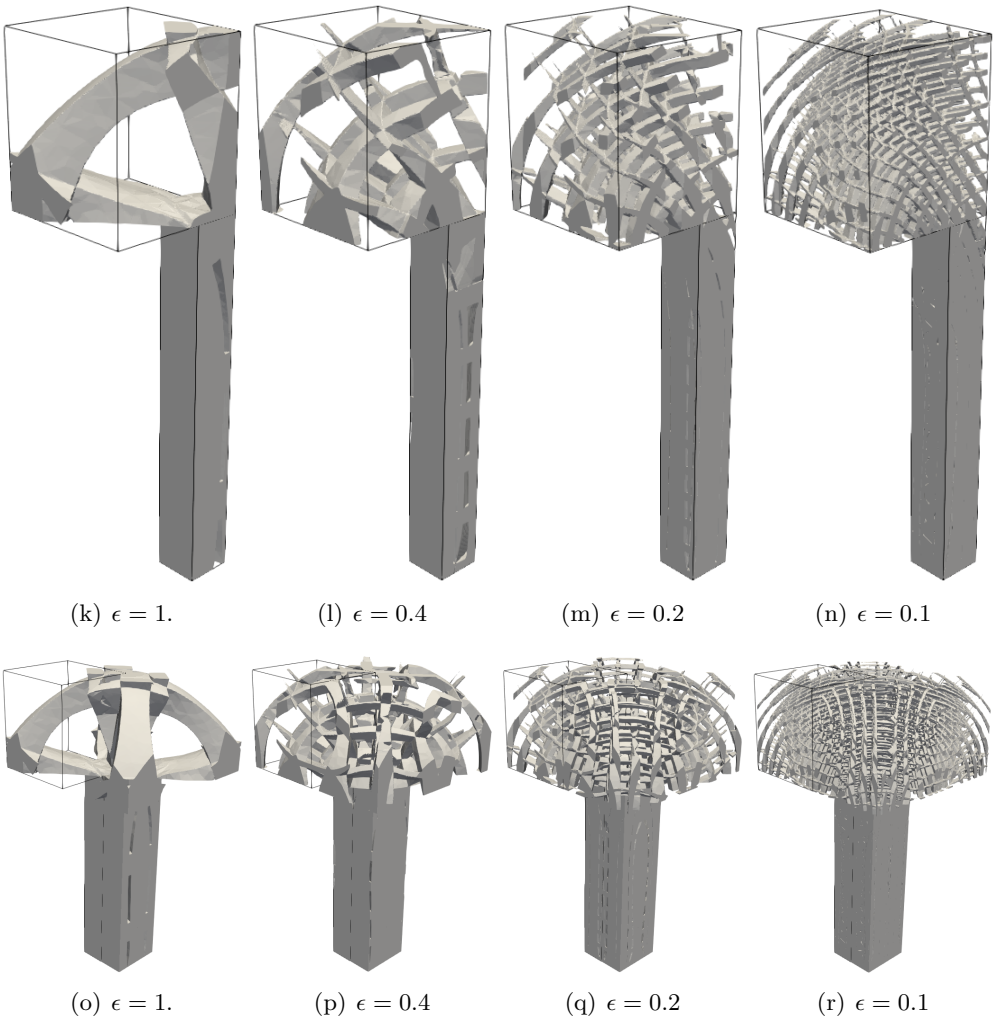

(k) $\epsilon = 1.$ (l) $\epsilon = 0.4$ (m) $\epsilon = 0.2$ (n) $\epsilon = 0.1$

(o) $\epsilon = 1.$ (p) $\epsilon = 0.4$ (q) $\epsilon = 0.2$ (r) $\epsilon = 0.1$

Figure 7.21: $\Omega_\epsilon(\varphi, m)$ for several ϵ in the electrical mast test case on the quarter of the whole domain (up), and on the whole domain (down).

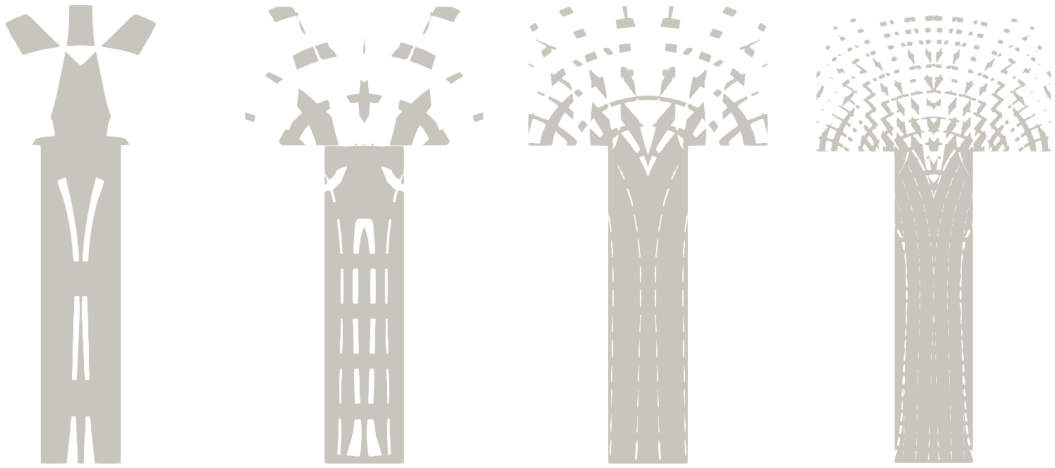

(a) $\epsilon = 1.$ (b) $\epsilon = 0.4$ (c) $\epsilon = 0.2$ (d) $\epsilon = 0.1$

Figure 7.22: Slices of normal x_1 of $\Omega_\epsilon(\varphi, m)$ for several ϵ for the electrical mast test.

$$R_{12}(\omega) = \begin{pmatrix} \sqrt{2}\omega_{1,1}\,\omega_{2,1} & \sqrt{2}\omega_{1,1}\,\omega_{3,1} & \sqrt{2}\omega_{2,1}\,\omega_{3,1} \\ \sqrt{2}\omega_{1,2}\,\omega_{2,2} & \sqrt{2}\omega_{1,2}\,\omega_{3,2} & \sqrt{2}\omega_{2,2}\,\omega_{3,2} \\ \sqrt{2}\omega_{1,3}\,\omega_{2,3} & \sqrt{2}\omega_{1,3}\,\omega_{3,3} & \sqrt{2}\omega_{2,3}\,\omega_{3,3} \end{pmatrix}, \tag{7.31}$$

$$R_{21}(\omega) = \begin{pmatrix} \sqrt{2}\omega_{1,1}\,\omega_{1,2} & \sqrt{2}\omega_{2,1}\,\omega_{2,2} & \sqrt{2}\omega_{3,1}\,\omega_{3,2} \\ \sqrt{2}\omega_{1,1}\,\omega_{1,3} & \sqrt{2}\omega_{2,1}\,\omega_{2,3} & \sqrt{2}\omega_{3,1}\,\omega_{3,3} \\ \sqrt{2}\omega_{1,2}\,\omega_{1,3} & \sqrt{2}\omega_{2,2}\,\omega_{2,3} & \sqrt{2}\omega_{3,2}\,\omega_{3,3} \end{pmatrix}, \tag{7.32}$$

$$R_{22}(\omega) = \begin{pmatrix} \omega_{1,1}\,\omega_{2,2} + \omega_{1,2}\,\omega_{2,1} & \omega_{1,1}\,\omega_{3,2} + \omega_{1,2}\,\omega_{3,1} & \omega_{2,1}\,\omega_{3,2} + \omega_{2,2}\,\omega_{3,1} \\ \omega_{1,1}\,\omega_{2,3} + \omega_{1,3}\,\omega_{2,1} & \omega_{1,1}\,\omega_{3,3} + \omega_{1,3}\,\omega_{3,1} & \omega_{2,1}\,\omega_{3,3} + \omega_{2,3}\,\omega_{3,1} \\ \omega_{1,3}\,\omega_{2,2} + \omega_{1,2}\,\omega_{2,3} & \omega_{1,3}\,\omega_{3,2} + \omega_{1,2}\,\omega_{3,3} & \omega_{2,3}\,\omega_{3,2} + \omega_{2,2}\,\omega_{3,3} \end{pmatrix}. \tag{7.33}$$

Chapter 8

Coupling the homogenization method and the level-set method

Contents

Efficient topology optimization method of structures made of composite materials, using the homogenization theory have been presented. We also presented a deshomogenization process yielding optimized genuine structures in 2D and in 3D, straightforwardly manufacturable by additive manufacturing processes.

Using the homogenization method, the external border of the structure is not explicitly known. In practice, it is only available after the deshomogenization process, and a fortiori after the optimization process. Thus, neither geometric constraint nor design-dependent loads can easily be taken into account with this topology optimization method.

The solution presented here relies on coupling two shape optimization methods, namely the homogenization method, and the level-set method. Indeed, in the level-set method, the external border of the structure is clearly identified during the whole optimization process. We propose here to optimize at once the general shape of the structure, given by a level-set function, and the distribution of the composite material in the shape.

In Section 8.1, the level-set method is briefly presented.

In Section 8.2, the coupling of both methods is explained. The coupled optimization algorithm is given, and successfully tested on a bridge and on a cantilever.

In Section 8.2.6, a coating-constraint is added to the optimization problem, in order to have an external layer of solid material on the final structure. Other approaches have been proposed. In [Wu 2018], an adapted SIMP method including adapted filters is used to optimize a bone-like structure. In [Wang 2013] the parameters of the bars of an internal truss are optimized, the objective is to lighten a shape by filling it with a lightweight frame structure. In [Dapogny 2017], a level-set method is proposed to optimize a structure featuring an anisotropic coating and filling with a uniform composite material. The main novelty of our method consists in optimizing the distribution of the given composite material filling the shape, and doing it at the same time as the external shape optimization.

In Section 8.2.7, we focus on design-dependent load cases, [Chen 2001, Bourdin 2003, Allaire 2004b]. Our method is successfully extended and tested for such a load, namely a uniform hydraulic pressure load.

8.1 Level-set method

8.1.1 Shape derivative

The notion of shape derivative was first introduced by Hadamard and has been well developed since, see for instance []. We recall here only few classical results required for the present work.

Let Ω be a smooth reference open set, $\theta \in W^{1,\infty}(\mathbb{R}^N, \mathbb{R}^N)$ and Id the identity map. If θ is small enough, the map $Id + \theta$ is a diffeomorphism in $\mathbb{R}^N$. Hence we can consider the domains:

$$\Omega_\theta = (Id + \theta)(\Omega)\,.$$

Definition 8.1.1. A functional $J(\Omega)$ is said to be shape differentiable at Ω if there exists a continuous linear form $J'(\Omega)$ on $W^{1,\infty}(\mathbb{R}^N, \mathbb{R}^N)$ such that, for all $\theta \in W^{1,\infty}(\mathbb{R}^N, \mathbb{R}^N)$:

$$J((I+\theta)(\Omega)) = J(\Omega) + J'(\Omega)(\theta) + o(\theta) \quad \text{with } \lim_{\theta \to 0} \frac{|o(\theta)|}{||\theta||} = 0\,.$$

Remark 16. *The shape derivative defined here is the Fréchet derivative. Others could be defined, like the Gateaux derivative.*

Lemma 8.1.1. *Let Ω be a smooth bounded open set, $\phi_v(x) \in W^{1,1}(\mathbb{R}^N)$ and $\phi_s(x) \in W^{2,1}(\mathbb{R}^N)$. Let two functionals J_v and J_s be defined by:*

$$J_v(\Omega) = \int_\Omega \phi_v(x)dx \quad J_s(\Omega) = \int_{\partial\Omega} \phi_s(x)ds\,.$$

The two functionals are differentiable at Ω and for all $\theta \in C^1(\mathbb{R}^N, \mathbb{R}^N)$ we have:

$$J'_v(\Omega)(\theta) = \int_\Omega \operatorname{div}(\theta(x)\phi_v(x))dx = \int_{\partial\Omega} \theta(x)\cdot n(x)\phi_v(x)ds$$

and

$$J'_s(\Omega)(\theta) = \int_{\partial\Omega} \theta(x)\cdot n(x)(\frac{\partial\phi_s}{\partial n} + H\phi_s)ds\,,$$

where n is the unit normal of $\partial\Omega$, and H is the mean curvature of $\partial\Omega$ defined by $H = \operatorname{div} n$.

The proof of this lemma relies on a change of variable, which is valid because θ is a diffeomorphism.

8.1.2 Shape derivative in linear elasticity

Let Ω be a smooth bounded open set of $D \subset \mathbb{R}^N$, occupied by a linear elastic material whose Hooke's law is denoted by A. The boundary $\partial\Omega$ is divided in three disjoint parts: $\partial\Omega = \Gamma_N \cup \Gamma_D \cup \Gamma_0$.

A surface load $g \in H^1(D)^N$ is applied on Γ_N (Neumann boundary conditions) and the structure is clamped on Γ_D (Dirichlet boundary conditions). The boundary Γ_0 is free of charge. The linear elasticity system reads as:

$$\begin{cases} -\operatorname{div}(Ae(u)) = 0 & \text{in } \Omega \\ (Ae(u))n = g & \text{on } \Gamma_N \\ u = 0 & \text{on } \Gamma_D \\ (Ae(u))n = 0 & \text{on } \Gamma_0 \end{cases}, \tag{8.1}$$

where u is the displacement field, $e(u) = \frac{1}{2}(\nabla u + \nabla u^T)$ is the strain field, and n is the unit normal on $\partial\Omega$. This problem admits a unique solution $u \in H^1(\Omega)^N$. Here we consider only problems without bulk load, but there will be no major difference if one would take bulk forces into account. We assume that the boundaries Γ_D and Γ_N are fixed: only the free boundary Γ_0 is varying during the optimization.

Let $J(\Omega)$ be the objective function, only the case of the compliance will be considered here:

$$J(\Omega) = \int_\Omega Ae(u) : e(u)dx = \int_{\Gamma_N} g \cdot u ds. \tag{8.2}$$

In order to minimize J, a gradient algorithm is used. It is an iterative method: shapes Ω_n are successively computed. The main idea is to slightly distort a shape to define the next one. Hence, a small vector field θ_n is computed at each step, thanks to the shape derivative of the objective function.

Lemma 8.1.2. *Let $\theta \in W^{1,\infty}(\mathbb{R}^N, \mathbb{R}^N)$. Assume that $g \in H^2(\Omega)$ and that the solution u of (8.1) is in $H^2(\Omega)^N$. Assume that $\theta = 0$ on $\Gamma_D \cup \Gamma_N$. The shape derivative of the functional $J(\Omega)$ defined by (8.2) is:*

$$J'(\Omega)(\theta) = -\int_{\Gamma_0} (Ae(u) : e(u))\theta \cdot n dx\,.$$

Proof. The proof relies on the Céa's method. To be perfectly rigorous, we should also proved that the solution u of (8.1) is Gateau differentiable with respect to the shape, thanks to a change of variable of type: $\Omega = (Id + t\theta)(\Omega_0)$, see []. Let $V = \{\phi \in H^1(D)^N \text{ such that } \phi = 0 \text{ on } \Gamma_D\}$. We introduce the following Lagrangian $L(\Omega, v, q)$, where $v, q \in V$,

$$L(\Omega, v, q) = \int_\Omega (Ae(v) : e(q)dx - \int_{\Gamma_N} g \cdot q ds + \int_\Omega Ae(v) : e(v)dx\,,$$

where q is the Lagrange multiplier for the elasticity problem. The partial derivative of L with respect to q in the direction $\phi \in H^1(\mathbb{R}^N, \mathbb{R}^N)$ is given by:

$$< \frac{\partial L}{\partial q}(\Omega, v, q), \phi >= \int_\Omega Ae(v) : e(\phi)dx - \int_{\Gamma_N} g \cdot \phi ds\,.$$

If we take ϕ with compact support in Ω, we recover the state equation in Ω. This partial derivative is equal to zero if and only if $v = u(\Omega)$, the unique solution of (8.1).

The partial derivative of L with respect to v in the direction $\phi \in H^1(\mathbb{R}^N, \mathbb{R}^N)$ is given by:

$$< \frac{\partial L}{\partial v}(\Omega, v, q), \phi >= \int_\Omega Ae(q) : e(\phi)dx + \int_{\Gamma_N} g \cdot \phi ds\,.$$

When it vanishes, it leads to the adjoint state equation, which is nothing but the state equation with a surface load equal to $-g$. Indeed, it is very well known that the compliance minimization is a self-adjoint problem. This partial derivative is equal to zero if and only if $q = -u(\Omega)$, the unique solution of (8.1).

The objective function is given by: $J(\Omega) = L(\Omega, u(\Omega), -u(\Omega))$. Hence the shape derivative of the objective function is given by the partial derivative of L with respect to Ω at $(\Omega, u(\Omega), -u(\Omega))$. Thanks to Lemma 8.1.2:

$$\begin{aligned} J'(\Omega)(\theta) &= < \frac{\partial L}{\partial \Omega}(\Omega, u(\Omega), -u(\Omega)), \theta > \\ &= -\int_{\partial\Omega} (Ae(u(\Omega)) : e(u(\Omega)))(\theta \cdot n)ds \end{aligned}$$

□

8.1.3 Geometric constraints

In linear elasticity, if the objective function is reduced to the compliance without any constraints over the final shape, the optimal shape is given by $\Omega = D$: a structure which occupies the whole working domain. Hence, geometric constraints are introduced. The more classical geometric constraints are on the total volume of the shape and on its perimeter. A first approach consists in imposing this constraint at every step of the optimization algorithm. However, this could be not effective, because too restrictive. Indeed, between two iterations, there is no freedom to break the geometric constraints in order to eventually get out of a local minimum. A second approach consists in introducing some penalization terms in the Lagrangian function, with a Lagrange multiplier. This more flexible approach enables to get out of eventual local minima. However, the Lagrange multipliers have to be carefully chosen. If they are too small, they would not have any impact on the final shape. But if they are too large, the actual approach will lead to the same pitfalls as the previous one: it would not be able to get out of eventual local minima.

If the volume (resp. the perimeter) of the final shape have to reach a target volume V_T (resp. a target perimeter P_T), we introduce the following function $f_V(\Omega)$ (resp. $f_P(\Omega)$):

$$f_V(\Omega) = (\int_\Omega dx - V_T)^2 \quad \text{and} \quad f_P(\Omega) = (\int_{\partial\Omega} dx - P_T)^2\,. \tag{8.3}$$

If the volume (resp. the perimeter) of the final shape have only to be minimized, we introduce the following function $f_V(\Omega)$ (resp. $f_P(\Omega)$):

$$f_V(\Omega) = \int_\Omega dx \quad \text{and} \quad f_P(\Omega) = \int_{\partial\Omega} dx\,. \tag{8.4}$$

The shape derivatives of all these functions are given by Lemma 8.1.1.

8.1.4 Implicit description of the shape

In order to describe implicitly the shape $\Omega \subset D$, a level-set function φ is introduced, such that:

$$\begin{cases} \varphi(x) = 0 & \text{if } x \in \partial\Omega \cap D \\ \varphi(x) < 0 & \text{if } x \in \Omega \\ \varphi(x) > 0 & \text{if } x \in D \setminus \Omega \end{cases}$$

A classical example of level-set function, and the one that will be used on all the following, is the signed distance function:

Definition 8.1.2. Let $\Omega \subset \mathbb{R}^N$ be a Lipschitz open set. The *signed distance function* to Ω, denoted by $d_\Omega : \mathbb{R}^N \to \mathbb{R}$, is defined as:

$$d_\Omega(x) = \begin{cases} -d(x, \partial\Omega) & \text{if } x \in \Omega \\ 0 & \text{if } x \in \partial\Omega \\ d(x, \partial\Omega) & \text{if } x \notin \overline{\Omega} \end{cases}, \tag{8.5}$$

where $d(\cdot, \partial\Omega)$ is the usual Euclidean distance to the boundary $\partial\Omega$.

The skeleton Σ of $\partial\Omega$ is defined as:

$$\Sigma = \left\{ x \in \mathbb{R}^N \,|\, (d_\Omega)^2 \text{ is not differentiable in } x \right\}$$

At every point $x \in \partial\Omega$, the unit normal vector to Ω is given by: $n(x) = \nabla d_\Omega(x)$. We can extend to $\Omega \setminus \Sigma$ this unit vector field. Since Σ has zero Lebesgue measure in $\mathbb{R}^N$, thanks to Rademacher's theorem, the normal is not defined over Σ but this has no real incidence for the following.

8.1.5 Evolution of the shape

We recall that between two iterations, the new shape is given by a slight distortion of the previous one. Hence, we have to define this process. We will consider that the shape depends fictively on the time t and so evolves in time. Thanks to the implicit description of the shape, the shape $\Omega(t)$ is given at time $t \in \mathbb{R}^+$ by:

$$\{x(t) \in D | \varphi(t, x(t)) < 0\}\,.$$

The evolution of the shape is characterized by a velocity, equal to the descent direction $\theta(t, x(t))$ given by the gradient of the Lagrangian. This leads to a transport equation:

$$\frac{\partial\varphi}{\partial t}(t, x) + \theta(t, x(t) \cdot \nabla\varphi(t, x) = 0 \text{ in } D\,, \tag{8.6}$$

In the classical level-set method, meaning with no composite material, the velocity is given at the boundary of the shape, and aligned with the normal to the frontier. It is then extended to the whole working domain. The transport equation yields an Hamilton-Jacobi equation. However, in the following, the shape is filled with a modulated composite material. This one has also to be advected. Hence, we can no longer assume the velocity field to be normal to the boundary, neither approximate it in the whole domain. The equation (8.6) is the one used here to update the shape at each iteration.

In practice, the same velocity is kept for a short while of time dt. If the Lagrangian of the new shape is lower than the previous, the new shape is validated. Else, the shape is rejected and the time interval is divided by two. Hence, the interval of time dt has to be chosen carefully at the beginning. If it is too high, the descent direction computed at $t = 0$ will not be admissible during all the time interval. If it is too small, the shape will evolve very slightly and a lot of iterations will be required until convergence of the optimization algorithm.

Numerically, we need to compute a velocity field in the whole domain D. If the descent direction is known only at a part of the border $\partial\Omega$, the velocity will be extended in the whole domain, this point will be developed in the following.

The *advect* library has been used to solve numerically the transport equation. For all theoretical questions about the implementation and the use of viscosity solutions, one can refer to [Bui 2012]. In order to compute the signed distance function for new shapes, we use the *mshdist* library [Dapogny 2012].

8.1.6 Algorithm of shape optimization by the level-set method

The shape optimization algorithm follows the following steps:

1. Initialization of the shape Ω_0.
2. Iteration until convergence, for $n \geq 0$:
   (a) Computation of the solution u_n of the linear elasticity (8.1).
   (b) Computation the descent direction θ_{n+1} as the partial derivative of the Lagrangian.
   (c) Updating the shape Ω_{n+1} using the Hamilton Jacobi equation.
   (d) Verification that the new shape improves the Lagrangian, else, reduction of the time interval dt and rejection of the new shape: $\Omega_{n+1} = \Omega_n$.

This algorithm ensures to find a local minimum of the Lagrangian, which depends in part of the initialization of the shape Ω_0. Indeed, as seen in Chapter 1, the global minimum is not a genuine structure and so can not be reach using a level-set method.

8.2 Coupling the homogenization and the level-set methods

The purpose of this chapter is to propose a coupling of the homogenization and level-set methods in order to obtain a smooth exterior boundary of a finely perforated lattice structure. At the difference with the first section, the shape Ω is no longer occupied by a constant isotropic material A, but by a composite material.

8.2.1 Elastic phases

We consider two elastic phases: the first occupies the shape Ω, the second one the domain $D \setminus \Omega$.

The first phase is a composite material made of two phases: void and isotropic material whose tensor will be denoted A. We will assume that the effective composite material is orthotropic and that its microstructure is parametrized by geometric parameters m. Its effective elasticity tensor will be denoted $A^*(m)$. Since the phase is not isotropic but orthotropic, it might be oriented according to an angle α. Hence the complete elastic tensor will be given by:

$$R(\alpha)A^*(m)R(\alpha)^T\,,$$

where R is the rotation operator of fourth-order tensor defined by 4.7 in Chapter 4. The volumic density of the material will be denoted $\rho(m) \in [0;1]$, it depends of the geometric parameters of the material, but obviously not of its orientation. When the density ρ is equal to zero, the composite material is void. When the density ρ is equal to one, the composite material is full and $A^* = A$.

In the following numerical tests, the material featuring square cells and rectangular holes, presented in Section 2 Chapter 4 will be used. However we emphasize that the above method is not restricted to this particular material.

The second phase is an ersatz material, in order to mimic void while avoiding the stiffness matrix to be singular. It is a very commonly used method in shape optimization. Its elastic tensor A_e is taken equal to 10^{-3} of A, the full isotropic material making up the composite material.

8.2.2 Description of the structures in the coupling method

The set of admissible structures in homogenization method is given by:

$$\Big\{(m,\alpha) \in L^\infty(D,[0;1]^2 \times \mathbb{R} \quad | \quad \int_D \rho(m)dx = V_T\Big\}\,,$$

where $\rho(m)$ is the density of the microstructure.

The structures $\Omega \subset D$ in level-set method are described using a level-set function ϕ :

$$\Omega = \big\{x \in D \quad | \quad \phi(x) < 0\big\}.$$

The structures in the coupling method are described with:
- a level-set function ϕ, which gives the subset of the working domain D where the structure is,
- the geometry parameters $m \in L^\infty(\Omega,[0;1]^2)$ of the material, and its orientation $\alpha \in L^\infty(\Omega,\mathbb{R})$.

8.2.3 Optimization problem

Let $D \subset \mathbb{R}^2$ be a fixed smooth bounded open set (the working domain). Let $\Omega \subset D$ be a bounded open set occupied by a homogenized elastic material, characterized by its geometric parameters $m \in L^\infty(\Omega, [0;1])$ and its orientation $\alpha \in L^\infty(\Omega, \mathbb{R})$, its homogenized elasticity tensor is denoted $A^*(m)$. The boundary of Ω contains Γ_N and Γ_D, with respectively Neumann and Dirichlet boundary conditions. The boundary parts Γ_N and Γ_D are assumed to be fixed in the optimization process.

The displacement u and the stress tensor σ are then solution of the system:

$$\left\{\begin{array}{ll} \mathrm{div}(\sigma) = 0 & \text{in } \Omega \\ \sigma = R(\alpha)A^*(m)e(u) & \text{in } \Omega \\ u = 0 & \text{on } \Gamma_D \\ \sigma \cdot n = g & \text{on } \Gamma_N \\ \sigma \cdot n = 0 & \text{on } \partial\Omega \setminus (\Gamma_D \cup \Gamma_N) \end{array}\right. ,$$

where $e(u) = \frac{1}{2}(\nabla u + \nabla u^T)$ is the strain tensor.

Let $\mathcal{U}_{\text{ad}}$ be the set of admissible shapes, defined by:

$$\mathcal{U}_{\text{ad}} = \{\Omega \subset D | \Gamma_N \subset \partial\Omega, \Gamma_D \subset \partial\Omega, \}\,.$$

Let V_T be the target, and $\rho(m)$ be the density of the homogenized material. Let the cost function $J(\Omega, m, \alpha)$ be a combination of of the compliance and of the volume constraint, namely:

$$J(\Omega, m, \alpha) = \int_\Omega R(\alpha)A_0^*(m)^{-1}R(\alpha)^T\sigma : \sigma dx + \gamma(\int_\Omega \rho(x)dx - V_T)^2\,,$$

where $\gamma > 0$ is the weight for the volume constraint.

The minimization problem reads as:

$$\left\{\begin{array}{c} \inf \\ \sigma \in H_0(\Omega) \\ \Omega \in \mathcal{U}_{\text{ad}} \\ m \in L^\infty(\Omega, [0;1]) \\ \alpha \in L^\infty(\Omega, \mathbb{R}) \end{array}\right. \int_\Omega R(\alpha)A_0^*(m)^{-1}R(\alpha)^T\sigma : \sigma dx + \gamma(\int_\Omega \rho(x)dx - V_T)^2\,,$$

with

$$H_0(\Omega) = \left\{\tau \in L^2(\Omega, \mathcal{M}_2^s) | \begin{array}{l} \mathrm{div}(\tau) = 0 \text{ in } \Omega \\ \tau n = g \text{ on } \Gamma_N \\ \tau n = 0 \text{ on } \partial\Omega \setminus (\Gamma_D \cup \Gamma_N) \end{array}\right\}.$$

In order to solve this problem, we use an alternate minimization algorithm [Allaire 2002b], minimizing successively with respect to the stress field σ, the microstructure m and the orientation α of the cell, and finally the shape Ω.

Minimization with respect to the stress field. For given design fields (Ω, m, α), the minimization with respect to the stress field σ amounts to solve the elasticity problem with a material of elasticity tensor equal to $R(\alpha)A^*(m)R(\alpha)^T$ in Ω, and to A_ϵ in $D \subset \Omega$.

Minimization with respect to the microstructure. For a given stress field σ and a shape Ω, a gradient algorithm is used to minimize with respect to m. We recall that the compliance minimization is self-adjoint. The descent direction dm_i is given by the derivative of J with respect to m

$$< \frac{\partial J(\Omega, m, \alpha,)}{\partial m_i}, h >= \int_\Omega (-\frac{\partial A^*(m)}{\partial m_i} R(\alpha)^T\sigma : R(\alpha)^T\sigma + 2\gamma(\int_\Omega \rho(m)dx - V_T)\frac{\partial \rho(m)}{\partial m_i})h\, dx\,.$$

Hence,

$$dm_i = \frac{\partial A^*(m)}{\partial m_i} R(\alpha)^T\sigma : R(\alpha)^T\sigma - 2\gamma(\int_\Omega \rho(m)dx - V_T)\frac{\partial \rho(m)}{\partial m_i}. \tag{8.7}$$

The update at iteration n is given by $m_i^{n+1} = m_i^n + \mu_m dm_i$, with $mu_m > 0$ is the step size.

Minimization with respect to the orientation. We recall that the homogenized material is orthotropic. Hence, its optimal orientation for a given stress field σ is given by the principal directions of σ. This result is an extension of the Pedersen formulas [Pedersen 1989]. By choosing to align the vector $a_1 = (\cos(\alpha); \sin(\alpha))$ with the eigenvector of σ of smallest eigenvalue (possibly negative), the angle α is then defined modulo π.

Minimization with respect to the shape. For a given stress field σ, a gradient algorithm is used to minimize with respect to Ω. When the shape Ω is moved by θ, the microstructure is not defined in $(Id + \theta)(\Omega) \setminus \Omega$. Hence, we decided to advect also the microstructure m, which consequently depends here on the shape Ω. The orientation α is updated using the Pedersen formulas. Other approaches are possible, like extending by continuity the actual microstructure, but it has not been investigated here.

For all $\theta \in C^1(D, D)$ we have:

$$\begin{aligned} J'(\Omega, m, \alpha)(\theta) \;=\; & \textstyle\int_{\Gamma_0}(-R(\alpha)A^*(m)R(\alpha)^T e(u) : e(u))\theta.n ds \\ & + \textstyle\int_\Omega(-R(\alpha)\frac{\partial A^*}{\partial m}(m)R(\alpha)^T e(u) : e(u))\nabla m \cdot \theta dx \\ & + \textstyle\int_\Omega(-(\frac{\partial R}{\partial \alpha}(\alpha)A^*(m)R(\alpha)^T + R(\alpha)A^*(m)\frac{\partial R^T}{\partial \alpha}(\alpha))e(u) : e(u))\nabla \alpha \cdot \theta dx \\ & + \textstyle\int_{\Gamma_0} 2\gamma\rho(m)(\int_\Omega \rho(m)dx - V_T)\theta \cdot n ds \\ & + 2\gamma(\textstyle\int_\Omega \rho(m)dx - V_T)\int_\Omega(\frac{\partial \rho(m)}{\partial m}\nabla m \cdot \theta)\,, \end{aligned} \tag{8.8}$$

Let $\theta \in C^1(D, D)$ be the solution of the variational formulation:

$$\forall t \in C^1(D, D) \quad \int_D \theta \cdot t\, dx = -J'(\Omega, m, \alpha)(t)\,. \tag{8.9}$$

We recall that the shape Ω is described by a level-set function φ, namely the signed distance function defined by (8.5). At each iteration, the level-set function and the microstructure are updated by advection during a period dt, using the Hamilton-Jacobi equation (8.6).

8.2.4 Implementation

We described here the numerical implementation of the optimization algorithm.

Complete optimization algorithm. The optimization algorithm is an iterative method, structured as follows:

1. Initialization of the design parameters (Ω, m, α)
2. Iteration until convergence for $n \geq 0$:
   (a) Computation of σ^n through a problem of linear elasticity for the structure characterized by $(\Omega^n, m^n, \alpha^n)$.
   (b) Updating the orientation $\tilde{\alpha}$, using the Pedersen formulas.
   (c) Updating the design parameters $\tilde{m}$, using (8.7).
   (d) Updating the level-set function φ^{n+1} and the design parameters m^{n+1} by advection of respectively φ^n and $\tilde{m}$, using (8.9). The shape Ω^{n+1} is described by the level-set function φ^{n+1}.
   (e) Computation of σ through a problem of linear elasticity for the structure characterized by $(\Omega^{n+1}, m^{n+1}, \alpha^n)$.
   (f) Updating the orientation α^{n+1}, using the Pedersen formulas.

We emphasize that the domain $D \setminus \Omega$ is numerically fulfilled with an ersatz material. Hence, the stress tensor is computed in the whole domain D, and the orientation α as well. There is no numerical limitation at step (2e) of the algorithm, when the orientation of the new structure is given by the old orientation.

We implemented the topology optimization in the finite element software FreeFem++ [Hecht 2012] (see [Allaire 2006] for the use of FreeFem++ in optimal design). All unknowns are discretized using P_1-functions.

The implementation of the minimization with respect to the stress field, the design parameters m and the orientation α is exactly the same as the one presented in Section 4 of Chapter 4. Hence, it is not reproduced here.

Minimization with respect to the shape. The shape is described by the level-set function φ. This function is discretized using P_1 finite elements.

The descent direction θ is computed using a H^1 equivalent norm, by solving the following variational formulation: $\forall t \in C^1(D, D)$

$$\int_D \theta \cdot t + \eta^2 \nabla\theta : \nabla t \, dx = -J'(\Omega, m, \alpha, \ell)(t) \,,$$

where J' is given by (8.8), and $\eta > 0$ is a small coefficient, which typically depends on the size of the elements of the mesh. The purpose of this small coefficient is to numerically regularize the partial derivatives on a length scale of order η and to limit the checkerboard effect [Sigmund 1998].

The derivative of J features linear integral along Γ_0. Since numerically mesh adaptation is not used here, this border is not exactly discretized on the mesh. Hence we use the regularization method, proposed by [Osher 2006], to approximate those integrals. One can refer to [Feppon 2017] for an other implementation of this method in shape optimization. Let $\epsilon > 0$ be a small coefficient, typically the characteristic size of the edges of the mesh. Let f be a P_1 discretized function. The linear integral $\int_{\Gamma_0} f(s)\theta \cdot n\, ds$ is numerically approximated by:

$$\int_\Omega \delta_\epsilon(x) f(x)\theta \cdot n\, dx\,,$$

where

$$\delta_\epsilon(x) = \begin{cases} 0 & \text{if } |\delta_\Omega(x)| > \epsilon \\ \dfrac{1}{2\epsilon}(1+\cos(\dfrac{\pi}{\epsilon}\delta_\Omega(x))) & \text{else} \end{cases}.$$

The level set function and the design parameters are then updated by advection during a period dt. In practice, we use an adaptive period dt. At each iteration, if the newly computed homogenized structure is accepted, the period is increased of 20%. On the contrary, if the newly computed structure is rejected, the period is divided by two. Moreover, the initialization of dt is given by:

$$dt = \frac{h_{\max}}{||\theta||_{L^\infty}}\,,$$

where $h_{\max}$ is the maximal size of the edges of the mesh. The idea is to prevent the shape to move too much between two iterations.

The advection of those functions is done with the library *advection*, [Bui 2012]. The advected level-set function is then again updated, using the library *mshdist*, in order to be the signed distance function of the advected shape.

Bounds on the density. If the effective material can reach a density equal to zero (meaning to be equivalent to the ersatz material), the level-set function disappears. Then, a lower bound is taken for the density of the effective material. Here for the sake of simplicity, the geometric parameters m_i are bounded. This no perfect because the cell can not reach the phases where it features only two parallel bars.

If we want to work only on the density, we could add a penalization term like $\int_\Omega (f(\rho(x))^2 dx$ for example, where f is a penalization function, equal to around one for low densities ($0 \leq \rho < \rho_{min}$) and equal to around zero for other densities ($\rho_{min} \leq \rho \leq 1$). This has not been investigated here.

8.2.5 Numerical results

8.2.5.a Cantilever case

We have numerically implemented the optimization algorithm for the cantilever problem, see Figure 8.1(a) for the boundary conditions. The domain size is 20×20 and it is discretized by a structured triangular mesh, featuring about 800 vertices. The target volume is fixed to 30% of the working domain. The optimized density is displayed on Figure 8.1(b).

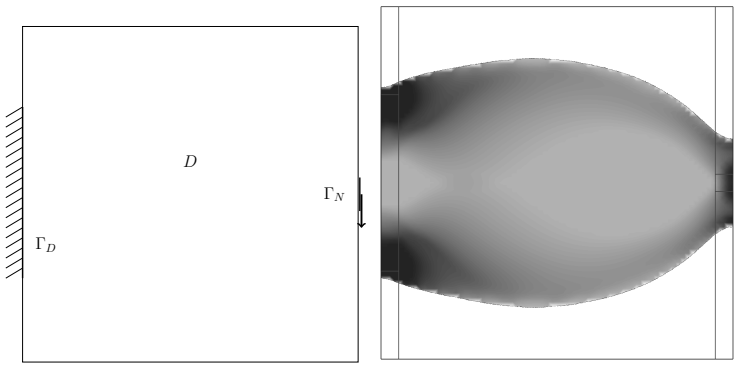

(a) Load case (b) Optimized density

Figure 8.1: Cantilever test case

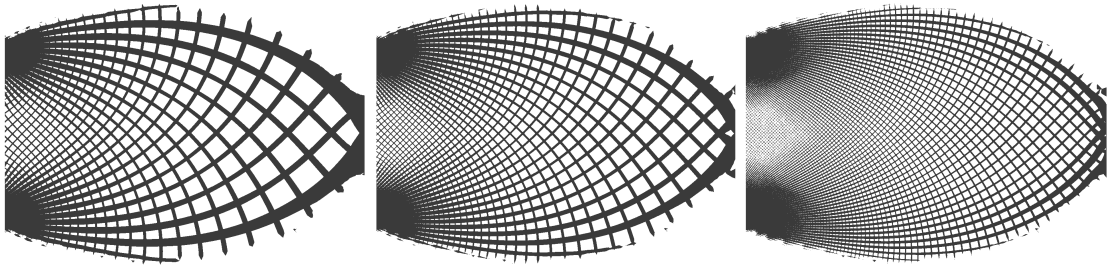

(a) $\varepsilon = 0.2$ (b) $\varepsilon = 0.1$ (c) $\varepsilon = 0.05$

Figure 8.2: $\Omega_\varepsilon(\varphi, m)$ for several ε in the case of the cantilever

The optimized orientation of the structure is then regularized with the same method than in Chapter 4. A diffeormorphism corresponding to the regularized orientation is then computed, like in Section 5 of Chapter 4. A sequence of genuine shapes $\Omega_\varepsilon(m)$ can then be computed, see Figure 8.2.

8.2.5.b Bridge case

We have numerically implemented the optimization algorithm for the bridge problem, see Figure 8.3 for the boundary conditions. The domain size is 22×13 and it is discretized by a structured triangular mesh, featuring about 1000 vertices. The target volume is fixed to 30% of the working domain.

8.2.5.c Discussion

The genuine shapes $\Omega_\varepsilon(\varphi, m)$ are not post-treated here. Thanks to the shape Ω, there is no very thin bars in the whole domain, contrary to non post-treated structures of Chapter 4. Nevertheless, the external border is not very smooth: it features stumps of bars. The same post-treatment method as the one presented in Chapter 4, Section 5, could be used here to

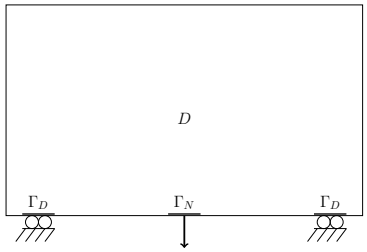

Figure 8.3: Boundary conditions for a bridge

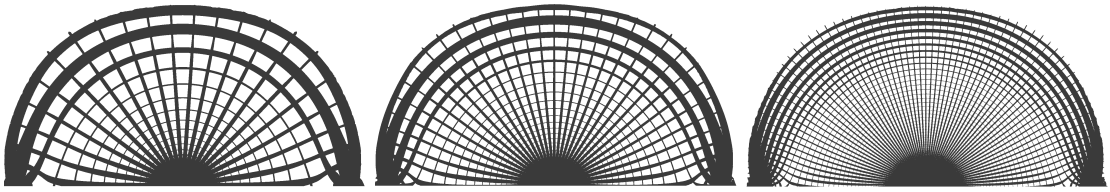

(a) $\varepsilon = 0.2$ (b) $\varepsilon = 0.1$ (c) $\varepsilon = 0.05$

Figure 8.4: $\Omega_\varepsilon(\varphi, m)$ for several ε in the case of the bridge

clean the structures. However we could also fix this problem during the optimization process by imposing a coating to the structure. This is the subject of the next section.

8.2.6 With geometric constraints: optimization of coated structures

Thanks to the shape Ω, we can now consider more sophisticated geometric constraints. Indeed, the genuine external border of the final structure is known all the time. This is not the case where only the homogenized method is used : the external border of the shape is known only at the end, after the deshomogenization step.

We want to impose the final structure to feature a coating of full material and of width h. This is motivated by diverse reasons. For example, if the final structure is coated, no post-treatment will be required to clean it of little bars. The external border will fit perfectly the level-set function and so will be smooth. An other kind of reason is industrial. A coated structure will not be susceptible to be fulfill by dust during its use, which could damage it or limit its performances.

The coated structures are also known as in-fill structures, or structures featuring a crust. Other approaches have been developed, [Wu 2018, Wang 2013]. They mostly rely on a SIMP method, and do not use a specific microstructure: the frame structure inside the shape is also optimized using a SIMP type method. The motivations are multiple: mimicking the structure of porous bones [Wu 2018], or reduce the quantity of material to fulfill structures, produced with additive manufacturing processes, [Wang 2013].

Let Ω_h be the domain of the coating, it is defined by:

$$\Omega_h = \{x \in \Omega | d_\Omega(x) > -h\}\,.$$

Two main approaches are possible to impose a coat. The first consists in considering as admissible structures only structures featuring a coating. Hence the homogenized material is

now restricted to the domain $\Omega \setminus \Omega_h$. During the advection of the shape, the width of the domain Ω_h has to be kept equal to h. The derivative of the cost function with respect to the shape has to taken into account this new constraint. This results in a very complex equation, featuring in particular integral along rays. Those terms are not easy to compute numerically.

On other difficulty remains in the modelization of the interface between the coating and the effective material. In the case of a sharp interface, we face new difficulties linked to the non continuity of the displacement around the interface. A smooth transition is then preferable, see [Allaire 2014] for more details.

To conclude, this approach has been explored, but with no satisfactory results. Indeed, the set of admissible shapes is so restricted than the optimization algorithm is quickly trapped in local minima.

The second approach consists in penalizing the density in the domain of the coating. We add a new term in the cost function:

$$I(\Omega, m) = \gamma_h \left(\int_{\Omega_h} (\rho(m) - 1) dx \right)^2 .$$

We emphasize that this term is an integral over Ω_h, defined using the signed distance function d_Ω. The proposition 3.5 of [Allaire 2014] gives its derivative:

Proposition 8.2.1. *Assume $\Omega \subset D$ is an open set of class C^1 and fix a point $x \notin \Sigma$, the skeleton of $\partial\Omega$. Then $\theta \mapsto d_{(Id+\theta)\Omega}(x)$ is Gateaux differentiable at $\theta = 0$, as an application from $W^{1,\infty}(D, \mathbb{R}^n)$ into $\mathbb{R}$ and its derivative is*

$$d'_\Omega(\theta)(x) = -\theta(p_{\partial\Omega(x)}) \cdot n(p_{\partial\Omega(x)}) , \tag{8.10}$$

where $p_{\partial\Omega(x)}$ is the projection on $\partial\Omega$, defined for $x \notin \Sigma$.

Proposition 8.2.2. *Let $\phi \in W^{1,1}(\mathbb{R}^N)$ and let K be the functional defined by: $K = \int_{\Omega_h} \phi(x) dx$.*
The derivative of the functional K is:

$$K'(\Omega)(\theta) = \int_{\partial\Omega} \phi(x)\theta(x) \cdot n(x)\, ds - \int_{\partial\Omega} \phi(y)\theta(y) \cdot n(y) dy$$

Proof. Let $\epsilon > 0$ a small coefficient, let χ_ϵ be the function defined by:

$$\chi_\epsilon(t) = \begin{cases} 0 & \text{if } t < -\epsilon \\ \frac{1}{2}(\sin(\frac{\pi}{2\epsilon}t) + 1) & \text{if } |t| \leq \epsilon \\ 1 & \text{if } t > \epsilon \end{cases} \tag{8.11}$$

Its derivative χ'_ϵ is given by:

$$\chi'_\epsilon(t) = \begin{cases} 0 & \text{if } |t| > \epsilon \\ \frac{\pi}{4\epsilon}\cos(\frac{\pi}{2\epsilon}t) & \text{if } |t| \leq \epsilon \end{cases} \tag{8.12}$$

Let $\chi_{\Omega_{h,\epsilon}}$ be the function defined by $\chi_{\Omega_{h,\epsilon}} = \chi_\epsilon(-h + d_\Omega(x))$. Hence, we get

$$\Omega_h = \{x \in \Omega | \chi_{\Omega_{h,\epsilon}}(x) < \frac{1}{2}\} .$$

Let the functional K_ϵ be defined by:

$$K_\epsilon(\Omega) = \int_\Omega \chi_{\Omega_{h,\epsilon}} \phi(x) dx \,.$$

It converges in the sense of distributions to $K(\Omega)$, when ϵ goes to zero.

Thanks to Proposition 8.2.1, the derivative of $K_\epsilon(\Omega)$ is:

$$\begin{aligned} K'_\epsilon(\Omega)(\theta) &= \int_{\partial\Omega 0} \phi(x)\theta(x)\cdot n(x)\, ds - \int_\Omega \frac{\partial \chi_{\Omega_{h,\epsilon}}}{\partial d_\Omega} \phi(x)\theta(p_{\partial\Omega(x)})\cdot n(p_{\partial\Omega(x)}) dx \\ &= \int_{\partial\Omega} \phi(x)\theta(x)\cdot n(x)\, ds - \int_{\partial\Omega} \left(\int_{-\epsilon}^{\epsilon} \frac{\pi}{4\epsilon} \cos(\frac{\pi}{2\epsilon} t) \phi(y + (t-h)n(y)) dt \right) \theta(y)\cdot n(y) dy \\ &\underset{\epsilon\to 0}{\longrightarrow} \int_{\partial\Omega} \phi(x)\theta(x)\cdot n(x)\, ds - \int_{\partial\Omega} \phi(y - hn(y))\theta(y)\cdot n(y) dy \end{aligned}$$

□

This leads straightforwardly to the derivative of the coating penalization term $I(\Omega, m)$:

Proposition 8.2.3. *Assume $\Omega \subset D$ is an open set of class C^1 and fix a point $x \notin \Sigma$, the skeleton of $\partial\Omega$. Then $\theta \to I((Id+\theta)\Omega, m)(x)$ is Gateaux differentiable at $\theta = 0$, as an application from $W^{1,\infty}(D, \mathbb{R}^n)$ into $\mathbb{R}$ and its derivative is*

$$\begin{aligned} I'(\Omega, m, \alpha)(\theta) &= 2\gamma_h \left(\textstyle\int_{\Omega_h} (\rho(m) - 1) dx\right) \int_{\Omega_h} \frac{\partial \rho(m)}{\partial m} \nabla m \cdot \theta dx \\ &\quad + 2\gamma_h \left(\textstyle\int_{\Omega_h} (\rho(m) - 1) dx\right) \int_{\Gamma_0} (\rho(m) - 1)\theta(x)\cdot n(x)\, ds \\ &\quad + 2\gamma_h \left(\textstyle\int_{\Omega_h} (\rho(m) - 1) dx\right) \int_{\Gamma_0} (\rho(m(x - hn(x))) - 1)\theta(x)\cdot n(x)\, ds \,, \end{aligned} \tag{8.13}$$

The derivative of the new objective function is simply given by adding (8.13) to (8.8). The descent direction θ is then again computed as the solution of a variational formulation, similar to (8.9).

The optimization algorithm is then identical to the one described in Section 8.2.4.

8.2.6.a Numerical results

The above algorithm has been implemented in FreeFem++, for a cantilever test case. The boundary conditions are identical to the previous section, see Figure 8.1(a).

Numerically, the derivative (8.13) is complex to implement because of its third term. Indeed, the value of the density ρ has to be computed along the rays emerging from the border Γ_0. In fact, we expect the coating to appear thanks to the homogenization part of the algorithm. It is indeed the only way to increase density locally, no matter of the neighbour density. The level-set part of the algorithm only moves the density inside the shape. Hence, the second and the third terms of (8.13) are expecting to be negligible during the whole optimization process. The third one, being complex to be implemented, is neglected. We will see in the following that does impact neither the convergence of the algorithm, nor the presence of a coating.

The volume constraint is set to 40% of the whole working domain. We run the algorithm for two different widths h of coating: $h = 0.7$ and $h = 2.1$, and two different upper bounds for the geometric parameters m_i: $m_{\max} = 0.8$ and $m_{\max} = 0.9$. The results are displayed on Figure 8.5.

One can check that the final densities feature a coating of constant width. For the thin coating ($h = 0.7$), the final shapes depend on the minimal admissible value of the density: the smaller, the vaster the final shape. Indeed, without lower bound for the density, the shape Ω converges to the whole domain D. This can be explained by the fact that the optimized shape computed with only the homogenization method, see Chapter 4, features microstructure on the whole domain, and no real void.

For the large coating ($h = 2.1$), the shapes are less vast. Indeed, the volume of the coating is closed to the target volume, and the inner of the shape has also to be fulfilled, since the density zero is not admissible. In fact, for $m_{\max} = 0.8$, the final volume is not equal to the volume target. To respect the volume constraint was too detrimental for the compliance.

The optimized structures are deshomogenized according to the method presented on Chapter 4. The orientation is first regularized. Then a diffeomorphism φ is computed from the regularized orientation. Deshomogenized structures $\Omega_\varepsilon(\varphi, m)$ are computed for several values of ε, the characteristic period of the periodic cells. Results are displayed on Figure 8.6. Those genuine shapes do not require any post-treatment in order to clean them. The external border is smooth and regular thanks to the presence of the coating.

8.2.7 Design-dependent loads

Thanks to the shape Ω, we can now consider design-dependent loads. Indeed, the genuine external border of the final structure is known all the time. This is not the case where only the homogenized method is used : the external border of the shape is known only at the end, after the deshomogenization step.

We consider here the case of a pressure load $p_0 n$, where p_0 is a given pressure. The elasticity problem reads as:

$$\begin{cases} \operatorname{div}(\sigma) = 0 & \text{in } \Omega \\ \sigma = R(\alpha)A^*(m)e(u) & \text{in } \Omega \\ u = 0 & \text{on } \Gamma_D \\ \sigma \cdot n = p_0 & \text{on } \Gamma_N \end{cases},$$

where the border Γ_N is varying during the optimization process.

8.2.7.a Minimization problem

The compliance $I(\Omega, m, \alpha)$ of the structure is given by: $I(\Omega, m, \alpha) = \int_{\Gamma_N} p_0 n \cdot u = \int_\Omega \operatorname{div}(p_0 u) dx$.

The volume is penalized using (8.4), and with a weight $\eta > 0$.

Hence the objective function J is given by:

$$J(\Omega, m, \alpha) = I(\Omega, m, \alpha) + \eta \int_\Omega dx\,. \tag{8.14}$$

We have the following proposition, see Corollary 9 of [Allaire 2004b]:

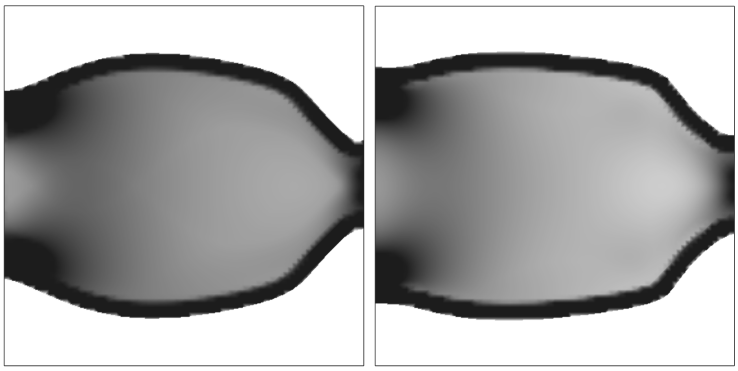

(a) $h = 0.7$ and $m_{\max} = 0.8$ (b) $h = 0.7$ and $m_{\max} = 0.9$

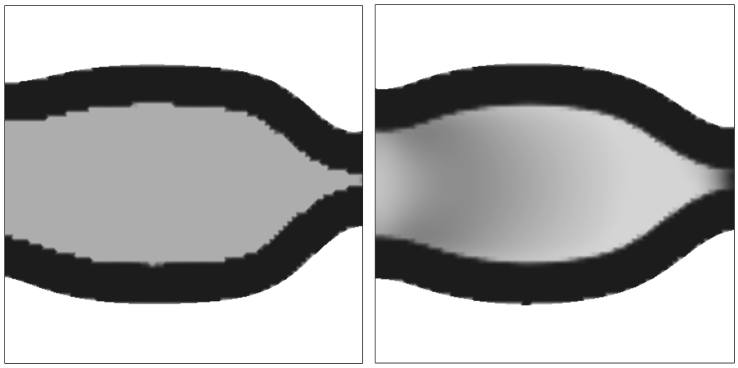

(c) $h = 2.1$ and $m_{\max} = 0.8$ (d) $h = 2.1$ and $m_{\max} = 0.9$

Figure 8.5: Optimized density in the case of the cantilever for two different values of coating width and of upper bound on m_i

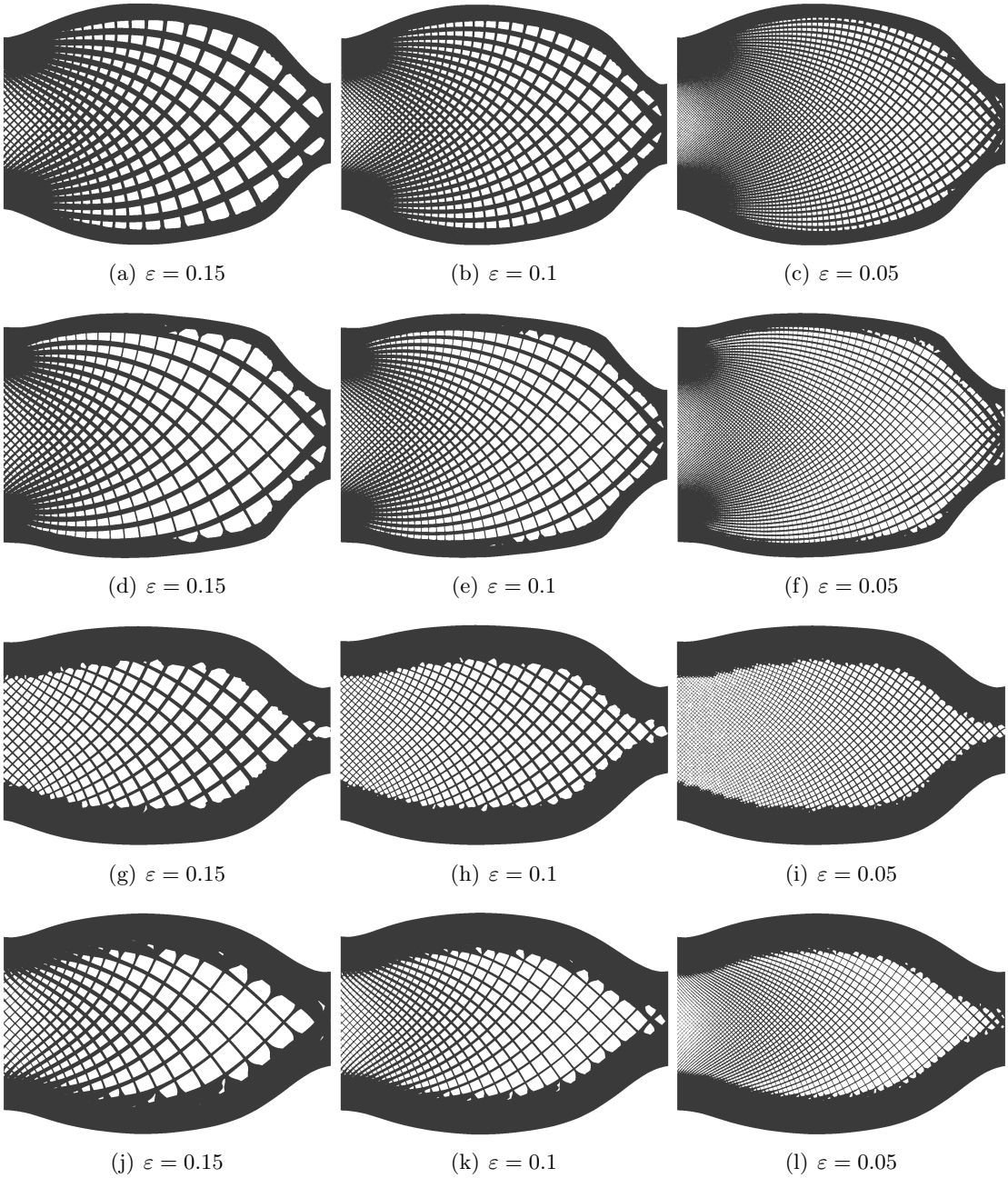

(a) $\varepsilon = 0.15$ (b) $\varepsilon = 0.1$ (c) $\varepsilon = 0.05$

(d) $\varepsilon = 0.15$ (e) $\varepsilon = 0.1$ (f) $\varepsilon = 0.05$

(g) $\varepsilon = 0.15$ (h) $\varepsilon = 0.1$ (i) $\varepsilon = 0.05$

(j) $\varepsilon = 0.15$ (k) $\varepsilon = 0.1$ (l) $\varepsilon = 0.05$

Figure 8.6: $\Omega_\varepsilon(\varphi, m)$ for several ε in the case of the cantilever

Proposition 8.2.4. *Let Ω be a smooth bounded open set and $\theta \in W^{1,\infty}(\mathbb{R}^N, \mathbb{R}^N)$. Assume that the solution u of (8.14) is smooth, say $u \in H^2(\Omega)^N$. The shape derivative of the objective function defined by (8.14) is:*

$$J'(\Omega, m, \alpha) = \int_{\Gamma_N} \theta \cdot n(2\,\mathrm{div}(p_0 u) - R(\alpha)A^*(m)e(u) : e(u))ds + \eta \int_{\Gamma_N} \theta \cdot n\, ds \tag{8.15}$$

Proof. The Lagrangian of the problem is defined for $(v, q) \in H^1(\mathbb{R}^N, \mathbb{R}^N)^2$ by:

$$L(\Omega, v, q, m, \alpha) = \int_\Omega \mathrm{div}(p_0 v)dx + \int_\Omega R(\alpha)A^*(m)e(v) : e(q)dx - \int_\Omega \mathrm{div}(p_0 q)dx + \eta \int_\Omega dx\,.$$

The compliance minimization is self-adjoint. Hence the adjoint state of the problem is $p = -u$, with u solution of (8.14).

The objective function is given by $J(\Omega, m, \alpha) = L(\Omega, u, -u, m, \alpha))$. Its shape derivative is given by the partial derivative of L with respect to Ω at $(\Omega, u, -u)$. Thanks to Lemma 8.1.1, for all $\theta \in W^{1,\infty}(\mathbb{R}^N, \mathbb{R}^N)$, such that θ is equal to zero on $\partial\Omega \setminus \Gamma_N$:

$$\begin{aligned} J'(\Omega, m, \alpha)(\theta) &= \int_{\Gamma_N} \mathrm{div}(p_0 u)\theta \cdot n\, dx + \int_{\Gamma_N} R(\alpha)A^*(m)e(u) : (-e(u))\theta \cdot n\, dx - \int_{\Gamma_N} \mathrm{div}(-p_0 u)\theta \cdot n\, dx \\ &= \int_{\Gamma_N} (2\,\mathrm{div}(p_0 u) - R(\alpha)A^*(m)e(u) : e(u))\theta \cdot n\, dx \end{aligned} \tag{8.16}$$

□

The optimization algorithm is then identical to the one described in Section 8.2.4.

8.2.7.b Numerical results

The above algorithm has been implemented in FreeFem++. The domain size is 22×10. The structure is clamped on two unit segments of the bottom border, see Figure 8.7(a). The pressure load p_0 is set to minus one. The weight of the volume penalization is $\eta = 0.1$. The upper bound on the geometric parameters m_i is $m_{\max} = 0.8$.

The optimized density is displayed on Figure 8.7(b). The final structure features a large coating, we emphasize that it was not a requirement: we do not impose a coating with the method of the previous section. The interior of the structure is filled with a composite material of uniform density, the lowest admissible. The optimization process tends to make disappear the composite material. It is not optimal to have composite material under the coating with this objective function. Our result is similar to the one in [Chen 2001], where no microstructure is used to optimize the shape.

The orientation is regularized according to the method presented at Chapter 5, it features a singularity. A diffeomorphism φ is then computed from the regularized orientation: it distorts a regular grid in order to align the bars with the given local orientation. Genuine shapes $\Omega_\varepsilon(\varphi, m)$ are then computed on a finer mesh, they are displayed on Figures 8.7(c) and 8.7(d).

The use of a lattice material in this particular case is not relevant. However, the method is proved to be effective. Other load cases should be investigated. For example the method could be used to optimize a dam like in [Bourdin 2003]: a pressure of uniform direction is applied on a part of the structure, mimicking the behaviour of fluid inside the dam. This is an ongoing work.

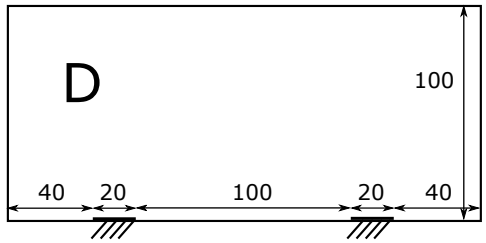

(a) Boundary conditions

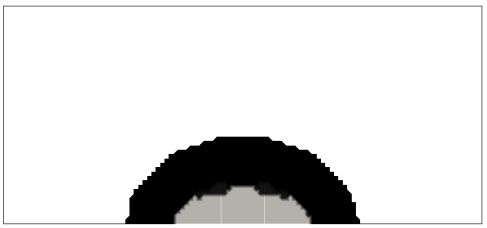

(b) Optimized density

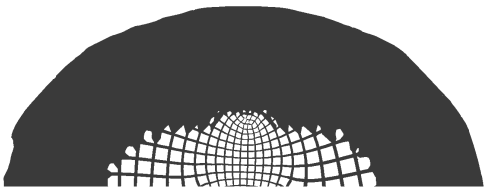

(c) $\Omega_\varepsilon(\varphi, m)$ with $\varepsilon = 0.01$

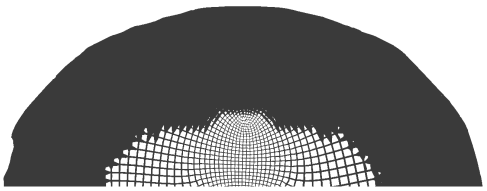

(d) $\Omega_\varepsilon(\varphi, m)$with $\varepsilon = 0.005$

Figure 8.7: Numerical results in a design-dependent load case

Conclusion and perspectives

In this thesis, an efficient topology optimization method of structures made of lattice materials, using the homogenization theory has been presented. We investigated isotropic and orthotropic microstructures in 2D and in 3D. In particular, the orientation of the orthotropic composite materials has been taken into account during the optimization process. These materials are adapted for particular shape optimization problems, namely the compliance and the stress minimization in a single-load case. Other objective functions have to be investigated. The crucial point is the optimization of the orientation of the lattice material. Indeed, the Pedersen formulas have no extension to other objective functions. A gradient based algorithm is not adapted to optimize the orientation, because of the numerous local minima. Other approaches have to be developed, like a local global minimization of the orientation. Nevertheless, such a strategy is only possible for particular cost functions. Indeed, it requires to introduce a local optimality criteria on the orientation. It should be efficient for example in multiple-loads compliance minimization.

On an other side, the use of other microstructures has to be investigated. For example, orthotropic materials are not adapted to multiple-loads compliance minimization. Indeed they are stiff in only two orthogonal principal directions. Consequently, they can not support efficiently stresses in several directions. We have shown that isotropic lattice materials are adequate candidates for this problem. Nevertheless, some anisotropic microstructures could possibly be more optimal.

The collaboration with Jonas Martinez will continue. In particular, shape optimization using 3D stochastic materials will be implemented. The particular interest of these materials relies on the fact that their geometry files, used as input for additive manufacturing machines, are very light. Indeed, it contains only the distribution of the parameters in the working domain and not a complete and fine description of the structure. An additive manufacturing machine builds the structure layer by layer. With stochastic material, the current layer is computed on the fly with respect to the previous one and the current parameters of the material. A similar approach to build structures made of modulated periodic lattice material could lighten the geometric files and should be investigated.

We presented a deshomogenization process yielding optimized genuine structures in 2D and in 3D, straightforwardly manufacturable by additive manufacturing processes. This method could be extended to other applications. First it could be used in structures conception. Indeed, uniform periodic lattice microstructures are increasingly used by industrials to fill structures, in order to lighten them (instead of filling them with solid material). However, they do not have adapted software to design such structures. Our deshomogenization method could be helpful. Moreover, the given volume could be filled with periodic cells which are aligned with the external boundaries: the orientation of the cells being known at the external frontier, it can be extended to the whole domain, and possibly regularized. Second, this method could be used for unstructured meshes generation, where the elements have to be oriented according to a given orientation field.

To conclude, we would like to print deshomogenized structures, the generation of the geom-

etry files is already implemented. Hence we could confirm that they are manufacturable, but also perform experimental tests to check their physical behaviour.

Appendix

Appendix A

Deshomogenization with arbitrary periodic microstructures

The purpose of this short chapter is to show how to extend the deshomogenization method relying on a diffeomorphism, to any periodic microstructure described by a level-set function.

A.1 Periodic microstructures

Let $Y = [-0.5; 0.5]^N$ be the unit cube. In the following, only the case where $N = 2$ is illustrated. Indeed $3D$-structures are difficult to display in $2D$-figures, however the exact same method is still valid. Let Y_0 be a unit periodic cell, whose microstructure is given by a level-set function $\psi : Y \to \mathbb{R}$:

$$Y_0 = \{y \in Y \,|\, \psi(y) < 0\}.$$

We emphasize that the geometry of the microstructure can be parametrized by parameters p. In this case, the corresponding level-set function will be denoted $\psi(p)$.

Examples:
The following microstructures are chosen to illustrate the method and not for any mechanical interest.
• The microstructure of a square cell featuring a central circular hole of radius $r \in [0; 0.5]$, see Figure A.1(a), is given by the level-set function:

$$\psi(r)(y_1, y_2) = r^2 - (y_1^2 + y_2^2).$$

• The microstructure of a square cell featuring a central ellipse of semi-major axis a, semi-minor axis b and orientation θ, see Figure A.1(b), is given by the level-set function:

$$\psi(a, b, \theta)(y_1, y_2) = 1 - \left(\left(\frac{\cos(\theta) y_1 + \sin(\theta) y_2}{a} \right)^2 + \left(\frac{\sin(\theta) y_1 - \cos(\theta) y_2}{b} \right)^2 \right).$$

• The microstructure of a square cell featuring a central rectangular hole with round corners, see Figure A.1(c), is given by the level-set-function:

$$\psi(a_1, a_2)(y_1, y_2) = 1 - \left(\left| \frac{y_1}{a_1} \right|^p + \left| \frac{y_2}{a_2} \right|^p \right)^{\frac{1}{p}},$$

with $p > 1$.

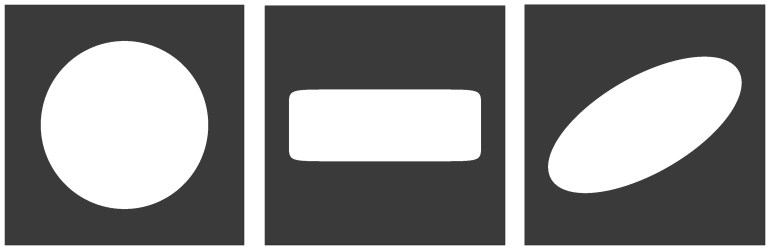

(a) Circular hole (b) Rounded square hole (c) Elliptical hole

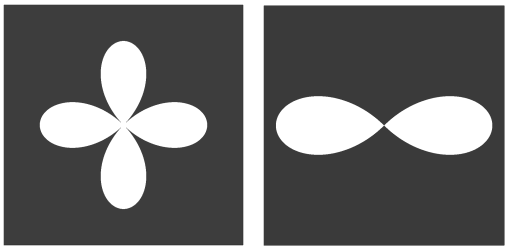

(d) Four-lobed hole (e) Two-lobed hole

Figure A.1: Several design of periodic cells

• The microstructure of a square cell featuring a central four-lobed hole of radius $r \in [0; 0.5]$, see Figure A.1(d), is given by the level-set-function:

$$\psi(r)(y_1, y_2) = r\frac{|y_1^2 - y_2^2|}{y_1^2 + y_2^2 + \eta^2} - \sqrt{y_1^2 + y_2^2},$$

with η a small coefficient.

• The microstructure of a square cell featuring a central two-lobed hole of radius $r \in [0; 0.5]$, see Figure A.1(d), is given by the level-set-function:

$$\psi(r)(y_1, y_2) = r\frac{y_1^2 - y_2^2}{y_1^2 + y_2^2 + \eta^2} - \sqrt{y_1^2 + y_2^2},$$

with η a small coefficient.

A.2 Deshomogenization

Let $D \subset \mathbb{R}^N$, with $N = 2$ or 3, be the working domain.
Let $\varphi : D \to \mathbb{R}^N$ be a diffeomorphism.
We want to tile D with periodic microstructures, of characteristic size $\varepsilon > 0$, and distorted according to the diffeomorphism φ.
The i^{th} coordinate of the point $M(x_1, ..x_N)$ in the corresponding distorted periodic cell is given by:

$$z_i = \varphi_i(x_1, ..x_N) - \left(E(\frac{\varphi_i(x_1, ..x_N)}{\varepsilon}) + \frac{1}{2}\right),$$

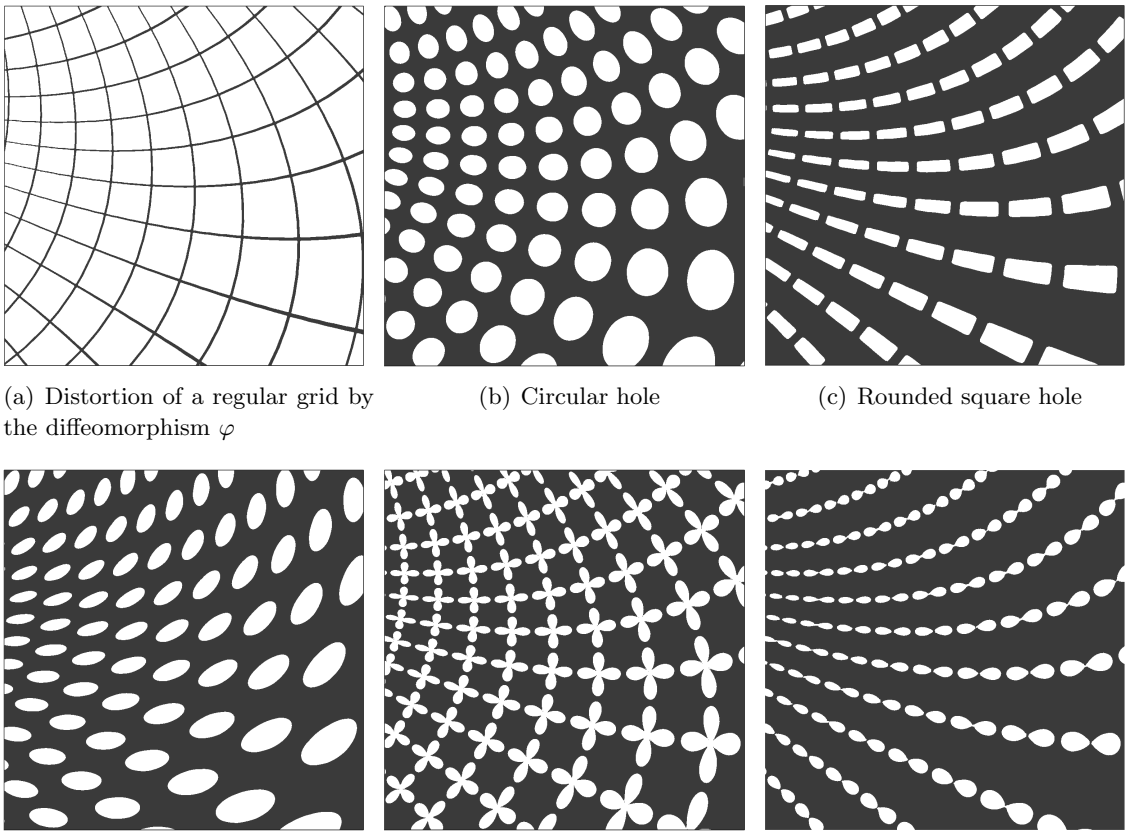

(a) Distortion of a regular grid by the diffeomorphism φ

(b) Circular hole

(c) Rounded square hole

(d) Elliptical hole

(e) Four-lobed hole

(f) Two-lobed hole

Figure A.2: Tiled square with uniform microstructures

where E stands for the floor function.

Hence the final structure is given by the level-set function $\Psi : D \to \mathbb{R}$ given by:

$$\Psi(x_1, ..x_N) = \psi(p)(z_1, .., z_N),$$

where $\psi(p)$ is the level-set function describing the microstructure.

The final structures made with the previous microstructures have been computed for arbitrary diffeomorphisms. In Figure A.2, the parameters of the microstructures are uniform in the whole domain. The distortion of a regular grid is given as reference, see Figure A.2(a).

Obviously, the parameters may vary in the domain, in order to modulate the microstructure, see Figure A.3.

To conclude, this method is still valid when the diffeomorphism features singularities, see Figure A.4, the distortion of a regular grid is displayed in Figure A.4(a).

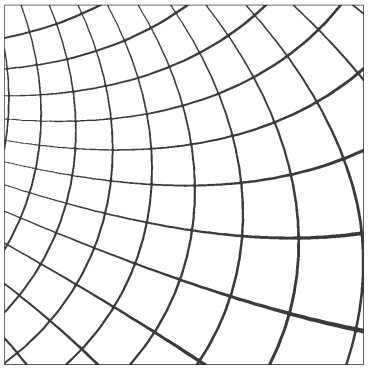

(a) Distortion of a regular grid by the diffeomorphism φ

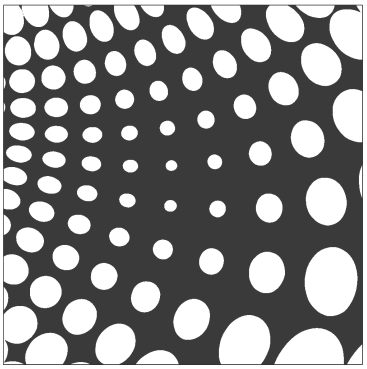

(b) Circular hole, whose radius r is modulated

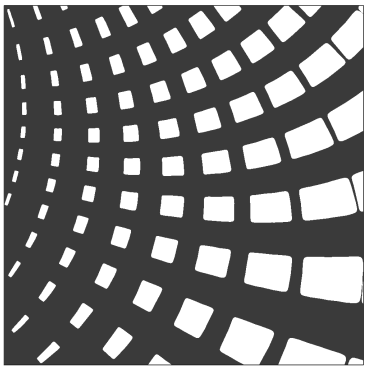

(c) Rounded square hole, whose realtive dimension a_2 is modulated

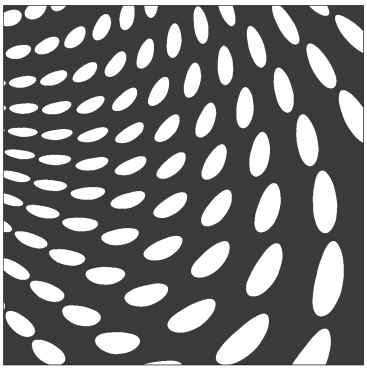

(d) Elliptical hole, whose orientation θ is modulated

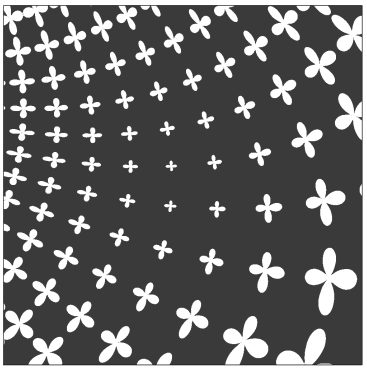

(e) Four-lobed hole, whose radius r is modulated

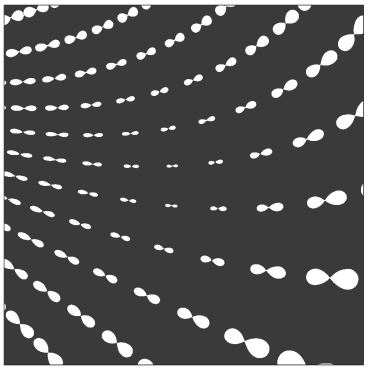

(f) Two-lobed hole, whose radius r is modulated

Figure A.3: Tiled square with modulated microstructures

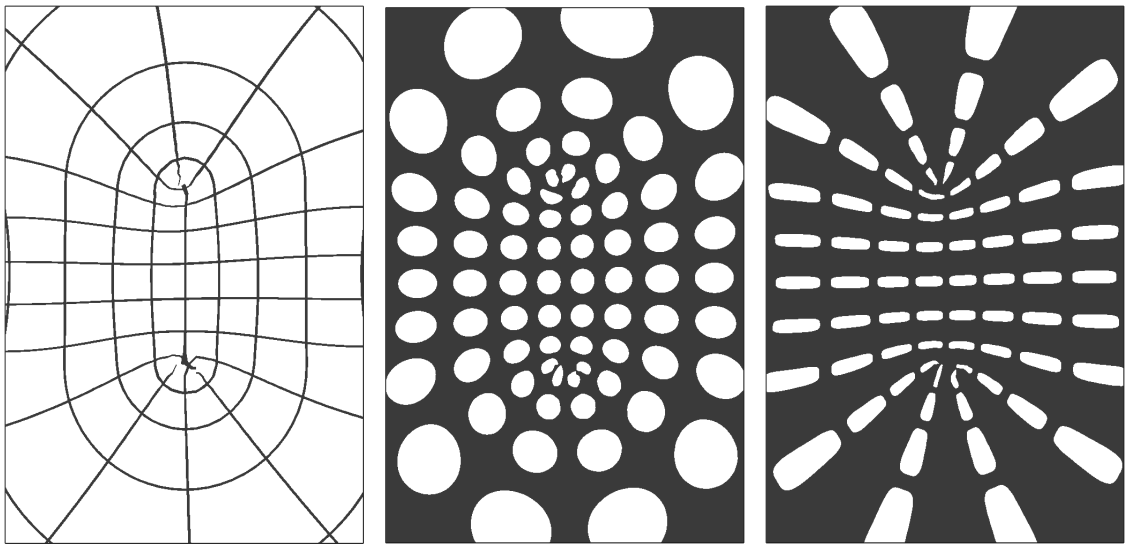

(a) Distortion of a regular grid by the diffeomorphism φ

(b) Circular hole

(c) Rounded square hole

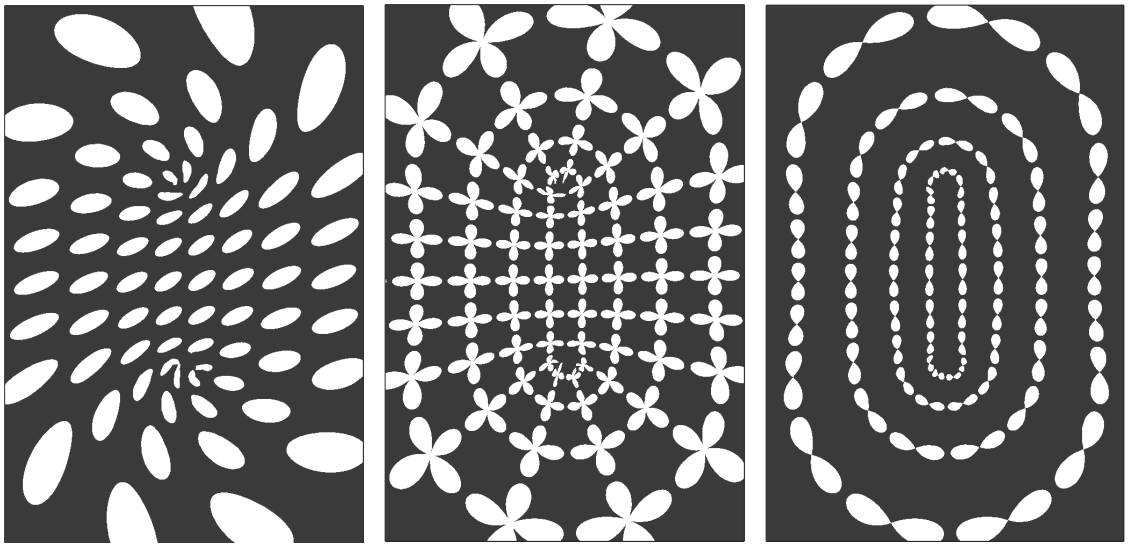

(d) Rounded square hole

(e) Four-lobed hole

(f) Two-lobed hole

Figure A.4: Tiled domain with uniform microstructures, in presence of singularities

Appendix B

Deshomogenization when the orientation is given up to a rotation

This short chapter is an extension to Chapter 5. In Chapter 5, we present a method to integrate an irrotational vector field on a differentiable manifold, when the orientation is given up to a π-rotation. The method can be straightly extended to the cases where the orientation is known up to a $\frac{\pi}{n}$-rotation, with $n \in \mathbb{N}^*$.

B.1 Context

Let $D \subset \mathbb{R}^2$ be an open subset. Let $\alpha : D \to \mathbb{R}/\frac{\pi}{n}\mathbb{Z}$ be an orientation angle: the orientation is given up to a rotation of angle $\frac{\pi}{n}$ where $n \in \mathbb{N}^*$.

Let introduce the unit vector field $b = (\cos(2n\alpha), \sin(2n\alpha))$: it is continuous on D.

We assume in the following that the orientation satisfies the conformity condition, see Section 4.5.2 for more details.

B.2 Simply connected domain

B.2.1 Integrability of the vector field

We assume here that the working domain D is simply connected.

Let $\mathcal{D}$ be the differentiable manifold defined by:

$$\mathcal{D} = \{(x, T) \,|\, T^n = b\}.$$

The manifold $\mathcal{D}$ consists in $2n$ disjoint copies of D. On each of those copies, the vector field T is continuous. Moreover, from one copy to another, the vector field T is rotated of $\frac{\pi k}{n}$, with $k \in \mathbb{Z}^*$. Hence, each copy can be labeled. The first one is arbitrarily chosen, and denoted D_1. The i^{th} copy D_i satisfies:

$$\forall x \in D \quad T_i(x) = R\left(\frac{(i-1)\pi}{n}\right) T_1(x),$$

where $R(\theta)$ is the rotation matrix of angle θ, and T_i is the value of T on the copy D_i.

Proposition B.2.1. *Assuming all the previous settings, there exists a function $\varphi \in C^1(\mathcal{D}, \mathbb{R}^2)$ such that:*

$$\forall (x,T) \in \mathcal{D} \quad \varphi(x,T) = R(\frac{\pi}{n})\varphi(x, R(\frac{\pi}{n})T), \tag{B.1}$$

and that satisfies:

$$\begin{cases} e^r T = \nabla \varphi_1 & \text{on } \mathcal{D} \\ e^r R\left(\frac{\pi}{2}\right) T = \nabla \varphi_2 & \text{on } \mathcal{D} \end{cases},$$

where $R(\theta)$ is the rotation matrix of angle θ, and $r : \mathcal{D} \to \mathbb{R}$ is the dilatation factor defined by (4.7).

Proof. On each copy D_i of D, thanks to Poincaré lemma, there exists functions $\varphi_{i,1}$ and $\varphi_{i,2}$ such that:

$$\begin{cases} e^r T_i = \nabla \varphi_{i,1} \\ e^r R\left(\frac{\pi}{2}\right) T_i = \nabla \varphi_{i,2} \end{cases}.$$

Hence, we get:

$$\forall i \in \{1, .., 2n\} \quad \begin{cases} \nabla \varphi_{i,1} = R\left(\frac{(i-1)\pi}{n}\right) \nabla \varphi_{1,1} \\ \nabla \varphi_{i,2} = R\left(\frac{(i-1)\pi}{n}\right) \nabla \varphi_{1,2} \end{cases}.$$

Possibly by adding constants, we can assume that:

$$\varphi_i = R\left(\frac{(i-1)\pi}{n}\right) \varphi_1 .$$

□

B.2.2 Numerical implementation

For details about the numerical implementation, one can read Section 4.5.5.

Here is the main difference with Chapter 4: to take into account the rotation condition (B.1), both components of φ have to be simultaneously computed.

We recall that P_1 finite elements are used to discretize φ. Let $\mathcal{V}_h$ be the Lagrange finite elements of degree one on $\mathcal{D}$ with values in $\mathbb{R}^2$, that satisfy the rotation condition (B.1). Let W_h be the P_1 discontinuous Galerkin elements on D, with values in $\mathbb{R}^2$,.

To compute the diffeomorphism φ, we introduce an interpolation operator I_h from $\mathcal{V}_h$ onto W_h. This interpolation operator I_h is a sparse matrix that is computed by going through all the elements of the mesh and by determining a coherent orientation on each element. This means that for any triangle, its all vertices belong to the same copy D_i of D. Numerically, for a given element, the orientation will be said *coherent*, if the three orientation vectors of the vertices belong to the same $\frac{\pi}{2n}$ angular sector.

Technically, at each triangle, one vertex is arbitrarily chosen and its current orientation vector $v_0 = (\cos(\alpha_0), \sin(\alpha_0))$ is taken as reference. On the ith vertex of the triangle, the current

orientation vector $v_i = (\cos(\alpha_i), \sin(\alpha_i))$ is rotated of an angle $\frac{\pi}{n}$ until the angle between v_0 and v_i is lower than $\frac{\pi}{2n}$. Let n_i be the number of necessar iterations of rotations. The interpolation operator on the ith vertex is then equal to the rotation matrix of an angle $n_i\frac{\pi}{n}$. Once the interpolation operator I_h has been computed, the same variationnal formulation than in Section 4.5.5, see Equation (4.36), is solved.

Remark 17. *Let φ be a diffeomorphism corresponing to a vector field defined up to a $\frac{\pi}{n}$-rotation. Only periodic microstructures, which are invariant by a $\frac{\pi}{n}$-rotation, can be deshomogenized using this diffeomorphism. Hence, in practice, n will be equal to 1, 2 or 3. We emphasize that the case where $n = 1$ is the one studied in Chapter 4.*

B.2.3 Numerical results

Vector field defined up to a $\frac{\pi}{2}$ rotation. An arbitrary orientation vector field, defined up to a $\frac{\pi}{2}$ rotation, is taken, see Figure B.1. The corresponding diffeomorphism φ is computed according to the above method, see Figure B.2. The numerical components of φ are not continuous on the mesh: their gradient suddenly turn of an angle $\frac{\pi}{2}$ where the orientation vector field jumps too. Indeed, the elements of the mesh do not necessarily belong to the same copy D_i of D. However, the structure deshomogenized using this diffeomorphism φ is smooth, see Figure B.3(c). The periodic microstructure chosen here for the deshomogenization is a square holed by a square, with relative dimensions $m \in [0; 1]$.

We emphasize that the sets of deshomogenized bars, see Figures B.3(a) and B.3(b) are not continuous, since they are respectively defined by:

$$\Omega_{i,\varphi,\varepsilon}(m) = \left\{ x \in D \,|\, \cos(\frac{2\pi}{\varepsilon}\varphi_i) > \cos(\pi(1 - m(x))) \right\},$$

where $\varepsilon > 0$ is the characteristic period of the composite. However, these sets are perfectly complementar and their union yield a final smooth structure.

Vector field defined up to a $\frac{\pi}{3}$ rotation. An arbitrary orientation vector field, defined up to a $\frac{\pi}{3}$ rotation, is taken, see Figure B.4. The corresponding diffeomorphism φ is computed according to the above method, see Figure B.5. Here again, the numerical components of φ are not continuous on the mesh: their gradient suddenly turn of an angle $\frac{\pi}{3}$ where the orientation vector field jumps too. Indeed, the elements of the mesh do not necessarily belong to the same copy D_i of D. However, the structure deshomogenized using this diffeomorphism φ is smooth, see Figure B.6(d). The periodic microstructure chosen here is the reinforced honeycomb see

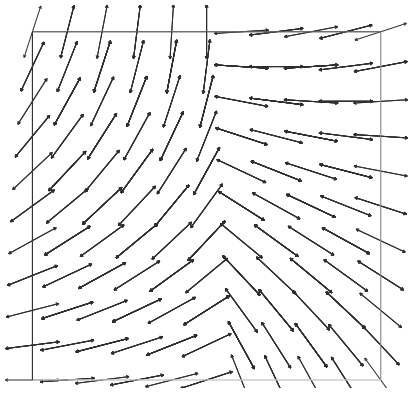

Figure B.1: Orientation up to a $\frac{\pi}{2}$-rotation

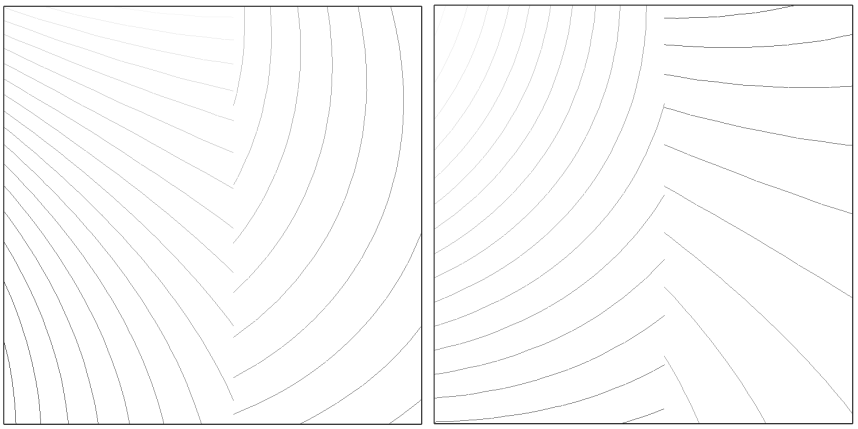

(a) (b)

Figure B.2: Diffeomorphism φ corresponding to the vector field defined up to a $\frac{\pi}{2}$-rotation

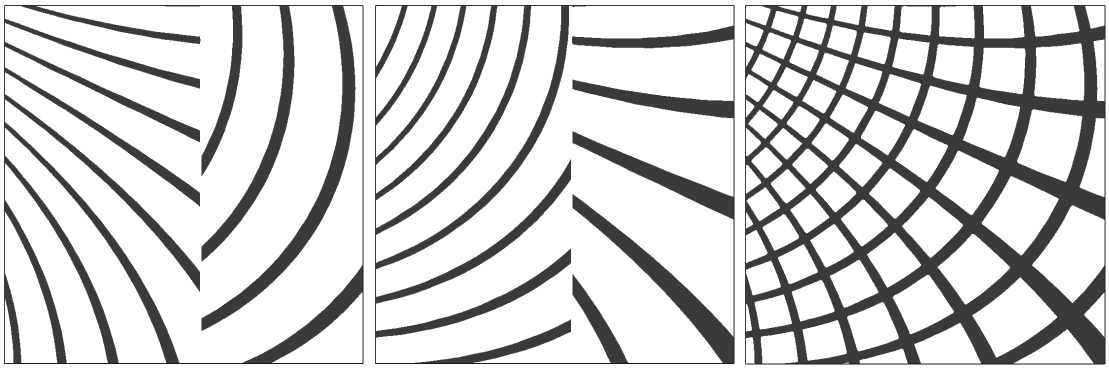

(a) $\Omega_{1,\varphi,\varepsilon}$ (b) $\Omega_{2,\varphi,\varepsilon}$ (c) Deshomogenized structure

Figure B.3: Deshomogenization process

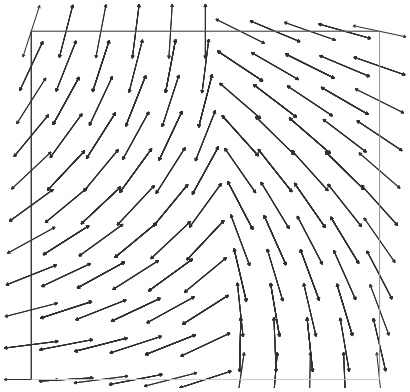

Figure B.4: Orientation up to a $\frac{\pi}{3}$–rotation

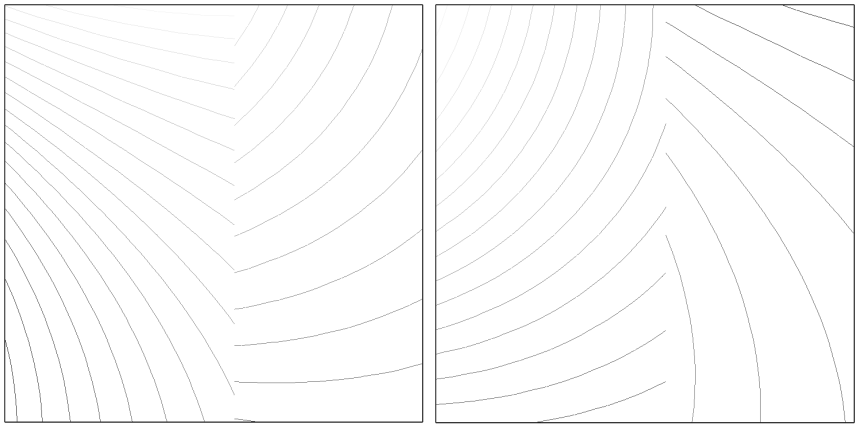

(a) φ_1 (b) φ_2

Figure B.5: Diffeomorphism φ corresponding to the vector field defined up to a $\frac{\pi}{3}$–rotation

Figure 3.1(b). For details about the deshomogenization process for this microstructure, see Section 3.4.2.

We emphasize that the sets of deshomogenized bars, see Figures B.6(a), B.6(b) and B.6(c) are not continuous. However, these sets are perfectly complementar and their union yield a final smooth structure.

B.3 Non simply connected domain

B.3.1 Correction functions

In the case where the working domain D is not simply connected, the manifold $\mathcal{D}$ is no longer the union of disjoint copies of D: copies are glued to each other. The previous approach is no longer valid. However, using the same process than the one described in Chapter 5, correction functions

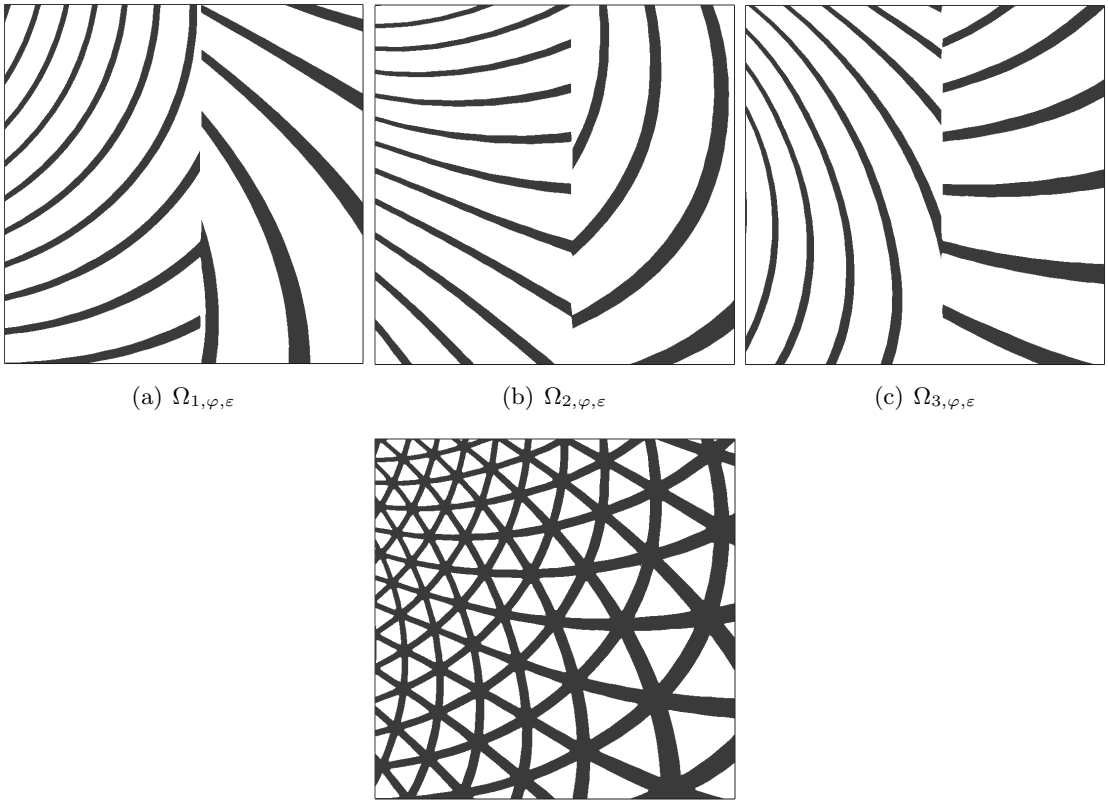

(a) $\Omega_{1,\varphi,\varepsilon}$ (b) $\Omega_{2,\varphi,\varepsilon}$ (c) $\Omega_{3,\varphi,\varepsilon}$

(d) Deshomogenized structure

Figure B.6: Deshomogenization process

are introduced in order to compute a continuous diffeomorphism φ. The main difference is that correction functions have now two components, and satisfy the rotation condition (B.1).

B.3.2 Spotting the singularities

A discretized orientation vector field may feature singularities, meaning points where the linear interpolation yield a null vector, see Proposition 5.3.2. In the case of an orientation field α defined up to a $\frac{\pi}{n}$–rotation, singularites may also occur.

Assuming the orientation is discretized using P_1 finite elements, singularities can numerically be spotted thanks to Proposition 5.3.1, applied to the vector fields $w = e^r b$, where r is the dilatation factor defined by (4.7). Briefly, a triangle K of the mesh contains a singularity if and only if at least two scalar products $w^i \cdot w^j$ are negative, where w_i is the value of w at the i^{th} vertex of the triangle K.

B.3.3 Numercial results

We do not give here details about the numerical implementation, but numerical results are briefly displayed.

Arbitrary orientation vector fields, defined up to a $\frac{\pi}{2}$ (resp. $\frac{\pi}{3}$) rotation and featuring singularities, are taken, see Figure B.7 (resp Figure B.10). The corresponding diffeomorphisms φ are computed according to the method presented in Chapter 5, see Figure B.8 (resp Figure B.11). The numerical components of φ are not continuous on the mesh. However, the structures deshomogenized using these diffeomorphisms are smooth, see Figure B.9(c) and B.12(d).

We emphasize that the sets of deshomogenized bars, see Figures B.9 and B.12 are not continuous. However, these sets are perfectly complementar and their union yield a final smooth structure. In particular, the connectivity of the bars is perfect along the cut lines used to define the correction functions.

Besides, there is an odd number of cells around the singularities, respectively 3 and 5 for the square cells, in red in Figure B.9(d), and 5 and 7 for the hexagonal cells, in red in Figure B.12(e). This would never occur on a regular grid: this illustrates clearly the effect of the correction functions on the diffeomorphism.

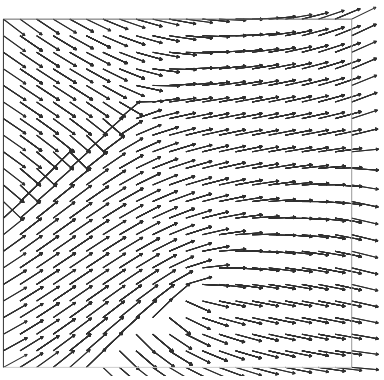

Figure B.7: Orientation up to a $\frac{\pi}{2}$-rotation

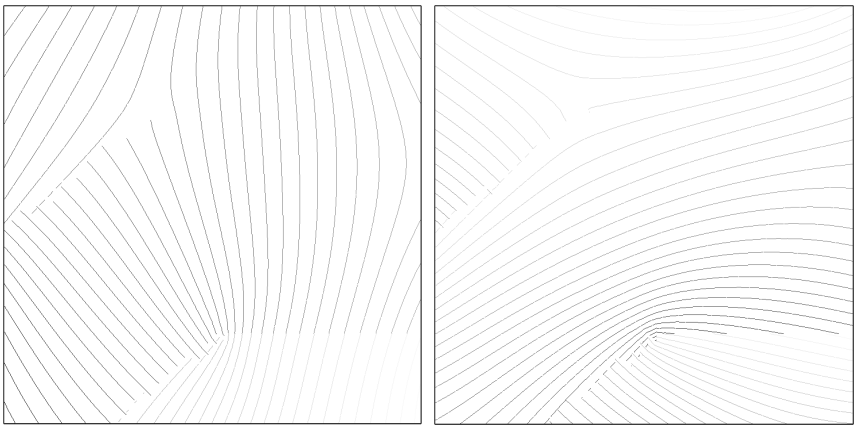

(a) φ_1 (b) φ_2

Figure B.8: Diffeomorphism corresponding to the vector field defined up to a $\frac{\pi}{2}$-rotation and featuring two singularities

φ_1

(a) $\Omega_{1,\varphi,\varepsilon}$ (b) $\Omega_{2,\varphi,\varepsilon}$

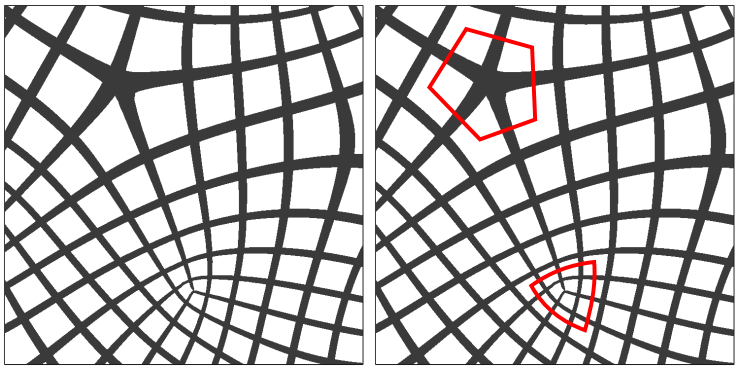

(c) Deshomogenized structure (d) Deshomogenized structure, in red, odd number of cells around the singularities

Figure B.9: Deshomogenization process

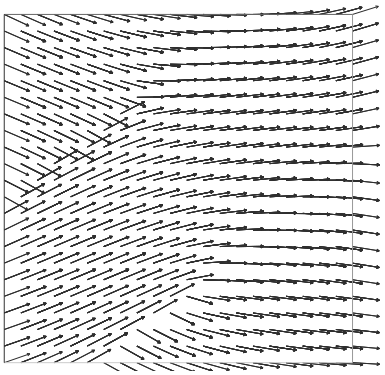

Figure B.10: Orientation up to a $\frac{\pi}{3}$-rotation

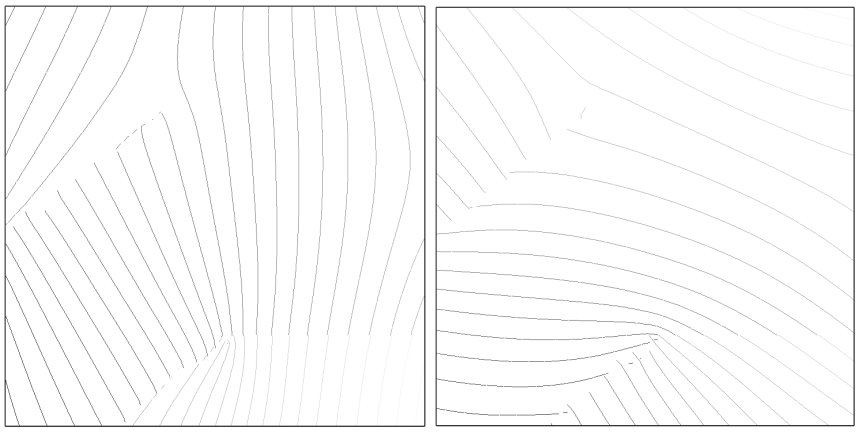

(a) φ_1 (b) φ_2

Figure B.11: Diffeomorphism corresponding to the vector field defined up to a $\frac{\pi}{3}$-rotation and featuring two singularities

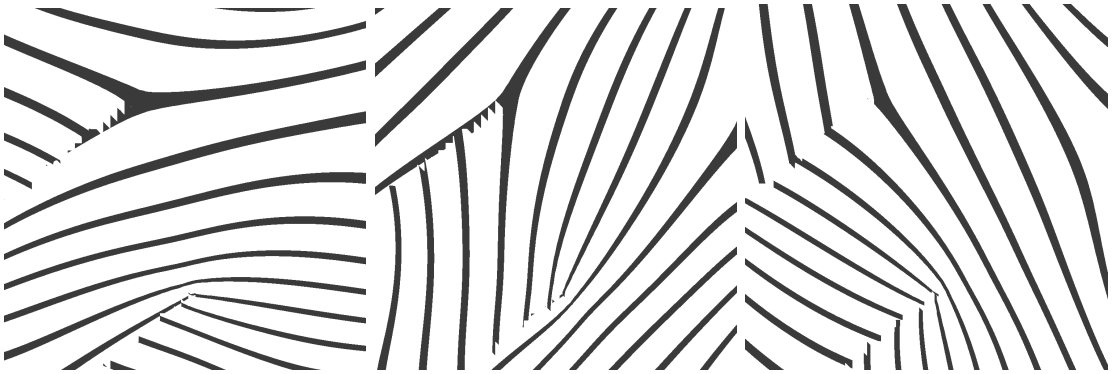

(a) $\Omega_{1,\varphi,\varepsilon}$ (b) $\Omega_{2,\varphi,\varepsilon}$ (c) $\Omega_{3,\varphi,\varepsilon}$

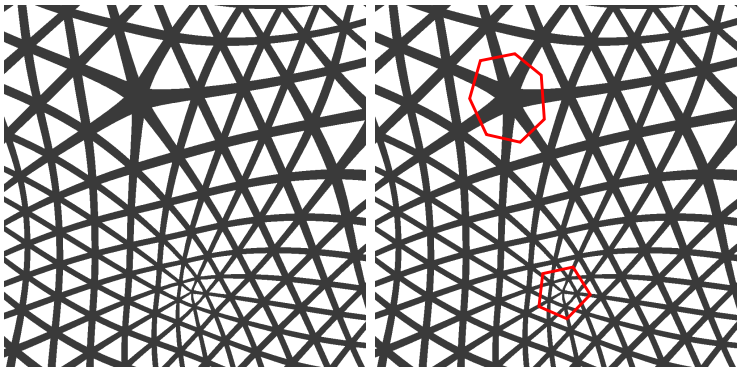

(d) Deshomogenized structure (e) Deshomogenized structure, in red, odd number of cells around the singularities

Figure B.12: Deshomogenization process

Appendix C

3D deshomogenization method for a non simply connected domain

In Section 4.5 of Chapter 4, we presented how to compute a $2D$ map whose gradient is aligned with a given orientation. In Chapter 5, this method has been extended to the general case, namely when the working domain is non simply connected.

In Chapter 7, the $2D$-method has been adapted to the $3D$ case, when the the working domain is simply connected. This short chapter is dedicated to the extension of the $3D$-method when the working domain features drilled holes. The approach is the same as the one presented in Chapter 5: the proofs are not detailed here.

C.1 Integrability of a $3D$ vector field on a non simply connected domain

Let $D \subset \mathbb{R}^3$ be an open subset featuring n_H holes $(H_i)_{1 \leq i \leq n_H}$. We assume that all those holes are loops (like in a torus) and not cavities. As in Chapter 5, we cut the domain D in order to connect the holes to the external border. However, there are no longer cut lines but cut surfaces, still denoted Γ_i, see Figure C.1. The new working domain $\tilde{D}$ is given by: $\tilde{D} = D \setminus \{\Gamma_i\}_{1 \leq i \leq n_H}$.

Let w be an irrotational vector field on D. There exists a continuous function $\tilde{\varphi}$ on $\tilde{D}$ such that: $\nabla \tilde{\varphi} = w$.

The jump of the function φ through the cut surfaces Γ_i is constant. Hence particular correction functions $\psi_i \in C^1(D, \mathbb{R}/\mathbb{Z})$ are introduced. We emphasize that their values are in $\mathbb{R}/\mathbb{Z}$.

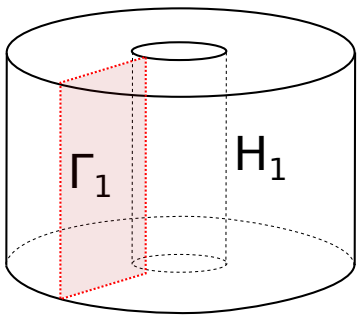

Figure C.1: The non simply connected domain D is cut along a surface Γ_1

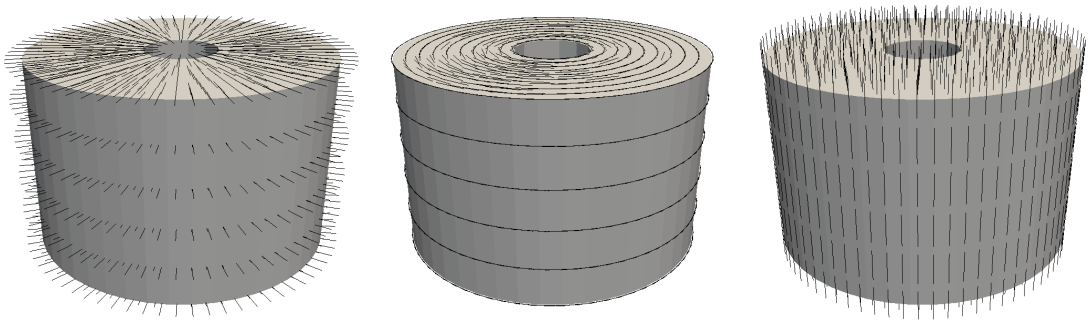

(a) ω_1 (b) ω_2 (c) ω_3

Figure C.2: Orientation

Hence there exists real coefficients c_i such that:

$$\forall x \in \tilde{D} \quad w(x) = \nabla\tilde{\varphi}(x) + \sum_{i=1}^{n_H} c_i \nabla\psi_i(x)$$

and such that the function $\varphi = \tilde{\varphi} + \sum_{i=1}^{n_H} c_i\psi_i$ can continuoulsy be extended to D.

C.2 Numerical examples

C.2.1 Theoretical test case

In this example, the working domain is a tube: its external radius is 4, its internal radius is 1 and its height is 5.

We chose an arbitrary orientation vectors field:

$$\begin{cases} \omega_1 = (\dfrac{x}{\sqrt{x^2+y^2}}, \dfrac{y}{\sqrt{x^2+y^2}}, 0) \\ \omega_2 = (-\dfrac{y}{\sqrt{x^2+y^2}}, \dfrac{x}{\sqrt{x^2+y^2}}, 0) \\ \omega_3 = (0,0,1) \end{cases}.$$

The three vector fields are respectively displayed in Figure C.2.

The diffeomorphism φ has been computed according to the method developed in Chapter 7 by taking into account the correction functions.

The microstructures used here is the periodic cubic square, holed from end to end with rectangular holes, see Figure 7.1. We took uniform microstructure: $m_i = 0.7$. The deshomogenization process is detailed in Section 7.5.1.

Let $\Omega_{i,\varphi,\varepsilon}$ be the subsets defined by:

$$\Omega_{i,\varphi,\varepsilon} = \left\{ x \in D \,|\, \cos(\frac{2\pi}{\varepsilon}\varphi_i(x)) > \cos(\pi(1 - m_i(x)) \right\},$$

see Figures C.3(a), C.3(b) and C.3(c). One can check that the normals to this sets of surfaces are aligned with the orientation vectors ω_i.

The sets of parallel bars featuring in the final structure are given by the intersections in pairs of the previous subsets, see Figures C.3(d), C.3(e) and C.3(f).

The final structure is displayed in Figure C.3(g). It is smooth: the bars are well connected around the cut surface Γ_1. The orientation of the cells is respected.

One can notice that the considered orientation is similar to the one of the $2D$ optimized wheel under normal loading, see Figure 5.24(c), but extruded in $3D$. As expected, an horizontal slice of the final structure is identical to the final structure of the wheel, see Figure 5.24(l).

C.2.2 Optimization of a tube

In this example, the working domain D is still the tube. The main difference is that the considered orientation is not arbitrary anymore, but the result of a shape optimization.

The structure is clamped on its bottom face. A unit tangential load is applied on its upper face, see Figure C.4. The optimized homogenized structure is computed with the method presented in Chapter 7. The microstructure is the same cubic periodic cell, see Figure 7.1. Here, the relative dimensions m_i of the holes are fixed to 0.7. Only the orientation of the cells is optimized.

The optimized orientation vector fields are displayed in Figure C.5. Contrary to the previous example, this orientation is not a $2D$ orientation extruded in $3D$.

The deshomogenization process is displayed in Figure C.6, and the final structure in Figure C.6(g). Here again, the connectivity of the final structure is perfect and the orientation of the cells is respected.

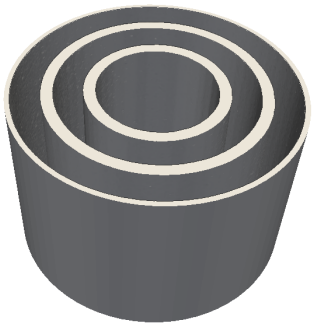

(a) $\Omega_1 = \Omega_{1,\varphi,0.2}$

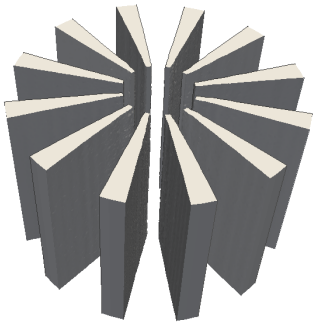

(b) $\Omega_2 = \Omega_{2,\varphi,0.2}$

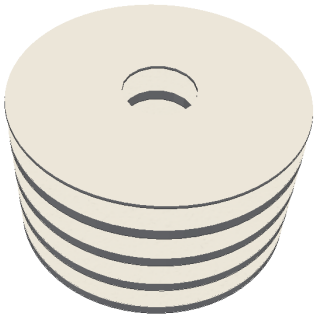

(c) $\Omega_3 = \Omega_{3,\varphi,0.2}$

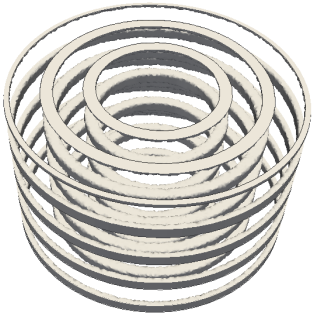

(d) $\Omega_{12} = \Omega_1 \cap \Omega_2$

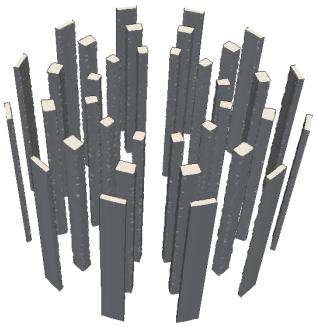

(e) $\Omega_{13} = \Omega_1 \cap \Omega_3$

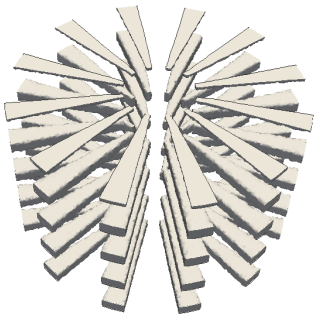

(f) $\Omega_{23} = \Omega_2 \cap \Omega_3$

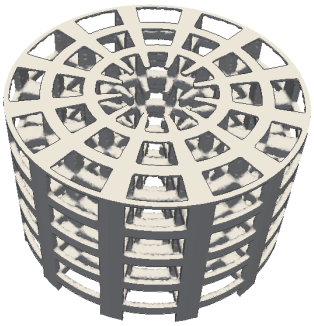

(g) Final structure

Figure C.3: Deshomogenization process

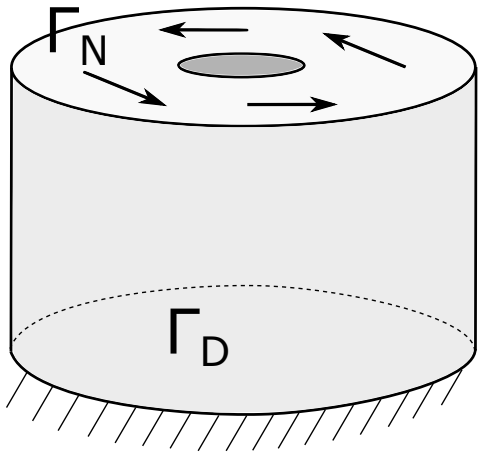

Figure C.4: Boundary conditions for the tube case

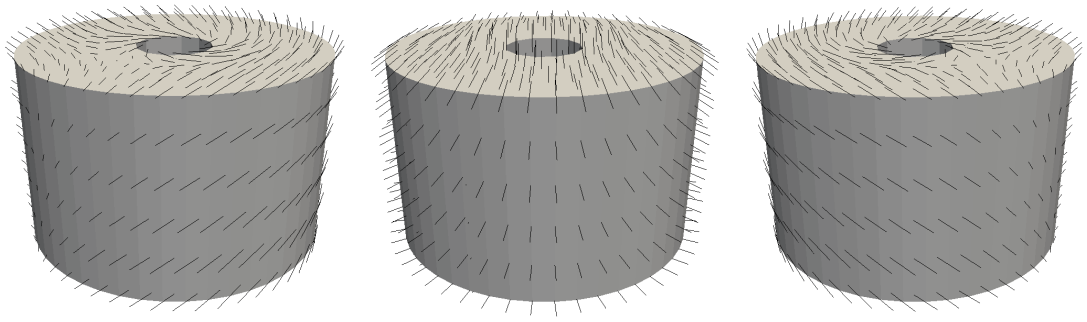

(a) ω_1 (b) ω_2 (c) ω_3

Figure C.5: Orientation of the cells

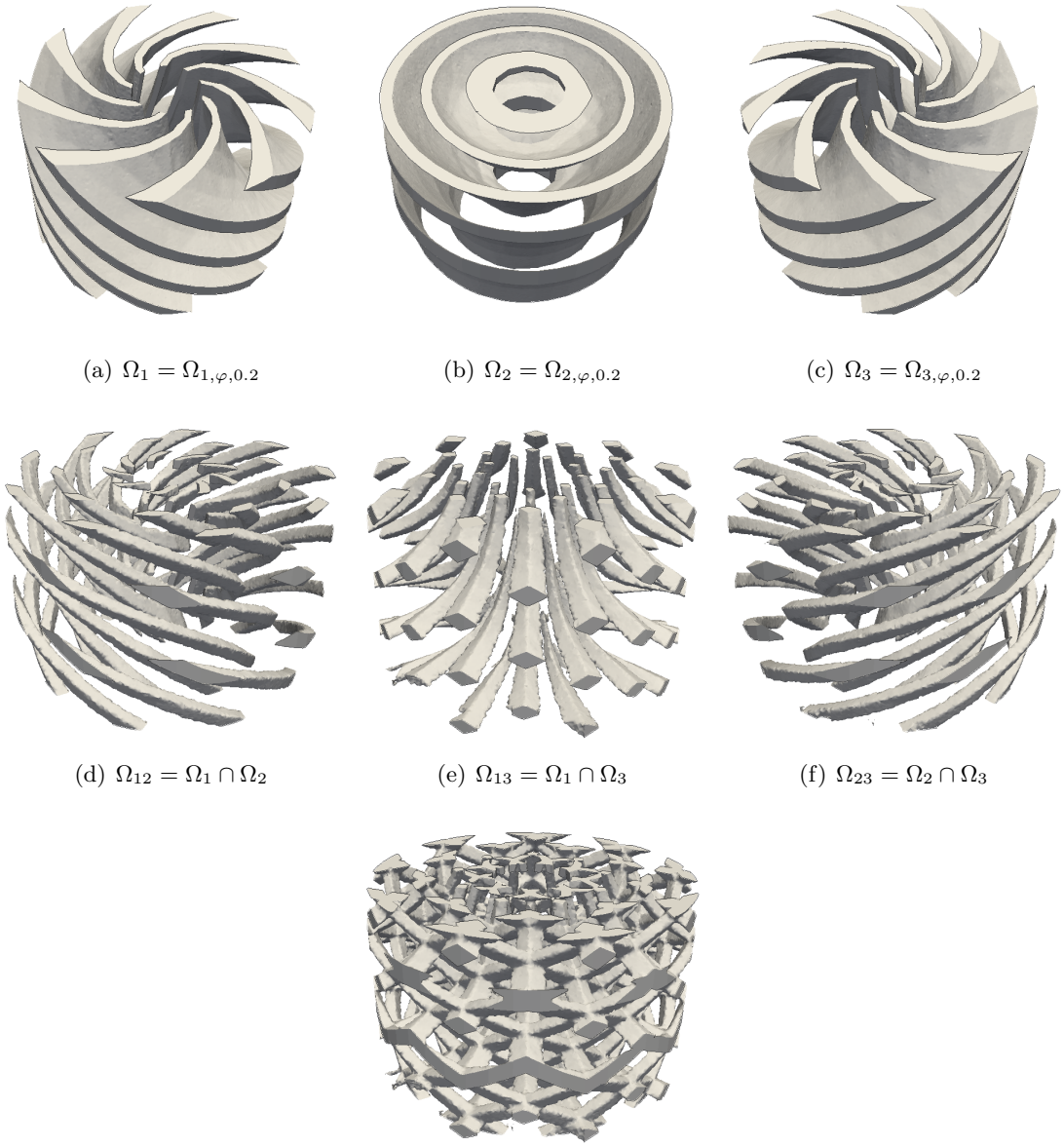

(a) $\Omega_1 = \Omega_{1,\varphi,0.2}$ (b) $\Omega_2 = \Omega_{2,\varphi,0.2}$ (c) $\Omega_3 = \Omega_{3,\varphi,0.2}$

(d) $\Omega_{12} = \Omega_1 \cap \Omega_2$ (e) $\Omega_{13} = \Omega_1 \cap \Omega_3$ (f) $\Omega_{23} = \Omega_2 \cap \Omega_3$

(g) Final structure

Figure C.6: Deshomogenization process

Bibliography

[Abad 2013] Ehsan Masoumi Khalil Abad, Sajad Arabnejad Khanoki and Damiano Pasini. *Fatigue design of lattice materials via computational mechanics: Application to lattices with smooth transitions in cell geometry.* International Journal of Fatigue, vol. 47, pages 126–136, 2013.

[Allaire 1993] G. Allaire and G. A. Francfort. A numerical algorithm for topology and shape optimization, chapitre Topology Design of Structures, pages 239–248. Springer Netherlands, 1993.

[Allaire 1997] Grégoire Allaire, Eric Bonnetier, Gilles Francfort and François Jouve. *Shape optimization by the homogenization method.* Numer. Math., vol. 76, no. 1, pages 27–68, 1997.

[Allaire 2002a] Grégoire Allaire. Shape optimization by the homogenization method, volume 146. Springer Science & Business Media, 2002.

[Allaire 2002b] Grégoire Allaire, François Jouve and Anca-Maria Toader. *A level-set method for shape optimization.* Comptes Rendus Mathematique, vol. 334, no. 12, pages 1125–1130, 2002.

[Allaire 2004a] Grégoire Allaire, F Jouve and H Maillot. *Topology optimization for minimum stress design with the homogenization method.* Structural and Multidisciplinary Optimization, vol. 28, no. 2-3, pages 87–98, 2004.

[Allaire 2004b] Grégoire Allaire, François Jouve and Anca-Maria Toader. *Structural optimization using sensitivity analysis and a level-set method.* Journal of computational physics, vol. 194, no. 1, pages 363–393, 2004.

[Allaire 2006] Grégoire Allaire and Olivier Pantz. *Structural optimization with FreeFem++.* Structural and Multidisciplinary Optimization, vol. 32, no. 3, pages 173–181, 2006.

[Allaire 2007] Grégoire Allaire. Conception optimale de structures, volume 58. Springer, 2007.

[Allaire 2014] Grégoire Allaire, Charles Dapogny, Gabriel Delgado and Georgios Michailidis. *Multi-phase structural optimization via a level set method.* ESAIM: control, optimisation and calculus of variations, vol. 20, no. 2, pages 576–611, 2014.

[Allaire 2018] Grégoire Allaire, Perle Geoffroy-Donders and Olivier Pantz. *Topology optimization of modulated and oriented periodic microstructures by the homogenization method.* Computers and Mathematics with Applications, 2018.

[Ambrosio 1993] Luigi Ambrosio and Giuseppe Buttazzo. *An optimal design problem with perimeter penalization.* Calculus of Variations and Partial Differential Equations, vol. 1, no. 1, pages 55–69, 1993.

[Amstutz 2006] Samuel Amstutz and Heiko Andrä. *A new algorithm for topology optimization using a level-set method.* Journal of Computational Physics, vol. 216, no. 2, pages 573–588, 2006.

[Andreassen 2014] Erik Andreassen, Boyan S Lazarov and Ole Sigmund. *Design of manufacturable 3D extremal elastic microstructure.* Mechanics of Materials, vol. 69, no. 1, pages 1–10, 2014.

[Aubry 1999] Sylvie Aubry. *Etude théorique et numérique de quelques problèmes d'optimisation de forme à l'aide de méthodes d'homogénéisation.* PhD thesis, Université Pierre et Marie Curie, 1999.

[Barbarosie 1997] C Barbarosie. *Optimization of perforated domains through homogenization.* Structural optimization, vol. 14, no. 4, pages 225–231, 1997.

[Barbarosie 2010a] Cristian Barbarosie and Anca-Maria Toader. *Shape and topology optimization for periodic problems.* Structural and Multidisciplinary Optimization, vol. 40, no. 1, pages 393–408, 2010.

[Barbarosie 2010b] Cristian Barbarosie and Anca-Maria Toader. *Shape and topology optimization for periodic problems. II. Optimization algorithm and numerical examples.* Struct. Multidiscip. Optim., vol. 40, no. 1-6, pages 393–408, 2010.

[Bendsøe 1988] Martin Philip Bendsøe and Noboru Kikuchi. *Generating optimal topologies in structural design using a homogenization method.* Computer methods in applied mechanics and engineering, vol. 71, no. 2, pages 197–224, 1988.

[Bendsøe 1989] Martin P Bendsøe. *Optimal shape design as a material distribution problem.* Structural and multidisciplinary optimization, vol. 1, no. 4, pages 193–202, 1989.

[Bendsøe 1994] M. P. Bendsøe, JM Guedes, Robert B Haber, P Pedersen and JE Taylor. *An Analytical Model to Predict Optimal Material Properties in the Context of Optimal Structural Design.* J. Appl. Mech., vol. 61, no. 4, pages 930–937, 1994.

[Bendsøe 1999] Martin P Bendsøe and Ole Sigmund. *Material interpolation schemes in topology optimization.* Archive of applied mechanics, vol. 69, no. 9, pages 635–654, 1999.

[Bendsoe 2003] Martin Philip Bendsoe and Ole Sigmund. Topology optimization: theory, methods, and applications. Springer Science & Business Media, 2003.

[Boscain 2016] Ugo Boscain, Ludovic Sacchelli and Mario Sigalotti. *Generic singularities of line fields on 2D manifolds.* Differential Geometry and its Applications, vol. 49, pages 326–350, 2016.

[Bourdin 2001] Blaise Bourdin. *Filters in topology optimization.* International journal for numerical methods in engineering, vol. 50, no. 9, pages 2143–2158, 2001.

[Bourdin 2003] Blaise Bourdin and Antonin Chambolle. *Design-dependent loads in topology optimization.* ESAIM: Control, Optimisation and Calculus of Variations, vol. 9, pages 19–48, 2003.

[Brennan-Craddock 2011] James Brennan-Craddock. *The Investigation of a Method to Generate Conformal Lattice Structures for Additive Manufacturing.* PhD thesis, Loughborough Univ., 2011.

[Briane 1994] Marc Briane. *Correctors for the homogenization of a laminate.* Adv. Math. Sci. Appl, vol. 4, no. 2, pages 357–379, 1994.

[Bruns 2005] TE Bruns. *A reevaluation of the SIMP method with filtering and an alternative formulation for solid–void topology optimization.* Structural and Multidisciplinary Optimization, vol. 30, no. 6, pages 428–436, 2005.

[Bui 2012] C Bui, Charles Dapogny and Pascal Frey. *An accurate anisotropic adaptation method for solving the level set advection equation.* International Journal for Numerical Methods in Fluids, vol. 70, no. 7, pages 899–922, 2012.

[Céa 1986] Jean Céa. *Conception optimale ou identification de formes, calcul rapide de la dérivée directionnelle de la fonction coût.* ESAIM: Mathematical Modelling and Numerical Analysis, vol. 20, no. 3, pages 371–402, 1986.

[Céa 2000] Jean Céa, Stéphane Garreau, Philippe Guillaume and Mohamed Masmoudi. *The shape and topological optimizations connection.* Computer methods in applied mechanics and engineering, vol. 188, no. 4, pages 713–726, 2000.

[Chambolle 2003] Antonin Chambolle. *A density result in two-dimensional linearized elasticity, and applications.* Archive for rational mechanics and analysis, vol. 167, no. 3, pages 211–233, 2003.

[Chen 2001] Bing-Chung Chen and Noboru Kikuchi. *Topology optimization with design-dependent loads.* Finite Elements in Analysis and Design, vol. 37, no. 1, pages 57–70, 2001.

[Chen 2007] Yong Chen. *3D Texture Mapping for Rapid Manufacturing.* Comput. Aided Des. Appl., vol. 4, no. 6, pages 761–771, 2007.

[Cramer 2016a] Andrew D Cramer, Vivien J Challis and Anthony P Roberts. *Microstructure interpolation for macroscopic design.* Structural and Multidisciplinary Optimization, vol. 53, no. 3, pages 489–500, 2016.

[Cramer 2016b] Andrew D Cramer, Vivien J Challis and Anthony P Roberts. *Physically Realisable 3D Bone Prosthesis Design with Interpolated Microstructures.* Journal of Biomechanical Engineering, 2016.

[Dapogny 2012] Charles Dapogny and Pascal Frey. *Computation of the signed distance function to a discrete contour on adapted triangulation.* Calcolo, vol. 49, no. 3, pages 193–219, 2012.

[Dapogny 2017] Charles Dapogny, Rafael Estevez, Alexis Faure and Georgios Michailidis. *Shape and topology optimization considering anisotropic features induced by additive manufacturing processes.* 2017.

[Daynes 2017] Stephen Daynes, Stefanie Feih, Wen Feng Lu and Jun Wei. *Optimisation of functionally graded lattice structures using isostatic lines.* Materials & Design, vol. 127, pages 215–223, 2017.

[Do Carmo 2012] M P Do Carmo. Differential forms and applications. Springer Science & Business Media, 2012.

[Dolean 2015] Victorita Dolean, Pierre Jolivet and Frédéric Nataf. An introduction to domain decomposition methods: algorithms, theory, and parallel implementation, volume 144. SIAM, 2015.

[Du 2018] Zongliang Du and Hyunsun A. Kim. *Multiscale Design Considering Microstructure Connectivity.* In 2018 AIAA/ASCE/AHS/ASC Structures, Structural Dynamics, and Materials Conference, 2018.

[El Majd 2008] Badr Abou El Majd, Jean-Antoine Désidéri and Régis Duvigneau. *Multilevel strategies for parametric shape optimization in aerodynamics.* European Journal of Computational Mechanics/Revue Européenne de Mécanique Numérique, vol. 17, no. 1-2, pages 149–168, 2008.

[Eschenauer 2001] Hans A Eschenauer and Niels Olhoff. *Topology Optimization of Continuum Structures: A Review.* Applied Mechanics Reviews, vol. 54, no. 4, page 331, 2001.

[Feppon 2017] Florian Feppon, G Michailidis, MA Sidebottom, Grégoire Allaire, BA Krick and N Vermaak. *Introducing a level-set based shape and topology optimization method for the wear of composite materials with geometric constraints.* Structural and Multidisciplinary Optimization, vol. 55, no. 2, pages 547–568, 2017.

[Francfort 1986] Gilles A Francfort and François Murat. *Homogenization and optimal bounds in linear elasticity.* Archive for Rational mechanics and Analysis, vol. 94, no. 4, pages 307–334, 1986.

[Fuchs 2005] MB Fuchs, S Jiny and N Peleg. *The SRV constraint for 0/1 topological design.* Structural and Multidisciplinary optimization, vol. 30, no. 4, pages 320–326, 2005.

[Geihe 2013] Benedict Geihe, Martin Lenz, Martin Rumpf and Rüdiger Schultz. *Risk averse elastic shape optimization with parametrized fine scale geometry.* Mathematical Programming, vol. 141, no. 1-2, page 383, 2013.

[Gibson 1999] Lorna J Gibson and Michael F Ashby. Cellular solids: structure and properties. Cambridge university press, 1999.

[Gorguluarslan 2017] Recep M Gorguluarslan, Umesh N Gandhi, Yu Yang Song and Seung-Kyum Choi. *An improved lattice structure design optimization framework considering additive manufacturing constraints.* Rapid Prototyping Journal, vol. 23, no. 2, 2017.

[Gray 1918] Henry Gray. *Anatomy of the human body. Philadelphia: Lea & Febiger, Bartleby. com, 2000*, 1918.

[Groen 2017] Jeroen Peter Groen and Ole Sigmund. *Homogenization-based topology optimization for high-resolution manufacturable micro-structures.* International Journal for Numerical Methods in Engineering, 2017.

[Guest 2006] James K Guest and Jean H Prévost. *Optimizing multifunctional materials: design of microstructures for maximized stiffness and fluid permeability.* International Journal of Solids and Structures, vol. 43, no. 22-23, pages 7028–7047, 2006.

[Hashin 1963] Zvi Hashin and Shmuel Shtrikman. *A variational approach to the theory of the elastic behaviour of multiphase materials.* Journal of the Mechanics and Physics of Solids, vol. 11, no. 2, pages 127–140, 1963.

[Haslinger 1995] Jaroslav Haslinger and Jan Dvořák. *Optimum composite material design.* ESAIM: Mathematical Modelling and Numerical Analysis, vol. 29, no. 6, pages 657–686, 1995.

[Hecht 2012] Frédéric Hecht. *New development in FreeFem++.* Journal of numerical mathematics, vol. 20, no. 3-4, pages 251–266, 2012.

[Henrot 2006] Antoine Henrot and Michel Pierre. Variation et optimisation de formes: une analyse géométrique, volume 48. Springer Science & Business Media, 2006.

[Hyun 2002] Sangil Hyun and Salvatore Torquato. *Optimal and manufacturable two-dimensional, Kagome-like cellular solids.* Journal of Materials Research, vol. 17, no. 1, pages 137–144, 2002.

[Jones 1975] Robert M Jones. Mechanics of composite materials, volume 193. Scripta Book Company Washington, DC, 1975.

[Joshi 2009] Dhananjay S Joshi, Xijia Zhu and Kanwerdip Singh. *Parametric shape optimization.* SAE International Journal of Materials and Manufacturing, vol. 1, no. 1, pages 763–767, 2009.

[Kawohl 2007] Bernhard Kawohl, Olivier Pironneau, Luc Tartar and J-P Zolesio. Optimal shape design: Lectures given at the joint cim/cime summer school held in troia (portugal), june 1-6, 1998. Springer, 2007.

[Khanoki 2012] Sajad Arabnejad Khanoki and Damiano Pasini. *Multiscale design and multiobjective optimization of orthopedic hip implants with functionally graded cellular material.* Journal of biomechanical engineering, vol. 134, no. 3, page 031004, 2012.

[Kim 2000] Yoon Young Kim and Gil Ho Yoon. *Multi-resolution multi-scale topology optimization—a new paradigm.* International Journal of Solids and Structures, vol. 37, no. 39, pages 5529–5559, 2000.

[Kočvara 2007] Michal Kočvara and Michael Stingl. *Free Material Optimization for Stress Constraints.* Struct. Multidiscip. Opt., vol. 33, no. 4, pages 323–335, 2007.

[Kohn 1986] Robert V. Kohn and Gilbert Strang. *Optimal design and relaxation of variational problems. I.* Comm. Pure Appl. Math., vol. 39, no. 1, pages 113–137, 1986.

[Lagae 2010] Ares Lagae, Sylvain Lefebvre, Rob Cook, Tony DeRose, George Drettakis, David S Ebert, JP Lewis, Ken Perlin and Matthias Zwicker. *A survey of procedural noise functions.* Computer Graphics Forum, vol. 29, no. 8, pages 2579–2600, 2010.

[Li 2006] Ke Li, X-L Gao and Ghatu Subhash. *Effects of cell shape and strut cross-sectional area variations on the elastic properties of three-dimensional open-cell foams.* Journal of the Mechanics and Physics of Solids, vol. 54, no. 4, pages 783–806, 2006.

[Li 2015] Dawei Li, Ning Dai, Xiaotong Jiang and Xiaosheng Chen. *Interior Structural Optimization Based on the Density-Variable Shape Modeling of 3D Printed Objects.* The International Journal of Advanced Manufacturing Technology, vol. 83, no. 9-12, 2015.

[Lin 2004] Cheng Yu Lin, Noboru Kikuchi and Scott J Hollister. *A novel method for biomaterial scaffold internal architecture design to match bone elastic properties with desired porosity.* Journal of biomechanics, vol. 37, no. 5, pages 623–636, 2004.

[Lipton 2002] Robert Lipton. *Design of functionally graded composite structures in the presence of stress constraints.* International journal of solids and structures, vol. 39, no. 9, pages 2575–2586, 2002.

[Liu 2008] Ling Liu, Jun Yan and Gengdong Cheng. *Optimum structure with homogeneous optimum truss-like material.* Computers & Structures, vol. 86, no. 13-14, pages 1417–1425, 2008.

[Luo 2007] Lingai Luo, Yilin Fan and Daniel Tondeur. *Heat exchanger: from micro-to multi-scale design optimization.* International journal of energy research, vol. 31, no. 13, pages 1266–1274, 2007.

[Lurie 1982] K. A. Lurie, A. V. Cherkaev and A. V. Fedorov. *Regularization of optimal design problems for bars and plates. I, II.* J. Optim. Theory Appl., vol. 37, no. 4, pages 499–522, 523–543, 1982.

[Martínez 2016] Jonàs Martínez, Jérémie Dumas and Sylvain Lefebvre. *Procedural Voronoi Foams for Additive Manufacturing.* ACM Transactions on Graphics, vol. 35, no. 4, pages 44:1–44:12, 2016.

[Martínez 2017a] Jonàs Martínez, Haichuan Song, Jérémie Dumas and Sylvain Lefebvre. *Orthotropic k-nearest foams for additive manufacturing.* ACM Transactions on Graphics, vol. 36, no. 4, pages 121:1–121:12, 2017.

[Martínez 2017b] Jonàs Martínez, Haichuan Song, Jérémie Dumas and Sylvain Lefebvre. *Orthotropic k-nearest foams for additive manufacturing.* ACM Transactions on Graphics (TOG), vol. 36, no. 4, page 121, 2017.

[Michailidis 2014] Georgios Michailidis. *Manufacturing constraints and multi-phase shape and topology optimization via a level-set method.* PhD thesis, Ecole Polytechnique X, 2014.

[Milton 2002] Graeme W Milton. The theory of composites. Cambridge University Press, May 2002.

[Moller 2003] Jesper Moller and Rasmus Plenge Waagepetersen. Statistical inference and simulation for spatial point processes. CRC Press, 2003.

[Moller 2012] Jesper Moller. Lectures on random voronoi tessellations, volume 87. Springer Science & Business Media, 2012.

[Murat 1985] F. Murat and L. Tartar. *Calcul des variations et homogénéisation*. In Homogenization methods: theory and applications in physics (Bréau-sans-Nappe, 1983), volume 57 of *Collect. Dir. Études Rech. Élec. France*, pages 319–369. Eyrolles, Paris, 1985.

[Murat 1997] François Murat and Luc Tartar. *H-convergence*. In Topics in the mathematical modelling of composite materials, pages 21–43. Springer, 1997.

[Neuber 1961] Heinz Neuber. Theory of notch stresses: principles for exact calculation of strength with reference to structural form and material, volume 4547. USAEC Office of Technical Information, 1961.

[Norris 2005] Andrew N Norris. *Optimal orientation of anisotropic solids*. The Quarterly Journal of Mechanics and Applied Mathematics, vol. 59, no. 1, pages 29–53, 2005.

[Novotny 2012] Antonio André Novotny and Jan Sokolowski. Topological derivatives in shape optimization. Springer Science & Business Media, 2012.

[Osher 1988] Stanley Osher and James A Sethian. *Fronts propagating with curvature-dependent speed: algorithms based on Hamilton-Jacobi formulations*. Journal of computational physics, vol. 79, no. 1, pages 12–49, 1988.

[Osher 2001] Stanley J Osher and Fadil Santosa. *Level set methods for optimization problems involving geometry and constraints*. Journal of Computational Physics, vol. 171, no. 1, pages 272–288, 2001.

[Osher 2006] Stanley Osher and Ronald Fedkiw. Level set methods and dynamic implicit surfaces, volume 153. Springer Science & Business Media, 2006.

[Panetta 2015] Julian Panetta, Qingnan Zhou, Luigi Malomo, Nico Pietroni, Paolo Cignoni and Denis Zorin. *Elastic Textures for Additive Fabrication*. ACM Trans. Graph., vol. 34, no. 4, pages 135:1–135:12, 2015.

[Pantz 2008] Olivier Pantz and Karim Trabelsi. *A post-treatment of the homogenization method for shape optimization*. SIAM Journal on Control and Optimization, vol. 47, no. 3, pages 1380–1398, 2008.

[Pantz 2010] Olivier Pantz and Karim Trabelsi. *Construction of minimization sequences for shape optimization*. In Methods and Models in Automation and Robotics (MMAR), 2010 15th International Conference on, pages 278–283. IEEE, 2010.

[Pedersen 1989] Pauli Pedersen. *On optimal orientation of orthotropic materials.* Structural Optimization, vol. 1, no. 2, pages 101–106, 1989.

[Radman 2013] A. Radman, X. Huang and Y. M. Xie. *Topology Optimization of Functionally Graded Cellular Materials.* Journal of Materials Science, vol. 48, no. 4, pages 1503–1510, 2013.

[Rešetnjak 1967] Ju. G. Rešetnjak. *Liouville's conformal mapping theorem under minimal regularity hypotheses.* Sibirsk. Mat. Ž., vol. 8, pages 835–840, 1967.

[Robbins 2016] J. Robbins, S.J. Owen, B.W. Clark and T.E. Voth. *An Efficient and Scalable Approach for Generating Topologically Optimized Cellular Structures for Additive Manufacturing.* Additive Manufacturing, 2016.

[Roberts 2002] AP Roberts and Edward J Garboczi. *Elastic properties of model random three-dimensional open-cell solids.* Journal of the Mechanics and Physics of Solids, vol. 50, no. 1, pages 33–55, 2002.

[Rodrigues 2002] H Rodrigues, Jose M Guedes and MP Bendsoe. *Hierarchical optimization of material and structure.* Structural and Multidisciplinary Optimization, vol. 24, no. 1, pages 1–10, 2002.

[Rosen 2007] David W. Rosen. *Computer-Aided Design for Additive Manufacturing of Cellular Structures.* Computer-Aided Design and Applications, vol. 4, no. 5, pages 585–594, 2007.

[Rozvany 2001] G. I. N. Rozvany. *Aims, Scope, Methods, History and Unified Terminology of Computer-Aided Topology Optimization in Structural Mechanics.* Struct. Multidiscip. Opt., vol. 21, no. 2, pages 90–108, 2001.

[Rozvany 2009] George IN Rozvany. *A critical review of established methods of structural topology optimization.* Structural and multidisciplinary optimization, vol. 37, no. 3, pages 217–237, 2009.

[Sandier 2008] Etienne Sandier and Sylvia Serfaty. Vortices in the magnetic ginzburg-landau model, volume 70. Springer Science & Business Media, 2008.

[Savvas 2016] Dimitrios Savvas, George Stefanou and Manolis Papadrakakis. *Determination of RVE size for random composites with local volume fraction variation.* Computer Methods in Applied Mechanics and Engineering, vol. 305, pages 340 – 358, 2016.

[Schramm 1993] Uwe Schramm and Walter D Pilkey. *The coupling of geometric descriptions and finite elements using NURBs—A study in shape optimization.* Finite elements in analysis and design, vol. 15, no. 1, pages 11–34, 1993.

[Schumacher 2015] Christian Schumacher, Bernd Bickel, Jan Rys, Steve Marschner, Chiara Daraio and Markus Gross. *Microstructures to control elasticity in 3D printing.* ACM Transactions on Graphics (TOG), vol. 34, no. 4, page 136, 2015.

[Sethian 1999] James Albert Sethian. Level set methods and fast marching methods: evolving interfaces in computational geometry, fluid mechanics, computer vision, and materials science, volume 3. Cambridge university press, 1999.

[Sethian 2000] James A Sethian and Andreas Wiegmann. *Structural boundary design via level set and immersed interface methods.* Journal of computational physics, vol. 163, no. 2, pages 489–528, 2000.

[Sigmund 1994a] Ole Sigmund. *Design of material structures using topology optimization.* PhD thesis, Technical University of Denmark Denmark, 1994.

[Sigmund 1994b] Ole Sigmund. *Materials with prescribed constitutive parameters: an inverse homogenization problem.* International Journal of Solids and Structures, vol. 31, no. 17, pages 2313–2329, 1994.

[Sigmund 1995] O. Sigmund. *Tailoring materials with prescribed elastic properties.* Mech. Mater., vol. 20, no. 4, pages 351–368, 1995.

[Sigmund 1998] Ole Sigmund and Joakim Petersson. *Numerical instabilities in topology optimization: a survey on procedures dealing with checkerboards, mesh-dependencies and local minima.* Structural optimization, vol. 16, no. 1, pages 68–75, 1998.

[Sigmund 1999] O Sigmund and S Torquato. *Design of Smart Composite Materials Using Topology Optimization.* Smart Materials and Structures, vol. 8, no. 3, page 365, 1999.

[Sigmund 2007] Ole Sigmund. *Morphology-based black and white filters for topology optimization.* Structural and Multidisciplinary Optimization, vol. 33, no. 4-5, pages 401–424, 2007.

[Sokolov 2016] Dmitry Sokolov, Nicolas Ray, Lionel Untereiner and Bruno Lévy. *Hexahedral-Dominant Meshing.* ACM Transactions on Graphics, vol. 35, no. 5, 2016.

[Sokolowski 2001] Jan Sokolowski and Antoni Żochowski. *Topological derivative in shape optimization.* In Encyclopedia of Optimization, pages 2625–2626. Springer, 2001.

[Staten 2007] Matthew L. Staten. Why is hex meshing so hard? Presentation at Sandia National Laboratories (URL), 2007.

[Suzuki 1991] Katsuyuki Suzuki and Noboru Kikuchi. *A homogenization method for shape and topology optimization.* Computer methods in applied mechanics and engineering, vol. 93, no. 3, pages 291–318, 1991.

[Šverák 1993] Vladimir Šverák. *On optimal shape design.* Journal de mathématiques pures et appliquées, vol. 72, no. 6, pages 537–551, 1993.

[Tartar 1978] L Tartar. *Cours Peccot au College de France, mar (1977), partially written in: F.* Murat, H-Convergence, Séminaire d'Analyse Fonctionelle et Numérique de l'Université d'Alger, duplicated, page 34, 1978.

[Tartar 1979] Luc Tartar. *Compensated compactness and applications to partial differential equations.* In Nonlinear analysis and mechanics: Heriot-Watt symposium, volume 4, pages 136–212, 1979.

[Tartar 1985] L Tartar. *Estimations fines de coefficients homogeneises.* In Ennio De Giorgi's Colloquium. Pitman Research Notes in Math., London, 1985.

[Vidimče 2013] Kiril Vidimče, Szu-Po Wang, Jonathan Ragan-Kelley and Wojciech Matusik. *OpenFab: A Programmable Pipeline for Multi-Material Fabrication.* ACM Trans. Graph., vol. 32, no. 4, page 1, 2013.

[Vidimče 2016] Kiril Vidimče, Alexandre Kaspar, Ye Wang and Wojciech Matusik. *Foundry: Hierarchical Material Design for Multi-Material Fabrication.* In Proc. of the 29th Annual Symposium on User Interface Software and Technology–UIST'16, 2016.

[Viertel 2017] Ryan Viertel and Braxton Osting. *An approach to quad meshing based on harmonic cross-valued maps and the Ginzburg-Landau theory.* arXiv preprint arXiv:1708.02316, 2017.

[Vigdergauz 1999] S Vigdergauz. *Energy-minimizing inclusions in a planar elastic structure with macroisotropy.* Structural optimization, vol. 17, no. 2-3, pages 104–112, 1999.

[Wall 2008] Wolfgang A Wall, Moritz A Frenzel and Christian Cyron. *Isogeometric structural shape optimization.* Computer methods in applied mechanics and engineering, vol. 197, no. 33-40, pages 2976–2988, 2008.

[Wang 2003] Michael Yu Wang, Xiaoming Wang and Dongming Guo. *A level set method for structural topology optimization.* Computer methods in applied mechanics and engineering, vol. 192, no. 1-2, pages 227–246, 2003.

[Wang 2005] Hongqing Wang, Yong Chen and David W. Rosen. *A Hybrid Geometric Modeling Method for Large Scale Conformal Cellular Structures.* In Volume 3: 25th Computers and Information in Engineering Conference, Parts A and B, 2005.

[Wang 2013] Weiming Wang, Tuanfeng Y Wang, Zhouwang Yang, Ligang Liu, Xin Tong, Weihua Tong, Jiansong Deng, Falai Chen and Xiuping Liu. *Cost-effective printing of 3D objects with skin-frame structures.* ACM Transactions on Graphics (TOG), vol. 32, no. 6, page 177, 2013.

[Wang 2017] Yiqiang Wang, Feifei Chen and Michael Yu Wang. *Concurrent design with connectable graded microstructures.* Computer Methods in Applied Mechanics and Engineering, vol. 317, pages 84–101, 2017.

[Wang 2018a] Chuang Wang, Ji Hong Zhu, Wei Hong Zhang, Shao Ying Li and Jie Kong. *Concurrent topology optimization design of structures and non-uniform parameterized lattice microstructures.* Structural and Multidisciplinary Optimization, vol. 58, no. 1, pages 35–50, Jul 2018.

[Wang 2018b] Yiqiang Wang, Lei Zhang, Stephen Daynes, Hongying Zhang, Stefanie Feih and Michael Yu Wang. *Design of graded lattice structure with optimized mesostructures for additive manufacturing.* Materials & Design, vol. 142, pages 114 – 123, 2018.

[Weintraub 1997] Steven H Weintraub. Differential forms: a complement to vector calculus. Academic Press, 1997.

[Wu 2018] Jun Wu, Niels Aage, Rüdiger Westermann and Ole Sigmund. *Infill optimization for additive manufacturing—approaching bone-like porous structures.* IEEE transactions on visualization and computer graphics, vol. 24, no. 2, pages 1127–1140, 2018.

[Xia 2008] Qi Xia and Michael Yu Wang. *Simultaneous optimization of the material properties and the topology of functionally graded structures.* Computer-Aided Design, vol. 40, no. 6, pages 660–675, 2008.

[Xia 2015] Liang Xia and Piotr Breitkopf. *Design of Materials Using Topology Optimization and Energy-Based Homogenization Approach in Matlab.* Struct. Multidiscip. Opt., vol. 52, no. 6, 2015.

[Xie 2012] Yi Min Xie, Zhi Hao Zuo, Xiaodong Huang and Jian Hua Rong. *Convergence of topological patterns of optimal periodic structures under multiple scales.* Structural and Multidisciplinary Optimization, vol. 46, no. 1, pages 41–50, 2012.

[Xu 2009] X. Frank Xu and Xi Chen. *Stochastic homogenization of random elastic multi-phase composites and size quantification of representative volume element.* Mechanics of Materials, vol. 41, no. 2, pages 174 – 186, 2009.

[Yan 2014] X Yan, X Huang, Y Zha and YM Xie. *Concurrent topology optimization of structures and their composite microstructures.* Computers & Structures, vol. 133, pages 103–110, 2014.

[Zhang 2015] Pu Zhang, Jakub Toman, Yiqi Yu, Emre Biyikli, Mesut Kirca, Markus Chmielus and Albert C To. *Efficient design-optimization of variable-density hexagonal cellular structure by additive manufacturing: theory and validation.* Journal of Manufacturing Science and Engineering, vol. 137, no. 2, page 021004, 2015.

[Zhou 1991] M. Zhou and G.I.N. Rozvany. *The COC algorithm, Part II: Topological, geometrical and generalized shape optimization.* Computer Methods in Applied Mechanics and Engineering, vol. 89, no. 1–3, pages 309 – 336, 1991. Second World Congress on Computational Mechanics.

[Zhou 2008] Shiwei Zhou and Qing Li. *Design of graded two-phase microstructures for tailored elasticity gradients.* Journal of Materials Science, vol. 43, no. 15, page 5157, 2008.

[Zhu 2017] Bo Zhu, Mélina Skouras, Desai Chen and Wojciech Matusik. *Two-Scale Topology Optimization with Microstructures.* ACM Trans. Graph., vol. 36, no. 5, pages 164:1–164:16, July 2017.

[Zuo 2013] Zhi Hao Zuo, Xiaodong Huang, Jian Hua Rong and Yi Min Xie. *Multi-scale design of composite materials and structures for maximum natural frequencies.* Materials & Design, vol. 51, pages 1023–1034, 2013.

université PARIS-SACLAY | École doctorale de mathématiques Hadamard (EDMH)

Titre : Méthode d'homogénéisation pour l'optimisation topologique de structures composées de matériau lattice

Mots Clefs : optimisation topologique, méthode d'homogénéisation, matériau lattice, matériau cellulaire, fabrication additive

Résumé : Les développements récents des méthodes de fabrication additive permettent aujourd'hui d'envisager l'usinage de pièces à la topologie complexe, composées de microstructures. Ceci ranime l'intérêt pour les méthodes d'optimisation topologique par méthode d'homogénéisation, développées dans les années 80 et quelque peu oubliées par manque d'applications industrielles. L'objectif de cette thèse est de fournir des méthodes d'optimisation topologique pour des structures constituées de matériau lattice localement périodique, c'est-à-dire dont la microstructure est modulée au sein de la pièce. Trois phases ont été définies. La première consiste à calculer les propriétés élastiques homogénéisées de microstructures en fonction de paramètres définissant leur géométrie. Dans la seconde étape, on optimise la structure constituée de matériau homogénéisé selon les paramètres géométriques de la microstructure ainsi que son orientation. Une structure homogénéisée n'est pas usinable en l'état. En effet, l'homogénéisation revient à considérer que la taille des cellules la composant converge vers zéro. Dans une troisième étape, on propose donc de déshomogénéiser la structure optimisée, c'est-à-dire de construire une suite de structures convergeant vers elle. Pour cela, on introduit un difféomorphisme déformant une grille régulière de sorte que chaque cellule soit orientée selon l'orientation optimale. Nous présentons dans cette thèse les détails de cette méthode, pour des microstructures élastiques isotropes et orthotropes, en deux et en trois dimensions. Nous proposons également un couplage de cette méthode avec la méthode d'optimisation de forme par les lignes de niveau, ce qui permet notamment d'inclure des contraintes géométriques sur les structures finales.

Title : Homogenization method for topology optimization of structures built with lattice materials

Keys words : topology optimization, homogenization method, lattice material, cellular material, additive manufacturing

Abstract : Thanks to the recent developments of the additive manufacturing processes, structures built with modulated microstructures and featuring a complex topology are now manufacturable. This leads to a resurrection of the homogenization method for shape optimization, an approach developed in the 80's but which progressively faded away because yielding too complex structures for manufacturing processes at this time.
The goal of this thesis is to develop shape optimization methods for structures built with modulated locally periodic lattice microstructures.
Three steps have been defined. The first consists in computing the homogenized, or effective, elastic properties of microstructures according to few parameters characterizing their geometry. In the second step, the geometric properties of the microstructure and its orientation are optimized in the working domain, yielding a homogenized optimized structure. Such a structure is nevertheless not straightforwardly manufacturable. Indeed, the homogenization is equivalent to have a structure featuring cells whose size is converging to zero. Hence, in the third and last step, a deshomogenization process is proposed. It consists in building a sequence of genuine structures converging to the homogenized optimal structures. The key point is to respect locally the orientation of the cells, which is performed thanks to a grid diffeomorphism.
In this thesis, we present the details of the whole method, for isotropic and orthotropic microstructures, in 2D and in 3D. A coupling of this method with the level-set shape optimization method is also presented, thanks which the set of geometric constraints on the final structures may be enlarged.